Xiaoyan Lei

High Speed Railway Track Dynamics

Models, Algorithms and Applications

Science Press
Beijing

Springer

High Speed Railway Track Dynamics

Xiaoyan Lei

High Speed Railway Track Dynamics

Models, Algorithms and Applications

Science Press
Beijing

Springer

Xiaoyan Lei
Railway Environmental Vibration and Noise
Engineering Research Center of the
Ministry of Education
East China Jiaotong University
Nanchang
China

ISBN 978-981-10-2037-7 ISBN 978-981-10-2039-1 (eBook)
DOI 10.1007/978-981-10-2039-1

The print edition is not for sale in China Mainland. Customers from China Mainland please order the print book from: Science Press

Library of Congress Control Number: 2016946622

Printed on acid-free paper

This Springer imprint is published by Springer Nature
The registered company is Science Press, Beijing and Springer Nature Singapore Pte Ltd
The registered company address is: 152 Beach Road, #22-06/08 Gateway East, Singapore 189721, Singapore

Foreword

In recent years, the construction and operation of Chinese high-speed railways has scored remarkable achievements, making great contribution to the sound and fast development of national economy. It has been widely acclaimed by the whole society and become another example of the world high-speed railway development. By the end of 2015, China had over 17,000 km newly built high-speed railway lines in operation, ranking the first in the world. In field of high-speed railway system, China is credited with the most comprehensive technologies, the strongest integration capability, the fastest running speed, the longest operation mileage, and the largest scale construction in the world.

The high-speed railway construction started late in China, so it has not accumulated sufficient theoretical and practical experience. Undoubtedly, it has been faced with a series of technical problems and challenges during the process of high-speed railway construction and operation, which requires the strong academic and technical support. The high-speed railway track structure consists of the rail, the rail pads and fastenings, the track slab, the cement asphalt mortar filling layer, the concrete basement, the subgrade, and the ground (or bridge). But there are great differences in the material properties and the structures, many technological difficulties, and complicated service environments. Besides, the train speed is over 200–300km/h. All these issues are closely related to the wheel-rail dynamics. Thus, high-speed railway track dynamics is the key basic discipline to ensure the safe operation of trains. When the train speed increases, the interactions between the locomotive, rolling stock, and track structure significantly increase. The environment of dynamic system becomes deteriorated, and the safety and stability of high-speed train and the reliability of track structure are thus faced with severe tests. When the train is running at high-speed, the influence of the plane and profile conditions of lines and track irregularities on passengers' comfort and the influence of the running train on the surrounding environment will be magnified, and the consequences of train accidents will become more hazardous. All of these must be explored based on high-speed railway track dynamics. Therefore, the in-depth study of high-speed trains and track interaction mechanism will provide the necessary

theoretical guidance for the design of the high-speed rail system and the operation of high-speed trains.

The book, entitled *High-Speed Railway Track Dynamics*, is a summary of the theoretical and practical research findings on high-speed railway track dynamics made by the author and his research team. It systematically introduces the latest research findings of the author and his research team, focusing on the high-speed railway track dynamics theories, models, algorithms, and engineering applications. The book is mainly featured by the frontier research contents, complete theoretical system, correct and effective model and algorithms, and rich engineering applications. What are particularly worth mentioning in the book are the author's researches in aspects of track element and vehicle element model and algorithm, moving element method for dynamic analysis of the vehicle and track coupling system, cross-iteration algorithm for dynamic analysis of the vehicle and track coupling system, dynamic behavior analysis for the track transition between ballast track and ballastless track, and environmental vibration analysis induced by overlapping subways, which are of great innovation and application value. The series of research findings have been published in the related famous international academic journals, such as *Journal of Vibration and Control*, *Journal of Transportation Engineering*, *Journal of Rail and Rapid Transit*, and *Journal of Sound and Vibration*, which are widely recognized and cited by the fellow scholars at home and abroad.

I strongly believe that the publication of this book will provide an important theoretical guidance for Chinese high-speed railway track design, construction, and operation, making great contributions to promoting the scientific development of railway engineering discipline and the railway technological progress and realizing the sustainable development of Chinese high-speed railways.

January 2016

Mengshu Wang
Academician of Chinese Academy of Engineering

Preface

Since the world's first high-speed railway has been constructed and put into operation, the high-speed railway is highly competitive compared to other means of transportation for its distinct advantages in speed, convenience, safety, comfort, environment-friendly design, large capacity, low energy consumption, all-weather transportation, etc. According to the statistics from the International Union of railways (UIC), up to November 1, 2013, the total operation mileage of the high-speed railways of other countries and regions in the world is 11605 km. 4883-km high-speed railways are under construction, and 12570-km high-speed railways are planned to be constructed. The total operation mileage of high-speed railways in China are 11028 km, and 12000-km lines are under construction. The total operation mileage of Chinese high-speed railways accounts for half of that of the world's high-speed railways. China has become a country with the longest operation mileage and the largest scale construction in the world in high-speed railway. Meanwhile, 18 cities in China (including Hong Kong) possess urban rail transit with a total mileage of 2100 km, and 2700-km lines are under construction, ranking the first in the world. The high-speed railways and rail transit system have become the important engines to drive the socioeconomic development. The independent innovation of high-speed railway technology has become the major national strategic demand.

However, with the rising running speed of trains, the increased transportation density, and the increased transportation loads, the interaction between train and track has become intensified. To adapt to this change in railway development, the countries all over the world have strengthened the railway technological innovation and widely adopted new technologies, designs, materials, processes, and modern management methods in railway engineering. Hence, the concept of modern railway track has emerged. Modern railway track is developed with the advent of high-speed railway and heavy-haul railway, which must meet the fast and high-speed demand of passenger transport and the fast and heavy-haul demand of freight transport. Compared with the conventional railway track, the modern track has the following characteristics: ① high-standard subgrade; ② new subrail

foundation; ③ heavy and super-long continuous welded rail; ④ the scientific management of track maintenance; and ⑤ the organization of safe operations and coordination of railway and environment. Obviously, the traditional track mechanics and structural analysis methods cannot satisfy the needs of modern railway track analysis and design. Owing to the rapid development of computers and numerical methods in recent decades, new theories and methods are applied to the track mechanics and track engineering, making it possible to solve many problems which seemed impossibly hard to solve in the past and those complex problems emerging in the process of railway modernization.

This book is a systematic summary of the related theoretical and applied research findings on high-speed railway track dynamics made by the author and his research team over a decade. In the past decades, sponsored by many projects, such as the Natural Science Foundation of China (50268001, 50568002, 50978099, U1134107, 51478184), International Cooperation and Exchange Project (2010DFA82340), Natural Science Foundation of Jiangxi Province (0250034, 0450012), Sino-Austria, Sino-Japan, Sino-Britain, and Sino-America Scientific Cooperation Projects, "Sponsor Program for Key Teachers of Colleges and Universities" of the Ministry of Education (GG-823-10404-1001), Science and Technology Development Plan of China Railway Bureau (98G33A), Outstanding Science & Technology Innovation Team of Jiangxi Province (20133BCB24007), and the Training Program of the Leading Personnel of Key Disciplines and Technologies of Jiangxi Province (020001), the author and his research team have conducted the in-depth and systematic researches on high-speed railway track dynamics, environmental vibration and noise induced by railway traffic, and engineering applications of track dynamics and have achieved fruitful research findings, most of which belong to the frontier issues of the track dynamics theory. Participants in the research team are as follows: Xiaoyan Lei, Liu Linya, Feng Qingsong, Zhang Pengfei, Liu Qingjie, Luo Kun, Luo Wenjun, Fang Jian, Zhang Bin, Xu Bin, Wang Jian, Tu Qinming, Zeng Qine, Lai Jianfei, Wu Shenhua, Sun Maotang, and Xiong Chaohua.

The draft of this book has been used as the textbook for postgraduate students majoring in road and railway engineering in East China Jiaotong University for several years. The book falls into 15 Chapters: 1. Track Dynamics Research Contents and Related Standards; 2. Analytic Method for Dynamic Analysis of the Track Structure; 3. Fourier Transform Method for Dynamic Analysis of the Track Structure; 4. Analysis of Vibration Behavior of the Elevated Track Structure; 5. Track Irregularity Power Spectrum and Numerical Simulation; 6. Model for Vertical Dynamic Analysis of the Vehicle-Track Coupling System; 7. A Cross-Iteration Algorithm for Vehicle-Track Coupling Vibration Analysis; 8. Moving Element Model and Its Algorithm; 9. Model and Algorithm for Track Element and Vehicle Element; 10. Dynamic Analysis of the Vehicle-Track Coupling System with Finite Elements in a Moving Frame of Reference; 11. Model for Vertical Dynamic Analysis of the Vehicle-Track-Subgrade-Ground Coupling System; 12. Analysis of Dynamic Behavior of the Train-Ballast Track-Subgrade

Coupling System; 13. Analysis of Dynamic Behavior of the Train-Slab Track-Subgrade Coupling System; 14. Analysis of Dynamic Behavior of the Transition Section Between Ballast Track and Ballastless Track; and 15. Environmental Vibration Analysis Induced by Overlapping Subways.

Compared with similar studies, the contents of the five chapters, that is, the cross iteration algorithm for vehicle-track coupling vibration analysis, model and algorithm for track element and vehicle element, finite elements in a moving frame of reference for dynamic analysis of the vehicle-track coupling system, dynamic behavior analysis for the transition between ballast track and ballastless track, and environmental vibration analysis induced by overlapping subways, have distinct characteristics, which may be considered as the author's original findings.

With original concepts, systematic theories, and advanced algorithms, this book attempts at introducing to the readers the latest research findings and developments at home and abroad in high-speed railway track dynamics. It lays great emphasis on precision and completeness of its content. All the chapters are interrelated yet relatively independent, which makes it possible for the readers to browse through the book or just focus on special topics. It combines theories with practice to provide abundant information in the hope of enlightening and helping readers. Any comments and suggestions concerning the book are welcome and appreciated.

On the occasion of the publication of this book, I would like to express my sincere thanks to institutions and people that have been funding, supporting, and caring about my research work and the publication of this book! I would like to extend my special gratitude to Profs. Du Qinghua and Wang Mengshu, academicians of China Academy of Engineering, Mr. Guan Tianbao, senior engineer of Shanghai Railway Bureau, and Profs. Tong Daxun and Wang Wusheng from Tongji University, for their longtime care, guidance, and help. Particularly gratefully, academician Wang takes the trouble to write the foreword for this book. I am also deeply indebted to the translation team, Tang Bin, Lu Xiuying, Yang Zuhua, Liu Qingxue, Li Xing, and Huang Qunhui, from School of Foreign Languages in ECJTU for their translation work. Last but not least, my heartfelt thanks go to my colleagues, postgraduate students, and Mr. Wei Yingjie, editor of Science Press. The publication of this book is the result of their joint efforts.

Kongmu Lakeside Xiaoyan Lei
2016

About the Book

High-speed railway is highly competitive compared to other means of transportation for its distinct advantages in speed, convenience, safety, comfort, environment-friendly design, large capacity, low energy consumption, all-weather transportation, etc. In recent years, there has been a boom in the construction of high-speed railways throughout the world. To adapt to the fast development of the design and construction of high-speed railways, it is essential to further theoretical studies in high-speed railway track dynamics. As a systematic summary of the relevant research findings on high-speed railway track dynamics made by the author and his research team over a decade, this book explores the frontier issues concerning the basic theory of high-speed railway, covering the dynamics theories, models, algorithms, and engineering applications of the high-speed train-track coupling system.

Characterized by original concepts, systematic theories, and advanced algorithms, this book lays great emphasis on precision and completeness of its content. All chapters are interrelated yet relatively independent, which makes it possible for the readers to browse through the book or just focus on special topics. It combines theories with practice to provide abundant information in the hope of introducing to the readers the latest research findings and developments in high-speed railway track dynamics. The book can be used both as textbook or reference book for undergraduates, postgraduates, teachers, engineers, and technicians involved in civil engineering, transportation, highway, and railway engineering.

Contents

About the Author

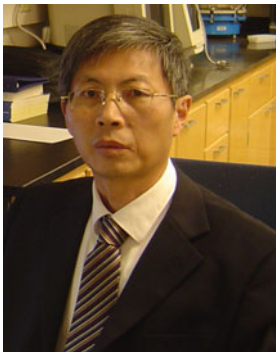

Xiaoyan Lei is a professor and doctoral supervisor of East China Jiaotong University, chair professor of Jiangxi Jingang Scholars, and director of Railway Environmental Vibration and Noise Engineering Research Center of the Ministry of Education.

He received his Ph.D. degree in solid mechanics from Tsinghua University in 1989. He served as a visiting scholar at University of Innsbruck, Austria, during 1991–1994, a visiting professor at Kyushu Institute of Technology, Japan, in 2001, and a senior research fellow at the University of Kentucky, USA, in 2007. He has been awarded many academic titles including the first- and second-rank talents of the National Talents Project, the leading personnel of key disciplines and technologies of Jiangxi Province and the leading talent of Jiangxi Ganpo Talent Candidates 555 Program. His academic positions include the senior member of American Society of Mechanical Engineers (ASME), executive director of China Communication and Transportation Association, director general of Theoretical and Applied Mechanics Society of Jiangxi Province, and deputy director general of Railway Society of Jiangxi Province. In addition, he works as the editorial member of *Journal of the China Railway Society, Journal of Railway Science and Engineering, Journal of Urban Mass Transit, Journal of Transportation Engineering and Information, International Journal of Rail Transportation, Journal of Civil Engineering Architecture, and Education Research Monthly.*

He has undertaken more than 60 scientific research projects at all levels, including National Key Basic Research Program of China, Key International Cooperation and Exchange Project, Natural Science Foundation of China, Natural Science Foundation of Jiangxi Province, Key International Bidding Project, Projects from the Ministry of Education, China Railway Corporation and Science and Technology Development Plan of Jiangxi Province, and Enterprise Commissioned Cooperation Projects. His publications cover over 200 academic

papers and 6 monographs on railway engineering. He is also the author of 6 invention patents and 18 computer software copyrights. There is a long list of his academic awards: the 2nd prize of National Science and Technology Progress Award in 2011, the 1st prize of Natural Science Award of Jiangxi Province in 2005, the 1st prize of Science and Technology Progress Award of Jiangxi Province in 2007, the 1st prize of Railway Science and Technology Award in 2011, the 2nd prize of Natural Science of the Ministry of Education, the 1st prize of Excellent Teaching Award of Jiangxi Province, and the prize of the first batch Three One Hundred Original Natural Science Books sponsored by General Administration of Press and Publication of the People's Republic of China. As a leading expert and distinguished professor, he has presided over the appraisal and evaluation of more than 10 scientific research projects.

His research interests focus mainly on high-speed railway track dynamics and environmental vibration and noise induced by railway traffic.

Chapter 1
Track Dynamics Research Contents and Related Standards

With increasing train speed, axle loads, traffic density, and the wider engineering applications of new vehicles and track structures, the interaction between vehicle and track has become more complex. Accordingly, the train running safety and stability are more affected by increased dynamic stresses. Dynamic loads acted on the tracks by vehicles fall into three categories: moving axle loads, dynamic loads of fixed points, and moving dynamic loads. Axle loads, due to their moving loading points, are dynamic loads for the track-subgrade-ground system, though irrelevant to the vehicle dynamics and constant in size. As soon as the speed of moving axle loads approaches the critical velocity of the track, the track is subjected to violent vibration. Dynamic loads of fixed points come from the impacts of vehicles passing by the fixed irregularity on track, such as rail joints, the welding slag of continuously welded rail and turnout frogs. Moving dynamic loads are induced by wheel-rail contact irregularities. The dynamics analysis of the train-track system lays a good foundation for investigating the complicated wheel-rail relationship and interaction mechanism, which provides essential references for guiding and optimizing vehicle and track structure designs.

1.1 A Review of Track Dynamics Research

Up to the present, scholars both at home and abroad have achieved a wealth of research findings about the establishment of track dynamics models and numerical methods. Studies on track dynamics models have experienced a development process from simple to complex. Historically, moving loads and vehicle structures have been the earliest practical issues in structure dynamics, especially in the train-track system. Knothe and Grassie [1–3] published several papers concerning track dynamics and vehicle-track interaction in frequency domain. Mathews [4, 5] found out solutions to the dynamic problems of any moving loads on infinite elastic foundation beam by means of Fourier transform method (FTM) and the moving

X. Lei, *High Speed Railway Track Dynamics*,
DOI 10.1007/978-981-10-2039-1_1

coordinate system. The Fourier transform method (FTM), as a method of frequency domain analysis, was applied by Trochanis [6], Ono and Yamada [7] in some related studies. Jezequel [8] simplified the track structure into infinite Euler–Bernoulli beam on elastic foundation, regarding the train loads as concentrated force of uniform motion and considering its rotation and transverse shear effects. Through modal superposition, Timoshenko [9] figured out the governing differential equation for moving loads on simply supported beams in time domain, while Warburton solved this equation by using analytical methods, and he also proved the deflection of beams would reach a maximum under moving loads at a certain speed [10]. Cai et al. [11], by modal superposition, studied the dynamic response of infinite beams over periodic bearings under moving loads.

All the above-mentioned studies have considered the track beam as the continuum and solved governing differential equations through analytical methods. Though simple, these approaches are not feasible for multi-DOF (degree of freedom) vehicle-track system, which have provided limited significance in track dynamics. In recent years, the finite element method (FEM) has been widely applied in practical engineering projects. FEM involves formulating element matrix and deriving finite element equations by discretizing the track structure into finite elements and assuming the displacement function for each element. Venancio Filho [12] reviewed how FEM had been used as a numerical method for analyzing dynamic response by moving loads on homogeneous beams. It can be seen that FEM is a popular solution to problems concerning the train-track dynamics. Olsson [13] applied the FEM to explore the effects of different vehicle models, vibration modes, and track surface irregularities and adopted the slab and column elements to simulate bridge vibration problems. Fryba [14] put forward stochastic finite element analysis method for uniform moving loads on elastic foundation beams. Thambiratnam and Zhuge established a finite element analysis model for elastic simply supported beams of any length [15, 16]. Nielsen and Igeland [17] setup a finite element model integrating bogies, rails, sleepers, and subgrades into a whole, analyzing such influence factors as the rail wear, wheel flat and sleeper dangling by applying the complex mode superposition. Zheng and Fan [18] studied stability problems of the train-track system. Koh et al. [19] put forward a new moving element method, which was formulated on a relative coordinate moving with trains, while the ordinary FEM is based on a fixed coordinate. Auersch [20] established the joint solution combining the FEM and boundary element method (BEM) to analyze the track structure model with or without ballast pads in three-dimensional space, and he discussed the parameter effects such as ballast pad stiffness, unsprung mass of the vehicle, track quality, and subgrade stiffness. Clouteau [21] proposed the efficient algorithm for subway vibration analysis based on FEM–BEM coupling method. The key point of the algorithm is to consider the track periodicity along the tunnel direction by applying the Floquet transform. Andersen and Jones compared the differences between two-dimensional and three-dimensional models by coupling the finite element–boundary element method, and they discovered that the two-dimensional model was suitable for qualitative analysis and could quickly obtain relevant results [22, 23]. Thomas [24] established a multi-body vehicle-track

model to explore effects of crosswind on snake movement of high-speed trains at the curve section, analyzing impacts of crosswind strength, and vehicle parameters on the dynamic response of trains. Ganesh Babu [25], by FEM, in light of parameter changes in subgrades, ballasts, and rail pads, analyzed track modulus of prestressed concrete sleeper and wooden sleeper track structures. Cai [26] processed the ground into porous elastic semi-infinite domain media and studied effects of wheel-rail interaction on ground environmental vibrations when the trains were passing based on Biot porous elastic dynamics theory.

Since the early 1990s, many domestic researchers have conducted theoretical and applied researches in the field of vehicle-track coupling dynamics. Zhai Wanming published his academic paper "*The Vertical Model of Vehicle-track System and Its Coupling Dynamics*" [27] in 1992 and his academic monograph *Vehicle-Track Coupling Dynamics* [28] in 1997. In 2002, he published another paper entitled "*New Advance in Vehicle-track Coupling Dynamics*," [29] summarizing the research history and progress about vehicle-track coupling dynamics both at home and abroad. Xiaoyan Lei and his research team also carried out systematic studies concerning models and numerical methods of track dynamics [30–32]. He published his academic monograph *Numerical Analysis of Railway Track Structure* in 1998, which introduced in detail the track model of a single wheel with primary suspension system, the track model of semi-vehicle and whole vehicle with primary and secondary suspension system and numerical methods for solving vibration equations of vehicle and track coupling system [33]. There are more domestic researches in this field worthy to be mentioned. Xu Zhisheng developed an analysis software for vehicle-track coupling vibration based on Timoshenko beam model by the vehicle-track coupling dynamics theory. Besides, he analyzed the vertical vibration characteristics of the vehicle-track system and compared with simulation results obtained from the software based on Euler beam model [34, 35]. His findings show that simulation results for both softwares are basically the same, but in a higher frequency domain, the difference of natural frequency between the two methods is obvious with Timoshenko beam model better reflecting the high frequency characteristics of wheel-rail system. Xie Weiping and Zhen Bin obtained analytical expressions of steady dynamic response for infinite Winkler beam under the variable moving loads by adopting the Fourier transform and Residue theory. Compared with Kenney's classical solution process, their solution has a more explicit physical meaning [36]. Luo [37] studied the relationship between the rail natural vibration frequency and temperature force by establishing the dynamic finite element model of continuous welded rail (CWR), which involved rails, fasteners, and sleepers and probed into effects of rail section properties, rail wear, rail pad, and fastener stiffness and torsional rigidity on the dynamic model calculations. Results show that the proposed model can more accurately analyze the intrinsic link between rails' longitudinal force and vibration characteristics of continuous welded rail track structures. Wei Qingchao established the horizontal and vertical vehicle-track coupling dynamics simulation model for linear motor subway systems. He calculated dynamic response of linear motor vehicles and track structures under the conditions of different track structures (tracks with embedded long

sleepers or the slab tracks), different subplate bearing stiffness, and damping and conducted a comparative analysis accordingly [38]. His findings are as follows: The car body vertical acceleration on tracks with embedded long sleepers is slightly larger than that on slab tracks while the rail lateral acceleration and vertical displacement of slab tracks are slightly larger than those of tracks with embedded long sleepers; increasing damping in the subplate is beneficial for reducing slab vibration of the track; the influence of subplate stiffness on the wheel-rail forces, rail displacement, and motor air gap is small; when subplate stiffness increases, the slab displacement decreases while the acceleration increases. In light of the turnouts, bridge structures, and layouts, Gao et al. [39] setup the welded turnout spatial coupling model and analyzed its spatial mechanical properties from the aspects of temperature loads, vertical loads, and rail lateral deformation. Feng [40] derived the flexibility matrix of ballast track-subgrade-foundation system at rail contact points by use of the Fourier transform and the transfer matrix. He built up the analytical model of vertical coupling vibration for vehicle-ballast track-subgrade-layered foundation in view of track irregularities and analyzed the vibration of embankment body-foundation system caused by single TGV high speed train. Meanwhile, he investigated effects of train speed, track irregularity, subgrade stiffness, and embankment soil stiffness on the embankment body vibration. His findings are as follows: The vertical displacement of the embankment body is caused by the moving train axle loads; with the increase in train speed, the "volatility" of embankment vibration increases significantly; subgrade stiffness and embankment soil stiffness have significant impact on embankment vibration. Bian Xuecheng and Chen Yunmin studied the coupling vibration of track and layered ground under moving loads by using dynamic substructure method which dealt with sleepers' impact of discrete support [41, 42]. Later they further investigated ground vibration problems by stratified transfer matrix method [43]. Xie [44, 45], Nie [46], Lei [47–50], He [51], and Li [52]' all adopted analytical wave number—frequency domain method to establish the single or multi-layer track structure model, thus exploring the track and ground vibrations generated by high-speed trains. Their studies are summarized as follows: The faster the train runs, the larger the vibration response of the track and ground is; when the train speeds are below, near, or above the ground surface wave velocity, the ground vibration may appear differently; when the train reaches a certain critical velocity, strong vibration of the track and ground would happen; and when the high-speed train passes on the soft soil foundation, strong vibration phenomenon may occur too. Wua Yean-Seng and Yang Yeong-Bin from Taiwan University proposed semi-analytical model to analyze the ground vibration induced by moving loads of elevated railways and obtained acting force on the pier top based on the elastic support beam model under moving axle loads. By lumped parameter model, they worked out interaction force between pier foundations and the surrounding soil, from which the vibration level of elastic half-space ground is then obtained [53]. Xia He and Cao Yanmei et al. from Beijing Jiaotong University established the train-track–ground coupling model by analytical wave number—frequency domain method. They regarded the ground-track system as Euler beam model with periodic support on three-dimensional layered ground and illustrated

the ground vibration response under the dynamic wheel-rail force generated by moving train axle loads and track irregularities [54].

Liu et al. [55] maintained that it was necessary to develop space coupling vibration model of wheel-rail system because in many cases wheel-rail vibration identified with space vibration with obvious coupling features. Li and Zeng [56] established the vehicle–tangent track space coupling vibration analysis model by way of vehicle-track coupling dynamics, which is characterized by the discretization of the track into 30-DOF spatial track elements, and the use of artificial bogie crawl waves as the excitation source. Liang [57] and Su [58] explored vibration effects of subgrade structures in detail and carried out researches about the vertical coupling dynamics of vehicle-track-subgrade. Wang [59], Luo [60, 61], and Cai Chengbiao studied relevant dynamic problems when high speed, rising speed, or fast trains run through bridge-subgrade transition sections by using the vehicle-track vertical unification model from References [27, 28], which would provide a theoretical basis for the foundation reinforcement, deformation control, and reasonable length of high-speed railway road-bridge transition sections. Wang [62] and Ren [63], respectively, explored interaction between the vehicles and the turnouts by means of the vehicle-track coupling dynamics theory and applied their findings into dynamic analysis of rising speed turnouts in China, which can offer references for improved designs of rising speed turnouts.

As the vehicle dynamic action on the track is a random process, it may be appropriate to make random vibration analysis of vehicle-track system for comprehensively understanding of the wheel-rail interaction mechanism. Random vibration of the vehicle-track coupling is generally studied under two excitation models: fixed-point excitation model and moving-point excitation model. The former one focuses on backward movement of track irregularity excitation at a certain speed by assuming that vehicles and tracks are stationary; the latter one firstly involves reversing the track irregularity sample based on power spectrum of the track irregularity, then solving for the time domain response of the system through numerical integration method, and finally deriving the power spectrum of the system response from the Fourier transform of the time domain response by assuming that trains are moving at a certain speed on the tracks. Chen [64] and Lei [65], Lei and Mao [66] worked out the random vibration response of vehicle-track coupling system by moving-point excitation model, which takes nonlinear wheel-rail contact force into consideration. But this approach requires large amounts of computation due to the step by step integration. Meanwhile, there might be some analytical errors in both the time domain samples of the track irregularities obtained from track spectrum inversion and the estimation of power spectrum based on response of the time domain analysis results. Lu et al. [67] established a vehicle-track random vibration analysis model, and proposed the pseudo-excitation method and dual algorithm, which considered the vertical and rotational vibration effect of the vehicle with 10-DOF (degrees of freedom) and simulated the track into infinite periodic Euler beam with rails, sleepers, and ballasts. It maintains that supposing the vehicle is stationary, there might exist moving random irregularity

spectrum on the track surface under the excitation of tracks, which moves at the train speed in the opposite direction.

From the above-mentioned literature review, it can be safely concluded that abundant findings have been achieved among scholars both at home and abroad in the field of track dynamics models and approaches. It should be pointed out that more related in-depth researches are under way.

1.2 Track Dynamics Research Contents

When the train moves along tracks, both of them are bound to induce vibration in all directions due to the following factors:

1. Locomotive dynamic power. It includes the cyclic force of the steam locomotive wheels' eccentric block and the vibration of diesel locomotive's power units;
2. Speed. When moving along irregular tracks at a certain speed, the locomotive and the train induce dynamic action;
3. Track irregularity. It is caused by rail surface wear, uneven foundation elasticity, failure of some sleepers, lack of rail fasteners conformance, gap between different track parts, and loose ties under the sleepers.
4. Rail joints and welding slag of continuously welded rail. When a train moves through the rail joints and welding slag, additional dynamic forces would be induced;
5. Continuous irregularity caused by eccentricity of wheel installment and impulse irregularity caused by wheel flats and uneven wheel tread wear.

The train consists of locomotive, car body, bogie, primary and secondary suspension system, and wheel sets. The train and track constitute a coupling system when the train moves along the track. The dynamic analysis of such a system chiefly covers:

1. Exploration of trains' safety along the tracks
   It is known that the train induces structural vibration when it moves along tracks. Through simulation analysis of the train and track coupling system, such parameters as dynamic stress and deflection for train and track, lateral force, derailment coefficient, and wheel load reduction rate can be derived, by which the safety of the locomotives and vehicles running on the track can be evaluated.
2. Exploration of trains' riding quality
   Riding quality of the locomotive and the passenger train is evaluated by comfortableness of engine drivers and passengers. When the train moves along tracks, the vehicle vibration frequency and acceleration and vibration amplitude should be controlled to ensure riding quality.
3. Evaluation of existing tracks, parameters selection, and optimization of locomotive, rolling stock unit, and track structures through theoretical analysis and experimental study. This may provide guidance for new track design.

With the ever increasing train speed, the growing freight train loads and the diversification of working conditions, it is of great significance to make an in-depth study of wheel-rail dynamics.

1.3 Limits for Safety and Riding Quality and Railway Environmental Standards

1.3.1 Safety Limit for Regular Trains

The evaluation parameters of train safety include derailment coefficient, lateral force, wheel load reduction rate, and overturning coefficient, and the like. Safety evaluation standards for regular trains are *Railway vehicles-Specification for evaluation the dynamic performance and accreditation test* (GB5599-85) and *Specification for Evaluation and Accreditation Test of Locomotive Dynamic Performance* (TB/T—2360—93).

Derailment coefficient is the parameter for evaluating whether the derailment is caused by the gradual uprise of wheel rims to the rail head under the lateral force. China's locomotive derailment coefficient limit is shown in Table 1.1 and China's derailment coefficient limit for freight and passenger vehicles is shown in Table 1.2[68].

It should be pointed out that despite distinct safety standards established in many countries the principles for train safety are the same. For instance, it is specified in European nations that derailment coefficient averages for $Q/P < 0.8$ within 2-meter movable sections whereas evaluation standard in Japan is $Q/P \leq 0.8$ (duration $t \geq 0.05$ s), and $\frac{Q}{P} \leq \frac{0.04}{t}$ ($t \leq 0.05$ s).

Lateral force limit is applied for evaluating whether trains movement would induce gauge widening (spike pulling) or serious track deformation. Lateral force limit is shown in Table 1.3.

Wheel load reduction rate is applied for determining whether derailment is caused by excess reduction of wheel load on one track side. Wheel load reduction rate limit is shown in Table 1.4.

Overturning coefficient is applied for determining whether the train will overturn under the lateral wind force, centrifugal force, and lateral vibration inertial force. Overturning coefficient limit is defined as follows:

Table 1.1 Locomotive derailment coefficient limit

Derailment coefficient	Excellent	Good	Qualified
Q/P	0.6	0.8	0.9

Note P stands for vertical force between steerable wheels of the locomotive and rails; Q for lateral force between steerable wheels and rails

Table 1.2 Freight and passenger vehicles' derailment coefficient limit

Derailment coefficient	Primary limit (qualified)	Secondary limit (safer)
Q/P	≤1.2	≤1.0

Table 1.3 Lateral force limit/kN

Lateral force	Primary limit (qualified)	Secondary limit (safer)
Q	$Q \leq 29 + 0.3P$	$Q \leq 19 + 0.3P$

Table 1.4 Wheel load reduction rate limit

Wheel load reduction rate	Primary limit (qualified)	Secondary limit (safer)
$\frac{\Delta P}{\bar{P}} = \frac{P_1 - P_2}{P_1 + P_2}$	≤0.65	≤0.60

Note ΔP for wheel load reduction; $\bar{P}$ for total wheel load of two wheels

$$D = \frac{P_d}{P_{\text{st}}} < 0.8 \tag{1.1}$$

where P_d is the lateral dynamic load applied to the vehicle, and P_{st} is the wheel static load. The critical condition for overturning is $D = 1$.

1.3.2 Riding Quality Limits for Regular Trains

Riding quality is evaluated, respectively, by riding index and vibration acceleration. Riding index is derived as follows:

$$W = 2.7 \sqrt[10]{a^3 f^5 F(f)} = 0.896 \sqrt[10]{\frac{A^3 F(f)}{f}} \tag{1.2}$$

where W is for riding index, $a(\text{cm})$ for vibration displacement amplitude, and $A(\text{cm/s}^2)$ for vibration acceleration amplitude; $f(\text{Hz})$ is for vibration frequency; $F(f)$ is a function relating to vibration frequency, known as frequency correction coefficient, as is shown in Table 1.5.

Table 1.5 Frequency correction coefficient

Vertical vibration		Lateral vibration	
0.5–5.9 Hz	$F(f) = 0.325f^2$	0.5–5.4 Hz	$F(f) = 0.8f^2$
5.9–20 Hz	$F(f) = 400/f^2$	5.4–26 Hz	$F(f) = 650/f^2$
>20 Hz	$F(f) = 1$	>26 Hz	$F(f) = 1$

The aforementioned riding index applies to continuous vibration of single frequency. In fact, vehicle vibration is random. As the acceleration measured includes the entire natural frequency of vehicle vibration, it should be grouped based on the frequency to reveal statistically the riding index of different acceleration of each frequency. Hence, the overall riding index is calculated as follows:

$$W = \left(W_1^{10} + W_2^{10} + W_3^{10} + \cdots + W_n^{10}\right)^{\frac{1}{10}} \tag{1.3}$$

where W_1, W_2,…, W_n stands for respective riding index derived from acceleration amplitude of each frequency which is obtained by frequency spectrum analysis. Generally speaking, the measurement period for riding index is 18 s. Frequency spectrum can be derived from fast Fourier transformation (FFT), and then by weighted frequency the riding index is obtained.

Major evaluation parameters of locomotive riding index are vertical and lateral vibration acceleration of the vehicle body, as well as effective value of weighted acceleration of driver's cabin. China's locomotive riding index limits are shown in Table 1.6.

Riding quality of freight and passenger vehicles denotes comfort of passengers and integrity of cargo delivery, evaluated by riding index and vibration acceleration, respectively. Riding quality limits for China's freight and passenger trains are shown in Table 1.7.

Table 1.6 Locomotive riding index limits

Riding quality	$A_{max}/(m/s^2)$		$A_w/(m/s^2)$		W
	Vertical	Lateral	Vertical	Lateral	
Excellent	2.45	1.47	0.393	0.273	2.75
Good	2.95	1.96	0.586	0.407	3.10
Qualified	3.63	2.45	0.840	0.580	3.45

Note A_{max} is for maximum vibration acceleration; A_w is for effective value of weighted acceleration, a frequency factor taking into account of drivers' feeling and fatigue, which represents a riding index for evaluating the suspension system of the locomotive; W is for riding index

Table 1.7 Riding quality limit for freight and passenger trains

Riding quality	Riding index W	
	Passenger train	Freight train
Excellent	<2.5	<3.5
Good	2.5–2.75	3.5–4.0
Passing	2.75–3.0	4.0–4.25

Note ① Evaluation for vertical and lateral riding quality are the same; ② Freight trains maximum vibration acceleration is also its vibration strength limit, with 0.7 g for vertical vibration and 0.5 g for lateral vibration

1.3.3 Safety and Riding Quality Limit for Rising Speed Trains

According to *Temporary Technical Regulation for Rising Speed of Existing Railways* issued by China's Ministry of Railway, safety and riding quality index should meet the requirements of the dynamic performance standards for rising speed of freight and passenger locomotives, the major technical performance specifications of rising speed passenger trains and EMUs, and the major technical performance specifications for rising speed of regular freight trains [69], as is shown, respectively, in Tables 1.8, 1.9 and 1.10.

Table 1.8 Dynamic performance standards for rising speed freight and passenger locomotives

Parameters	Standards
Derailment coefficient	≤0.8
Wheel load reduction rate	Quasi-static ≤0.65; dynamic <0.8
Lateral wheelset force/kN	$Q \leq 0.85\left(10 + P_0/3\right)$, P_0 for static wheel load/kN
Vibration acceleration of vehicle body/ (m/s^2)	Vertical: excellent 2.45, good 2.95, qualified 3.63
	Lateral: excellent 1.47, good 1.76, qualified 2.45
Riding quality index (vertical and lateral)	Excellent 2.75, good 3.10, qualified 3.45

Note ① If derailment coefficient >0.8, duration of t should be checked. For continuous measurement, the maximum derailment coefficient should meet $\left(\frac{Q}{P}\right)_{\max} \leq \frac{0.04}{t}$ ($t < 0.05$ s); For discontinuous measurement, the two consecutive derailment coefficient peaks exceeding 0.8 should not be allowed. If wheel load reduction rate >0.65, duration of t should also be checked. For continuous measurement, the maximum wheel load reduction rate should satisfy $\left(\frac{\Delta P}{P}\right) < 0.8$ ($t < 0.05$ s); For discontinuous measurement, the two consecutive wheel load reduction rate peaks exceeding 0.65 should not be allowed

Table 1.9 Technical specifications for rising speed passenger trains and EMUs

Parameters	Standards
Derailment coefficient	≤0.8
Wheel load reduction rate	≤0.65
Lateral wheelset force/kN	$Q \leq 0.85\left(10 + \frac{1}{3}\left(P_{st1} + P_{st2}\right)\right)$, P_{st1}, P_{st2} for static wheel load of right and left wheel, respectively/kN
Riding quality index (vertical and lateral)	Excellent 2.5, good 2.75, qualified 3.0 (2.75 for new trains)

Note This is applicable to the power-distributed EMUs and power-centralized passenger vehicles. Power-centralized power cars should follow the technical specifications for locomotive standards

Table 1.10 Technical specifications for rising speed regular freight trains

Parameters	Specifications
Derailment coefficient	≤1.0 (secondary limit); ≤1.2 (primary limit)
Wheel load reduction rate	≤0.6 (secondary limit); ≤0.65 (primary limit)
Lateral force/kN	$Q \leq 29 + 0.3P_{st}$, P_{st} for static wheel load,/kN
Lateral wheelset force/(kN)	$Q \leq 0.85\left(15 + \frac{1}{2}(P_{st1} + P_{st2})\right)$, P_{st1}, P_{st2} for static wheel load of right and left wheel respectively,/kN
Car body vibration acceleration/(m/s^2)	Vertical: ≤7.0
	Lateral: ≤5.0
Riding index (vertical and lateral)	Excellent 3.5, good 4.0, qualified 4.25 (4.0 for new trains)

1.3.4 Railway Noise Standards in China

Emission Standards and Measurement Methods of Railway Noise on the Boundary Alongside Railway Line (GB 12525-90) issued by China in November 1990 has explicitly set the railway boundary noise limit as shown in Table 1.11 [70]. When passing through crowded urban areas, the radiation noise has to comply with the "Sound Environmental Quality Standards" (GB 3096-2008). The standards have specified the maximum limits of environmental noise for five types of urban areas, as is shown in Table 1.12 [71].

1.3.5 Railway Noise Standards in Foreign Countries

Since sound level A has taken the less sensitivity of the human ear to low frequency noise into consideration and has a greater amount of correction on low frequency, it can better reflect human's subjective assessment on all kinds of noises, and thus it is widely used in noise rating. Besides, in light of the impact of noise duration, equivalent continuous sound level A-weighting L_{eq} is adopted to evaluate the noise generated by transportation. Just like traffic noise, $L_{A_{eq}}$ is also a priority evaluation value in railway noise. For high-speed railways, France and Japan adopt $L_{A_{max}}$, because the daily amount of trains running by is not unchangeable. Some European countries set a slightly lower standard for railway noise than that of road traffic noise. In Switzerland, the limit for railway noise can be liberalized by 5 dB(A). If the amount of trains passing by every day is too small, the limit can be liberalized to

Table 1.11 Railway boundary noise limit $L_{A_{eq}}$/dB (A) (GB 12525-1990)

Daytime	70
Nighttime	70

Table 1.12 Standard of environmental noise of urban area $L_{A_{eq}}$/dB(A)

Category		Daytime	Nighttime
0		50	40
1		55	45
2		60	50
3		65	55
4	4a	70	55
	4b	70	60

Notes
0: applicable to rehabilitation and recuperation areas, where special quietness is needed
1: applicable to areas which mainly function as residential, health care, cultural and educational, scientific research and planning, and municipal office areas, where quietness should be kept
2: applicable to areas which mainly function as commercial finance and terminal markets, or areas with residential, commercial, and industrial functions mixed together, and thus quietness for residence should be kept
3: applicable to areas which mainly function as industrial production and warehouse logistics, where serious impact of industrial noise on the surrounding areas should be prevented
4: applicable to areas within a certain distance from the main roads, where serious impact of traffic noise on the surrounding areas should be prevented. Two types are included: 4a and 4b. 4a mainly refers to the two sides of expressways, first-class highways, second-class highways, urban expressways, urban arterial roads, urban sub-distributors, urban mass transits (on the ground), and inland waterways; while 4b mainly refers to the two sides of trunk railways

15 dB(A). The allowable liberalization on railway noise limit is based on extensive social survey. With the same value of $L_{A_{eq}}$, it is generally acknowledged that the impact of railway noise is less serious than road traffic noise. Tables 1.13 and 1.14 illustrate the railway noise limit in some countries and areas.

1.3.6 Noise Limit for Railway Locomotives and Passenger Trains in China

With the railway network extending to major cities, towns, and rural areas, railway environmental protection has captured people's increasing attention. Railway noise is the main issue of railway environmental protection. It is not only directly related to the health of passengers, railway staffs, and residents along the lines but also to the safety of trains. For example, if the noise, vibration, temperature, or humidity in the cab is not controlled properly, it will affect the mood and productivity of the staff and crew, which may result in safety problems.

Noise limit for railway locomotives and passenger trains in China are shown in Tables 1.15, 1.16, 1.17, 1.18 and 1.19.

Table 1.13 Railway noise limit in some countries and areas/dB(A)

Country	Evaluation index	Type of lines	Daytime	Rest time	Nighttime	Monitoring site
Australia	$L_{A_{eq},24h}$	New railway lines	70			–
	$L_{A_{max}}$		95			
Austria	$L_r = L_{A_{eq}} - 5$	New and reconstructed railway lines	60–65		50–55	–
Denmark	$L_{A_{eq},24h}$	New railway lines	60			Outdoor free field
	$L_{A_{max}}$	New railway lines	85			
	$L_{A_{eq},24h}$	Existing lines	65			
French	$L_{A_{eq},12h}$	New high-speed railway lines	60–65			Outdoor free field
Germany	$L_r = L_{A_{eq}} - 5$	New residential areas	50–55		40–45	Outdoor free field
		Reconstructed railway lines	59		49	
England	$L_{A_{eq}}$	New residential areas	50		42	Outdoor free field
		New railway lines with insulation measures	68		63	
Hongkong, China	$L_{A_{eq},24h}$	New residential areas	65			–
Japan	$L_{A_{max}}$	Standard for Tohoku Shinkansen	70			Outdoor free field
Korea	$L_{A_{eq}}$	Environmental standard for newly constructed lines and existing lines	65		55	–
Netherland	$L_{A_{eq}}$	Allowable maximum value for new lines and existing lines	70 (+3)	65 (+3)	60 (+3)	Outdoor free field
Norway	$L_{A_{eq},24h}$ $L_{A_{max}}$ $L_{A_{max}}$	Newly constructed railways	60			Outdoor free field
		Newly constructed railways	80			
		Existing lines	76			

(continued)

Table 1.13 (continued)

Country	Evaluation index	Type of lines	Daytime	Rest time	Nighttime	Monitoring site
Sweden	$L_{A_{eq},24h}$	New lines and new residential areas	60			Outdoor free field
		Existing lines	75			
Swiss	$L_r = L_{A_{eq}} - 5$ K = −5 to −15 Depending on the number of trains	Newly constructed railways	55		45	Outdoor free field
		Impact threshold	60		50	
		Warning value	70		65	

Table 1.14 Noise limit for high-speed trains in foreign countries/dB(A)

High-speed trains	Speed of trains/(km/h)						
	160	200	240	250	270	300	400
Regular fast trains	85	88	–	91	–	–	–
German ICE-V high-speed trains	79	82	–	85	–	89	102
German Transrapid maglev trains	–	84	–	89	–	92	100
French TGV-PSE high-speed trains	–	92	–	95	–	–	–
French TGV-A high-speed trains	–	87	–	–	–	94	100
Spanish Talgo—Pendular high-speed trains	–	82	–	–	–	–	–
Japanese Tohoku Shinkansen	–	–	80	–	81	–	–

Table 1.15 Radiation noise limit for railway locomotives/dB(A)

Noise	Electric locomotive	Diesel locomotive	Steam locomotive
Radiation noise limit	90	95	100

Note: ① Measure at 7.5 m from the track center, 1.5 m from the track surface, and at the height of 3.5 m when necessary; ② For overhauled diesel locomotives, allowable error cannot exceed 3 dB (A); ③ Whistling noise is not accounted; and ④ The speed is 120 km/h or below

1.3.7 Environmental Vibration Standards in China's Urban Areas

Standard of environmental vibration in urban area is shown in Table 1.20. It stipulates the standard values of vertical vibration level Z for all types of city areas and applies to consecutive steady vibration, impact vibration, and random vibration [72].

Table 1.16 Noise limit for the railway locomotive cabs/dB(A)

Types of locomotives	Testing speed/(km/h)		Steady noise	Equivalent sound level L_{eq}
	Passenger	Freight		
Diesel locomotives	90	70	80	85
Electric locomotives	90	70	78	85
Steam locomotives	80	60	85	90

Note: ① For diesel and steam locomotives, measure at 1.2 m from the cab's floor surface. ② For new or overhauled locomotives, evaluate the interior steady noise. ③ For locomotives in operation, adopt the equivalent continuous sound level $L_{A_{eq}}$

Table 1.17 Noise limit for railway locomotives/dB(A)

Types of noise	Diesel and electric locomotives	Steam locomotives
Steady noise	80	85
Equivalent sound level $L_{A_{eq}}$	85	90

Note Monitoring noise cannot exceed 70 dB(A) measured from 30 m and 24 h

Table 1.18 Noise limit for multiple unit trains/dB(A)

Types of multiple unit trains	Cab	Passenger compartment	Trailer		Machine room of DMU
			Cushioned passenger compartment	Semi-cushioned passenger compartment	
EMUs	78	75	65	68	–
DMUs	78	75	65	68	90

Table 1.19 Noise limit for passenger trains/dB(A)

Cushioned berth	Semi-cushioned berth and cushioned seat	Semi-cushioned seat, dining car, luggage car, crew compartment of mail car (air-conditioned)	Semi-cushioned seat, dining car, luggage car, crew compartment of generator car (non- air conditioned)	Suburbs seat, kitchen in the dining car, luggage car and the office of mail car	Control room of the generator car
65	68	68	70	75	80

Note ① When the passenger train is running at the speed of 80 km/h, measured at 1.2 m from the floor. ② When the train is not in motion but the air conditioning unit and generators are running at full capacity, the allowable noise outside the train is 85 dB(A), measured at 3.5 m from the track center and 1.9 m from the track surface. ③ When the train is stationary but the air conditioning unit and generators are running at full capacity, interior noise is 3 dB(A) lower than allowable noise for the running train

Table 1.20 Standard of environmental vibration in urban area/dB (GB 10070-88)

Types of areas	Time	Allowable standard value of vertical vibration level Z
Special residential areas	Daytime	65
	Nighttime	65
Residential, cultural and educational areas	Daytime	70
	Nighttime	67
Mixed areas, CBDs	Daytime	75
	Nighttime	72
Industrial zones	Daytime	75
	Nighttime	72
Two sides of main roads	Daytime	75
	Nighttime	72
Two sides of trunk railways	Daytime	80
	Nighttime	80

Notes
(1) The "daytime" and "nighttime" are defined by the local government according to local habits and alteration of seasons
(2) "Two sides of main roads" refers to the sides of roads where the vehicle flow exceeds 100/h
(3) "Two sides of trunk railways" refers to residential areas 30 m away from the outer rail with a daily flow of no less than 20 trains
(4) Measurement and evaluation is carried out according to "Measuring Method for Environmental Vibration in Urban Areas" (GB 10071-88)

1.3.7.1 Vertical Vibration Level Z

Vertical vibration level Z is defined as follows:

$$VL_Z = 20\lg(a'_{\text{rms}}/a_0) \tag{1.4}$$

$$a'_{\text{rms}} = \sqrt{\sum a^2_{\text{frms}} \times 10^{0.1c_{\text{f}}}} \tag{1.5}$$

$$a_{\text{frms}} = \left[\frac{1}{T}\int_0^{\text{T}} a_f^2(t)\text{d}t\right]^{1/2} \tag{1.6}$$

where a_0 is the reference acceleration, generally $a_0 = 10^{-6}\,\text{m/s}^2$; a'_{rms} is the modified acceleration RMS (m/s^2); a_{frms} is the vibration acceleration RMS of frequency f; T is the measurement time of vibration; c_{f} is the sensory modification value of vertical vibration acceleration. The specific values are shown in Table 1.21.

Table 1.21 Sensory modification value of vertical and horizontal vibration acceleration (ISO2631/1-1985)

Modification value		Central frequency of one-third octave/(Hz)								
		1	2	4	6.3	8	16	31.5	63	90
Vertical	Modification value (dB)	−6	−3	0	0	0	−6	−12	−18	−21
	Allowable deviation (dB)	+2 −5	+2 −2	+1.5 −1.5	+1 −1	0 −2	+1 −1	+1 −1	+1 −2	+1 −3
Horizontal	Modification value (dB)	3	3	−3	−7	−9	−15	−21	−27	−30
	Allowable deviation (dB)	+2 −5	+2 −2	+1.5 −1.5	+1 −1	+1 −1	+1 −1	+1 −1	+1 −2	+1 −3

1.3.7.2 Calculation of Vertical Vibration Level Z

Calculation steps for vertical vibration level Z are as follows:

1. Select a section of the acceleration record $a(t)$, to analyze by the fast Fourier transform (FFT) method and calculate the power spectrum density function (PSDF), $s_a(f)$

$$s_a(f) = 2\frac{|a(f)|^2}{T} \tag{1.7}$$

   where $|a(f)|$ = FFT amplitude; T = time period of $a(t)$; and f = frequency (Hz).
2. Calculate the total power P_{f_l,f_u} of a certain frequency band

$$P_{f_l,f_u} = \int_{f_l}^{f_u} s_a(f)\mathrm{d}f \tag{1.8}$$

   where f_l, f_u, and f_c are lower band, upper band, and center frequencies, respectively. Calculation of frequency band adopts one-third octave band as stated by international standard ISO2631. The relationship among upper, lower, and center frequencies of one-third octave band is as follows. See Table 1.22.

Table 1.22 Central frequency, upper and lower frequency of one-third octave band/(Hz)

Central frequency	Upper and lower frequency	Central frequency	Upper and lower frequency	Central frequency	Upper and lower frequency
4	3.6–4.5	16	14.3–17.8	63	56.2–70.8
5	4.5–5.6	20	17.8–22.4	80	70.8–89.1
6.3	5.6–7.1	25	22.4–28.2	100	89.1–112
8	7.1–8.9	31.5	28.2–35.5	125	112–141
10	8.9–11.1	40	35.5–44.7	160	141–178
12.5	11.1–14.3	50	44.7–56.2	200	178–224

$$f_c = \sqrt[6]{2} f_l = \frac{f_u}{\sqrt[6]{2}}$$

3. Calculate the root mean square (RMS), a_{frms}

$$a_{frms} = \sqrt{P_{f_l, f_u}} \tag{1.9}$$

4. Calculate the modified acceleration RMS

$$a'_{rms} = \sqrt{\sum a^2_{frms} \times 10^{0.1 c_f}} \tag{1.10}$$

5. Calculate vibration level Z VL_z (dB)

$$VL_z = 20 \lg(a'_{rms}/a_0) \tag{1.11}$$

where a'_{rms} is the RMS of vibration acceleration (m/s^2); a_0 is the reference acceleration, generally taken as $a_0 = 10^{-6}$ m/s^2.

1.3.8 Limit for Building Vibration Caused by Urban Mass Transit

Standard for Limit and Measuring Method of Building Vibration and Secondary Noise Caused by Urban Rail Transit was enacted by the Ministry of Housing and Urban-rural Development of China in March 2009, as is shown in Table 1.23 [73].

Table 1.23 Indoor vibration limit for buildings along urban mass transit/dB

Types of areas	Application scope	Daytime (6:00–22:00)	Nighttime (22:00–6:00)
1	Special residential areas	65	62
2	Residential, cultural and educational areas	65	62
3	Mixed areas, CBDs	70	67
4	Industrial zones	75	72
5	Two sides of main roads	75	72

Note 1 "Special residential areas" refer to residential areas where special quietness is needed
2 "Residential, cultural and educational areas" refer to pure residential areas, and areas for cultural, educational, and institutional use
3 "Mixed areas" generally refers to areas where industry, business, residence, and light traffic are not clearly divided, and CBDs are concentrated business downtown areas
4 "Industrial zones" are areas clearly partitioned for industrial use in a city or region
5 "Two sides of main roads" refers to the sides of roads where the vehicle flow is above 100/h

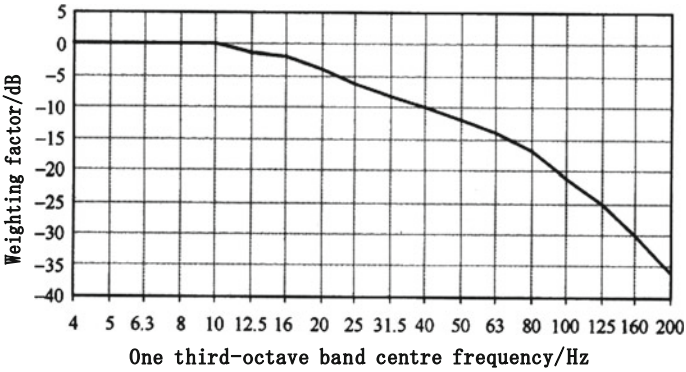

Fig. 1.1 Acceleration weighting factor Z of one-third octave band center frequency

Table 1.24 Z acceleration weighting factor of one-third octave center frequency

Central frequency of one-third octave/Hz	4	5	6.3	8	10	12.5	16	20	25
Weighting factor/dB	0	0	0	0	0	−1	−2	−4	−6
Central frequency of one-third octave/Hz	31.5	40	50	63	80	100	125	160	200
Weighting factor/dB	−8	−10	−12	−14	−17	−21	−25	−30	−36

Monitoring site can be located on the ground floor inside a building or on the building foundation within 0.5 m of the exterior wall. Data of the vertical vibration acceleration are processed by weighting factor Z of center frequency with one-third octave, as is shown in Fig. 1.1 or is modified by Table 1.24 to get the vibration acceleration level of each central frequency.

1.4 Standards of Track Maintenance for High-Speed Railway

Theoretical analysis, and practice have proved that on the one hand track irregularity directly affects safety and stability of high-speed running, and on the other hand, the dynamic load induced by track irregularity further accelerates the track deterioration and the developing of irregularity. Therefore, the scientific and

economical track maintenance is necessary in actual operations so as to keep them in good conditions for a longer period of time, ensuring the safety, and stability of high-speed running.

High-speed railway management and maintenance are based on the track inspection and the dynamic effects of track irregularity on high-speed trains and tracks. The track inspection is implemented by advanced track recording cars, rail destructive inspection cars, and other inspection devices as well as the visual patrol inspection of railway maintenance staff. The scientific evaluation of track conditions will be made through inspection. According to the measuring data and evaluation results, various parameters of the track conditions will be managed according to different levels, and the appropriate maintenance plans will be made. As for the local residual track irregularity and track fault which seriously affect the safety and stability of high speed running, the urgent repair measures and train speed limit must be taken.

1.4.1 Standards of Track Maintenance for French High-Speed Railway

The track maintenance and management of French high-speed railway can be divided into 4 levels according to the track irregularity conditions.

1. Target value—the quality standards that must be reached after laying and maintenance of the new lines.
2. Warning value—the value that the track irregularity reaches or exceeds, which should be observed closely. Its developments and changes should be analyzed, and the maintenance programs should be made.
3. Intervention value—as for the sites or districts that reach or exceed the value, the necessary maintenance must be implemented, generally within 15 days, to achieve the target value.
4. Limit speed—for the sites or sections that reach or exceed the value, the train must slow down and any possible means including manual work can be employed to regulate and eliminate it.

The standards of track maintenance for French high-speed railways are shown in Table 1.25.

1.4.2 Standards of Track Maintenance and Management for Japanese Shinkansen High-Speed Railway

The track maintenance and management of Japanese Shinkansen high-speed railway can be divided into 5 levels according to the track irregularity conditions. With

Table 1.25 Standards of track maintenance and management for French high-speed railway

Category	Lateral vibration acceleration/ (m/s^2)		Track profile/mm		Track alignment/mm	
	Car body	Bogie	Half peak with 12.2 m basal length	Peak-peak with 31 m basal length	Half peak with 10 m basal length	Peak-peak with 33 m basal length
Target value	–	–	3	–	2	–
Warning value	1.2	3.5	5	10	6	12
Intervention value	2.2	6	10	18	8	16
Limit speed	2.8	8	15	24	12	20

further speed rising, 40-m chord is added in the maintenance standards. The standards of track maintenance and management for Japanese Shinkansen high-speed railway are shown in Table 1.26.

1.4.3 Standards of Track Maintenance and Management for German High-Speed Railway

The track irregularity maintenance and management of German high-speed railway can be divided into 5 levels, as shown in Table 1.27.

1. SR_0—It means a large safety reserve of track irregularity and a good condition of track regularity.
2. SR_A—It is called as the safety reserve release value. Exceeding it indicates that the track irregularity begins to affect safety reserve, which needs careful evaluation.
3. SR_{100}—It indicates that the track irregularity affect safety reserve as well as the rationality of technical and economic reserve, which needs to arrange for maintenance.
4. SR_{lim}—Exceeding it indicates that the track irregularity has large effects on safety reserve as well as the locomotive and rolling stock and track damage (norms do not allow), which needs urgent repairs.
5. $SR_{\text{ultimate value}}$—It is the limit value directly affecting safety, that is, the safety reserve of track irregularity is running out. The high-speed trains must run within the speed limit and any necessary repair measures need to be employed to eliminate it.

Table 1.26 Standards of track maintenance and management for Japanese Shinkansen high-speed railway

Category			Target value of working acceptance	Target value of planned maintenance	Target value of comfort maintenance	Target value of safety maintenance	Target value of slow speed maintenance
Track irregularity	10 m chord	Track profile/mm	≤4	6	7	10	15
		Track alignment/mm	≤3	4	4	6	9
		Gauge/mm	≤±2	+6, −4	+6, −4	+6, −4	–
		Track cross level/mm	≤3	5	5	7	–
		Planarity/ (mm/2.5 m)	≤3	4	5	6	–
	40 m chord	Track profile/mm	7–10				
		Track alignment/mm	6–7				
Vibration acceleration of car body	Vertical g/(amplitude)		–	0.25	0.25	0.35	0.45
	Lateral g/(amplitude)		–	0.20	0.20	0.30	0.35

(1) Target value of working acceptance—the target quality value that must be reached after maintenance and engineering construction
(2) Target value of planned maintenance—the target value of track irregularity maintenance that needs to be determined while making maintenance plans
(3) Target value of comfortableness maintenance—the target value ensuring the trains in good and comfortable conditions
(4) Target value of safety maintenance—when the value of track irregularity reaches or exceeds it, which will significantly affects the safety of high-speed running, the urgent repair measures must be taken before the deadline (generally within 15 days)
(5) Target value of slow speed maintenance—when the value of track irregularity reaches or exceeds it, the train must slow down and any possible means can be employed to eliminate it

Table 1.27 Standards of track maintenance and management for German high-speed railway

Number	Category	Measuring reference line/(m)	Peak type	SR_0	SR_A	SR_{100}	$SR_{\lim}$	SR ultimate value
1	Profile/mm	2.6/6.0	Peak/peak	6	10	14	20	35
2	Twist/mm	2.5	Mean/peak	1.3	2.0	3.0	–	–
3	Cross level/mm	–	Mean/peak	4	6	8	12	20
4	Track alignment/mm	4.0/6.0	Peak/peak	6	10	14	20	35

Table 1.28 Standards of the response of locomotive and rolling stock to the track irregularity

Number	Evaluating index	Evaluation level coefficient k				
		Reference value	SR_0	SR_A	SR_{100}	$SR_{\lim}$
1	Lateral force/kN	$\left(10+\frac{2}{3}Q\right)k$	0.5	1.0	1.3	1.5
2	Lateral acceleration peak/peak/(m/s^2)	$2.5k$	0.7	1.0	1.3	1.5
3	Lateral acceleration RMS value	$0.5k$	0.4	1.0	1.3	1.5
4	Maximum vertical force/kN	$170k$	0.8	1.0	1.3	1.5
5	Minimum vertical force/kN	Q_0k	0.6	0.4	0.3	–
6	Vertical acceleration peak/peak/(m/s^2)	$2.5k$	0.7	1.0	1.3	1.5
7	Vertical acceleration RMS value	$0.5k$	0.4	1.0	1.3	1.5

Note In the table, Q_0 refers to static wheel load; RMS (root-mean-square) refers to root mean square, $x_{\text{rms}}=\left(\frac{1}{T}\int_0^T x^2\mathrm{d}x\right)^{1/2}$

Besides directly evaluating the track irregularity, German high-speed railway manages the response value of locomotive and rolling stock induced by the track irregularity, as shown in Table 1.28.

1.4.4 Standards of Track Maintenance and Management for British High-Speed Railway

The track irregularity management of British high-speed railway, like that of most countries, involves both residual track irregularity and the section irregularity condition. For British high-speed railway the standard deviation σ of per 200 m

Table 1.29 Standards of track irregularity management for British high-speed railway

Wavelength/m	Amplitude standard	
	When the train can meet stable requirements/mm	When the increased dynamic load conditions are met/mm
0.5	–	0.1
1	–	0.3
2	–	0.6
5	–	2.5
10	5	–
20	9	–
50	16	–

Table 1.30 The management standards of standard deviation for British track irregularity

Speed/(km/h)	Profile/(mm)				Track alignment/(mm)			
	<42 m wavelength		42–84 m wavelength		<42 m wavelength		42–84 m wavelength	
	Mean	Max	Mean	Max	Mean	Max	Mean	Max
175	1.8	2.9	3.2	5.7	1.1	1.9	2.6	4.6
200	1.5	2.4	2.7	4.7	0.9	1.6	2.2	3.9
225	1.3	2.0	2.3	4.0	0.8	1.4	1.8	3.2
250	1.1	1.7	1.9	3.3	0.7	1.1	1.5	2.7

track element is used for track irregularity maintenance and management, thereby the relevant maintenance programs are made.

In recent years, with the further rising train speed, besides the standard deviation of track irregularity maintenance standards under wavelength 42 m, the standard deviation of 42–84 m wavelength are also included. And the track section element extends from 200 to 400 m. The standards of residual track irregularity and section track irregularity for British high-speed railways are shown in Tables 1.29 and 1.30, respectively.

1.4.5 The Measuring Standards of Track Geometry for Korean High-Speed Railway (Dynamic)

The PLASSER' EM120 track recording car is employed for inspecting rails by Korean high-speed railway. The measuring standards of track geometry for Korean high-speed railway are shown in Table 1.31.

Table 1.31 The measuring standards of track geometry for Korean high-speed railway

Category	Measuring chord	Maximum deviation of new lines/(mm)	Temporary repair standard/(mm)	Speed limit standard/(mm)
Profile	Short chord 10 m	2	10	15
	Long chord 30 m	5	18	24
Track alignment	Short chord 10 m	3	8	12
	Long chord 30 m	6	16	20
Twist	3 m	3	7	15

Note
(1) The management value of 10-m short chord applies to the speed of 150–200 km/h
(2) The management value of 30-m long chord applies to the speed of 250–300 km/h
(3) When it reaches or exceeds the temporary repair standard, prompt maintenance must be implemented (According to the actual situation, the maintenance must be implemented within 1 month, 2 weeks, 1 week, or immediately)
(4) When it reaches or exceeds the speed limit standard, speed limit measures must be taken immediately (According to the actual situation, the speed limit can be 230 km/h, 170 km/h, or slower)

1.4.6 Standards of Track Maintenance for Chinese High-Speed Railway

The standards of track maintenance and management for Chinese high-speed railway include: the deviation value of track dynamic geometry for Passenger-Dedicated Line 300–350 km/h, as shown in Table 1.32. The deviation value of track static geometry tolerance for high-speed main lines is shown in Table 1.33. The deviation value of turnout static geometry tolerance for high-speed main line is shown in Table 1.34.

1.4.7 The Dominant Frequency Range and Sensitive Wavelength of European High-Speed Train and Track Coupling System

The dominant frequency range and sensitive wavelength of European high-speed train and track coupling system are shown in Table 1.35. In the structure design of the vehicle-track coupling system, the dominant frequency of the vehicle and the track structure should be avoided being close to that of the coupling system.

Table 1.32 The deviation value of track dynamic geometry for Passenger-Dedicated Line 300–350 km/h

Category		Working acceptance	Planned maintenance	Comfort-ableness	Temporary repairs	Speed limit 200 km/h
		–	I	II	III	IV
1.5–42 m wavelength	Profile/mm	3	5	8	10	11
	Track alignment/mm	3	4	5	6	7
1.5–120 m wavelength	Profile/mm	4	7	9	12	15
	Track alignment/mm	4	6	8	10	12
Gauge/(mm)		+3, −2	+4, −3	+6, −4	+7, −5	+8, −6
Cross level/(mm)		3	5	6	7	8
Twist/(mm)		3	4	6	7	8
Vertical acceleration of car body/(m/s^2)		–	1.0	1.5	2.0	2.5
Lateral acceleration of car body/(m/s^2)		–	0.6	0.9	1.5	2.0

Table 1.33 The deviation value of track static geometry tolerance for high-speed main lines

Category	Temporary maintenance value	Speed limit maintenance value	
		Speed limit 200 km/h maintenance value	Speed limit 160 km/h maintenance value
Profile/(mm)	7	8	11
Track alignment/(mm)	5	7	9
Gauge/(mm)	+5, −3	+6, −4	+8, −6
Cross level/(mm)	7	8	10
Twist/(mm)	5	6	8

Note
(1) Track alignment deviation is the maximum vector with 10-m chord measuring method
(2) Track profile deviation is the maximum vector with 10-m chord measuring method
(3) The basal length of twist is 2.5 m

Table 1.34 The deviation value of turnout static geometry tolerance for high-speed main lines

Category	Working acceptance	Temporary maintenance value	Speed limit value	
			Speed limit 200 km/h	Speed limit 160 km/h
Profile/(mm)	2	7	8	11
Tangent track alignment/(mm)	2	5	7	9
Curve track alignment/(mm)	2	4	–	–
Turnout gauge/(mm)	+2, −1	+5, −2	+6, −4	+8, −6
Gauge of tip track/(mm)	+1, −1	+3, −2	+6, −4	+8, −6
Cross level/(mm)	2	7	8	10
Lead curve exceeding reversely/(mm)	0	3	–	–
Twist/(mm)	2	5	6	8
Check gauge/(mm)	No less than 1391 mm			

Note
(1) Track alignment deviation is the maximum vector with 10-m chord measuring method
(2) Track profile deviation is the maximum vector with 10-m chord measuring method
(3) The basal length of twist is 2.5 m
(4) The gauge tolerance deviation of special turnout is checked according to the design drawings

Table 1.35 The dominant frequency range and sensitive wavelength of European high-speed train and track coupling system

Structure	Dominant frequency range/(Hz)	Sensitive wavelength and wavelength of inducing the periodic track irregularity/(m)			
		160 km/h	200 km/h	300 km/h	350 km/h
Car body	1–2	22.0–44.0	27.8–55.6	41.5–83.0	48.5–97.0
Bogie	8–12	3.5–5.0	4.6–7.0	6.9–10.4	8.1–12.1
Track	30–60	0.7–1.4	0.9–1.8	1.4–2.8	1.6–3.2

1.5 Vibration Standards of Historic Building Structures

Historic buildings refer to those buildings in all ages which are of great value to the study of social politics, economy, and cultural development. Figures 1.2, 1.3 and 1.4 are the national key cultural relic protection sites. Figures 1.5 and 1.6 are provincial and municipal key cultural relic protection sites, respectively. Figure 1.7 is Tengwang Pavilion built in the 4th year of Yonghui in Tang Dynasty—the leading tower of the three famous ones in South China. The other two towers are Yellow Crane Tower in Wuhan and Yueyang Tower in Hunan. Tengwang Pavilion had been rebuilt for 29 times in the history, and it has been destroyed and rebuilt many times. The present Tengwang Pavilion was built in October 8, 1989. It was rebuilt according to "*The Draft Drawing of Tengwang Pavilion Reconstruction Plan*" drawn by Liang Sicheng in 1985, which was a pseudo-historic building with

Fig. 1.2 The Yonghe Lama Temple in Beijing (National)

Fig. 1.3 The Museum of Bayi Nanchang Uprising in Nanchang (National)

Fig. 1.4 The Guifeng Pagoda in Heyuan, Guangdong (National)

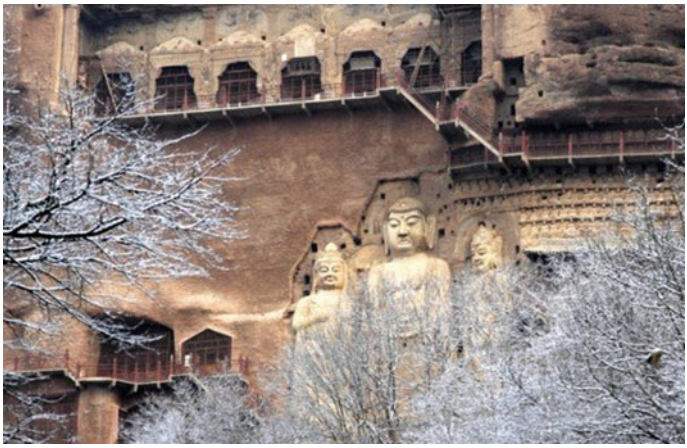

Fig. 1.5 The Maiji Mountain Grottoes in Tianshui, Gusu (National)

Fig. 1.6 The Jiangxi Exhibition Center in Nanchang (Provincial)

steel and reinforced concrete structure. Compared with the traditional timber architecture in the history, it has no historical value, and its artistic value is not up to the standards of cultural relics. Thus, although it is very famous, Tengwang Pavilion is not listed as a national key cultural relic protection site (Fig. 1.8).

The vibration evaluation index of historic building structure adopts the allowable vibration velocity, which should be selected according to structure type, protection level, and the propagating speed of elastic wave in the historic building structure. The allowable vibration velocity of different types of historic buildings are shown in Tables 1.36, 1.37, 1.38 and 1.39 [74].

Fig. 1.7 The Memorial of Bayi Nanchang Uprising in Nanchang (Municipal)

Fig. 1.8 The Famous Tengwang Pavilion in South China

Table 1.36 Allowable vibration velocity of historic brick structure/(mm/s)

Protection level	Control point location	Control point direction	Brick structure V_p (m/s)		
			<1600	1600–2100	>2100
National cultural relic protection unit	The highest point of bearing structure	Lateral	0.15	0.15–0.20	0.20
Provincial cultural relic protection unit	The highest point of bearing structure	Lateral	0.27	0.27–0.36	0.36
Municipal and county cultural relic protection unit	The highest point of bearing structure	Lateral	0.45	0.45–0.60	0.60

Note When V_p is between 1600 and 2100 m/s, the allowable vibration velocity can be determined by interpolation method

Table 1.37 Allowable vibration velocity of historic stone structure/(mm/s)

Protection level	Control point location	Control point direction	Stone structure V_p (m/s)		
			<2300	2300–2900	>2900
National key cultural relic protection unit	The highest point of bearing structure	Lateral	0.20	0.20–0.25	0.25
Provincial cultural relic protection unit	The highest point of bearing structure	Lateral	0.36	0.36–0.45	0.45
Municipal and county cultural relic protection unit	The highest point of bearing structure	Lateral	0.60	0.60–0.75	0.75

Note When V_p is between 2300 and 2900 m/s, the allowable vibration velocity is determined by interpolation method

Table 1.38 Allowable vibration velocity of historic timber structure/(mm/s)

Protection level	Control point location	Control point direction	Along the wood grain V_p (m/s)		
			<4600	4600–5600	>5600
National key cultural relic protection unit	Top of top-floor pillar	Lateral	0.18	0.18–0.22	0.22
Provincial cultural relic protection unit	Top of top-floor pillar	Lateral	0.25	0.25–0.30	0.30
Municipal and county cultural relic protection unit	Top of top-floor pillar	Lateral	0.29	0.29–0.35	0.35

Note When V_p is between 4600 and 5600 m/s, the allowable vibration velocity is determined by interpolation method

Table 1.39 Allowable vibration velocity of grottoes/(mm/s)

Protection level	Control point location	Control point direction	Rock type	Rock V_p (m/s)		
National key cultural relic protection unit	Grotto roof	Three directions	Sandstone	<1500	1500–1900	>1900
				0.10	0.10–0.13	0.13
			Gravel	<1800	1800–2600	>2600
				0.12	0.12–0.17	0.17
			Limestone	<3500	3500–4900	>4900
				0.22	0.22–0.31	0.31

Note The three directions refer to radial, tangential, and vertical; when V_p is between 1500–1900, 1800–2600, and 3500–4900 m/s, the allowable vibration velocity is determined by interpolation method

References

1. Knothe KL, Grassie SL (1993) Modeling of railway track and vehicle track interaction at high-frequencies. Veh Syst Dyn 22(3–4):209–262
2. Grassie SL, Gregory RW, Johnson KL (1982) The dynamic response of railway track to high frequency lateral excitation. J Mech Eng Sci 24(2):91–95
3. Grassie SL, Gregory RW, Johnson KL (1982) The dynamic response of railway track to high frequency longitudinal excitation. J Mech Eng Sci 24(2):97–102
4. Mathews PM (1958) Vibrations of a beam on elastic foundation. Zeitschrift fur Angewandte Mathematik und Mechanik 38:105–115
5. Mathews PM (1959) Vibrations of a beam on elastic foundation. Zeitschrift fur Angewandte Mathematik und Mechanik 39:13–19
6. Trochanis AM, Chelliah R, Bielak J (1987) Unified approach for beams on elastic foundation for moving load. J Geotech Eng 112:879–895
7. Ono K, Yamada M (1989) Analysis of railway track vibration. J Sound Vib 130:269–297
8. Jezequel L (1981) Response of periodic systems to a moving load. J Appl Mech 48:613–618
9. Timoshenko S, Young DH, Weaver JRW (1974) Vibration problems in engineering, 4th edn. Wiley, New York
10. Warburton GB (1976) The dynamic behavior of structures. Pergamon Press, Oxford
11. Cai CW, Cheung YK, Chan HC (1988) Dynamic response of infinite continuous beams subjected to a moving force-an exact method. J Sound Vib 123(3):461–472
12. Venancio Filho F (1978) Finite element analysis of structures under moving loads. Shock Vib Digest 10:27–35
13. Olsson M (1985) Finite element modal co-ordinate analysis of structures subjected to moving loads. J Sound Vib 99(1):1–12
14. Fryba L, Nakagiri S, Yoshikawa N (1993) Stochastic finite element for a beam on a random foundation with uncertain damping under a moving force. J Sound Vib 163:31–45
15. Thambiratnam DP, Zhuge Y (1993) Finite element analysis of track structures. J Microcomput Civil Eng 8:467–476
16. Thambiratnam D, Zhuge Y (1996) Dynamic analysis of beams on an elastic foundation subjected to moving loads. J Sound Vib 198(2):149–169
17. Nielsen JCO, Igeland A (1995) Vertical dynamic interaction between train and track-influence of wheel and track imperfections. J Sound Vib 187(5):825–839
18. Zheng DY, Fan SC (2002) Instability of vibration of a moving train and rail coupling system. J Sound Vib 255(2):243–259

19. Koh CG, Ong JSY, Chua DKH, Feng J (2003) Moving element method for train-track dynamics. Int J Numer Meth Eng 56:1549–1567
20. Auersch L (2006) Dynamic axle loads on tracks with and without ballast mats: numerical results of three-dimensional vehicle–track–soil models. J Rail Rapid Transit 220:169–183 (Proceedings of the Institution of Mechanical Engineers. Part F)
21. Clouteau D, Arnst M, Al-Hussaini TM, Degrande G (2005) Free field vibrations due to dynamic loading on a tunnel embedded in a stratified medium. J Sound Vib 283(1–2):173–199
22. Andersen L, Jones CJC (2002) Vibration from a railway tunnel predicted by coupled finite element and boundary element analysis in two and three dimensions. In: Proceedings of the 4th structural dynamics—EURODYN. Munich, Germany, pp 1131–1136
23. Andersen L, Jones CJC (2006) Coupled boundary and finite element analysis of vibration from railway tunnels-a comparison of two and three-dimensional models. J Sound Vib 293(3–5):611–625
24. Thomas D (2010) Dynamics of a high-speed rail vehicle negotiating curves at unsteady crosswind. J Rail Rapid Transit 224(6):567–579 (Proceedings of the Institution of Mechanical Engineers. Part F)
25. Ganesh Babu K, Sujatha C (2010) Track modulus analysis of railway track system using finite element model. J Vib Control 16(10):1559–1574
26. Cai Y, Sun H, Xu C (2010) Effects of the dynamic wheel-rail interaction on the ground vibration generated by a moving train. Int J Solids Struct 47(17):2246–2259
27. Wanming Z (1992) The vertical model of vehicle-track system and its coupling dynamics. J China Railway Soc 14(3):10–21
28. Wanming Z (2007) Vehicle-track coupling dynamics, 3rd edn. Science Press, Beijing
29. Wanming Z (2002) New advance in vehicle-track coupling dynamics. China Railway Sci 23 (4):1–13
30. Xiaoyan Lei (1994) Finite element analysis of wheel-rail interaction. J China Railway Soc 16 (1):8–17
31. Xiaoyan Lei (1997) Dynamic response of high-speed train on ballast. J China Railway Soc 19 (1):114–121
32. Xiaoyan Lei (1998) Research on parameters of dynamic analysis model for railway track. J Railway Eng Soc 2:71–76
33. Lei X (1998) Numerical analysis method of railway track structure. China Railway Publishing House, Beijing
34. Xu Z, Zhai W, Wang K, Wang Q (2003) Analysis of vehicle-track system vibration: comparison between Timoshenko beam and Euler beam track model. Earthq Eng Eng Vib 23 (6):74–79
35. Xu Z, Zhai W, Wang K (2003) Analysis of vehicle-track coupling vibration based on Timoshenko beam model. J Southwest Jiaotong Univ 38(1):22–27
36. Xie W, Zhen B (2005) Steady-state dynamic analysis of Winkler beam under moving loads. J Wuhan Univ Technol 27(7):61–63
37. Luo Y, Shi D, Tan X (2008) Finite element analysis of dynamic characteristic on continuous welded rail track under longitudinal temperature force. Chin Q Mech 29(2):284–290
38. Wei Q, Deng Y, Feng Y (2008) Study on vibration characteristics of metro track structure of linear induction motor. Railway Archit 3:84–88
39. Gao L, Tao K, Qu C, Xin T (2009) Study on the spatial mechanical characteristics of welded turnout on the ridges for passenger dedicated lines. China Railway Sci 30(1):29–34
40. Feng Q, Lei X, Lian S (2010) Vibration analysis of high-speed railway subgrade-ground system. J Railway Sci Eng 7(1):1–6
41. Bian X, Yunmin C (2005) Dynamic analyses of track and ground coupled system with high-speed train loads. Chin J Theor Appl Mech 37(4):477–484
42. Bian X (2005) Dynamic analysis of ground and tunnel responses due to high-speed train moving loads. Doctor's Dissertation of Zhejiang University, Hangzhou
43. Bian X, Yunmin C (2007) Characteristics of layered ground responses under train moving loads. Chin J Rock Mech Eng 26(1):182–189

44. Xie W, Hu J, Xu J (2002) Dynamic responses of track-ground system under high-speed moving loads. Chin J Rock Mech Eng 21(7):1075–1078
45. Xie W, Wang G, Yu Y (2004) Calculation of soil deformation induced by moving load. Chin J Geotech Eng 26(3):318–322
46. Nie Z, Liu B, Li L, Ruan B (2006) Study on the dynamic response of the track/subgrade under moving load. China Railway Sci 27(2):15–19
47. Lie X (2006) Study on critical velocity and vibration boom of track. J Geotech Eng 28(3):419–422
48. Lei X (2007) Dynamic analyses of track structure with fourier transform technique. J China Railway Soc 29(3):67–71
49. Lei X (2006) Study on ground waves and track vibration boom induced by high speed trains. J China Railway Soc 28(3):78–82
50. Lei X (2007) Analyses of track vibration and track critical velocity for high-speed railway with fourier transform technique. China Railway Sci 28(6):30–34
51. He Z, Zhai W (2007) Ground vibration generated by high-speed trains along slab tracks. China Railway Sci 28(2):7–11
52. Li Z, Gao G, Feng S, Shi G (2007) Analysis of ground vibration induced by high-speed train. J Tongji Univ (Sci) 35(7):909–914
53. Wua Y-S, Yang Y-B (2004) A semi-analytical approach for analyzing ground vibrations caused by trains moving over elevated bridges. Soil Dyn Earthq Eng 24:949–962
54. Xia H, Cao YM, De Roeck G (2010) Theoretical modeling and characteristic analysis of moving-train induced ground vibrations. J Sound Vib 329:819–832
55. Liu X, Wang P, Wan F (1998) A space-coupling vibration model of wheel/rail system and its application. J China Railway Soc 20(3):102–108
56. Li D, Zeng Q (1997) Dynamic analysis of train-tangent track space coupling time varying system. J China Railway Soc 19(1):101–107
57. Liang B, Cai Y, Zhu D (2000) Dynamic analysis on vehicle-subgrade model of vertical coupled system. J China Railway Soc 22(5):65–71
58. Su Q, Cai Y (2001) A spatial time-varying coupling model for dynamic analysis of high speed railway subgrade. J Southwest Jiaotong Univ 36(5):509–513
59. Wang Q, Cai C, Luo Q, Cai Y (1998) Allowable values of track deflection angles on high speed railway bridge-subgrade transition sections. J China Railway Soc 20(3):109–113
60. Luo Q, Cai Y, Zhai W (1999) Dynamic performance analyses of high-speed railway bridge-subgrade transition. Eng Mech 16(5):65–70
61. Luo Q, Cai Y (2000) Study on deformation limit and reasonable length of high-speed railway bridge-subgrade transition section. Railway Stand Des 6–7:2–4
62. Wang P (1997) Dynamic research on turnout wheel-track system. Doctor's Dissertation of Southwest China Jiaotong University, Chengdu
63. Ren Z (2000) Dynamic research on vehicle-turnout system. Doctor's Dissertation of Southwest China Jiaotong University, Chengdu
64. Chen G (2000) Analysis of random vibration of vehicle-track coupling system. Doctor's Dissertation of Southwest China Jiaotong University, Chengdu
65. Lei X (2002) New methods of track dynamics and engineering. China Railway Publishing House, Beijing
66. Lei X, Mao L (2001) Analyses of dynamic response of vehicle and track coupling system with random irregularity of rail vertical profile. China Railway Sci 22(6):38–43
67. Lu F, Kennedy D, Williams FW, Lin JH (2008) Symplectic analysis of vertical random vibration for coupled vehicle–track systems. J Sound Vib 317:236–249
68. National Standard of the People's Republic of China (1985) Railway vehicle specification for evaluation the dynamic performance and accreditation Test (GB 5599-85). China Railway Publishing House, Beijing
69. Professional Standard of the People's Republic of China (2007) Temporary regulation for Newly Built 300–350 km/h passenger dedicated line. Railway Construction No. 47. China Railway Publishing House, Beijing

70. National Standard of the People's Republic of China (1990) Emission standards and measurement methods of railway noise on the boundary alongside railway line (GB 12525-90). China Environmental Science Press, Beijing
71. National Standard of the People's Republic of China (2008) Standard of environmental noise of urban area (GB3096-2008). China Environmental Science Press, Beijing
72. National Standard of the People's Republic of China (1989) Standard of environmental vibration in urban area (GB 10070-88). China Environmental Science Press, Beijing
73. Professional Standard of the People's Republic of China (2009) Standard for limit and measuring method of building vibration and secondary noise caused by urban rail transit (JGJ/T170-2009). China Architecture & Building Press, Beijing
74. National Standard of the People's Republic of China (2009) Technical specifications for protection of historic buildings against man-made vibration (GB 50452-2008). China Architecture and Building Press, Beijing

Chapter 2
Analytic Method for Dynamic Analysis of the Track Structure

With the ongoing operation of high-speed and heavy-haul railways, dynamic analysis of the track structure has become a significant research topic in the field of railway engineering. By establishing the continuous elastic beam model of track structure, analytic method for dynamic analysis of track structure is discussed, and characteristics of ground surface waves and the strong track vibration induced by high-speed trains are analyzed by the analytic method. Finally, effects of track stiffness on track critical velocity and track vibration are investigated.

2.1 Studies of Ground Surface Wave and Strong Track Vibration Induced by High-Speed Train

It is understood that the increase in train speed may cause the increased dynamic action induced by the train on track and ground surface. This occurrence is especially serious under the high-speed operation. Studies have shown that when train speed reaches or exceeds some critical velocities, there would be surface waves induced by high-speed trains causing strong vibration of track structure. Meanwhile, owing to the wave propagation through ballast and subgrade, there would be strong vibration and structure-borne noise of surrounding buildings along the railway lines. In the track-ballast-subgrade-ground system, there are mainly two kinds of critical wave velocity: the wave velocity of Rayleigh wave on ground surface and the minimum phase velocity of the bending wave propagating in the track, which is also called track critical velocity. The track critical velocity varies according to different physical properties of the ground media. When the track foundation is soft subgrade, it is easy for high-speed trains to reach and exceed these two kinds of critical wave velocity. Madshus and Kaynia [1] from Sweden discovered this phenomenon in testing X2000 high-speed train. In the recent years, related studies have been emerging [1–5].

X. Lei, *High Speed Railway Track Dynamics*,
DOI 10.1007/978-981-10-2039-1_2

2.1.1 The Continuous Elastic Beam Model of Track Structure

To simplify the analysis, track critical velocity and strong track vibration are investigated by use of the analytic method in the following. The continuous elastic beam model of track structure is established as shown in Fig. 2.1.

According to D'Alembert principle, the differential equation for track vibration excluding damping is [6]

$$EI\frac{\partial^4 w}{\partial x^4}+m\frac{\partial^2 w}{\partial t^2}+kw=-F\delta(x-Vt) \tag{2.1}$$

where E, I stand for elasticity modulus and inertia moment around the horizontal axis; w is rail vertical deflection, and m is track mass per unit length; k is equivalent track stiffness, and δ is Dirac function; V is train speed, and F is wheelset load.

Defining

$$\varepsilon_1^2=\frac{m}{4EI},\quad \varepsilon_2^4=\frac{\mathrm{k}}{4EI} \tag{2.2}$$

Equation (2.1) then can be transformed into

$$\frac{\partial^4 w}{\partial x^4}+4\varepsilon_1^2\frac{\partial^2 w}{\partial t^2}+4\varepsilon_2^4 w=-\frac{F}{EI}\delta(x-Vt) \tag{2.3}$$

Firstly, let us consider the free vibration. Supposing $F=0$, the solution for (2.3) is

$$w(x,t)=\mathrm{e}^{\frac{j2\pi(x-ct)}{\lambda}} \tag{2.4}$$

where λ is vibration wavelength, and c is vibration wave propagation velocity.

Substituting (2.4) into (2.3), it has

$$c=\frac{1}{2\varepsilon_1}\left(\frac{\lambda^2\varepsilon_2^4}{\pi^2}+\left(\frac{2\pi}{\lambda}\right)^2\right)^{\frac{1}{2}} \tag{2.5}$$

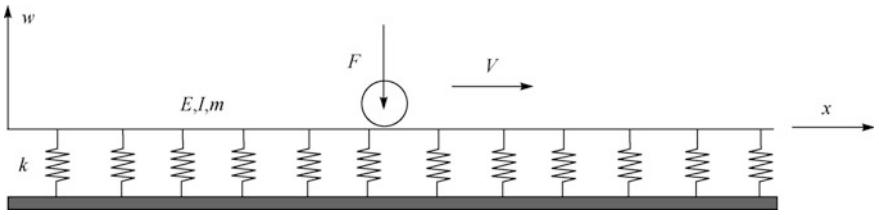

Fig. 2.1 The continuous elastic beam model of track structure

When $\lambda = \frac{\sqrt{2}\pi}{\varepsilon_2}$, c obtains the minimum, then there derives

$$c_{\min} = \sqrt[4]{\frac{4kEI}{m^2}} \tag{2.6}$$

$c_{\min}$ is the minimum phase velocity of the bending wave in track structure, also called track critical velocity.

Secondly, let us considering the wheelset load F, the solution is $w(x - Vt)$. Introducing $z = x - Vt$, Eq. (2.3) can be transformed into

$$\frac{\partial^4 w}{\partial z^4} + 4\varepsilon_1^2 V^2 \frac{\partial^2 w}{\partial z^2} + 4\varepsilon_2^4 w = -\frac{F}{EI}\delta(z) \tag{2.7}$$

Characteristic equation for (2.7) is

$$p^4 + 4\varepsilon_1^2 V^2 p^2 + 4\varepsilon_2^4 = 0 \tag{2.8}$$

The solution for the above characteristic equation is related to coefficient. When $V < \frac{\varepsilon_2}{\varepsilon_1}$ (note: The existing domestic and international track structures all meet this inequality), the solution for (2.8) is

$$p = \pm\alpha \pm j\beta \tag{2.9}$$

where

$$\alpha = \left(\varepsilon_2^2 - V^2\varepsilon_1^2\right)^{\frac{1}{2}}, \quad \beta = \left(\varepsilon_2^2 + V^2\varepsilon_1^2\right)^{\frac{1}{2}} \tag{2.10}$$

Then, the solution for (2.7) should be

$$w(z) = \mathrm{e}^{\alpha z}(D_1 \cos\beta z + D_2 \sin\beta z) + \mathrm{e}^{-\alpha z}(D_3 \cos\beta z + D_4 \sin\beta z) + \varphi(z) \tag{2.11}$$

In the above equation, $\varphi(z)$ is related to external load. When $z = 0$, x is located at the wheel-rail contact point. When $z \neq 0$ and $\varphi(z) = 0$, (2.11) can be turned into

$$\begin{aligned} w_1(z) &= \mathrm{e}^{\alpha z}(D_1 \cos\beta z + D_2 \sin\beta z) \qquad z \leq 0 \\ w_2(z) &= \mathrm{e}^{-\alpha z}(D_3 \cos\beta z + D_4 \sin\beta z) \quad z > 0 \end{aligned} \tag{2.12}$$

Four undetermined coefficients in the above equations can be derived from four boundary conditions when $z = 0$. They are

$$w_1|_{z=0} = w_2|_{z=0}, \quad \left.\frac{\partial w_1}{\partial z}\right|_{z=0} = 0, \quad \left.\frac{\partial w_2}{\partial z}\right|_{z=0} = 0, \quad EI\left.\frac{\partial^3 w_1}{\partial z^3}\right|_{z=0} = \frac{F}{2} \tag{2.13}$$

The solution for (2.7) can be finally figured out as follows:

$$w(z) = -\frac{F}{8EI\alpha\varepsilon_2^2} e^{-\alpha|z|}\left(\cos\beta z + \frac{\alpha}{\beta}\sin\beta|z|\right) \tag{2.14}$$

Under the multiple moving wheelset loads, the differential equation for track vibration is

$$EI\frac{\partial^4 w}{\partial x^4} + m\frac{\partial^2 w}{\partial t^2} + kw = -\sum_{i=1}^{N} F_i\delta(x - a_i - Vt) \tag{2.15}$$

where F_i is the load of the i th wheelset; a_i is the distance between the first wheelset and the ith wheelset; N is the total number of the wheelsets. The solution for (2.15) can be derived from the single moving wheelset solution (2.14) through superposition principle.

2.1.2 Track Equivalent Stiffness and Track Foundation Elasticity Modulus

The track equivalent stiffness k and the track foundation elasticity modulus E_s are closely related. Vesic [7] worked out the relationship between the track equivalent stiffness modeled as Euler beam on semi-infinite domain and the track foundation elasticity modulus. On such basis, Heelis [8] proposed the following formula for calculating track equivalent stiffness k.

$$k = \frac{0.65E_s}{1 - \upsilon_s^2}\sqrt[12]{\frac{E_s B^4}{EI}} \tag{2.16}$$

where E_s is the track foundation elasticity modulus (unit: $\mathrm{MN/m^2}$); υ_s is Poisson's ratio; B is the sleeper length, usually 2.5–2.6 m; EI is the rail flexural modulus (unit: $\mathrm{MN\,m^2}$); k is the track equivalent stiffness (unit: $\mathrm{MN/m^2}$).

Under general circumstances, approximately the track foundation elasticity modulus E_s is $50 - 100\,\mathrm{MN/m^2}$. When $E_s = 50\,\mathrm{MN/m^2}$ and Poisson's ratio $\upsilon_s = 0.35$, then $k = 56.148\,\mathrm{MN/m^2}$ according to (2.16). In case of soft foundation, $E_s = 10\,\mathrm{MN/m^2}$ or even lower, resulting in $k = 9.82\,\mathrm{MN/m^2}$.

2.1.3 Track Critical Velocity

As mentioned above, Eq. (2.6) is the computational formula for track critical velocity, which is related to the track equivalent stiffness k, the rail flexural modulus EI, and the track mass per unit length m. In calculating m, masses of the rail, sleeper, and ballast should be included. For instance, if the rail is 60 kg/m, with the sleeper allocation being 1760 sleepers/km, the ballast thickness 30 cm, the ballast shoulder breadth 35 cm, and the ballast density 2000 kg/m^3, the track critical velocity corresponding to three different kinds of track foundation elasticity modulus can be calculated as shown in Table 2.1.

From Table 2.1, it can be observed that when $E_s = 10\,\text{MN/m}^2$, $c_{\min} = 91.34\,\text{m/s} = 328.8\,\text{km/h}$ and when $E_s = 5\,\text{MN/m}^2$, $c_{\min} = 75.70\,\text{m/s} = 272.5\,\text{km/h}$. These two velocities can be easily exceeded by high-speed trains.

2.1.4 Analysis of Strong Track Vibration

2.1.4.1 Analysis of Strong Track Vibration Under a Moving Wheelset Load

When the track foundation elasticity modulus $E_s = 50\,\text{MN/m}^2$, the track critical velocity $c_{\min} = 141.24\,\text{m/s}$ according to Table 2.1. Supposing a wheelset load (axle load $F = 170$ KN) moving over the track at four different speeds, respectively (V = 110, 130, 135, and 140 m/s), track vibration is analyzed accordingly, as is indicated by the track vibration deflection curve in Fig. 2.2. It can be seen from this figure that strong track vibration would be induced when the wheelset moves at the speed of 140 m/s, which is approaching the track critical velocity.

Table 2.1 The track critical velocity corresponding to different track foundation elasticity modulus

Parameters	$E_s/(\text{MN/m}^2)$	$k/(\text{MN/m}^2)$	$EI/(\text{MN m}^2)$	$m/(\text{kg/m})$	$B/(m)$	$c_{\min}/(\text{m/s})$
Compacted clay	50	56.15	13.25	2735	2.5	141.24
Loam	10	9.82	13.25	2735	2.5	91.34
Soft subgrade	5	4.63	13.25	2735	2.5	75.70

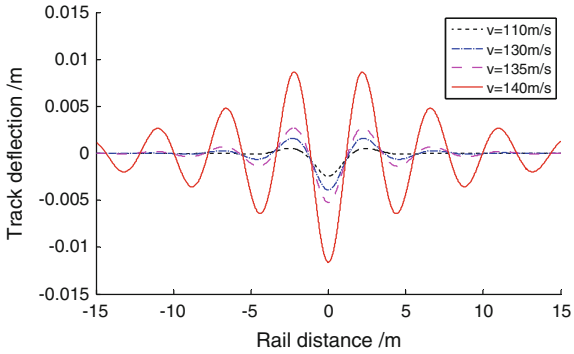

Fig. 2.2 The track vibration deflections by a moving wheelset load at different speeds

2.1.4.2 Analysis of Strong Track Vibration Induced by a High-Speed Train

Track vibration is investigated by Fig. 2.3, the computational model, when the high-speed train moves at different speeds. Supposing the train marshaled by one TGV high-speed motor car and four TGV high-speed trailers. Parameters for TGV high-speed motor car and trailers are given in Chap. 6. Computational results are presented in Figs. 2.4 and 2.5, which represent the track deflections for $E_s = 50\,\mathrm{MN/m^2}$ and $E_s = 10\,\mathrm{MN/m^2}$, respectively. In these two figures, effects of two kinds of rail flexural stiffness EI on track deflection are shown, with the solid line being the track deflection for the flexural stiffness $EI = 13.25\,\mathrm{MN\,m^2}$ (namely the flexural stiffness for two rails of $60\,\mathrm{kg/m}$), and the dotted line being the track deflection for the flexural stiffness EI doubles (namely increasing two guard rails of $60\,\mathrm{kg/m}$).

Based on the above computational results, some conclusions are summarized as follows [9–11]:

(1) When the train speed approaches the track critical velocity, strong track vibration will be induced, as is shown in Figs. 2.2, 2.4 and 2.5.
(2) Track foundation elasticity modulus is the main factor for influencing the track critical velocity. In particular when the track foundation is the soft subgrade, the track critical velocity is much low, which can be easily exceeded by medium-speed or high-speed trains.

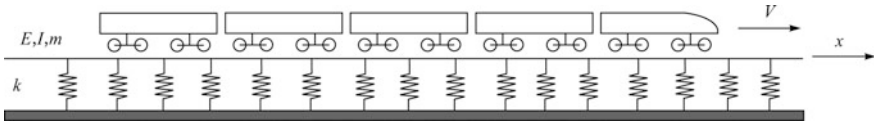

Fig. 2.3 The computational model of a TGV high-speed train

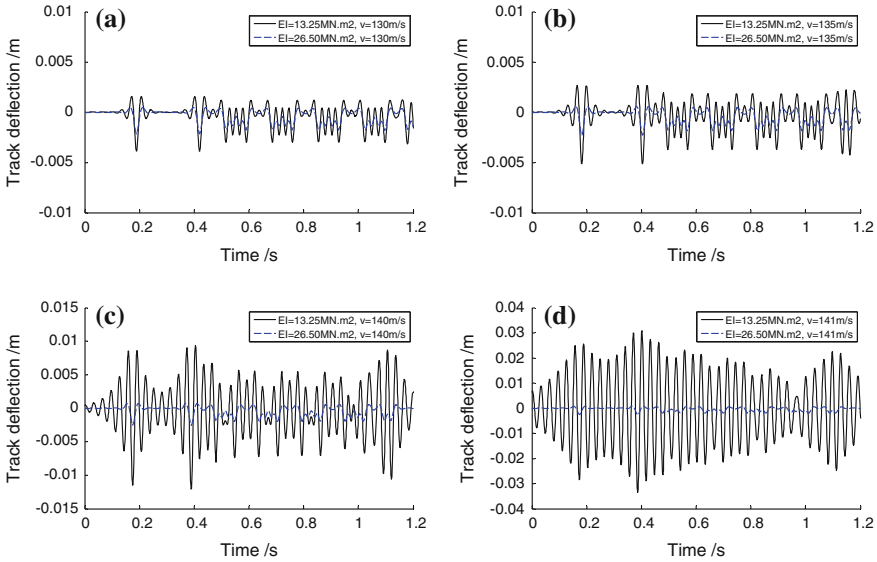

Fig. 2.4 The track deflections for $E_s = 50\,\mathrm{MN/m^2}$, **a** for train speed of 130 m/s, **b** for train speed of 135 m/s, **c** for train speed of 140 m/s and **d** for train speed of 141 m/s

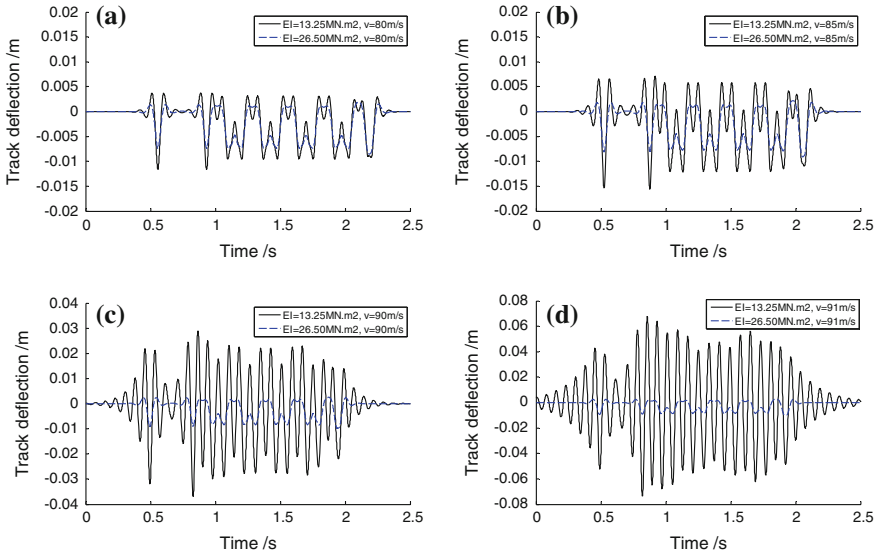

Fig. 2.5 The track deflections for $E_s = 10\,\mathrm{MN/m^2}$, **a** for train speed of 80 m/s, **b** for train speed of 85 m/s, **c** for train speed of 90 m/s and **d** for train speed of 91 m/s

(3) When the train speed is lower than the track critical velocity, the increase in rail flexural stiffness has not obvious effects on reducing track deformation, as shown in Figs. 2.4a, b and 2.5a, b. However, when the train speed approaches the track critical velocity, the increase in the rail flexural stiffness has significant effects on track deformation reduction, as shown in Figs. 2.4c, d and 2.5c, d.
(4) The rail flexural stiffness has certain effects on track vibration waveform and amplitude. When the rail flexural stiffness is small, the vibration waveform is multiple, and the amplitude is large and vice versa. When the train speed approaches the track critical velocity, this phenomenon is particularly obvious, as indicated in Figs. 2.4c, d and 2.5c, d. The more frequent the vibration is, the larger the amplitude is and the more likely it is for the ballast to come into liquefaction, which would reduce the stability of the track foundation.

2.2 Effects of Track Stiffness Abrupt Change on Track Vibration

In railway lines, there are a large number of bridges, grade crossings, and rigid culverts. In track transition from the subgrade to abutment, or grade crossing and/or culverts, there appears uneven track stiffness. In some cases, there would be track stiffness abrupt change. Experiments have shown that when the train moves through areas of stiffness abrupt change, additional dynamic action would be significantly induced resulting in large track deformation. The vehicle riding comfort would be damaged, or at worst, the train operation accident would be caused. There are abundant studies on uneven stiffness of railway track both at home and abroad [12–17], though with some findings, but are limited to experimental methods.

In this section, effects of track stiffness abrupt change on track vibration are investigated by the analytic method for dynamic analysis of track structure. By establishing the simplified analytic model, impacts of track irregularity, foundation stiffness, and train speed on track vibration are analyzed.

2.2.1 Track Vibration Model in Consideration of Track Irregularity and Stiffness Abrupt Change Under Moving Loads

To simplify the analysis, the analytic method is adopted to investigate the effects of track irregularity and stiffness abrupt change on track vibration under a moving wheelset load at constant speed V. The simplified analytic model is shown in Fig. 2.6. The coordinate origin is set at the point of stiffness abrupt change. On the left side of the origin, the track foundation stiffness is k_1, and the deflection is w_1;

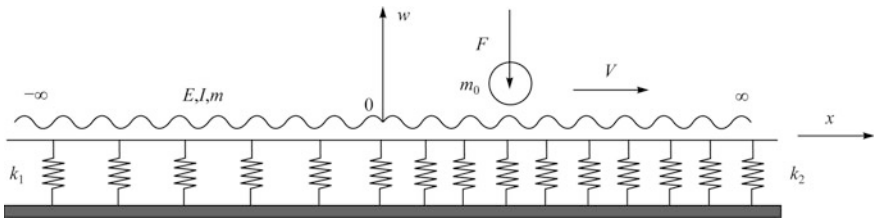

Fig. 2.6 Track vibration model in consideration of track irregularity and stiffness abrupt change under moving loads

on the right side of the origin, the track foundation stiffness is k_2, and the deflection is w_2. Taking w_1 for instance, according to D'Alembert's principle, the track vibration differential equation excluding damping is

$$EI\frac{\partial^4 w_1}{\partial x^4}+m\frac{\partial^2 w_1}{\partial t^2}+k_1 w_1=-\left(F+m_0\frac{\partial^2(w_1+\eta)}{\partial t^2}\right)\delta(x-Vt) \tag{2.17}$$

where E, I stand for track elasticity modulus and inertia moment around the horizontal axis; w is track vertical deflection; η is track irregularity; m is track mass per unit length; k_1 is track foundation stiffness, and F represents the moving wheelset load; m_0 is the wheelset mass; V is the wheelset moving speed, and δ is Dirac function.

Supposing the track irregularity η is a cosine function

$$\eta=a\left[1-\cos\frac{2\pi(x-Vt)}{l}\right] \tag{2.18}$$

In this function, a is the amplitude of track irregularity; l is the track irregularity wavelength.

Defining

$$\varepsilon_1^2=\frac{m}{4EI},\quad \gamma_1^4=\frac{k_1}{4EI} \tag{2.19}$$

equation (2.17) can be transformed into

$$\frac{\partial^4 w_1}{\partial x^4}+4\varepsilon_1^2\frac{\partial^2 w_1}{\partial t^2}+4\gamma_1^4 w_1=-\frac{1}{EI}\left(F+m_0\frac{\partial^2(w_1+\eta)}{\partial t^2}\right)\delta(x-Vt) \tag{2.20}$$

The solution for the above equation is related to $(x-Vt)$, in other words, $w_1=w_1(x-Vt)$. By introducing $z=x-Vt$, (2.20) can be changed into

$$\frac{\partial^4 w_1}{\partial z^4} + 4\varepsilon_1^2 V^2 \frac{\partial^2 w_1}{\partial z^2} + 4\gamma_1^4 w_1 = -\frac{1}{EI}\left(F + m_0 \frac{\partial^2 (w_1 + \eta)}{\partial t^2}\right)\delta(z) \tag{2.21}$$

The characteristic equation for (2.21) is

$$p^4 + 4\varepsilon_1^2 V^2 p^2 + 4\gamma_1^4 = 0 \tag{2.22}$$

The solution for the above characteristic equation is related to coefficient. In case $V < \frac{\gamma_1}{\varepsilon_1}$, Eq. (2.22) can be solved into

$$p = \pm\alpha_1 \pm j\beta_1 \tag{2.23}$$

where

$$\alpha_1 = \left(\gamma_1^2 - V^2\varepsilon_1^2\right)^{\frac{1}{2}}, \quad \beta_1 = \left(\gamma_1^2 + V^2\varepsilon_1^2\right)^{\frac{1}{2}} \tag{2.24}$$

Thus, the solution for (2.21) can be obtained as

$$w_1(z) = \mathrm{e}^{\alpha_1 z}(D_1 \cos\beta_1 z + D_2 \sin\beta_1 z) + \mathrm{e}^{-\alpha_1 z}(D_3 \cos\beta_1 z + D_4 \sin\beta_1 z) + \varphi_1(z) \tag{2.25}$$

where $\varphi_1(z)$ is related to external load. When $z = 0$, x is located at the wheel-rail contact point. When $z \neq 0$, $\varphi_1(z) = 0$; when $z \to -\infty$, w_1 should be finite value; therefore, $D_3 = D_4 = 0$, and Eq. (2.25) can be transformed into

$$w_1(z) = \mathrm{e}^{\alpha_1 z}(D_1 \cos\beta_1 z + D_2 \sin\beta_1 z) \quad z \leq 0 \tag{2.26}$$

where D_1, D_2 are undetermined coefficients associated with the boundary conditions.

Similarly, the track vibration differential equation on the right side of the coordinate origin is

$$EI\frac{\partial^4 w_2}{\partial x^4} + m\frac{\partial^2 w_2}{\partial t^2} + k_2 w_2 = -\left(F + m_0 \frac{\partial^2 (w_2 + \eta)}{\partial t^2}\right)\delta(x - Vt) \tag{2.27}$$

where w_2 is the vertical deflection of the right track, and k_2 is the right track foundation stiffness. Following the solution method of (2.17), Eq. (2.27) can be solved to obtain

$$w_2(z) = \mathrm{e}^{-\alpha_2 z}(D_3 \cos\beta_2 z + D_4 \sin\beta_2 z) \quad z \geq 0 \tag{2.28}$$

where

$$\alpha_2 = \left(\gamma_2^2 - V^2\varepsilon_2^2\right)^{\frac{1}{2}}, \quad \beta_2 = \left(\gamma_2^2 + V^2\varepsilon_2^2\right)^{\frac{1}{2}} \tag{2.29}$$

$$\varepsilon_2^2 = \frac{m}{4EI}, \quad \gamma_2^4 = \frac{k_2}{4EI} \tag{2.30}$$

D_3, D_4 are undetermined coefficients associated with the boundary conditions.

The four undetermined coefficients in (2.26) and (2.28) can be derived from the four boundary conditions when $z = 0$. They are

$$w_1|_{z=0} = w_2|_{z=0} \tag{2.31}$$

$$\left.\frac{\partial w_1}{\partial z}\right|_{z=0} = \left.\frac{\partial w_2}{\partial z}\right|_{z=0} \tag{2.32}$$

$$\left.\frac{\partial^2 w_1}{\partial z^2}\right|_{z=0} = \left.\frac{\partial^2 w_2}{\partial z^2}\right|_{z=0} \tag{2.33}$$

$$-\left.\frac{\partial^3 w_1}{\partial z^3}\right|_{z=0} + \left.\frac{\partial^3 w_2}{\partial z^3}\right|_{z=0} = -\left.\left(\frac{F}{EI} + m_0\frac{\partial^2(w_2+\eta)}{\partial t^2}\right)\right|_{z=0} \tag{2.34}$$

Substituting (2.26) and (2.28) into the above four boundary conditions, the following solutions can be obtained through redundant derivation [17, 18].

$$w_1(z) = \mathrm{e}^{\alpha_1 z}(C_1\cos\beta_1 z + C_2\sin\beta_1 z)C_3 \quad z<0 \tag{2.35}$$

$$w_2(z) = \mathrm{e}^{-\alpha_2 z}(C_1\cos\beta_2 z + \sin\beta_2 z)C_3 \quad z\geq 0 \tag{2.36}$$

where

$$C_1 = \frac{2\beta_2(\alpha_1+\alpha_2)}{(\alpha_1+\alpha_2)^2 + \beta_1^2 - \beta_2^2}$$

$$C_2 = -\frac{\beta_2\left[(\alpha_1+\alpha_2)^2 - \beta_1^2 + \beta_2^2\right]}{\beta_1\left[(\alpha_1+\alpha_2)^2 + \beta_1^2 - \beta_2^2\right]}$$

$$C_3 = -\frac{F + m_0 a\left(2\pi V/l\right)^2}{EI(G_1C_1 + G_2C_2 + G_3 + G)}$$

$$G = \frac{m_0V^2}{EI}\left[(\alpha_2^2 - \beta_2^2)C_1 - 2\alpha_2\beta_2\right]$$

$$G_1 = -\alpha_1^3 - \alpha_2^3 + 3\alpha_1\beta_1^2 + 3\alpha_2\beta_2^2$$

$$G_2 = -3\alpha_1^2\beta_1 + \beta_1^3$$

$$G_3 = 3\alpha_2^2\beta_2 - \beta_2^3$$

From (2.35) and (2.36), the track accelerations can be derived as follows:

$$\frac{\partial^2 w_1}{\partial t^2} = V^2 \mathrm{e}^{\alpha_1 z}\left\{\left[(\alpha_1^2 - \beta_1^2)C_1 + 2\alpha_1\beta_1 C_2\right]\cos\beta_1 z + \left[(\alpha_1^2 - \beta_1^2)C_2 - 2\alpha_1\beta_1 C_1\right]\sin\beta_1 z\right\}C_3 \quad z<0 \tag{2.37}$$

$$\frac{\partial^2 w_2}{\partial t^2} = V^2 \mathrm{e}^{-\alpha_2 z}\left\{\left[(\alpha_2^2 - \beta_2^2)C_1 - 2\alpha_2\beta_2\right]\cos\beta_2 z + \left[(\alpha_2^2 - \beta_2^2) + 2\alpha_2\beta_2 C_1\right]\sin\beta_2 z\right\}C_3 \quad z\geq 0 \tag{2.38}$$

Under multiple moving wheelset loads, the differential equation corresponding to (2.17) for track vibration is

$$EI\frac{\partial^4 w_1}{\partial x^4} + m\frac{\partial^2 w_1}{\partial t^2} + k_1 w_1 = -\sum_{i=1}^{N}\left(F_i - m_{0i}\frac{\partial^2(w_1+\eta)}{\partial t^2}\right)\delta(x - a_i - Vt) \tag{2.39}$$

where F_i is the moving load of the ith wheelset; m_{0i} is the mass of the ith wheelset; a_i is the distance between the first wheelset and the i th wheelset; N is the total number of the wheelsets.

The solution for (2.39) can be derived from the solution Eqs. (2.35) and (2.36) under a moving wheelset load through superposition principle.

2.2.1.1 Effects of Track Irregularity and Track Stiffness Abrupt Change on Track Vibration

It is verified that track vibration response is related to the track equivalent stiffness k_1, k_2, the rail flexural modulus EI, the track irregularity amplitude a, the wavelength l, the wheelset load F, the wheelset mass m_0, the wheelset moving speed V, and the track mass m per unit length. In calculating m, the mass of the rail, the sleeper, and the ballast should be included. In order to better probe into effects of track irregularity and track stiffness abrupt change on track vibration, the following analysis is conducted under two conditions of track regularity and irregularity (the periodic irregularity with wavelength $l = 2$ m and amplitude a = 1 mm) and in four cases of track stiffness ratio, namely $k_2/k_1 = 1$, $k_2/k_1 = 2$, $k_2/k_1 = 5$, and $k_2/k_1 = 10$. The track parameters under different conditions are as follows: the rail of 60 kg/m, the sleeper allocation of 1760 sleepers/km, the ballast thickness of

Table 2.2 Computational parameters

Cases	$k_1/(\mathrm{MN/m^2})$	$k_2/(\mathrm{MN/m^2})$	$EI/(\mathrm{MN\,m^2})$	$m/(\mathrm{kg/m})$	$m_0/(\mathrm{kg})$	$F/(\mathrm{KN})$
Case 1	k_2	118	13.25	2735	2000	170
Case 2	$\frac{k_2}{2}$	118	13.25	2735	2000	170
Case 3	$\frac{k_2}{5}$	118	13.25	2735	2000	170
Case 4	$\frac{k_2}{10}$	118	13.25	2735	2000	170

30 cm, the ballast shoulder breadth of 35 cm, the ballast density of 2000 kg/m^3, and the track foundation elasticity modulus $E_s = 100\ \mathrm{MN/m^2}$, as is clearly shown in Table 2.2.

2.2.1.2 Analysis of Track Vibration Under a Moving Wheelset Load

Track vibration is analyzed under a moving wheelset load at different speeds V = 60, 70, 80, and 90 m/s. Meanwhile, four kinds of track stiffness abrupt change and two conditions of track regularity and irregularity (the wavelength l = 2 m and amplitude a = 1 mm) are taken into account as well. Relationships between the track deflection and the total amplitude of acceleration with the wheelset moving speed are indicated in Figs. 2.7 and 2.8. The total amplitude of acceleration is defined as the difference between the maximum and the minimum of the vibratory magnitude.

2.2.1.3 Analysis of Track Vibration Induced by a High-Speed Train

Analysis of track vibration is carried out for a high-speed train passing at the speed V = 90 m/s. The train is marshaled by one TGV high-speed motor car and four

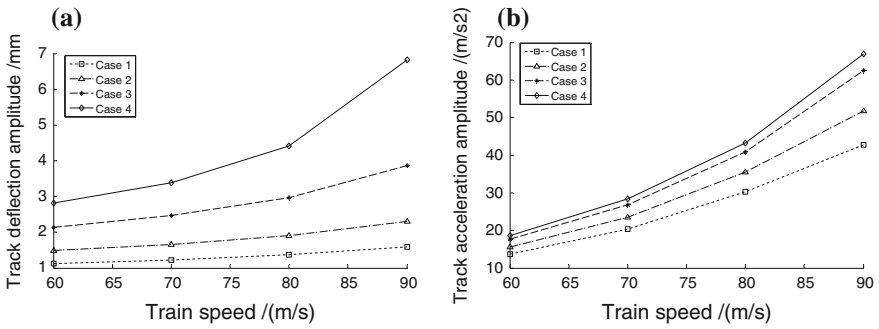

Fig. 2.7 The track deflection amplitude and the track acceleration amplitude for smooth track under a moving wheelset load: **a** The track deflection amplitude and **b** the track acceleration amplitude

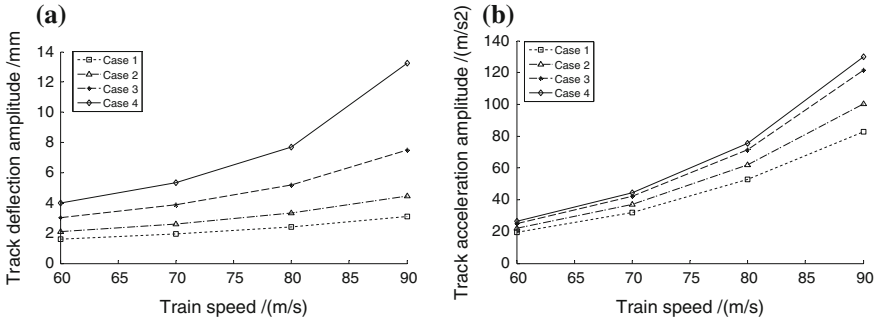

Fig. 2.8 The track deflection amplitude and the track acceleration amplitude for track irregularities ($a = 1$ mm) under a moving wheelset load: **a** the track deflection amplitude and **b** the track acceleration amplitude

TGV high-speed trailers (computational parameters for TGV high-speed motor car and trailers are noted in Chap. 6). The computational model is shown in Fig. 2.9. Four kinds of track stiffness abrupt change and two conditions of track regularity and irregularity (the wavelength $l = 2$ m and amplitude $a = 1$ mm) are taken into account for analyzing the track vibration. Computational results include the track deflection, velocity, acceleration, and time history curve of wheel-rail force at the point of stiffness abrupt change, as can be seen in Figs. 2.10, 2.11, 2.12 and 2.13. Figure 2.14 shows the dynamic coefficient curve for smooth track with different track stiffness ratio.

From the above computational results, conclusions can be drawn as follows [17, 18]:

(1) Track stiffness abrupt change has effects on track vibration. As is shown in Figs. 2.7, 2.8, 2.10 and 2.13, the bigger the difference of track stiffness ratio is, the larger the dynamic response is induced.
(2) For the fixed track stiffness ratio, the faster the train speed is, the larger the dynamic response of the structure is induced. This is clearly presented in Figs. 2.7 and 2.8.

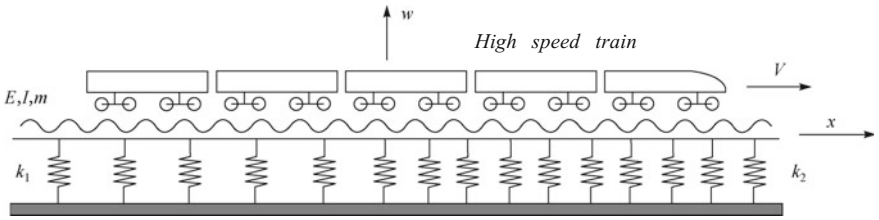

Fig. 2.9 Analysis model of the track vibration induced by a high-speed train

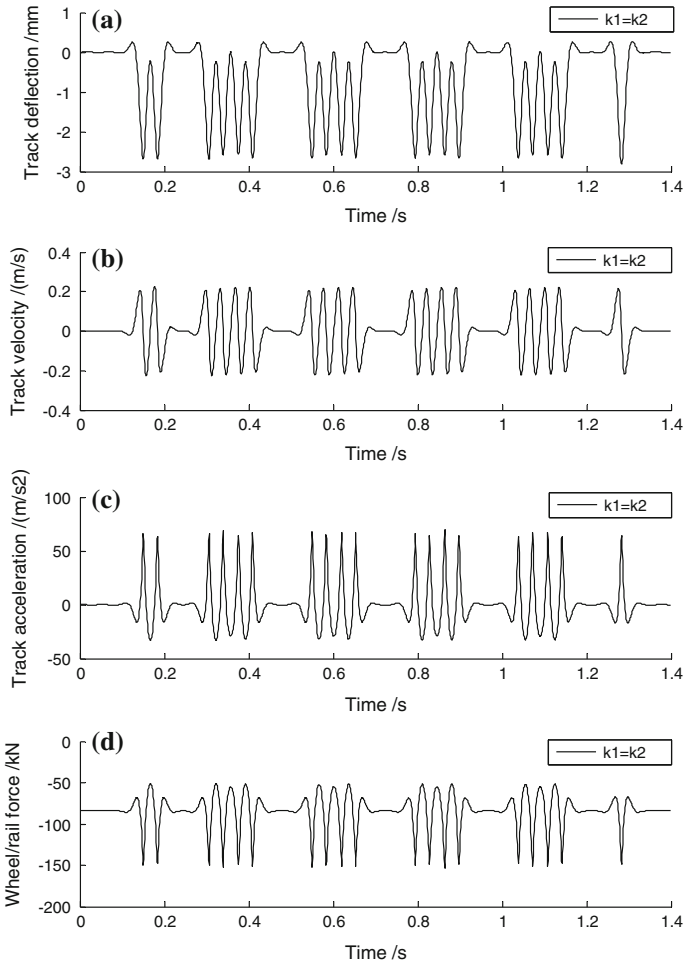

Fig. 2.10 Time history of the track deflection, velocity, and acceleration as well as the wheel-rail force at the point of stiffness abrupt change ($k_1 = k_2$, $a = 1$ mm)

(3) Track irregularity has significant impact on track vibration. The bigger the track irregularity amplitude is, the larger the dynamic response of the structure is induced.

(4) When track stiffness ratio $k_2/k_1 = 2$, $k_2/k_1 = 5$, and $k_2/k_1 = 10$, the total amplitude of the track deflection is 1.44, 2.42, and 4.27 times of those of the uniform track stiffness, and the total amplitude of the track velocity is 1.27, 1.84, and 2.73 times of those of the uniform track stiffness. In addition, the total amplitude of the track acceleration and the wheel-rail force is 1.18, 1.38, and 1.43 times of those of the uniform track stiffness. As for the acceleration and the wheel-rail force, the two parameters, which exert rather bigger influence on track structure, have greater effects on track vibration if the track

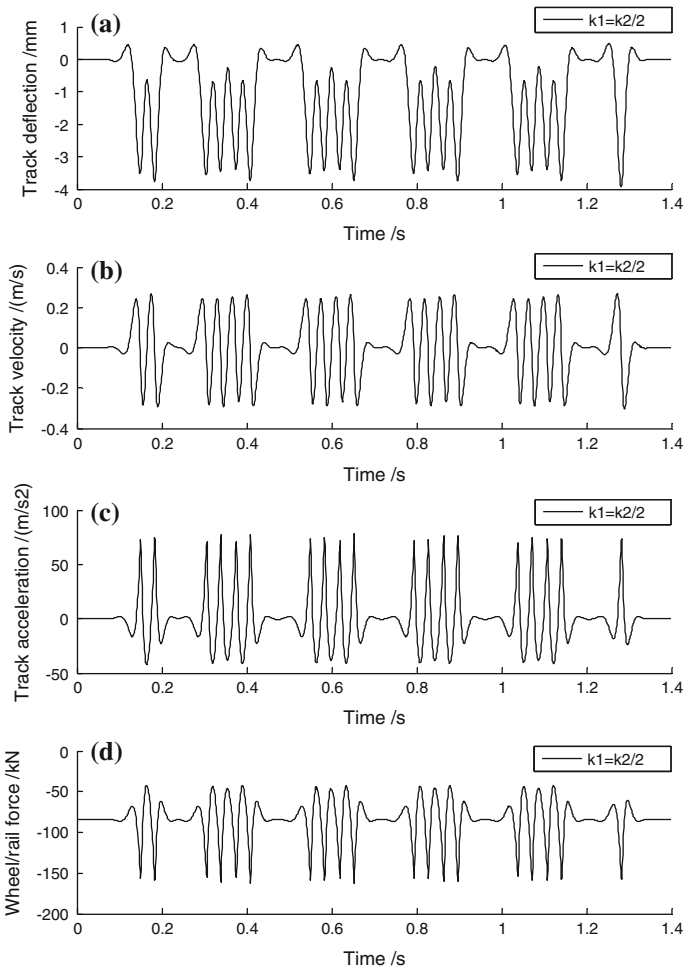

Fig. 2.11 Time history of the track deflection, velocity, and acceleration as well as the wheel-rail force at the point of stiffness abrupt change ($k_1 = \frac{k_2}{2}$, $a = 1$ mm)

stiffness difference is within the range of 5 times; their effects on track vibration are on the decrease if the track stiffness difference is over 5 times. These are illustrated in Figs. 2.7 and 2.8.

(5) The total amplitude represents the amplitude of structural vibration. The enlarged amplitude signifies the stronger structural vibration, which may cause subgrade liquefaction and reduce the stability of the structural foundation. When the track stiffness ratio reaches five times or more, the upper and lower oscillation waveform amplitude is approximate, which is harmful to track structural stability and should be avoided. These are illustrated in Figs. 2.12 and 2.13.

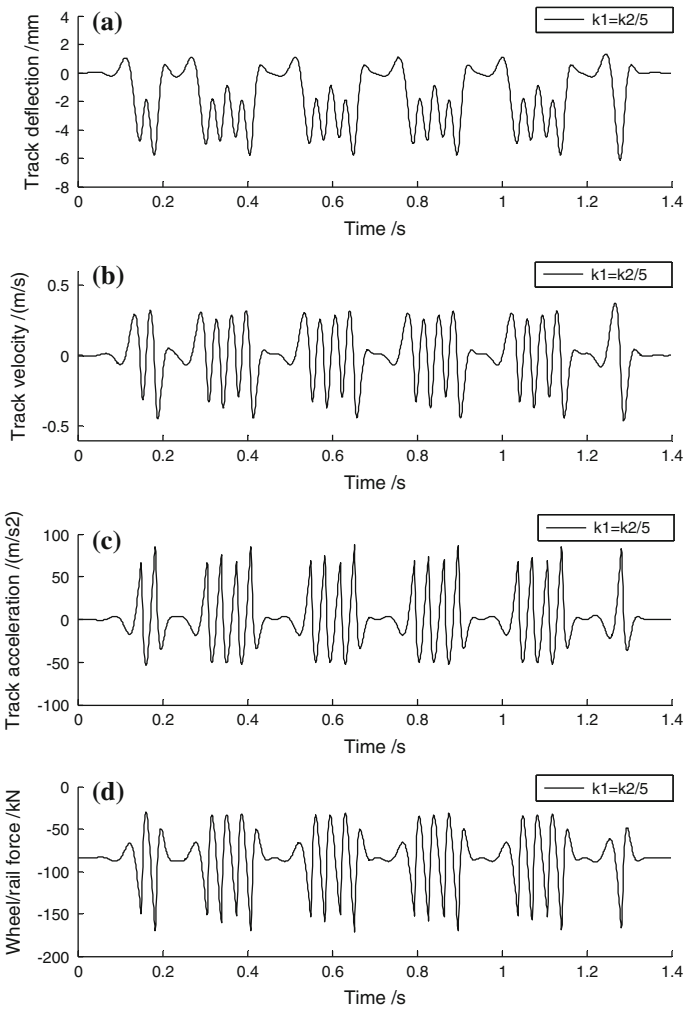

Fig. 2.12 Time history of the track deflection, velocity, and acceleration as well as the wheel-rail force at the point of stiffness abrupt change ($k_1 = k_2/5$, $a = 1$ mm)

2.2.2 The Reasonable Distribution of the Track Stiffness in Transition

The reasonable distribution of the track stiffness in transition should meet the following requirements:

(1) Ensure the equal track stiffness in track transition as much as possible.
(2) Make sure smooth transition of track stiffness if it is hard to guarantee the equal stiffness so that track dynamic deflection, acceleration, and wheel-rail

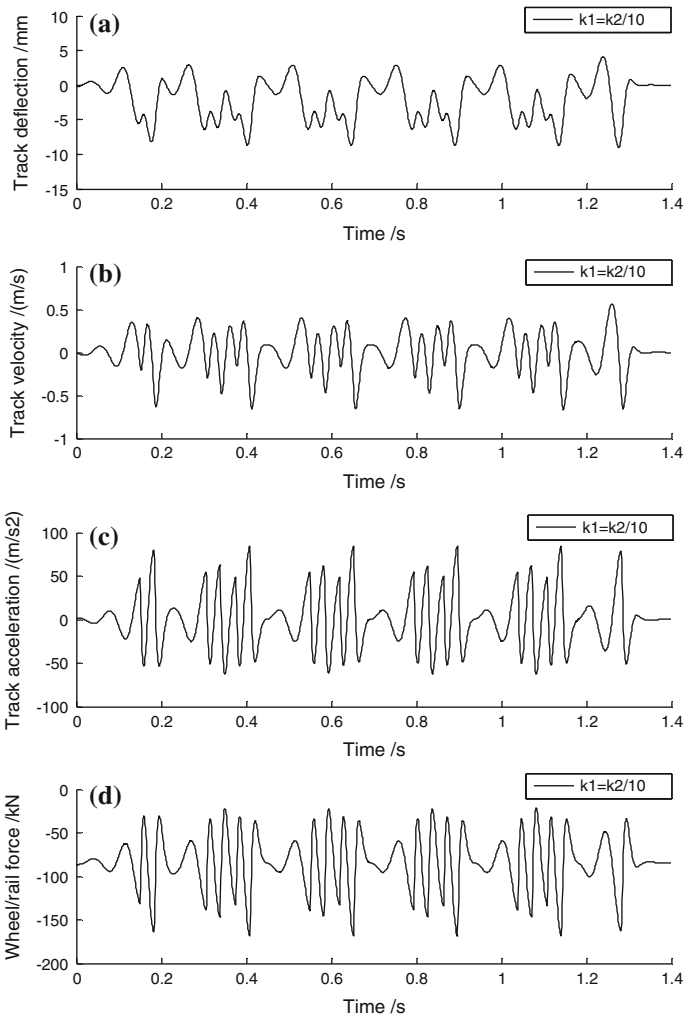

Fig. 2.13 Time history of the track deflection, velocity, and acceleration as well as the wheel-rail force at the point of stiffness abrupt change ($k_1 = \frac{k_2}{10}$, $a = 1$ mm)

contact force would not change too much, thus resulting in great impacts to track transition.

For smoothing track stiffness in transition, it is advisable to install elastic rail pad on sleepers at rigid zones or lay rubber layer or ballast under the sleepers in order to increase the elasticity of the related section. It is also feasible to increase the track foundation stiffness by use of long sleepers, guard rails at transition sections, and the concrete approach slab and bolster at bridgehead. Besides, for increasing the

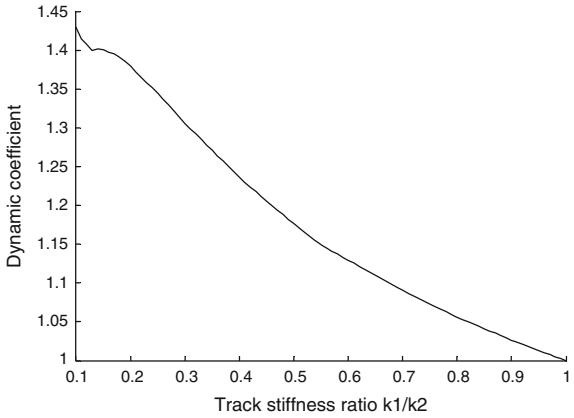

Fig. 2.14 The dynamic coefficient curve for smooth track with different track stiffness ratio

track stiffness, it is preferable to lay geosynthetic material on the ballast bottom, replace the sand layer with asphalt mortar, or adopt coarse ingredients filling and reinforced soil embankment. The distance for smooth transition of track stiffness depends on the train speed, which shows the faster the speed is, the longer the distance is [19].

According to results of Fig. 2.14, when $k_1/k_2 \geq 1/2$, the dynamic coefficient $\alpha = 1.17$. Based on this, the following suggestions are proposed for the design of the reasonable track stiffness in transition: (1) adopting the stratified reinforcement at the transition sections, usually 3–4 layers, for convenient construction. (2) The dynamic coefficient induced by train in track transition and the stiffness ratio of each layer should meet such conditions as $\alpha \leq 1.2$ and $1/2 \leq k_1/k_2 \leq 1$. (3) The distance of smooth transition for each layer is $l = 5 - 10$ m. When the train speed $V \leq 160$ km/h, then $l = 5$ m, and when the train speed $V > 160$ km/h, then $l = 10$ m. This is illustrated in Fig. 2.15.

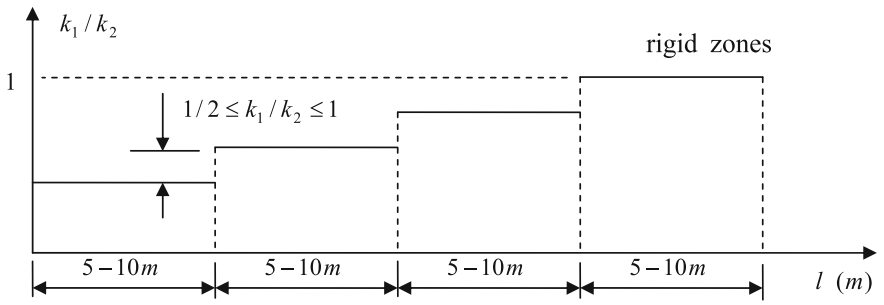

Fig. 2.15 Track stiffness at the stratified reinforcement transition section

References

1. Madshus C, Kaynia A (1998) High speed railway lines on soft ground: dynamic response of rail-embankment-soil system. NGI515177-1
2. Krylov VV (1994) On the theory of railway induced ground vibrations. J Phys 4(5):769–772
3. Krylov VV (1995) Generation of ground vibrations by super fast trains. Appl Acoust 44:149–164
4. Krylov VV, Dawson AR (2000) Rail movement and ground waves caused by high speed trains approaching track-soil critical velocities. Proc Instit Mech Eng Part F J Rail Rapid Transit 214 (F):107–116
5. Xiaoyan Lei, Xiaozhen Sheng (2004) Railway traffic noise and vibration. Science Press, Beijing
6. Belzer AI (1988) Acoustics of solids. Springer, Berlin
7. Vesic AS (1961) Beams on elastic subgrade and the Winkler hypothesis. In: Proceedings of the 5th international conference on soil mechanics and foundation engineering vol 1. Paris, France, pp 845–851
8. Heelis ME, Collop AC, Dawson AR, Chapman DN (1999) Transient effects of high speed trains crossing soft soil. In: Barends et al. (eds) Geotechnical engineering for transportation infrastructure. Balkema, Rotterdam, pp 1809–1814
9. Lei X, Sheng X (2008) Advanced studies in modern track theory, 2nd edn. China Railway Publishing House, Beijing
10. Lei X (2006) Study on critical velocity and vibration boom of track. Chin J Geotech Eng 28 (3):419–422
11. Lei X (2006) Study on ground waves and track vibration boom induced by high speed trains. J China Railway Soc 28(3):78–82
12. Kerr AD, Moroney BE (1995) Track transition problems and remedies. Bull 742-Am Railway Eng Assoc Bull 742:267–297
13. Kerr AD (1987) A method for determining the track modulus using a locomotive or car on multi-axle trucks. Proc Am Railway Eng Assoc 84(2):270–286
14. Kerr AD (1989) On the vertical modulus in the standard railway track analyses. Rail Int 235 (2):37–45
15. Moroney BE (1991) A study of railroad track transition points and problems. Master's thesis of University of Delaware, Newark
16. Lei X, Mao L (2004) Dynamic response analyses of vehicle and track coupled system on track transition of conventional high speed railway. J Sound Vib 271(3):1133–1146
17. Lei X (2006) Effects of abrupt changes in track foundation stiffness on track vibration under moving loads. J Vibr Eng 19(2):195–199
18. Lei X (2006) Influences of track transition on track vibration due to the abrupt change of track rigidity. China Railway Sci 27(5):42–45
19. Liu L, Lei X, Liu X Designing and dynamic performance evaluation of roadbed-bridge transition on existing railways. Railway Stand Des 504(1):9–10

Chapter 3
Fourier Transform Method for Dynamic Analysis of the Track Structure

High-speed railways have many advantages in medium- or long-distance transport, such as being fast, comfortable, energy-saving, and environment-friendly. Along with the increase of train speed, dynamic action of trains on tracks and ground is enlarged apparently, which would be more severe when train runs at high speed. Researches both at home and abroad [1–4] have revealed that when train speed approaches or exceeds some critical velocity, the ground surface waves would be induced by high-speed trains, causing strong vibration of the track structure, which might affect trains' safety and comfort or even worse result in the train derailment. Madshus and Kaynia [1] from Sweden noted this phenomenon in testing the high-speed train X2000, maintaining that coefficient of dynamic force during the strong vibration of track structure induced by the high-speed train was 10 times as much as the normal cases. Surface waves and strong track vibration induced by high-speed trains have drawn much concern from scholars and railway enterprises all over the world. Quite a number of studies concerning track vibration and surface waves have been emerging in recent years [1–7].

In this chapter, Fourier transform method is applied into dynamic analysis of the track structure. Firstly, Fourier transform is performed for the track structure vibration equation, and the vibration displacement is solved in the Fourier transform domain. Next, the vibration response of the track structure can be obtained through fast inverse discrete Fourier transform.

3.1 Model of Single-Layer Continuous Elastic Beam for the Track Structure

The single-layer continuous elastic beam model for the track structure is shown in Fig. 3.1. Its vibration differential equation is

X. Lei, *High Speed Railway Track Dynamics*,
DOI 10.1007/978-981-10-2039-1_3

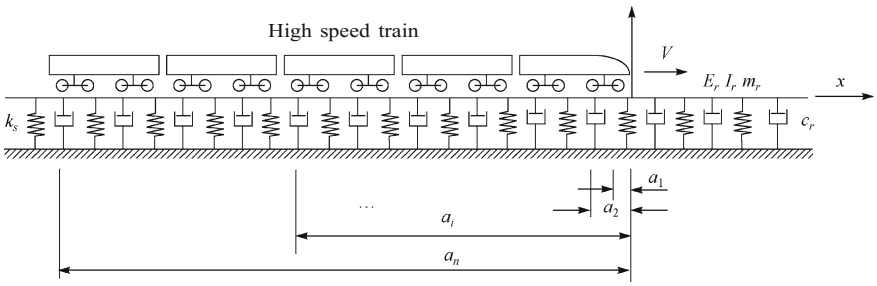

Fig. 3.1 Single-layer continuous elastic beam model of track structure

$$E_{\mathrm{r}}I_{\mathrm{r}}\frac{\partial^4 w}{\partial x^4}+m_{\mathrm{r}}\frac{\partial^2 w}{\partial t^2}+c_{\mathrm{r}}\frac{\partial w}{\partial t}+k_{\mathrm{s}}w=-\sum_{l=1}^{n}F_l\delta(x-Vt-a_l) \tag{3.1}$$

where $E_{\mathrm{r}}, I_{\mathrm{r}}$ are denoted as rail elasticity modulus and inertia moment around the horizontal axis; $w(x,t)$ represents rail vertical deflection and m_{r} is track mass per unit length; c_{r} is equivalent damping of track structure; k_{s} is track foundation equivalent stiffness, and δ is Dirac function; V is the train moving speed and F_l represents 1/2 axle load of the lth wheelset; a_l is the distance between the lth wheelset and the coordinate origin when $t=0$; n is the total number of wheelsets.

3.1.1 Fourier Transform

Fourier transform is defined as [8, 9]

$$W(\beta,t)=\int_{-\infty}^{\infty}w(x,t)\mathrm{e}^{-i\beta x}\mathrm{d}x \tag{3.2}$$

And the inverse Fourier transform is

$$w(x,t)=\frac{1}{2\pi}\int_{-\infty}^{\infty}W(\beta,t)\mathrm{e}^{i\beta x}\mathrm{d}\beta \tag{3.3}$$

where β is denoted as vibration wave number (unit: rad/m). Applying Fourier transform to (3.1), it has

$$E_{\mathrm{r}}I_{\mathrm{r}}(i\beta)^4W(\beta,t)+m_{\mathrm{r}}\frac{\partial^2W(\beta,t)}{\partial t^2}+c_{\mathrm{r}}\frac{\partial W(\beta,t)}{\partial t}+k_{\mathrm{s}}W(\beta,t)=-\sum_{l=1}^{n}F_l\mathrm{e}^{-i\beta(a_l+Vt)} \tag{3.4}$$

Supposing the vehicle load is harmonic excitation, namely $F_l=F_l\mathrm{e}^{i\Omega t}$, the right-hand item of (3.4) can be written into

$$\begin{aligned}-\sum_{l=1}^{M}F_l\mathrm{e}^{-i\beta(a_l+Vt)}\mathrm{e}^{i\Omega t}&=-\sum_{l=1}^{M}F_l\mathrm{e}^{-i\beta a_l}\mathrm{e}^{i(\Omega-\beta V)t}\\&=-\sum_{l=1}^{M}F_l\mathrm{e}^{-i\beta a_l}\mathrm{e}^{i\omega t}\\&=-\tilde{F}(\beta)\mathrm{e}^{i\omega t}=-\bar{F}(\beta,t)\end{aligned} \tag{3.5}$$

where

$$\bar{F}(\beta,t)=\tilde{F}(\beta)\mathrm{e}^{i\omega t},\quad \tilde{F}(\beta)=\sum_{l=1}^{n}F_l\mathrm{e}^{-i\beta a_l} \tag{3.6}$$

Due to the fact that the vehicle load is harmonic excitation, the displacement response can be expressed as

$$W(\beta,t)=\tilde{W}(\beta)\mathrm{e}^{i\omega t} \tag{3.7}$$

where $\omega=\Omega-\beta V$ and Ω is load excitation frequency (unit: rad/s).

Substituting (3.5) and (3.6) into (3.4), it yields

$$E_{\mathrm{r}}I_{\mathrm{r}}\beta^4\tilde{W}(\beta)-m_{\mathrm{r}}\omega^2\tilde{W}(\beta)+i\omega c_{\mathrm{r}}\tilde{W}(\beta)+k_{\mathrm{s}}\tilde{W}(\beta)=-\tilde{F}(\beta) \tag{3.8}$$

Equation (3.8) is solved into

$$\tilde{W}(\beta)=-\frac{\tilde{F}(\beta)}{E_{\mathrm{r}}I_{\mathrm{r}}\beta^4-m_{\mathrm{r}}(\Omega-\beta V)^2+ic_{\mathrm{r}}(\Omega-\beta V)+k_{\mathrm{s}}} \tag{3.9}$$

Substitute the above equation firstly into (3.7) and then (3.3) and carry out the inverse Fourier transform, namely

$$\tilde{w}(x,t)=\frac{1}{2\pi}\int_{-\infty}^{\infty}W(\beta,t)\mathrm{e}^{i\beta x}\mathrm{d}\beta \tag{3.10}$$

The final solution is

$$w(x,t) = \tilde{w}(x,t)\mathrm{e}^{i\varphi} \tag{3.11}$$

where φ is the phase angle of the complex displacement $\tilde{w}(x,t)$.

3.1.2 Inverse Discrete Fourier Transform

The inverse Fourier transform (3.10) can be expressed as

$$\tilde{w}(x,t) = \frac{1}{2\pi}\int_{-\infty}^{\infty} W(\beta,t)\mathrm{e}^{i\beta x}\mathrm{d}\beta \approx \frac{\Delta\beta}{2\pi}\sum_{j=-N+1}^{N} W(\beta_j,t)\mathrm{e}^{i\beta_j x} \tag{3.12}$$

Taking [10]

$$\beta_k = (k-N)\Delta\beta - \frac{\Delta\beta}{2}, \quad k = 1,2,\ldots,2N \tag{3.13}$$

And substituting (3.13) into (3.12), it has

$$\tilde{w}(x_m,t) \approx \frac{\Delta\beta}{2\pi}\sum_{k=1}^{2N} W(\beta_k,t)\mathrm{e}^{i\beta_k x_m} \tag{3.14}$$

where

$$x_m = (m-N)\Delta x, \quad m = 1,2,\ldots,2N \tag{3.15}$$

and

$$\Delta x\Delta\beta = \Delta x\frac{2\pi}{L} = \frac{L}{2N}\frac{2\pi}{L} = \frac{\pi}{N} \tag{3.16}$$

where L is spatial period in $\left(-\frac{L}{2}, \frac{L}{2}\right)$.

Thus, there is

$$\Delta x = \frac{\pi}{N\Delta\beta}$$

Hence,

$$\beta_k x_m = -\left(N-\frac{1}{2}\right)(m-N)\frac{\pi}{N} + (k-1)(m-N)\frac{\pi}{N} \tag{3.17}$$

Substituting (3.17) into (3.14), then

$$\tilde{w}(x_m,t) \approx \frac{\Delta\beta}{2\pi} e^{-i\left(N-\frac{1}{2}\right)(m-N)\pi/N} \sum_{k=1}^{2N} W(\beta_k,t) e^{i(k-1)(m-N)\pi/N}. \tag{3.18}$$

3.1.3 Definition of Inverse Discrete Fourier Transform in MATLAB

The inverse discrete Fourier transform in MATLAB is defined as follows:

$$\tilde{w}_1(x_j,t) = \frac{1}{2N} \sum_{k=1}^{2N} W(\beta_k,t) e^{i(k-1)(j-1)\pi/N} \tag{3.19}$$

After the inverse discrete Fourier transform by use of MATLAB software, it is necessary to reorder the results. The relationship between the reordered results $\widehat{w}(x_m,t)$ and the calculated results $\tilde{w}_1(x_j,t)$ in MATLAB can be summarized as follows:

(1) When j is within the range of $1 - (N + 1)$, $m = j + N - 1$ is modified, that is,

$$\widehat{w}(x_m,t) = \widehat{w}\left(x_{j+N-1},t\right) = \tilde{w}_1\left(x_j,t\right) \tag{3.20a}$$

Hence, there derive

$$\begin{aligned} &\widehat{w}(x_N,t) = \tilde{w}_1(x_1,t) \\ &\widehat{w}(x_{N+1},t) = \tilde{w}_1(x_2,t) \\ &\cdots \\ &\widehat{w}(x_{2N},t) = \tilde{w}_1(x_{N+1},t) \end{aligned}$$

(2) When j is within the range of $(N + 2) - 2N$, $m = j - N - 1$ is modified, that is,

$$\widehat{w}(x_m,t) = \widehat{w}\left(x_{j-N-1},t\right) = \tilde{w}_1\left(x_j,t\right) \tag{3.20b}$$

Thus, there derive

$$\begin{aligned}\widehat{w}(x_1,t) &= \tilde{w}_1(x_{N+2},t)\\ \widehat{w}(x_2,t) &= \tilde{w}_1(x_{N+3},t)\\ &\cdots\\ \widehat{w}(x_{N-1},t) &= \tilde{w}_1(x_{2N},t)\end{aligned}$$

Comparing (3.18) and (3.19), it has

$$\tilde{w}(x_m,t) \approx \frac{\Delta\beta \cdot N}{\pi} \mathrm{e}^{-i\left(N-\frac{1}{2}\right)(m-N)\pi/N} \widehat{w}(x_m,t) \tag{3.21}$$

Substituting (3.21) into (3.11), and there is

$$w(x_m,t) = \tilde{w}(x_m,t)\mathrm{e}^{i(\varphi+\Omega t)} \tag{3.22}$$

where φ is the phase angle of the complex displacement $\tilde{w}(x_m,t)$.

3.2 Model of Double-Layer Continuous Elastic Beam for the Track Structure

Slab track structure in tunnel can be simplified into a double-layer continuous elastic beam model, as is shown in Fig. 3.2. Its vibration differential equation is

$$\begin{aligned}&E_\mathrm{r}I_\mathrm{r}\frac{\partial^4 w}{\partial x^4} + m_\mathrm{r}\frac{\partial^2 w}{\partial t^2} + c_\mathrm{r}\left(\frac{\partial w}{\partial t} - \frac{\partial y}{\partial t}\right) + k_\mathrm{p}(w-y) = -\sum_{l=1}^{n} F_l\delta(x-Vt-a_l)\\ &E_\mathrm{s}I_\mathrm{s}\frac{\partial^4 y}{\partial x^4} + m_\mathrm{s}\frac{\partial^2 y}{\partial t^2} + c_\mathrm{s}\frac{\partial y}{\partial t} - c_\mathrm{r}\left(\frac{\partial w}{\partial t} - \frac{\partial y}{\partial t}\right) + k_\mathrm{s}y - k_\mathrm{p}(w-y) = 0\end{aligned} \tag{3.23}$$

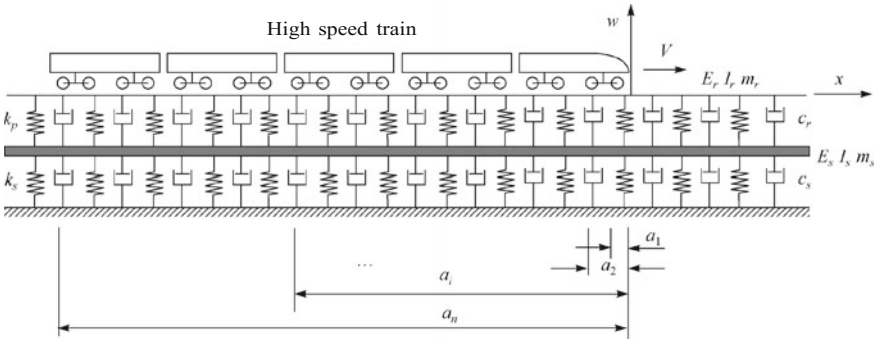

Fig. 3.2 Double-layer continuous elastic beam model of track structure

In this equation, E_r, I_r are denoted as rail elasticity modulus and inertia moment around the horizontal axis; $w(x,t)$ represents rail vertical deflection; E_s, I_s are track slab elasticity modulus and inertia moment around the horizontal axis; $y(x,t)$ is track slab vertical deflection; m_r is rail mass per unit length and m_s is track slab mass per unit length; c_r is the rail pad and fastener damping; k_p is the rail pad and fastener stiffness; c_s represents damping of CAM (cement asphalt mortar) or track slab foundation and k_s represents stiffness of CAM (cement asphalt mortar) or track slab foundation. Other parameters are specified in Eq. (3.1).

Perform the Fourier transform for (3.23) and suppose

$$\begin{aligned} F(\beta,t) &= \tilde{F}(\beta)\mathrm{e}^{i\omega t} \\ W(\beta,t) &= \tilde{W}(\beta)\mathrm{e}^{i\omega t} \\ Y(\beta,t) &= \tilde{Y}(\beta)\mathrm{e}^{i\omega t} \end{aligned} \tag{3.24}$$

where

$$\tilde{F}(\beta) = \sum_{l=1}^{M} F_l \mathrm{e}^{-i\beta a_l}$$

Then, there derives

$$E_r I_r \beta^4 \tilde{W} - m_r \omega^2 \tilde{W} + i\omega c_r\left(\tilde{W} - \tilde{Y}\right) + k_p\left(\tilde{W} - \tilde{Y}\right) = -\tilde{F} \tag{3.25}$$

$$E_s I_s \beta^4 \tilde{Y} - m_s \omega^2 \tilde{Y} + i\omega c_s \tilde{Y} - i\omega c_r\left(\tilde{W} - \tilde{Y}\right) + k_s \tilde{Y} - k_p\left(\tilde{W} - \tilde{Y}\right) = 0 \tag{3.26}$$

Through the simultaneous solution for both (3.25) and (3.26), there are

$$\tilde{W}(\beta) = -\frac{A}{AB - C^2}\tilde{F}(\beta) \tag{3.27}$$

$$\tilde{Y}(\beta) = \frac{C}{A}\tilde{W}(\beta) \tag{3.28}$$

where

$$\begin{aligned} A &= E_s I_s \beta^4 - m_s \omega^2 + i\omega(c_s + c_r) + k_s + k_p \\ B &= E_r I_r \beta^4 - m_r \omega^2 + i\omega c_r + k_p \\ C &= i\omega c_r + k_p \end{aligned} \tag{3.29}$$

Substitute (3.27) and (3.28) into (3.24) and perform the inverse Fourier transform, and there are

$$\tilde{w}(x,t) = \frac{1}{2\pi}\int_{-\infty}^{\infty} W(\beta,t)\mathrm{e}^{i\beta x}\mathrm{d}\beta \tag{3.30}$$

$$\tilde{y}(x,t) = \frac{1}{2\pi}\int_{-\infty}^{\infty} Y(\beta,t)\mathrm{e}^{i\beta x}\mathrm{d}\beta \tag{3.31}$$

Finally, the solutions are obtained as follows:

$$w(x,t) = \tilde{w}(x,t)\mathrm{e}^{i(\varphi_w+\Omega t)} \tag{3.32}$$

$$y(x,t) = \tilde{y}(x,t)\mathrm{e}^{i\left(\varphi_y+\Omega t\right)} \tag{3.33}$$

where φ_w and φ_y are the phase angles for the complex displacements $\tilde{w}(x,t)$ and $\tilde{y}(x,t)$, respectively.

3.3 Analysis of High-Speed Railway Track Vibration and Track Critical Velocity

Based on the models of the single-layer and the double-layer continuous elastic beam for the track structure, dynamic analyses of the track structure for high-speed railways are carried out, and calculation method for the critical velocity of track structure is put forward.

3.3.1 Analysis of the Single-Layer Continuous Elastic Beam Model

Track critical velocity refers to a certain velocity which induces strong vibration of track structure as soon as the train speed reaches it. For the single-layer continuous elastic beam model of track structure, the track critical velocity c_{crit} is given in (2.6) of Chap. 2, that is,

$$c_{\mathrm{crit}} = \sqrt[4]{\frac{4k_{\mathrm{s}}EI}{m_{\mathrm{r}}^2}} \tag{3.34}$$

The critical velocity of track structure is in relation to track foundation equivalent stiffness k_s, rail flexural modulus EI, and track mass m_r per unit length [3, 4]. For single-layer continuous elastic beam model, mass of the rail, sleeper, and ballast should be included in calculating m_r.

Track foundation equivalent stiffness k_s and track foundation elasticity modulus are related in the following way [11].

$$k_s = \frac{0.65E_s}{1-\upsilon_s^2}\sqrt[12]{\frac{E_s B^4}{EI}} \tag{3.35}$$

where E_s refers to track foundation elasticity modulus (unit: $\mathrm{MN/m^2}$). υ_s is Poisson's ratio; B is sleeper length, usually 2.5–2.6 m; EI is rail flexural modulus (unit: $\mathrm{MN \times m^2}$). Generally, the track foundation elasticity modulus E_s is $50-100\,\mathrm{MN/m^2}$ approximately; for the soft foundation, $E_s = 10\,\mathrm{MN/m^2}$ or even lower.

Now the track vibration is examined in details for the high-speed train running at different speeds, as is shown in Fig. 3.2. Suppose the train is marshaled by one TGV high-speed motor car and 4 TGV high-speed trailers (computational parameters for TGV high-speed motor car and trailers are given in Chap. 6). Track parameters are the continuously welded rail of 60 kg/m, the rail flexural modulus $EI = 2 \times 6.625\,\mathrm{MN\,m^2}$, the sleeper allocation of 1760 sleepers/km, sleeper length of 2.6 m, ballast thickness of 35 cm, ballast shoulder breadth of 50 cm, and ballast density of $2000\,\mathrm{kg/m^3}$. By use of Eq. (3.34) and Fourier transform, the track critical velocities are calculated and results are compared in Table 3.1. Figures 3.3 and 3.5 denote the corresponding maximum track vibration deflections for different train speed when $E_s = 2 \times 50\,\mathrm{MN/m^2}$ and $E_s = 2 \times 10\,\mathrm{MN/m^2}$. Figures 3.4 and 3.6 present the rail deflections in the corresponding Fourier domain when $E_s = 2 \times 50\,\mathrm{MN/m^2}$, $V = 149\,\mathrm{m/s}$ and $E_s = 2 \times 10\,\mathrm{MN/m^2}$, $V = 97\,\mathrm{m/s}$. These two figures also show effects of track equivalent damping on track vibration wave distribution along the track coordinate. From these figures, it can be found that in case of soft subgrade, the track critical velocity might decrease, namely $c_{crit} = 97\,\mathrm{m/s} = 349\,\mathrm{km/h}$, which is easily exceeded by high-speed trains, thus inducing strong track vibration.

Table 3.1 Track parameters and the minimum track critical velocity (single-layer continuous elastic beam model)

Parameters	$E_s/(\mathrm{MN/m^2})$	$c_r/(\mathrm{kN\,s/m^2})$	$m_r/(\mathrm{kg/m})$	$F_l/(\mathrm{kN})$	$c_{crit}/(\mathrm{m/s})$ Fourier transform results	$c_{crit}/(\mathrm{m/s})$ Equation (3.34)
Clayey soil subgrade	2 × 50	0	3600	85	149	148.5
Soft subgrade	2 × 10	0	3600	85	97	96.0

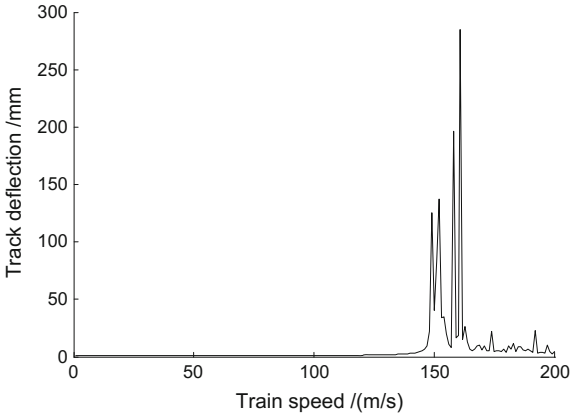

Fig. 3.3 The corresponding maximum track vibration deflection for different train speeds ($E_s = 2 \times 50\,\mathrm{MN/m^2}$)

3.3.1.1 Analysis of Double-Layer Continuous Elastic Beam Model

Now let us analyze effects of track parameters on track critical velocity and track vibration based on the model shown in Fig. 3.2. Analyses are carried out for the following six cases:

Case 1 Effect of rail pad and fastener stiffness $k_p = 2 \times 150,\ 2 \times 100,\ 2 \times 50,\ 2 \times 25\,\mathrm{MN/m^2}$ on track critical velocity ($E_s = 2 \times 50\,\mathrm{MN/m^2}$; $c_r = c_s = 0$), respectively;

Case 2 Effect of track foundation stiffness $E_s = 2 \times 100,\ 2 \times 50,\ 2 \times 10,\ 2 \times 2\,\mathrm{MN/m^2}$ on track critical velocity ($k_p = 2 \times 100\,\mathrm{MN/m^2}$; $c_r = c_s = 0$), respectively;

Case 3 Effect of rail pad and fastener stiffness $k_p = 2 \times 100,\ 2 \times 50,\ 2 \times 25,\ 2 \times 5\,\mathrm{MN/m^2}$ on track vibration ($E_s = 2 \times 50\,\mathrm{MN/m^2}$; $c_r = c_s = 2 \times 50\,\mathrm{kN\,s/\,m^2}$; $V = 149\,\mathrm{m/s}$), respectively;

Case 4 Effect of track foundation stiffness $E_s = 2 \times 100,\ 2 \times 50,\ 2 \times 10,\ 2 \times 2\,\mathrm{MN/m^2}$ on track vibration ($k_p = 2 \times 100\,\mathrm{MN/m^2}$; $c_r = c_s = 2 \times 50\,\mathrm{kN\,s/m^2}$; $V = 149\,\mathrm{m/s}$), respectively;

Case 5 Effect of rail pad and fastener damping $c_r = 0,\ 2 \times 25,\ 2 \times 50,\ 2 \times 100\,\mathrm{kN\,s/m^2}$ on track vibration ($E_s = 2 \times 50\,\mathrm{MN/m^2}$; $k_p = 2 \times 100\,\mathrm{MN/m^2}$; $c_s = 2 \times 50\,\mathrm{kN\,s/m^2}$; $V = 149\,\mathrm{m/s}$), respectively;

Case 6 Effect of track foundation damping $c_s = 2 \times 5,\ 2 \times 25,\ 2 \times 50,\ 2 \times 100\,\mathrm{kN\,s/m^2}$ on track vibration ($E_s = 2 \times 50\,\mathrm{MN/m^2}$, $k_p = 2 \times 100\,\mathrm{MN/m^2}$, $c_r = 2 \times 50\,\mathrm{kN\,s/m^2}$, $V = 149\,\mathrm{m/s}$), respectively.

The computational parameters and the results are presented in Tables 3.2 and 3.3. Figures 3.7 and 3.8 illustrate the effects of the rail pad and fastener stiffness and the track foundation stiffness on track critical velocity, respectively. Figures 3.9, 3.10, 3.11 and 3.12 show the effects of the rail pad and fastener stiffness, the track foundation stiffness, the rail pad and fastener damping, and

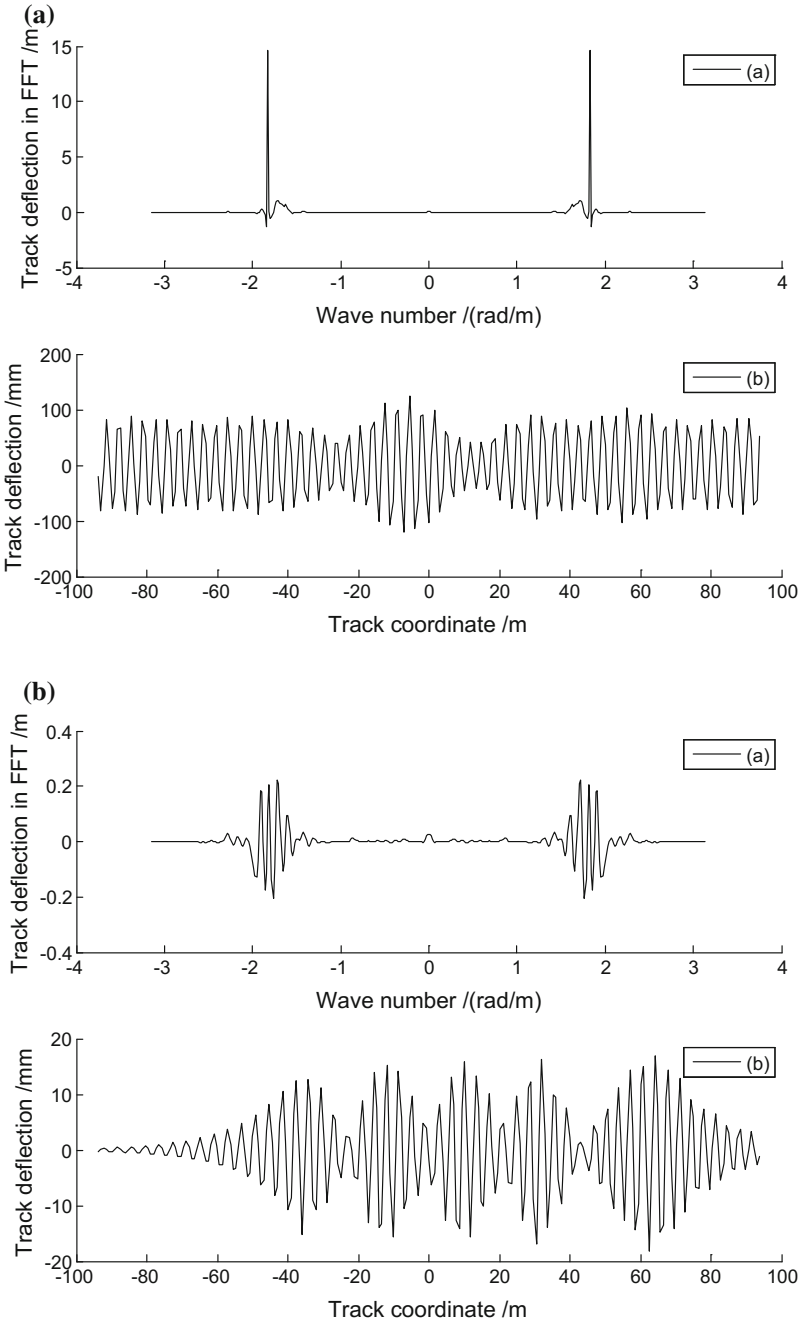

Fig. 3.4 Effects of damping on track deflection ($E_s = 2 \times 50\,\mathrm{MN/m^2}$, $V = 149\,\mathrm{m/s}$). **a** $c_r = 0$. **b** $c_r = 2 \times 5\,\mathrm{kN\,s/m^2}$. **c** $c_r = 2 \times 25\,\mathrm{kN\,s/m^2}$. **d** $c_r = 2 \times 50\,\mathrm{kN\,s/m^2}$

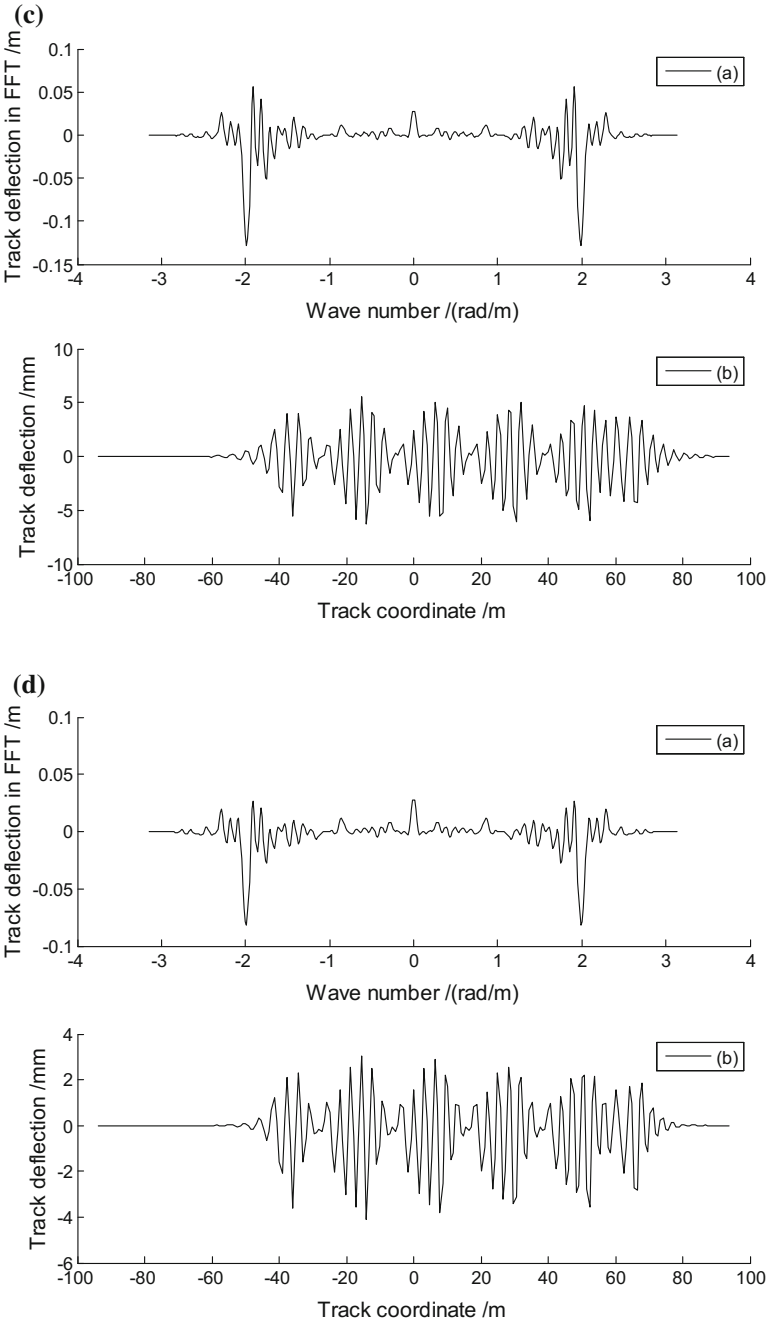

Fig. 3.4 (continued)

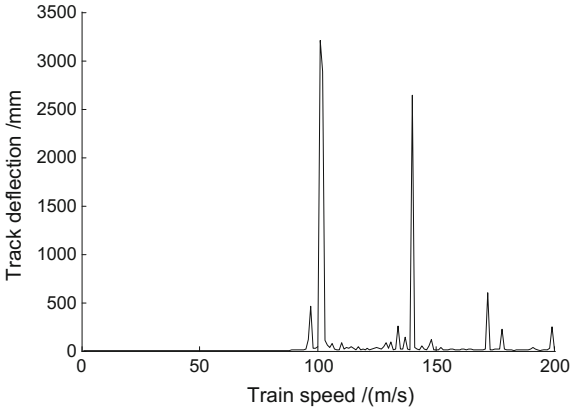

Fig. 3.5 The corresponding maximum track vibration deflection for different train speeds ($E_s = 2 \times 10\,\mathrm{MN/m^2}$)

the track foundation damping on track vibration, respectively. Based on the calculated results, some conclusions are drawn as follows [12]:

(1) Effect of the rail pad and fastener stiffness on track critical velocity is random, as is shown in Table 3.2 and Fig. 3.7.
(2) Track foundation stiffness has significant effects on track critical velocity. The track critical velocity increases with the increase of the track foundation stiffness, as is shown in Table 3.3 and Fig. 3.8.
(3) Effect of the rail pad and fastener stiffness on track vibration is not obvious, as is shown in Fig. 3.9.
(4) Track foundation stiffness has effects on track vibration. Increase of the track foundation stiffness is beneficial for track stability.
(5) The rail pad and fastener damping and the track foundation damping are sensitive to track vibration. Damping may decrease the occurrence of strong track vibration. But when there is c_r (or c_s), change of c_s (or c_r) does not affect track vibration much.
(6) When track foundation stiffness E_s remains unchanged, the minimum track critical velocities calculated by the single-layer and the double-layer continuous elastic beam model as well as Eq. (3.34) are almost the same, as is shown in Tables 3.1, 3.2 and 3.3. To simplify the calculation, it is suggested that the formula (3.34) can be employed to calculate the minimum critical velocity for the track structure.

Usually there are numerous critical velocities for the track structure and it is the minimum track critical velocity that should be noted in engineering projects. The minimum track critical velocity might be low in the condition of soft subgrade, which is easily exceeded by high-speed trains and accordingly causes strong track vibration or derailment. It should also be pointed out that the track critical velocity is difficult to be obtained through the analytic method for double-layer continuous elastic beam model.

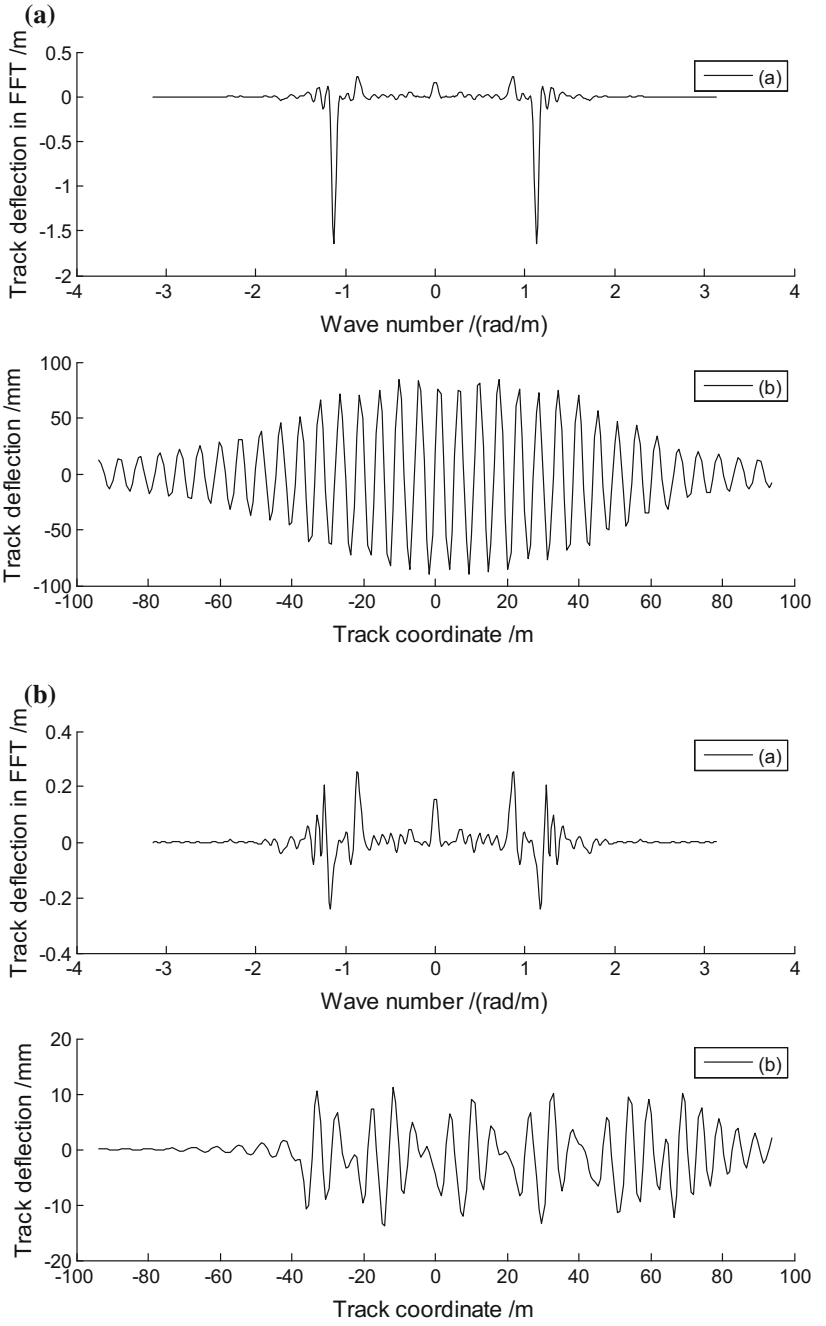

Fig. 3.6 Effects of damping on track deflection ($E_s = 2 \times 10\,\mathrm{MN/m^2}$, $V = 97\,\mathrm{m/s}$). **a** $c_r = 0$. **b** $c_r = 2 \times 5\,\mathrm{kN\,s/m^2}$. **c** $c_r = 2 \times 25\,\mathrm{kN\,s/m^2}$. **d** $c_r = 2 \times 50\,\mathrm{kN\,s/m^2}$

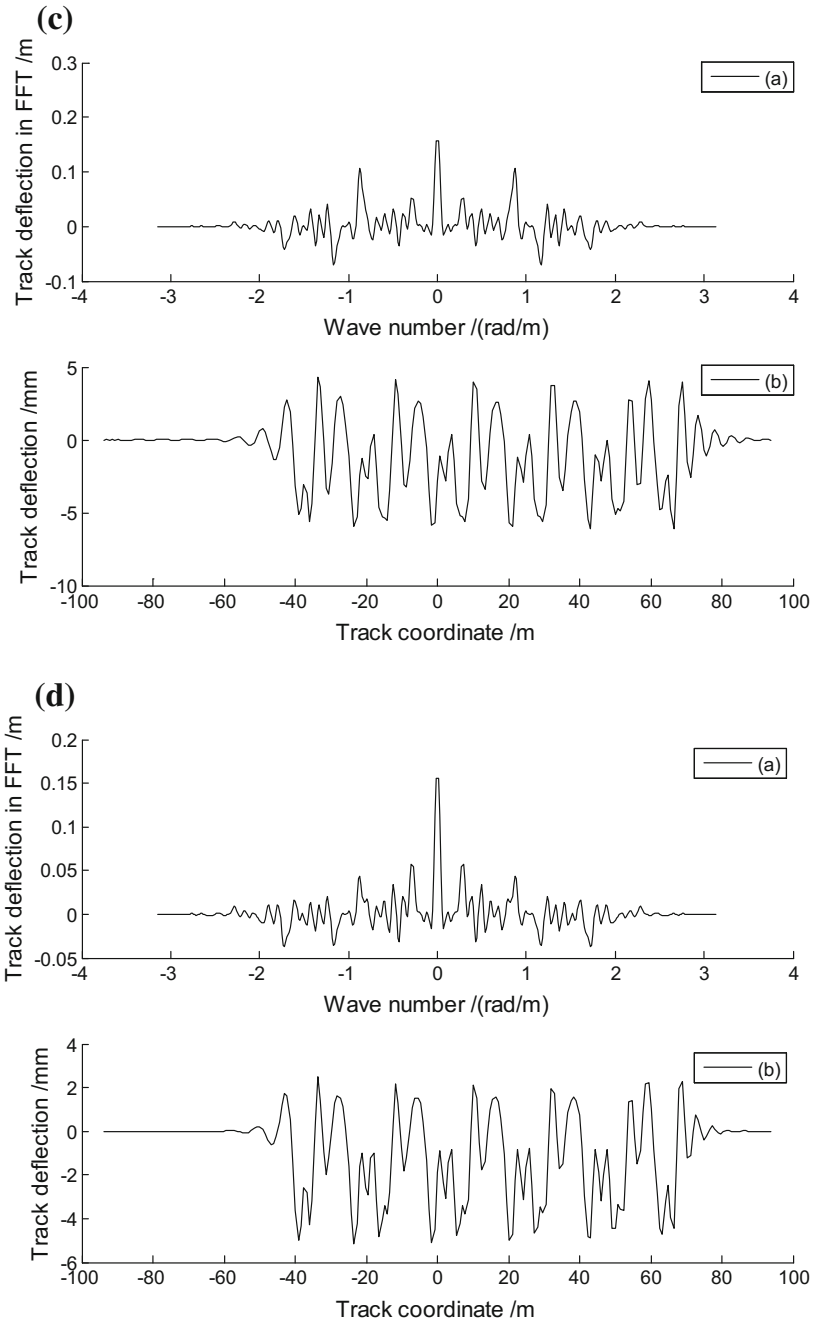

Fig. 3.6 (continued)

Table 3.2 Track parameters and the minimum track critical velocity (Case 1)

Parameters	$k_p/(\mathrm{MN/m^2})$	$E_s/(\mathrm{MN/m^2})$	$c_r/(\mathrm{kN\,s/m^2})$	$c_s/(\mathrm{kN\,s/m^2})$	$m_r/(\mathrm{kg/m})$	$m_t/(\mathrm{kg/m})$	$c_{crit}/(\mathrm{m/s})$
Case 1	2 × 150	2 × 50	0	0	120	3480	139
	2 × 100						149
	2 × 50						129
	2 × 25						123

Table 3.3 Track parameters and the minimum track critical velocity (Case 2)

Parameters	$E_s/(\mathrm{MN/m^2})$	$k_p/(\mathrm{MN/m^2})$	$c_r/(\mathrm{kN\,s/m^2})$	$c_s/(\mathrm{kN\,s/m^2})$	$m_r/(\mathrm{kg/m})$	$m_t/(\mathrm{kg/m})$	$c_{crit}/(\mathrm{m/s})$
Case 2	2 × 100	2 × 100	0	0	120	3480	158
	2 × 50						148
	2 × 10						97
	2 × 2						83

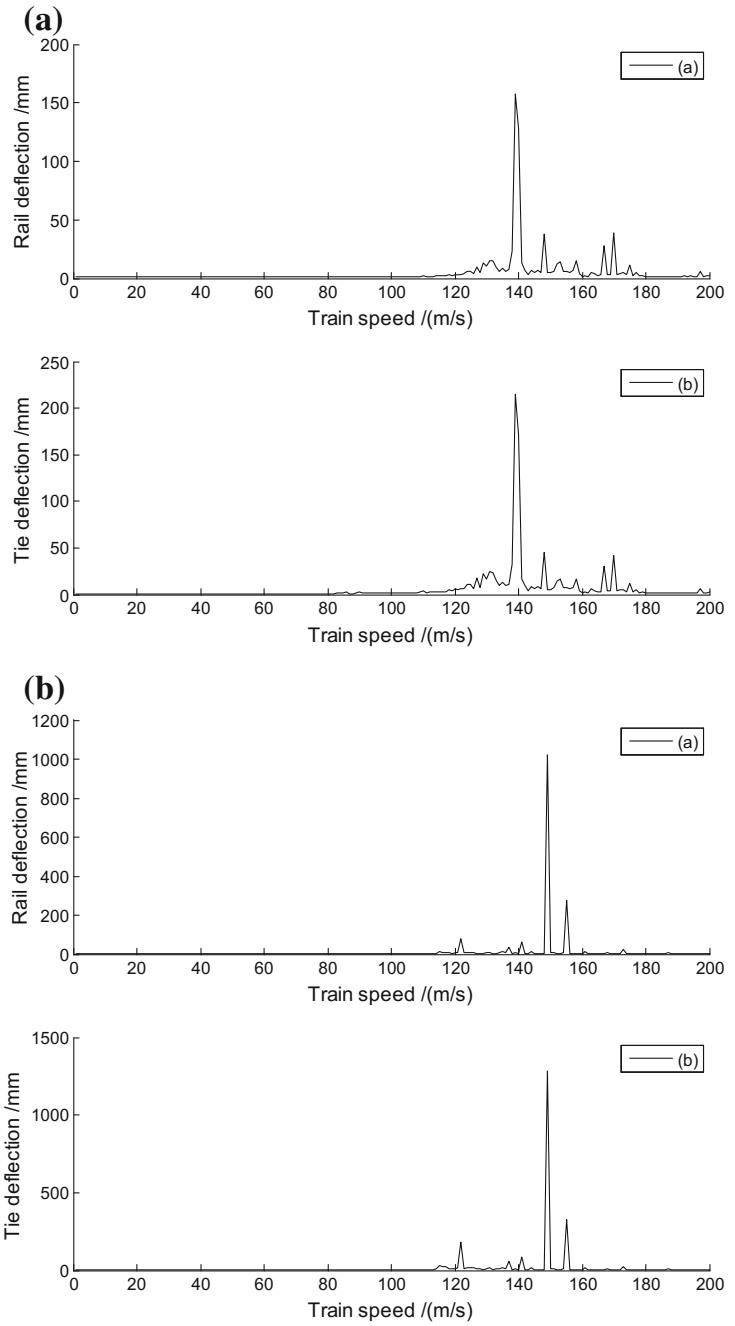

Fig. 3.7 Effect of the rail pad and fastener stiffness on track critical velocity ($E_s = 2 \times 50\,\mathrm{MN/m^2}$; $c_r = c_s = 0$). **a** $k_p = 2 \times 150\ \mathrm{MN/m^2}$; $V_{crit} = 139\ \mathrm{m/s}$. **b** $k_p = 2 \times 100\ \mathrm{MN/m^2}$; $V_{crit} = 149\ \mathrm{m/s}$. **c** $k_p = 2 \times 50\ \mathrm{MN/m^2}$; $V_{crit} = 129\ \mathrm{m/s}$. **d** $k_p = 2 \times 25\ \mathrm{MN/m^2}$; $V_{crit} = 123\ \mathrm{m/s}$

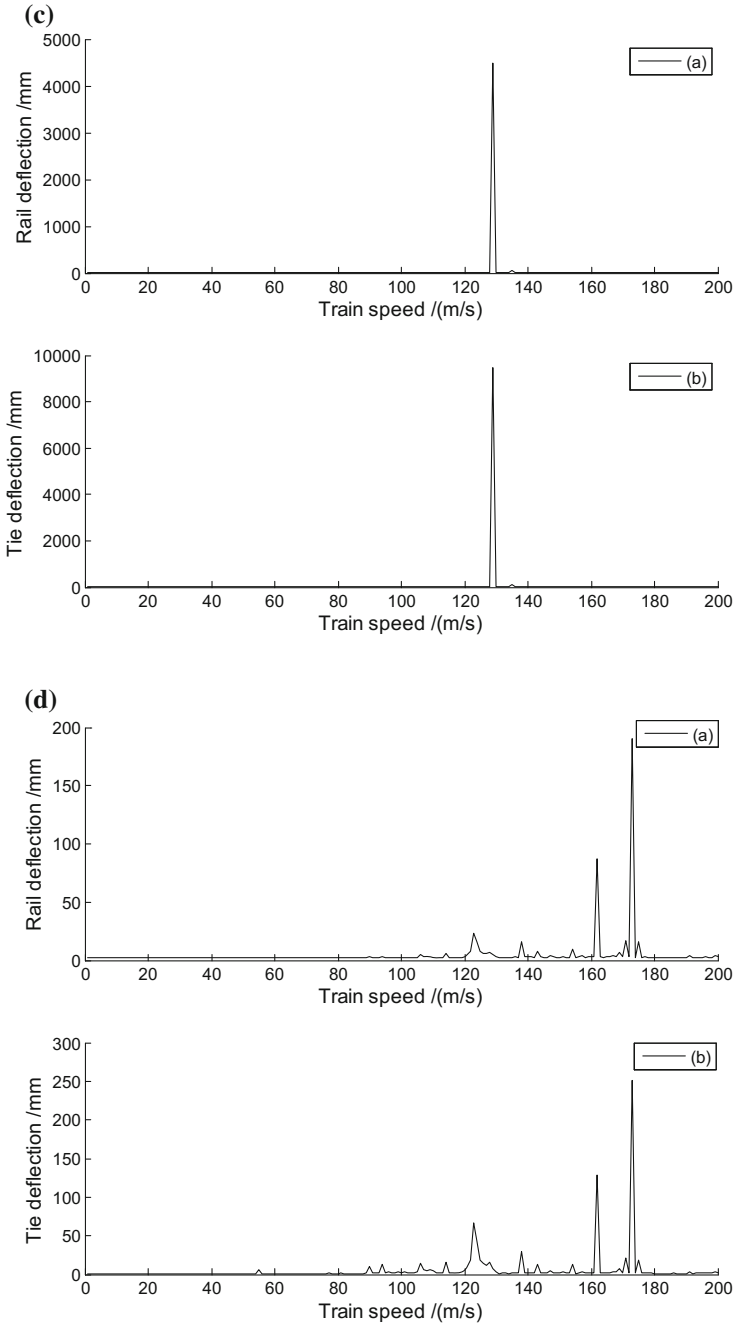

Fig. 3.7 (continued)

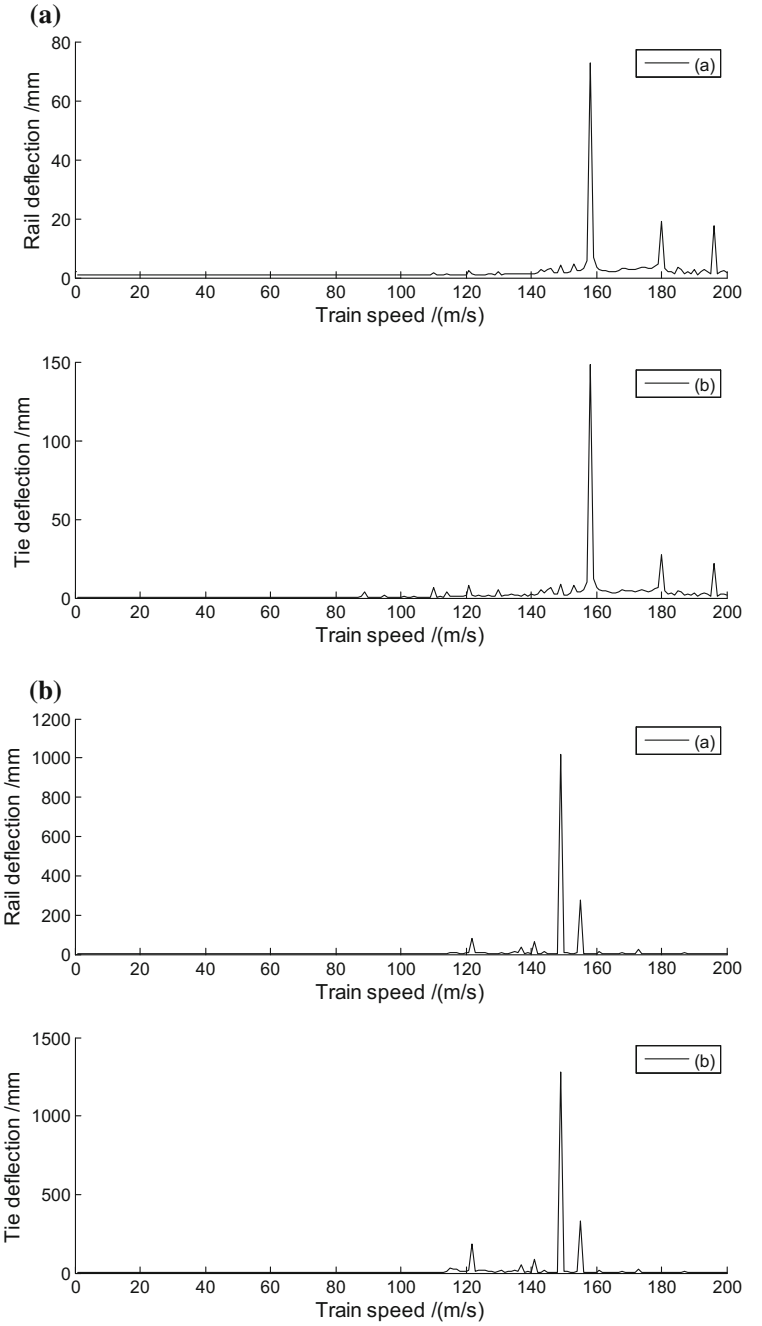

Fig. 3.8 Effect of the track foundation stiffness on track critical velocity ($k_p = 2\times 100\,\mathrm{MN/m^2}$; $c_r = c_s = 0$). **a** $E_s = 2 \times 100\,\mathrm{MN/m^2}$; $V_{crit} = 158\,\mathrm{m/s}$. **b** $E_s = 2 \times 50\,\mathrm{MN/m^2}$; $V_{crit} = 148\,\mathrm{m/s}$. **c** $E_s = 2 \times 10\,\mathrm{MN/m^2}$; $V_{crit} = 97\,\mathrm{m/s}$. **d** $E_s = 2 \times 2\,\mathrm{MN/m^2}$; $V_{crit} = 83\,\mathrm{m/s}$

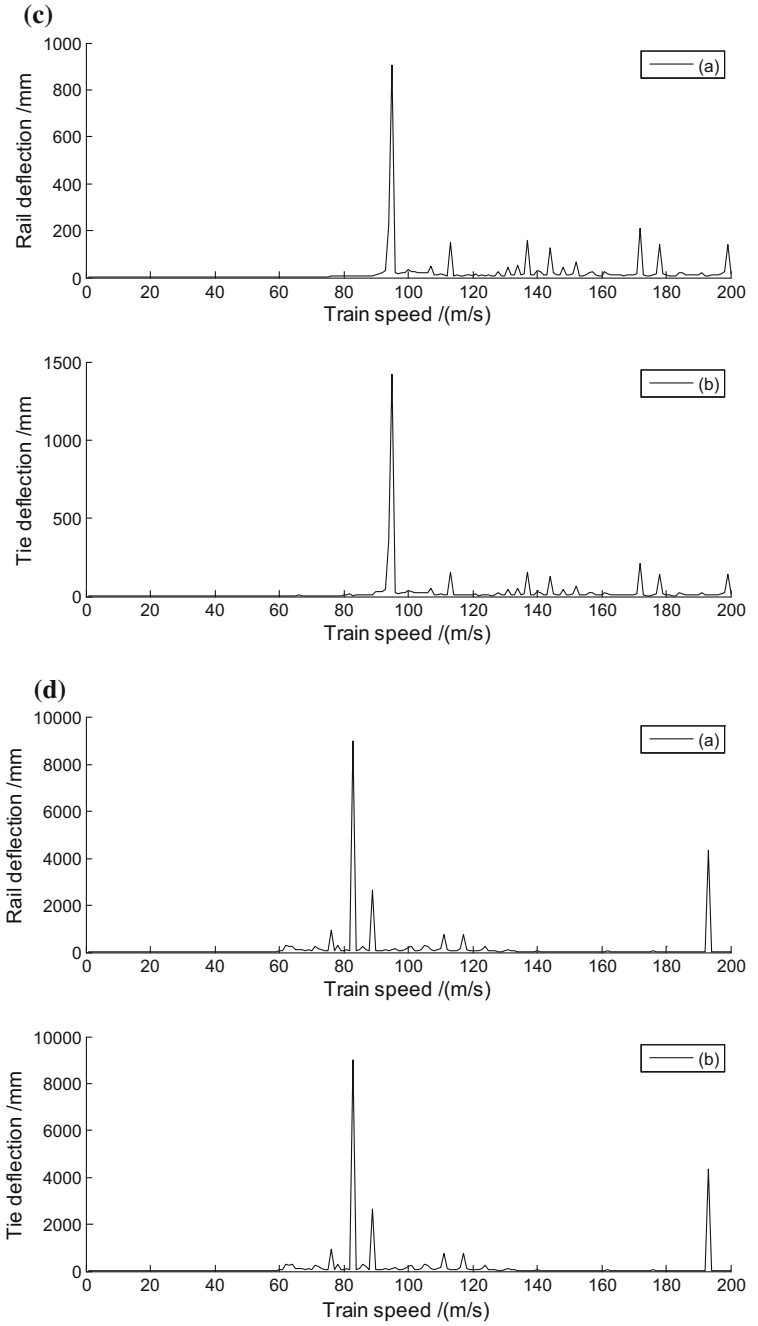

Fig. 3.8 (continued)

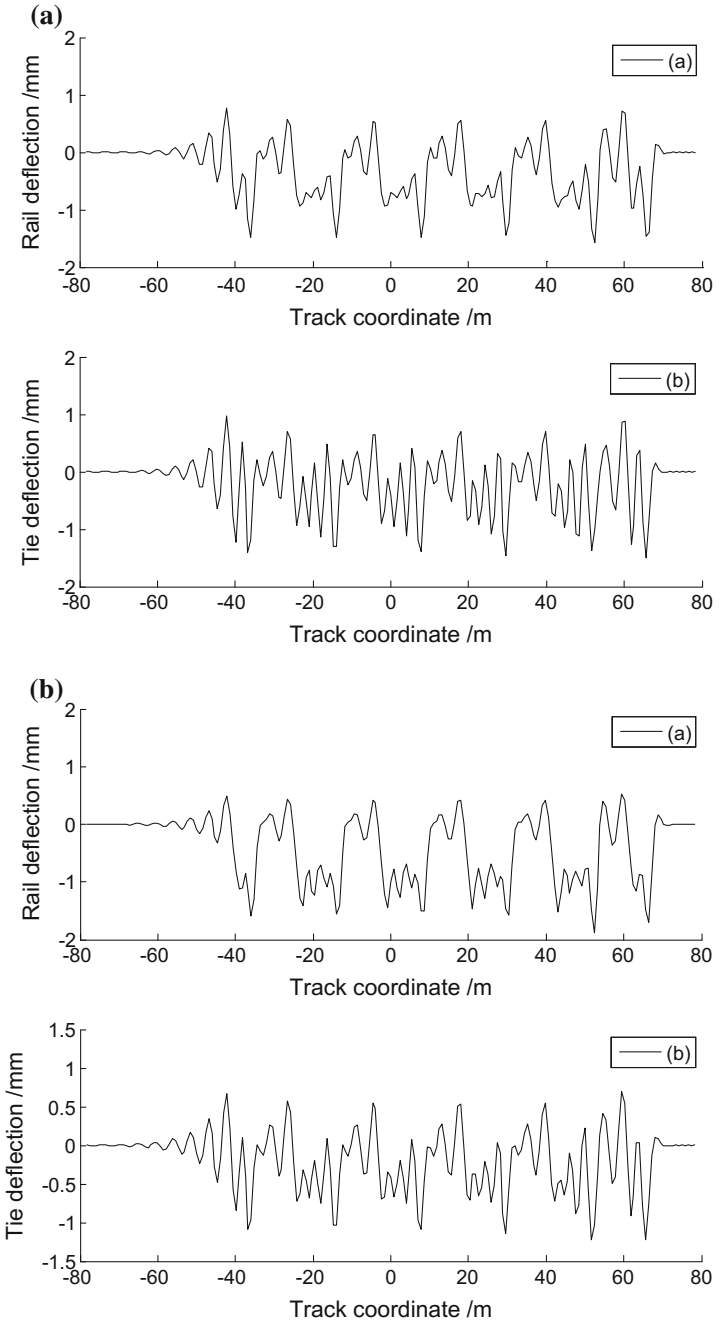

Fig. 3.9 Effect of the rail pad and fastener stiffness on track vibration ($E_s = 2 \times 50\,\mathrm{MN/m^2}$; $c_r = c_s = 2 \times 50\,\mathrm{kN\,s/m^2}$; $V = 149\,\mathrm{m/s}$). **a** $k_p = 2 \times 100\,\mathrm{MN/m^2}$. **b** $k_p = 2 \times 50\,\mathrm{MN/m^2}$. **c** $k_p = 2 \times 25\,\mathrm{MN/m^2}$. **d** $k_p = 2 \times 5\,\mathrm{MN/m^2}$

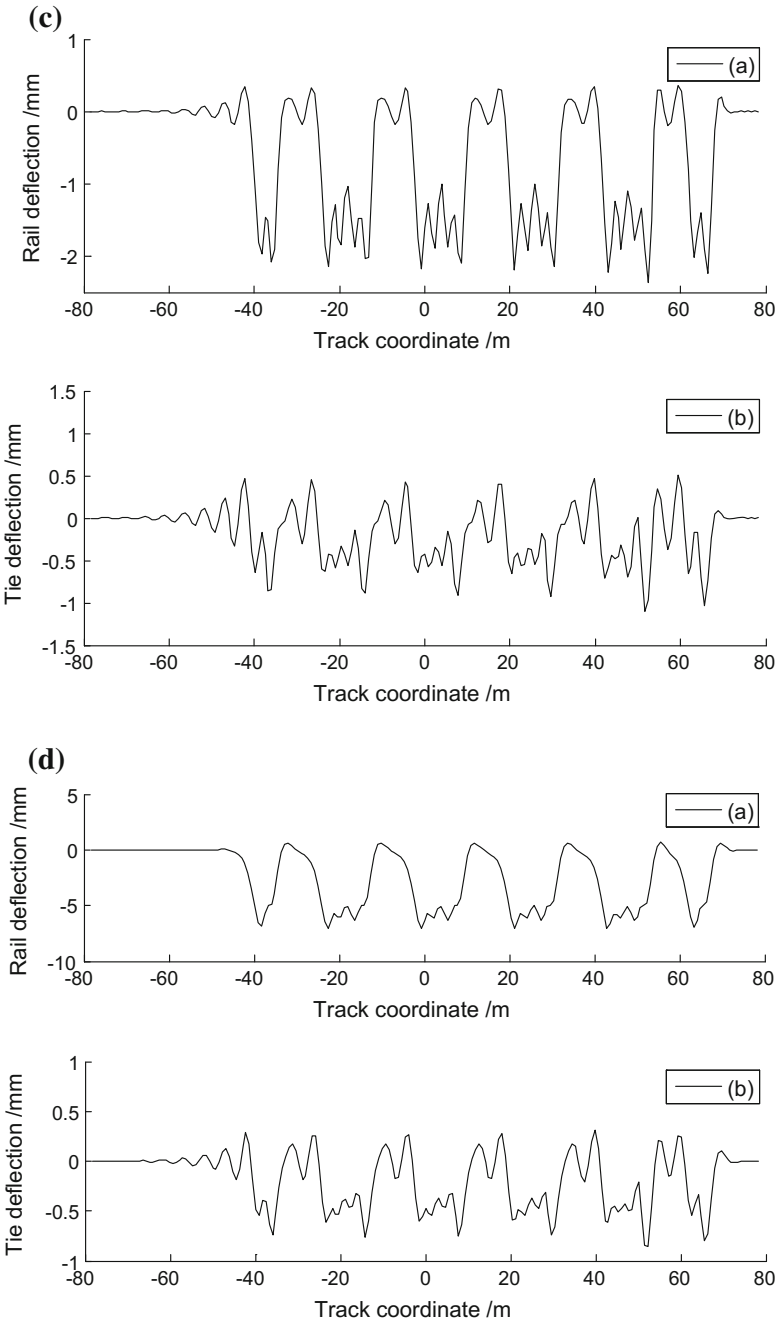

Fig. 3.9 (continued)

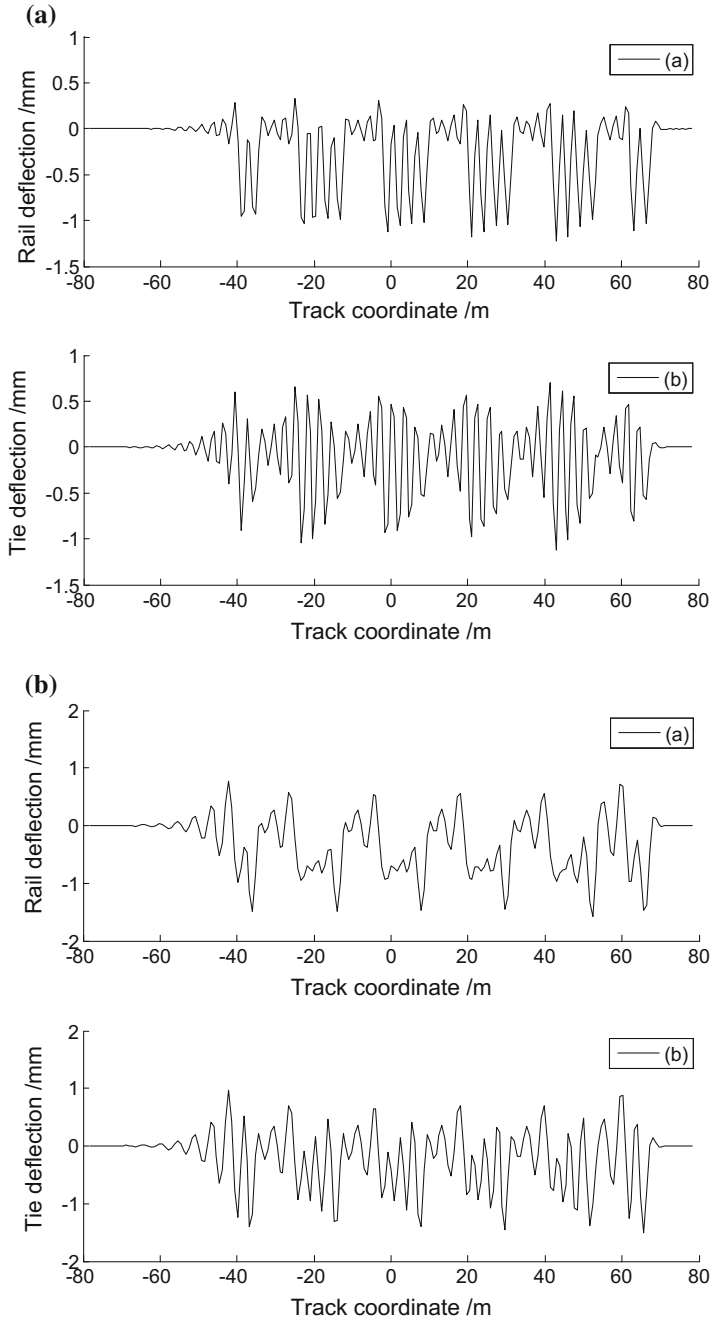

Fig. 3.10 Effect of the track foundation stiffness on track vibration ($k_p = 2 \times 100\,\mathrm{MN/m^2}$; $c_r = c_s = 2 \times 50\,\mathrm{kN\,s/m^2}$; $V = 149\,\mathrm{m/s}$). **a** $E_s = 2 \times 100\,\mathrm{MN/m^2}$. **b** $E_s = 2 \times 50\,\mathrm{MN/m^2}$. **c** $E_s = 2 \times 10\,\mathrm{MN/m^2}$. **d** $E_s = 2 \times 2\,\mathrm{MN/m^2}$

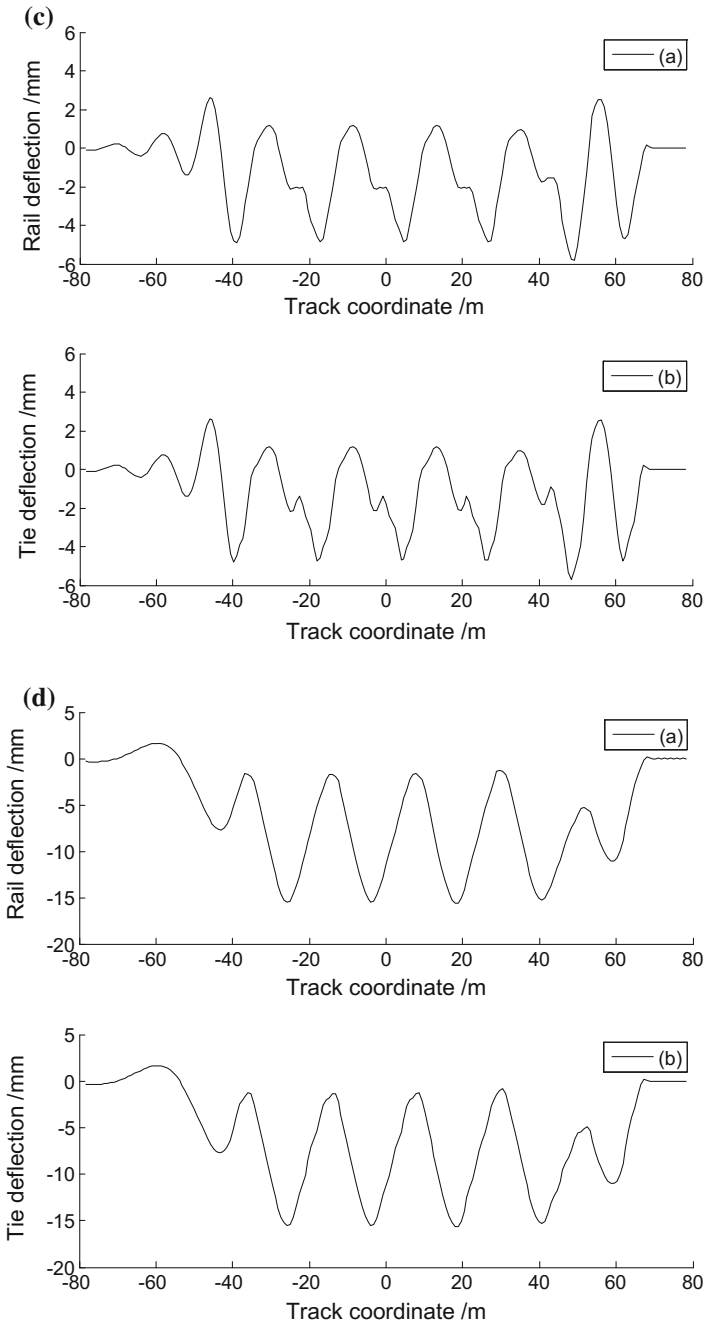

Fig. 3.10 (continued)

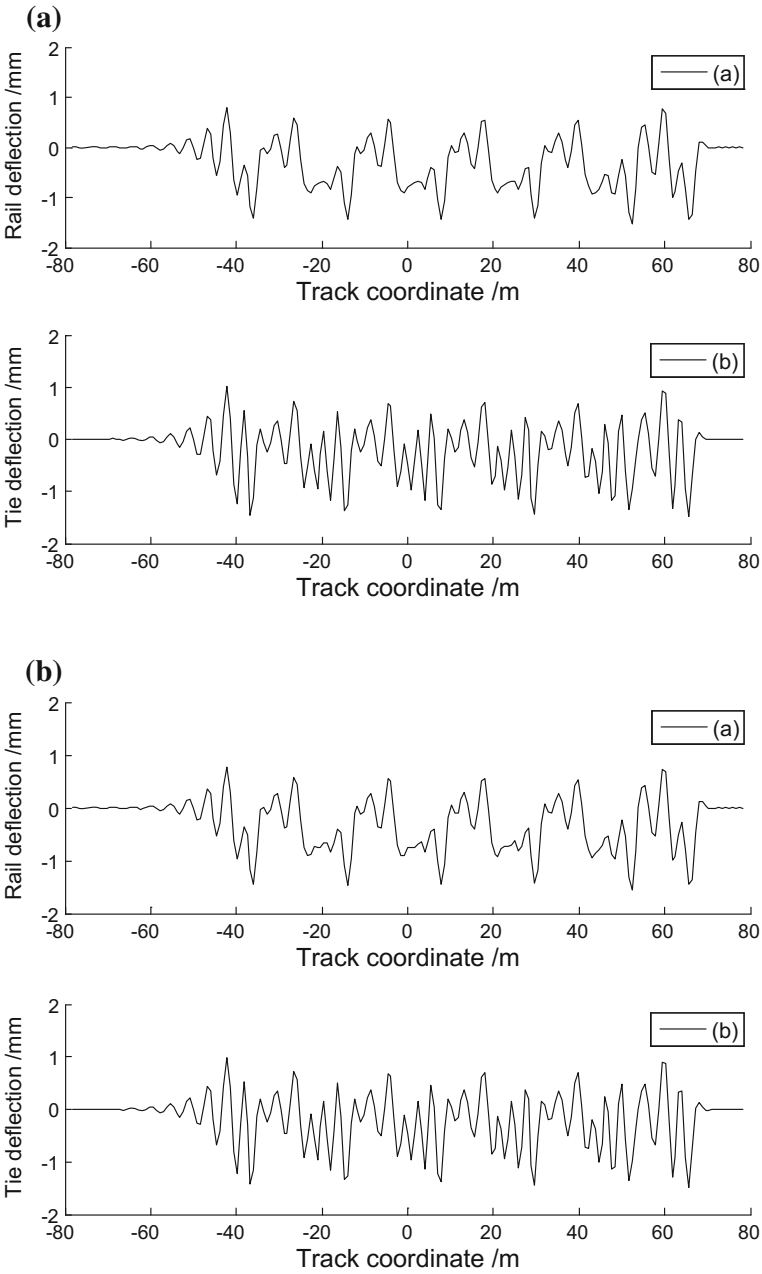

Fig. 3.11 Effect of the rail pad and fastener damping on track vibration ($E_s = 2 \times 50\,\mathrm{MN/m^2}$; $k_p = 2 \times 100\,\mathrm{MN/m^2}$; $c_s = 2 \times 50\,\mathrm{kN\,s/m^2}$; $V = 149\,\mathrm{m/s}$). **a** $c_r = 0\,\mathrm{kN\,s\,/m^2}$. **b** $c_r = 2 \times 25\,\mathrm{kN\,s/m^2}$. **c** $c_r = 2 \times 50\,\mathrm{kN\,s/m^2}$. **d** $c_r = 2 \times 100\,\mathrm{kN\,s/m^2}$

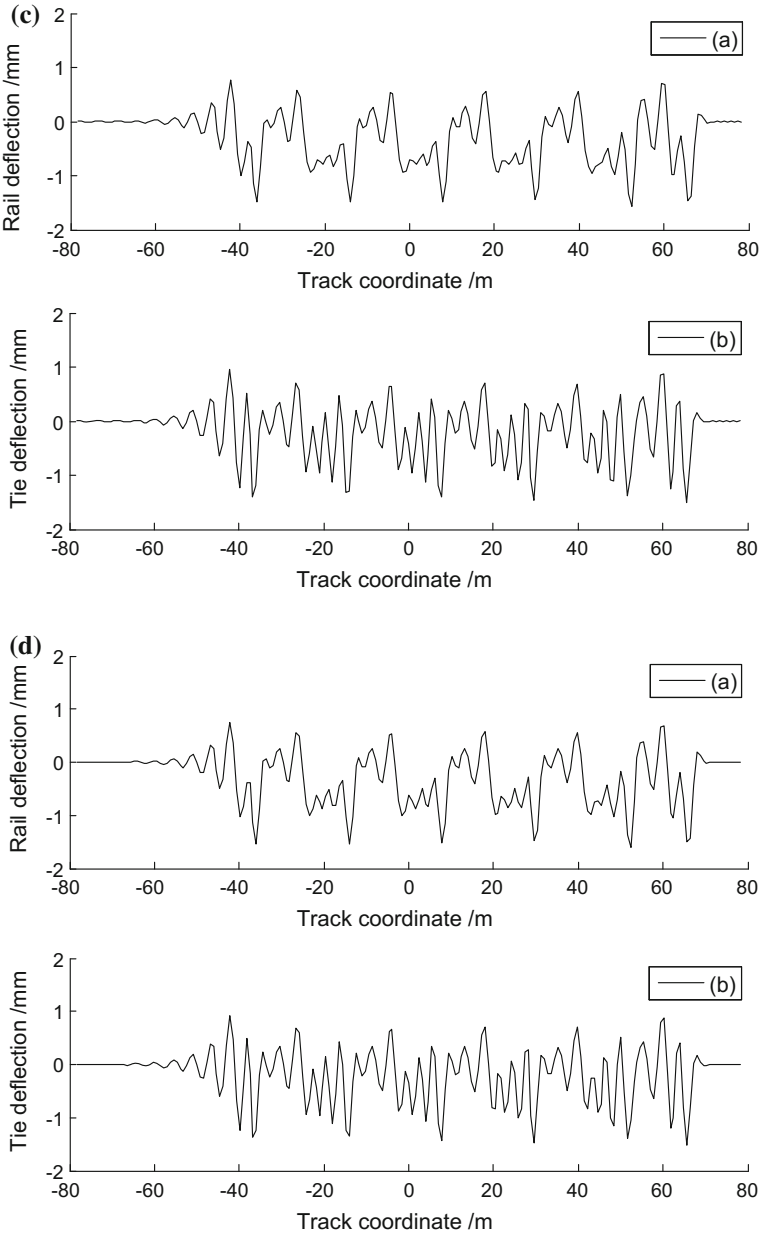

Fig. 3.11 (continued)

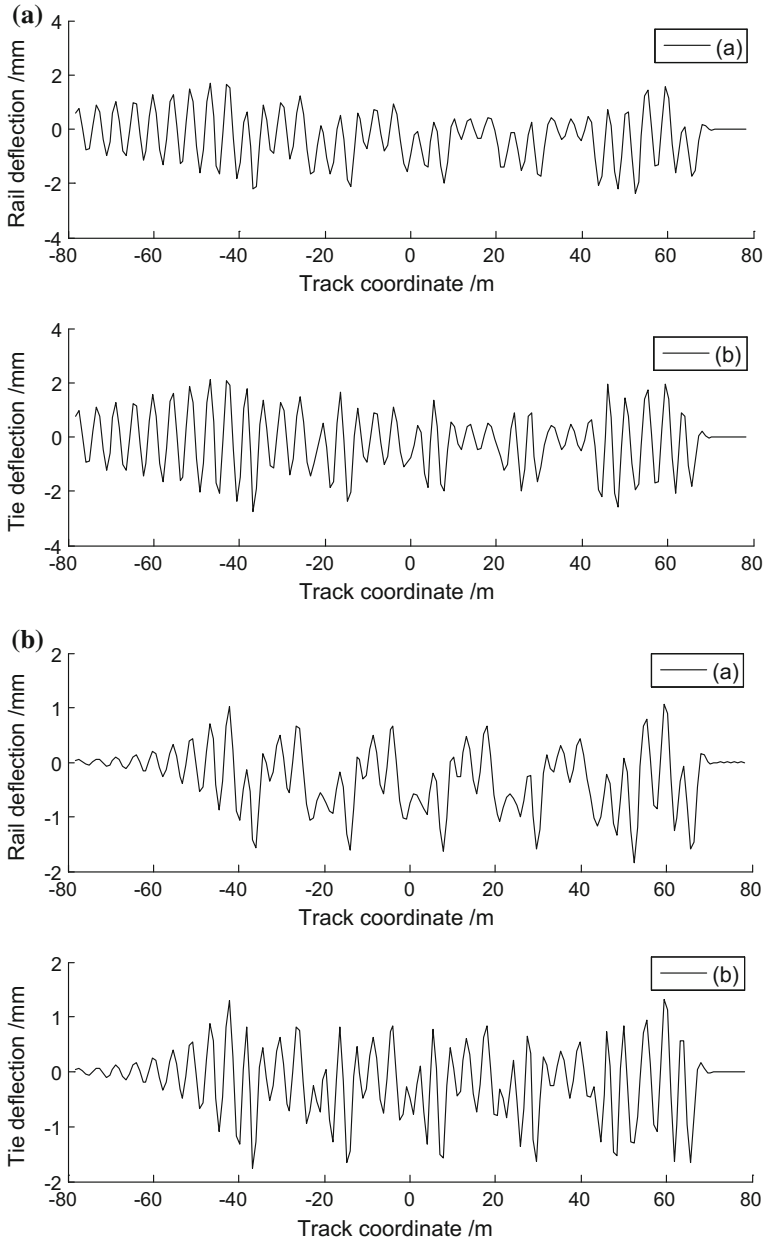

Fig. 3.12 Effect of the track foundation damping on track vibration ($E_s = 2 \times 50\,\mathrm{MN/m^2}$; $k_p = 2 \times 100\,\mathrm{MN/m^2}$; $c_r = 2 \times 50\,\mathrm{kN\,s/m^2}$; $V = 149\,\mathrm{m/s}$). **a** $c_s = 2 \times 5\,\mathrm{kN\,s/m^2}$. **b** $c_s = 2 \times 25\,\mathrm{kN\,s/m^2}$. **c** $c_s = 2 \times 50\,\mathrm{kN\,s/m^2}$. **d** $c_s = 2 \times 100\,\mathrm{kN\,s/m^2}$

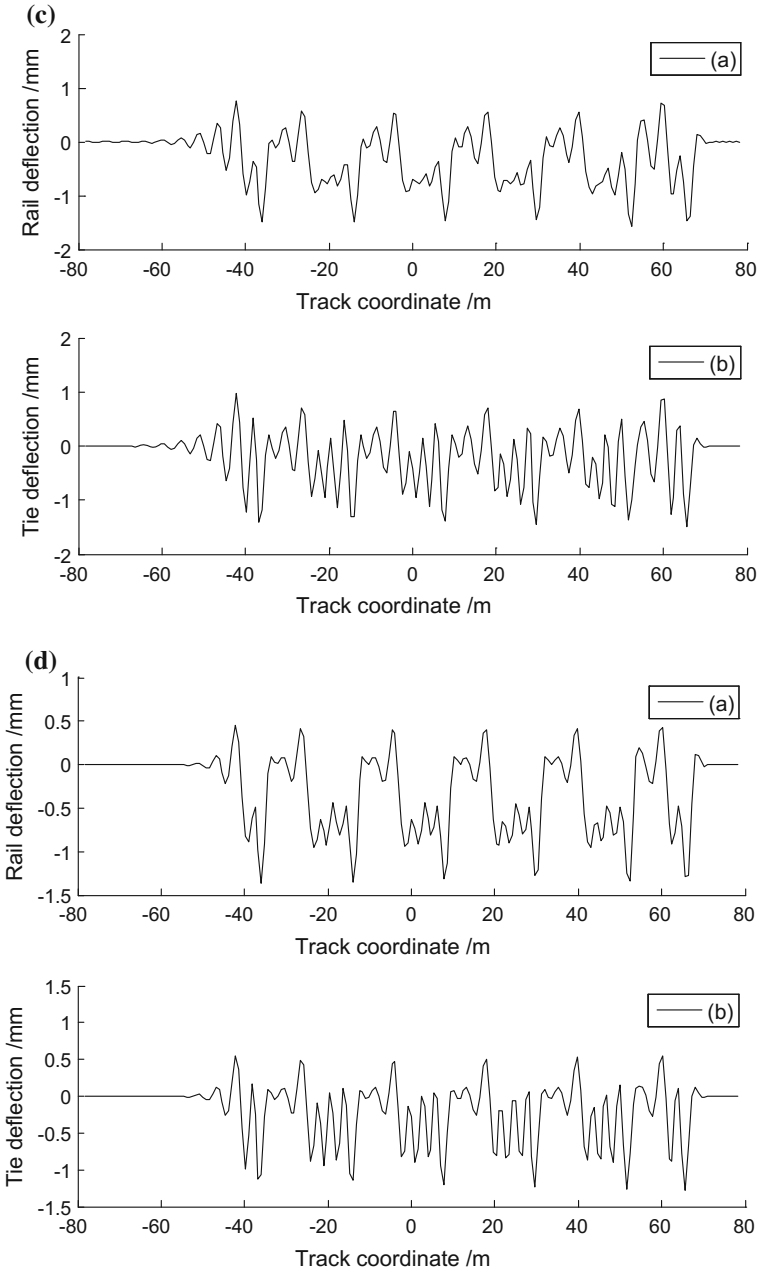

Fig. 3.12 (continued)

In summary, the above discussion deals with solution for dynamic response of track structure and track critical velocity through Fourier transform based on the single-layer and double-layer continuous elastic beam models of track structure. As application example, the track critical velocities for high-speed trains are investigated by means of Fourier transform. And the effects of the rail pad and fastener stiffness, the track foundation stiffness, the rail pad and fastener damping, and the track foundation damping on track vibration are analyzed. Finally, some significant conclusions are obtained. Fourier transform method is simple and feasible for dynamic analysis of the track structure under moving loads, which has the advantage of easy programming by use of MATLAB software.

3.4 Vibration Analysis of Track for Railways with Mixed Passenger and Freight Traffic

To ease the heavy railway transport, China has been implementing large-scale railway speeding and modification for existing lines. Meanwhile, quite a number of dedicated passenger lines have been constructed. For some modified existing lines and dedicated passenger lines at the early stage of operation, the mixed passenger and freight transportation mode has been adopted. In this section, the three-layer continuous elastic beam model of track structure is developed in consideration of track random irregularity, and the numerical method for solving the three-layer continuous elastic beam model of track structure is discussed by way of Fourier transform. Finally, the corresponding vibration characteristics of track structure are investigated in detail, which is induced by mixed passenger and freight trains at different speeds.

3.4.1 Three-Layer Continuous Elastic Beam Model of Track Structure

The traditional ballast track structure can be simplified into a three-layer continuous elastic beam model, as is shown in Fig. 3.13. And its differential equation of vibration is [14, 15]

$$\begin{aligned} &E_{\mathrm{r}} I_{\mathrm{r}} \frac{\partial^4 w}{\partial x^4} + m_{\mathrm{r}} \frac{\partial^2 w}{\partial t^2} + c_{\mathrm{r}} \left(\frac{\partial w}{\partial t} - \frac{\partial z}{\partial t} \right) + k_{\mathrm{p}} (w - z) \\ &\quad = -\sum_{l=1}^{n} \left(F_l + m_w \frac{\partial^2 \eta}{\partial t^2} \right) \delta (x - V_t - a_l) \end{aligned} \tag{3.36}$$

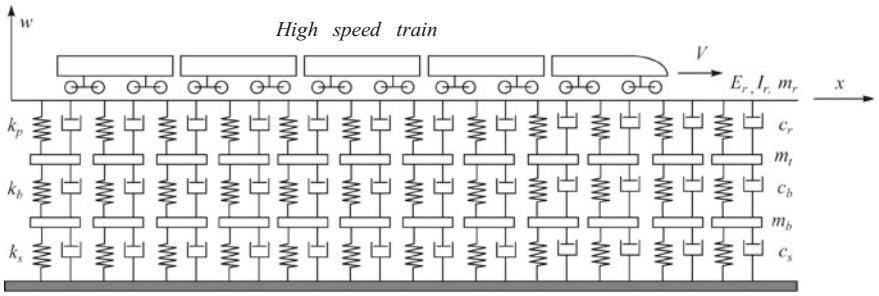

Fig. 3.13 Three-layer continuous elastic beam model of track structure

$$m_t \frac{\partial^2 z}{\partial t^2} + c_\mathrm{b}\left(\frac{\partial z}{\partial t} - \frac{\partial y}{\partial t}\right) - c_\mathrm{r}\left(\frac{\partial w}{\partial t} - \frac{\partial z}{\partial t}\right) + k_\mathrm{b}(z-y) - k_\mathrm{p}(w-z) = 0 \tag{3.37}$$

$$m_\mathrm{b} \frac{\partial^2 y}{\partial t^2} + c_\mathrm{s} \frac{\partial y}{\partial t} - c_\mathrm{b}\left(\frac{\partial z}{\partial t} - \frac{\partial y}{\partial t}\right) + k_\mathrm{s} y - k_\mathrm{b}(z-y) = 0 \tag{3.38}$$

where w represents the rail vertical deflection and m_r is the rail mass per unit length; k_p is denoted as the rail pad and fastener stiffness per unit length and c_r is the rail pad and fastener damping per unit length; z represents the sleeper vertical deflection and m_t is the sleeper mass per unit length; k_b is denoted as the ballast stiffness per unit length and c_b is the ballast damping per unit length; y is the vertical deflection of ballast and m_b the ballast mass per unit length; k_s represents the subgrade equivalent stiffness per unit length and c_s the subgrade equivalent damping per unit length; δ is Dirac function and V the train speed; F_l stands for 1/2 axle load of the lth wheelset and m_w the lth wheel mass. a_l is the distance between the lth wheelset and the coordinate origin when $t = 0$; n is the total number of wheelsets and $\eta(x = V_t)$ represents the track random irregularity.

3.4.2 Numerical Simulation of Track Random Irregularity

The sample function of the track random irregularity $\eta(x = vt)$ can be simulated by trigonometry series as [13]

$$\eta = \sum_{k=1}^{N_k} \eta_k \sin(\omega_k x + \phi_k) \tag{3.39}$$

where η_k is a Gaussian random variable with expectation zero and variance σ_k and is independent for $k = 1, 2, \ldots, N$, ϕ_k is a random variable with uniformity distribution in $0 \sim 2\pi$ and is independent for $k = 1, 2, \ldots, N$ too. η_k and φ_k are

independent with each other and can be generated by computer with such multiplicative method, Monte Carlo method, or other algorithm of generating pseudo random variable.

In order to obtain variance σ_k, a frequency band $\Delta\omega$ is defined as follows:

$$\Delta\omega = (\omega_u - \omega_l)/N_k \tag{3.40}$$

where ω_l and ω_u are lower and upper limit frequencies of power spectral density function and N_k is a sufficient large division number.

Defining

$$\omega_k = \omega_l + \left(k - \frac{1}{2}\right)\Delta\omega, \quad k = 1, 2, \ldots, N_k \tag{3.41}$$

it has

$$\sigma_k^2 = 4S_x(\omega_k)\Delta\omega, \quad k = 1, 2, \ldots, N_k \tag{3.42}$$

In above computation, $\omega_\mathrm{l}, \omega_\mathrm{u}$ and ω_k in (3.40)–(3.42) represent spatial frequency (unit: rad/m). The effective power spectral density $S_x(\omega_k)$ is assumed in the range of ω_l to ω_u and beyond this scope $S_x(\omega_k)$ is taken as zero. It is proved that the power spectral density function of the sample function composed by equations from (3.39) to (3.42) is $S_x(\omega)$ and ergodic as well [9].

Federal Railroad Administration (FRA) in USA obtained the power spectral density of track irregularity based on the large quantities of measured data and then fit it into a function expressed by cutoff frequency and roughness constant. Wavelength range for those functions is from 1.524 to 304.8 m. And, the track irregularity is categorized into 6 levels.

The power spectral density of American track vertical profile irregularity is

$$S_\mathrm{v}(\omega) = \frac{kA_\mathrm{v}\omega_\mathrm{c}^2}{(\omega^2 + \omega_\mathrm{c}^2)\omega^2}\ \mathrm{cm}^2/\mathrm{rad/m} \tag{3.43}$$

In this equation, k is usually 0.25; ω_c and A_v are shown in Table 3.4.

Table 3.4 American track irregularity spectrum parameters

Parameters	Parameter value for each level of track					
Line level	1	2	3	4	5	6
$A_\mathrm{v}/(\mathrm{cm}^2\ \mathrm{rad/m})$	1.2107	1.0181	0.6816	0.5376	0.2095	0.0339
$\omega_\mathrm{c}/(\mathrm{rad/m})$	0.8245	0.8245	0.8245	0.8245	0.8245	0.8245

3.4.3 Fourier Transform for Solving Three-Layer Continuous Elastic Beam Model of Track Structure

Fourier transform and inverse Fourier transform are defined as follows:

$$W(\beta,t)=\int_{-\infty}^{\infty} w(x,t)\mathrm{e}^{-i\beta x}\mathrm{d}x \tag{3.44}$$

$$w(x,t)=\frac{1}{2\pi}\int_{-\infty}^{\infty} W(\beta,t)\mathrm{e}^{i\beta x}\mathrm{d}\beta \tag{3.45}$$

where β is vibration wave number (unit: rad/m).

From (3.39), the following is derived:

$$\frac{\partial^2\eta}{\partial t^2}=-\sum_{k=1}^{N_k}\eta_k\omega_k^2v^2\sin(\omega_k x+\phi_k) \tag{3.46}$$

If Fourier transform is conducted to the right-hand item of (3.36), then there is

$$I_{\text{right}}=-\left\{\sum_{l=1}^{M}\left(F_l+m_w\frac{\partial^2\eta}{\partial t^2}\right)\mathrm{e}^{-i\beta a_l}\right\}\mathrm{e}^{-i\beta vt}=\tilde{F}(\beta)\mathrm{e}^{-i\beta vt} \tag{3.47}$$

where

$$\tilde{F}(\beta)=-\sum_{l=1}^{M}\left(F_l+m_w\frac{\partial^2\eta}{\partial t^2}\right)\mathrm{e}^{-i\beta a_l} \tag{3.48}$$

Apply Fourier transform to Eqs. (3.36), (3.37), and (3.38), and suppose

$$F(\beta,t)=\tilde{F}(\beta)\mathrm{e}^{i\omega t} \tag{3.49}$$

$$W(\beta,t)=\tilde{W}(\beta)\mathrm{e}^{i\omega t} \tag{3.50}$$

$$Z(\beta,t)=\tilde{Z}(\beta)\mathrm{e}^{i\omega t} \tag{3.51}$$

$$Y(\beta,t)=\tilde{Y}(\beta)\mathrm{e}^{i\omega t} \tag{3.52}$$

where $\omega=\Omega-\beta V$ and Ω is external load excitation frequency (unit: rad/m).

Then, there are

$$EI\beta^4\tilde{W} - m_r\omega^2\tilde{W} + i\omega c_r\left(\tilde{W} - \tilde{Z}\right) + k_p\left(\tilde{W} - \tilde{Z}\right) = \tilde{F} \tag{3.53}$$

$$-m_t\omega^2\tilde{Z} + i\omega c_b\left(\tilde{Z} - \tilde{Y}\right) - i\omega c_r\left(\tilde{W} - \tilde{Z}\right) + k_b\left(\tilde{Z} - \tilde{Y}\right) - k_p\left(\tilde{W} - \tilde{Z}\right) = 0 \tag{3.54}$$

$$-m_b\omega^2\tilde{Y} + i\omega c_s\tilde{Y} - i\omega c_b\left(\tilde{Z} - \tilde{Y}\right) + k_s\tilde{Y} - k_b\left(\tilde{Z} - \tilde{Y}\right) = 0 \tag{3.55}$$

Perform simultaneous solution for the above three equations from (3.53) to (3.55), and then, there obtain

$$\tilde{W}(\beta) = \frac{\left[AB - (i\omega c_b + k_b)^2\right]\tilde{F}(\beta)}{C\left[AB - (i\omega c_b + k_b)^2\right] - A\left(i\omega c_r + k_p\right)^2} \tag{3.56}$$

$$\tilde{Z}(\beta) = \frac{A\left(i\omega c_r + k_p\right)}{AB - (i\omega c_b + k_b)^2}\tilde{W}(\beta) \tag{3.57}$$

$$\tilde{Y}(\beta) = \frac{i\omega c_b + k_b}{A}\tilde{Z}(\beta) \tag{3.58}$$

Here, we have

$$\begin{aligned} A &= -m_b\omega^2 + i\omega(c_s + c_b) + k_s + k_b \\ B &= -m_t\omega^2 + i\omega(c_b + c_r) + k_b + k_p \\ C &= EI\beta^4 - m_r\omega^2 + i\omega c_r + k_p \end{aligned}$$

Substitute the three equations from (3.56) to (3.58) into (3.50)–(3.52) and perform the inverse Fourier transform, and there are

$$\tilde{w}(x,t) = \frac{1}{2\pi}\int_{-\infty}^{\infty} W(\beta,t)\mathrm{e}^{i\beta x}\mathrm{d}\beta$$

$$\tilde{z}(x,t) = \frac{1}{2\pi}\int_{-\infty}^{\infty} Z(\beta,t)\mathrm{e}^{i\beta x}\mathrm{d}\beta$$

$$\tilde{y}(x,t) = \frac{1}{2\pi}\int_{-\infty}^{\infty} Y(\beta,t)\mathrm{e}^{i\beta x}\mathrm{d}\beta$$

Finally, we obtain

$$w(x,t) = \tilde{w}(x,t)\mathrm{e}^{i(\varphi_w + \Omega t)} \tag{3.59}$$

$$z(x,t) = \tilde{z}(x,t)\mathrm{e}^{i\left(\varphi_z + \Omega t\right)} \tag{3.60}$$

$$y(x,t) = \tilde{y}(x,t)\mathrm{e}^{i\left(\varphi_y + \Omega t\right)} \tag{3.61}$$

In these equations, φ_w, φ_z, and φ_y are phase angles for the complex displacements $\tilde{w}(x,t)$, $\tilde{z}(x,t)$, and $\tilde{y}(x,t)$, respectively. Based on the three equations from (3.59) to (3.61), the velocity and the acceleration of the rail, the sleeper, and the ballast, as well as the dynamic pressure on the ballast and the subgrade, can be figured out.

3.4.3.1 Vibration Analysis of Track Structure for Railways with Mixed Passenger and Freight Traffic

The present model will be used to evaluate track vibrations for Chinese railways with mixed passenger and freight traffic [14, 15]. Two types of trains, i.e., passenger trains and freight trains will be considered. The passenger train is composed of a Chinese locomotive and eight YZ25 cars while the freight train is a combination of a Chinese locomotive and fifteen C60 wagons. The axle loads and the wheelset masses are 142.5 kN and 2200 kg for YZ25 car and 210 kN and 3300 kg (including associated bogie frame mass) for C60 wagon, respectively.

The track under the consideration is the Chinese conventional railway with mixed passenger and freight traffic, composed of 60 kg/m heavy continuous welded long rails, ballast track, the rail flexural modulus $EI = 2 \times 6.625\,\mathrm{MN} \times \mathrm{m}^2$ type-III sleeper with sleeper interval of 0.60 m, and the track irregularity simulated into six levels as well. Other computational parameters are given in Table 3.5.

Vibration responses are analyzed separately when the passenger train and freight train run at different speeds including 60, 80, 100, 120, 140, 160, 180, and 200 km/h.

Computational results are shown in Figs. 3.14, 3.15, 3.16 and 3.17, which illustrate, respectively, effects of the passenger train and the freight train running at different speeds on the rail displacements, the rail accelerations, the sleeper

Table 3.5 Computational parameters for the track

Track structure	Mass per unit length/(kg)	Stiffness per unit length/(MN/m^2)	Damping per unit length/(kN s/m^2)
Rail	60	80/0.6	50/0.6
Sleeper	340/0.6	120/0.6	60/0.6
Ballast	2718	425	90/0.6

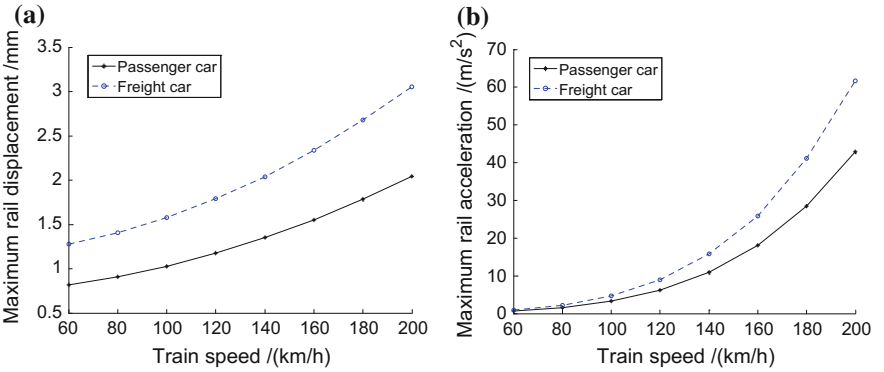

Fig. 3.14 Effect of train speed on the rail displacements and the rail accelerations. **a** Rail displacement. **b** Rail acceleration

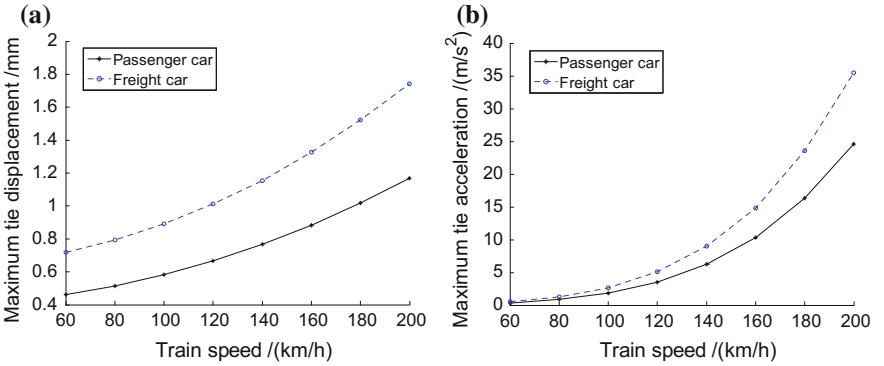

Fig. 3.15 Effect of train speed on the sleeper displacements and accelerations. **a** Sleeper displacement. **b** Sleeper acceleration

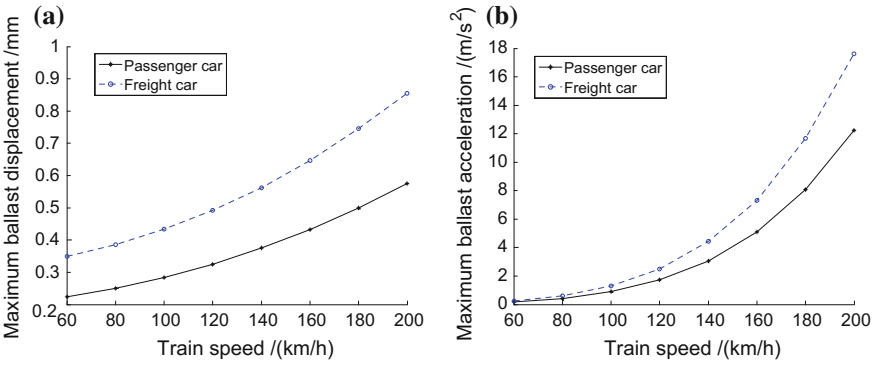

Fig. 3.16 Effect of train speed on the ballast displacements and accelerations. **a** Ballast displacement. **b** Ballast acceleration

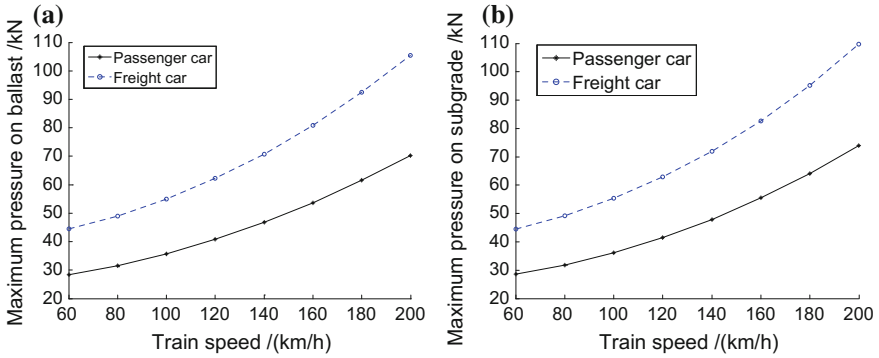

Fig. 3.17 Effect of train speed on the dynamic pressure on ballast and subgrade. **a** Dynamic pressure on ballast. **b** Dynamic pressure on subgrade

displacements, the sleeper accelerations, the ballast displacements, the ballast accelerations, and the dynamic pressures on the sleeper and on the subgrade.

Based on the above-calculated results, some conclusions may be drawn as follows:

(1) The dynamic response of the track structure increases with the increase of both passenger and freight train speed. Among the four quantities, i.e., the displacement, the acceleration, and the dynamic forces on the ballast and on the subgrade, the ones highly influenced by the speed of the trains are the rail acceleration, the sleeper acceleration, and the ballast acceleration. These accelerations increase distinctively especially when the train speed exceeds 100 km/h.

(2) Under the condition of the same train speed, the track dynamic response induced by the freight train is larger than that induced by the passenger train. The track displacement, acceleration, and dynamic pressure caused by the freight train is approximately 45–50 %, 40–50 %, and 50–60 % larger than those caused by the passenger train, respectively, which indicates that track deflection and dynamic pressure induced by the passenger train running at the speed of 200 km/h are equal to those induced by the freight train at the speed of 140 km/h. This phenomenon may be attributed to two reasons: the freight train has larger axle load than that of the passenger train, namely 210 and 142.5 kN; length between the truck centers for the freight train is smaller than that of the passenger train, namely 8.7 and 18.0 m. Thus, for dedicated railways with mixed passenger and freight traffic, the most unfavorable condition may happen to the freight train. And larger dynamic action would be induced in case the train is marshaled by mixed empty and heavy vehicles, which has been verified by site tests.

At present, existing railways in China mainly adopt mixed passenger and freight transport mode. The mixed passenger and freight traffic poses higher demands on

the curved and straight segments of railway lines, because the superelevation of curves needs to take both freight and passenger train into account, and in the meantime it must restrict the maximum weight, length, and speed. In foreign countries, there are the railway lines of mixed passenger and freight traffic, and the high-speed railway lines for freight traffic, such as Shinkansen in Japan. But the precondition is that those freight cars are of light type, unlike the heavy cars in China. Mixed passenger and freight traffic may cause bigger harm to tracks induced by trains. A passenger train is like a private car while a freight train is like a truck on highways, which causes enormous impacts on track structure due to its heavy load and slow speed. If the passenger train speed increases and the freight train speed remains unchanged, the transportation capacity for the freight train would be reduced conversely. The problem can be solved by separating the freight train from the passenger train and by building separate passenger and freight dedicated lines. It is an inevitable trend to implement diversion of the passenger and freight traffic. Recently, China has been endeavoring to construct dedicated lines for passenger trains, which is certain to be able to ease the transportation pressure greatly.

3.5 Vibration Analysis of Ballast Track with Asphalt Trackbed Over Soft Subgrade

The USA-led railways in North America mainly take on freight transportation, and 70 % railway lines in USA are heavy-haul ones. The standard axle load for heavy-haul trains in North America is 33 tons and the maximum axle load is up to 39 tons. The heavy-haul train is formed by 108 freight cars and 3–6 locomotives, whose total mass reaches 13,600 tons. To improve load-bearing capacity for the track foundation of heavy-haul railways, it is common in USA to lay an asphalt layer under the ballast over soft subgrade or at sections with unfavorable geographical conditions, which is clearly shown in Fig. 3.18. The typical asphalt layer is 3.7 m wide and 125–150 mm thick, while in areas with poor geographical conditions it can be 200 mm thick. Thickness of the ballast over asphalt layer is usually 200–300 mm. It is advisable to mix a certain percentage of rubber particles into asphalt in order to upgrade the elasticity of the ballast track with asphalt trackbed, thus controlling vibration and noise in special areas of mass transit. Ballast track with asphalt trackbed can be widely applied for main lines, at turnouts, in the tunnels, in road-bridge transition and road-tunnel transition sections, and at

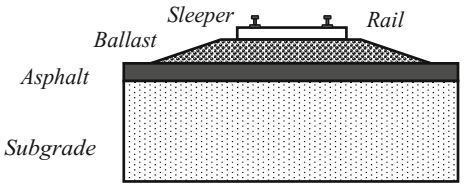

Fig. 3.18 Cross section of the ballast track with asphalt trackbed over soft subgrade

grade crossings as well. Practice has proved that the use of the ballast track with asphalt trackbed can greatly improve the stability of track structure and increase track elasticity. Meanwhile, the asphalt layer is quite waterproof, which can prevent mud pumping of the track structure and reduce track faults.

In this section, the four-layer continuous elastic beam model of track structure is established in consideration of railway random irregularities, and the numerical methods for solving the four-layer continuous elastic beam model of track structure is discussed by means of Fourier transform. Besides, vibration analysis of the ballast track with asphalt trackbed, and parameter analyses of the asphalt layer thickness, rubber content in asphalt, and elasticity modulus of soft subgrade on track vibration are carried out.

3.5.1 Four-Layer Continuous Elastic Beam Model of Track Structure

The ballast track structure with asphalt trackbed over soft subgrade can be simplified into a four-layer continuous elastic beam model, as is shown in Fig. 3.19. The vibration differential equations are [16]

$$E_{\mathrm{r}}I_{\mathrm{r}}\frac{\partial^4 w}{\partial x^4}+m_{\mathrm{r}}\frac{\partial^2 w}{\partial t^2}+c_{\mathrm{p}}\left(\frac{\partial w}{\partial t}-\frac{\partial z}{\partial t}\right)+k_{\mathrm{p}}(w-z)=-\sum_{l=1}^{n}\left(F_l+m_w\frac{\partial^2 \eta}{\partial t^2}\right)\delta(x-V_t-a_l) \tag{3.62}$$

$$m_t\frac{\partial^2 z}{\partial t^2}+c_{\mathrm{b}}\left(\frac{\partial z}{\partial t}-\frac{\partial y}{\partial t}\right)-c_{\mathrm{p}}\left(\frac{\partial w}{\partial t}-\frac{\partial z}{\partial t}\right)+k_{\mathrm{b}}(z-y)-k_{\mathrm{p}}(w-z)=0 \tag{3.63}$$

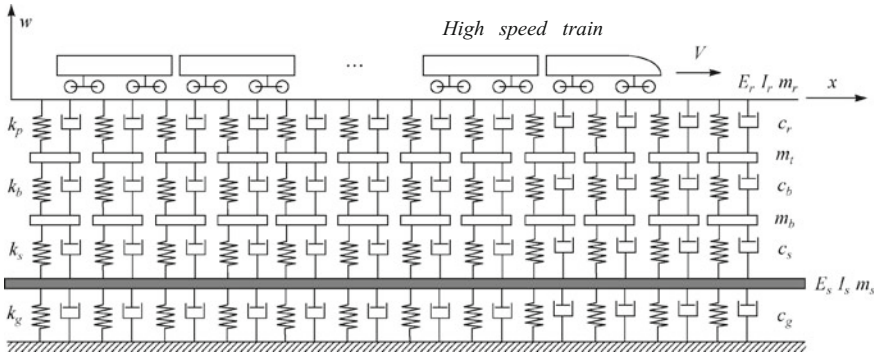

Fig. 3.19 Computational model for vibration analysis of ballast track with asphalt trackbed

$$m_{\mathrm{b}}\frac{\partial^2 y}{\partial t^2}+c_{\mathrm{s}}\left(\frac{\partial y}{\partial t}-\frac{\partial g}{\partial t}\right)-c_{\mathrm{b}}\left(\frac{\partial z}{\partial t}-\frac{\partial y}{\partial t}\right)+k_{\mathrm{s}}(y-g)-k_{\mathrm{b}}(z-y)=0 \tag{3.64}$$

$$E_{\mathrm{s}}I_{\mathrm{s}}\frac{\partial^4 g}{\partial x^4}+m_{\mathrm{s}}\frac{\partial^2 g}{\partial t^2}+c_{\mathrm{g}}\frac{\partial g}{\partial t}-c_{\mathrm{s}}\left(\frac{\partial y}{\partial t}-\frac{\partial g}{\partial t}\right)+k_{\mathrm{g}}g-k_{\mathrm{s}}(y-g)=0 \tag{3.65}$$

In these equations, w, z, y, and g represent the vertical deflection of rail, sleeper, ballast, and asphalt layer, respectively; E_{r} and I_{r} are rail elasticity modulus and inertia moment around the horizontal axis; m_{r} is rail mass per unit length, k_{p} is rail pad and fastener stiffness per unit length, and c_{r} stands for rail pad and fastener damping per unit length; m_t signifies sleeper mass per unit length, k_{b} is the stiffness of ballast per unit length, and c_{b} the ballast damping per unit length; m_{b} represents ballast mass per unit length, k_{s} is the equivalent stiffness of asphalt layer per unit length, and c_{s} stands for the equivalent damping of asphalt layer per unit length. E_{s} and I_{s} are denoted as the elasticity modulus and the inertia moment around the horizontal axis of asphalt layer, and m_{s} is the asphalt layer mass per unit length; k_{g} is the equivalent stiffness of soft subgrade per unit length, and c_{g} is the equivalent damping of soft subgrade per unit length; x is track longitudinal coordinate and $\delta(x-V_t-a_l)$ is Dirac function. V is train speed and F_l is 1/2 axle load of the lth wheelset; m_w is mass of the lth wheel; a_l is the distance between the coordinate origin and the lth wheelset when $t=0$; n is the total number of train wheelsets and $\eta(x=V_t)$ signifies track random irregularity.

3.5.2 Fourier Transform for Solving Four-Layer Continuous Elastic Beam Model of Track Structure

Fourier transform and inverse Fourier transform are defined as

$$W(\beta,t)=\int_{-\infty}^{\infty}w(x,t)\mathrm{e}^{-i\beta x}\mathrm{d}x \tag{3.66}$$

$$w(x,t)=\frac{1}{2\pi}\int_{-\infty}^{\infty}W(\beta,t)\mathrm{e}^{i\beta x}\mathrm{d}\beta \tag{3.67}$$

where β represents vibration wave number (unit: rad/m).

Perform Fourier transform to the four equations from (3.62) to (3.65) and suppose $W(\beta,t)$, $Z(\beta,t)$, $Y(\beta,t)$, $G(\beta,t)$, and $F(\beta,t)$ are harmonic functions, namely

$$W(\beta,t)=\tilde{W}(\beta)\mathrm{e}^{i\omega t} \tag{3.68}$$

$$Z(\beta,t) = \tilde{Z}(\beta)\mathrm{e}^{i\omega t} \tag{3.69}$$

$$Y(\beta,t) = \tilde{Y}(\beta)\mathrm{e}^{i\omega t} \tag{3.70}$$

$$G(\beta,t) = \tilde{G}(\beta)\mathrm{e}^{i\omega t} \tag{3.71}$$

$$F(\beta,t) = \tilde{F}(\beta)\mathrm{e}^{i\omega t} \tag{3.72}$$

$$\tilde{F}(\beta) = \sum_{l=1}^{n}\left(-F_l + m_w\frac{\partial^2\eta}{\partial t^2}\right)\mathrm{e}^{-\beta a_l} \tag{3.73}$$

In these functions, $\omega = \Omega - \beta V$ and Ω is external load excitation frequency (unit: rad/m).

Then, there are

$$\left(E_\mathrm{r}I_\mathrm{r}\beta^4 - m_\mathrm{r}\omega^2 + i\omega c_\mathrm{p} + k_\mathrm{p}\right)\tilde{W}(\beta) - \left(i\omega c_\mathrm{p} + k_\mathrm{p}\right)\tilde{Z}(\beta) = \tilde{F}(\beta) \tag{3.74}$$

$$\left[-m_t\omega^2 + i\omega\left(c_\mathrm{b} + c_\mathrm{p}\right) + k_\mathrm{b} + k_\mathrm{p}\right]\tilde{Z}(\beta) - (i\omega c_\mathrm{b} + k_\mathrm{b})\tilde{Y}(\beta) - \left(i\omega c_\mathrm{p} + k_\mathrm{p}\right)\tilde{W}(\beta) = 0 \tag{3.75}$$

$$\left[-m_\mathrm{b}\omega^2 + i\omega(c_\mathrm{s} + c_\mathrm{b}) + k_\mathrm{s} + k_\mathrm{b}\right]\tilde{Y}(\beta) - (i\omega c_\mathrm{s} + k_\mathrm{s})\tilde{G}(\beta) - (i\omega c_\mathrm{b} + k_\mathrm{b})\tilde{Z}(\beta) = 0 \tag{3.76}$$

$$\left[E_\mathrm{s}I_\mathrm{s}\beta^4 - m_\mathrm{s}\omega^2 + i\omega\left(c_\mathrm{g} + c_\mathrm{s}\right) + k_\mathrm{g} + k_\mathrm{s}\right]\tilde{G}(\beta) - (i\omega c_\mathrm{s} + k_\mathrm{s})\tilde{Y}(\beta) = 0 \tag{3.77}$$

Defining

$$\begin{aligned} A_1 &= E_\mathrm{r}I_\mathrm{r}\beta^4 - m_\mathrm{r}\omega^2 + i\omega c_\mathrm{p} + k_\mathrm{p} \\ A_2 &= -m_t\omega^2 + i\omega\left(c_\mathrm{b} + c_\mathrm{p}\right) + k_\mathrm{b} + k_\mathrm{p} \\ A_3 &= -m_\mathrm{b}\omega^2 + i\omega(c_\mathrm{s} + c_\mathrm{b}) + k_\mathrm{s} + k_\mathrm{b} \\ A_4 &= E_\mathrm{s}I_\mathrm{s}\beta^4 - m_\mathrm{s}\omega^2 + i\omega\left(c_\mathrm{g} + c_\mathrm{s}\right) + k_\mathrm{g} + k_\mathrm{s} \end{aligned} \tag{3.78}$$

$$\begin{aligned} B_1 &= i\omega c_\mathrm{p} + k_\mathrm{p} \\ B_2 &= i\omega c_\mathrm{b} + k_\mathrm{b} \\ B_3 &= i\omega c_\mathrm{s} + k_\mathrm{s} \end{aligned} \tag{3.79}$$

Through the simultaneous solution for the above four equations from (3.74) to (3.77), there obtain

$$\tilde{W}(\beta) = \frac{A_2(A_3A_4 - B_3B_3) - A_4B_2B_2}{A_1A_2(A_3A_4 - B_3B_3) - A_1A_4B_2B_2 - (A_3A_4 - B_3B_3)B_1B_1}\tilde{F}(\beta) \tag{3.80}$$

$$\tilde{Z}(\beta) = \frac{(A_3A_4 - B_3B_3)B_1}{A_2(A_3A_4 - B_3B_3) - A_4B_2B_2}\tilde{W}(\beta) \tag{3.81}$$

$$\tilde{Y}(\beta) = \frac{A_4B_2}{A_3A_4 - B_3B_3}\tilde{Z}(\beta) \tag{3.82}$$

$$\tilde{G}(\beta) = \frac{B_3}{A_4}\tilde{Y}(\beta) \tag{3.83}$$

Substituting Eqs. (3.80)–(3.83) into (3.68)–(3.71) and making inverse Fourier transform, it has

$$\tilde{w}(x,t) = \frac{1}{2\pi}\int_{-\infty}^{\infty} W(\beta,t)\mathrm{e}^{i\beta x}\mathrm{d}\beta \tag{3.84}$$

$$\tilde{z}(x,t) = \frac{1}{2\pi}\int_{-\infty}^{\infty} Z(\beta,t)\mathrm{e}^{i\beta x}\mathrm{d}\beta \tag{3.85}$$

$$\tilde{y}(x,t) = \frac{1}{2\pi}\int_{-\infty}^{\infty} Y(\beta,t)\mathrm{e}^{i\beta x}\mathrm{d}\beta \tag{3.86}$$

$$\tilde{g}(x,t) = \frac{1}{2\pi}\int_{-\infty}^{\infty} G(\beta,t)\mathrm{e}^{i\beta x}\mathrm{d}\beta \tag{3.87}$$

Hence, there derive

$$w(x,t) = \tilde{w}(x,t)\mathrm{e}^{i\varphi_w} \tag{3.88}$$

$$z(x,t) = \tilde{z}(x,t)\mathrm{e}^{i\varphi_z} \tag{3.89}$$

$$y(x,t) = \tilde{y}(x,t)\mathrm{e}^{i\varphi_y} \tag{3.90}$$

$$g(x,t) = \tilde{g}(x,t)\mathrm{e}^{i\varphi_g} \tag{3.91}$$

In the above equations, φ_w, φ_z, φ_y, and φ_g are the corresponding phase angles for complex displacements $\tilde{w}(x,t)$, $\tilde{z}(x,t)$, $\tilde{y}(x,t)$, and $\tilde{g}(x,t)$, respectively. Based on the four equations from (3.88) to (3.91), not only the velocity and acceleration of the rail, sleeper, ballast, and asphalt layer but also the dynamic pressure on the sleeper, ballast, asphalt layer, and soft subgrade can be figured out.

3.5.3 Vibration Analysis of Ballast Track with Asphalt Trackbed Over Soft Subgrade

Based on the above-proposed model, the vibration analysis of ballast track with asphalt trackbed over soft subgrade can be carried out [16].

Some track parameters are listed as follows: the continuously welded rail of 60 kg/m, the ballast track with asphalt trackbed, the rail flexural modulus $E_rI_r = 2 \times 6.625\,\text{MN} \times \text{m}^2$, type-III prestressed concrete sleeper with sleeper length of 2.6 m and sleeper interval of 0.60 m, ballast shoulder breadth $b = 30\,\text{cm}$, ballast thickness $H_b = 30\,\text{cm}$, and ballast density $\rho = 2000\,\text{kg/m}^3$. The track irregularities are simulated into six levels as well. Other parameters are given in details in Table 3.6. The mass of the asphalt trackbed depends on the thickness and the density of the material and it varies for each case. The equivalent stiffness k_s and damping c_s from the asphalt trackbed are different with different rubber contents, which can be evaluated by the data of Table 3.7. Parameters for crumb rubber-modified asphalt (CRMA) are listed in Table 3.7 which shows that the rubber-modified asphalt cannot only increases the damping of the asphalt mix but also increases the shear strength. For CRMA with 20 % rubber content, the average damping ratio is approximately 9.5 %. For the asphalt mix without crumb rubber, the damping ratio is approximately 5.5 %. Unsaturated subgrade soils have an average damping ratio of approximately 3.8 %, much less than CRMA under similar stress and strain conditions. Stiffness of soft subgrade per unit length k_g can be derived by elasticity modulus E_s of soft subgrade based on Eq. (3.35).

The train is formed by eight CRH3 motor cars, whose axle load is 142.5 kN, with the train speed of 200 km/h.

Table 3.6 Track parameters

Track structure	Mass per unit length/(kg)	Stiffness per unit length/(MN/m^2)	Damping per unit length/(kN s/m^2)
Rail	60	–	–
Sleeper	340/0.6	80/0.6	50/0.6
Ballast	2790	120/0.6	60/0.6
Asphalt layer	Variable	Variable	variable
Soft subgrade	–	Variable	90/0.6

Table 3.7 Parameters for crumb rubber-modified asphalt

Cases	Rubber content/(%)	Rubber density/(kg/m^3)	Rubber shear modulus/(MPa)	Damping ratio
1	0	2511	750	0.055
2	10	2500	890	0.065
3	20	2480	980	0.095

Vibration analyses of the track with asphalt trackbed over soft subgrade are carried out by considering the following three cases [16]:

Case 1 Influence of three asphalt thicknesses H_a, 10, 15, and 20 cm for crumb rubber-modified asphalt trackbed with rubber content C_a = 20 % and subgrade modulus E_s = 20 MPa, on track vibration;

Case 2 Influence of three rubber contents C_a, 0, 10, and 20 % for crumb rubber-modified asphalt trackbed with asphalt thickness H_a = 20 cm and subgrade modulus E_s = 20 MPa, on track vibration;

Case 3 Influence of three soft subgrade modulus E_s, 20, 25, and 30 MPa for crumb rubber-modified asphalt trackbed with rubber content C_a = 20 % and asphalt thickness H_a = 20 cm, on track vibration.

Results for each case are compared with those of the conventional ballast track with soft subgrade. The conventional ballast track herein is similar as the asphalt track except that the asphalt layer is substituted for the sub-ballast on an equal thickness basis.

The calculated outputs include maximum deflections of the rail, sleeper, ballast, and asphalt trackbed and maximum accelerations of the rail, sleeper, ballast, and asphalt trackbed as well as maximum dynamic pressures (i.e., forces on sleeper spacing) on the sleeper, ballast, asphalt trackbed, and subgrade, respectively. The computational results are depicted in Figs. 3.20, 3.21, 3.22, 3.23, 3.24, 3.25, 3.26, 3.27 and 3.28, which show the effects of different asphalt thickness H_a and different rubber content C_a as well as different subgrade modulus E_s on track vibration.

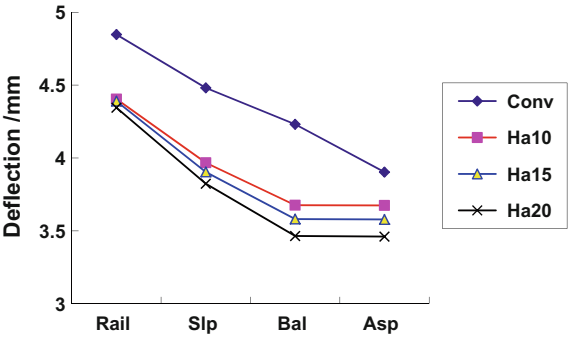

Fig. 3.20 Influence of asphalt thickness H_a with C_a = 20 % and E_s = 20 MPa on deflections of the track (*Slp* sleeper, *Bal* Ballast, *Asp* Asphalt, *Conv* Conventional ballast track with soft subgrade, H_a Thickness of the asphalt layer)

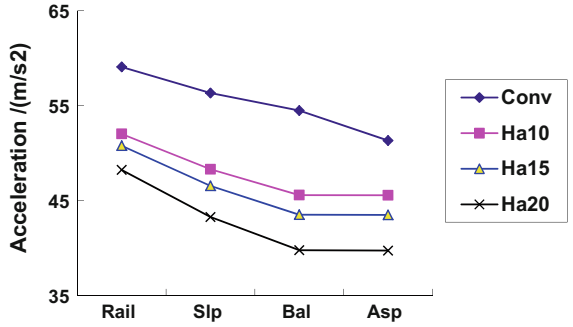

Fig. 3.21 Influence of asphalt thickness H_a with C_a = 20 % and E_s = 20 MPa on accelerations of the track (*Slp* sleeper, *Bal* Ballast, *Asp* Asphalt, *Conv* Conventional ballast track with soft subgrade, H_a Thickness of the asphalt layer)

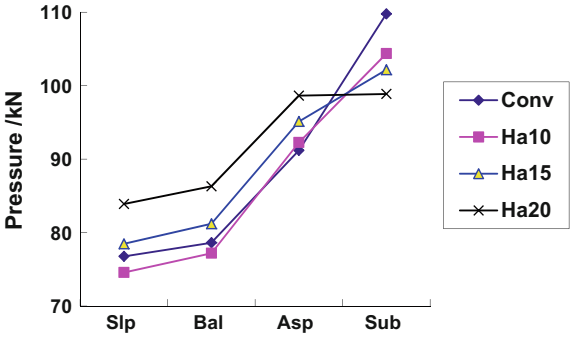

Fig. 3.22 Influence of asphalt thickness H_a with C_a = 20 % and E_s = 20 MPa on pressures on the track (*Slp* sleeper, *Bal* Ballast, *Asp* Asphalt, *Sub* Subgrade, *Conv* Conventional ballast track with soft subgrade, H_a Thickness of the asphalt layer)

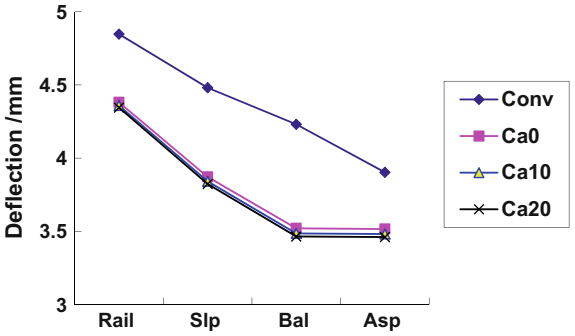

Fig. 3.23 Influence of rubber content C_a with H_a = 20 cm and E_s = 20 MPa on deflections of the track (*Slp* sleeper, *Bal* Ballast, *Asp* Asphalt, *Conv* Conventional ballast track with soft subgrade, C_a Rubber content of the asphalt layer)

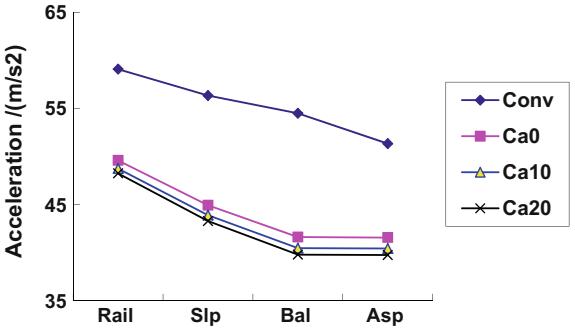

Fig. 3.24 Influence of rubber content C_a with H_a = 20 cm and E_s = 20 MPa on accelerations of the track (*Slp* sleeper, *Bal* Ballast, *Asp* Asphalt, *Conv* Conventional ballast track with soft subgrade, C_a Rubber content of the asphalt layer)

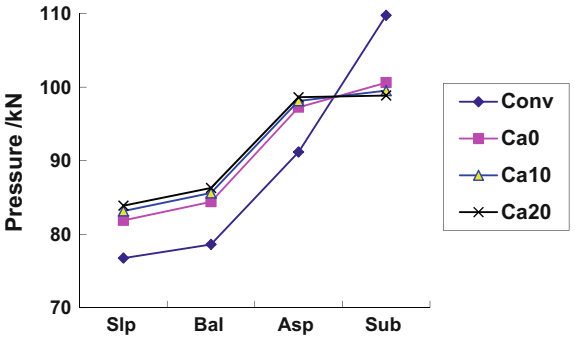

Fig. 3.25 Influence of rubber content C_a with H_a = 20 cm and E_s = 20 MPa on pressures on the track (*Slp* sleeper, *Bal* Ballast, *Asp* Asphalt, *Sub* Subgrade, *Conv* Conventional ballast track with soft subgrade, C_a Rubber content of the asphalt layer)

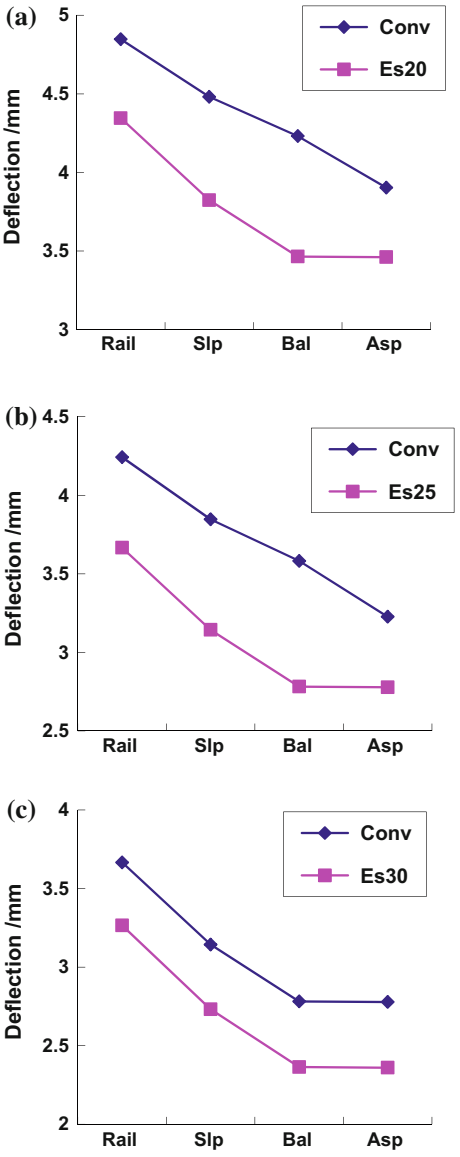

Fig. 3.26 Influence of subgrade module E_s with C_a = 20 % and H_a = 20 cm on deflections of the track (*Slp* sleeper, *Bal* Ballast, *Asp* Asphalt, *Conv* Conventional ballast track with soft subgrade, E_s subgrade module). **a** E_s = 20 MPa. **b** E_s = 25 MPa. **c** E_s = 30 MPa

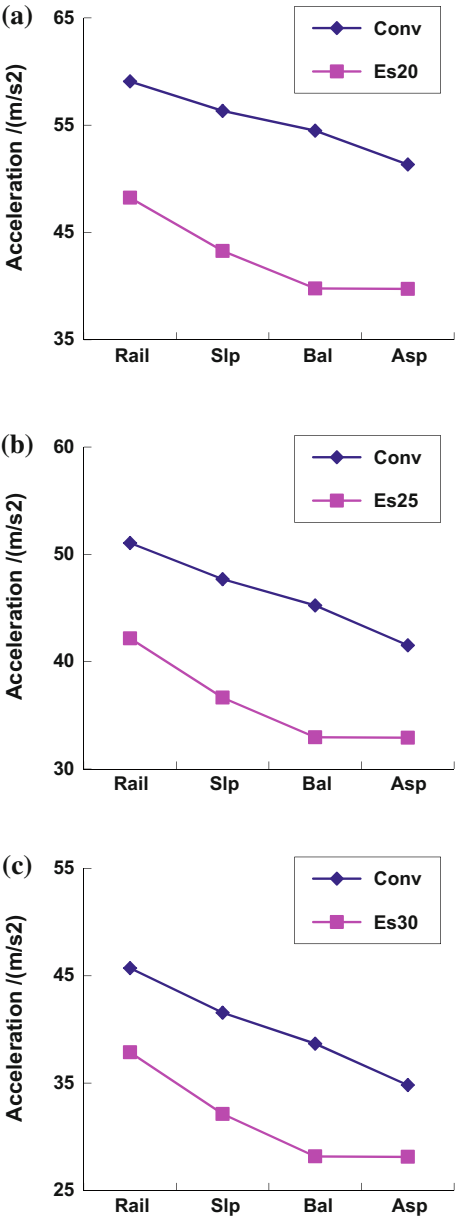

Fig. 3.27 Influence of subgrade module E_s with C_a = 20 % and H_a = 20 cm on accelerations of the track (*Slp* sleeper, *Bal* Ballast, *Asp* Asphalt, *Conv* Conventional ballast track with soft subgrade, E_s subgrade module). **a** E_s = 20 MPa. **b** E_s = 25 MPa. **c** E_s = 30 MPa

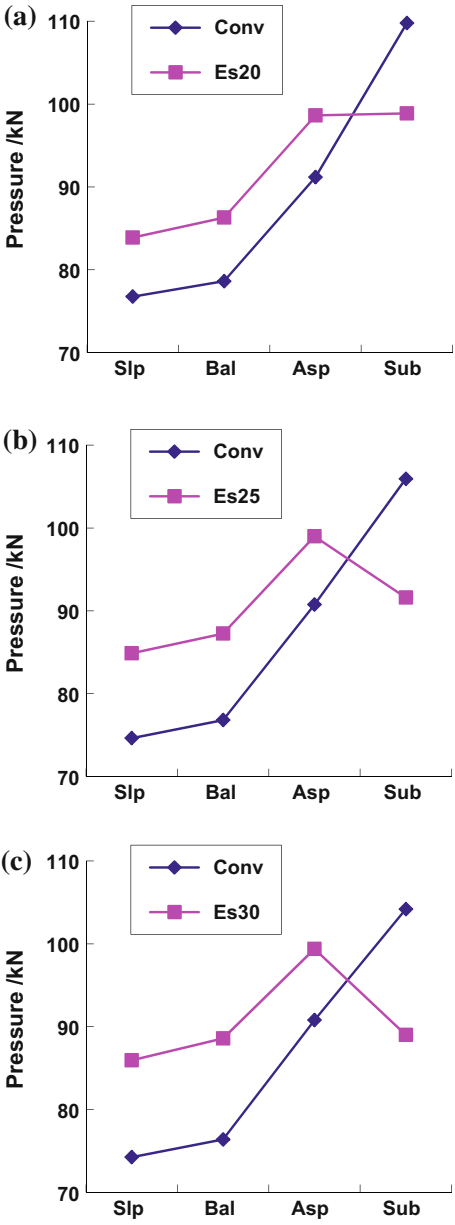

Fig. 3.28 Influence of subgrade module E_s with C_a = 20 % and H_a = 20 cm on pressures on the track (*Slp* sleeper, *Bal* Ballast, *Asp* Asphalt, *Sub* Subgrade, *Conv* Conventional ballast track with soft subgrade, E_s subgrade module).
a E_s = 20 MPa.
b E_s = 25 MPa.
c E_s = 30 MPa

According to the related computational results, conclusions are drawn as follows:

(1) Use of the asphalt trackbed as a substitute for sub-ballast in ballast track with soft subgrade can significantly reduce the deflections and accelerations of the rail, sleeper, ballast, and asphalt and the pressures on the subgrade, as shown in Figs. 3.20, 3.21 and 3.22. This pressure is the primary source to stimulate vibration to nearby buildings. Reduction of the pressure is essential to control the environment vibration and structure-borne noise induced by railways. The dynamic response of the track decreases with the increase of the thickness of the asphalt trackbed.

(2) Figures 3.23, 3.24 and 3.25 indicate both the asphalt and the crumb rubber-modified asphalt trackbed can greatly suppress the deflections and accelerations of the rail, sleeper, ballast, and asphalt and the pressures on the subgrade for ballast track with soft subgrade. However, the crumb rubber-modified asphalt mat only slightly improves the abatement of dynamic responses of the track compared with the normal asphalt trackbed.

(3) Considering the stiffness and the damping ratio and the inertia moment for the crumb rubber-modified asphalt trackbed, the most effective one to influence the capacity of reducing track vibration is the resistant bending modulus of the material $E_s I_s$. Due to the beam action of the track (partly from rail panel and partly from the asphalt layer), which distributes the concentrated wheel loadings over several sleepers and the confined, high-modulus ballast layers, serve to effectively reduce the heavy wheel loadings.

(4) Figures 3.26, 3.27 and 3.28 demonstrate that using asphalt trackbeds instead of sub-ballast has the distinctive effect in reducing vibration of ballast track over soft subgrade. For deflections and accelerations of the rail, sleeper, ballast, and asphalt, the maximum reduction can be up to 14.1 and 18.6 %, respectively, compared with the conventional ballast track with soft subgrade. The maximum reductions of pressures on the subgrade can be up to 14 %.

(5) Ballast track with asphalt trackbed is particularly applicable to heavy-haul railways or railway lines over soft subgrade owing to the fact that the asphalt layer is waterproof and the ballast track with asphalt trackbed has less faults and longer service life.

References

1. Madshus C, Kaynia A (1998) High speed railway lines on soft ground: dynamic response of rail-embankment-soil system. GI515177-1
2. Krylov VV (1994) On the theory of railway-induced ground vibrations. J Phys 4(5):769–772
3. Krylov VV (1995) Generation of ground vibrations by super fast trains. Appl Acoust 44:149–164

4. Krylov VV, Dawson AR (2000) Rail movement and ground waves caused by high speed trains approaching track-soil critical velocities. In: Proceedings of the institution of mechanical engineers, part F. Journal of rail and rapid transit, 214(F):107–116
5. Lei X (2006) Study on critical velocity and vibration boom of track. Chin J Geotech Eng 28 (3):419–422
6. Lei X (2006) Study on ground waves and track vibration boom induced by high speed trains. J China Railway Soc 28(3):78–82
7. Lei X (2007) Analyses of track vibration and track critical velocity for high-speed railway with Fourier transform technique. China Railway Sci 28(6):30–34
8. Sheng X, Jones CJC, Thompson DJ (2004) A theoretical model for ground vibration from trains generated by vertical track irregularities. J Sound Vib 272(3–5):937–965
9. Sheng X, Jones CJC, Thompson DJ (2004) A theoretical study on the influence of the track on train-induced ground vibration. J Sound Vib 272(3–5):909–936
10. Sheng X (2002) Ground vibrations generated from trains. Doctor's Dissertation of University of Southampton, UK
11. Vesic AS (1961) Beams on elastic subgrade and the Winkler hypothesis. In: Proceedings of the 5th international conference on soil mechanics and foundation engineering, Paris, France, (1):845–851
12. Lei X (2007) Dynamic analyses of track structure with Fourier transform technique. China Railway Sci 29(3):67–71
13. Lei X, Sheng X (2008) Advanced studies in modern track theory, 2 edn. China Railway Publishing House, Beijing
14. Lei X et al (2007) Vibration analysis of track for railways with passenger and freight traffic. J Railway Eng Soc 29(3):67–71
15. Lei X, Rose JG (2008) Track vibration analysis for railways with mixed passenger and freight traffic. J Rail Rapid Transit Proc Inst Mech Eng 222(4):413–421
16. Lei X, Rose JG (2008) Numerical investigation of vibration reduction of ballast track with asphalt trackbed over soft subgrade. J Vib Control 14(12):1885–1902

Chapter 4
Analysis of Vibration Behavior of the Elevated Track Structure

The elevated track structure, which has many advantages, such as less land occupation, less settlement, low construction and operation costs, and effective relief of the urban traffic congestion, is widely used in high-speed railway and urban mass transit. However, its loud vibration noise has certain influence on the environment along the railway [1]. By establishing an analytic model and the three-dimensional finite element model of the elevated track structure, the vibration distribution regularity of two types of elevated track structure, that is, the box girder and the U-beam, is investigated, and the attenuation characteristics of environmental vibration induced by elevated track structure with different distances is analyzed. Finally, the adaptability of these two models is compared.

4.1 Basic Concept of Admittance

4.1.1 Definition of Admittance

Admittance is an important index for structure vibration study. Admittance (Y) is defined as the ratio of the response complex amplitude and the excitation complex amplitude generated by the structure while it is subject to harmonic excitation, namely the response caused by unit loads. Response can be displacement, velocity, acceleration, stress, and strain. It is proved by theory and experiment that admittance is related to the inherent characteristics of the structure, such as mass, elasticity, and damping of the structure.

As shown in Fig. 4.1, if force F_j is exerted on point j and response X_i is generated on any point i, then the displacement admittance between i and j can be expressed as follows: $Y_{ij} = \frac{X_i}{F_j}$. If the response point and the excitation point are different, the generated admittance is called cross-point admittance. Impedance is the reciprocal of admittance, namely $Z_{ij} = 1/Y_{ij}$. If response point and excitation

X. Lei, *High Speed Railway Track Dynamics*,
DOI 10.1007/978-981-10-2039-1_4

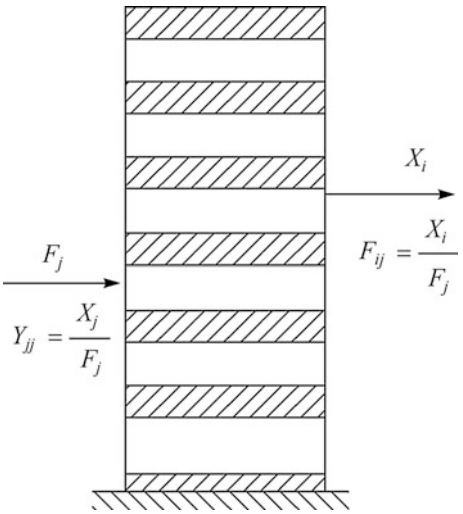

Fig. 4.1 The concept of admittance

Table 4.1 Structure admittance

Symbol	Name	Expression
Y_X	Displacement admittance, dynamic flexibility/(m/N)	X_j/F_j
Y_V	Velocity admittance/(m/s/N)	V_j/F_j
Y_A	Acceleration admittance/(m/s^2/N)	A_j/F_j

point are the same point, the generated admittance is called loading point admittance $Y_{jj} = \frac{X_j}{F_j}$. Table 4.1 shows the symbols, names, expressions, and unit of structure loading point admittance.

4.1.2 Computational Method of Admittance

As mentioned above, the mechanical admittance of stable linear vibration system is equal to the ratio of steady response and the exerted harmonic excitation complex or amplitude. For single degree-of-freedom system, shown in Fig. 4.2, the vibration differential equation is as follows:

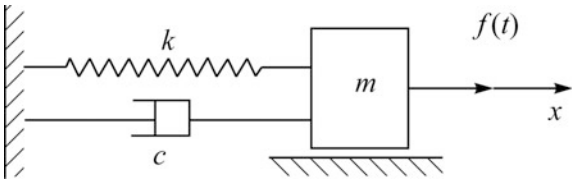

Fig. 4.2 Single degree-of-freedom system model

$$m\frac{\mathrm{d}^2x}{\mathrm{d}t^2}+c\frac{\mathrm{d}x}{\mathrm{d}t}+kx=f(t) \tag{4.1}$$

where m stands for mass, c is damping coefficient, k is stiffness, and $f(t)$ is excitation force.

Suppose the excitation force of the system is as follows:

$$f(t)=\overline{F}\mathrm{e}^{i\omega t} \tag{4.2}$$

The steady-state displacement response is as follows:

$$x(t)=\overline{X}\mathrm{e}^{i\omega t} \tag{4.3}$$

Velocity response is as follows:

$$\dot{x}(t)=i\omega\overline{X}\mathrm{e}^{i\omega t}=\overline{V}\mathrm{e}^{i\omega t} \tag{4.4}$$

Acceleration response is as follows:

$$\ddot{x}(t)=-\omega^2\overline{X}\mathrm{e}^{i\omega t}=\overline{A}\mathrm{e}^{i\omega t} \tag{4.5}$$

The displacement admittance of the system can be expressed as follows:

$$Y_x=\frac{X_j}{F_j}=\frac{x(t)}{f(t)}=\frac{\overline{X}\mathrm{e}^{i\omega t}}{\overline{F}\mathrm{e}^{i\omega t}}=\frac{\overline{X}}{\overline{F}}=\frac{1}{k-\omega^2m+i\omega c} \tag{4.6}$$

The velocity admittance can be expressed as follows:

$$Y_{\dot{x}}=\frac{\dot{x}(t)}{f(t)}=\frac{\overline{V}\mathrm{e}^{i\omega t}}{\overline{F}\mathrm{e}^{i\omega t}}=\frac{\overline{V}}{\overline{F}}=i\omega Y_x \tag{4.7}$$

And the acceleration admittance can be expressed as follows:

$$Y_{\ddot{x}}=\frac{\ddot{x}(t)}{f(t)}=\frac{\overline{A}\mathrm{e}^{i\omega t}}{\overline{F}\mathrm{e}^{i\omega t}}=\frac{\overline{A}}{\overline{F}}=-\omega^2Y_x \tag{4.8}$$

4.1.3 Basic Theory of Harmonic Response Analysis

Harmonic response analysis is used to analyze the steady-state response of linear structure system under harmonic load, in order to calculate the response of the structure at different frequencies and get response curve with frequency variation, such as displacement-frequency curve, velocity-frequency curve, and acceleration-frequency curve. Its input is harmonic load, such as force, pressure, and forced displacement.

Actually, harmonic response analysis is to solve the vibration equation of the structure.

$$\boldsymbol{M}\ddot{\boldsymbol{u}} + \boldsymbol{C}\dot{\boldsymbol{u}} + \boldsymbol{K}\boldsymbol{u} = \boldsymbol{F} \tag{4.9}$$

Where $\boldsymbol{M}$ is mass matrix, $\boldsymbol{C}$ is damping matrix, $\boldsymbol{K}$ is stiffness matrix, $\ddot{\boldsymbol{u}}$ is node acceleration vector, $\dot{\boldsymbol{u}}$ is node velocity vector, $\boldsymbol{u}$ is node displacement vector, and $\boldsymbol{F}$ is load vector exerted on the structure.

Different from the general situation, $\boldsymbol{F}$ and $\boldsymbol{u}$ are complex vectors in the above vibration Eq. (4.9):

$$\boldsymbol{F} = \boldsymbol{F}_{\max} \mathrm{e}^{i\Psi} \mathrm{e}^{i\omega t} = (\boldsymbol{F}_1 + i\boldsymbol{F}_2)\mathrm{e}^{i\omega t} \tag{4.10}$$

$$\boldsymbol{u} = \boldsymbol{u}_{\max} \mathrm{e}^{i\Psi} \mathrm{e}^{i\omega t} = (\boldsymbol{u}_1 + i\boldsymbol{u}_2)\mathrm{e}^{i\omega t} \tag{4.11}$$

Hence, the vibration equation for harmonic response analysis is as follows:

$$\left(-\omega^2\boldsymbol{M} + i\omega\boldsymbol{C} + \boldsymbol{K}\right)(\boldsymbol{u}_1 + i\boldsymbol{u}_2) = (\boldsymbol{F}_1 + i\boldsymbol{F}_2) \tag{4.12}$$

where $\boldsymbol{F}_{\max}$ and $\boldsymbol{u}_{\max}$ stand for load amplitude and displacement amplitude, respectively; i is imaginary unit $\sqrt{-1}$; ω is circular frequency; Ψ is phase angle for load function; t is time; and $\boldsymbol{F}_1$ and $\boldsymbol{u}_1$ are load real part and displacement real part, respectively; $\boldsymbol{F}_2$ and $\boldsymbol{u}_2$ stand for load imaginary part and displacement imaginary part, respectively.

The definition of admittance shows that the vibration characteristics of structure admittance can be analyzed by harmonic response analysis. The finite element analysis software ANSYS has special harmonic response analysis function. ANSYS software has three solutions: full, reduce, and mode superposition. In the following sections, the ANSYS software will be adopted to analyze the harmonic response of the structure. Next, the vibration response of elevated track structure will be investigated by importing the results of the harmonic response analysis into MATLAB programming tools.

4.2 Analysis of Vibration Behavior of the Elevated Bridge Structure

By establishing the analytic beam model and finite element model of the elevated bridge structure, the influence of the elevated bridge structure on the vibration characteristics of track system can be analyzed. In the analytic beam model, the bridge is assumed as Euler beam with free boundary and the bearing simplified as a linear spring with structural damping, as shown in Fig. 4.3 [2]. This chapter mainly

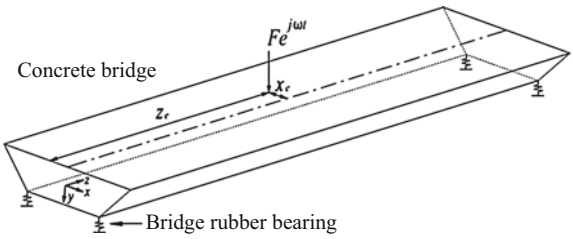

Fig. 4.3 The elevated bridge structure model

studies the vertical vibration characteristics of the elevated track structure, without considering the pier-ground-bridge-coupled vibration. Because the vertical stiffness and inertia are usually much larger than the rubber bearing, the pier can be simplified as a rigid support. A simple analytic beam model or finite element model can be adopted for the bridge.

4.2.1 Analytic Beam Model

In analytic beam model, the bridge is assumed as Euler–Bernoulli beam with free boundary, and the cross-sectional model is shown in Fig. 4.4. Double tracks are laid on bridge deck, and the track center line is located near the junction of top board, flange, and the web. Due to the deviation of track center line from the transverse symmetric center of bridge cross section, torsional and bending vibration of the bridge will occur at the same time when the vehicle is running. Thus, in the analytic model of the elevated track-bridge, the torsional and the bending vibration should be considered, and at the same time, the analysis is simplified by ignoring the warping effect.

As shown in Fig. 4.4, when the bridge cross-sectional shear center and the bridge centroid are in the same vertical line, its vertical bending vibration and torsional vibration around oz axle (bridge center line) are approximately decoupled. Assume harmonic load $Fe^{i\omega t}$ is exerted on bridge track center line and the coordinates are (x_e, z_e), and as shown in Figs. 4.3 and 4.4, without considering the warping effect, the differential equations for bending vibration and torsional vibration of the bridge are as follows [2]:

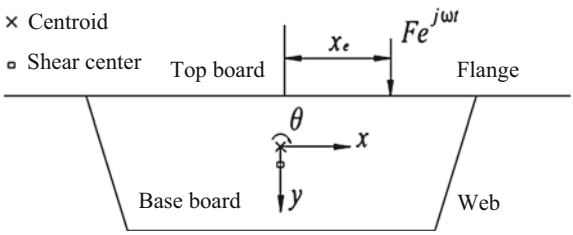

Fig. 4.4 Bridge cross-sectional model

Table 4.2 Loss factors for various materials

Material	Loss factor η	Material	Loss factor η
Steel and iron	0.0001–0.0006	Plexiglass	0.02–0.04
Aluminum	0.0001	Plastic	0.005
Copper	0.002	Wood fiber board	0.01–0.03
Magnesium	0.0001	Sandwich plate	0.01–0.013
Zinc	0.0003	Cork	0.13–0.17
Tin	0.002	Brick	0.01–0.02
Glass	0.0006–0.002	Concrete	0.015–0.05
Large damping plastic	0.1–10	Damping rubber	0.1–5.0
Viscoelastic material	0.2–5.0	Sand (dry sand)	0.12–0.6

$$\rho A\frac{\partial^2 y}{\partial t^2}+EI(1+i\eta)\frac{\partial^4 y}{\partial t^4}=F\mathrm{e}^{i\omega t}\delta(z-z_e) \tag{4.13}$$

$$\rho I_P\frac{\partial^2 \theta}{\partial t^2}-GJ_t(1+i\eta)\frac{\partial^2 \theta}{\partial z^2}=Fx_e\mathrm{e}^{i\omega t}\delta(z-z_e) \tag{4.14}$$

where y is vertical displacement of the bridge; θ is torsion angle of the bridge; ρ is material density; A and I are bridge cross-sectional area and sectional moment of inertia around the horizontal axis, respectively; E is elasticity modulus of material; G is shear modulus of material; η is loss factor shown in Table 4.2 for various materials; I_P is polar moment of inertia of cross section; and J_t is torsional moment of inertia.

Based on mode superposition method, the vertical displacement and the torsional angle of the bridge can be written as follows:

$$y=\sum_{n=1}^{N_B}\phi_n(z)p_n(t),\quad \theta=\sum_{n=1}^{N_T}\varphi_n(z)q_n(t) \tag{4.15a, b}$$

where $\phi_n(z)$ and $\varphi_n(z)$ stand for the regularized mode shape function of the nth bending vibration mode and torsional vibration mode of free boundary beam, respectively; p_n and q_n are corresponding modal coordinates; and N_B and N_T are mode number of bending vibration and torsional vibration, respectively.

$$\begin{cases}\phi_1(z)=\dfrac{1}{\sqrt{\rho AL}},\\ \phi_2(z)=\dfrac{1}{\sqrt{\rho AL}}\sqrt{3}(1-2z/L),\quad 0\le z\le L\\ \phi_n(z)=\dfrac{1}{\sqrt{\rho AL}}[\cosh k_n z+\cos k_n z-C_n(\sinh k_n z+\sin k_n z)],\quad n\ge 3\end{cases} \tag{4.16a}$$

$$\begin{cases} \varphi_1(z) = \dfrac{1}{\sqrt{\rho I_P L}}, & 0 \le z \le L \\ \varphi_n(z) = \sqrt{\dfrac{2}{\rho I_P L}} \cos \dfrac{(n-1)\pi z}{L}, & n \ge 2 \end{cases} \tag{4.16b}$$

where L is the bridge span; k_n is the nth bending vibration mode wave number; C_n is the corresponding coefficient, as shown in Table 4.3; and $\phi_1(z)$, $\phi_2(z)$, and $\varphi_1(z)$ are rigid modes. According to the orthogonality principle, the regularized mode shape function satisfies the following equations:

$$\int_0^L \rho A \phi_{m(z)} \phi_{n(z)} \mathrm{d}z = \begin{cases} 1, m = n \\ 0, m \ne n \end{cases}; \quad \int_0^L EI \phi_{m(z)} \phi''''_{n(z)} \mathrm{d}z = \begin{cases} \omega_n^2, m = n \\ 0, m \ne n \end{cases} \tag{4.17a}$$

$$\int_0^L \rho I_P \varphi_{m(z)} \varphi_{n(z)} \mathrm{d}z = \begin{cases} 1, m = n \\ 0, m \ne n \end{cases}; \quad \int_0^L GJ_t \varphi_{m(z)} \varphi''_{n(z)} \mathrm{d}z = \begin{cases} \omega_{tn}^2, m = n \\ 0, m \ne n \end{cases} \tag{4.17b}$$

where ω_n and ω_{tn} are the natural frequency of the nth bending vibration and torsional vibration of the bridge, respectively, which can be expressed as follows:

$$\omega_n = k_n^2 \sqrt{\frac{EI}{\rho A}}, \qquad \omega_{tn} = \frac{(n-1)\pi}{L} \sqrt{\frac{GJ_t}{\rho I_P}} \tag{4.18a, b}$$

By substituting Eq. (4.15a, b) into Eqs. (4.13) and (4.14), we have

$$\rho A \sum_{n=1}^{N} \phi_n \ddot{p}_n(t) + EI(1 + i\eta) \sum_{n=1}^{N} \phi_n''''(z) p_n(t) = F \mathrm{e}^{i\omega t} \delta(z - z_e) \tag{4.19}$$

$$\rho I_P \sum_{n=1}^{N} \varphi_n \ddot{q}_n(t) - GJ_t(1 + i\eta) \sum_{n=1}^{N} \varphi_n''(z) q_n(t) = F x_e \mathrm{e}^{i\omega t} \delta(z - z_e) \tag{4.20}$$

Both ends of Eqs. (4.19) and (4.20), respectively, are multiplied by mode shape function and integrated over the bridge length, and orthogonality of mode shape function is used to obtain

Table 4.3 Mode shape function parameter of Euler–Bernoulli beam with free boundary

Order n	1	2	3	4	5	≥ 6
C_n	–	–	0.9825	1.0008	1.0000	1.0000
$k_n L$	0	0	4.7300	7.8532	10.996	$(2n-3)\pi/2$

$$\ddot{p}_n(t) + \omega_n^2(1+i\eta)p(t) = F\phi_n(z_e)\mathrm{e}^{i\omega t} \tag{4.21}$$

$$\ddot{q}_n(t) - \omega_{tn}^2(1+i\eta)q_n(t) = Fx_e\varphi_n(z_e)\mathrm{e}^{i\omega t} \tag{4.22}$$

Solving formulas (4.21) and (4.22), we can obtain

$$p_n(t) = P_n\mathrm{e}^{i\omega t} = \frac{F\phi_n(z_e)}{(1+i\eta)\omega_n^2 - \omega^2}\mathrm{e}^{i\omega t}, \quad q_n(t) = Q_n\mathrm{e}^{i\omega t} = \frac{Fx_e\varphi_n(z_e)}{(1+i\eta)\omega_{tn}^2 - \omega^2}\mathrm{e}^{i\omega t} \tag{4.23a, b}$$

By substituting Eq. (4.23a, b) into Eq. (4.15a, b), the vertical displacement amplitude $Y(z)$ and the torsion angle amplitude $\theta(z)$ of the bridge can be calculated. And the dynamic flexibility function of the bridge can be expressed as follows:

$$\gamma_b(x,z;x_e,z_e) = \frac{Y(z)+x\theta(z)}{F} = \sum_{n=1}^{N_B}\frac{\phi_n(z)\phi_n(z_e)}{(1+i\eta)\omega_n^2 - \omega^2} + \sum_{n=1}^{N_T}\frac{xx_e\varphi_n(z)\varphi_n(z_e)}{(1+i\eta)\omega_{tn}^2 - \omega^2} \tag{4.24}$$

According to the concept of dynamic flexibility, the steady displacement response amplitude of the elevated track-bridge structure can be expressed as follows:

$$Y_v(x,z) = F\gamma_b(x,z;x_e,z_e) - \sum_{n=1}^{4}F_{vbn}\gamma_b(x,z;x_{vbn},z_{vbn}) \tag{4.25}$$

where F_{vbn} is the nth force of the bridge rubber bearing; x_{vbn} and z_{vbn} are the horizontal and the vertical coordinates of the bridge bearing. Likewise, the force amplitude of the bridge bearing can be expressed as follows:

$$F_{vbn} = k_{vb}(1+i\eta_{vb})Y_v(x_{vbn},z_{vbn}) \tag{4.26}$$

where k_{vb} is stiffness of the bridge bearing and η_{vb} is loss factor of the bridge bearing.

Substituting the vertical displacement of the bridge rubber bearing derived from Eq. (4.25) into Eq. (4.26), we get

$$-\frac{F_{vbn}}{k_{vb}(1+i\eta_{vb})} = F\gamma_b(x_{vbn},z_{vbn};x_e,z_e) - \sum_{m=1}^{4}F_{vbn}\gamma_b(x_{vbn},z_{vbn};x_{vbn},z_{vbn}), \quad n = 1,2,3,4 \tag{4.27}$$

Substituting the force of the bridge bearing derived from solving formula (4.27) into Eq. (4.25), the displacement response of the elevated track-bridge structure $Y_v(x,z)$ can be obtained, and the dynamic flexibility of the elevated track-bridge can be expressed as follows:

$$\gamma(x,z;x_e,z_e)=\frac{Y_v(x,z)}{F} \tag{4.28}$$

According to the definition of velocity admittance, the velocity admittance amplitude of the elevated track-bridge is as follows:

$$\dot{Y}_v(x,z)=\frac{i\omega Y_v(x,z)}{F} \tag{4.29}$$

4.2.2 Finite Element Model

The finite element analysis software ANSYS is used to establish the box girder bridge structure. SOLID 45 element is used to simulate the box girder, and COMBIN 14 element is used to simulate the elastic bearing of the bridge [3]. The actual geometrical dimension of the box girder is shown in Fig. 4.5, and the length of the bridge is 32 m. Because the influence of the bridge pier on bridge vibration is ignored, the bridge pier is simplified as fixed three degree-of-freedom displacement constraints. The bridge structure parameters are shown in Table 4.4.

Mapping mesh method is used to discretize the bridge, and the finite element mesh of the box girder structure is shown in Fig. 4.6.

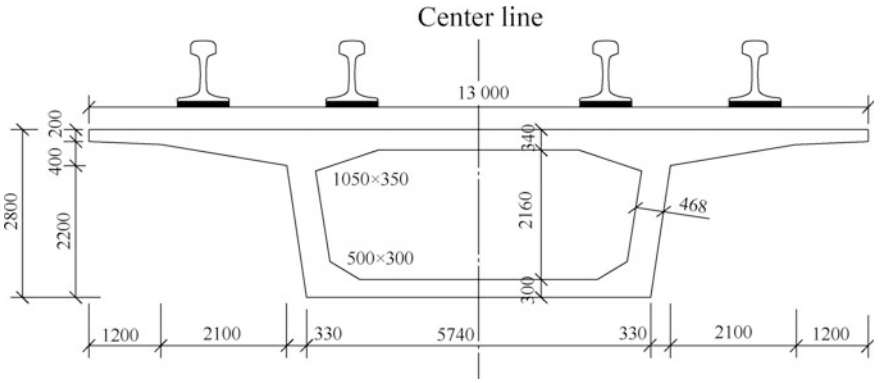

Fig. 4.5 Geometrical dimensions of box girder cross section

Table 4.4 Bridge structure parameter

Parameter	Value
Elasticity modulus/(Gpa)	36.2
Density/(kg/m^3)	2500
Poisson's ratio	0.2
Damping ratio	0.03
Stiffness of bridge bearing/(kN/m)	3.38×10^6

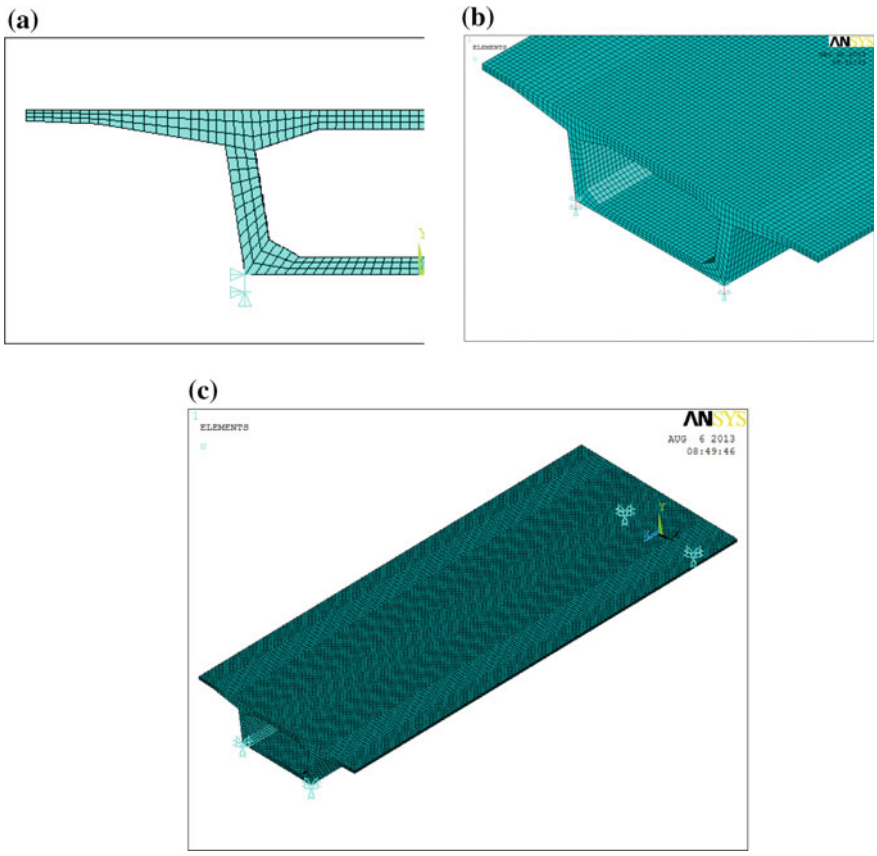

Fig. 4.6 Finite element mesh of the box girder structure. **a** Cross section displacement constraint. **b** Partial enlarged view. **c** Finite element mesh of the box girder

4.2.3 Comparison Between Analytic Model and Finite Element Model of the Elevated Track-Bridge

As shown in Fig. 4.4, a loading point is selected on the center of the bridge span, and the loading point and the other point of 4.5 m away from the loading point are selected as response points, respectively. The loading point velocity admittance and the cross-point velocity admittance for the elevated track-bridge structure can be calculated by employing the analytic model and the finite element model, respectively. The frequency range of traffic noise of the elevated track is mainly of middle and low frequency, among which the main frequency range is below 1000 Hz [1]; thus, only the calculated results below 1000 Hz will be analyzed, as shown in Fig. 4.7 [4].

It is shown in Fig. 4.7 that below 13 Hz, the calculated results of the two models are of no significant difference. The amplitude of the analytic model is slightly

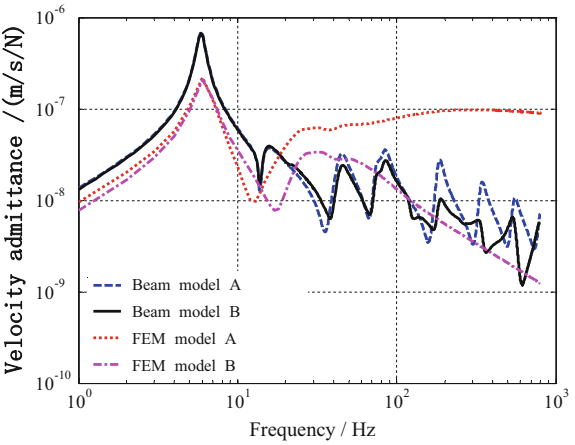

Fig. 4.7 The bridge velocity admittance derived from the analytic model and the finite element model (*A* loading point velocity admittance and *B* cross-point velocity admittance)

larger than that of the finite element model, and both of which appear the first-order peak at about 6 Hz and the second-order peak at about 13 Hz. Above 13 Hz, there is a significant difference between these two models, indicating that the vibration amplitude of the finite element model is significantly larger than that of the analytic model. The amplitude of the analytic model attenuates rapidly, while the finite element model attenuates insignificantly, which indicates that in high-frequency range, the box girder is not suitably simulated by the simple beam model.

4.2.4 The Influence of the Bridge Bearing Stiffness

Five different kinds of the bridge bearing stiffness are considered to investigate its influence on the bridge structure vibration: $k_{vb}, 2k_{vb}, 5k_{vb}, 10k_{vb}, 100k_{vb}$, where $k_{vb} = 3.38 \times 10^9$ N/m. The calculated results are shown in Fig. 4.8 [4]. The first-order bridge vibration frequency increases with the increase of the bridge bearing stiffness, while the vibration amplitude decreases. With the increase of the frequency, the influence of the bearing stiffness on velocity admittance gets smaller and smaller. Above 100 Hz or more, the bridge bearing stiffness barely has influence on bridge vibration.

4.2.5 The Influence of the Bridge Cross Section Model

In recent years, the U-beam has been used in the urban elevated track structure. Compared with the box girder, the U-beam has the following advantages: (1) It beautifies the city landscape and can reduce 50 % visual impact; (2) it reduces 1.5–2 m construction height of the station buildings; and (3) with wheel-rail noise

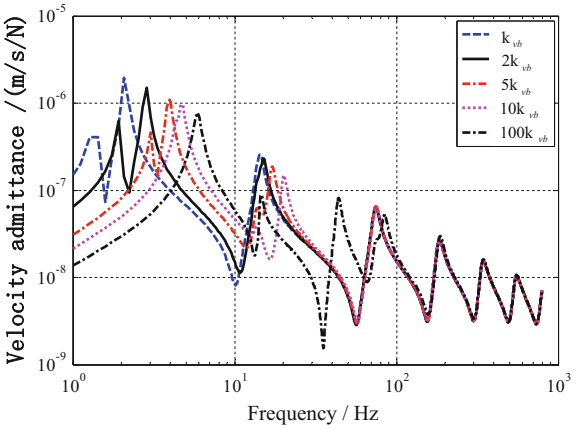

Fig. 4.8 The influence of the bridge bearing stiffness on bridge velocity admittance

insulation function, the web on both sides can reduce the use of noise barrier. At present, the U-beam has been used in the elevated track of many cities in China, such as Chongqing Metro 1, Nanjing Metro 2, and South extension section of the elevated line of Shanghai mass transit 8. In order to explore the influence of the bridge cross-sectional model on the vibration characteristics of the elevated bridge structure, the bridge vibration characteristics corresponding to the U-beam and the box girder cross-sectional models are compared and analyzed. The geometrical dimensions are shown in Fig. 4.9. ANSYS software is used to establish the U-beam model, and the finite element mesh is shown in Fig. 4.10. The loading point velocity admittance of these two kinds of bridge cross section is shown in Fig. 4.11 [4].

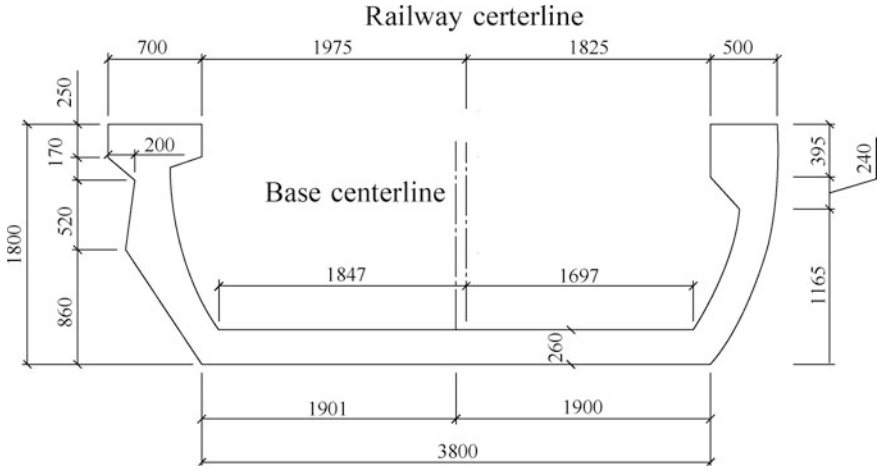

Fig. 4.9 Geometrical dimensions of the U-beam cross section (unit: mm)

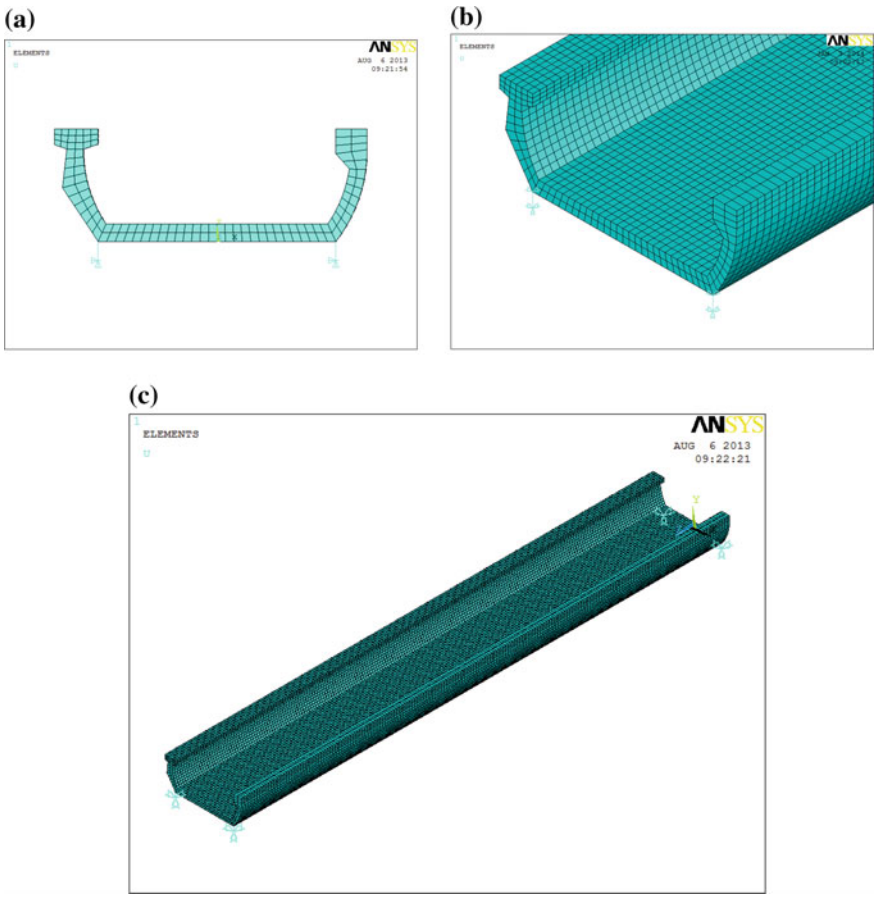

Fig. 4.10 Finite element mesh of the U-beam. **a** Cross section displacement constraint. **b** Partial enlarged view. **c** Finite element mesh of the U-beam

It is shown in Fig. 4.11 that below 25 Hz, the velocity admittance amplitude of the U-beam is much larger than that of the box girder and the first-order frequency of the U-beam is at about 3 Hz and that of the box girder is at about 6 Hz, which corresponds to the natural frequency of the bridge, since the mass of the U-beam per unit length is less than that of the box girder. Above 25 Hz, the amplitude of two kinds of cross section is almost the same. Hence, the change of the bridge cross-sectional model makes no difference to bridge vibration in low-frequency range, from a few tens Hertz to hundreds of Hertz.

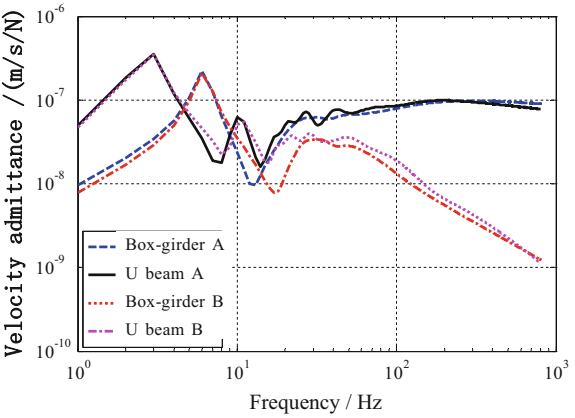

Fig. 4.11 The influence of the bridge cross-sectional model on the bridge velocity admittance (*A* loading point velocity admittance and *B* cross-point velocity admittance)

4.3 Analysis of Vibration Behavior of the Elevated Track Structure

4.3.1 Analytic Model of the Elevated Track-Bridge System

For the analysis of the vibration characteristics of the elevated track-bridge system, the elevated track-bridge system model is established, as shown in Fig. 4.12. In the figure, rail is connected directly on the elevated bridge by rail pads and fasteners. Suppose that the rail is infinite Euler–Bernoulli beam, the rail pad and fastener is a damping spring system with discrete supports, and the bridge is considered as a free beam with finite length supported by four elastic bearings on the pier. Assuming the pier is rigid, the bridge can be simplified with the analytic beam model. For the double track-bridge, the interaction of the two tracks is ignored and only the right-hand side of the track and the elevated bridge system are taken as research objects. To simplify the analysis, only the structure of one bridge span is considered. The dynamic flexibility method is used to study the vertical vibration of the

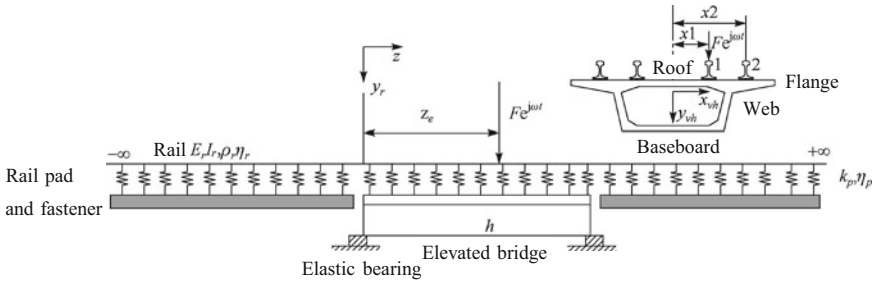

Fig. 4.12 The analytic model of the elevated track-bridge coupling system

track. The dynamic flexibility is defined as the displacement $Y(z)$ caused by the action of unit harmonic load, namely:

$$\gamma = Y(z)/F(\omega) \tag{4.30}$$

Assuming the harmonic load $Fe^{i\omega t}$ acts on rail 1 which is at the longitudinal position $z = z_e$, the vibration differential equations for rail 1 and rail 2 are as follows [2]:

$$\rho_r A_r \frac{\partial^2 y_{r1}}{\partial t^2} + E_r I_r (1 + i\eta_r) \frac{\partial^4 y_{r1}}{\partial t^4} = Fe^{i\omega t}\delta(z - z_e) - \sum_{n=1}^{N} f_{1n}\delta(z - z_{1n}) \tag{4.31}$$

$$\rho_r A_r \frac{\partial^2 y_{r2}}{\partial t^2} + E_r I_r (1 + i\eta_r) \frac{\partial^4 y_{r2}}{\partial t^4} = -\sum_{n=1}^{N} f_{2n}\delta(z - z_{2n}) \tag{4.32}$$

where y_{rj} is the vertical displacement of the rail j; ρ_r and E_r are the density and elasticity modulus of the rail; η_r is loss factor; A_r and I_r are cross-sectional area and moment of inertia around horizontal axle; f_{jn} is the force of the nth rail pad and fastener under rail z_{jn}; z_{jn} is longitudinal position of the rail pad and fastener; j = 1 and 2; $N = N_r \times N_v$ is the total number of the rail pads and fasteners under one rail; N_v is the number of the elevated bridge spans and 1 is taken in Fig. 4.1; N_r is the number of the rail pads and fasteners on one elevated bridge span; and δ is Dirac-delta function.

Only consider the steady-state response of the system, namely $y_{rj} = Y_{rj}e^{i\omega t}$ and $f_{jn} = F_{jn}e^{i\omega t}$, which is substituted into (4.31) and (4.32), and we obtain

$$-\rho_r A_r \omega^2 Y_{r1} + E_r I_r (1 + i\eta_r) Y_{r1}'''' = F\delta(z - z_e) - \sum_{n=1}^{N} F_{1n}\delta(z - z_{1n}) \tag{4.33}$$

$$-\rho_r A_r \omega^2 Y_{r2} + E_r I_r (1 + i\eta_r) Y_{r2}'''' = -\sum_{n=1}^{N} F_{2n}\delta(z - z_{2n}) \tag{4.34}$$

where Y_{rj} is the vertical displacement amplitude of rail j; F_{jn} is the force amplitude of the nth rail pad and fastener under rail j, j = 1 and 2; and superscript "′" means the differential of the longitudinal coordinate.

Since the linear system satisfies the superposition principle, the displacement of the rail is equal to the superposition of the displacements caused by all forces exerted on it (include the external loads and the rail pad and fastener force). The displacement caused by each force is equal to the product of the force and the

corresponding dynamic flexibility, and the steady-state displacement amplitude can be expressed as follows:

$$Y_{r1}(z) = F\alpha(z, z_e) - \sum_{n=1}^{N} F_{1n}\alpha(z, z_{1n}) \tag{4.35}$$

$$Y_{r2}(z) = -\sum_{n=1}^{N} F_{2n}\alpha(z, z_{2n}) \tag{4.36}$$

where $\alpha(z_1, z_2)$ is dynamic flexibility function of the rail (modeled as infinite Euler–Bernoulli beam), namely the steady displacement amplitude of $z = z_1$, induced by unit harmonic load acted on $z = z_2$. The steady-state displacement amplitude can be calculated by the following formula [2]:

$$\alpha(z_1, z_2) = \frac{1}{4E_r I_r(1 + i\eta_r)k^3}(ie^{ik|z_2 - z_1|} - ie^{-k|z_2 - z_1|}) \tag{4.37}$$

where $k = \sqrt[4]{\frac{\rho_r A_r \omega^2}{E_r I_r(1 + i\eta_r)}}$ is complex wave number, and its real part and imaginary part are larger than zero to ensure that the value in the bracket gradually tends to zero with the increase of the distance between the loading point z_2 and the response point z_1.

Similarly, the steady-state displacement response of the elevated bridge h is as follows:

$$Y_h(x_h, z_h) = \sum_{j=1}^{2}\sum_{m=1}^{N_r} F_{jhm}\gamma(x_h, z_h; x_j, z_{jhm}) \tag{4.38}$$

where F_{jhm} is the force of the mth rail pad and fastener corresponding to rail j on the elevated bridge h; z_{jhm} is the longitudinal position of the mth rail pad and fastener in the local coordinate system of the elevated bridge h; x_j is the transversal position of rail j in the local coordinate system, j = 1 and 2; and γ is dynamic flexibility function of the elevated bridge, as shown in formula (4.28).

When $n = (h-1)N_r + m$, F_{jn}, and F_{jhm} correspond to the same force of the rail pad and fastener, the displacement of the rail pad and fastener is as follows:

$$Y_{kjn} = -\frac{F_{jn}}{k_p(1 + i\eta_p)} = -\frac{F_{jhm}}{k_p(1 + i\eta_p)} = Y_{rj}(z_{jn}) - Y_h(x_j, z_{jhm}), j = 1, 2 \tag{4.39}$$

Substituting (4.35), (4.36), and (4.38) into (4.39), we have

$$-\frac{F_{1n}}{k_p(1+i\eta_p)} = -\frac{F_{1hm}}{k_p(1+i\eta_p)} = F\alpha(z_{1n}, z_e) - \sum_{k=1}^{N} F_{1k}\alpha(z_{1n}, z_{1k}) - \sum_{j=1}^{2}\sum_{l=1}^{N_P} F_{jhl}\gamma(x_{1,}z_{1hm}; x_j, z_{jhl}) \tag{4.40}$$

$$-\frac{F_{2n}}{k_p(1+i\eta_p)} = -\frac{F_{2hm}}{k_p(1+i\eta_p)} = -\sum_{k=1}^{N} F_{2k}\alpha(z_{2n}, z_{2k}) - \sum_{j=1}^{2}\sum_{l=1}^{N_P} F_{jhl}\gamma(x_{2,}z_{2hm}; x_j, z_{jhl}) \tag{4.41}$$

Equations (4.40) and (4.41) can be written in matrix form as follows:

$$\mathbf{RF} = \mathbf{Q} \tag{4.42}$$

where $\mathbf{R}$ is the dynamic flexibility matrix of system of $2N \times 2N$ dimension which is comprised of the rail dynamic flexibility α, the rail pad and fastener dynamic flexibility $1/k_p(1+i\eta_p)$, and the elevated bridge dynamic flexibility γ; $\mathbf{F}$ is 2N column vector comprised of the rail pad and fastener forces in two rails; $\mathbf{Q}$ is 2N load vector whose value is $F\alpha(z_{1n}, z_e)$, $n = 1, 2, \ldots,$ N; and the rest element is zero.

The force of the rail pad and fastener can be obtained from (4.42), which is substituted into (4.35) to obtain the rail displacement amplitude in loading point $Y_{r1}(z_e)$. According to the definition of the velocity admittance, the amplitude of the rail velocity admittance is as follows:

$$\dot{Y}_{r1}(z_e) = \frac{i\omega Y_{r1}(z_e)}{F} \tag{4.43}$$

Supposing the elevated bridge foundation is rigid support, Eqs. (4.40) and (4.41) can be rewritten as follows:

$$-\frac{F_{1n}}{k_p(1+i\eta_p)} = -\frac{F_{1hm}}{k_p(1+i\eta_p)} = F\alpha(z_{1n}, z_e) - \sum_{k=1}^{N} F_{1k}\alpha(z_{1n}, z_{1k}) \tag{4.44}$$

$$-\frac{F_{2n}}{k_p(1+i\eta_p)} = -\frac{F_{2hm}}{k_p(1+i\eta_p)} = -\sum_{k=1}^{N} F_{2k}\alpha(z_{2n}, z_{2k}) \tag{4.45}$$

The above admittance is the elevated bridge velocity admittance with the rigid support foundation.

4.3.2 Finite Element Model

To estimate the vibration characteristics of the elevated track structure, three-dimensional elevated track-box girder coupling system model is established with finite element method. Beam element 188 is used to simulate the rail, and the linear spring-damping element COMBIN 14 is used to simulate the rail pad and fastener and the bridge bearing. For the roadbed and the bridge, the block element Solid 45 is used. The influence of the bridge pier on the vibration of the track structure is ignored, and the fixed constraint boundary is adopted to simulate the bridge pier. Track structure parameters are shown in Table 4.5.

To analyze the influence of the elevated track-bridge structure model on track vibration characteristics, the finite element models of the two different cross-sectional models, i.e., the elevated track-box girder and the elevated track U-beam, are established, respectively, as shown in Figs. 4.13 and 4.14 [4].

4.3.3 Damping of the Bridge Structure

According to Energy Conservation Law, without external energy, due to the effect of physical damping, vibration of the structure will be steady with time passing. Damping can consume the vibration energy of the system, and normally, vibration damping exists in every structure. As basic parameter of structure dynamic analysis, damping, which is one of the important factors affecting vibration response of the vehicle-bridge coupling system, will directly affect the analysis results of structure dynamic response [3]. Currently, the value of the bridge structure damping largely depends on experiential formula and experiential value. It is generally believed that damping is mainly caused by viscoelastic materials, viscous damping, friction

Table 4.5 Track structure parameters

Structure	Parameter	Value
Rail with 60 kg/m	Elasticity modulus E_r/GPa	206
	Density ρ_r /(kg/m^3)	7830
	Cross-sectional area A_r/(m^2)	7.745×10^{-3}
	Cross-sectional moment of inertia I_r/(m^4)	3.217×10^{-5}
	Poisson's ratio υ_r	0.3
	Loss factor η_r	0.01
	Sleeper interval d_p/(m)	0.625
	Loss factor of the rail pad and fastener η_p	0.25
Track slab	Density ρ /(kg/m^3)	2500
	Poisson's ratio ρ/(kg/m^3)	0.176
	Elasticity modulus E/(GPa)	39

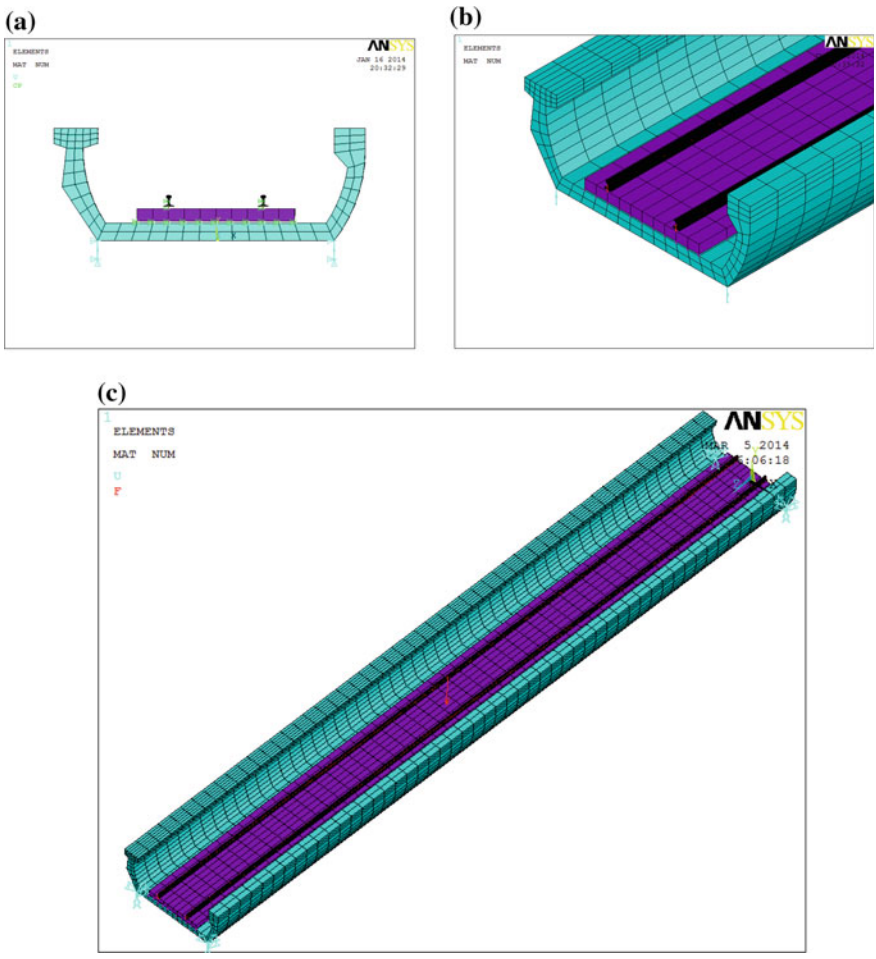

Fig. 4.13 Finite element model of the elevated track U-beam coupling system. **a** Displacement constraint of cross section. **b** Partial enlarged view. **c** Finite element mesh of the U-beam

damping between two solids, and the installment of artificial electromagnetic damper. When external medium damper and interior material damper work together, normally the Rayleigh damping model is employed and its mathematic formula is expressed as follows [5, 6]:

$$\boldsymbol{C} = \alpha \boldsymbol{M} + \beta \boldsymbol{K} \tag{4.46}$$

where $\boldsymbol{M}$ and $\boldsymbol{K}$ are mass matrix and stiffness matrix of the bridge structure; α, β are constants of the Rayleigh damping.

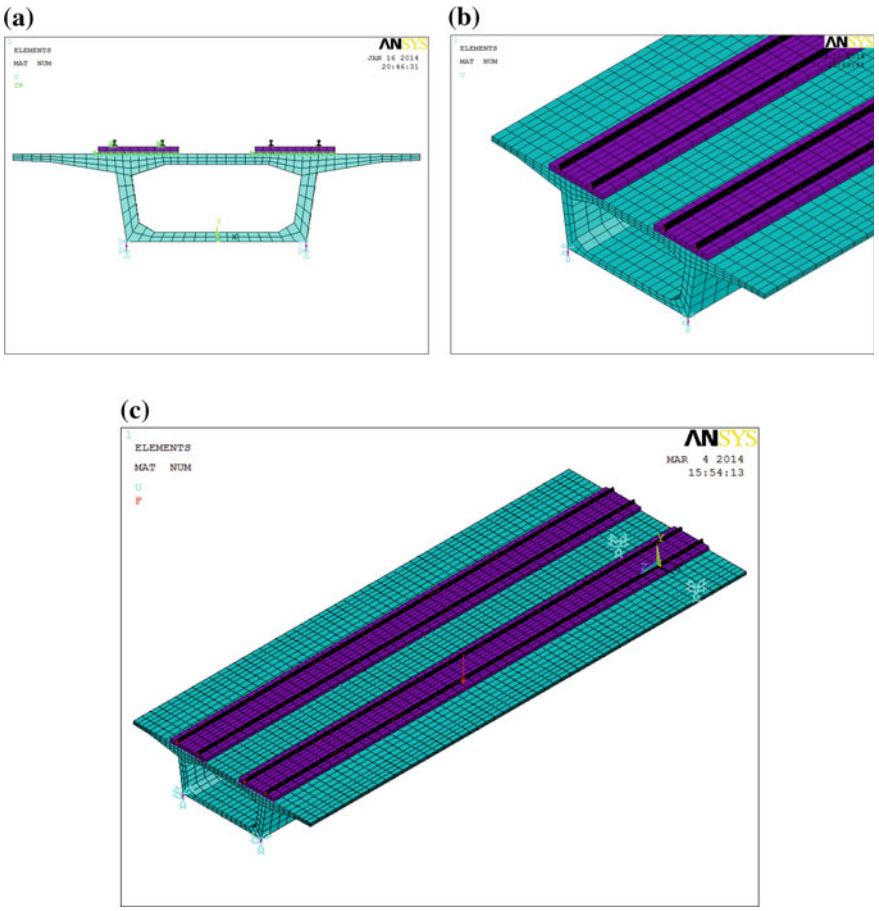

Fig. 4.14 Finite element model of the elevated track-box girder coupling system. **a** Displacement constraint of cross section. **b** Partial enlarged view. **c** Finite element mesh of the box girder

If the natural frequencies of any two vibration modes and their corresponding damping ratios are known, the damping constants can be calculated by the following formula:

$$\alpha = \frac{2(\xi_j\omega_i - \xi_i\omega_j)\omega_i\omega_j}{\omega_i^2 - \omega_j^2}, \quad \beta = \frac{2(\xi_j\omega_i - \xi_i\omega_j)}{\omega_i^2 - \omega_j^2} \tag{4.47}$$

where ω_i, ω_j are the natural vibration frequency of the ith and jth vibration mode, and $\omega = 2\pi f$; ξ_i, ξ_j are the damping ratio of the ith and jth vibration mode.

The natural frequencies ω_i and ω_j mainly depend on the frequency which influences the bridge vibration. Normally, the natural frequency of the first two orders is taken to calculate the damping coefficient. The damping ratio for the concrete bridge is generally within 0.01–0.05, and here, 0.03 is taken for calculation.

4.3.4 Parameter Analysis of the Elevated Track-Bridge System

4.3.4.1 The Influence of the Bridge Foundation

To analyze the influence of the elevated bridge foundation on elevated track vibration, the analytic method is used to investigate the elevated track velocity admittance with rigid foundation and box girder foundation. The calculated result is shown in Fig. 4.15 [4, 7].

As shown in Fig. 4.15, below frequency 20 Hz, the difference between the track velocity admittance amplitude of the two foundations is large, which indicates that the elevated bridge foundation has significant influence on track vibration. There is a peak at frequency 6 Hz, which corresponds to the natural frequency of the elevated bridge. While above 20 Hz, the two curves almost overlap, which indicates that the elevated bridge foundation has no influence on track vibration. Meanwhile, an obvious peak exists at 200 Hz for the two foundations, which corresponds to the natural frequency of the rail-rail pad and fastener system.

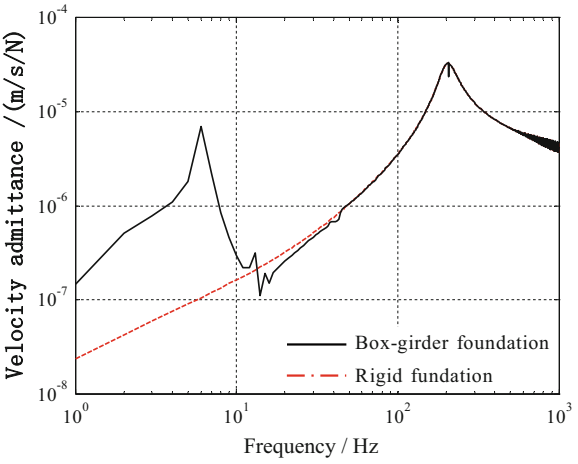

Fig. 4.15 The influence of the track foundation on elevated track velocity admittance

4.3.4.2 The Influence of the Rail Pad and Fastener Stiffness

The stiffness of the rail pad and fastener directly influences the coupling behavior between the track and the elevated bridge. The influence of four different kinds of the rail pad and fastener stiffness, 30, 60, 100, and 200 MN/m, on the velocity admittance of the elevated track structure, is considered. The calculated result is shown in Fig. 4.16 [4, 7].

It is shown in Fig. 4.16, the resonance frequency of the elevated track is closely related to the rail pad and fastener. With the increase of the rail pad and fastener stiffness, the resonance frequencies are 147, 200, 266, and 370 Hz, respectively,and the corresponding resonance peaks decline. Below 147 Hz, the bigger the rail pad and the fastener the stiffness is, the smaller the amplitude of the track velocity admittance will be; the smaller the rail pad and the fastener the stiffness, the bigger the coupling effect between the track and the elevated bridge structure; over the natural frequency of the rail pad and the fastener—the track system, the track vibration tends to decline and the bigger the stiffness of the rail pad and fastener is, the more rapidly the decrease speed will be. Above 800 Hz, the stiffness of the rail pad and fastener has no essential influence on track vibration.

4.3.4.3 The Influence of the Bridge Cross Section Model

The influence of two kinds of the bridge cross-sectional models, i.e., the U-beam and the box girder, on velocity admittance of the elevated track is considered, and the calculated results are shown in Fig. 4.17 [4, 7].

It is shown in Fig. 4.17 that the vibration curves of the elevated track, corresponding to the two kinds of the bridge cross-sectional models, the U-beam and the box girder, basically agree with each other. The cross-sectional model of the bridge structure will influence track vibration mainly below frequency 30 Hz. Within this frequency band range, the natural frequency of the U-beam is slightly smaller than that of the box girder, largely because the bend-resistant stiffness of the U-beam is

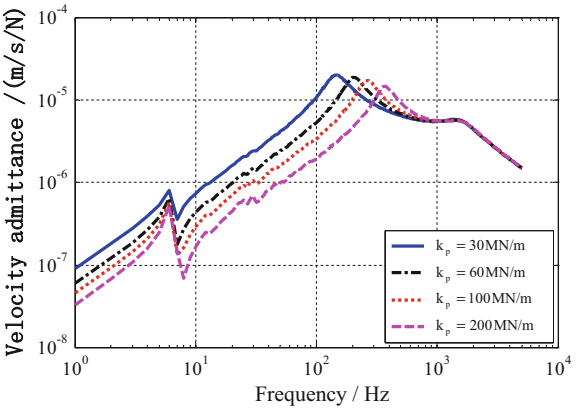

Fig. 4.16 The influence of the rail pad and fastener stiffness on velocity admittance of the elevated track

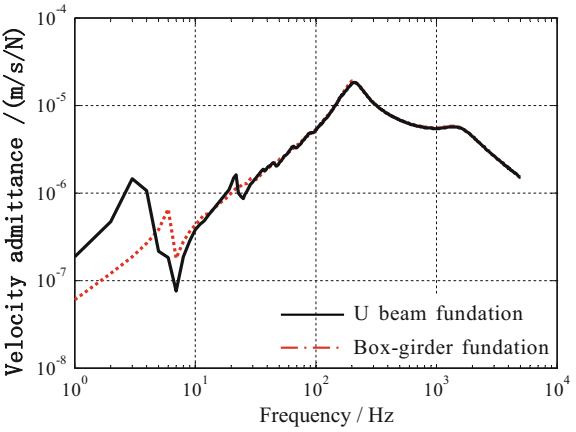

Fig. 4.17 The influence of the bridge cross-sectional model on velocity admittance of the elevated track

less than that of the box girder. It is shown in the figure that the vibration amplitude of the U-beam is obviously larger than that of the box girder. In vibration process, the box girder chamber and web can effectively restrain the vertical vibration of its roof board. Whereas above 30 Hz, the velocity admittance curves of the track structure corresponding to the two bridge cross-sectional models almost overlap, which indicates that within this frequency band range, the influence of the two types of the bridge cross-sectional model on vibration of the track structure is the same.

4.3.4.4 The Influence of the Bridge Structure Damping

The bridge structure damping has certain influence on track vibration. The influence of the following three kinds of damping ratio $\xi = 0.01, \xi = 0.03, \xi = 0.05$ on the velocity admittance of the elevated track structure is considered, and the Rayleigh damping constant corresponding to different damping ratio is shown in Fig. 4.18. The calculated result is shown in Table 4.6 [4, 7].

It is shown in Fig. 4.18 that the influence of the bridge structure damping on the elevated track vibration mainly concentrates on the natural frequencies, 5.97, 200, and 1051 Hz, respectively. Around these three natural frequencies, the track velocity admittance amplitude decreases with increase of the damping ratio. Within other frequency range, change of the damping ratio has no influence on track vibration and the three curves almost overlap completely.

4.3.4.5 The Influence of the Bridge Bearing Stiffness

To study the influence of the bridge bearing stiffness on track vibration, the influence of three different kinds of the bridge bearing stiffness, k_{vb}, $2k_{vb}$, and $5k_{vb}$

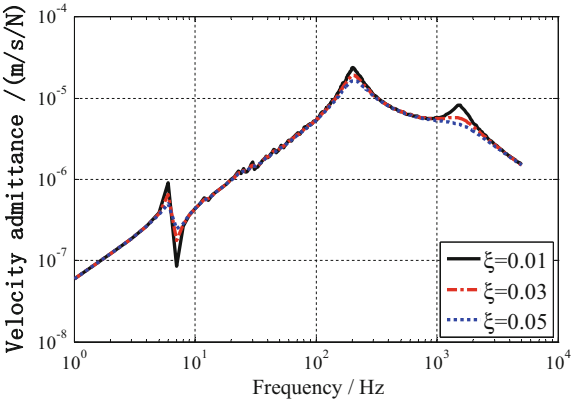

Fig. 4.18 The influence of the bridge structure damping on velocity admittance of the elevated track

Table 4.6 The Rayleigh damping constant corresponding to different damping ratio

Damping ratio	ω_i	ω_j	α	β
$\xi = 0.01$	5.97	200	0.7285	1.55×10^{-5}
$\xi = 0.03$	5.97	200	2.1854	4.64×10^{-5}
$\xi = 0.05$	5.97	200	3.6400	7.73×10^{-5}

(k_{vb} = 3.38 × 10^6 kN/m), on the velocity admittance of the elevated track structure are considered. The calculated result is shown in Fig. 4.19 [4, 7].

It is shown in Fig. 4.19 that these three curves almost overlap with a slight change around 6 Hz, the natural frequency of the elevated bridge, which indicates that the bridge bearing stiffness only has slight influence on track vibration.

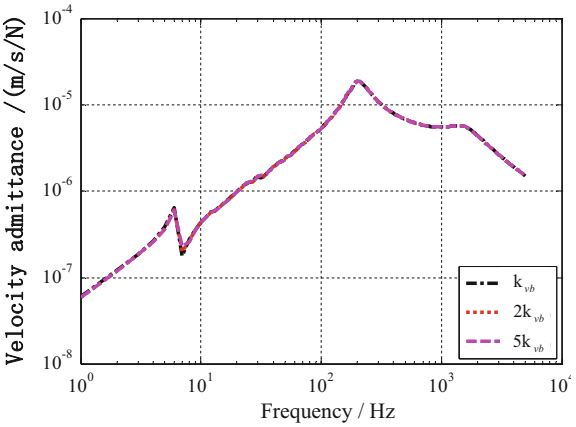

Fig. 4.19 The influence of the bridge bearing stiffness on the velocity admittance of the elevated track

4.4 Analysis of Vibration Attenuation Behavior of the Elevated Track Structure

4.4.1 The Attenuation Rate of Vibration Transmission

When the rail is excited at one point, the vibration will transmit to both ends along the rail and the vibration attenuates with the increase of distance. Its attenuation characteristics can be expressed with loss factor. The bigger the loss factor is, the more rapidly the vibration attenuates. The vibration attenuation along the track is related to the exciting frequency. In the following, the vibration transmission characteristics of the track structure along its length under different exciting frequencies will be analyzed and the fitting attenuation curves will be obtained, as shown in Fig. 4.20. The calculated result of attenuation rate of the track vibration transmission is shown in Fig. 4.21. For comparison, the measured attenuation rate of the track vibration transmission in Reference [8] is given, as shown in Fig. 4.22 [4, 9].

By comparing Fig. 4.21 with Fig. 4.22, it can be observed that the trend of calculated attenuation rate is consistent with that of the measured attenuation rate. At frequencies below 10 Hz, the attenuation rate value is relatively small. Between 10 and 100 Hz, the attenuation rate value is bigger. However, at frequencies above the rail—the rail pad and fastener resonance frequency (about 200 Hz), the track attenuation rate begins to decrease rapidly. Above 700 Hz, the attenuation rate rises again. At 5000 Hz, it appears an attenuation rate peak.

To study the influence of the elevated track structure parameters on track structure loss factor, influences of different kinds of the track foundation, the bridge cross-sectional model, the rail pad and fastener, the damping ratio, and the bridge bearing stiffness on the vibration attenuation rate of the elevated track are considered. The calculated results are shown in Figs. 4.23, 4.24, 4.25, 4.26 and 4.27 [4, 9].

It is shown in Fig. 4.23 that below the resonance frequency 200 Hz, the attenuation rate of the elevated box girder foundation is obviously lower than that of the rigid foundation, which indicates that the track vibration, laid on elevated box girder, is much bigger than that on the rigid foundation. Above 200 Hz, there is no significant difference for the vibration attenuation rates between these two track foundations.

It is shown in Fig. 4.24 that below the resonance frequency 200 Hz, the bridge cross-sectional model has significant influence on track vibration attenuation rate. The attenuation rate of the box girder is obviously bigger than that of the U-beam, indicating that the vibration reduction effects of the box girder is better than that of the U-beam.

It is shown in Fig. 4.25 that below the track resonance frequency 147 Hz, corresponding to the rail pad and fastener stiffness 30 MN/m, the track vibration attenuation rate increases with the decrease of the rail pad and fastener stiffness, whereas within the frequency range of 147–1000 Hz, the track vibration attenuation

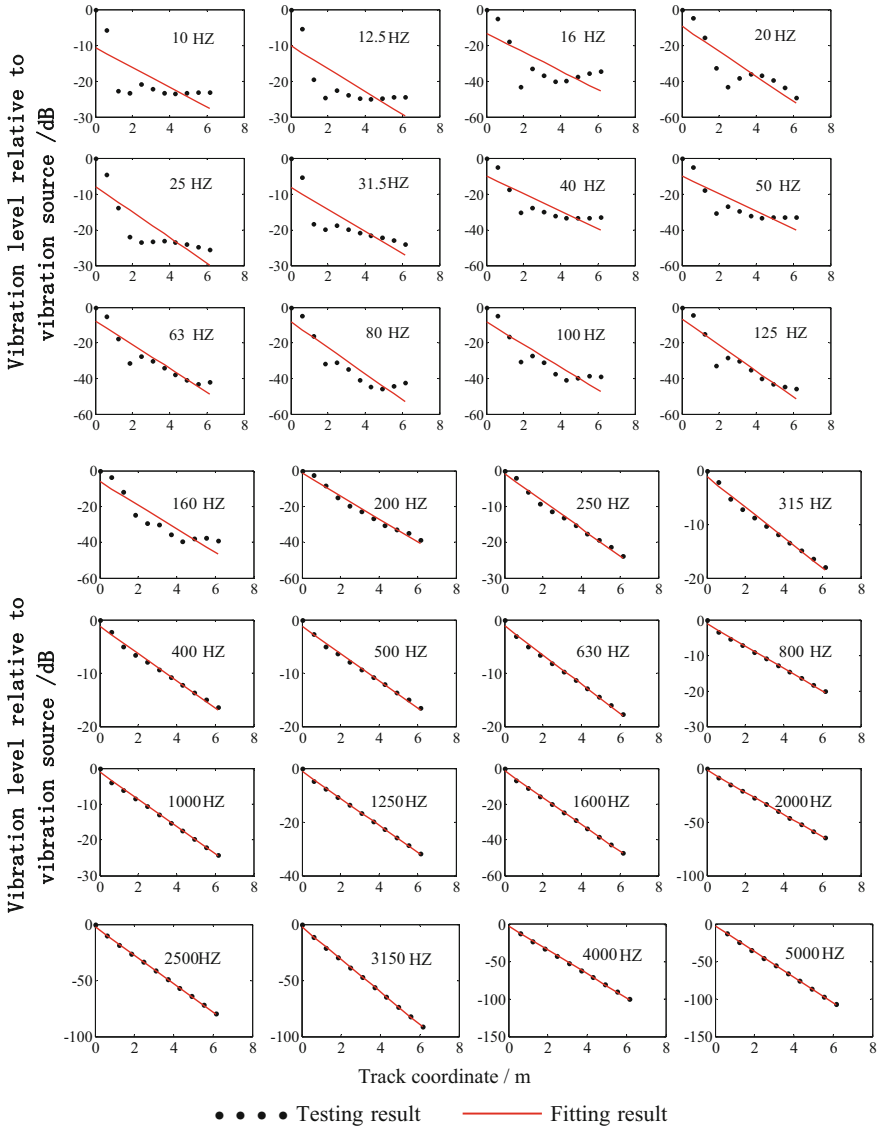

Fig. 4.20 The distribution of track vibration along the rail

rate will also increase with the increase of the rail pad and fastener stiffness and the attenuation rate tends to vary curvedly with frequency. Above 1000 Hz, the rail pad and fastener stiffness barely has influence on track vibration attenuation rate. From the perspective of reducing vibration and noise, it is benefit to adopt the weak rail pad and fastener stiffness.

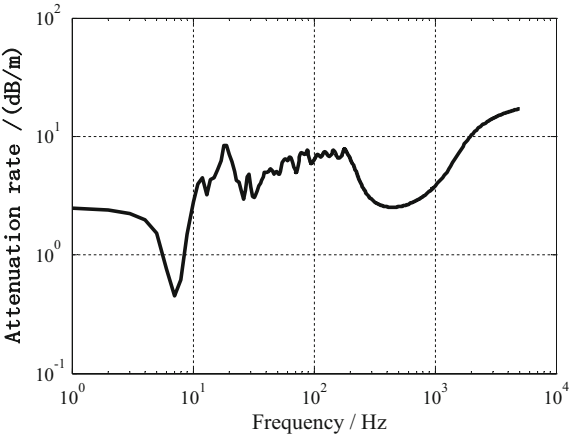

Fig. 4.21 The calculated track vibration attenuation rate

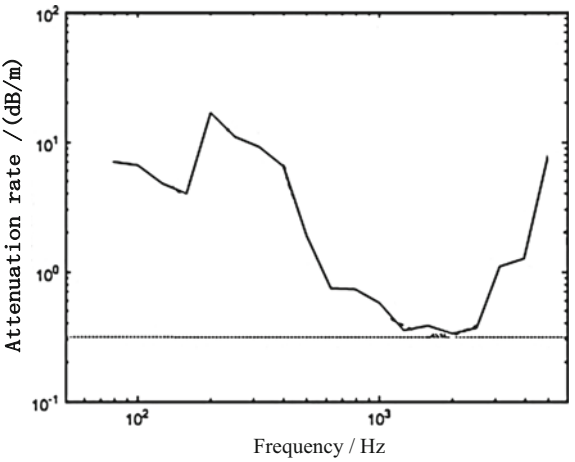

Fig. 4.22 The measured track vibration attenuation rate

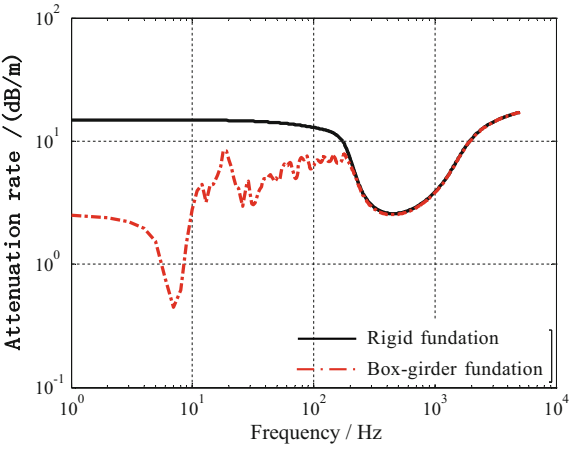

Fig. 4.23 The influence of the track foundation on the attenuation rate of track vibration

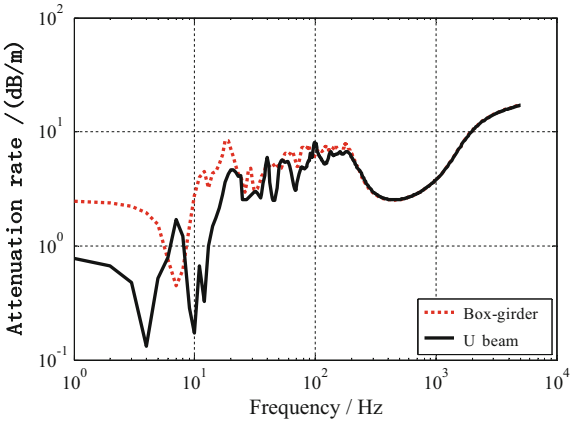

Fig. 4.24 The influence of the bridge cross-sectional model on track vibration attenuation rate

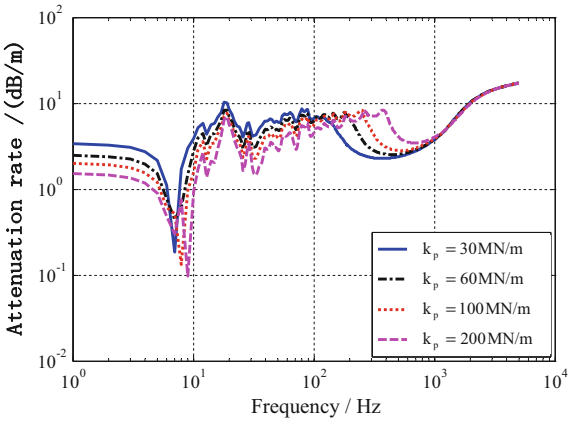

Fig. 4.25 The influence of the rail pad and fastener stiffness on track vibration attenuation rate

It is shown in Fig. 4.26 that the influence range of different structure damping ratio on track vibration attenuation rate is mainly concentrated on the peak. Below the resonance frequency 200 Hz, the bigger the damping ratio is, the smaller the track attenuation rate at the peak will be. Within the range of 200–2000 Hz, the track attenuation rate increases significantly with the increase of the structure damping ratio. Above 2000 Hz, the damping ratio of the bridge structure basically has no influence on track vibration attenuation.

It is shown in Fig. 4.27 that the bridge bearing stiffness has slight influence on track vibration attenuation. At the frequencies above 200 Hz, the bridge bearing stiffness has almost no influence on track vibration attenuation, which is mostly consistent with the findings of Sect. 4.3.4.5.

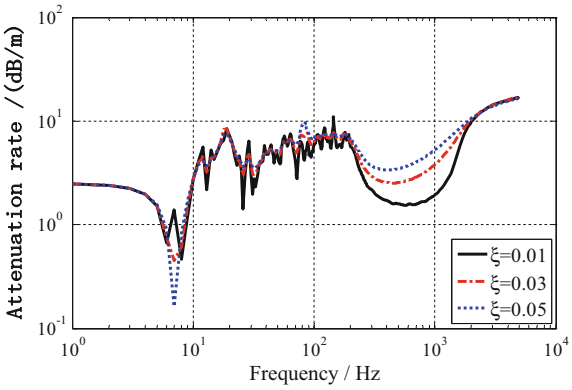

Fig. 4.26 The influence of the damping ratio on track vibration attenuation rate

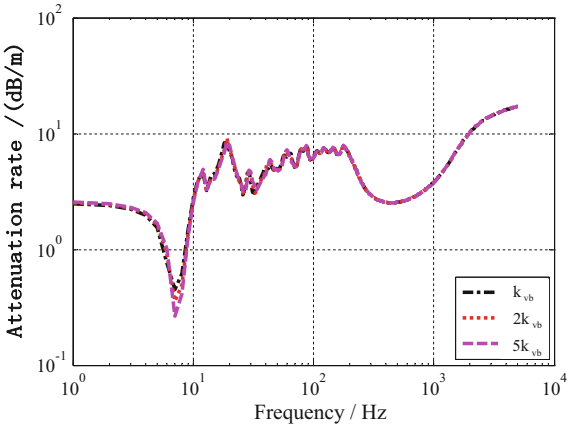

Fig. 4.27 The influence of the bridge bearing stiffness on track vibration attenuation rate

4.4.2 Attenuation Coefficient of Rail Vibration

The attenuation coefficient of rail vibration η_{RV} is another important index specified for rail transmission attenuation, and its definition is as follows:

$$\eta_{RV} = -\frac{\Delta_V}{2k_{RV}} \tag{4.48}$$

where Δ_V is the ratio of the rail vertical vibration attenuation and the distance (unit: dB/m). k_{RV} is wave number of rail bending vibration, and the computational formula is as follows:

$$k_{RV} = \sqrt[4]{\left(\frac{\omega}{r_{RV}c_l}\right)^2} \tag{4.49}$$

where r_{RV} is rail vertical bending radius of gyration; $r_{RV} = \sqrt{I_x/A}$ and I_x, A stand for rail sectional moment of inertia around the horizontal axis and rail cross-sectional area, respectively; c_l is rail longitudinal wave velocity, $c_l = \sqrt{\frac{E}{\rho}}$ where E is elasticity modulus and ρ is material density.

References

1. He J, Wan Q, Jiang W (2007) Analysis of the elevated urban rail transit noise. Urban Mass Transit 10(8):57–60
2. Li Z (2010) Study on modeling, prediction and control of structure-borne noise from railway viaduct. Doctor's Dissertation of Shanghai Jiaotong University, Shanghai
3. D Hou, X Lei, Q Liu (2006) Analysis of dynamical responses of floating slab track system. J Railway Eng Soc 11(8):18–24
4. Zeng Q (2007) The prediction model and analysis of wheel-rail noise of elevated rail. Master's thesis of East China Jiaotong University, Nanchang
5. L Fan (1997) Bridge seismic. Tongji University Press, Shanghai
6. Cai C (2004) Theory and application of train-track-bridge coupling vibration in high speed railways. Doctor's Dissertation of Southwest Jiaotong University, Chengdu
7. Zeng Q, Mao S, Lei X (2013) Analysis on vibration characteristics of elevated track structure. J East China Jiaotong Univ 30(6):1–5
8. Jones CJC, Thompson DJ, Diehl RJ (2006) The use of decay rates to analyze the performance of railway track in rolling noise generation. J Sound Vib 293(3–5):485–495
9. Zeng Q, Lei X (2014) The analysis of elevated rail wheel-rail noise and prediction. Urban Mass Transit 17(12):57–60

Chapter 5
Track Irregularity Power Spectrum and Numerical Simulation

The railway track is an engineering structure whose operation and maintenance are undertaken at the same time. Due to long-time running, the accumulated deformation of track structure is increasing, which would cause various kinds of track irregularities: track profile irregularity, track cross-level irregularity, track alignment irregularity and track gauge irregularity. These irregularities will greatly excite the detrimental vibration between vehicle and track, not only deteriorating the train running quality, but also posing extremely unfavorable effects on the parts damage of wheel-rail system and the track quality. The measured data at home and abroad demonstrate that track irregularity is essentially a random process and it is processed as stationary ergodic random process in simulation analysis of track structure and is the exciting source of the random vibration of vehicle-track system. Therefore, to study and measure the statistical characteristics of track irregularity is the basis for investigating the random vibration of vehicle-track system.

The measurement of track irregularity statistical characteristics has long been the study focus outside China. In 1964, the British Railway Administration initiated related researches [1]. Britain, Japan, Germany, America, Russia, India, and Czech Republic have measured their own power spectral density of track irregularity and correlation function, respectively. China has also done a lot of research in this area. In 1982, Luo Lin from China Academy of Railway Sciences studied the measuring methods of different kinds of track irregularity. In 1985, the random vibration research laboratory of the former Changsha Railway Institute (now Central South University) divided the track irregularity into elastic irregularity and geometric irregularity. By analyzing and processing the track irregularity measured along Beijing-Guangzhou line, different kinds of track irregularity spectrum and the analytic expression of the irregularity power spectral density of Chinese first-class trunk track were obtained [2].

X. Lei, *High Speed Railway Track Dynamics*,
DOI 10.1007/978-981-10-2039-1_5

5.1 Basic Concept of Random Process

Let E be a random test, $S = \{e\}$ is the sample space of test. If for each $e \in S$, we can always determine the function about time t corresponding to it according to a certain rule.

$$x(e,t) \quad t \in T \tag{5.1}$$

As a result, for all the $e \in S$, a family of function about time t will be got. We refer to this family of function about time t as the random process [3]. And each function of the family is referred to as the sample function of the random process, as is shown in Fig. 5.1.

The further explanation of the above definition is as below:

(1) For the specific $e_i \in S$, namely for a specific test result, $x(e_i, t)$ is a defined sample function, which can be interpreted as a physical realization of the random process and can be commonly denoted as $x_i(t)$.
(2) For each fixed time, such as $t = t_1 \in T$, $x(e, t_1)$ is a random variable.

According to explanation (2), the random process can be defined in another form:

If $x(t_1)$ is a random variable for each fixed time $t_1 \in T$, $x(t)$ is referred to as a random process. In other words, the random process is a family of random variable depending on the time t.

For example, if $x(t) = a\cos(\omega t + \theta)$, a, ω are constants, θ is random variable evenly distributed in $(0, 2\pi)$, it has

$$x_i(t) = a\cos(\omega t + \theta_i).$$

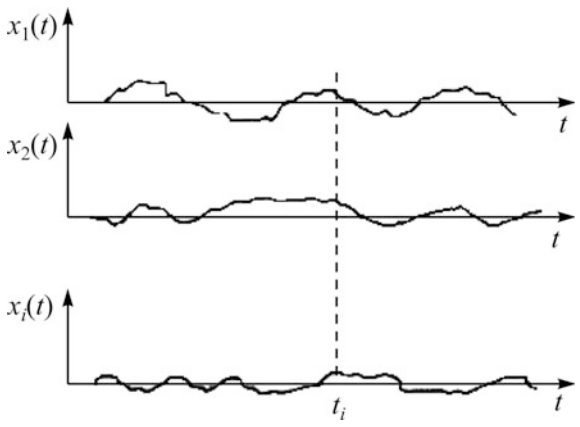

Fig. 5.1 The sample function of random process

5.1.1 Stationary Random Process

In actual engineering, there are quite a number of random processes. Both the present condition and the previous condition have strong influence on the future condition.

The characteristic of a stationary random process is that the statistical properties of the process do not change with time translation or time origin selection.

The numerical characteristics of a random process are as follows.

Let $x(t)$ be a random process, for fixed time t_1, $x(t_1)$ is a random variable, and its mean or mathematical expectation is normally related to t_1, which is denoted as follows:

$$\mu(t_1) = E[x(t_1)] = \int_{-\infty}^{+\infty} x_1 f_1(x_1, t_1) \mathrm{d}x_1 \tag{5.2}$$

where $f_1(x_1, t_1)$ is one-dimensional probability density of $x(t)$, $\mu(t_1)$ is the mean of $x(t)$.

Mean square deviation is as follows:

$$\sigma^2(t) = E\{[x(t) - \mu(t)]^2\} \tag{5.3}$$

where $\sigma(t)$ is mean square deviation, denoting the deviation of random process $x(t)$ relative to mean at time t, as is shown in Fig. 5.2.

The numerical characteristics of a stationary random process are as follows:

(1) The mean value is constant;
(2) The autocorrelation function is the function of single variable $\tau = t_2 - t_1$.

The autocorrelation function is defined as follows:

$$R(t_1, t_2) = E[x(t_1)x(t_2)] = \int_{-\infty}^{+\infty} \int_{-\infty}^{+\infty} x_1 x_2 f_2(x_1 x_2; t_1 t_2) \mathrm{d}x_1 x_2 \tag{5.4}$$

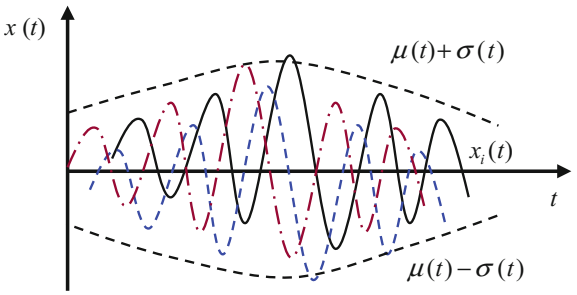

Fig. 5.2 The digital characteristics of a random process

or

$$R(\tau) = E[x(t)x(t+\tau)] = \int_{-\infty}^{+\infty}\int_{-\infty}^{+\infty} x_1 x_2 f_2(x_1 x_2; \tau) dx_1 x_2. \tag{5.5}$$

5.1.2 Ergodic

Definition: Let $x(t)$ be a stationary process,

(1) If $\langle x(t)\rangle = E[x(t)] = \mu$, the mean of process $x(t)$ is ergodic.
Under normal circumstances, a different sample function $x(t)$ has a different time mean, which is a random variable. If the mathematical expectation (statistical mean) of $x(e,t)$ is equal to the time mean of its sample function $x(t)$ with probability 1, the mean of $x(e,t)$ is ergodic.
(2) If $\langle x(t)x(t+\tau)\rangle = E[x(t)x(t+\tau)] = R(\tau)$, the autocorrelation function of process $x(t)$ is ergodic;
(3) If the mean and autocorrelation function of process $x(t)$ are ergodic, $x(t)$ is ergodic.

The time mean and time-correlation function mean of random process $x(t)$ are defined as follows:

$$\langle x(t)\rangle = \underbrace{\lim}_{T\to\infty} \frac{1}{2T}\int_{-T}^{T} x(t)\mathrm{d}t \tag{5.6}$$

$$\langle x(t)x(t+\tau)\rangle = \underbrace{\lim}_{T\to\infty} \frac{1}{2T}\int_{-T}^{T} x(t)x(t+\tau)\mathrm{d}t \tag{5.7}$$

For an ergodic process, the digital characteristics can be obtained according to a single sample function.

5.2 Random Irregularity Power Spectrum of the Track Structure

As is shown in Fig. 5.3, there are different kinds of track irregularity: profile, cross-level, alignment, gauge, and twist.

Track irregularity can be simulated as random function changing with the length of rail line. The random function can be considered as random wave which is the superposition of a series of harmonic waves with different wavelength, amplitude, and phase [1].

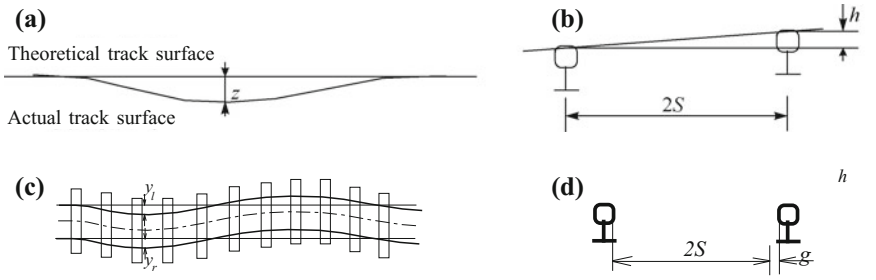

Fig. 5.3 Track geometric irregularity. *a* Profile irregularity. *b* Cross level irregularity. *c* Alignment irregularity. *d* Gauge irregularity

Power spectral density (PSD) function is the most important and commonly used statistical function to express the track irregularity taken as stationary random process. In engineering, power spectrum diagram is often used to describe the change of spectral density function with frequency. Track irregularity power spectrum diagram is a continuously changing curve with spectral density as vertical coordinate and frequency or wavelength as horizontal coordinate, which clearly indicates that the irregularity changes with frequency. Generally, it is more convenient to use spatial frequency $f(\text{cycle/m})$ or $\omega(\text{rad/m})$ to describe the track irregularity. The relationship between them, and the relationship with time frequency $F(\text{cycle/s})$ and $\Omega(\text{rad/s})$ are

$$\begin{cases} \omega = 2\pi f \\ \omega = \Omega / V \\ f = F / V \end{cases} \tag{5.8}$$

where V is the train speed (m/s).

The unit of the track irregularity power spectral density is commonly $\text{mm}^2/\text{cycle/m}$, $\text{mm}^2/\text{rad/m}$, or $\text{cm}^2/\text{cycle/m}$, $\text{cm}^2/\text{rad/m}$, or $\text{m}^2/\text{cycle/m}$, $\text{m}^2/\text{rad/m}$.

5.2.1 American Track Irregularity Power Spectrum

Based on a large number of field measured data, Federal Railroad Administration of America (FRA) obtained irregularity power spectral density function of rail line, which was fitted to a function expressed by cutoff frequency and roughness constant [4]. The applicable wavelength range for the function is 1.524–304.8 m. The track irregularity in the USA can be divided into six levels.

Track profile irregularity power spectral density function (the profile irregularity of rail surface along the track extension direction) is as follows:

$$S_{\mathrm{v}}(\omega)=\frac{kA_{\mathrm{v}}\omega_{\mathrm{c}}^2}{(\omega^2+\omega_{\mathrm{c}}^2)\omega^2}\ (\mathrm{cm}^2/\mathrm{rad/m}) \tag{5.9}$$

Track alignment irregularity power spectral density function (the irregularity of track centerline along track extension direction) is as follows:

$$S_{\mathrm{a}}(\omega)=\frac{kA_{\mathrm{a}}\omega_{\mathrm{c}}^2}{(\omega^2+\omega_{\mathrm{c}}^2)\omega^2}\ (\mathrm{cm}^2/\mathrm{rad/m}) \tag{5.10}$$

Track cross-level and gauge irregularity power spectral density function (track cross-level irregularity refers to the irregularity along the track extension direction caused by the height difference between the corresponding points of left rail and right rail; track gauge irregularity refers to the gauge deviation irregularity of left rail and right rail along the track extension direction) is as follows:

$$S_{\mathrm{c}}(\omega)=\frac{4\,kA_{\mathrm{v}}\omega_{\mathrm{c}}^2}{(\omega^2+\omega_{\mathrm{c}}^2)\left(\omega^2+\omega_{\mathrm{s}}^2\right)}\ (\mathrm{cm}^2/\mathrm{rad/m}) \tag{5.11}$$

where $S(\omega)$ is track irregularity power spectral density function ($\mathrm{cm}^2/\mathrm{rad/m}$), ω is spatial frequency (rad/m), ω_{c} and ω_{s} are cutoff frequency (rad/m), A_{v} and A_{a} are roughness coefficients (cm^2 rad/m), related to line level, and their values are shown in Table 5.1. k is generally 0.25.

5.2.2 *Track Irregularity Power Spectrum for German High-Speed Railways [5]*

Track profile irregularity power spectral density function is as follows:

$$S_{\mathrm{v}}(\omega)=\frac{A_{\mathrm{v}}\omega_{\mathrm{c}}^2}{(\omega^2+\omega_{\mathrm{r}}^2)\left(\omega^2+\omega_{\mathrm{s}}^2\right)}(\mathrm{m}^2/\mathrm{rad/m}) \tag{5.12}$$

Table 5.1 Parameters of American track irregularity power spectral density function

Parameter	Parameter values for different line levels					
	1	2	3	4	5	6
$A_{\mathrm{v}}/(\mathrm{cm}^2$ rad/m)	1.2107	1.0181	0.6816	0.5376	0.2095	0.0339
$A_{\mathrm{a}}/(\mathrm{cm}^2$ rad/m)	3.3634	1.2107	0.4128	0.3027	0.0762	0.0339
$\omega_{\mathrm{s}}/$(rad/m)	0.6046	0.9308	0.8520	1.1312	0.8209	0.4380
$\omega_{\mathrm{c}}/$(rad/m)	0.8245	0.8245	0.8245	0.8245	0.8245	0.8245

Table 5.2 Parameters of track irregularity power spectral density function for German high-speed railways

Track grade	$\omega_c/(\text{rad/m})$	$\omega_r/(\text{rad/m})$	$\omega_s/(\text{rad/m})$	$A_a/(10^{-7}\text{m rad})$	$A_v/(10^{-7}\text{m rad})$	$A_g/(10^{-7}\text{ m rad})$
Low interference	0.8246	0.0206	0.4380	2.119	4.032	0.532
High interference	0.8246	0.0206	0.4380	6.125	10.80	1.032

Track alignment irregularity power spectral density function is as follows:

$$S_a(\omega) = \frac{A_a\omega_c^2}{(\omega^2+\omega_r^2)(\omega^2+\omega_s^2)}\,(\text{m}^2/\text{rad/m}) \tag{5.13}$$

Track cross-level irregularity power spectral density function is as follows:

$$S_c(\omega) = \frac{A_v\omega_c^2\omega^2}{(\omega^2+\omega_r^2)(\omega^2+\omega_c^2)(\omega^2+\omega_s^2)}\,(\text{m}^2/\text{rad/m}) \tag{5.14}$$

Track gauge irregularity power spectral density function is as follows:

$$S_g(\omega) = \frac{A_g\omega_c^2\omega^2}{(\omega^2+\omega_r^2)(\omega^2+\omega_c^2)(\omega^2+\omega_s^2)}\,(\text{m}^2/\text{rad/m}) \tag{5.15}$$

where the parameters ω_c, ω_r, ω_s, A_a, A_v, and A_g are shown in Table 5.2.

5.2.3 *Japanese Track Irregularity Sato Spectrum*

The formula of track irregularity power spectral density function introduced by Sato, a Japanese scholar, to analyze the wheel-rail high-frequency vibration is as follows [6]:

$$S(\omega) = \frac{A}{\omega^3}\,(\text{m}^2/\text{rad/m}) \tag{5.16}$$

where ω is roughness frequency (rad/m), and A is a roughness coefficient of wheel-rail surface, $A = 4.15 \times 10^{-8} \sim 5.0 \times 10^{-7}$.

Belonging to the wheel-rail joint spectrum, as excitation input spectrum of wheel-rail random high-frequency vibration and noise radiation model, the power spectrum has been applied widely.

5.2.4 Chinese Trunk Track Irregularity Spectrum

5.2.4.1 Track Irregularity Spectrum of Former Changsha Railway Institute [7]

The former Changsha Railway Institute carried out three tests of track irregularity on China's Beijing-Guangzhou rail line by ground testing methods and obtained the statistical characteristics of Chinese first-grade trunk track irregularity spectrum.

Track profile irregularity power spectral density function is as follows:

$$S_{\mathrm{v}}(f) = 2.755 \times 10^{-3} \frac{f^2 + 0.8879}{f^4 + 2.524 \times 10^{-2} f^2 + 9.61 \times 10^{-7}} \ (\mathrm{mm}^2/\mathrm{cycle/m}) \tag{5.17}$$

Track alignment irregularity power spectral density function is as follows:

$$S_{\mathrm{a}}(f) = 9.404 \times 10^{-3} \frac{f^2 + 9.701 \times 10^{-2}}{f^4 + 3.768 \times 10^{-2} f^2 + 2.666 \times 10^{-5}} \ (\mathrm{mm}^2/\mathrm{cycle/m}) \tag{5.18}$$

Track cross-level irregularity power spectral density function is as follows:

$$S_{\mathrm{c}}(f) = 5.100 \times 10^{-8} \frac{f^2 + 6.346 \times 10^{-3}}{f^4 + 3.157 \times 10^{-2} f^2 + 7.791 \times 10^{-6}} \ (\mathrm{mm}^2/\mathrm{cycle/m}) \tag{5.19}$$

Track gauge irregularity power spectral density function is as follows:

$$S_{\mathrm{g}}(f) = 7.001 \times 10^{-3} \frac{f^2 - 3.863 \times 10^{-2}}{f^4 - 3.355 \times 10^{-2} f^2 - 1.464 \times 10^{-5}} \ (\mathrm{mm}^2/\mathrm{cycle/m}) \tag{5.20}$$

where $S(f)$ is track irregularity power spectral density ($\mathrm{mm}^2/\mathrm{cycle/m}$), and f is spatial frequency ($\mathrm{cycle/m}$).

5.2.4.2 Track Irregularity Spectrum of Chinese Academy of Railway Sciences

(1) Track irregularity spectrum of Chinese trunk railway test line [8].

The 60 kg/m continuously welded rail track across sections has been used as the track structure of China's high-speed and quasi-high-speed railway test line. China Academy of Railway Sciences has comprehensively measured the test line and by fitting the data, obtained the track irregularity power spectral density function which

Table 5.3 Parameters of Chinese trunk track irregularity power spectral density function

Irregularity	A	B	C	D	E	F	G
Left profile	0.1270	−2.1531	1.5503	4.9835	1.3891	−0.0327	0.0018
Right profile	0.3326	−1.3757	0.5497	2.4907	0.4057	0.0858	−0.0014
Left alignment	0.0627	−1.1840	0.6773	2.1237	−0.0847	0.034	−0.0005
Right alignment	0.1595	−1.3853	0.6671	2.3331	0.2561	0.0928	−0.0016
Cross-level	0.3328	−1.3511	0.5415	1.8437	0.3813	0.2068	−0.0003

reflects the characteristics of China's 60 kg/m continuously welded rail tracks across sections.

$$S(f) = \frac{A(f^2 + Bf + C)}{f^4 + Df^3 + Ef^2 + Ff + G} \tag{5.21}$$

where $S(f)$ is track irregularity power spectral density ($\text{mm}^2/\text{cycle/m}$), and f is spatial frequency (cycle/m).

Parameters *A, B, C, D, E, F,* and *G* are listed in Table 5.3.

(2) Track irregularity of Chinese three heavy-haul rising-speed trunk: Beijing-Guangzhou, Beijing-Shanghai, and Beijing-Harbin rail line [8].

The fitting expression of the track irregularity power spectral density of the three heavy-haul rising-speed trunk, Beijing-Guangzhou, Beijing-Shanghai and Beijing-Harbin rail line, is still as Eq. (5.21), and the fitting curve parameters are shown in Table 5.4.

(3) Track shortwave irregularity spectrum [8].

The wavelength range of the above track irregularity power spectrum is from a few meters to tens of meters, only suitable for the random vibration analysis of vehicles and bridge structure. It cannot meet the need of studying the random vibration of track structure, because the vibration-dominant frequency of unsprung mass and subrail structure can be from hundreds to thousands of Hertz. Therefore, China Academy of Railway Sciences carried out field measurement of the track vertical irregularity of Shijiazhuang-Taiyuan rail line by using the ground measurement method and the Colmar rail wear measuring instrument. Through the regression analysis, the vertical irregularity power spectral density function of the 50 kg/m standard rail line was obtained.

Table 5.4 Parameters of track irregularity power spectral density for three heavy-haul rising-speed trunk

Irregularity	A	B	C	D	E	F	G
Left profile	1.1029	−1.4709	0.5941	0.8480	3.8061	−0.2500	0.0112
Right profile	0.8581	−1.4607	0.5848	0.0407	2.8428	−0.1989	0.0094
Left alignment	0.2244	−1.5746	0.6683	−2.1466	1.7665	−0.1506	0.0052
Right alignment	0.3743	−1.5894	0.7265	0.4553	0.9101	−0.0270	0.0031
Cross-level	0.1214	−2.1603	2.0214	4.5089	2.2227	−0.0396	0.0073

$$S(f) = \frac{0.036}{f^{3.15}} \left(\text{mm}^2/\text{cycle/m}\right) \tag{5.22}$$

The spectral density of the above formula is applicable for the track shortwave irregularity with the wavelength range of 0.001–1 m.

(4) Ballastless track irregularity spectrum of high-speed railway [9].

Xiong Kang from China Academy of Railway Sciences obtained the gauge, cross-level, alignment, and profile irregularity spectrum fitting formula for China's high-speed railway ballastless track by statistical analysis of the irregularity inspection data on high-speed railway ballastless track, including Beijing-Shanghai, Beijing-Guangzhou, Zhengzhou-Xi'an, Shanghai-Hangzhou, Shanghai-Nanjing, Hefei-Bengbu, Guangzhou-Shenzhen, and Beijing-Tianjin Intercity Rail [9]. The track irregularity data were collected by the CRH2-150C high-speed multi-purpose inspection train. The maximum inspection wavelength of track profile and alignment was 120 m.

The ballastless track irregularity spectrum of high-speed railway can conduct piecewise fitting of the power function shown as below [9]:

$$S(f) = \frac{A}{f^k} \left(\text{mm}^2/\text{cycle/m}\right) \tag{5.23}$$

where f is spatial frequency, A and k are coefficients.

All the fitting coefficients in the irregularity spectrum formula (5.23) of high-speed railway ballastless track are shown in Table 5.5, and all the fitting section transition points are shown in Table 5.6. It can be seen that the track gauge, cross-level, and alignment irregularity can be expressed piecewise by three power functions, whereas the track profile irregularity needs to be expressed piecewise by four power functions. From comparisons between the measured track irregularity spectrum and the fitting track irregularity spectrum, it can be seen that the fitting track irregularity spectrum with piecewise power functions can reflect the trend of the measured track irregularity spectrum quite well.

5.2.5 *The Track Irregularity Spectrum of Hefei-Wuhan Passenger-Dedicated Line [10]*

Hefei-Wuhan passenger-dedicated line starts from Hefei city of Anhui Province in the east to Wuhan city of Hubei Province in the west with the total mileage of 356 km. It was jointly constructed by the former Ministry of Railways and the local government and its design speed was 250 km/h. Hefei-Wuhan passenger-dedicated line is the part of China's Shanghai-Wuhan-Chengdu fast railway and the important part of national plan "4 north–south and 4 east–west" high-speed passenger

Table 5.5 Fitting coefficients of ballastless track irregularity spectrum in high-speed railway

Irregularity item	Section 1		Section 2		Section 3		Section 4	
	A	k	A	k	A	k	A	k
Gauge irregularity	5.4978×10^{-2}	0.8282	5.0701×10^{-3}	1.9037	1.8778×10^{-4}	4.5948	–	–
Cross-level irregularity	3.6148×10^{-3}	1.7278	4.3685×10^{-2}	1.0461	4.5867×10^{-3}	2.0939	–	–
Alignment irregularity	3.9513×10^{-3}	1.8670	1.1047×10^{-2}	1.5354	7.5633×10^{-4}	2.8171	–	–
Profile irregularity	1.0544×10^{-5}	3.3891	3.5588×10^{-3}	1.9271	1.9784×10^{-2}	1.3643	3.9488×10^{-4}	3.4516

Table 5.6 The spatial frequency (1/m) and the corresponding wavelength (m) in subsection of high-speed railway ballastless track irregularity spectrum

Irregularity item	Sections 1 and 2		Sections 2 and 3		Sections 3 and 4	
	Spatial frequency	Spatial wavelength	Spatial frequency	Spatial wavelength	Spatial frequency	Spatial wavelength
Gauge irregularity	0.1090	9.2	0.2938	3.4	–	–
Cross-level irregularity	0.0258	38.8	0.1163	8.6	–	–
Alignment irregularity	0.0450	22.2	0.1234	8.1	–	–
Profile irregularity	0.0187	53.5	0.0474	21.1	0.1533	6.5

transport network. The whole project was started in September 2005. Its commissioning and testing was completed and it was put into operation at the end of 2008. There are 171 large, medium, and small bridges along the line with the total mileage of 118.819 km, accounting for 33.1 % of the total mileage of the main line; there are 37 tunnels with a total mileage of about 64.076 km, accounting for 17.83 % of the main line. In EMU inspection section (the mileage scope is K486–K663), the track types mainly include crushed stone bed ballast track over subgrade and crushed stone bed ballast track over bridge, crushed stone bed ballast track in tunnel, and double-block monolithic bed ballastless track in long and large tunnel.

The Hefei section inspection center of Shanghai Railway Bureau employed No. 0 and No. 100 high-speed multi-purpose inspection trains to detect the track irregularity of Hefei-Wuhan passenger-dedicated line from March 2009 to September 2009 with once or twice detection every month, collecting 30 times of the track irregularity data from the mileage scope of K486–K663 section. We select and make the statistical analysis of the track irregularity data collected by No. 0 high-speed multi-purpose inspection train in March, April, May, June, July, August, and September. Because the length of the crushed stone bed ballast track in tunnel and double-block monolithic bed ballastless track over bridge of Hefei-Wuhan passenger-dedicated line was short, very inadequate measured data were collected. Therefore, only the three types of track structure irregularity data will be analyzed: (1) crushed stone bed ballast track structure over subgrade; (2) crushed stone bed ballast track structure over bridge; (3) double-block monolithic bed ballastless track in tunnel. There are three types of track irregularity: (1) profile irregularity; (2) alignment irregularity; (3) cross-level irregularity.

Based on the analysis of the detection data of Hefei-Wuhan passenger-dedicated line, the nonlinear least-square method is used to fit the profile irregularity, alignment irregularity and cross-level irregularity power spectral density function of Hefei-Wuhan passenger-dedicated line. The fitting formula is obtained as follows:

Table 5.7 Fitting parameters of irregularity power spectrum for ballast track over subgrade

Parameter	A_1	A_2	A_3
Profile irregularity	0.000991	0.017876	0.017838
Alignment irregularity	0.001747	0.187256	0.002413
Cross-level irregularity	0.001474	0.003237	0.199733

Table 5.8 Fitting parameters of irregularity power spectrum for ballast track over bridge

Parameter	A_1	A_2	A_3
Profile irregularity	0.000849	0.006523	0.006519
Alignment irregularity	0.001723	0.050175	0.004021
Cross-level irregularity	0.004854	0.564343	0.001622

Table 5.9 Fitting parameters of irregularity power spectrum for ballast track in tunnel

Parameter	A_1	A_2	A_3
Profile irregularity	0.002252	0.058017	0.017164
Alignment irregularity	0.001368	0.015602	0.023396
Cross-level irregularity	0.000870	0.012326	0.033728

$$S(f) = \frac{A_1}{(A_2^2 + f^2)(A_3^2 + f^2)} \tag{5.24}$$

where $S(f)$ is power spectral density function (mm^2 m); f are spatial frequency (cycle/m); A_i is undetermined coefficient, i = 1, 2, 3, the unit of A_1 is mm^2 /m^3, the unit of A_2 and A_3 is m^{-1}, their values are shown in Tables 5.7, 5.8 and 5.9. The comparisons between the fitting power spectral density curve and the measured curve are shown in Figs. 5.4, 5.5 and 5.6.

5.2.6 *Comparison of the Track Irregularity Power Spectrum Fitting Curves*

Track irregularity power spectrum fitting curves of some country will be compared, including American spectrum, German high- and low- interference spectrum, Chinese trunk spectrum, and Hefei-Wuhan passenger-dedicated line spectrum, which are shown in Figs. 5.7, 5.8 and 5.9 [10].

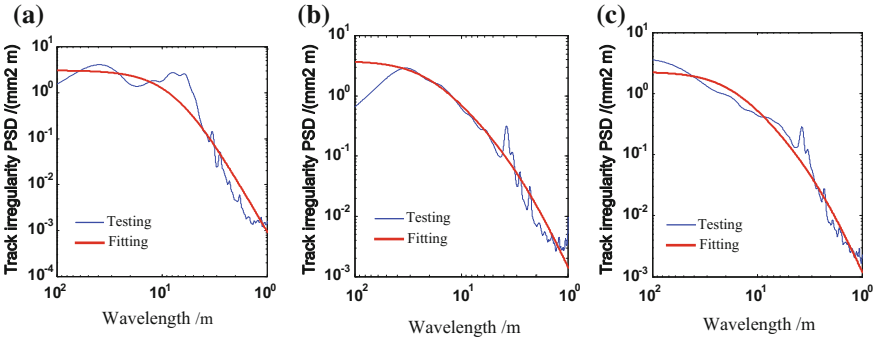

Fig. 5.4 The fitting curve of irregularity power spectrum for ballast track over subgrade of Hefei-Wuhan passenger-dedicated line. *a* Profile irregularity. *b* Alignment irregularity. *c* Cross level irregularity

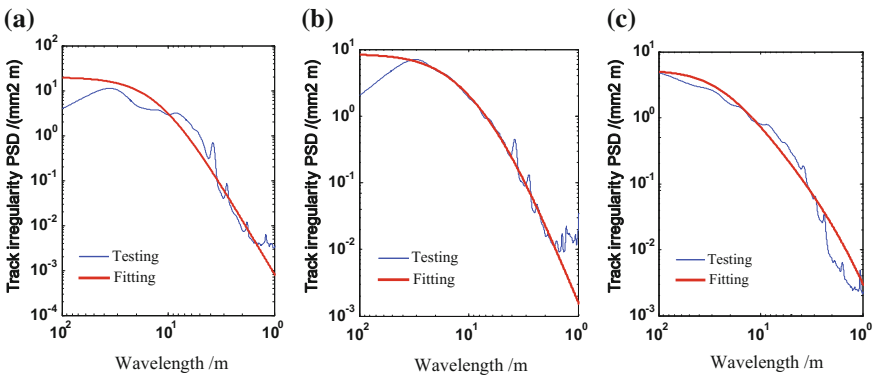

Fig. 5.5 The fitting curve of irregularity power spectrum for ballast track over bridge of Hefei-Wuhan passenger-dedicated linetrack irregularity of passenger-dedicated line. *a* Profile irregularity. *b* Alignment irregularity. *c* Cross level irregularity

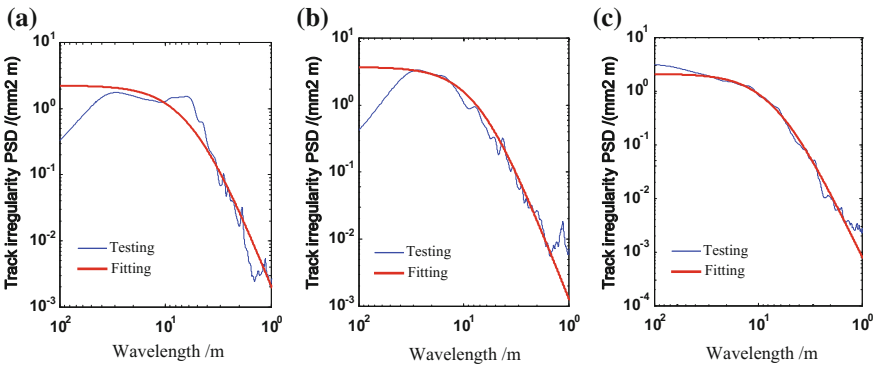

Fig. 5.6 The fitting curve of irregularity power spectrum for ballast track in tunnel of Hefei-Wuhan passenger-dedicated line. *a* Profile irregularity. *b* Alignment irregularity. *c* Cross level irregularity

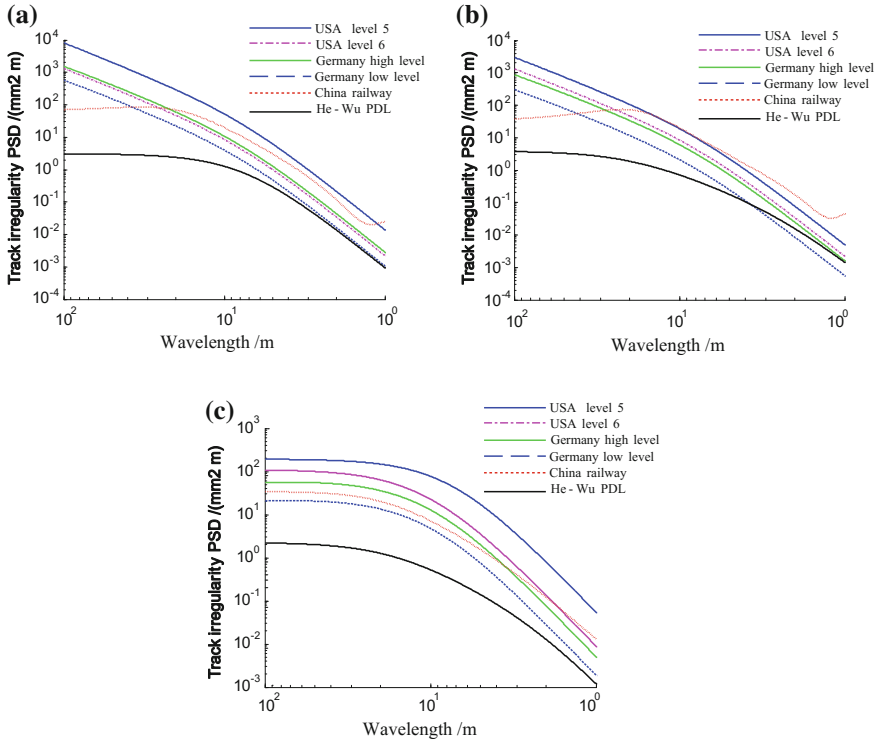

Fig. 5.7 The comparison of irregularity power spectrum fitting curves for ballast track structure over subgrade. *a* Profile irregularity. *b* Alignment irregularity. *c* Cross level irregularity

(1) Ballast track structure over subgrade

Figure 5.7a indicates that for the profile irregularity of ballast track over subgrade, the track spectrum of Hefei-Wuhan passenger-dedicated line is obviously superior to that of Chinese trunk spectrum, American spectrum, and German spectrum. Within the wavelength range of 1–5 m, the track spectral density of the passenger-dedicated line is close to and slightly superior to German low-interference spectrum.

Figure 5.7b indicates that for the alignment irregularity of ballast track over subgrade, the power spectral density of Hefei-Wuhan passenger-dedicated line is relatively larger but obviously lower than Chinese trunk spectrum and American track irregularity PSD for line level 5. Within the analyzed wavelength range, the track spectrum of the passenger-dedicated line is superior to American track irregularity PSD for line level 6 and close to the latter with the decrease of wavelength. Compared with German high-interference spectrum, the track spectrum of the passenger-dedicated line is much lower. While within the wavelength range of about 1 m the track spectrum of the passenger-dedicated line is close to German high-interference spectrum. Within the wavelength range of 1–4 m, the

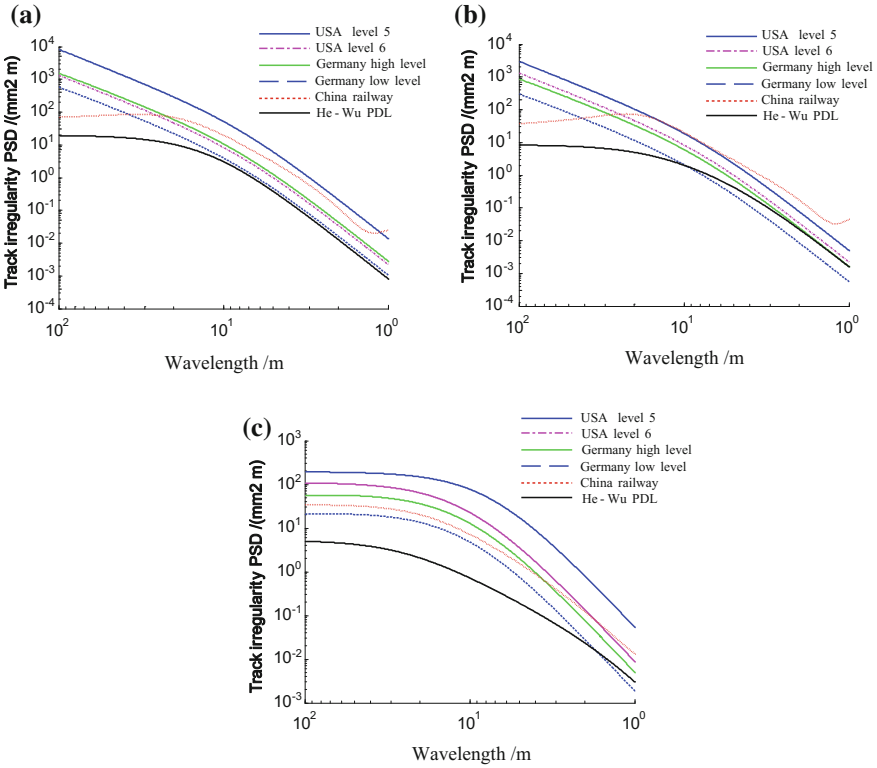

Fig. 5.8 The comparison of irregularity power spectrum fitting curves for ballast track structure over bridge. *a* Profile irregularity. *b* Alignment irregularity. *c* Cross level irregularity

track spectral density of the passenger-dedicated line is larger than German low-interference spectrum; within the wavelength range of 4–50 m, the track spectral density of the passenger-dedicated line is lower than German low-interference spectrum.

Figure 5.7c indicates that the cross-level irregularity of ballast track over subgrade of Hefei-Wuhan passenger-dedicated line has been well controlled. Within the analyzed wavelength range, the track spectral density of the passenger-dedicated line is obviously lower than Chinese trunk spectrum, German low-interference spectrum, and American track irregularity PSD for line level 6.

(2) Ballast track structure over bridge.

Figure 5.8a indicates that for the profile irregularity of ballast track over bridge, the track spectral density of Hefei-Wuhan passenger-dedicated line is close to and lower than German low-interference spectrum within the wavelength range of 1–10 m. Within the wavelength range of 10–50 m, the profile irregularity of ballast track over bridge is obviously lower than German low-interference spectrum. Within the

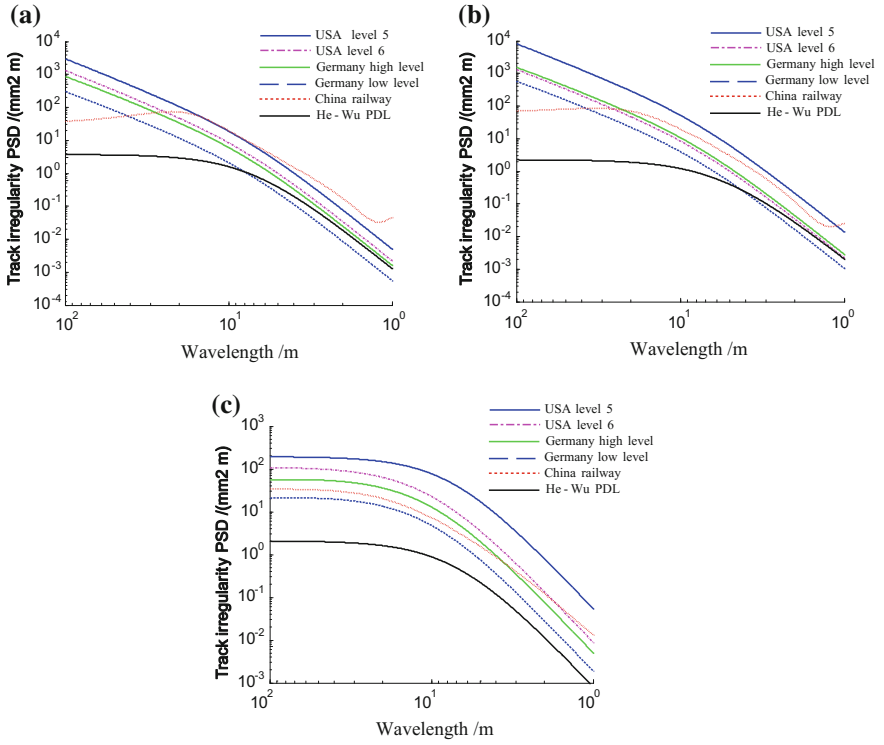

Fig. 5.9 The comparison of irregularity power spectrum fitting curves for ballast track structure in tunnel. *a* Profile irregularity. *b* Alignment irregularity. *c* Cross level irregularity

analyzed wavelength range, the track spectrum of Hefei-Wuhan passenger-dedicated line is obviously superior to American track irregularity PSD for line level 6 and Chinese trunk spectrum.

Figure 5.8b indicates that for the alignment irregularity of ballast track over bridge, the track spectral density of Hefei-Wuhan passenger-dedicated line is relatively larger but lower than Chinese trunk spectrum. Within the analyzed wavelength range, the track spectrum of the passenger-dedicated line is superior to American track irregularity PSD for line level 6 and close to the latter with the decrease of wavelength. Compared with German high-interference spectrum, the track spectrum of the passenger-dedicated line is lower; within the wavelength range of 1–2 m, they are very close to each other. Within the wavelength range of 1–10 m, the track spectral density of the passenger-dedicated line is larger than German low-interference spectrum; within the wavelength range of 10–50 m, the track spectral density of the passenger-dedicated line is lower than German low-interference spectrum.

Figure 5.8c indicates that for the cross-level irregularity of ballast track over bridge, within the analyzed wavelength range, the track spectral density of the passenger-dedicated line is obviously lower than Chinese trunk spectrum, German high-interference spectrum, and American spectrum for line level 6. Within the wavelength range of about 1.0–1.7 m, the track spectral density of the passenger-dedicated line is larger than German low-interference spectrum but obviously lower than the latter within other wavelength range.

(3) Ballast track structure in tunnel.

Figure 5.9a indicates that for the profile irregularity of ballast track in tunnel, the track spectral density of Hefei-Wuhan passenger-dedicated line is relatively larger, but obviously lower than Chinese trunk spectrum and American track irregularity PSD for line level 5. Within the analyzed wavelength range, the track spectrum of the passenger-dedicated line is superior to American track irregularity PSD for line level 6 and is close to the latter with the decrease of wavelength, especially obvious for the short wavelength of about 1 m. Compared with German high-interference spectrum, the track spectrum of the passenger-dedicated line is lower and is constantly close to German high-interference spectrum with the decrease of wavelength. Within the wavelength range of 1–4 m, the track spectral density of the passenger-dedicated line is larger than German low-interference spectrum; within the wavelength range of 4–50 m, the power spectral density of the passenger-dedicated line is lower than German low-interference spectrum.

Figure 5.9b indicates that for the alignment irregularity of ballast track in tunnel, the track spectral density of Hefei-Wuhan passenger-dedicated line is obviously superior to Chinese trunk spectrum. Within the analyzed wavelength range, the track spectrum of the passenger-dedicated line is lower than American track irregularity PSD for line level 6 and German high-interference spectrum and is constantly close to the latter two with the decrease of wavelength. Within the wavelength range of 1–8 m, the track spectral density of the passenger-dedicated line is larger than German low-interference spectrum; within the wavelength range of 8–50 m, the track spectral density of the passenger-dedicated line is lower than German low-interference spectrum.

Figure 5.9c indicates that the cross-level irregularity of ballast track in tunnel of Hefei-Wuhan passenger-dedicated line has been well controlled, which is obviously lower than Chinese trunk spectrum, German spectrum, and American spectrum.

When the track irregularity power spectrum is used to simulate the actual irregularity, the analyzed wavelength range of the track irregularity should be correctly determined. The lower limit of the track irregularity wavelength should include the short irregularity wavelength of the actual rail corrugation, rail joint, and turnout area of railway track. According to the investigation, the short irregularity wavelength is generally not less than 0.1 m. Thus, the lower limit of the track irregularity wavelength, namely the shortest irregularity wavelength, can be determined as 0.1 m. When the train speed is 100–400 km/h, the excited vibration frequency induced by 0.1 m wavelength track irregularity is 278–1111 Hz, which

Table 5.10 The vertical natural vibration frequency of Chinese locomotive and rolling stock

Vibration type	Shaoshan 1, electrified locomotive	Beijing 3000, diesel locomotive	Dongfeng 4, diesel locomotive	Transfer type 8, freight train		202 bogie passenger train		101 bogie passenger train
				Old 608	New 702	With damper	Without damper	
Bouncing	3.29	1.47	1.67	3.17–3.48	3.25–3.52	1.39	1.33	1.95
Pitch	3.57	1.78–2.0	1.78	3.75–3.90	5.5–5.6	1.46	1.26	2.08

can obviously meet the requirement of track structure vibration analysis. The shorter wavelength track irregularity is mainly related to wheel-rail noise. And the upper limit of the track irregularity wavelength should be determined by the car body natural vibration frequency and train speed V. The vertical natural vibration frequencies for main types of China locomotive and rolling stock are shown in Table 5.10. The natural vibration frequencies of car body lateral vibration basically agree with those of car body vertical vibration. If the minimum vibration frequency of the system is $F_{\min}$ (generally 0.5–1 Hz), the upper limit of the wavelength can be determined as follows: $V/F_{\min}$.

To sum up, when the locomotive and rolling stocks are running at different speed, the excited vibration frequency induced by track irregularity should cover all the main frequencies of locomotive and rolling stock and track structure. Therefore, the wavelength range of the track irregularity should be as follows [1]:

$$\lambda = 0.1 - V/F_{\min}\,(\mathrm{m}). \tag{5.25}$$

5.3 Numerical Simulation for Random Irregularity of the Track Structure

Power spectral density function can only be directly input in the analysis of linear random vibration frequency domain. As for the nonlinear random vibration problem (strictly speaking, vehicle-track coupling system belongs to nonlinear problem), the most effective method is to obtain the random exciting sample as input followed by adopting the numerical method to calculate the system random response. Therefore, it is necessary to discuss the numerical simulation of track irregularity random process.

Let the track irregularity sample be as follows:

$$\eta = \eta(x) \tag{5.26}$$

where $\eta(x)$ is the track irregularity of coordinate x and is a random function. The numerical simulation of the track irregularity is to seek the sample function $\eta(x)$ with spectrum density expressed by Eqs. (5.9)–(5.24).

At present, the most commonly used numerical methods for simulation of the track irregularity include secondary filtering method [1], triangle series method [12], white noise filtering method, and periodic diagram approach [1]. The secondary filtering method needs to design the filter. The different suitable filter needs to be designed for the track irregularity of different power spectral density functions. Usually, it is not easy. As a result, this method lacks generality. In the following, the trigonometric series method which is widely applied in engineering will be introduced.

5.4 Trigonometric Series Method

5.4.1 Trigonometric Series Method (1)

Let the mean of stationary Gaussian processes $\eta(x)$ be zero and the power spectral density function be $S_x(\omega)$. The sample function of $\eta(x)$ can be approximately simulated by the trigonometric series.

$$\eta^d(x) = \sum_{k=1}^{N} a_k \sin(\omega_k x + \phi_k) \tag{5.27}$$

where a_k is the Gaussian random variable with mean 0; standard deviation σ_k, and it is independent with each other for $k = 1, 2, \ldots, N$. ϕ_k, independent with a_k, is the same random variable evenly distributed within the scope of $0 \sim 2\pi$ and is independent with each other for $k = 1, 2, \ldots, N$. σ_k can be determined by the following method.

Within the positive region of the power spectral density function$S_x(\omega)$ of $\eta(x)$, the value between the lower limit frequency ω_l and the upper limit frequency ω_u is divided by N, as is shown in Fig. 5.10.

Let

$$\Delta\omega = (\omega_u - \omega_l)/N \tag{5.28}$$

Supposing

$$\omega_k = \omega_l + \left(k - \frac{1}{2}\right)\Delta\omega \quad k = 1, 2, \ldots, N \tag{5.29}$$

It has

$$\sigma_k^2 = 4S_x(\omega_k)\Delta\omega \quad k = 1, 2, \ldots, N \tag{5.30}$$

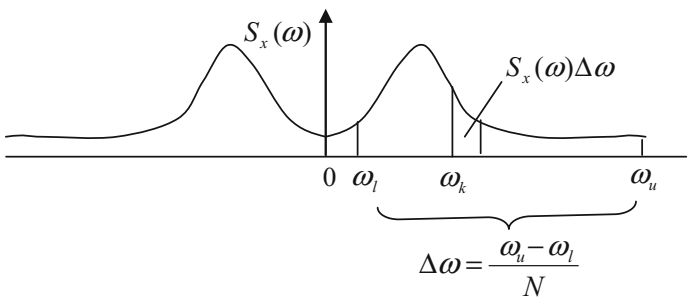

Fig. 5.10 The division of power spectral density function $S_x(\omega)$

Namely, the effective power of $S_x(\omega)$ is regarded as within the scope of $\omega_l - \omega_u$ and the value beyond the scope of $\omega_l - \omega_u$ is regarded as 0. ω_k and σ_k can be calculated based on the relation in Fig. 5.10. ω_l, ω_u and ω_k in formula (5.28)–(5.30) are spatial frequencies, the unit is rad/m; and N is sufficiently large integer.

It can be proved that the spectral density function of sample function $\eta(x)$, calculated by formula (5.27)–(5.30), is $S_x(\omega)$ and ergodic [11].

5.4.2 Trigonometric Series Method (2)

Let the mean of stationary Gaussian processes $\eta(x)$ be zero and the power spectral density function $S_x(\omega)$. The sample function of $\eta(x)$ can be approximately simulated by the following trigonometric series [12].

$$\eta^d(x) = \sum_{k=1}^{N} \{a_k \cos \omega_k x + b_k \sin \omega_k x\} \tag{5.31}$$

where a_k is the Gaussian random variable with mean 0 and standard deviation σ_k, and it is independent with each other for $k = 1, 2, \ldots, N$. b_k is unrelated to a_k, which is independent Gaussian random variable with mean 0 and standard deviation σ_k, and is independent with each other for $k = 1, 2, \ldots, N$. Again, let

$$\sigma_k^2 = 2S_x(\omega_k)\Delta\omega, \quad k = 1, 2, \ldots, N \tag{5.32}$$

$\Delta\omega$, ω_k are given by formula (5.28), (5.29), respectively.

5.4.3 Trigonometric Series Method (3)

Let the mean of Stationary Gaussian Processes $\eta(x)$ be zero and the power spectral density function $S_x(\omega)$. The sample function of $\eta(x)$ can be approximately simulated by the following trigonometric series [12].

$$\eta^d(x) = \sum_{k=1}^{N} a_k \cos(\omega_k x + \phi_k) \tag{5.33}$$

where a_k is the Gaussian random variable with mean 0 and standard deviation σ_k and is independent with each other for $k = 1, 2, \ldots, N$. ϕ_k, independent with a_k, is the same random variable evenly distributed within the scope of $0 \sim 2\pi$ and is independent with each other for $k = 1, 2, \ldots, N$.

$$\sigma_k^2 = 4S_x(\omega_k)\Delta\omega \quad k = 1, 2, \ldots, N \tag{5.34}$$

$\Delta\omega$ and ω_k are given by formula (5.28), (5.29), respectively.

5.4.4 Trigonometric Series Method (4)

Let the mean of Stationary Gaussian Processes $\eta(x)$ be zero and the power spectral density function $S_x(\omega)$. The sample function of $\eta(x)$ can be approximately simulated by the following trigonometric series [12].

$$\eta^d(x) = \sigma_x \sqrt{\frac{2}{N}} \sum_{k=1}^{N} \cos(\omega_k x + \phi_k) \tag{5.35}$$

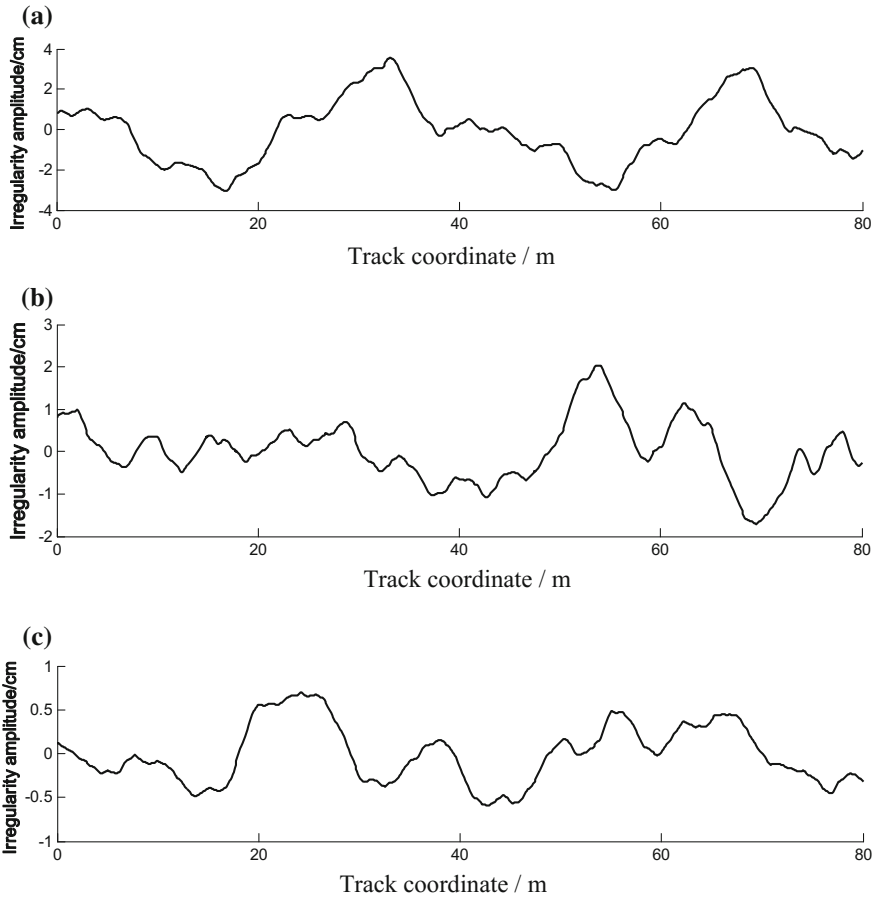

Fig. 5.11 The simulated track profile irregularity sample with trigonometric series. *a* The track profile irregularity sample for line level 4. *b* The track profile irregularity sample for line level 5. *c* The track profile irregularity sample for line level 6

where

$$\sigma_x^2 = \int_{-\infty}^{\infty} S_x(\omega)\mathrm{d}\omega \tag{5.36}$$

ω_k is the random variable with the probability density function $p(\omega) = \frac{S_x(\omega)}{\sigma_x^2}$; φ_k is the same random variable evenly distributed within the scope of $0 \sim 2\pi$ and is independent with each other for $k = 1, 2, \ldots, N$.

5.4.5 *Sample of the Track Structure Random Irregularity*

In this calculation example, the track profile irregularity space sample as exciting input is obtained by borrowing the track profile irregularity spectrum of American AAR standard for line level 4, 5, 6 and employing the trigonometric series, as is shown in formula (5.9). Take the spatial wavelength as 0.5–50 m, the corresponding ω_l and ω_u is $2\pi(0.02 - 2)\mathrm{rad/m}$, respectively, and N is 2500. The typical track profile irregularity samples corresponding to line level 4, 5, and 6 are shown in Fig. 5.11.

References

1. Chen G (2000) Random vibration analysis of vehicle-track coupling system. Doctor's Dissertation of Southwest Jiaotong University, Chengdu
2. Lei X (2002) New methods of track dynamics and engineering. China Railway Publishing House, Beijing
3. Sheng Z, Xie S, Pan C (2001) Probability theory and mathematical statistics. Higher Education Press, Beijing
4. Futian Wang (1994) Vehicle system dynamics. China Railway Publishing House, Beijing
5. Southwest Jiaotong University (1993) Deutsche Bundesbahn IC-Express Assignment for technical design. Department of science and technology, Ministry of Railway
6. Yoshihiko SATO (1977) Study on high-frequency vibrations in track operated high-speed trains. Q Rep18(3)
7. The random vibration research laboratary of Changsha Railway Institute (1985) Study on random excitation function of vehicle/track system. J Changsha Railway Inst (2):1–36
8. Luo L, Wei S (1999) Study on our country's trunk track irregularity power spectrum. China Academy of Railway Sciences, Beijing
9. Kang X, Liu X et al (2014) The ballestless track irregularity spectrum of high-speed railway. Sci China Sci Technol 44(7):687–696
10. Fang J (2013) The effects of track irregularity on the elevated track structure vibration characteristics of high-speed passenger dedicated line. Doctor's Dissertation of Tongji University, Shanghai
11. Cao X et al (1987) Dynamic analysis of bridge structure. China Railway Publishing House, Beijing
12. Xing G (1977) Random vibration analysis. Seismological Press, Beijing

Chapter 6
Model for Vertical Dynamic Analysis of the Vehicle-Track Coupling System

With the sustained and rapid social and economic development in China, there is an increasing demand for railway passenger and freight transport, making it vital and urgent for freight trains to increase their capacity and passenger trains to improve their speed and riding quality on the premise of assuring traffic safety. Thus, it is necessary to predict the dynamic characteristics of wheel-rail interaction for the design and to make new types of rolling stocks and the construction and maintenance of railways. Railways with better dynamic performance are essential for safe and stable running of the trains as vehicles with better dynamic performance will reduce their damage to railways in the interactions between vehicles and railways. However, despite human beings' capability to simulate accurately the motion of a flying object in the space and to keep a precise control of it as well, it is still impossible for human beings to simulate wheel-rail interaction in an accurate way, which means the wheel-rail relationship and the vehicle-track interaction still remain as difficult problems in the dynamic study of vehicles and tracks. Rolling stocks and track structure constitute an integrated system, in which they interrelate and interact with each other. Therefore, during the study of dynamic performance of rolling stocks, railways cannot simply be regarded as external exciting disturbance. In other words, railways itself do not own the characteristics of excitation that lie independently of the trains. Vibration in the system is induced by the random wheel and rail irregularities.

The method of simulated analysis is taken by many people in various countries in order to have a close study on the dynamic characteristics of track structure, with the advantage of replacing the costly and time-consuming physical tests to conduct numerical simulation study on the problems in question. In recent years, various computational models have been developed [1–22], and some progress has been achieved.

In this chapter, as the base of track structure vibration analysis, the fundamental theory of dynamic finite element method is introduced, and various analysis models of vehicle-track coupling system are discussed.

X. Lei, *High Speed Railway Track Dynamics*,
DOI 10.1007/978-981-10-2039-1_6

6.1 Fundamental Theory of Dynamic Finite Element Method

6.1.1 A Brief Introduction to Dynamic Finite Element Method

Great progress has been made in response analysis of the structure subjected to dynamic load, as a result of various practical needs such as dynamic analysis of nuclear power stations, dams, and high-rise buildings under earthquake load; dynamic analysis of offshore platform under wind, wave, and fluid load; and vibration analysis of railway track structure under moving trains and dynamic analysis of various mechanical equipment in the process of high-speed operation or under impact load, which is a necessary step to guarantee good working performance, safety, and reliability of the structure or the machinery. Besides, the progress made in dynamic analysis of various complex structures is also the result of the application of high-performance computers and the development of numerical method, especially finite element analysis.

In case of structure under the dynamic loads, displacement, velocity, acceleration, strain, and stress are all a function of time. Take the two-dimensional problem as an example, the fundamental steps of finite element dynamic analysis can be described as follows [23, 24]:

(1) Discretization of continuous medium
In dynamic analysis, due to the introduction of time coordinate, the problem should be dealt with in domain (x, y, t). Partial discretization method is generally adopted in finite element analysis; namely, discretization is used in space alone, while difference method is employed on time scale.

(2) Constructing interpolation function
Since only the physical space domain is discretized, displacements u, v at any point within the element can be expressed as follows:

$$\begin{aligned} u(x, y, t) &= \sum_{i=1}^{n} N_i(x, y) u_i(t) \\ v(x, y, t) &= \sum_{i=1}^{n} N_i(x, y) v_i(t) \end{aligned} \tag{6.1}$$

where u, v are displacements in point (x, y) of the element; N_i is the interpolation function; u_i, v_i are element node displacements; and n is the total element node number.

Equation (6.1) can be expressed in matrix

$$\boldsymbol{f} = \boldsymbol{N}\boldsymbol{a}^e \tag{6.2}$$

where $\boldsymbol{f}$ is the element displacement vector; $\boldsymbol{N}$ is the interpolation function matrix; and $\boldsymbol{a}^e$ is the element node displacement vector.

$$\boldsymbol{f} = \begin{Bmatrix} u(x,y,t) \\ v(x,y,t) \end{Bmatrix}$$

$$\boldsymbol{N} = \begin{bmatrix} N_1 & O & N_2 & O_1 & \cdots & N_n & O \\ O & N_1 & O & N_2 & & O & N_n \end{bmatrix}$$

$$\boldsymbol{a}^e = \{ \boldsymbol{a}_1 \quad \boldsymbol{a}_2 \quad \cdots \quad \boldsymbol{a}_n \}^{\mathrm{T}}$$

$$\boldsymbol{a}_i = \begin{Bmatrix} u_i(t) \\ v_i(t) \end{Bmatrix}$$

In dynamic problems, node displacement $\boldsymbol{a}^e$ is a function of time.

(3) Forming element characteristic matrix and characteristic vector.

Element strain vector and stress vector can be derived based on Eq. (6.2)

$$\boldsymbol{\varepsilon} = \boldsymbol{B}\boldsymbol{a}^e \tag{6.3}$$

$$\boldsymbol{\sigma} = \boldsymbol{D}\boldsymbol{\varepsilon} = \boldsymbol{D}\boldsymbol{B}\boldsymbol{a}^e \tag{6.4}$$

where $\boldsymbol{\varepsilon}$ is the element strain vector, $\boldsymbol{B}$ is the strain matrix, $\boldsymbol{\sigma}$ is the element stress vector, and $\boldsymbol{D}$ is the elasticity matrix.

Velocity at any point (x, y) of the element can be derived through differentiating the displacement by time:

$$\dot{\boldsymbol{f}}(x,y,t) = \boldsymbol{N}(x,y)\dot{\boldsymbol{a}^e}(t) \tag{6.5}$$

where $\boldsymbol{a}^e$ is the node velocity vector of the element.

Dynamic equation of the structure can be established based on *Hamilton's* principle or *Lagrange* equation as well, and the latter can be expressed as follows:

$$\frac{\mathrm{d}}{\mathrm{d}t}\frac{\partial L}{\partial \dot{\boldsymbol{a}}} - \frac{\partial L}{\partial \boldsymbol{a}} + \frac{\partial R}{\partial \dot{\boldsymbol{a}}} = \boldsymbol{0} \tag{6.6}$$

where L is the *Lagrange* function.

$$L = T - \Pi_{\mathrm{p}} \tag{6.7}$$

$T, \Pi_{\mathrm{p}}, R, \boldsymbol{a}$ and $\dot{\boldsymbol{a}}$ are the kinetic energy, potential energy, dissipation energy, node displacement vector, and node velocity vector of the system, respectively.

The kinetic energy and potential energy of the element can be expressed, respectively, as follows:

$$T^e = \frac{1}{2}\int_{\Omega^e} \rho \dot{\boldsymbol{f}}^{\mathrm{T}} \dot{\boldsymbol{f}} \mathrm{d}\Omega \tag{6.8}$$

$$\Pi_{\mathrm{p}}^e = \frac{1}{2}\int_{\Omega^e} \boldsymbol{\varepsilon}^{\mathrm{T}} \boldsymbol{D} \boldsymbol{\varepsilon} \mathrm{d}\Omega - \int_{\Omega^e} \boldsymbol{f}^{\mathrm{T}} \boldsymbol{b} \mathrm{d}\Omega - \int_{\Gamma_\sigma} \boldsymbol{f}^{\mathrm{T}} \boldsymbol{q} \mathrm{d}\Gamma \tag{6.9}$$

where ρ is the density of material. The first item on the right of Eq. (6.9) represents element strain energy, and the second and the third items represent potential energy of the external forces, among which $\boldsymbol{b}, \boldsymbol{q}$ represent the body force vector and surface force vector acting on the element.

With regard to element dissipation energy, assuming the damping force is proportional to the velocity of each particle, it can be expressed as follows:

$$R^e = \frac{1}{2}\int_{\Omega^e} \mu \dot{\boldsymbol{f}}^{\mathrm{T}} \dot{\boldsymbol{f}} \mathrm{d}\Omega \tag{6.10}$$

where μ is the damping coefficient.

Substituting Eq. (6.2) into Eqs. (6.8)–(6.10), it has

$$\begin{aligned} T^e &= \frac{1}{2}(\dot{\boldsymbol{a}}^e)^{\mathrm{T}} \boldsymbol{m}^e \dot{\boldsymbol{a}}^e \\ \Pi_{\mathrm{p}}^e &= \frac{1}{2}(\boldsymbol{a}^e)^{\mathrm{T}} \boldsymbol{k}^e \boldsymbol{a}^e - (\boldsymbol{a}^e)^{\mathrm{T}} \boldsymbol{Q}^e \\ R^e &= \frac{1}{2}(\dot{\boldsymbol{a}}^e)^{\mathrm{T}} \boldsymbol{c}^e \dot{\boldsymbol{a}}^e \end{aligned} \tag{6.11}$$

where

$$\boldsymbol{m}^e = \int_{\Omega^e} \rho \boldsymbol{N}^{\mathrm{T}} \boldsymbol{N} \mathrm{d}\Omega, \quad \boldsymbol{k}^e = \int_{\Omega^e} \boldsymbol{B}^{\mathrm{T}} \boldsymbol{D} \boldsymbol{B} \mathrm{d}\Omega, \quad \boldsymbol{c}^e = \int_{\Omega^e} \mu \boldsymbol{N}^{\mathrm{T}} \boldsymbol{N} \mathrm{d}\Omega \tag{6.12}$$

They are mass matrix, stiffness matrix, and damping matrix of the element, respectively.

$$\boldsymbol{Q}^e = \int_{\Omega^e} \boldsymbol{N}^{\mathrm{T}} \boldsymbol{b} \mathrm{d}\Omega + \int_{\Gamma_\sigma} \boldsymbol{N}^{\mathrm{T}} \boldsymbol{q} \mathrm{d}\Gamma \tag{6.13}$$

$\boldsymbol{Q}^e$ is the equivalent node load vector of the element.

(4) Assembling matrices and vectors of each element to form the dynamic finite element equation of the whole system.
Assembling T^e, Π_p^e, R^e of each element to obtain T, Π_p, R of the system

$$\begin{aligned} T &= \sum_e T^e = \frac{1}{2}\dot{\boldsymbol{a}}^{\mathrm{T}}\boldsymbol{M}\dot{\boldsymbol{a}} \\ \Pi_p &= \sum_e \Pi_p^e = \frac{1}{2}\boldsymbol{a}^{\mathrm{T}}\boldsymbol{K}\boldsymbol{a} - \boldsymbol{a}^{\mathrm{T}}\boldsymbol{Q} \\ R &= \sum_e R^e = \frac{1}{2}\dot{\boldsymbol{a}}^{\mathrm{T}}\boldsymbol{C}\dot{\boldsymbol{a}} \end{aligned} \tag{6.14}$$

where

$$\boldsymbol{M} = \sum_e \boldsymbol{m}^e, \quad \boldsymbol{K} = \sum_e \boldsymbol{k}^e, \quad \boldsymbol{C} = \sum_e \boldsymbol{c}^e, \quad \boldsymbol{Q} = \sum_e \boldsymbol{Q}^e \tag{6.15}$$

They are global mass matrix, global stiffness matrix, global damping matrix, and global load vector of the system, respectively
Next, by substituting Eq. (6.14) into *Lagrange* equation (6.6), the dynamic finite element equation of the system can be obtained

$$\boldsymbol{M}\ddot{\boldsymbol{a}}(t) + \boldsymbol{C}\dot{\boldsymbol{a}}(t) + \boldsymbol{K}\boldsymbol{a}(t) = \boldsymbol{Q}(t) \tag{6.16}$$

This is a second-order ordinary differential equation, where $\ddot{\boldsymbol{a}}(t)$ is the node acceleration vector of the system.

(5) Computation of the strain and stress of the structure
By solving the system dynamic finite element equation (6.16), the node displacement vector $\boldsymbol{a}(t)$ is obtained. The element strain vector $\boldsymbol{\varepsilon}(t)$ and stress vector $\boldsymbol{\sigma}(t)$ can be calculated based on Eq. (6.3) and Eq. (6.4).
As can be observed from the above steps, since the kinetic energy and dissipation energy may occur in the energy equation, mass matrix and damping matrix are introduced in dynamic analysis, compared with static analysis, so that the final solved equation obtained is a second-order ordinary differential equation set rather than algebraic equation set. As for the solution of a second-order ordinary differential equation set, in principle, some common methods of ordinary differential equation set (such as Runge–Kutta method) can be used for solution. But in the finite element dynamic analysis, because of the high order of the solved equation set, these commonly used methods are generally not efficient and economical and more often numerical integration method is used instead.

6.1.2 Beam Element Theory

6.1.2.1 Element Stiffness Matrix

As for two-dimensional beam element with two nodes, each node has three degrees of freedom, as shown in Fig. 6.1.

Assuming the displacement mode of beam element is

$$u = \alpha_1 + \alpha_2 x \tag{6.17}$$

$$v = \beta_1 + \beta_2 x + \beta_3 x^2 + \beta_4 x^3 \tag{6.18}$$

where α_i, β_i are six undetermined generalized coordinates and can be represented by six node displacements of the element.

Substituting node coordinate $i(0), j(l)$ into Eq. (6.17), it has

$$\begin{bmatrix} 1 & 0 \\ 1 & l \end{bmatrix} \begin{Bmatrix} \alpha_1 \\ \alpha_2 \end{Bmatrix} = \begin{Bmatrix} u_i \\ u_j \end{Bmatrix} \tag{6.19}$$

Solve for α_1, α_2 as

$$\begin{Bmatrix} \alpha_1 \\ \alpha_2 \end{Bmatrix} = \begin{bmatrix} 1 & 0 \\ -\frac{1}{l} & \frac{1}{l} \end{bmatrix} \begin{Bmatrix} u_i \\ u_j \end{Bmatrix} \tag{6.20}$$

$\beta_1 - \beta_4$ in Eq. (6.18) can be determined according to the node displacements $v_i, \theta_i, v_j, \theta_j$. Based on Eq. (6.18), it has

$$\theta = -\frac{\mathrm{d}v}{\mathrm{d}x} = -\beta_2 - 2\beta_3 x - 3\beta_4 x^2 \tag{6.21}$$

Substituting the node coordinates into Eqs. (6.18) and (6.21), it has

$$\begin{bmatrix} 1 & 0 & 0 & 0 \\ 0 & -1 & 0 & 0 \\ 1 & l & l^2 & l^3 \\ 0 & -1 & -2l & -3l^2 \end{bmatrix} \begin{Bmatrix} \beta_1 \\ \beta_2 \\ \beta_3 \\ \beta_4 \end{Bmatrix} = \begin{Bmatrix} v_i \\ \theta_i \\ v_j \\ \theta_j \end{Bmatrix} \tag{6.22}$$

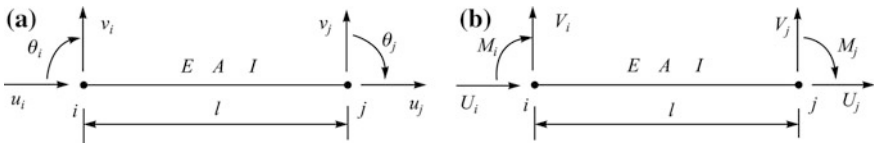

Fig. 6.1 Beam element with 2 nodes and 6 degrees of freedom

Solving the above equation, it yields

$$\begin{Bmatrix} \beta_1 \\ \beta_2 \\ \beta_3 \\ \beta_4 \end{Bmatrix} = \begin{bmatrix} 1 & 0 & 0 & 0 \\ 0 & -1 & 0 & 0 \\ -\frac{3}{l^2} & \frac{2}{l} & \frac{3}{l^2} & \frac{1}{l} \\ \frac{2}{l^3} & -\frac{1}{l^2} & -\frac{2}{l^3} & -\frac{1}{l^2} \end{bmatrix} \begin{Bmatrix} v_i \\ \theta_i \\ v_j \\ \theta_j \end{Bmatrix} \tag{6.23}$$

By substituting Eqs. (6.20) and (6.23) into (6.17) and (6.18), the element displacements expressed by interpolation function and node displacements can be obtained

$$\begin{aligned} u &= N_1 u_i + N_4 u_j \\ v &= N_2 v_i + N_3 \theta_i + N_5 v_j + N_6 \theta_j \end{aligned} \tag{6.24}$$

where N_1–N_6 are displacement interpolation functions, which are the functions of local coordinate x.

$$\begin{aligned} &N_1 = 1 - \tfrac{x}{l}, \quad N_2 = 1 - \tfrac{3}{l^2}x^2 + \tfrac{2}{l^3}x^3, \quad N_3 = -x + \tfrac{2}{l}x^2 - \tfrac{1}{l^2}x^3 \\ &N_4 = \tfrac{x}{l}, \qquad N_5 = \tfrac{3}{l^2}x^2 - \tfrac{2}{l^3}x^3, \qquad N_6 = \tfrac{1}{l}x^2 - \tfrac{1}{l^2}x^3 \end{aligned} \tag{6.25}$$

Defining the element node displacement vector

$$\boldsymbol{a}^e = \{ u_i \quad v_i \quad \theta_i \quad u_j \quad v_j \quad \theta_j \}^{\mathrm{T}}$$

Equation (6.24) can be rewritten in matrix form as follows:

$$\boldsymbol{f} = \begin{Bmatrix} u \\ v \end{Bmatrix} = \boldsymbol{N}\boldsymbol{a}^e \tag{6.26}$$

where

$$\boldsymbol{N} = \begin{bmatrix} N_1 & 0 & 0 & N_4 & 0 & 0 \\ 0 & N_2 & N_3 & 0 & N_5 & N_6 \end{bmatrix} \tag{6.27}$$

Element strain can be derived by the element displacement obtained. As for rods with large slenderness, shear deformation can be ignored and this strain only includes axial deformation and bending deformation

$$\boldsymbol{\varepsilon} = \begin{Bmatrix} \varepsilon_\chi \\ k_\chi \end{Bmatrix} = \begin{Bmatrix} \frac{\mathrm{d}u}{\mathrm{d}x} \\ \frac{\mathrm{d}^2 v}{\mathrm{d}x^2} \end{Bmatrix} = \boldsymbol{L}\boldsymbol{f} \tag{6.28}$$

where $\boldsymbol{L}$ is a differential operator.

$$\boldsymbol{L} = \begin{bmatrix} \frac{\mathrm{d}}{\mathrm{d}x} & 0 \\ 0 & \frac{\mathrm{d}^2}{\mathrm{d}x^2} \end{bmatrix} \tag{6.29}$$

Substituting Eq. (6.26) into (6.28), it has

$$\boldsymbol{\varepsilon} = \boldsymbol{B}\boldsymbol{a}^e \tag{6.30}$$

where

$$\boldsymbol{B} = \boldsymbol{L}\boldsymbol{N} = [\boldsymbol{B}_i \quad \boldsymbol{B}_j] \tag{6.31}$$

$$\boldsymbol{B}_i = \begin{bmatrix} a_i & 0 & 0 \\ 0 & b_i & c_i \end{bmatrix} \quad \boldsymbol{B}_j = \begin{bmatrix} a_j & 0 & 0 \\ 0 & b_j & c_j \end{bmatrix} \tag{6.32}$$

In the above equations,

$$\begin{aligned} a_j &= -a_i = \tfrac{1}{l}, \quad & b_j &= -b_i = \tfrac{6}{l^2} - \tfrac{12}{l^3}x \\ c_i &= \tfrac{4}{l} - \tfrac{6}{l^2}x, & c_j &= \tfrac{2}{l} - \tfrac{6}{l^2}x \end{aligned}$$

Element stiffness matrix can be calculated according to the following equation:

$$\begin{aligned} \boldsymbol{k}^e &= \int_{\Omega^e} \boldsymbol{B}^{\mathrm{T}}\boldsymbol{D}\boldsymbol{B}\mathrm{d}\Omega = \int_{\Omega^e} \begin{bmatrix} \boldsymbol{B}_i^{\mathrm{T}} \\ \boldsymbol{B}_j^{\mathrm{T}} \end{bmatrix} [D][\boldsymbol{B}_i \quad \boldsymbol{B}_j]\mathrm{d}\Omega \\ &= \begin{bmatrix} \boldsymbol{k}_{ii} & \boldsymbol{k}_{ij} \\ \boldsymbol{k}_{ji} & \boldsymbol{k}_{jj} \end{bmatrix} \end{aligned} \tag{6.33}$$

where the submatrix $\boldsymbol{k}_{\mathrm{rs}}$ is

$$\begin{aligned} \boldsymbol{k}_{\mathrm{rs}} &= \int_{\Omega^e} \boldsymbol{B}_{\mathrm{r}}^{\mathrm{T}}\boldsymbol{D}\boldsymbol{B}_{\mathrm{s}}\mathrm{d}\Omega \\ &= \int_l \begin{bmatrix} a_{\mathrm{r}} & 0 \\ 0 & b_{\mathrm{r}} \\ 0 & c_{\mathrm{r}} \end{bmatrix} \begin{bmatrix} EA & 0 \\ 0 & EI \end{bmatrix} \begin{bmatrix} a_{\mathrm{s}} & 0 & 0 \\ 0 & b_{\mathrm{s}} & c_{\mathrm{s}} \end{bmatrix} \mathrm{d}x \end{aligned} \tag{6.34}$$

A and I are the beam cross-sectional area and section inertia moment, respectively, and *E* is the elasticity modulus of the material.

The explicit expression of the two-dimensional beam element stiffness matrix is

$$\boldsymbol{k}^e = \begin{bmatrix} \frac{EA}{l} & 0 & 0 & -\frac{EA}{l} & 0 & 0 \\ & \frac{12EI}{l^3} & -\frac{6EI}{l^2} & 0 & -\frac{12EI}{l^3} & -\frac{6EI}{l^2} \\ & & \frac{4EI}{l} & 0 & \frac{6EI}{l^2} & \frac{2EI}{l} \\ & & & \frac{EA}{l} & 0 & 0 \\ & \text{symmetry} & & & \frac{12EI}{l^3} & \frac{6EI}{l^2} \\ & & & & & \frac{4EI}{l} \end{bmatrix} \tag{6.35}$$

6.1.2.2 Equivalent Node Load Vector of Beam Element

Equivalent node load vector of the beam element $\boldsymbol{Q}^e$ is

$$\boldsymbol{Q}^e = \boldsymbol{Q}_q^e + \boldsymbol{Q}_b^e + \boldsymbol{Q}_p^e \tag{6.36}$$

where $\boldsymbol{Q}_q^e$, $\boldsymbol{Q}_b^e$, and $\boldsymbol{Q}_p^e$ are equivalent node load vectors induced by distributed loads, body forces, and concentrated loads, respectively, which can be calculated by the following equations:

$$\boldsymbol{Q}_q^e = \int_l \boldsymbol{N}^{\mathrm{T}} \boldsymbol{q} \mathrm{d}x \tag{6.37}$$

$$\boldsymbol{Q}_b^e = \int_{\Omega^e} \boldsymbol{N}^{\mathrm{T}} \boldsymbol{b} \mathrm{d}\Omega \tag{6.38}$$

$$\boldsymbol{Q}_p^e = \boldsymbol{N}^{\mathrm{T}} \boldsymbol{P} \tag{6.39}$$

In the following, some equivalent node load vectors for typical loads will be given.

(1) For uniformly distributed load, as shown in Fig. 6.2,

$$\boldsymbol{q} = \{ 0 \quad -q \}^{\mathrm{T}}$$

the equivalent node load vector induced by $\boldsymbol{q}$ can be derived according to Eq. (6.37).

$$\begin{aligned} \boldsymbol{Q}_q^e = \Big\{ 0 \quad -\tfrac{qa}{2l^3}(2l^3 - 2la^2 + a^3) \quad \tfrac{qa^2}{12l^2}(6l^2 - 8la + 3a^2) \\ 0 \quad -\tfrac{qa^3}{2l^3}(2l - a) \quad -\tfrac{qa^3}{12l^2}(4l - 3a) \Big\}^{\mathrm{T}} \end{aligned} \tag{6.40}$$

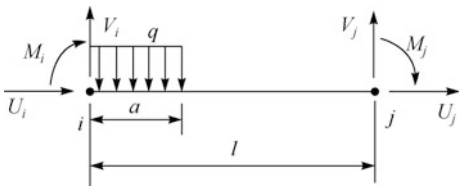

Fig. 6.2 Uniformly distributed load on beam element

When the load is applied on full span $(a = l)$, the above result will be

$$\boldsymbol{Q}_q^e = \left\{ 0 \quad -\tfrac{1}{2}ql \quad \tfrac{1}{12}ql^2 \quad 0 \quad -\tfrac{1}{2}ql \quad -\tfrac{1}{12}ql^2 \right\}^{\mathrm{T}} \tag{6.41}$$

(2) For vertical concentrated load, as indicated in Fig. 6.3, the equivalent node load vector is

$$\boldsymbol{Q}_p^e = \left\{ 0 \quad \frac{P_y b^2}{l^3}(l+2a) \quad -\frac{P_y ab^2}{l^2} \quad 0 \quad \frac{P_y a^2}{l^3}(l+2b) \quad \frac{P_y a^2 b}{l^2} \right\}^{\mathrm{T}} \tag{6.42}$$

(3) For longitudinal concentrated load, as indicated in Fig. 6.4, the equivalent node load vector is

$$\boldsymbol{Q}_p^e = \left\{ \frac{P_x b}{l} \quad 0 \quad 0 \quad \frac{P_x a}{l} \quad 0 \quad 0 \right\}^{\mathrm{T}} \tag{6.43}$$

6.1.2.3 Element Mass Matrix

Element mass matrix expressed by Eq. (6.12) is

$$\boldsymbol{m}^e = \int_{\Omega^e} \rho \boldsymbol{N}^{\mathrm{T}} \boldsymbol{N} \mathrm{d}\Omega \tag{6.44}$$

Equation (6.44) is called consistent mass matrix. This is because the mass distribution is according to the actual distribution in the derivation from element kinetic energy, and meanwhile, the displacement interpolation function adopts the same form as that used in the derivation of stiffness matrix from the potential energy. In addition, the so-called lumped mass matrix is also frequently used in the

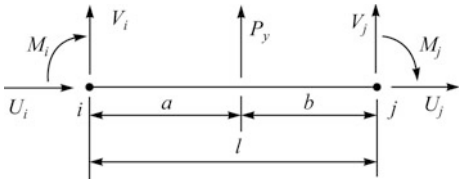

Fig. 6.3 Vertical concentrated load on beam element

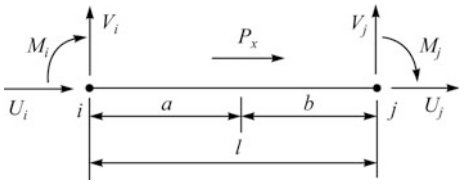

Fig. 6.4 Longitudinal concentrated load on beam element

finite element method. It is assumed that the element mass concentrates on each node, and the mass matrix thus obtained is a diagonal matrix.

Substituting interpolation function (6.27) of the beam element into Eq. (6.44), the following consistent mass matrix will be derived

$$\boldsymbol{m}^e = \frac{\rho A l}{420}\begin{bmatrix} 140 & 0 & 0 & 70 & 0 & 0 \\ & 156 & -22l & 0 & 54 & 13l \\ & & 4l^2 & 0 & -13l & -3l^2 \\ & & & 140 & 0 & 0 \\ & \text{symmetrical} & & & 156 & 22l \\ & & & & & 4l^2 \end{bmatrix} \tag{6.45}$$

where A is the cross-sectional area of the beam and l is the length of the beam element.

If one half of the element mass concentrates on each node, and ignores the rotation, the lumped mass matrix of the element will be

$$\boldsymbol{m}^e = \frac{\rho A l}{2}\begin{bmatrix} 1 & 0 & 0 & 0 & 0 & 0 \\ & 1 & 0 & 0 & 0 & 0 \\ & & 0 & 0 & 0 & 0 \\ & & & 1 & 0 & 0 \\ & \text{symmetrical} & & & 1 & 0 \\ & & & & & 0 \end{bmatrix} \tag{6.46}$$

Both the two kinds of mass matrices are used in actual analysis. In general, the results given by them are similar to each other. From Eq. (6.44), it can be seen that the integrand of the mass matrix of integral expression is the square of the interpolation function, and the stiffness matrix is the square of its derivative. So with the same requirement of precision, lower order interpolation function can be used in mass matrix. The lumped mass matrix, in essence, is such an alternative, which can simplify the computation. Especially in solving the dynamic finite element equation by the explicit scheme of direct integral, if the damping matrix is diagonal, it will avoid the decomposition of the equivalent stiffness matrix, which plays a key role in the nonlinear analysis.

6.1.2.4 Element Damping Matrix

Element damping matrix expressed by Eq. (6.12) is

$$\boldsymbol{c}^e = \int_{\Omega^e} \mu \boldsymbol{N}^{\mathrm{T}} \boldsymbol{N} \mathrm{d}\Omega \tag{6.47}$$

For the same reason as that of consistent mass matrix, Eq. (6.47) is called consistent damping matrix, as a result of assuming that damping force is proportional to the velocity of particle movement. Usually, the medium damping is simplified in this way. In this case, the element damping matrix is in proportion to element mass matrix.

In addition, there is the damping proportional to the strain velocity. For example, the damping caused by the internal friction of materials can be simplified in this way as well. Here, the dissipation energy function can be expressed as follows:

$$R^e = \frac{1}{2} \int_{\Omega^e} \mu \dot{\boldsymbol{\varepsilon}}^{\mathrm{T}} \boldsymbol{D} \dot{\boldsymbol{\varepsilon}} \mathrm{d}\Omega \tag{6.48}$$

Thus, the element damping matrix can be obtained

$$\boldsymbol{c}^e = \mu \int_{\Omega^e} \boldsymbol{B}^{\mathrm{T}} \boldsymbol{D} \boldsymbol{B} \mathrm{d}\Omega \tag{6.49}$$

It can be observed from the above equation that the damping matrix of the element is proportional to element stiffness matrix.

It is rather difficult to determine the damping matrix accurately in actual analysis, and usually, it is allowed to simplify the damping of the actual structure into two forms of linear combination, namely

$$\boldsymbol{c}^e = \alpha \boldsymbol{m}^e + \beta \boldsymbol{k}^e \tag{6.50}$$

This is called proportional damping or modal damping.

6.2 Finite Element Equation of the Track Structure

6.2.1 Basic Assumptions and Computing Model

The following basic assumptions are adopted in the establishment of vertical vibration model of the vehicle-track coupling system by finite element method

(1) Take into account vertical dynamic effect and longitudinal dynamic effect of the vehicle-track coupling system.
(2) Since the vehicle and the track are symmetrical about the centerline of the track, only half of the vehicle-track coupling system is used for ease of calculation.
(3) The upper structure in the vehicle and track coupling system is a complete locomotive or rolling stock unit with a primary and secondary suspension system, in which bouncing vibration and pitch vibration for both vehicle and bogie are considered.
(4) The hypothesis of a linear elastic contact between wheel and rail is used in coupling the vehicle and the track.
(5) The lower structure in the coupling system is the ballast track where rails are discretized into 2D beam element; the stiffness coefficient and damping coefficient of the rail pads and fasteners are denoted by k_{y1} and c_{y1}, respectively.
(6) Sleeper mass is dealt with as lumped mass, and only the vertical vibration effect is taken into account; the stiffness and damping coefficients of the ballast are denoted by k_{y2} and c_{y2}, respectively.
(7) Ballast mass is simplified as lumped mass, and only the vertical vibration effect is considered; the stiffness and damping coefficients of the subgrade are denoted by k_{y3} and c_{y3}, respectively.

The computing model of the vehicle-track coupling system is as shown in Fig. 6.5.

6.2.2 *Theory of Generalized Beam Element of Track Structure*

In order to facilitate the design of the computing program and reduce the bandwidth of global stiffness matrix, a model of generalized beam element of track structure has been proposed [1]. This element is composed of a segment of rails, sleepers, ballast, and subgrade between two adjacent sleepers, as shown in Fig. 6.6.

Defining the node displacement and node force of the generalized beam element of track structure as follows:

$$\boldsymbol{a}_1^e = \{\, u_1 \quad v_1 \quad \theta_1 \quad v_2 \quad v_3 \quad u_4 \quad v_4 \quad \theta_4 \quad v_5 \quad v_6 \,\}^{\mathrm{T}}$$
$$\boldsymbol{F}_1^e = \{\, U_1 \quad V_1 \quad M_1 \quad V_2 \quad V_3 \quad U_4 \quad V_4 \quad M_4 \quad V_5 \quad V_6 \,\}^{\mathrm{T}}$$

where $u_i, v_i\ (i = 1, 2, \ldots, 6)$ are the longitudinal (along the railway direction) and vertical node displacements and $\theta_i\ (i = 1, 4)$ is the rotational angle of node i; $U_i, V_i\ (i = 1, 2, \ldots, 6)$ are the longitudinal and vertical node forces, and $M_i\ (i = 1, 4)$ is the bending moment of the node i.

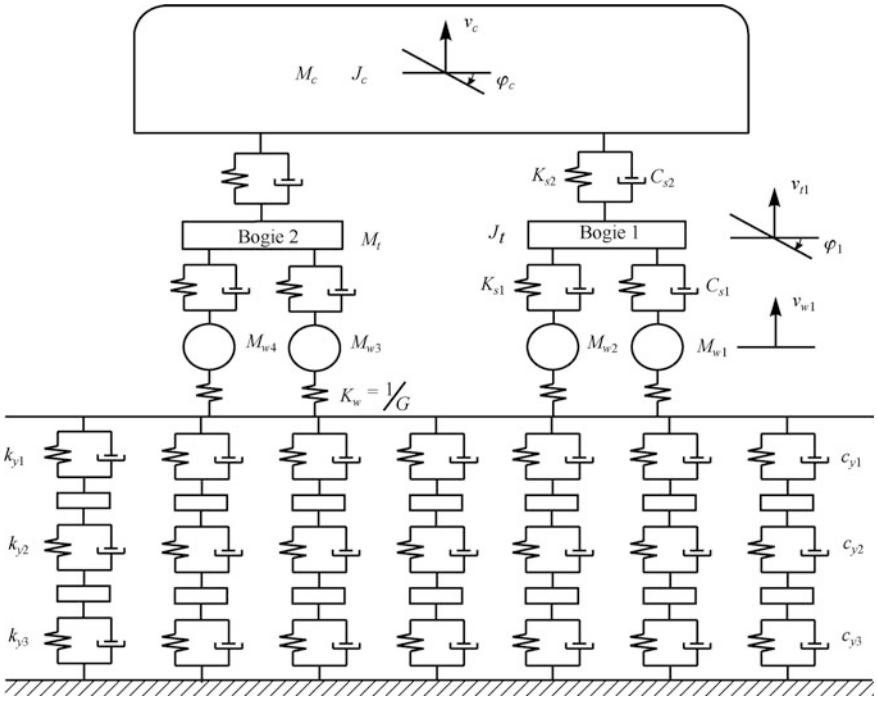

Fig. 6.5 Computing model of the vehicle-track system

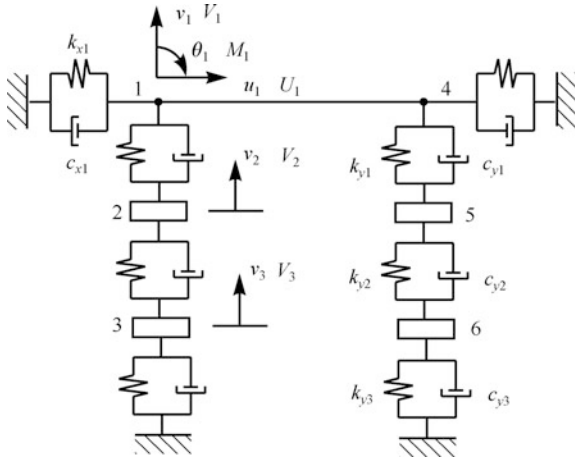

Fig. 6.6 Generalized beam element of track structure

(1) Element stiffness matrix

The enlarged generalized beam element stiffness matrix of track structure can be expressed as follows:

$$\boldsymbol{k}_{\mathrm{r}}^{e}=\begin{bmatrix} EA/l & 0 & 0 & 0 & 0 & -EA/l & 0 & 0 & 0 & 0 \\ & 12EI/l^3 & -6EI/l^2 & 0 & 0 & 0 & -12EI/l^3 & -6EI/l^2 & 0 & 0 \\ & & 4EI/l & 0 & 0 & 0 & 6EI/l^2 & 2EI/l & 0 & 0 \\ & & & 0 & 0 & 0 & 0 & 0 & 0 & 0 \\ & & & & 0 & 0 & 0 & 0 & 0 & 0 \\ & & & & & EA/l & 0 & 0 & 0 & 0 \\ & & \text{symmetrical} & & & & 12EI/l^3 & 6EI/l^2 & 0 & 0 \\ & & & & & & & 4EI/l & 0 & 0 \\ & & & & & & & & 0 & 0 \\ & & & & & & & & & 0 \end{bmatrix} \tag{6.51}$$

In generalized beam element model of track structure, besides the stiffness induced by rail strain energy, the stiffness induced by discrete elastic supports should also be taken into account.

Assuming that the elastic force is proportional to the node displacement, according to Fig. 6.6, it has

$$\begin{cases} U_{ie}=\frac{1}{2}k_{x1}u_i \\ V_{ie}=\frac{1}{2}k_{y1}(v_i-v_{i+1}) & (i=1,4) \\ M_{ie}=0 \end{cases} \tag{6.52}$$

$$V_{ie}=\frac{1}{2}k_{y2}(v_i-v_{i+1})-\frac{1}{2}k_{y1}(v_{i-1}-v_i) \quad (i=2,5)$$

$$V_{ie}=\frac{1}{2}k_{y3}v_i-\frac{1}{2}k_{y2}(v_{i-1}-v_i) \quad (i=3,6)$$

where k_{x1} and k_{y1} are the longitudinal and vertical stiffness coefficients of the rail pads and fasteners, respectively; k_{y2} and k_{y3} are the vertical stiffness coefficients of the ballast and the subgrade, respectively. The stiffness coefficient of the node i in (6.52) has 1/2 because the node stiffness induced by rail pads and fasteners, or ballast, or subgrade equals to the sum of the node stiffness of the two adjacent elements.

It can be written in matrix form as follows:

$$\boldsymbol{F}_{\mathrm{e}}^{e}=\boldsymbol{k}_{\mathrm{e}}^{e}\boldsymbol{a}^{e} \tag{6.53}$$

where $\boldsymbol{F}_{\mathrm{e}}^{e}$ is the elastic force vector of the generalized beam element and $\boldsymbol{k}_{\mathrm{e}}^{e}$ is the element stiffness matrix induced by discrete elastic supports.

$$\boldsymbol{k}_{\mathrm{e}}^{e}=\frac{1}{2}\begin{bmatrix} k_{x1} & 0 & 0 & 0 & 0 & 0 & 0 & 0 & 0 & 0 \\ & k_{y1} & 0 & -k_{y1} & 0 & 0 & 0 & 0 & 0 & 0 \\ & & 0 & 0 & 0 & 0 & 0 & 0 & 0 & 0 \\ & & & k_{y1}+k_{y2} & -k_{y2} & 0 & 0 & 0 & 0 & 0 \\ & & & & k_{y2}+k_{y3} & 0 & 0 & 0 & 0 & 0 \\ & & & & & k_{x1} & 0 & 0 & 0 & 0 \\ & & & & & & k_{y1} & 0 & -k_{y1} & 0 \\ & & & \text{symmetrical} & & & & 0 & 0 & 0 \\ & & & & & & & & k_{y1}+k_{y2} & -k_{y2} \\ & & & & & & & & & k_{y2}+k_{y3} \end{bmatrix} \tag{6.54}$$

The stiffness matrix of the generalized beam element of track structure can be derived by summing up Eqs. (6.51) and (6.54).

$$\boldsymbol{k}_{\mathrm{l}}^{e}=\boldsymbol{k}_{\mathrm{r}}^{e}+\boldsymbol{k}_{\mathrm{e}}^{e} \tag{6.55}$$

(2) Element mass matrix

The enlarged consistent mass matrix of the generalized beam element of track structure is

$$\boldsymbol{m}_{\mathrm{r}}^{e}=\frac{\rho Al}{420}\begin{bmatrix} 140 & 0 & 0 & 0 & 0 & 70 & 0 & 0 & 0 & 0 \\ & 156 & -22l & 0 & 0 & 0 & 54 & 13l & 0 & 0 \\ & & 4l^2 & 0 & 0 & 0 & -13l & -3l^2 & 0 & 0 \\ & & & 0 & 0 & 0 & 0 & 0 & 0 & 0 \\ & & & & 0 & 0 & 0 & 0 & 0 & 0 \\ & & & & & 140 & 0 & 0 & 0 & 0 \\ & & & \text{symmetrical} & & & 156 & 22l & 0 & 0 \\ & & & & & & & 4l^2 & 0 & 0 \\ & & & & & & & & 0 & 0 \\ & & & & & & & & & 0 \end{bmatrix} \tag{6.56}$$

where ρ is the rail density.

Besides the rail mass, the masses of the sleeper and the ballast should also be taken into account in the mass matrix of track structure. According to the basic assumptions (6) and (7), sleeper mass m_{t} and ballast mass m_{b} can be simplified as a concentrated mass in the generalized beam element of track structure, respectively.

$$\boldsymbol{m}_{\mathrm{b}}^{e}=\mathrm{diag}\left(0 \quad 0 \quad \tfrac{1}{4}m_{\mathrm{t}} \quad \tfrac{1}{4}m_{\mathrm{b}} \quad 0 \quad 0 \quad \tfrac{1}{4}m_{\mathrm{t}} \quad \tfrac{1}{4}m_{\mathrm{b}}\right) \tag{6.57}$$

Element mass matrix of track structure can be derived by summing up Eqs. (6.56) and (6.57).

$$\boldsymbol{m}_{\mathrm{l}}^{e} = \boldsymbol{m}_{\mathrm{r}}^{e} + \boldsymbol{m}_{\mathrm{b}}^{e} \tag{6.58}$$

where $\boldsymbol{m}_{\mathrm{r}}^{e}$ is the consistent mass matrix of the rail and $\boldsymbol{m}_{\mathrm{b}}^{e}$ is the mass matrix of the sleeper and ballast.

(3) Element damping matrix

Element damping matrix is often expressed as follows:

$$\boldsymbol{c}_{\mathrm{r}}^{e} = \alpha \boldsymbol{m}_{\mathrm{r}}^{e} + \beta \boldsymbol{k}_{\mathrm{r}}^{e} \tag{6.59}$$

This damping is called proportional damping, with α and β as damping coefficients, related to damping ratio and natural frequency of the system.

Just as in the discussion of element stiffness matrix of track structure, in addition to the proportional damping caused by rail, the damping force caused by discrete supports should also be taken into account here.

$$\begin{cases} U_{id} = \frac{1}{2} c_{x1} \dot{u}_i \\ V_{id} = \frac{1}{2} c_{y1} (\dot{v}_i - \dot{v}_{i+1}) & (i = 1, 4) \\ M_{id} = 0 \end{cases}$$
$$V_{id} = \frac{1}{2} c_{y2} (\dot{v}_i - \dot{v}_{i+1}) - \frac{1}{2} c_{y1} (\dot{v}_{i-1} - \dot{v}_i) \quad (i = 2, 5)$$
$$V_{id} = \frac{1}{2} c_{y3} \dot{v}_i - \frac{1}{2} c_{y2} (\dot{v}_{i-1} - \dot{v}_i) \quad (i = 3, 6) \tag{6.60}$$

where c_{x1} and c_{y1} represent the longitudinal and vertical damping coefficients of the rail pads and fasteners, respectively. c_{y2} and c_{y3} represent vertical damping coefficients of the ballast and the subgrade, respectively. For the same reason as in element stiffness matrix, the damping coefficient of the element in (6.60) has 1/2.

Equation (6.60) can be written in matrix form

$$\boldsymbol{F}_{\mathrm{c}}^{e} = \boldsymbol{c}_{\mathrm{c}}^{e} \dot{\boldsymbol{a}}^{e} \tag{6.61}$$

where $\boldsymbol{F}_{\mathrm{c}}^{e}$ is the damping force vector of the generalized beam element and $\boldsymbol{c}_{\mathrm{c}}^{e}$ is the damping force coefficient matrix of the generalized beam element. In generalized coordinate system, it has

$$\boldsymbol{c}_{\mathrm{c}}^{e} = \frac{1}{2} \begin{bmatrix} c_{x1} & 0 & 0 & 0 & 0 & 0 & 0 & 0 & 0 & 0 \\ & c_{y1} & 0 & -c_{y1} & 0 & 0 & 0 & 0 & 0 & 0 \\ & & 0 & 0 & 0 & 0 & 0 & 0 & 0 & 0 \\ & & & c_{y1} + c_{y2} & -c_{y2} & 0 & 0 & 0 & 0 & 0 \\ & & & & c_{y2} + c_{y3} & 0 & 0 & 0 & 0 & 0 \\ & & & & & c_{x1} & 0 & 0 & 0 & 0 \\ & & & & & & c_{y1} & 0 & -c_{y1} & 0 \\ & & & \text{symmetrical} & & & & 0 & 0 & 0 \\ & & & & & & & & c_{y1} + c_{y2} & -c_{y2} \\ & & & & & & & & & c_{y2} + c_{y3} \end{bmatrix} \tag{6.62}$$

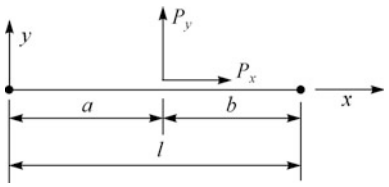

Fig. 6.7 Vertical and longitudinal concentrated forces on rail

Damping matrix of the generalized beam element of track structure can be derived by summing up Eqs. (6.59) and (6.62)

$$\boldsymbol{c}_{\mathrm{l}}^{e} = \boldsymbol{c}_{\mathrm{r}}^{e} + \boldsymbol{c}_{\mathrm{c}}^{e} \tag{6.63}$$

(4) Element equivalent node load vector
In vibration analysis of track structure, the vertical concentrated force induced by wheel loads and the longitudinal force induced by traction and braking are expressed by P_y and P_x, respectively, as shown in Fig. 6.7.
The element equivalent node load vector induced by vertical and longitudinal concentrated forces is

$$\boldsymbol{Q}_{\mathrm{l}}^{e} = \left\{ \tfrac{b}{l}P_x \quad -\tfrac{P_y b^2}{l^3}(l+2a) \quad \tfrac{P_y ab^2}{l^2} \quad 0 \quad 0 \quad \tfrac{a}{l}P_x \quad -\tfrac{P_y a^2}{l^3}(l+2b) \quad -\tfrac{P_y a^2 b}{l^2} \quad 0 \quad 0 \right\}^{\mathrm{T}} \tag{6.64}$$

(5) The dynamic finite element equation of track structure
The finite element equation to solve the dynamic problem of track structure can be derived based on Lagrange equation

$$\boldsymbol{M}_{\mathrm{l}}\ddot{\boldsymbol{a}}_{\mathrm{l}} + \boldsymbol{C}_{\mathrm{l}}\dot{\boldsymbol{a}}_{\mathrm{l}} + \boldsymbol{K}_{\mathrm{l}}\boldsymbol{a}_{\mathrm{l}} = \boldsymbol{Q}_{\mathrm{l}} \tag{6.65}$$

In the above equation, the subscript "*l*" represents the quantity of lower track structure, where

$$\boldsymbol{M}_{\mathrm{l}} = \sum_{e} \boldsymbol{m}_{\mathrm{l}}^{e}, \quad \boldsymbol{C}_{\mathrm{l}} = \sum_{e} \boldsymbol{c}_{\mathrm{l}}^{e}, \quad \boldsymbol{K}_{\mathrm{l}} = \sum_{e} \boldsymbol{k}_{\mathrm{l}}^{e}, \quad \boldsymbol{Q}_{\mathrm{l}} = \sum_{e} \boldsymbol{Q}_{\mathrm{l}}^{e} \tag{6.66}$$

They are global mass matrix, global damping matrix, global stiffness matrix, and global node load vector of track structure, respectively.

6.3 Model of Track Dynamics Under Moving Axle Loads

In recent years, new problems in the high-speed and heavy-haul railway transportation make it urgent for us to have a deeper understanding of wheel-rail dynamic interaction. Numerical analysis method is a powerful means to study

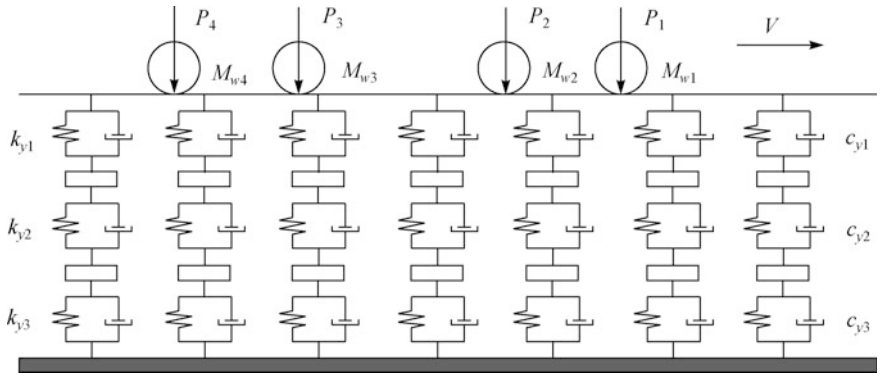

Fig. 6.8 The simple track dynamics model under moving axle loads

wheel-rail interaction. At present, there are many theoretical analysis models regarding vehicle-track-subgrade as an integrated system. Outstanding advantages of numerical analysis method are as follows: to predict the dynamic response and stability of track structure based on mathematic models and to assess the preliminary design of a new type of track structure which needs to implement field inspection as a rule. It is a commonly used approach in various types of computing models to describe a track structure with a system of complex dispersion parameters as a lumped parameter model with a single degree of freedom or a discrete structure with many degrees of freedom.

The simplest track dynamics model will be discussed first in this section. Regarding the train as the moving axle loads and without considering the primary and secondary suspension system of the vehicle, a track dynamics model under moving axle loads is established. In this model, pitch vibration and bouncing vibration of the locomotive and the sprung mass and unsprung mass of vehicle suspension system are ignored. The vehicle load is distributed into each wheelset evenly, and the inertial force of the wheel is taken into account. Since the pitch vibration and the bouncing vibration of sprung mass and unsprung mass are ignored, this model is relatively simple, and the entire length of the train can be chosen as computational object. The track dynamics model under moving axle loads is as shown in Fig. 6.8.

In Sect. 6.2, we have already established the finite element equation (6.65) of track structure, and here, we only need to add the vehicle mass and the wheelset mass into element mass matrix. It is noted that the position of the wheelset on the rail is a function of time, as shown in Fig. 6.9.

Fig. 6.9 Position of the wheelset on the rail

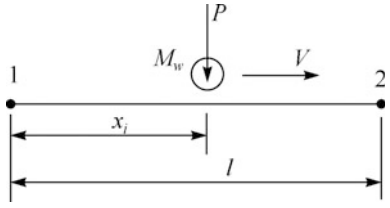

The additional mass matrix of the generalized track beam element caused by half unsprung wheelset mass is as follows:

$$\boldsymbol{m}_{\mathrm{w}}^{e} = \mathrm{diag}(\, m_{\mathrm{w1}} \quad m_{\mathrm{w1}} \quad 0 \quad 0 \quad 0 \quad m_{\mathrm{w2}} \quad m_{\mathrm{w2}} \quad 0 \quad 0 \quad 0 \,) \tag{6.67}$$

where $m_{\mathrm{w1}} = \left(1 - \frac{x_i}{l}\right) M_{\mathrm{w}}, \quad m_{\mathrm{w2}} = \frac{x_i}{l} M_{\mathrm{w}}, \quad M_{\mathrm{w}}$ is half unsprung wheelset mass.

Therefore, $\boldsymbol{m}_{\mathrm{l}}^{e}$ in the Eq. (6.58) can be simply modified to

$$\boldsymbol{m}_{\mathrm{l}}^{e} = \boldsymbol{m}_{\mathrm{r}}^{e} + \boldsymbol{m}_{\mathrm{b}}^{e} + \boldsymbol{m}_{\mathrm{w}}^{e} \tag{6.68}$$

Meanwhile, the axle load P of the moving train has to be imposed on the track structure as the concentrated force.

6.4 Vehicle Model of a Single Wheel With Primary Suspension System

The discussion in Sect. 6.3 ignored the effect of vehicle suspension system and coupling effect of the vehicle and the track. Ever since this section, following the principle of from the simple to the complex, the simple model, i.e., the vehicle model of a single wheel with primary suspension system, will be introduced first. Then, the vehicle model of half a car with primary and secondary suspension system, and finally, the vehicle model of a whole car with primary and secondary suspension system will be discussed. In discussing various vehicle models, the vertical upward direction of displacement and force is designated as positive, and the clockwise direction of rotational angle and torque is positive.

The model of a single wheel with primary suspension system is as shown in Fig. 6.10. In this model, only bouncing vibration of the vehicle is taken into account, and pitch vibration of the vehicle is ignored. Compared with the vehicle

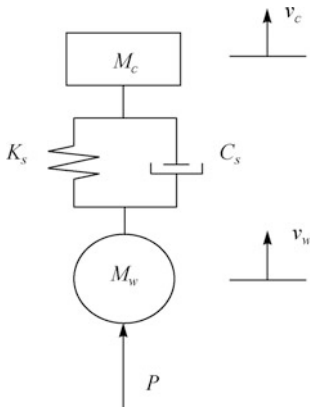

Fig. 6.10 Vehicle model of a single wheel with primary suspension system

mass, the bogie mass is relatively small, and the vibration of the vehicle is the main factor in the dynamic analysis of track structure. Thus, in order to simplify the computation, the bogie mass is incorporated into the wheelset, and the locomotive is regarded as single-layer dynamic system.

The springs of the primary and secondary suspension system are considered as a series system, and the equivalent stiffness K_s of the primary and secondary suspension system can be calculated by the series equation

$$K_{\mathrm{s}} = \frac{K_{\mathrm{s1}} K_{\mathrm{s2}}}{K_{\mathrm{s1}} + K_{\mathrm{s2}}} \tag{6.69}$$

where K_{s1} and K_{s2} are stiffness coefficients of the primary and secondary suspension system, respectively.

Vehicle bouncing vibration equation is

$$M_{\mathrm{c}}\ddot{v}_{\mathrm{c}} + C_{\mathrm{s}}(\dot{v}_{\mathrm{c}} - \dot{v}_{\mathrm{w}}) + K_{\mathrm{s}}(v_{\mathrm{c}} - v_{\mathrm{w}}) = -M_{\mathrm{c}}g \tag{6.70}$$

Wheel bouncing vibration equation is

$$M_{\mathrm{w}}\ddot{v}_{\mathrm{w}} - C_{\mathrm{s}}(\dot{v}_{\mathrm{c}} - \dot{v}_{\mathrm{w}}) - K_{\mathrm{s}}(v_{\mathrm{c}} - v_{\mathrm{w}}) = P \tag{6.71}$$

where M_c is the $1/2n$ vehicle mass (n is the wheelset number of a locomotive or vehicle); M_{w} is the 1/2 unsprung wheelset mass; and K_{s} and C_{s} are equivalent stiffness and damping coefficients of the single-layer dynamic system. $P = -M_{\mathrm{w}}g + F_{\mathrm{w}i}$, $F_{\mathrm{w}i}$ is the wheel-rail contact force and can be derived through Hertz equation according to the relative contact displacement of wheel and rail.

$$F_{\mathrm{w}i} = \begin{cases} \frac{1}{G^{3/2}}\left(\left|v_{\mathrm{w}i} - (v_{xi} + \eta_i)\right|\right)^{3/2} & v_{\mathrm{w}i} - (v_{xi} + \eta_i) \le 0 \\ 0 & v_{\mathrm{w}i} - (v_{xi} + \eta_i) > 0 \end{cases} \tag{6.72}$$

where $v_{\mathrm{w}i}$ and v_{xi} are the displacements of wheel and rail in the coordinate x_i; η_i is the irregularity of the rail surface; and G is the contact deflection coefficient, when the wheel is new tapered tread,

$$G = 4.57R^{-0.149} \times 10^{-8}\ (\mathrm{m/N^{2/3}}) \tag{6.73}$$

And when the wheel is worn profile tread,

$$G = 3.86R^{-0.115} \times 10^{-8}\ (\mathrm{m/N^{2/3}}) \tag{6.74}$$

Wheel-rail interaction can be analyzed with iteration method. The iteration algorithm used in solving the vehicle-track coupling equations will be introduced in more detail in Chap. 7.

Equations (6.70) and (6.71) can be written in matrix form

$$\boldsymbol{M}_{\mathrm{u}}\ddot{\boldsymbol{a}}_{\mathrm{u}} + \boldsymbol{C}_{\mathrm{u}}\dot{\boldsymbol{a}}_{\mathrm{u}} + \boldsymbol{K}_{\mathrm{u}}\boldsymbol{a}_{\mathrm{u}} = \boldsymbol{Q}_{\mathrm{u}} \tag{6.75}$$

In the above equation, the subscript "*u*" represents the upper structure, namely the vehicle system.

$$\boldsymbol{a}_{\mathrm{u}} = \{\, v_{\mathrm{c}} \quad v_{\mathrm{w}} \,\}^{\mathrm{T}}, \quad \dot{\boldsymbol{a}}_{\mathrm{u}} = \{\, \dot{v}_{\mathrm{c}} \quad \dot{v}_{\mathrm{w}} \,\}^{\mathrm{T}}, \quad \ddot{\boldsymbol{a}}_{\mathrm{u}} = \{\, \ddot{v}_{\mathrm{c}} \quad \ddot{v}_{\mathrm{w}} \,\}^{\mathrm{T}} \tag{6.76}$$

$$\boldsymbol{Q}_{\mathrm{u}} = \{\, -M_{\mathrm{c}}g \quad P \,\}^{\mathrm{T}} \tag{6.77}$$

$$\boldsymbol{M}_{\mathrm{u}} = \begin{bmatrix} M_{\mathrm{c}} & 0 \\ 0 & M_{\mathrm{w}} \end{bmatrix} \tag{6.78}$$

$$\boldsymbol{C}_{\mathrm{u}} = \begin{bmatrix} C_{\mathrm{s}} & -C_{\mathrm{s}} \\ -C_{\mathrm{s}} & C_{\mathrm{s}} \end{bmatrix} \tag{6.79}$$

$$\boldsymbol{K}_{\mathrm{u}} = \begin{bmatrix} K_{\mathrm{s}} & -K_{\mathrm{s}} \\ -K_{\mathrm{s}} & K_{\mathrm{s}} \end{bmatrix} \tag{6.80}$$

The vehicle model of a single wheel with primary suspension system has two degrees of freedom.

6.5 Vehicle Model of Half a Car With Primary and Secondary Suspension System

In this section, the vehicle model of half a car with primary and secondary suspension system will be discussed, as shown in Fig. 6.11. In the discussion of the vehicle model of half a car, half of the vehicle mass is taken as concentrated mass and its bouncing vibration is taken into account. But with regard to bogie, besides bouncing vibration, its pitch vibration has to be taken into account as well.

According to Fig. 6.11, bouncing vibration equation of the car body is

$$M_{\mathrm{c}}\ddot{v}_{\mathrm{c}} + (\dot{v}_{\mathrm{c}} - \dot{v}_{\mathrm{t}})C_{\mathrm{s2}} + (v_{\mathrm{c}} - v_{\mathrm{t}})K_{\mathrm{s2}} = -M_{\mathrm{c}}g \tag{6.81}$$

where M_{c} and v_{c} are ½ half car body mass and vertical displacement of the car body, respectively. K_{s1} and C_{s1} are stiffness and damping coefficients of the primary suspension system of the vehicle, while K_{s2} and C_{s2} are stiffness and damping coefficients of the secondary suspension system of the vehicle. v_{t} is the vertical displacement of the bogie.

Bouncing vibration equation of the bogie is

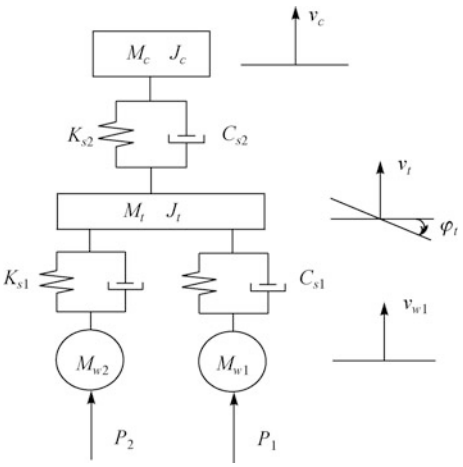

Fig. 6.11 Vehicle model of half a car with primary and secondary suspension system

$$\begin{aligned} M_t\ddot{v}_t &+ [(\dot{v}_t - \dot{v}_{w1} - \dot{\varphi}_t l_1) + (\dot{v}_t - \dot{v}_{w2} + \dot{\varphi}_t l_1)]C_{s1} \\ &+ [(v_t - v_{w1} - \varphi_t l_1) + (v_t - v_{w2} + \varphi_t l_1)]K_{s1} \\ &- (\dot{v}_c - \dot{v}_t)C_{s2} - (v_c - v_t)K_{s2} = -M_t g \end{aligned} \tag{6.82}$$

Pitch vibration equation of the bogie is

$$\begin{aligned} J_t\ddot{\varphi}_t &+ [-(\dot{v}_t - \dot{v}_{w1} - \dot{\varphi}_t l_1) + (\dot{v}_t - \dot{v}_{w2} + \dot{\varphi}_t l_1)]C_{s1} l_1 \\ &+ [-(v_t - v_{w1} - \varphi_t l_1) + (v_t - v_{w2} + \varphi_t l_1)]K_{s1} l_1 = 0 \end{aligned} \tag{6.83}$$

where M_t is the 1/2 bogie mass; J_t is the inertia moment of the bogie; φ_t is the rotational angle around the horizontal axis of the bogie; l_1 is the 1/2 of the bogie length; and v_{w1} and v_{w2} are the vertical displacements of wheel 1 and wheel 2, respectively.

Bouncing vibration equations of the two wheels are

$$M_{w1}\ddot{v}_{w1} - (\dot{v}_t - \dot{v}_{w1} - \dot{\varphi}_t l_1)]C_{s1} - (v_t - v_{w1} - \varphi_t l_1)K_{s1} = P_1 \tag{6.84}$$

$$M_{w2}\ddot{v}_{w2} - (\dot{v}_t - \dot{v}_{w2} + \dot{\varphi}_t l_1)]C_{s1} - (v_t - v_{w2} + \varphi_t l_1)K_{s1} = P_2 \tag{6.85}$$

where M_{wi} is the 1/2 unsprung mass of ith wheelset, $P_i = -M_{wi}g + F_{wi}$ and F_{wi} is the wheel-rail contact force and can be derived by Hertz Eq. (6.72) according to the relative contact displacement of wheel and rail.

Equations (6.81)–(6.85) can be written in matrix form

$$\boldsymbol{M}_u\ddot{\boldsymbol{a}}_u + \boldsymbol{C}_u\dot{\boldsymbol{a}}_u + \boldsymbol{K}_u\boldsymbol{a}_u = \boldsymbol{Q}_u$$

where

$$\begin{aligned} \boldsymbol{a}_{\mathrm{u}} &= \{\, v_{\mathrm{c}} \quad v_{\mathrm{t}} \quad \varphi_{\mathrm{t}} \quad v_{\mathrm{w1}} \quad v_{\mathrm{w2}} \,\}^{\mathrm{T}} \\ \ddot{\boldsymbol{a}}_{\mathrm{u}} &= \{\, \ddot{v}_{\mathrm{c}} \quad \ddot{v}_{\mathrm{t}} \quad \ddot{\varphi}_{\mathrm{t}} \quad \ddot{v}_{\mathrm{w1}} \quad \ddot{v}_{\mathrm{w2}} \,\}^{\mathrm{T}} \end{aligned} \tag{6.86}$$

$$\boldsymbol{Q}_{\mathrm{u}} = \{\, -M_{\mathrm{c}}g \quad -M_{\mathrm{t}}g \quad 0 \quad P_1 \quad P_2 \,\}^{\mathrm{T}} \tag{6.87}$$

$$\boldsymbol{M}_{\mathrm{u}} = \begin{bmatrix} M_{\mathrm{c}} & & & & 0 \\ & M_{\mathrm{t}} & & & \\ & & J_{\mathrm{t}} & & \\ & & & M_{\mathrm{w1}} & \\ 0 & & & & M_{\mathrm{w2}} \end{bmatrix} \tag{6.88}$$

$$\boldsymbol{C}_{\mathrm{u}} = \begin{bmatrix} C_{\mathrm{s2}} & -C_{\mathrm{s2}} & 0 & 0 & 0 \\ & C_{\mathrm{s2}} + 2C_{\mathrm{s1}} & 0 & -C_{\mathrm{s1}} & -C_{\mathrm{s1}} \\ & & 2C_{\mathrm{s1}}l_1^2 & C_{\mathrm{s1}}l_1 & -C_{\mathrm{s1}}l_1 \\ & \text{symmetrical} & & C_{\mathrm{s1}} & 0 \\ & & & & C_{\mathrm{s1}} \end{bmatrix} \tag{6.89}$$

$$\boldsymbol{K}_{\mathrm{u}} = \begin{bmatrix} K_{\mathrm{s2}} & -K_{\mathrm{s2}} & 0 & 0 & 0 \\ & K_{\mathrm{s2}} + 2K_{\mathrm{s1}} & 0 & -K_{\mathrm{s1}} & -K_{\mathrm{s1}} \\ & & 2K_{\mathrm{s1}}l_1^2 & K_{\mathrm{s1}}l_1 & -K_{\mathrm{s1}}l_1 \\ & \text{symmetrical} & & K_{\mathrm{s1}} & 0 \\ & & & & K_{\mathrm{s1}} \end{bmatrix} \tag{6.90}$$

The vehicle model of half a car with primary and secondary suspension system has 5 degrees of freedom.

6.6 Vehicle Model of a Whole Car With Primary and Secondary Suspension System

The vehicle model of a whole car with primary and secondary suspension system is as shown in Fig. 6.12. In the vehicle model of a whole car, bouncing vibration and pitch vibration of both the vehicle and the bogie are taken into account. The vehicle model of a whole car is in accordance with the actual situation as well.

Bouncing vibration equation of the car body is

$$\begin{aligned} M_{\mathrm{c}}\ddot{v}_{\mathrm{c}} + [(\dot{v}_{\mathrm{c}} - \dot{v}_{\mathrm{t1}} - \dot{\varphi}_{\mathrm{c}}l_2) + (\dot{v}_{\mathrm{c}} - \dot{v}_{\mathrm{t2}} + \dot{\varphi}_{\mathrm{c}}l_2)]C_{\mathrm{s2}} + \\ [(v_{\mathrm{c}} - v_{\mathrm{t1}} - \varphi_{\mathrm{c}}l_2) + (v_{\mathrm{c}} - v_{\mathrm{t2}} + \varphi_{\mathrm{c}}l_2)]K_{\mathrm{s2}} = -M_{\mathrm{c}}g \end{aligned} \tag{6.91}$$

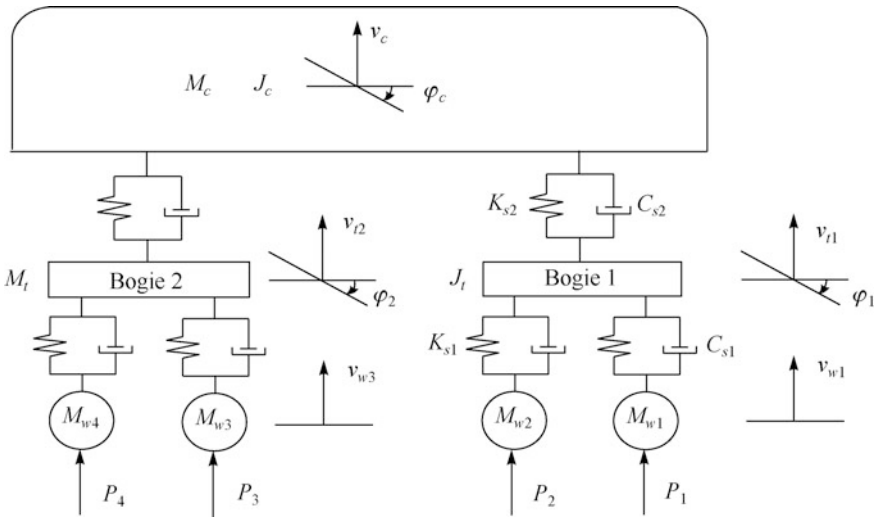

Fig. 6.12 Vehicle model of a whole car with primary and secondary suspension system

Pitch vibration equation of the car body is

$$\begin{aligned} J_c\ddot{\varphi}_c + [-(\dot{v}_c - \dot{v}_{t1} - \dot{\varphi}_c l_2) + (\dot{v}_c - \dot{v}_{t2} + \dot{\varphi}_c l_2)]C_{s2}l_2 + \\ [-(v_c - v_{t1} - \varphi_c l_2) + (v_c - v_{t2} + \varphi_c l_2)]K_{s2}l_2 = 0 \end{aligned} \tag{6.92}$$

Bouncing vibration equations of the two bogies are

$$\begin{aligned} M_t\ddot{v}_{t1} - (v_c - v_{t1} - \varphi_c l_2)K_{s2} - (\dot{v}_c - \dot{v}_{t1} - \dot{\varphi}_c l_2)C_{s2} + \\ [(v_{t1} - v_{w1} - \varphi_1 l_1) + (v_{t1} - v_{w2} + \varphi_1 l_1)]K_{s1} + \\ [(\dot{v}_{t1} - \dot{v}_{w1} - \varphi_1 l_1) + (\dot{v}_{t1} - \dot{v}_{w2} + \varphi_1 l_1)]C_{s1} = -M_t g \end{aligned} \tag{6.93}$$

$$\begin{aligned} M_t\ddot{v}_{t2} - (v_c - v_{t2} + \varphi_c l_2)K_{s2} - (\dot{v}_c - \dot{v}_{t2} + \dot{\varphi}_c l_2)C_{s2} + \\ [(v_{t2} - v_{w3} - \varphi_2 l_1) + (v_{t2} - v_{w4} + \varphi_2 l_1)]K_{s1} + \\ [(\dot{v}_{t2} - \dot{v}_{w3} - \dot{\varphi}_2 l_1) + (\dot{v}_{t2} - \dot{v}_{w4} + \dot{\varphi}_2 l_1)]C_{s1} = -M_t g \end{aligned} \tag{6.94}$$

Pitch vibration equations of the two bogies are

$$\begin{aligned} J_t\ddot{\varphi}_1 + [-(v_{t1} - v_{w1} - \varphi_1 l_1) + (v_{t1} - v_{w2} + \varphi_1 l_1)]K_{s1}l_1 + \\ [-(\dot{v}_{t1} - \dot{v}_{w1} - \dot{\varphi}_1 l_1) + (\dot{v}_{t1} - \dot{v}_{w2} + \dot{\varphi}_1 l_1)]C_{s1}l_1 = 0 \end{aligned} \tag{6.95}$$

$$\begin{aligned} J_t\ddot{\varphi}_2 + [-(v_{t2} - v_{w3} - \varphi_2 l_1) + (v_{t2} - v_{w4} + \varphi_2 l_1)]K_{s1}l_1 + \\ [-(\dot{v}_{t2} - \dot{v}_{w3} - \dot{\varphi}_2 l_1) + (\dot{v}_{t2} - \dot{v}_{w4} + \dot{\varphi}_2 l_1)]C_{s1}l_1 = 0 \end{aligned} \tag{6.96}$$

Bouncing vibration equations of the four wheels are

$$M_{w1}\ddot{v}_{w1} - (v_{t1} - v_{w1} - \varphi_1 l_1)K_{s1} - (\dot{v}_{t1} - \dot{v}_{w1} - \dot{\varphi}_1 l_1)C_{s1} = P_1 \tag{6.97}$$

$$M_{w2}\ddot{v}_{w2} - (v_{t1} - v_{w2} + \varphi_1 l_1)K_{s1} - (\dot{v}_{t1} - \dot{v}_{w2} + \dot{\varphi}_1 l_1)C_{s1} = P_2 \tag{6.98}$$

$$M_{w3}\ddot{v}_{w3} - (v_{t2} - v_{w3} - \varphi_2 l_1)K_{s1} - (\dot{v}_{t2} - \dot{v}_{w3} - \dot{\varphi}_2 l_1)C_{s1} = P_3 \tag{6.99}$$

$$M_{w4}\ddot{v}_{w4} - (v_{t2} - v_{w4} + \varphi_2 l_1)K_{s1} - (\dot{v}_{t2} - \dot{v}_{w4} + \dot{\varphi}_2 l_1)C_{s1} = P_4 \tag{6.100}$$

In the above equations, M_c is the 1/2 mass of the car body; v_c and φ_c are vertical displacement of the centroid of the car body and rotational angle around the horizontal axis, respectively; J_c is the inertia moment of the car body; v_{t1} and v_{t2} are vertical displacements of the front and back bogie centroid, respectively; φ_1 and φ_2 are front and back bogie rotational angles around the horizontal axis, respectively; $J_{t,}$ is the bogie inertia moment; $2l_1$ is the wheelbase, $2l_2$ is the distance between the bogie pivot centers, and the meaning of other symbols is the same as above.

Equations (6.91)–(6.100) can be written in matrix form

$$\boldsymbol{M}_u\ddot{\boldsymbol{a}}_u + \boldsymbol{C}_u\dot{\boldsymbol{a}}_u + \boldsymbol{K}_u\boldsymbol{a}_u = \boldsymbol{Q}_u$$

where

$$\begin{aligned}
\boldsymbol{a}_u &= \{\, v_c \quad \varphi_c \quad v_{t1} \quad v_{t2} \quad \varphi_1 \quad \varphi_2 \quad v_{w1} \quad v_{w2} \quad v_{w3} \quad v_{w4} \,\}^T \\
\dot{\boldsymbol{a}}_u &= \{\, \dot{v}_c \quad \dot{\varphi}_c \quad \dot{v}_{t1} \quad \dot{v}_{t2} \quad \dot{\varphi}_1 \quad \dot{\varphi}_2 \quad \dot{v}_{w1} \quad \dot{v}_{w2} \quad \dot{v}_{w3} \quad \dot{v}_{w4} \,\}^T \\
\ddot{\boldsymbol{a}}_u &= \{\, \ddot{v}_c \quad \ddot{\varphi}_c \quad \ddot{v}_{t1} \quad \ddot{v}_{t2} \quad \ddot{\varphi}_1 \quad \ddot{\varphi}_2 \quad \ddot{v}_{w1} \quad \ddot{v}_{w2} \quad \ddot{v}_{w3} \quad \ddot{v}_{w4} \,\}^T
\end{aligned} \tag{6.101}$$

$$\boldsymbol{Q}_u = \{\, -M_c g \quad 0 \quad -M_t g \quad -M_t g \quad 0 \quad 0 \quad P_1 \quad P_2 \quad P_3 \quad P_4 \,\}^T \tag{6.102}$$

$$\boldsymbol{M}_u = \mathrm{diag}\{\, M_c \quad J_c \quad M_t \quad M_t \quad J_t \quad J_t \quad M_{w1} \quad M_{w2} \quad M_{w3} \quad M_{w4} \,\} \tag{6.103}$$

$$\boldsymbol{C}_u = \begin{bmatrix}
2C_{s2} & 0 & -C_{s2} & -C_{s2} & 0 & 0 & 0 & 0 & 0 & 0 \\
 & 2C_{s2}l_2^2 & C_{s2}l_2 & -C_{s2}l_2 & 0 & 0 & 0 & 0 & 0 & 0 \\
 & & 2C_{s1}+C_{s2} & 0 & 0 & 0 & -C_{s1} & -C_{s1} & 0 & 0 \\
 & & & 2C_{s1}+C_{s2} & 0 & 0 & 0 & 0 & -C_{s1} & -C_{s1} \\
 & & & & 2C_{s1}l_1^2 & 0 & C_{s1}l_1 & -C_{s1}l_1 & 0 & 0 \\
 & & & & & 2C_{s1}l_1^2 & 0 & 0 & C_{s1}l_1 & -C_{s1}l_1 \\
 & & & & & & C_{s1} & 0 & 0 & 0 \\
 & & & & & & & C_{s1} & 0 & 0 \\
 & & & \text{symmetrical} & & & & & C_{s1} & 0 \\
 & & & & & & & & & C_{s1}
\end{bmatrix} \tag{6.104}$$

$$\boldsymbol{K}_{\mathrm{u}}=\begin{bmatrix} 2K_{\mathrm{s2}} & 0 & -K_{\mathrm{s2}} & -K_{\mathrm{s2}} & 0 & 0 & 0 & 0 & 0 & 0 \\ & 2K_{\mathrm{s2}}l_2^2 & K_{\mathrm{s2}}l_2 & -K_{\mathrm{s2}}l_2 & 0 & 0 & 0 & 0 & 0 & 0 \\ & & 2K_{\mathrm{s1}}+K_{\mathrm{s2}} & 0 & 0 & 0 & -K_{\mathrm{s1}} & -K_{\mathrm{s1}} & 0 & 0 \\ & & & 2K_{\mathrm{s1}}+K_{\mathrm{s2}} & 0 & 0 & 0 & 0 & -K_{\mathrm{s1}} & -K_{\mathrm{s1}} \\ & & & & 2K_{\mathrm{s1}}l_1^2 & 0 & K_{\mathrm{s1}}l_1 & -K_{\mathrm{s1}}l_1 & 0 & 0 \\ & & & & & 2K_{\mathrm{s1}}l_1^2 & 0 & 0 & K_{\mathrm{s1}}l_1 & -K_{\mathrm{s1}}l_1 \\ & & & & & & K_{\mathrm{s1}} & 0 & 0 & 0 \\ & & & & & & & K_{\mathrm{s1}} & 0 & 0 \\ & & & \text{symmetrical} & & & & & K_{\mathrm{s1}} & 0 \\ & & & & & & & & & K_{\mathrm{s1}} \end{bmatrix} \tag{6.105}$$

The vehicle model of a whole car with primary and secondary suspension system has 10 degrees of freedom.

6.7 Parameters for Vehicle and Track Structure

In the previous sections, various vehicle-track coupling system models are introduced. Whatever model it is, it needs some predetermined necessary parameters, such as the mass, inertia moment, stiffness, and damping coefficients of various parts of locomotives and vehicles; the mass, stiffness, and damping coefficients of various parts of track structure; and the wheel-rail contact stiffness. This section will focus on the parameter value range of the typical locomotives, vehicles, and various components of ballast track and ballastless track at home and abroad, for the readers' reference in computation.

6.7.1 Basic Parameters of Locomotives and Vehicles

Commonly used railway vehicles in China include C_{62A} and C_{75} freight cars, SWJ new heavy-haul freight cars, and HSC high-speed railway cars [20]. The geometric dimension of these vehicles is shown in Fig. 6.13, while their basic parameters are shown in Table 6.1.

The geometric dimension of German ICE high-speed motor cars and trailers is shown in Figs. 6.14, 6.15, while their basic parameters are shown in Tables 6.2, 6.3.

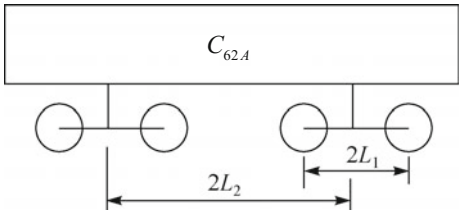

Fig. 6.13 Geometric dimension of the commonly used vehicles in China

Table 6.1 Basic parameters of commonly used railway vehicles in China

Vehicle type	C_{62A}	C_{75}	SWJ	HSC
Car body mass M_c /(kg)	77,000	91,800	91,100	52,000
Bogie mass M_t /(kg)	1100	1510	1950	3200
Wheel mass M_w /(kg)	1200	1295	1250	1400
Car body pitch inertia moment J_c /(kg/m^2)	1.2×10^6	4.22×10^6	4.28×10^6	2.31×10^6
Bogie pitch inertia moment J_t /(kg m^2)	760	1560	1800	3120
Vertical stiffness of primary suspension K_{s1} /(kN/m)	–	–	5×10^3	1.87×10^3
Vertical stiffness of secondary suspension K_{s2} /(kN/m)	5.32×10^3	5.014×10^3	–	1.72×10^3
Vertical damping of primary suspension C_{s1} /(kN s/m)	–	–	30	5×10^2
Vertical damping of secondary suspension C_{s2} /(kN s/m)	70	50	–	1.96×10^2
Fixed wheelbase $2l_1$ /(m)	1.75	1.75	1.75	2.50
Distance between bogie pivot centers $2l_2$ /(m)	8.50	8.70	8.70	18.0
Wheel radius/(m)	0.42	0.42	0.42	0.4575

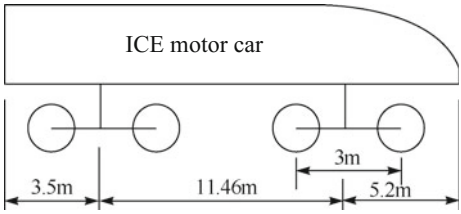

Fig. 6.14 ICE high-speed motor car

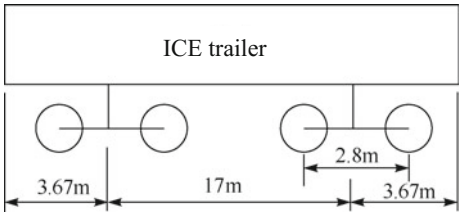

Fig. 6.15 ICE high-speed trailer

The geometric dimension of French TGV medium-speed motor cars, high-speed motor cars, and trailers are shown in Figs. 6.16, 6.17, while their basic parameters are shown in Tables 6.4, 6.5, 6.6.

Parameters of CRH3 high-speed motor cars in China are shown in Table 6.7

Table 6.2 Basic parameters of ICE high-speed motor car

Parameters	Value	Parameters	Value
Train speed $V/(\mathrm{km/h})$	≤ 300	Longitudinal stiffness of primary suspension K_{1x} (kN/m)	2×10^4
Axle load P/(kN)	195	Lateral stiffness of primary suspension K_{1y} (kN/m)	4.86×10^3
Car body mass M_c/(kg)	5.88×10^4	Vertical stiffness of primary suspension K_{1z} (kN/m)	2.418×10^3
Bogie mass M_t/(kg)	5.35×10^3	Longitudinal damping of primary suspension C_{1x} (kN s/m)	7.3×10^3
Wheelset mass M_w/(kg)	2.2×10^3	Lateral damping of primary suspension C_{1y} (kN s/m)	2.12×10^3
Car body roll inertia moment $J_{cx}/(\mathrm{kg\,m^2})$	1.337×10^5	Vertical damping of primary suspension C_{1z} (kN s/m)	30
Car body pitch inertia moment $J_{cy}/(\mathrm{kg\,m^2})$	3.089×10^6	Lateral stiffness of secondary suspension K_{2y} (kN/m)	187
Car body yawing inertia moment $J_{cz}/(\mathrm{kg\,m^2})$	3.089×10^6	Vertical stiffness of secondary suspension K_{2z} (kN/m)	1.52×10^3
Bogie roll inertia moment $J_{tx}/(\mathrm{kg\,m^2})$	2.79×10^3	Lateral damping of secondary suspension C_{2y} (kN s/m)	100
Bogie pitch inertia moment $J_{ty}/(\mathrm{kg\,m^2})$	5.46×10^2	Vertical damping of secondary suspension C_{2z} (kN s/m)	90
Bogie yawing inertia moment $J_{tz}/(\mathrm{kg\,m^2})$	6.6×10^3	Wheel radius r_0 m	0.46
Wheelset roll inertia moment $J_{wx}/(\mathrm{kg\,m^2})$	950	Transverse distance of primary suspension $2b_1$ m	2.0
Wheelset yawing inertia moment $J_{wz}/(\mathrm{kg\,m^2})$	950	Transverse distance of secondary suspension $2b_2$ m	2.284
Wheel flange friction coefficient μ_1	0.3	Distance between vehicle center and secondary suspension point h_1 m	0.9
Wheel tread friction coefficient μ_2	0.3	Distance between bogie center and secondary suspension point h_2 m	0.451
Clearance between wheel flange and gauge line δ/(m)	0.019	Distance between bogie center and wheelset center h_3 m	0.1

6.7.2 Basic Parameters of the Track Structure

(1) Stiffness of rail discrete support
If the rail is regarded as a continuous beam with finite discrete elastic supports, the stiffness k of the rail discrete support can be expressed as follows:

$$k = \frac{k_{pc} k_{bs}}{k_{pc} + k_{bs}} \tag{6.106}$$

Table 6.3 Basic parameters of ICE high-speed trailer

Parameters	Value	Parameters	Value
Train speed $V/(\mathrm{km/h})$	≤ 300	Longitudinal stiffness of primary suspension K_{1x} (kN/m)	7.3×10^3
Axle load P/(kN)	145	Lateral stiffness of primary suspension K_{1y} (kN/m)	2.12×10^3
Car body mass M_c/(kg)	4.55×10^4	Vertical stiffness of primary suspension K_{1z} (kN/m)	2.82×10^4
Bogie mass M_t/(kg)	3.09×10^3	Longitudinal damping of primary suspension C_{1x} (kN s/m)	41.6
Wheelset mass M_w/(kg)	1.56×10^3	Lateral damping of primary suspension C_{1y} (kN s/m)	29.5
Car body roll inertia moment $J_{cx}/(\mathrm{kg\,m^2})$	1.035×10^5	Vertical damping of primary suspension C_{1z} (kN s/m)	21.9
Car body pitch inertia moment $J_{cy}/(\mathrm{kg\,m^2})$	2.391×10^6	Lateral stiffness of secondary suspension K_{2y} (kN/m)	146
Car body yawing inertia moment $J_{cz}/(\mathrm{kg\,m^2})$	2.391×10^6	Vertical stiffness of secondary suspension K_{2z} (kN/m)	324
Bogie roll inertia moment $J_{tx}/(\mathrm{kg\,m^2})$	2.366×10^3	Lateral damping of secondary suspension C_{2y} (kN s/m)	17.5
Bogie pitch inertia moment $J_{ty}/(\mathrm{kg\,m^2})$	4.989×10^2	Vertical damping of secondary suspension C_{2z} (kN s/m)	29.2
Bogie yawing inertia moment $J_{tz}/(\mathrm{kg\,m^2})$	2.858×10^3	Wheel radius r_0 m	0.46
Wheelset roll inertia moment $J_{wx}/(\mathrm{kg\,m^2})$	678	Transverse distance of primary suspension $2b_1$ m	2.0
Wheelset yawing inertia moment $J_{wz}/(\mathrm{kg\,m^2})$	678	Transverse distance of secondary suspension $2b_2$ m	2.284
Wheel flange friction coefficient μ_1	0.3	Distance between vehicle center and secondary suspension point h_1 m	0.9
Wheel tread friction coefficient μ_2	0.2	Distance between bogie center and secondary suspension point h_2 m	0.451
Clearance between wheel flange and gauge line δ/(m)	0.019	Distance between bogie center and wheelset center h_3 m	0.1

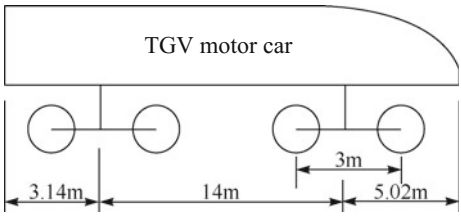

Fig. 6.16 TGV medium- and high-speed motor car

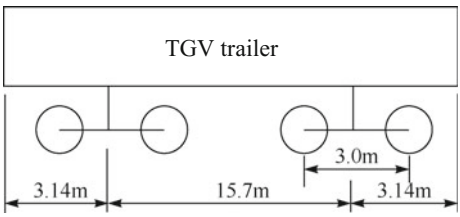

Fig. 6.17 TGV medium- and high-speed trailer

Table 6.4 Basic parameters of TGV medium-speed motor car

Parameters	Value	Parameters	Value
Train speed $V/(\text{km/h})$	≤ 270	Longitudinal stiffness of primary suspension K_{1x} (kN/m)	1×10^4
Axle load $P/(\text{kN})$	168	Lateral stiffness of primary suspension K_{1y} (kN/m)	5.0×10^3
Car body mass $M_c/(\text{kg})$	4.24×10^4	Vertical stiffness of primary suspension K_{1z} (kN/m)	1.04×10^3
Bogie mass $M_t/(\text{kg})$	3.4×10^3	Longitudinal damping of primary suspension C_{1x} (kN s/m)	60
Wheelset mass $M_w/(\text{kg})$	2.2×10^3	Lateral damping of primary suspension C_{1y} (kN s/m)	69.6
Car body roll inertia moment $J_{cx}/(\text{kg m}^2)$	1.015×10^5	Vertical damping of primary suspension C_{1z} (kN s/m)	50
Car body pitch inertia moment $J_{cy}/(\text{kg m}^2)$	1.064×10^6	Lateral stiffness of secondary suspension K_{2y} (kN/m)	200
Car body yawing inertia moment $J_{cz}/(\text{kg m}^2)$	8.672×10^5	Vertical stiffness of secondary suspension K_{2z} (kN/m)	500
Bogie roll inertia moment $J_{tx}/(\text{kg m}^2)$	3.2×10^3	Lateral damping of secondary suspension C_{2y} (kN s/m)	50
Bogie pitch inertia moment $J_{ty}/(\text{kg m}^2)$	7.2×10^3	Vertical damping of secondary suspension C_{2z} (kN s/m)	60
Bogie yawing inertia moment $J_{tz}/(\text{kg m}^2)$	6.8×10^3	Wheel radius r_0 m	0.43
Wheelset roll inertia moment $J_{wx}/(\text{kg m}^2)$	1630	Transverse distance of primary suspension $2b_1$ m	2.05
Wheelset yawing inertia moment $J_{wz}/(\text{kg m}^2)$	1630	Transverse distance of secondary suspension $2b_2$ m	2.05
Wheel flange friction coefficient μ_1	0.3	Distance between vehicle center and secondary suspension point h_1 m	0.38
Wheel tread friction coefficient μ_2	0.3	Distance between bogie center and secondary suspension point h_2 m	0.38
Clearance between wheel flange and gauge line $\delta/(\text{m})$	0.019	Distance between bogie center and wheelset center h_3 m	0.1

Table 6.5 Basic parameters of TGV medium-speed trailer

Parameters	Value	Parameters	Value
Train speed V/(km/h)	≤ 270	Longitudinal stiffness of primary suspension K_{1x}/ (kN/m)	5×10^4
Axle load P/(kN)	168	Lateral stiffness of primary suspension K_{1y}/ (kN/m)	5.0×10^3
Car body mass M_c/(kg)	4.4×10^4	Vertical stiffness of primary suspension K_{1z}/ (kN/m)	700
Bogie mass M_t/(kg)	1.7×10^3	Longitudinal damping of primary suspension C_{1x}/ (kN s/m)	60
Wheelset mass M_w/(kg)	1.9×10^3	Lateral damping of primary suspension C_{1y}/ (kN s/m)	69.6
Car body roll inertia moment J_{cx}/(kg m^2)	7.42×10^4	Vertical damping of primary suspension C_{1z}/ (kN s/m)	38
Car body pitch inertia moment J_{cy}/(kg m^2)	2.74×10^6	Lateral stiffness of secondary suspension K_{2y}/ (kN/m)	210
Car body yawing inertia moment J_{cz}/(kg m^2)	2.74×10^6	Vertical stiffness of secondary suspension K_{2z}/ (kN/m)	350
Bogie roll inertia moment J_{tx}/(kg m^2)	1600	Lateral damping of secondary suspension C_{2y}/ (kN s/m)	15
Bogie pitch inertia moment J_{ty}/(kg m^2)	1700	Vertical damping of secondary suspension C_{2z}/ (kN s/m)	40
Bogie yawing inertia moment J_{tz}/(kg m^2)	1700	Wheel radius r_0/ m	0.43
Wheelset roll inertia moment J_{wx}/(kg m^2)	1067	Transverse distance of primary suspension $2b_1$/ m	2.05
Wheelset yawing inertia moment J_{wz}/(kg m^2)	1067	Transverse distance of secondary suspension $2b_2$/ m	2.05
Wheel flange friction coefficient μ_1	0.3	Distance between vehicle center and secondary suspension point h_1/ m	0.49
Wheel tread friction coefficient μ_2	0.2	Distance between bogie center and secondary suspension point h_2/ m	0.49
Clearance between wheel flange and gauge line δ/(m)	0.019	Distance between bogie center and wheelset center h_3/ m	0.34

In the above equation, k is the equivalent stiffness resulting from the rail pads and fasteners, ballast, and subgrade connected in series; k_{bs} is the equivalent stiffness resulting from the ballast and subgrade connected in series, and k_{pc}, the stiffness of the rail pad and fastener, is equal to the sum of the rail pad stiffness k_p and the rail pad stiffness k_c, namely

$$k_{pc} = k_p + k_c \tag{6.107}$$

Table 6.6 Basic parameters of TGV high-speed motor car

Parameters	Value	Parameters	Value
Axle load P/(kN)	170	Vertical stiffness of primary suspension K_{s1}/(kN/m)	1.31×10^3
Car body mass M_c/(kg)	53.5×10^3	Vertical stiffness of secondary suspension K_{s2}/(kN/m)	3.28×10^3
Bogie mass M_t/(kg)	3.26×10^3	Vertical damping of primary suspension C_{s1}/(kN s/m)	30
Wheelset mass M_w/(kg)	2.0×10^3	Vertical damping of secondary suspension C_{s2}/(kN s/m)	90
Car body pitch inertia moment J_c/(kg m^2)	2.4×10^6	Wheel radius r_0/(m)	0.458
Bogie pitch inertia moment J_t/(kg m^2)	3.33×10^3	Fixed wheelbase $2l_1$/(m)	3.0

Table 6.7 Parameters of CRH3 high-speed motor car

Parameters	Value	Parameters	Value
Car body mass M_c/(kg)	40×10^3	Vertical damping of primary suspension C_{s1}/(kN s/m)	100
Bogie mass M_t/(kg)	3200	Vertical damping of secondary suspension C_{s2}/(kN s/m)	120
Wheelset mass M_w/(kg)	2400	Vertical stiffness of wheel-rail contact K_c/(kN/m)	1.325×10^6
Car body pitch inertia moment J_c/(kg m^2)	5.47×10^5	Fixed wheelbase $2l_1$/(m)	2.5
Bogie pitch inertia moment J_t/(kg m^2)	6800	Distance between bogie pivot centers $2l_2$/(m)	17.375
Vertical stiffness of primary suspension K_{s1}/(kN/m)	2.08×10^3	Length of the middle cars/(m)	24.775
Vertical stiffness of secondary suspension K_{s2}/(kN/m)	0.8×10^3	Length of the head car/(m)	25.675

In general, the rail fastener stiffness is small, while the rail pad stiffness is large.

The average stiffness of a set of rail fasteners is as follows:
For clip fasteners: $k_c = 2.94 - 3.92$ MN/m
For elastic rod rail fastener: $k_c = 3.92$ MN/m

The average stiffness of rubber rail pad is

For 12–14-mm high-strength rubber pads: $k_p = 49$ MN/m
For 7–8-mm rubber pads: $k_p = 117.6$ MN/m

The equivalent stiffness k_{bs} resulting from the ballast and subgrade connected in series is

$$k_{bs} = \frac{k_b k_s}{k_b + k_s} \tag{6.108}$$

The effective stiffness of the ballast depends on the load distribution, load acting area, and the elasticity of the ballast bed. Applying a simplified model with uniform load distributing tapered downward, and resulting in uniform pressure in same depth of the ballast, it has

$$k_b = \frac{c(l-b)E_b}{\ln\left[\frac{l(b+ch_b)}{b(l+ch_b)}\right]} \text{ (N/m)} \tag{6.109}$$

where E_b (N/m^2) is the ballast elasticity modulus; l is the length of the loading area, namely half of the effective supporting length of sleeper; b is the width of the load area, namely the average base width of the sleepers; h_b is the thickness of the ballast bed; $c = 2tg\varphi$, where φ is the friction angle of the ballast and φ's value range is 20°–35°.

If rail is regarded as a long infinite beam supported by continuous elastic foundation, the stiffness of the rail continuous support can be calculated according to the following equation:

$$K = \frac{k}{a} \left(\text{N/m}^2\right) \tag{6.110}$$

where a is the sleeper interval.

(2) Wheel-rail contact stiffness

Wheel-rail contact stiffness is not only related to wheel-rail contact force, relative contact displacement, and elasticity coefficient of the materials but also related to the wheel tread and the rail shape.

When wheel is new, rail and wheel can be regarded as cylinders. According to Hertz equation for two mutually perpendicular and contacted cylinders, it has

$$y = Gp^{2/3} \tag{6.112}$$

where y is the relative displacement between the wheel and the rail and p is the wheel-rail contact force and G is the deflection coefficient.

Equation (6.112) can be rewritten as follows:

$$p = \frac{1}{G^{3/2}} y^{3/2} = Cy^{3/2} \tag{6.113}$$

where $C = \frac{1}{G^{3/2}}$ is called stiffness coefficient.

By linearizing the Hertz nonlinear contact stiffness near the wheel static load p_0, namely

$$k_{\mathrm{w}} = \left.\frac{\mathrm{d}p}{\mathrm{d}y}\right|_{p=p_0} = \left.\frac{3}{2}Cy^{1/2}\right|_{p=p_0} = \frac{3}{2}p_0^{1/3}C^{2/3} = \frac{3}{2G}p_0^{1/3}\ (\mathrm{N/cm}) \tag{6.114}$$

Equation (6.113) is changed to

$$p = k_{\mathrm{w}}y \tag{6.115}$$

where k_{w} is called linearized stiffness coefficient of wheel-rail contact. Experimental results show that the rail type and the load variation have little impact on k_{w}, whereas the wheel diameter variation has great impact, which is usually within the range of 1225–1500 MN/m.

(3) Value range of the track structure parameters

Table 6.8 lists the value range of the parameters of conventional ballast track structure. Table 6.9 lists the parameters of ballast track structure of trunk lines. Table 6.10 lists the parameters of the Bögle slab track structure. Table 6.11 lists the parameters of conventional ballast track structure materials. Tables 6.12, 6.13, 6.14, 6.15 lists basic parameters of the rail, basic parameters of the sleepers, performance parameters of bar-spring clips, and static stiffness of rail rubber pads, respectively.

Table 6.8 Value range of the parameters of ballast track structure

Parameters	Value range
Rail pad stiffness k_{p}/(MN/m)	50–100
Rail fastener stiffness k_{c}/(MN/m)	2.94–3.92
Stiffness of rail pads and fasteners k_{pc}/(MN/m)	53–104
Damping of rail pads and fasteners c_{pc}/(kN s/m)	30–63
Ballast stiffness k_{b}/(MN/m)	165–220
Ballast damping c_{b}/(kN s/m)	55–82
Subgrade stiffness k_{s}/(MN/m)	40–133
Subgrade damping c_{s}/(kN s/m)	90–100
Joint stiffness of ballast and subgrade k_{bs}/(MN/m)	40–60 (newly built lines) 80–100 (existing lines)
Stiffness of the track with single rail (discrete supports) k/(MN/m)	14.4–23 (track of wooden sleepers) 34.5–48.9 (track of concrete sleepers) 40.25–57.5 (track of widen sleepers)
Lateral stiffness of sleepers k_1/(MN/m)	402.5
Lateral stiffness of sleepers k_2/(MN/m)	11.5
Wheel-track contact stiffness k_{w}/(MN/m)	1225–1500

Table 6.9 Parameters of ballast track structure of trunk lines

Parameters		Value
Rail	Mass/(kg/m)	60.64
	Section area/(cm^2)	77.45
	Moment of inertia around horizontal axis/(cm^4)	3217
	Elasticity modulus/(MPa)	2.06×10^5
Rail pad and fastener	Stiffness coefficient/(MN/m)	78
	Damping coefficient/(kN s/m)	50
	Mass/(kg)	3.0
Sleeper	Sleeper interval/(m)	0.60
	Mass/(kg)	250
	Length/(m)	2.6
	Width/(m)	0.25
	Height/(m)	0.20
	Basal area/(m^2)	0.6525 (Basal area of sleepers) 0.5073 (load area)
Ballast	Density/(kg/m^3)	2500
	Stiffness coefficient/(MN/m)	180
	Damping coefficient/(kN s/m)	60
	Thickness/(m)	0.35
Subgrade	Stiffness coefficient/(MN/m)	65
	Damping coefficient/(kN s/m)	90

Table 6.10 Parameters of Bögle slab track structure

Parameters		Value	Parameters	Value	
Track slab	Length/(mm)	6450	Concrete supporting layer	Length/(mm)	6450
	Width/(mm)	2550		Width/(mm)	2950
	Height/(mm)	200		Height/(mm)	300
	Density/(kg/m^3)	2500		Density/(kg/m^3)	2500
	Elasticity modulus/(MPa)	3.9×10^4		Elasticity modulus/(MPa)	3.0×10^4
Rail pad and fastener	Stiffness coefficient/(MN/m)	60	CA mortar	Stiffness coefficient/(MN/m)	900
	Damping coefficient/(kN s/m)	47.7		Damping coefficient/(kN s/m)	83
Subgrade	Stiffness coefficient/(MN/m)	60	Subgrade	Damping coefficient/(kN s/m)	90

Table 6.11 Parameters of materials for conventional ballast track structure

Parameters of materials	Elasticity modulus/(E (MPa))	Poisson's ratio υ	Density ρ/(kg/m^3)
Rail	2.1×10^5	0.30	7800
Sleeper	1.5×10^4	0.30	2800
Ballast	150	0.27	2500
Sub-ballast	50	0.35	2000
Subgrade	20	0.25	2000

Table 6.12 Basic rail parameters

Rail type	75	60	50	45	43
Mass per meter/(kg)	74.414	60.64	51.514	45.11	44.653
Section area/(cm^2)	90.06	77.45	65.8	57.61	57.0
Moment of inertia around horizontal axis/(cm^4)	4490	3217	2037	1606	1489
Moment of inertia around vertical axis/(cm^4)	661	524	377	283	260
Rail height/(mm)	192	176	152	145	140
Rail head width/(mm)	75	73	70	67	70
Rail base width/(mm)	150	150	132	126	114

Table 6.13 Basic parameters of sleeper

Type of sleepers	Mass/(kg)	Length/(m)	Average width of the bottom/(m)	Effective supporting length of half sleeper/(m)
Conventional wooden sleeper	100	2.5	0.19–0.22	1.1
Concrete sleeper of the existing lines (type I)	237	2.5	0.267	0.95
Widen concrete sleeper (chord type 76)	520	2.5	0.55	0.95
Sleeper of speed-rising main line (type II)	251	2.5	0.273	0.95
Sleeper of fast dedicated passenger line (type III)	340	2.6	0.29	1.175

Table 6.14 Parameters of bar-spring clips

Type of bar-spring clips	Clamping force/(kN)	Spring deflection/(mm)
Bar-spring clips (type I)	8.5	9
Bar-spring clips (type II)	10.8	11
Bar-spring clips (type III)	11.0	13

Table 6.15 Static stiffness of rubber pads

Type of railway	Type of rubber pads	Static stiffness/(MN/m)
Conventional existing lines	10–11	90–120
Quasi-high-speed railway	10–17	55–80
High-speed railway	High elasticity	40–60

References

1. Lei X (2002) New methods of track dynamics and engineering. China Railway Publishing House, Beijing
2. Knothe K, Grassie SL (1993) Modeling of railway track and vehicle/track interaction at high frequencies. Vehicle Syst Dyn 22(3/4):209–262
3. Trochanis AM, Chelliah R, Bielak J (1987) Unified approach for beams on elastic foundation for moving load. J Geotech Eng 112:879–895
4. Ono K, Yamada M (1989) Analysis of railway track vibration. J Sound Vib 130(2):269–297
5. Grassie SL, Gregory RW, Harrison D, Johnson KL (1982) The dynamic response of railway track to high frequency vertical excitation. J Mech Eng Sci 24:77–90
6. Cai Z, Raymond GP (1992) Theoretical model for dynamic wheel/rail and track interaction. In: Proceedings of the 10th international wheelset congress, Sydney, Australia, pp 127–131
7. Jenkins HH, Stephenson JE, Morland GA, Lyon D (1974) The effect of track and vehicle parameters on wheel/rail vertical dynamic forces. Railw Eng J 3:2–16
8. Kerr AD (1989) On the vertical modulus in the standard railway track analyses. Rail Int 235 (2):37–45
9. Ishida M, Miura S, Kono A (1998) Track deforming characteristics and vehicle running characteristics due to the settlement of embankment behind the abutment of bridges. RTRI Rep 12(3):41–46
10. Nielsen JCO (1993) Train/track interaction: coupling of moving and stationary dynamic system. Dissertation, Chalmers University of Technology, Gotebory, Sweden
11. Kisilowski J, Knothe K (1991) Advanced railway vehicle system dynamics. Wydawnictwa Naukowo- Techniczne, Warsaw, pp 74–78
12. Zhai WM, Sun X (1994) A detailed model for investigating vertical interactions between railway vehicle and track. Vehicle Syst Dyn Supp 23:603–615
13. Ishida M, Miura S, Kono A (1997) Track dynamic model and its analytical results. RTRI Rep 11(2):19–26
14. Ishida M (2000) The past and future of track dynamic models. RTRI Rep 14(4):1–6
15. Snyder JE, Wormley DN (1977) Dynamic interactions between vehicle and elevated, flexible, randomly irregular guide ways. J Dyn Control Syst 99:23–33
16. Roberts JB, Spanos PD (1990) Random vibration and statistical linearization. Wiley, New Jersey
17. Shinozuka M (1971) Simulation of multivariate and multidimensional random processes. J Acoustical Soc Am 49(1):357–368
18. Yang F, Fonder GA (1996) An iterative solution method for dynamic response of bridge-vehicles systems. J Earthq Eng Struct Dyn 25:195–215
19. Lei X, Wang J (2014) Dynamic analysis of the train and slab track coupling system with finite elements in a moving frame of reference. J Vib Control 20(9):1301–1317
20. Zhai W (2007) Vehicle-track coupling dynamics, 3rd edn. Science Publishing House, Beijing

21. Lei X, Zhang B, Liu Q (2010) Model of vehicle track elements for vertical dynamic analysis of vehicle track system. J Vib Shock 29(3):168–173
22. Feng Q, Lei X, Lian S (2008) Vibration analysis of high-speed tracks vibration with geometric irregularities. J Railw Sci Eng 21(6):559–564
23. Zienkiewicz OC (1977) The finite element method, 3rd edn. McGraw-Hill Inc., New York
24. Lei X (2000) The finite element method. China Railway Publishing House, Beijing

Chapter 7
A Cross-Iteration Algorithm for Vehicle-Track Coupling Vibration Analysis

In Chap. 6, the track dynamics model under the moving axle loads, the vehicle model of single wheel with primary suspension system, and the vehicle model of half a car and a whole car with primary and secondary suspension system are presented, and the associated dynamic finite element equations are derived. All these models share one common feature; that is, the vehicle equation and the track equation are not completely independent from each other, but are mutually coupled through wheel-rail contact force and wheel-rail contact displacement. Therefore, the equation to be solved is coupled equation of the vehicle-track system. Solutions to the coupled equation of the vehicle-track system have been discussed in many literature [1–4]. According to existed studies, the solutions can be roughly divided into two categories, one being iterative method [5–7] and the other being method based on energy principle [8–11]. A cross-iteration algorithm for vehicle-track coupling vibration analysis is to be discussed in this chapter, while the other method will be elaborated in Chaps. 8 and 9.

7.1 A Cross-Iteration Algorithm for Vehicle-Track Nonlinear Coupling System

Computation model for the vehicle-track coupling system is shown in Fig. 7.1. To solve the finite element equation, the coupled system is decomposed into the upper subsystem of the vehicle and the lower subsystem of the track. The cross-iteration algorithm is applied in the two systems.

In order to solve the dynamic equation of the vehicle-track coupling system, Newmark integration method is used and the detailed procedure of the cross-iteration algorithm is given as follows.

The equations to be solved in the upper and lower subsystems are second-order ordinary differential equations.

X. Lei, *High Speed Railway Track Dynamics*,
DOI 10.1007/978-981-10-2039-1_7

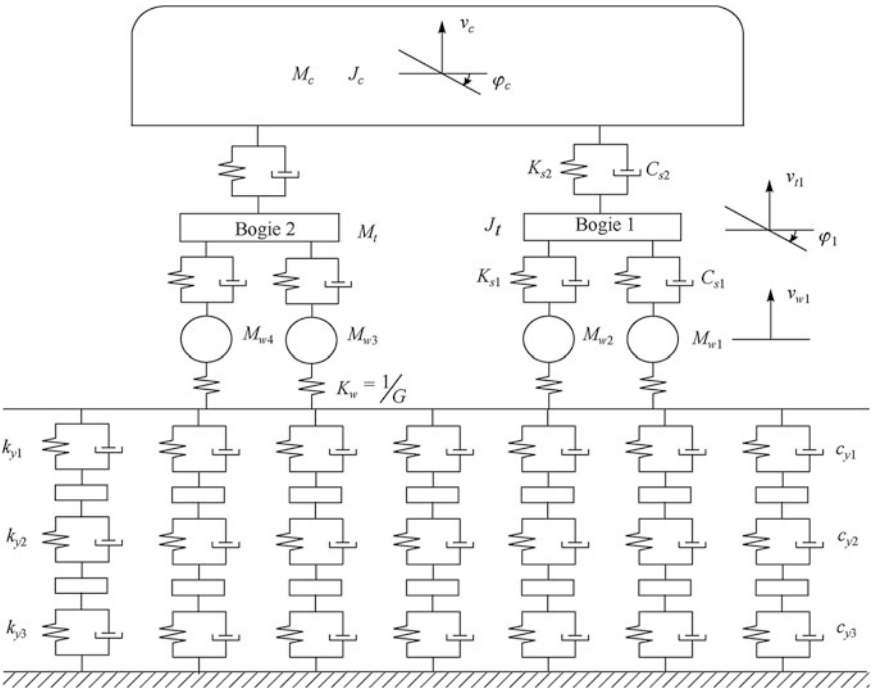

Fig. 7.1 Computation model for the vehicle-track coupling system

As shown in Fig. 7.2, the finite element equation for the vehicle substructure is

$$\boldsymbol{M}_{\mathrm{u}}\ddot{\boldsymbol{a}}_{\mathrm{u}} + \boldsymbol{C}_{\mathrm{u}}\dot{\boldsymbol{a}}_{\mathrm{u}} + \boldsymbol{K}_{\mathrm{u}}\boldsymbol{a}_{\mathrm{u}} = \boldsymbol{Q}_{\mathrm{ug}} + \boldsymbol{F}_{\mathrm{ul}} \tag{7.1}$$

where $\boldsymbol{M}_{\mathrm{u}}$, $\boldsymbol{C}_{\mathrm{u}}$, and $\boldsymbol{K}_{\mathrm{u}}$ denote mass matrix, damping matrix, and stiffness matrix of the vehicle subsystem; $\boldsymbol{a}_{\mathrm{u}}$, $\dot{\boldsymbol{a}}_{\mathrm{u}}$, and $\ddot{\boldsymbol{a}}_{\mathrm{u}}$ stand for displacement vector, velocity vector, and acceleration vector of the vehicle; $\boldsymbol{Q}_{\mathrm{ug}}$ is vehicle gravity vector; and $\boldsymbol{F}_{\mathrm{ul}}$ is wheel-rail contact force vector, which can be calculated by the following Hertz nonlinear formula

$$F_{\mathrm{ul}i} = \begin{cases} \frac{1}{G^{\frac{3}{2}}}\left|v_{\mathrm{w}i} - (v_{\mathrm{lc}i} + \eta_i)\right|^{\frac{3}{2}} & v_{\mathrm{w}i} - (v_{\mathrm{lc}i} + \eta_i) < 0 \\ 0 & v_{\mathrm{w}i} - (v_{\mathrm{lc}i} + \eta_i) \geq 0 \end{cases} \tag{7.2}$$

where G denotes contact deflection coefficient, $v_{\mathrm{w}i}$ is the ith wheel displacement, $v_{\mathrm{lc}i}$ and η_i stand for rail displacement and track irregularity value at the ith wheel-rail contact point.

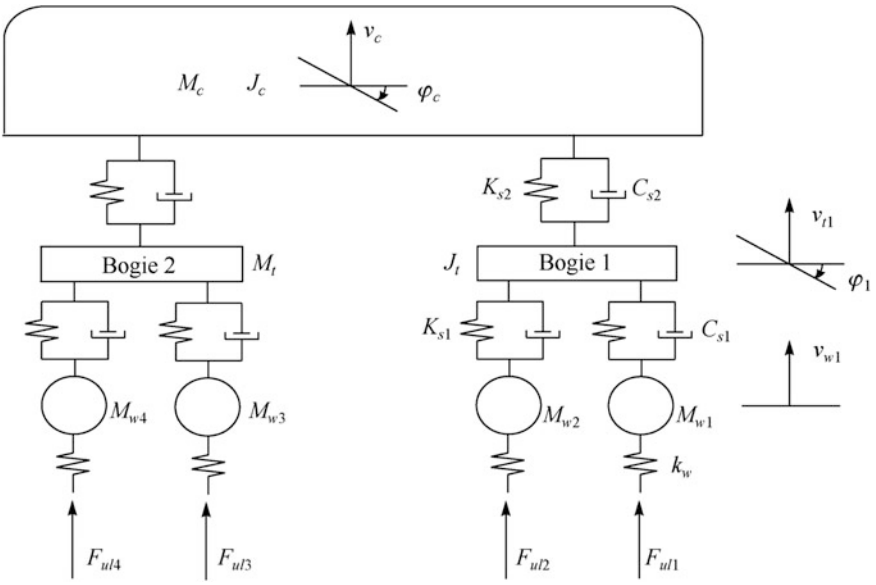

Fig. 7.2 Model of the vehicle as the upper subsystem

Linearizing the Hertz nonlinear stiffness, it has

$$\boldsymbol{F}_{\mathrm{ul}} = \begin{cases} -\boldsymbol{K}_{\mathrm{w}}(\boldsymbol{a}_{\mathrm{u}} - \boldsymbol{a}_{\mathrm{lc}} - \boldsymbol{\eta}) & (\boldsymbol{a}_{\mathrm{u}} - \boldsymbol{a}_{\mathrm{lc}} - \boldsymbol{\eta})_i < 0 \\ 0 & (\boldsymbol{a}_{\mathrm{u}} - \boldsymbol{a}_{\mathrm{lc}} - \boldsymbol{\eta})_i \geq 0 \end{cases} \tag{7.3}$$

where $\boldsymbol{K}_{\mathrm{w}}$ denotes the linearized wheel-rail contact stiffness matrix and $\boldsymbol{\eta}$ is track irregularity vector at wheel-rail contact point.

$$\boldsymbol{Q}_{\mathrm{ug}} = -g\{\, M_{\mathrm{c}} \quad 0 \quad M_{\mathrm{t}} \quad M_{\mathrm{t}} \quad 0 \quad 0 \quad M_{\mathrm{w1}} \quad M_{\mathrm{w2}} \quad M_{\mathrm{w3}} \quad M_{\mathrm{w4}} \,\}^{\mathrm{T}} \tag{7.4}$$

$$\boldsymbol{a}_{\mathrm{u}} = \{\, v_{\mathrm{c}} \quad \varphi_{\mathrm{c}} \quad v_{\mathrm{t1}} \quad v_{\mathrm{t2}} \quad \varphi_1 \quad \varphi_2 \quad v_{\mathrm{w1}} \quad v_{\mathrm{w2}} \quad v_{\mathrm{w3}} \quad v_{\mathrm{w4}} \,\}^{\mathrm{T}} \tag{7.5}$$

$$\boldsymbol{a}_{\mathrm{lc}} = \{\, 0 \quad 0 \quad 0 \quad 0 \quad 0 \quad 0 \quad v_{\mathrm{lc1}} \quad v_{\mathrm{lc2}} \quad v_{\mathrm{lc3}} \quad v_{\mathrm{lc4}} \,\}^{\mathrm{T}} \tag{7.6}$$

$$\boldsymbol{K}_{\mathrm{w}} = \mathrm{diag}\{\, 0 \quad 0 \quad 0 \quad 0 \quad 0 \quad 0 \quad k_{\mathrm{w}} \quad k_{\mathrm{w}} \quad k_{\mathrm{w}} \quad k_{\mathrm{w}} \,\} \tag{7.7}$$

In Eq. (7.7), k_{w} stands for wheel-rail linear contact stiffness.

$$k_{\mathrm{w}} = \frac{3}{2G} p_0^{1/3} \ (\mathrm{N/cm}) \tag{7.8}$$

where p_0 denotes static wheel load.

Substituting Eq. (7.3) into Eq. (7.1), it has

$$\boldsymbol{M}_{\mathrm{u}}\ddot{\boldsymbol{a}}_{\mathrm{u}} + \boldsymbol{C}_{\mathrm{u}}\dot{\boldsymbol{a}}_{\mathrm{u}} + (\boldsymbol{K}_{\mathrm{u}} + \boldsymbol{K}_{\mathrm{w}})\boldsymbol{a}_{\mathrm{u}} = \boldsymbol{Q}_{\mathrm{ug}} + \boldsymbol{K}_{\mathrm{w}}(\boldsymbol{a}_{\mathrm{lc}} + \boldsymbol{\eta}) \tag{7.9}$$

As shown in Fig. 7.3, the finite element equation for the track structure is

$$\boldsymbol{M}_{\mathrm{l}}\ddot{\boldsymbol{a}}_{\mathrm{l}} + \boldsymbol{C}_{\mathrm{l}}\dot{\boldsymbol{a}}_{\mathrm{l}} + \boldsymbol{K}_{\mathrm{l}}\boldsymbol{a}_{\mathrm{l}} = \boldsymbol{Q}_{\mathrm{lg}} - \boldsymbol{F}_{\mathrm{ul}} \tag{7.10}$$

where $\boldsymbol{M}_{\mathrm{l}}$, $\boldsymbol{C}_{\mathrm{l}}$, and $\boldsymbol{K}_{\mathrm{l}}$ denote mass matrix, damping matrix, and stiffness matrix of the track structure; $\boldsymbol{a}_{\mathrm{l}}$, $\dot{\boldsymbol{a}}_{l}$, and $\ddot{\boldsymbol{a}}_{l}$ stand for displacement vector, velocity vector, and acceleration vector of the track structure; and $\boldsymbol{Q}_{\mathrm{lg}}$ is gravity vector of the track structure.

Newmark integration method is used to solve the dynamic responses of the vehicle subsystem and the track subsystem, which is widely used in engineering practice [12]. If solutions ${}^{t-\Delta t}\boldsymbol{a}$, ${}^{t-\Delta t}\dot{\boldsymbol{a}}$, ${}^{t-\Delta t}\ddot{\boldsymbol{a}}$ at time step $(t - \Delta t)$ are known, solution ${}^{t}\boldsymbol{a}$ at time step (t) can be obtained by solving the following equation:

$$(\boldsymbol{K} + c_0\boldsymbol{M} + c_1\boldsymbol{C})^{t}\boldsymbol{a} = {}^{t}\boldsymbol{Q} + \boldsymbol{M}(c_0{}^{t-\Delta t}\boldsymbol{a}_{\mathrm{t}-\Delta \mathrm{t}} + c_2{}^{t-\Delta t}\dot{\boldsymbol{a}} + c_3{}^{t-\Delta t}\ddot{\boldsymbol{a}}) + \boldsymbol{C}(c_1{}^{t-\Delta t}\boldsymbol{a} + c_4{}^{t-\Delta t}\dot{\boldsymbol{a}} + c_5{}^{t-\Delta t}\ddot{\boldsymbol{a}}) \tag{7.11}$$

Velocity ${}^{t}\dot{\boldsymbol{a}}$ and acceleration ${}^{t}\ddot{\boldsymbol{a}}$ at time step (t) can be evaluated with Eqs. (7.12) and (7.13).

$${}^{t}\dot{\boldsymbol{a}} = {}^{t-\Delta t}\dot{\boldsymbol{a}} + c_6{}^{t-\Delta t}\ddot{\boldsymbol{a}} + c_7{}^{t}\ddot{\boldsymbol{a}} \tag{7.12}$$

$${}^{t}\ddot{\boldsymbol{a}} = c_0({}^{t}\boldsymbol{a} - {}^{t-\Delta t}\boldsymbol{a}) - c_2{}^{t-\Delta t}\dot{\boldsymbol{a}} - c_3{}^{t-\Delta t}\ddot{\boldsymbol{a}} \tag{7.13}$$

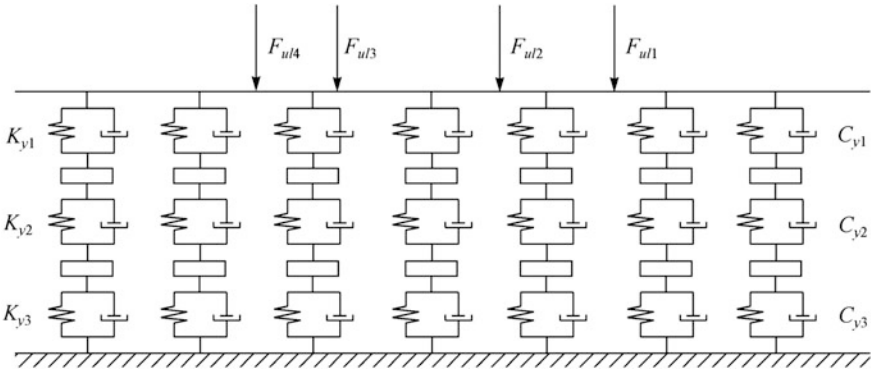

Fig. 7.3 Model of track structure as the lower subsystem

where $c_0 = \frac{1}{\alpha\Delta t^2}$, $c_1 = \frac{\delta}{\alpha\Delta t}$, $c_2 = \frac{1}{\alpha\Delta t}$, $c_3 = \frac{1}{2\alpha} - 1$, $c_4 = \frac{\delta}{\alpha} - 1$, $c_5 = \left(\frac{\delta}{2\alpha} - 1\right)\Delta t$, $c_6 = (1-\delta)\Delta t$, $c_7 = \delta\Delta t$, Δt is time step, and α, δ are Newmark parameters. When $\alpha = 0.25, \delta = 0.5$, solution of Newmark integration method is unconditionally stable [12].

The fundamental computation steps are summarized as follows:

I. **Initial Computation**

(1) In the first time step and first iteration, assume the initial displacement $\boldsymbol{a}_1^0$ of the track structure (usually taking $\boldsymbol{a}_1^0 = \mathbf{0}$). Based on the value of $\boldsymbol{a}_1^0$, the initial displacement of the rail $v_{\mathrm{lc}i}^0$ (i = 1, 2, 3, 4) can be derived at the i th wheel-rail contact point. Next, substituting $v_{\mathrm{lc}i}^0$ (i = 1, 2, 3, 4) into Eq. (7.6), the initial displacement vector $\boldsymbol{a}_{\mathrm{lc}}^0$ can be obtained.

(2) Substituting $\boldsymbol{a}_{\mathrm{lc}}^0$ into Eq. (7.9), the displacement $\boldsymbol{a}_u^0$, velocity $\dot{\boldsymbol{a}}_{\mathrm{u}}^0$, and acceleration $\ddot{\boldsymbol{a}}_u^0$ of the vehicle can be evaluated by solving the dynamic Eq. (7.9) of the vehicle.

II. **Step-by-step procedure in time domain**

Assume that in time step (t), the $(k-1)$th iteration has been performed, and vectors of the displacement, velocity, and acceleration at time step (t) for the vehicle and the track structure are known. Now let us consider the (k) th iteration.

(1) By substituting ${}^t\boldsymbol{a}_{\mathrm{u}}^{k-1}$ and ${}^t\boldsymbol{a}_{\mathrm{lc}}^{k-1}$ into Eq. (7.2), calculate the interaction force ${}^tF_{\mathrm{ul}i}^k (i = 1, 2, 3, 4)$ by the following formula:

$${}^tF_{\mathrm{ul}i}^k = \begin{cases} \frac{1}{G^{3/2}} \left| {}^tv_{\mathrm{w}i}^{k-1} - \left({}^tv_{\mathrm{lc}i}^{k-1} + {}^t\eta_i^{k-1}\right)\right|^{3/2} & {}^tv_{\mathrm{w}i}^{k-1} - \left({}^tv_{\mathrm{lc}i}^{k-1} + {}^t\eta_i^{k-1}\right) < 0 \\ 0 & {}^tv_{\mathrm{w}i}^{k-1} - \left({}^tv_{\mathrm{lc}i}^{k-1} + {}^t\eta_i^{k-1}\right) \geq 0 \end{cases}$$

(2) The relaxation method is introduced to modify the wheel-rail contact force ${}^tF_{\mathrm{ul}i}^k (i = 1, 2, 3, 4)$, that is

$${}^tF_{\mathrm{ul}i}^k = {}^tF_{\mathrm{ul}i}^{k-1} + \mu\left({}^tF_{\mathrm{ul}i}^k - {}^tF_{\mathrm{ul}i}^{k-1}\right) \tag{7.14}$$

where μ is relaxation coefficient which has to be in a certain range $(0 < \mu < 1)$ to ensure the convergence. It is demonstrated that $0.2 < \mu < 0.5$ is the optimal relaxation coefficient.

(3) Assembling ${}^tF_{\mathrm{ul}i}^k$ into the wheel-rail contact force vector ${}^t\boldsymbol{F}_{\mathrm{ul}}^k$, which is applied to the lower part of the track structure, as shown in Fig. 7.3, the

displacement ${}^{t}\boldsymbol{a}_{\mathrm{l}}^{k}$, velocity ${}^{t}\dot{\boldsymbol{a}}_{\mathrm{l}}^{k}$, and acceleration ${}^{t}\ddot{\boldsymbol{a}}_{\mathrm{l}}^{k}$ for the track structure can be evaluated by solving the differential Eq. (7.10) of the track structure.

(4) Based on ${}^{t}\boldsymbol{a}_{\mathrm{l}}^{k}$, the displacement ${}^{t}v_{\mathrm{lc}i}^{k}$ (i = 1, 2, 3, 4) of the rail can be obtained at the i th wheel-rail contact point, and the updated wheel-rail contact force ${}^{t}F_{\mathrm{ul}i}^{k}$ acting on the vehicle can be calculated with formula (7.2).

(5) Assembling the updated ${}^{t}F_{\mathrm{ul}i}^{k}$ into the wheel-rail contact force vector ${}^{t}\boldsymbol{F}_{\mathrm{ul}}^{k}$, which is applied to the upper structure as external forces, the displacement ${}^{t}\boldsymbol{a}_{\mathrm{u}}^{k}$, velocity ${}^{t}\dot{\boldsymbol{a}}_{\mathrm{u}}^{k}$, and acceleration ${}^{t}\ddot{\boldsymbol{a}}_{\mathrm{u}}^{k}$ for the vehicle can be evaluated by solving the differential Eq. (7.1) of the vehicle.

(6) Calculate track displacement difference and its norm as follows:

$$\{\Delta^{t}\boldsymbol{a}\}_{\mathrm{l}}^{k} = {}^{t}\boldsymbol{a}_{\mathrm{l}}^{k} - {}^{t}\boldsymbol{a}_{\mathrm{l}}^{k-1} \tag{7.15}$$

where ${}^{t}\boldsymbol{a}_{\mathrm{l}}^{k}$ and ${}^{t}\boldsymbol{a}_{\mathrm{l}}^{k-1}$ are displacement vectors of the track structure at current iteration and previous iteration, respectively.

Now, define the convergence criterion as follows:

$$\frac{\mathrm{Norm}\{\Delta^{t}\boldsymbol{a}\}_{\mathrm{l}}^{k}}{\mathrm{Norm}\left({}^{t}\boldsymbol{a}_{\mathrm{l}}^{k}\right)} \leq \varepsilon \tag{7.16}$$

where

$$\mathrm{Norm}\{\Delta^{t}\boldsymbol{a}\}_{\mathrm{l}}^{k} = \sum_{i=1}^{n}\{\Delta^{t}\boldsymbol{a}^{2}(i)\}_{\mathrm{l}}^{k}, \mathrm{Norm}\left({}^{t}\boldsymbol{a}_{\mathrm{l}}^{k}\right) = \sum_{i=1}^{n}\{{}^{t}\boldsymbol{a}_{\mathrm{l}}^{k2}(i)\}, \tag{7.17}$$

ε is a specified tolerance and assumed between 1.0×10^{-5} and 1.0×10^{-8}, usually sufficient to obtain the solution with reasonable accuracy.

(7) Checking the convergence criterion.

If the convergence criterion (7.16) is not satisfied, go to Stage II and enter the next iteration step $(k+1)$. If it is satisfied, proceed to the next instant $(t+\Delta t)$ and define

$$\begin{aligned} {}^{t+\Delta t}\boldsymbol{a}_{\mathrm{u}}^{0} &= {}^{t}\boldsymbol{a}_{\mathrm{u}}^{k}, \quad {}^{t+\Delta t}\dot{\boldsymbol{a}}_{\mathrm{u}}^{0} = {}^{t}\dot{\boldsymbol{a}}_{\mathrm{u}}^{k} \quad {}^{t+\Delta t}\ddot{\boldsymbol{a}}_{\mathrm{u}}^{0} = {}^{t}\ddot{\boldsymbol{a}}_{\mathrm{u}}^{k} \\ {}^{t+\Delta t}\boldsymbol{a}_{\mathrm{l}}^{0} &= {}^{t}\boldsymbol{a}_{\mathrm{l}}^{k}, \quad {}^{t+\Delta t}\dot{\boldsymbol{a}}_{\mathrm{l}}^{0} = {}^{t}\dot{\boldsymbol{a}}_{\mathrm{l}}^{k}, \quad {}^{t+\Delta t}\ddot{\boldsymbol{a}}_{\mathrm{l}}^{0} = {}^{t}\ddot{\boldsymbol{a}}_{\mathrm{l}}^{k} \end{aligned}$$

Hence, return to Stage II, enter the next time step, and continue the calculation until the last time step.

7.2 Example Validation

7.2.1 Verification

In order to verify the correctness of the cross-iteration algorithm for the model and the method proposed in this paper to calculate the example in the literature [9], analysis of dynamic response for vehicle and track is carried out, where Chinese high-speed train CRH3 with the speed of 200 km/h and the slab track of 60 kg/m continuously welded long rails are considered. As excitation source of the track profile irregularity, periodic sine function with amplitude 3 mm and wave length 12.5 m is adopted in the computation. Results derived from the two different computational methods will be compared.

Computation results obtained by the cross-iteration algorithm are shown in Figs. 7.4, 7.5, 7.6, 7.7, 7.8 and 7.9. Compared with those calculated by finite element method, well agreement between the two calculations was observed, which confirms the validity and practicability of the algorithm [14].

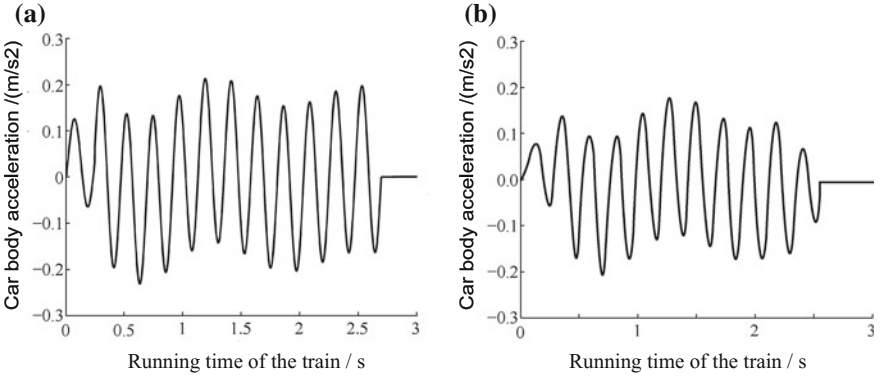

Fig. 7.4 Time history of the vertical car body acceleration. **a** The results in this paper and **b** the results with FEM

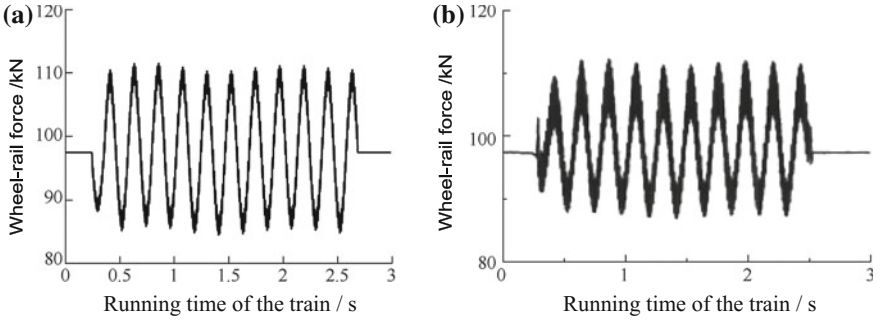

Fig. 7.5 Time history of the wheel-rail contact force. **a** The results in this paper and **b** The results with FEM

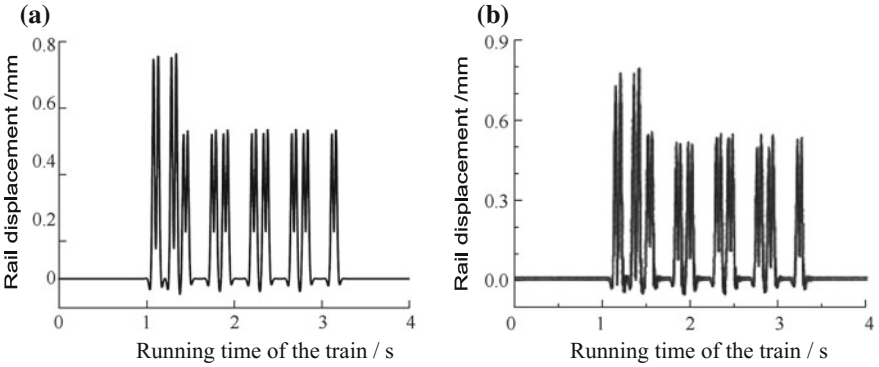

Fig. 7.6 Time history of the vertical rail displacement. **a** The results in this paper and **b** The results with FEM

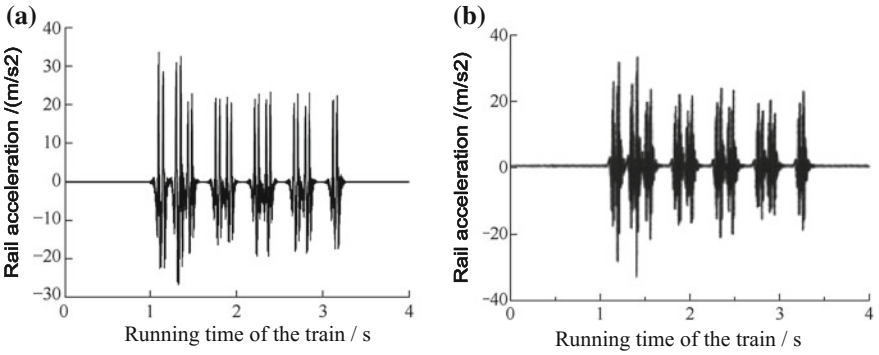

Fig. 7.7 Time history of the vertical rail acceleration. **a** The results in this paper and **b** The results with FEM

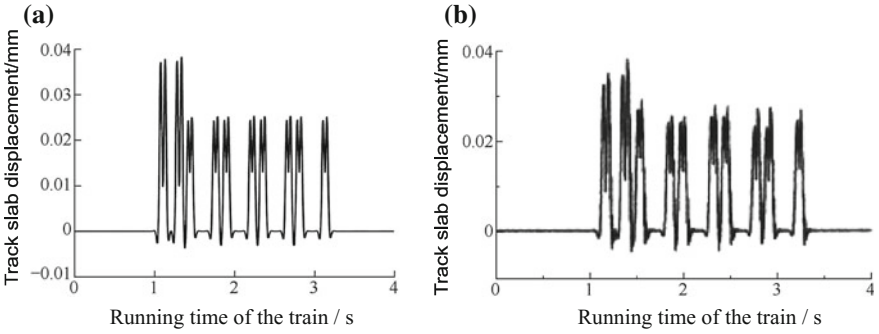

Fig. 7.8 Time history of the vertical track slab displacement. **a** The results in this paper and **b** The results with FEM

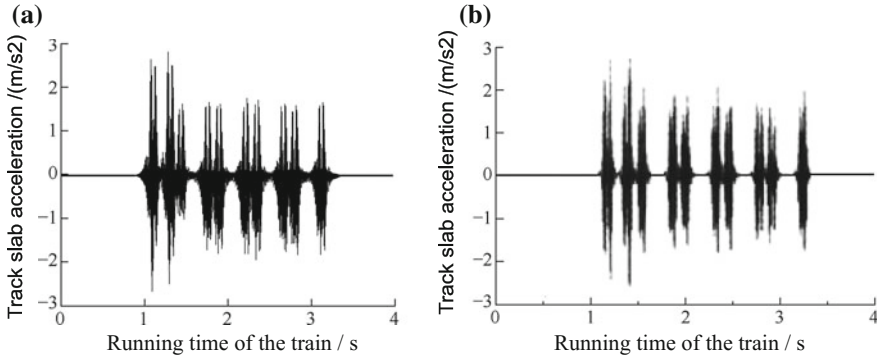

Fig. 7.9 Time history of the vertical track slab acceleration. **a** The results in this paper and **b** The results with FEM

Figures 7.10 and 7.11 show the iteration convergence process of the wheel-rail contact force and the rail displacement of the wheel-rail contact point at the time t [13]. It ban be observed that starting from the previous equilibrium state at the time $(t - \Delta t)$ the solution approaches convergence after several iterations.

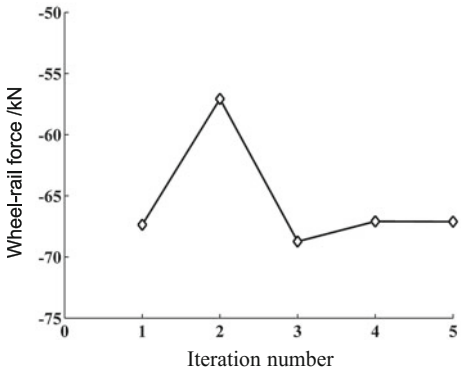

Fig. 7.10 Iteration process for wheel-rail contact force at time t

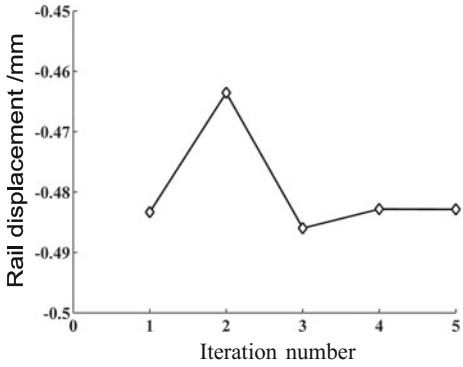

Fig. 7.11 Iteration process for rail displacement at wheel-rail contact point at time t

7.2.2 The Influence of Time Step

Take time step Δt as 0.05, 0.1, 0.5, and 1 ms to examine the influence of the time step on solving process of the vehicle-track coupling system equations, among which, the vehicle is Chinese high-speed train CRH3 with the train speed 250 km/h, the track structure is CRTS II slab track, and the convergence precision is 1.0×10^{-7}. Parameters of the high-speed train CRH3 and the CRTS II slab track are given in Tables 6.7 and 6.10 of Chap. 6.

Table 7.1 shows the number of iterations for solving the system equations with different time step. It is appointed in the paper that in every time step, solving the track system equation and the vehicle system equation, respectively, for once is considered as a cross-iteration for the coupling system for a time. The data given in the table are the maximum iteration number in the process of solving the coupling system equations.

It is shown in Table 7.1 that the shorter the time step, the closer the balance between the state of the system of the next moment and that of the previous moment, which indicates that it is easy to achieve a balance. As a result, the iteration number is a few, and the convergence speed is fast. Meanwhile, the influence of the relaxation coefficient on solving the system equations decreases gradually, but the computation efficiency is lower. In such a condition, by means of choosing a suitable relaxation coefficient, increasing the time step appropriately can improve the solution efficiency effectively. For instance, taking the computation time as 1 s and reducing the time step Δt from 0.5 to 0.1 ms, let us compare the solution efficiency. When $\Delta t = 0.5$ ms, the total iteration number for solving the system equations is $1/0.0005 \times (2 \times 78\ \% + 3 \times 22\ \%) = 4440$, among which, 2 and 3 stand for the iteration number in this case, 78 and 22 % for associated proportion. Likewise, when $\Delta t = 0.1$ ms, the total iteration number for solving the system equations is $1/0.0001 \times 2 \times 100\ \% = 20000$, the latter being 7.5 times of the former, and the solution efficiency is greatly reduced. Therefore, adoption of relaxation coefficient makes it possible to select a larger time step and can improve the computation efficiency.

However, if taking larger time step, solution of the system may seriously deviate from the balance of the previous moment to lose computation stability, which in turn results in the divergence of numerical solution to the system. Consequently, with regard to complex dynamics problems of the train-track coupling system, Newmark numerical integration is no longer unconditionally stable, and numerical instability may happen in some case.

Table 7.1 Number of iterations to solve for the system equations with different time step

Time step Δt/ms	Relaxation coefficient μ						
	0.1	0.2	0.3	0.4	0.5	0.6	0.7
0.05	2	2	2	2	2	2	2
0.1	2	2	2	2	2	2	2
0.5	7	4	3	2	2	2	3
1.0	7	4	3	3	4	6	10

7.2.3 The Influence of Convergence Precision

Taking convergence precision as 1.0×10^{-7}, 1.0×10^{-8}, 1.0×10^{-9} and 1.0×10^{-10}, and considering the ballast and the slab track, the influences of the convergence precision on dynamic responses of the two kinds of the track structure will be investigated in the following. The vehicle is Chinese high-speed train CRH3 with the train speed 250 km/h, and the track is CRTS II slab track for high-speed railways. Parameters of the high-speed train CRH3 and the CRTS II slab track are given in Table 6.7 and Table 6.10 of Chap. 6.

Figure 7.12 shows the influence of convergence precision on the iteration number of the system [13]. It is shown in the figure the iteration number for the slab track is more than that of the ballast track, and the reason for this is that the displacement degrees of freedom (DOFs) of the slab track element model are greater than those of the ballast track element model and the matrix order of the former is higher than that of the latter. However, when the relaxation coefficient is in range from 0.2 to 0.4, the iteration number of the two track systems differs slightly and the iteration number is reduced. Meanwhile, the higher the convergence precision is, the larger the iteration number is. While the relaxation coefficient is about 0.3, the iteration number does not increase with the higher convergence precision.

In addition, the convergence precision greatly influences dynamic response of the system. Figures 7.13 and 7.14 show the time history of the wheel-rail contact force with the relaxation coefficient as 0.1 and the convergence precision being 1.0×10^{-7} and 1.0×10^{-10}, respectively. The theoretical value of the wheel-rail contact force is 70 kN, and the maximum relative error calculated by computer program is 2–3 %. Therefore, in dynamic analysis of general structure, selecting convergence precision between 1.0×10^{-7} and 1.0×10^{-10} can satisfy the computing requirement, while in fine analysis, higher convergence precision should be adopted. It should be pointed out that when taking relaxation coefficient as 0.3, system dynamic response to different convergence precision differs insignificantly, which shows the relaxation coefficient has the effect of improving the iteration stability.

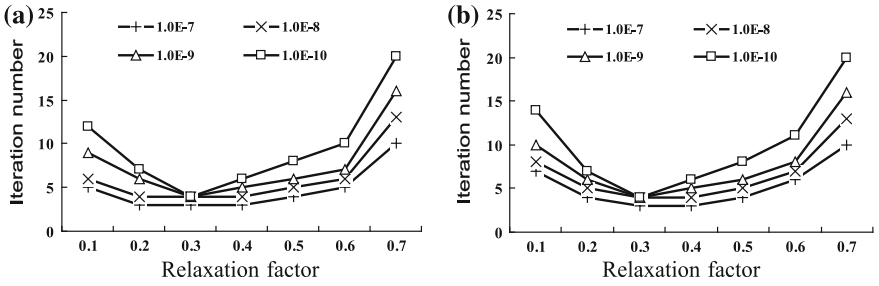

Fig. 7.12 The influence of convergence precision on the iteration number of the system. **a** Number of iteration of ballast track and **b** Number of iteration of slab track

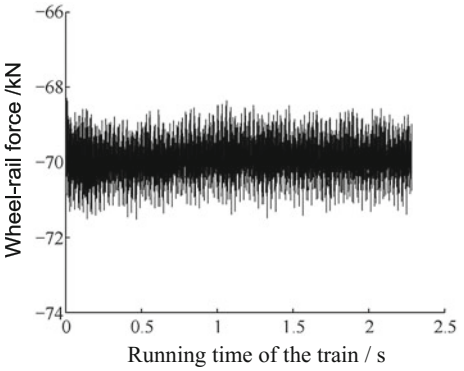

Fig. 7.13 Time history of wheel-rail contact force for convergence precision 1.0×10^{-7}

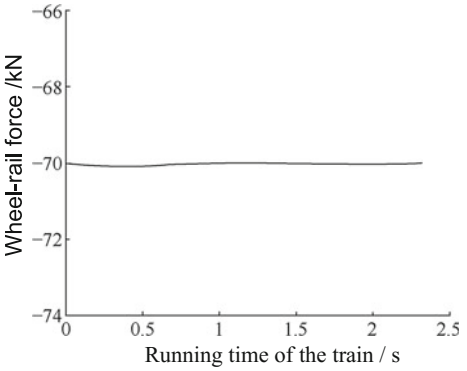

Fig. 7.14 Time history of wheel-rail contact force for convergence precision 1.0×10^{-10}

7.3 Dynamic Analysis of the Train-Track Nonlinear Coupling System

As an application example, the dynamic response analysis for the vehicle and track nonlinear coupling system induced by train running on the ballast track is carried out. The train considered here is Chinese high-speed train CRH3. Parameters for the high-speed train CRH3 and for the ballast track structure are given in Table 6.7 of Chap. 6 and Table 7.2 [11]. In order to reduce the boundary effect of the track structure, the total track length for computation is 300 m. Random irregularity of the track with line level 6 PSD of the United State is regarded as the external excitation. Influences of the linear and nonlinear wheel-rail contact models and different train speeds (V = 200, 250, 300 and 350 km/h) on the dynamic responses of the vehicle and the track are taken into account. The time step of numerical integration adopts 0.001 and 0.0005 s in linear and nonlinear contact models, respectively.

The results computed by varying train speeds and considering linear and nonlinear wheel-rail contact models upon the dynamic response of the train and the

Table 7.2 Parameters for ballast track structure

Parameter	Value	Parameter	Value
Mass of rail m_r/(kg)	60.64	Mass of ballast m_b/kg	560
Density of rail ρ_r/(kg m$^{-3)}$	7800	Stiffness of rail pad and fastener k_{y1}/(M N m^{-1})	78
Inertia moment of rail I_r/(cm^4)	3217	Damping of rail pad and fastener c_{y1}/(k N s m^{-1})	50
Elasticity modulus of rail E_r/(Mpa)	2.06×10^5	Stiffness of ballast bed k_{y2}/(M N m^{-1})	180
Sectional area of rail A_r/(cm^2)	77.45	Damping of ballast bed c_{y2}/(k N s m^{-1})	60
Sleeper interval l/(m)	0.568	Stiffness of subgrade k_{y3}/(M N m^{-1})	65
Mass of sleeper m_t/(kg)	250	Damping of subgrade c_{y3}/(k N s m^{-1})	90

track have been given in Tables 7.3, 7.4, 7.5, 7.6, 7.7, 7.8, 7.9, 7.10, 7.11 and 7.12, where the outputs are the maximum and the total amplitude of displacements and accelerations for the rail, the sleeper, the ballast, the wheel, the bogie and the car body, and the maximum and the total amplitude of the wheel-rail contact forces [14]. Figures 7.15 and 7.16 are the time history of the wheel-rail contact force for different train speeds [14].

It is indicated that the train speed has a great influence on the displacement of the track structure, shown in Tables 7.3, 7.4 and 7.5. With the increase of the train speed from 80 to 200 km/h, the total amplitudes of displacement for the rail, the sleeper, and the ballast in case of the wheel-rail linear contact model increase from 0.885, 0.559 and 0.413 mm to 1.35, 0.945, and 0.717 mm, respectively. The increases of

Table 7.3 The maximum and the total amplitude of the rail displacement

Speed/(km/h)	Wheel-rail linear contact			Wheel-rail nonlinear contact		
	Max/(mm)	Min/(mm)	Total amplitude/(mm)	Max/(mm)	Min/(mm)	Total amplitude/(mm)
200	0.054	−1.300	1.350	0.050	−1.100	1.150
160	0.050	−1.200	1.250	0.050	−0.879	0.929
120	0.048	−0.990	1.040	0.040	−0.847	0.887
80	0.051	−0.834	0.885	0.043	−0.901	0.944

Table 7.4 The maximum and the total amplitude of the sleeper displacement

Speed/(km/h)	Wheel-rail linear contact			Wheel-rail nonlinear contact		
	Max/(mm)	Min/(mm)	Total amplitude/(mm)	Max/(mm)	Min/(mm)	Total amplitude/(mm)
200	0.043	−0.902	0.945	0.040	−0.698	0.738
160	0.036	−0.769	0.805	0.038	−0.543	0.580
120	0.033	−0.630	0.663	0.027	−0.545	0.572
80	0.032	−0.526	0.559	0.028	−0.567	0.595

Table 7.5 The maximum and the total amplitude of the ballast displacement

Speed/(km/h)	Wheel-rail linear contact			Wheel-rail nonlinear contact		
	Max/(mm)	Min/(mm)	Total amplitude/(mm)	Max/(mm)	Min/(mm)	Total amplitude/(mm)
200	0.035	−0.682	0.717	0.034	−0.533	0.566
160	0.028	−0.574	0.602	0.031	−0.410	0.441
120	0.025	−0.468	0.493	0.021	−0.409	0.430
80	0.024	−0.389	0.413	0.021	−0.421	0.442

Table 7.6 The maximum and the total amplitude of the rail acceleration

Speed/(km/h)	Wheel-rail linear contact			Wheel-rail nonlinear contact		
	Max/(m/s^2)	Min/(m/s^2)	Total amplitude/(m/s^2)	Max/(m/s^2)	Min/(m/s^2)	Total amplitude/(m/s^2)
200	71.1	−112.8	183.9	101.9	−55.0	156.9
160	44.2	−86.5	130.7	81.2	−29.4	110.6
120	18.8	−57.6	76.4	56.2	−15.4	71.6
80	9.3	−27.7	37.1	24.7	−6.2	30.9

Table 7.7 The maximum and the total amplitude of the sleeper acceleration

Speed/(km/h)	Wheel-rail linear contact			Wheel-rail nonlinear contact		
	Max/(m/s^2)	Min/(m/s^2)	Total amplitude/(m/s^2)	Max/(m/s^2)	Min/(m/s^2)	Total amplitude/(m/s^2)
200	46.7	−31.5	78.2	25.7	−37.4	63.1
160	26.4	−25.1	51.5	23.8	−20.8	44.6
120	12.6	−21.6	34.2	19.7	−10.8	30.5
80	6.0	−7.7	13.8	7.4	−5.0	12.4

Table 7.8 The maximum and the total amplitude of the ballast acceleration

Speed/(km/h)	Wheel-rail linear contact			Wheel-rail nonlinear contact		
	Max/(m/s^2)	Min/(m/s^2)	Total amplitude/(m/s^2)	Max/(m/s^2)	Min/(m/s^2)	Total amplitude/(m/s^2)
200	37.2	−26.4	63.6	26.0	−31.7	57.7
160	20.9	−25.4	46.4	25.3	−16.6	41.9
120	9.6	−18.1	27.7	18.1	−8.8	26.9
80	4.9	−6.5	11.3	6.9	−4.4	11.3

Table 7.9 The maximum and the total amplitude of the wheel acceleration

Speed (km/h)	Wheel-rail linear contact			Wheel-rail nonlinear contact		
	Max/(m/s^2)	Min/(m/s^2)	Total amplitude/(m/s^2)	Max/(m/s^2)	Min/(m/s^2)	Total amplitude/(m/s^2)
200	37.0	−36.3	73.3	37.5	−35.6	73.0
160	29.1	−21.4	50.5	25.2	−28.2	53.3
120	21.2	−21.7	42.9	20.3	−20.5	40.8
80	24.6	−22.9	47.5	21.4	−22.7	44.1

Table 7.10 The maximum and the total amplitude of the bogie acceleration

Speed/ (km/h)	Wheel-rail linear contact			Wheel-rail nonlinear contact		
	Max/ (m/s^2)	Min/ (m/s^2)	Total amplitude/ (m/s^2)	Max/ (m/s^2)	Min/ (m/s^2)	Total amplitude/ (m/s^2)
200	6.98	−4.67	11.70	4.79	−6.77	11.60
160	5.22	−3.90	9.11	3.71	−4.95	8.66
120	5.29	−3.67	8.96	3.43	−4.81	8.24
80	4.11	−4.16	8.27	3.95	−3.75	7.70

Table 7.11 The maximum and the total amplitude of the car body acceleration

Speed/ (km/h)	Wheel-rail linear contact			Wheel-rail nonlinear contact		
	Max/ (m/s^2)	Min/ (m/s^2)	Total amplitude/ (m/s^2)	Max/ (m/s^2)	Min/ (m/s^2)	Total amplitude/ (m/s^2)
200	0.361	−0.423	0.784	0.354	−0.319	0.674
160	0.270	−0.311	0.581	0.317	−0.278	0.594
120	0.233	−0.286	0.518	0.285	−0.231	0.517
80	0.196	−0.255	0.451	0.253	−0.193	0.446

Table 7.12 The maximum and the total amplitude of the wheel-rail contact force

Speed/ (km/h)	Wheel-rail linear contact			Wheel-rail nonlinear contact		
	Max/(kN)	Min/(kN)	Total amplitude/(kN)	Max/(kN)	Min/(kN)	Total amplitude/(kN)
200	112.0	27.7	84.2	113.0	26.4	86.6
160	106.0	41.7	64.0	98.7	33.1	65.6
120	97.3	45.4	51.9	93.4	42.1	51.3
80	98.1	40.7	57.4	95.0	40.9	54.1

the amplitude ratio are 52.5, 69.1 and 73.6 %. The total amplitudes of displacement for the rail, the sleeper, and the ballast in case of the wheel-rail nonlinear contact model increase with the increase of the train speeds, but the increases are smaller at the speed of 120 km/h than those at the speed of 80 km/h, a little at the speed of 160 km/h than those at the speed of 120 km/h, and significant at the speed of 200 km/h.

The maximum and the total amplitudes of displacement for the rail, the sleeper, and the ballast in the linear contact model are larger than those in nonlinear contact model, and the increasing range is from 10 to 20 %. However, results for the speed of 80 km/h are opposite.

The maximum and the total amplitudes of acceleration for the rail, the sleeper, and the ballast increase with the increase of the train speed, as shown in Tables 7.6, 7.7 and 7.8.

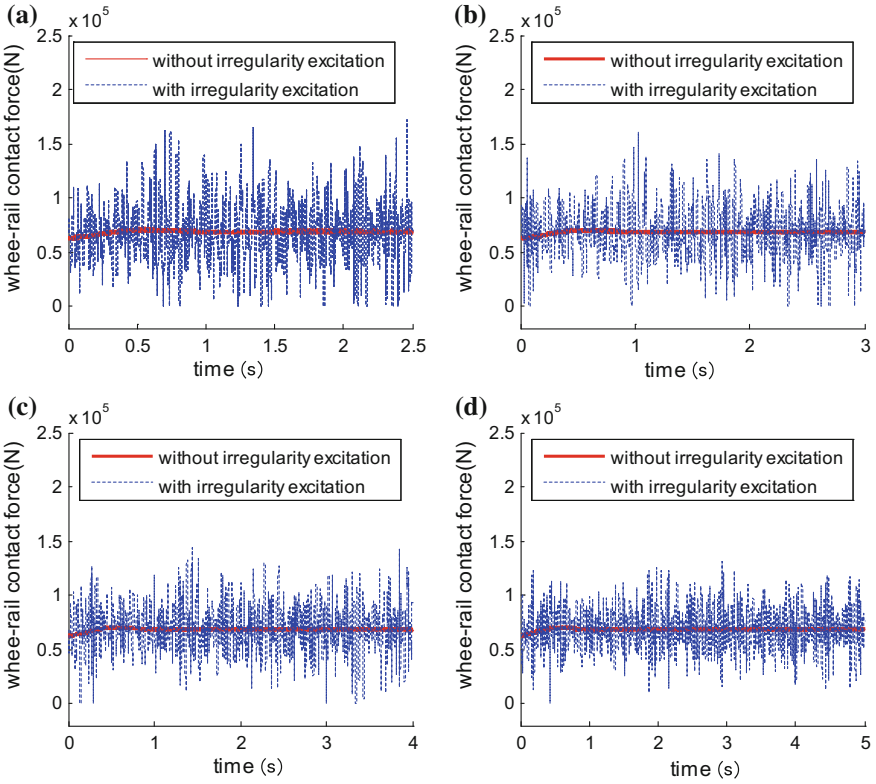

Fig. 7.15 Time history of the wheel-rail contact force with different train speeds in wheel-rail linear contact model. **a** At the speed of 350 km/h, **b** at the speed of 300 km/h, **c** at the speed of 250 km/h, and **d** at the speed of 200 km/h

With the increase of the train speed from 80 to 200 km/h, the total amplitudes of acceleration for the rail, the sleeper, and the ballast in case of the wheel-rail linear contact model increase from 37.1, 13.8, and 11.3 m/s^2 to 183.9, 78.2, and 63.6 m/s^2, respectively. The increases of the amplitude ratio are 395.7, 466.7, and 462.8 %. When the system is in wheel-rail nonlinear contact model, the increases of the amplitude ratio for the rail, the sleeper, and the ballast accelerations are 407.8, 408.9, and 410.6 %, respectively.

The maximum and the total amplitudes of acceleration for the rail, the sleeper, and the ballast in the linear contact model are larger than those in nonlinear contact model, and the difference is about 10–20 %. If the speed is larger, the difference will be more obvious.

As is indicated in Table 7.9, 7.10 and 7.11, with the increase of the train speed from 80 to 200 km/h, the total amplitudes of acceleration for the bogie and the car body in case of the wheel-rail linear contact model increase from 8.27 and 0.451 m/s^2 to 11.70 and 0.784 m/s^2, respectively. The increases of the amplitude

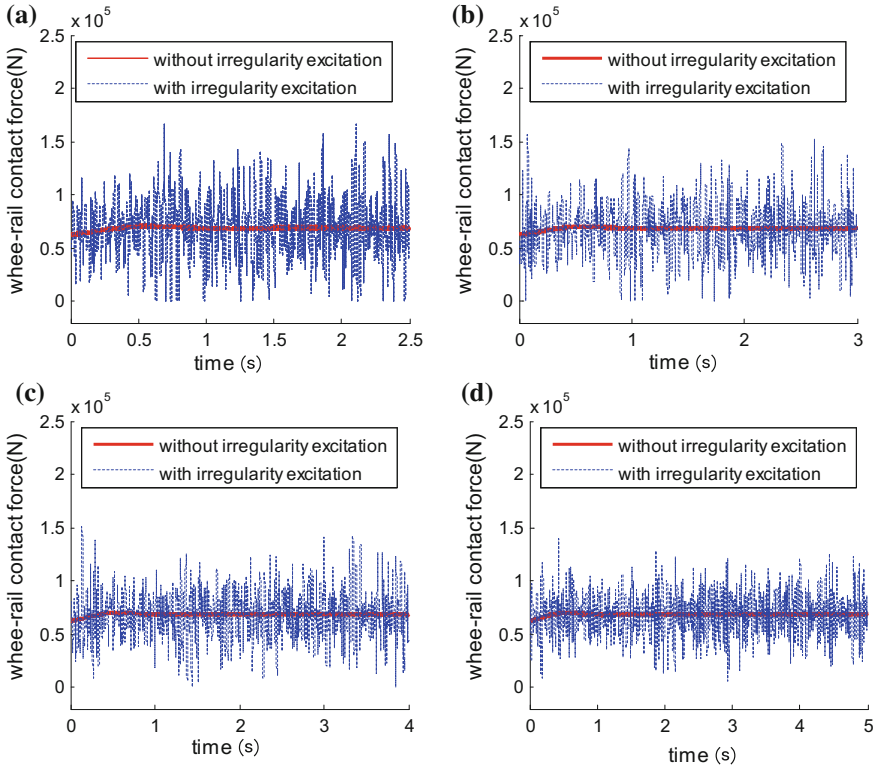

Fig. 7.16 Time history of the wheel-rail contact force with different train speeds in wheel-rail nonlinear contact model. **a** At the speed of 350 km/h, **b** at the speed of 300 km/h, **c** at the speed of 250 km/h, and **d** at the speed of 200 km/h

ratio are 41.5 and 73.8 %. In case of the wheel-rail nonlinear contact model, the increases of the amplitude ratio for the bogie and the car body accelerations are 50.6 and 51.1 %. The maximum wheel acceleration basically goes up with the increase of the train speed, but the total amplitude of the wheel acceleration at the speed of 80 km/h is larger than that at the speed of 120 km/h. The cause may be the track irregularity of individual point being too much.

The total amplitudes of acceleration for the bogie and the wheel in linear contact model are slightly larger than those in nonlinear contact model, and the differences are within 5 %. At the train speed of 200 km/h, the total amplitude of the car body acceleration in linear contact model is slightly larger than that in nonlinear contact model. However, at the other train speeds, the total amplitudes of the car body acceleration are nearly equal whether the wheel-rail contact is in linear or nonlinear contact model. What is more, the maximum and the total amplitudes of the car body acceleration are within the range of 1 m/s^2, which illustrate that the primary and

secondary suspension systems of the vehicle have an excellent influence on vibration and noise reduction.

As shown in Table 7.12 and Figs. 7.15 and 7.16, the maximum and the total amplitudes of the wheel-rail contact force basically increase with the increase of the train speed. However, the maximum and the total amplitudes of the wheel-rail contact force at the speed of 80 km/h are larger than those at the speed of 120 km/h. When the train speed increases from 120 to 200 km/h, the maximum and the total amplitudes of the wheel-rail contact force increase from 97.3 and 51.9 kN to 112 and 84.2 kN, respectively, in linear contact model. The increases of the amplitude ratio are 15.1 and 62.2 %. However, in nonlinear contact model, the maximum and the total amplitudes of the wheel-rail contact force increase from 93.4 and 51.3 kN to 113 and 86.6 kN, respectively, and the increases of the amplitude ratio are 20.9 and 68.8 %. The maximum wheel-rail contact forces in linear contact model are a little bit larger than those in nonlinear contact model, but the difference of the wheel-rail contact force amplitude in both of the linear and the nonlinear contact models is small.

7.4 Conclusions

A model for dynamic analysis of the vehicle-track nonlinear coupling system is established by finite element method. And, a cross-iteration algorithm is presented to solve the nonlinear dynamic equation of the vehicle-track coupling system. In simulation analysis, the whole system is divided into two subsystems, i.e., the vehicle subsystem considered as a rolling stock unit with a primary and secondary suspension system, and the track subsystem regarded as a three elastic beam model. Coupling of the two systems is achieved by equilibrium conditions for wheel-rail nonlinear contact forces and geometrical compatibility conditions. The test computation examples show that a relatively small time step has to be selected to ensure convergence, which will greatly increase the computation time. In order to solve this problem and accelerate the iterative convergence rate, a relaxation technique is introduced to modify the wheel-rail contact force. Based on the dynamic analysis of the high-speed train and slab track nonlinear coupling system, the following conclusions are obtained:

(1) The train speed has a significant influence on the dynamic responses of the train and the track structures. Regardless of the wheel-to-rail linear contact model or nonlinear contact model, the accelerations and the displacements of the rail, the sleeper, and the ballast, and the accelerations of the wheel, the bogie, and the car body, as well as the wheel-rail contact forces, increase with the increase of the train speeds, while the displacements of the wheel, the bogie, and the car body vary little with the train speed.
(2) Results of the dynamic responses for the train and the track structure with the wheel-to-rail linear contact model are larger than those with the wheel-to-rail

nonlinear contact model under the same train speed. The differences for the maximum and the total amplitudes of the displacements and the accelerations are in the range of 10 %, and the differences for the wheel-rail contact forces are within 5 %. Meanwhile, the train speed has a great influence on the difference for rail acceleration. The higher the train speed is, the larger the differences of the rail acceleration will be. The total amplitude of the rail acceleration with the wheel-to-rail linear contact model is twice as large as that with the wheel-to-rail nonlinear contact model at higher train speed, whereas the difference of the rail acceleration is within 5 % at lower train speed. Summarily, it is conservative and safer to make the design of the train and the track structure based on the calculated results with the wheel-to-rail linear contact model.

(3) The introduction of the relaxation coefficient to modify the wheel-rail contact force can evidently accelerate the convergence speed of the cross-iterative algorithm. The computation tests show that only 3–6 iteration steps are required to approach the convergence in each iteration.

(4) As the vehicle and track coupling nonlinear system is divided into the vehicle subsystem and the track subsystem, the dynamic equations of the two subsystems can be solved independently. This method can not only reduce the analysis scale of the problem, but also reduce the difficulty of the programming design. At the same time, the coefficient matrices of the finite element equation for the two subsystems are constant and symmetric, and inversing is only required once. In the computation procedure, the same inversed matrices can be substituted in every iteration and every time step. As a result, the computation speed is greatly enhanced. In contrast to the existing method of "set-in-right-position" to dynamic analysis of the vehicle-track coupling system, the coefficient matrices of the finite element equations change with the change of the position of the train on the track. Therefore, inversion calculation is necessary in every time step, which greatly reduces the computational efficiency. A conclusion, by simulating analysis of the dynamic responses for the vehicle and the track structure (which are induced by the train moving on the track with the length of 370 m), is obtained that the computing time in the ordinary computer workstation is of only 40-min duration with the cross-iteration algorithm, compared with the 150 min required by the method of "set-in-right-position." (Details of the computers and programming languages and systems employed are as follows: (1) CPU: Intel(R) core(TM) i5-2400 CPU @ 3.1 GHz 3.1 GHz, (2) RAM: 4.00 GB, and (3) programming languages: MATLAB R2010b.) The computation efficiency of the former method is 4–6 times higher than the latter under normal conditions. If the scale of the analyzed problem is larger, the computation efficiency will be higher.

It should be pointed out that the proposed algorithm has a general applicability, which can be used to analyze all kinds of the linear and the nonlinear problems under moving loads.

References

1. Clough RW, Penzien J (1995) Dynamic of structures (3rd Edition). Computers & Structures, Inc., Berkeley, pp 120–124
2. Rezaiee-Pajand M, Alamatian J (2008) Numerical time integration for dynamic analysis using a new higher order predictor-corrector method. Eng Comput 25(6):541–568
3. Chen C, Ricles JM (2010) Stability analysis of direct integration algorithms applied to MDOF nonlinear structural dynamics. J Eng Mech 136(4):485–495
4. Zhai WM (2007) Vehicle-track coupling dynamics (3rd edition). Science Press, Beijing
5. Zhang N, Xia H (2013) A vehicle-bridge interaction dynamic system analysis method based on inter-system iteration. China Railway Sci 34(5):32–38
6. Wu D, Li Q, Chen A (2007) Numerical stability of iterative scheme in solving coupled vibration of the train-bridge system. Chin Q Mech 28(3):405–411
7. Yang F, Fonder GA (1996) An iterative solution method for dynamic response of bridge-vehicles systems. J Earthq Eng Struct Dyn 25(2):195–215
8. Zhang B, Lei X (2011) Analysis on dynamic behavior of ballastless track based on vehicle and rack elements with finite element method. J China Railway Soc 33(7):78–85
9. Xiang J, Hao D, Zeng Q (2007) Analysis method of vertical vibration of train and ballastless track system with the lateral finite strip and slab segment element. J China Railway Soc 29(4): 64–69
10. Lei X (2002) New methods in railroad track mechanics and technology. China Railway Publishing House, Beijing
11. Lei X, Zhang B, Liu Q (2010) A track model for vertical vibration analysis of track-bridge coupling. J Vibr Shock 29(3):168–173
12. Lei X (2000) Finite element method. China Railway Publishing House, Beijing
13. Zhang B, Lei X, Luo Y (2016) Improved algorithm of iterative process for vehicle-track coupled system based on Newmark formulation. J Central South Univ (Sci Technol) 47(1): 298–306
14. Lei X, Wu S, Zhang B (2016) Dynamic analysis of the high speed train and slab track nonlinear coupling system with the cross iteration algorithm. J Nonlinear Dyn, vol 2016, Article ID 8356160, 17 pages, http://dx.doi.org/10.1155/2016/8356160

Chapter 8
Moving Element Model and Its Algorithm

Chapter 7 has investigated the cross iterative method that solves the dynamic response of the train-track coupling system. Merits of the method include being able to consider the nonlinear behavior of the wheel-rail contact and simple programming, but when it comes to linear problems, the method has no advantages in computational efficiency. Published literature just briefly mentioned using "set-in-the-right-position" rule to formulate the solution equation for the train-track coupling system, but did not present any detailed explanation or relevant formula [1–6]. In this chapter, three models are established from simple to complex: moving element model of a single wheel, moving element model of a single wheel with primary suspension system, and moving element model of a single wheel with primary and secondary suspension system. On the basis of these models, the algorithm for simultaneously solving for dynamic response of the train-track coupling system is discussed and the corresponding explicit formulas are presented.

8.1 Moving Element Model

In the model, the wheel moving on the rail is analyzed, as shown in Fig. 8.1. The wheel is simplified into a particle with a mass of m_w moving at a speed of V, and the rail is simulated as a two-dimensional beam element. Assume the wheel-rail contact is elastic and the contact stiffness is k_c. Such a model is called moving element model [1]. In Fig. 8.1, points 1 and 2 are the two nodes of the rail beam element, whose vertical displacements v_i and rotational angles θ_i $(i = 1, 2)$ are analyzed, respectively; point 3 is moving node, also called target node, whose vertical displacement is v_3; point c is wheel-rail contact point, whose vertical displacement is denoted as v_c.

The model has three nodes, marked as 1, 2, 3 and 5 DOFs (degrees of freedom). The distance between node c and node 1 is x_c, and the element length is l, as shown in Fig. 8.1.

X. Lei, *High Speed Railway Track Dynamics*,
DOI 10.1007/978-981-10-2039-1_8

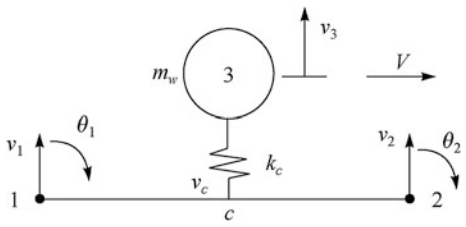

Fig. 8.1 Moving element model

In Chap. 6, plane beam element with two nodes has been discussed. The displacement of any point in the element can be expressed by interpolation function and element nodal displacements as

$$v = N_1 v_1 + N_2 \theta_1 + N_3 v_2 + N_4 \theta_2 \tag{8.1}$$

where N_1–N_4 are the interpolation function of plane beam element with two nodes

$$\begin{aligned} N_1 &= 1 - \frac{3}{l^2}x^2 + \frac{2}{l^3}x^3 \\ N_2 &= -x + \frac{2}{l}x^2 - \frac{1}{l^2}x^3 \\ N_3 &= \frac{3}{l^2}x^2 - \frac{2}{l^3}x^3 \\ N_4 &= \frac{1}{l}x^2 - \frac{1}{l^2}x^3 \end{aligned} \tag{8.2}$$

As for point c, its vertical displacement v_c can be written as

$$v_c = N_1 v_1 + N_2 \theta_1 + N_3 v_2 + N_4 \theta_2 \tag{8.3}$$

where N_1–N_4 are the respective interpolation function after letting $x = x_c$.

Let the nodal displacement vector of the moving element be

$$\boldsymbol{a}^e = \{ v_1 \quad \theta_1 \quad v_2 \quad \theta_2 \quad v_3 \}^{\mathrm{T}} \tag{8.4}$$

Vertical displacement of node 3 is v_3 and can be expressed as

$$v_3 = \boldsymbol{N}_3^{\mathrm{T}} \boldsymbol{a}^e \tag{8.5}$$

$$\dot{v}_3 = \boldsymbol{N}_3^{\mathrm{T}} \dot{\boldsymbol{a}}^e \tag{8.6}$$

where

$$\boldsymbol{N}_3^{\mathrm{T}} = \{ 0 \quad 0 \quad 0 \quad 0 \quad 1 \} \tag{8.7}$$

The vertical displacement of node c is v_c and can be expressed by interpolation function as

$$v_c = \{ N_1 \quad N_2 \quad N_3 \quad N_4 \quad 0 \} \boldsymbol{a}^e \tag{8.8}$$

Then it yields

$$v_3 - v_c = \{ -N_1 \quad -N_2 \quad -N_3 \quad -N_4 \quad 1 \} \boldsymbol{a}^e = \boldsymbol{N}_{3c}^{\mathrm{T}} \boldsymbol{a}^e \tag{8.9}$$

where

$$\boldsymbol{N}_{3c}^{\mathrm{T}} = \{ -N_1 \quad -N_2 \quad -N_3 \quad -N_4 \quad 1 \} \tag{8.10}$$

Applying Lagrange equation, that is

$$\frac{\mathrm{d}}{\mathrm{d}t} \frac{\partial L}{\partial \dot{\boldsymbol{a}}} - \frac{\partial L}{\partial \boldsymbol{a}} + \frac{\partial R}{\partial \dot{\boldsymbol{a}}} = 0 \tag{8.11}$$

where L is Lagrange function

$$L = T - \Pi \tag{8.12}$$

T is kinetic energy, Π is potential energy, and R is dissipated energy.
Kinetic energy of the moving element is

$$T = \frac{1}{2} m_w \dot{v}_3^2 = \frac{1}{2} m_w \left(\boldsymbol{N}_3^{\mathrm{T}} \dot{\boldsymbol{a}}^e \right)^{\mathrm{T}} \left(\boldsymbol{N}_3^{\mathrm{T}} \dot{\boldsymbol{a}}^e \right) = \frac{1}{2} (\dot{\boldsymbol{a}}^e)^{\mathrm{T}} \boldsymbol{m}_u^e \dot{\boldsymbol{a}}^e \tag{8.13}$$

where mass matrix of the moving element is

$$\boldsymbol{m}_u^e = m_w \boldsymbol{N}_3 \boldsymbol{N}_3^{\mathrm{T}} = \begin{bmatrix} 0 & 0 & 0 & 0 & 0 \\ 0 & 0 & 0 & 0 & 0 \\ 0 & 0 & 0 & 0 & 0 \\ 0 & 0 & 0 & 0 & 0 \\ 0 & 0 & 0 & 0 & m_w \end{bmatrix} \tag{8.14}$$

Potential energy of the moving element is

$$\begin{aligned} \Pi &= \frac{1}{2} k_c (v_3 - v_c)^2 + (v_3 m_w g) = \frac{1}{2} k_c \left(\boldsymbol{N}_{3c}^{\mathrm{T}} \boldsymbol{a}^e \right)^{\mathrm{T}} \boldsymbol{N}_{3c}^{\mathrm{T}} \boldsymbol{a}^e + (\boldsymbol{a}^e)^{\mathrm{T}} m_w g \hat{\boldsymbol{N}}_3 \\ &= \frac{1}{2} (\boldsymbol{a}^e)^{\mathrm{T}} \boldsymbol{k}_u^e \boldsymbol{a}^e - (\boldsymbol{a}^e)^{\mathrm{T}} \boldsymbol{Q}_u^e \end{aligned} \tag{8.15}$$

where stiffness matrix of the moving element is

$$\boldsymbol{k}_{\mathrm{u}}^{e}=k_{\mathrm{c}}\boldsymbol{N}_{3\mathrm{c}}\boldsymbol{N}_{3\mathrm{c}}^{\mathrm{T}}=k_{\mathrm{c}}\begin{bmatrix} N_1^2 & N_1N_2 & N_1N_3 & N_1N_4 & -N_1 \\ & N_2^2 & N_2N_3 & N_2N_4 & -N_2 \\ & & N_3^2 & N_3N_4 & -N_3 \\ & \text{symmetry} & & N_4^2 & -N_4 \\ & & & & 1 \end{bmatrix} \tag{8.16}$$

Element nodal load vector is

$$\boldsymbol{Q}_{\mathrm{u}}^{e}=\{0\quad 0\quad 0\quad 0\quad -m_{\mathrm{w}}g\}^{\mathrm{T}} \tag{8.17}$$

Substituting (8.13) and (8.15) into Lagrange equations (8.11) and (8.12), it yields dynamic equation of the moving element as

$$\boldsymbol{m}_{\mathrm{u}}^{e}\ddot{\boldsymbol{a}}+\boldsymbol{k}_{\mathrm{u}}^{e}\boldsymbol{a}=\boldsymbol{Q}_{\mathrm{u}}^{e} \tag{8.18}$$

8.2 Moving Element Model of a Single Wheel with Primary Suspension System

Figure 8.2 shows moving element model of a single wheel with primary suspension system. The model has four nodes, marked as 1, 2, 3, and 4, and 6 DOFs (degrees of freedom). Points 1 and 2 are the two nodes of the rail beam element, whose vertical displacements v_i and rotational angles θ_i $(i=1,2)$ are analyzed, respectively; point 3 is the node of the car body with its vertical displacement marked as v_3 and 1/8 mass of the car body as m_{c}; k_{s}, c_{s} are the equivalent stiffness and damping coefficients of the primary suspension system, respectively; point 4 is the

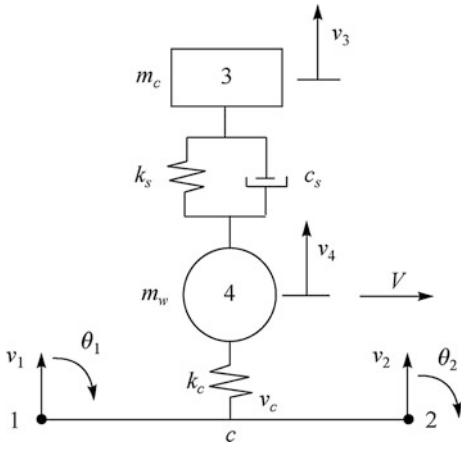

Fig. 8.2 Moving element model of a single wheel with primary suspension system

node of the wheel with its vertical displacement marked as v_4 and mass as m_w, and the wheel is moving at a constant velocity V; point c is the wheel-rail contact point with its vertical displacement denoted as v_c. The distance between node 1 and node c is x_c, the element length is l, and the wheel-rail contact stiffness is k_c.

Define the element nodal displacement vector as

$$\boldsymbol{a}^e = \{ v_1 \quad \theta_1 \quad v_2 \quad \theta_2 \quad v_3 \quad v_4 \}^{\mathrm{T}} \tag{8.19}$$

Vertical displacement of node 3 is v_3 and it has

$$v_3 = \boldsymbol{N}_3^{\mathrm{T}} \boldsymbol{a}^e \tag{8.20}$$

$$\dot{v}_3 = \boldsymbol{N}_3^{\mathrm{T}} \dot{\boldsymbol{a}}^e \tag{8.21}$$

where

$$\boldsymbol{N}_3^{\mathrm{T}} = \{ 0 \quad 0 \quad 0 \quad 0 \quad 1 \quad 0 \} \tag{8.22}$$

Vertical displacement of node 4 is v_4 and in the same way it has

$$v_4 = \boldsymbol{N}_4^{\mathrm{T}} \boldsymbol{a}^e \tag{8.23}$$

$$\dot{v}_4 = \boldsymbol{N}_4^{\mathrm{T}} \dot{\boldsymbol{a}}^e \tag{8.24}$$

where

$$\boldsymbol{N}_4^{\mathrm{T}} = \{ 0 \quad 0 \quad 0 \quad 0 \quad 0 \quad 1 \} \tag{8.25}$$

$$v_3 - v_4 = \boldsymbol{N}_{34}^{\mathrm{T}} \boldsymbol{a}^e \tag{8.26}$$

$$\dot{v}_3 - \dot{v}_4 = \boldsymbol{N}_{34}^{\mathrm{T}} \dot{\boldsymbol{a}}^e \tag{8.27}$$

where $\boldsymbol{N}_{34}^{\mathrm{T}} = \{ 0 \quad 0 \quad 0 \quad 0 \quad 1 \quad -1 \}$

Vertical displacement of node c is v_c and can be expressed by interpolation function as

$$v_c = \boldsymbol{N}_c^{\mathrm{T}} \boldsymbol{a}^e \tag{8.28}$$

where

$$\boldsymbol{N}_c^{\mathrm{T}} = \{ N_1 \quad N_2 \quad N_3 \quad N_4 \quad 0 \quad 0 \} \tag{8.29}$$

And it yields

$$v_4 - v_c = \boldsymbol{N}_{4c}^{\mathrm{T}} \boldsymbol{a}^e \tag{8.30}$$

where

$$\boldsymbol{N}_{4c}^{\mathrm{T}} = \{ -N_1 \quad -N_2 \quad -N_3 \quad -N_4 \quad 0 \quad 1 \} \tag{8.31}$$

Kinetic energy of the element is

$$\begin{aligned} T &= \frac{1}{2} m_c \dot{v}_3^2 + \frac{1}{2} m_w \dot{v}_4^2 = \frac{1}{2} m_c \left(\boldsymbol{N}_3^{\mathrm{T}} \dot{\boldsymbol{a}}^e \right)^{\mathrm{T}} \left(\boldsymbol{N}_3^{\mathrm{T}} \dot{\boldsymbol{a}}^e \right) + \frac{1}{2} m_w \left(\boldsymbol{N}_4^{\mathrm{T}} \dot{\boldsymbol{a}}^e \right)^{\mathrm{T}} \left(\boldsymbol{N}_4^{\mathrm{T}} \dot{\boldsymbol{a}}^e \right) \\ &= \frac{1}{2} (\dot{\boldsymbol{a}}^e)^{\mathrm{T}} \boldsymbol{m}_u^e \dot{\boldsymbol{a}}^e \end{aligned} \tag{8.32}$$

where the element mass matrix is

$$\boldsymbol{m}_u^e = m_c \boldsymbol{N}_3 \boldsymbol{N}_3^{\mathrm{T}} + m_w \boldsymbol{N}_4 \boldsymbol{N}_4^{\mathrm{T}} = \mathrm{diag}(0 \quad 0 \quad 0 \quad 0 \quad m_c \quad m_w) \tag{8.33}$$

Potential energy of the element is

$$\begin{aligned} \Pi &= \frac{1}{2} k_s (v_3 - v_4)^2 + \frac{1}{2} k_c (v_4 - v_c)^2 + (v_3 m_c g) + (v_4 m_w g) \\ &= \frac{1}{2} \boldsymbol{a}^{e\mathrm{T}} \left\{ k_s \boldsymbol{N}_{34} \boldsymbol{N}_{34}^{\mathrm{T}} + k_c \boldsymbol{N}_{4c} \boldsymbol{N}_{4c}^{\mathrm{T}} \right\} \boldsymbol{a}^e + (\boldsymbol{a}^e)^{\mathrm{T}} \{ m_c g \boldsymbol{N}_3 + m_w g \boldsymbol{N}_4 \} \\ &= \frac{1}{2} (\boldsymbol{a}^e)^{\mathrm{T}} \boldsymbol{k}_u^e \boldsymbol{a}^e - (\boldsymbol{a}^e)^{\mathrm{T}} \boldsymbol{Q}_u^e \end{aligned} \tag{8.34}$$

where the element stiffness matrix is

$$\begin{aligned} \boldsymbol{k}_u^e &= \boldsymbol{k}_s^e + \boldsymbol{k}_c^e = k_s \boldsymbol{N}_{34} \boldsymbol{N}_{34}^{\mathrm{T}} + k_c \boldsymbol{N}_{4c} \boldsymbol{N}_{4c}^{\mathrm{T}} \\ &= \begin{bmatrix} 0 & 0 & 0 & 0 & 0 & 0 \\ & 0 & 0 & 0 & 0 & 0 \\ & & 0 & 0 & 0 & 0 \\ & & & 0 & 0 & 0 \\ & \text{symmetry} & & & k_s & -k_s \\ & & & & & k_s \end{bmatrix} + k_c \begin{bmatrix} N_1^2 & N_1 N_2 & N_1 N_3 & N_1 N_4 & 0 & -N_1 \\ & N_2^2 & N_2 N_3 & N_2 N_4 & 0 & -N_2 \\ & & N_3^2 & N_3 N_4 & 0 & -N_3 \\ & & & N_4^2 & 0 & -N_4 \\ & \text{symmetry} & & & 0 & 0 \\ & & & & & 1 \end{bmatrix} \end{aligned} \tag{8.35}$$

Element nodal load vector is

$$\boldsymbol{Q}_u^e = \{ 0 \quad 0 \quad 0 \quad 0 \quad -m_c g \quad -m_w g \}^{\mathrm{T}} \tag{8.36}$$

Dissipated energy of the element is

$$R = \frac{1}{2} c_s (\dot{v}_3 - \dot{v}_4)^2 = \frac{1}{2} (\dot{\boldsymbol{a}}^e)^{\mathrm{T}} \boldsymbol{c}_{\mathrm{u}}^e \dot{\boldsymbol{a}}^e \tag{8.37}$$

where the element damping matrix is

$$\boldsymbol{c}_{\mathrm{u}}^e = c_s \boldsymbol{N}_{34} \boldsymbol{N}_{34}^{\mathrm{T}} = \begin{bmatrix} 0 & 0 & 0 & 0 & 0 & 0 \\ & 0 & 0 & 0 & 0 & 0 \\ & & 0 & 0 & 0 & 0 \\ & & & 0 & 0 & 0 \\ & \text{symmetry} & & & c_s & -c_s \\ & & & & & c_s \end{bmatrix} \tag{8.38}$$

Substituting (8.32), (8.34), and (8.37) into Lagrange equations (8.11) and (8.12), it obtains the dynamic equation for moving element of a single wheel with primary suspension system as

$$\boldsymbol{m}_{\mathrm{u}}^e \ddot{\boldsymbol{a}} + \boldsymbol{c}_{\mathrm{u}}^e \dot{\boldsymbol{a}} + \boldsymbol{k}_{\mathrm{u}}^e \boldsymbol{a} = \boldsymbol{Q}_{\mathrm{u}}^e \tag{8.39}$$

8.3 Moving Element Model of a Single Wheel with Primary and Secondary Suspension Systems

Figure 8.3 shows the moving element model of a single wheel with primary and secondary suspension systems. The model has 5 nodes and 6 DOFs (degrees of freedom). Points 1 and 2 are the two nodes of the rail beam element and their vertical displacements v_i and rotational angles θ_i $(i = 1, 2)$ are analyzed, respectively; point 3 is the node of the car body with its vertical displacement marked as v_3, and 1/8 mass of the car body as m_c; k_{s2} and c_{s2} are the respective stiffness and damping coefficients of secondary suspension system.

Point 4 is the node of the bogie with its vertical displacement marked as v_4 and 1/4 mass of the bogie as m_t; k_{s1}, c_{s1} are the respective stiffness and damping coefficients of primary suspension system; point 5 is the node of the wheel with its vertical displacement marked as v_5 and mass as m_w and the wheel is moving at a constant velocity V; point c is the wheel-rail contact point with its vertical displacement denoted as v_c. The distance between node 1 and node c is x_c, the element length is l, and the wheel-rail contact stiffness is k_c.

Define the element nodal displacement vector as

$$\boldsymbol{a}^e = \{ v_1 \quad \theta_1 \quad v_2 \quad \theta_2 \quad v_3 \quad v_4 \quad v_5 \}^{\mathrm{T}} \tag{8.40}$$

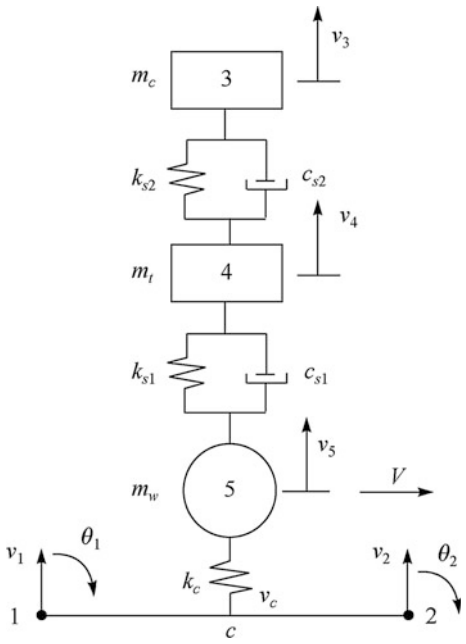

Fig. 8.3 Moving element model of a single wheel with primary and secondary suspension systems

Vertical displacement of node 3 is v_3, and it has

$$v_3 = \boldsymbol{N}_3^{\mathrm{T}} \boldsymbol{a}^e \tag{8.41}$$

$$\dot{v}_3 = \boldsymbol{N}_3^{\mathrm{T}} \dot{\boldsymbol{a}}^e \tag{8.42}$$

where

$$\boldsymbol{N}_3^{\mathrm{T}} = \{\, 0 \quad 0 \quad 0 \quad 0 \quad 1 \quad 0 \quad 0 \,\} \tag{8.43}$$

Vertical displacement of node 4 is v_4 and in the same way it has

$$v_4 = \boldsymbol{N}_4^{\mathrm{T}} \boldsymbol{a}^e \tag{8.44}$$

$$\dot{v}_4 = \boldsymbol{N}_4^{\mathrm{T}} \dot{\boldsymbol{a}}^e \tag{8.45}$$

where

$$\boldsymbol{N}_4^{\mathrm{T}} = \{\, 0 \quad 0 \quad 0 \quad 0 \quad 0 \quad 1 \quad 0 \,\} \tag{8.46}$$

And it has

$$v_3 - v_4 = \boldsymbol{N}_{34}^{\mathrm{T}} \boldsymbol{a}^e \tag{8.47}$$

$$\dot{v}_3 - \dot{v}_4 = \boldsymbol{N}_{34}^{\mathrm{T}} \dot{\boldsymbol{a}}^e \tag{8.48}$$

where

$$\boldsymbol{N}_{34}^{\mathrm{T}} = \{\, 0 \quad 0 \quad 0 \quad 0 \quad 1 \quad -1 \quad 0 \,\} \tag{8.49}$$

Vertical displacement of node 5 is v_5 and similarly it has

$$v_5 = \boldsymbol{N}_5^{\mathrm{T}} \boldsymbol{a}^e \tag{8.50}$$

$$\dot{v}_5 = \boldsymbol{N}_5^{\mathrm{T}} \dot{\boldsymbol{a}}^e \tag{8.51}$$

where

$$\boldsymbol{N}_5^{\mathrm{T}} = \{\, 0 \quad 0 \quad 0 \quad 0 \quad 0 \quad 0 \quad 1 \,\} \tag{8.52}$$

And it gets

$$v_4 - v_5 = \boldsymbol{N}_{45}^{\mathrm{T}} \boldsymbol{a}^e \tag{8.53}$$

$$\dot{v}_4 - \dot{v}_5 = \boldsymbol{N}_{45}^{\mathrm{T}} \dot{\boldsymbol{a}}^e \tag{8.54}$$

where

$$\boldsymbol{N}_{45}^{\mathrm{T}} = \{\, 0 \quad 0 \quad 0 \quad 0 \quad 0 \quad 1 \quad -1 \,\} \tag{8.55}$$

Vertical displacement of node c is v_{c}, which can be expressed by interpolation function as

$$v_{\mathrm{c}} = \boldsymbol{N}_{\mathrm{c}}^{\mathrm{T}} \boldsymbol{a}^e \tag{8.56}$$

where

$$\boldsymbol{N}_{\mathrm{c}}^{\mathrm{T}} = \{\, N_1 \quad N_2 \quad N_3 \quad N_4 \quad 0 \quad 0 \quad 0 \,\} \tag{8.57}$$

And it achieves

$$v_5 - v_{\mathrm{c}} = \boldsymbol{N}_{5\mathrm{c}}^{\mathrm{T}} \boldsymbol{a}^e \tag{8.58}$$

where

$$\boldsymbol{N}_{4c}^{\mathrm{T}} = \{ -N_1 \quad -N_2 \quad -N_3 \quad -N_4 \quad 0 \quad 0 \quad 1 \} \tag{8.59}$$

Kinetic energy of the element is

$$\begin{aligned} T &= \frac{1}{2} m_c \dot{v}_3^2 + \frac{1}{2} m_t \dot{v}_4^2 + \frac{1}{2} m_w \dot{v}_5^2 \\ &= \frac{1}{2} m_c \left(\boldsymbol{N}_3^{\mathrm{T}} \dot{\boldsymbol{a}}^e\right)^{\mathrm{T}} \left(\boldsymbol{N}_3^{\mathrm{T}} \dot{\boldsymbol{a}}^e\right) + \frac{1}{2} m_t \left(\boldsymbol{N}_4^{\mathrm{T}} \dot{\boldsymbol{a}}^e\right)^{\mathrm{T}} \left(\boldsymbol{N}_4^{\mathrm{T}} \dot{\boldsymbol{a}}^e\right) + \frac{1}{2} m_w \left(\boldsymbol{N}_5^{\mathrm{T}} \dot{\boldsymbol{a}}^e\right)^{\mathrm{T}} \left(\boldsymbol{N}_5^{\mathrm{T}} \dot{\boldsymbol{a}}^e\right) \\ &= \frac{1}{2} (\dot{\boldsymbol{a}}^e)^{\mathrm{T}} \boldsymbol{m}_u^e \dot{\boldsymbol{a}}^e \end{aligned} \tag{8.60}$$

where the element mass matrix is

$$\boldsymbol{m}_u^e = m_c \boldsymbol{N}_3 \boldsymbol{N}_3^{\mathrm{T}} + m_t \boldsymbol{N}_4 \boldsymbol{N}_4^{\mathrm{T}} + m_w \boldsymbol{N}_5 \boldsymbol{N}_5^{\mathrm{T}} = \mathrm{diag}(\, 0 \quad 0 \quad 0 \quad 0 \quad m_c \quad m_t \quad m_w \,) \tag{8.61}$$

Potential energy of the element is

$$\begin{aligned} \Pi &= \frac{1}{2} k_{s2} (v_3 - v_4)^2 + \frac{1}{2} k_{s1} (v_4 - v_5)^2 + \frac{1}{2} k_c (v_5 - v_c)^2 + (v_3 m_c g) + (v_4 m_t g) + (v_5 m_w g) \\ &= \frac{1}{2} \boldsymbol{a}^{e\mathrm{T}} \left\{ k_{s2} \boldsymbol{N}_{34} \boldsymbol{N}_{34}^{\mathrm{T}} + k_{s1} \boldsymbol{N}_{45} \boldsymbol{N}_{45}^{\mathrm{T}} + k_c \boldsymbol{N}_{5c} \boldsymbol{N}_{5c}^{\mathrm{T}} \right\} \boldsymbol{a}^e + (\boldsymbol{a}^e)^{\mathrm{T}} \{ m_c g \boldsymbol{N}_3 + m_t g \boldsymbol{N}_4 + m_w g \boldsymbol{N}_5 \} \\ &= \frac{1}{2} (\boldsymbol{a}^e)^{\mathrm{T}} \boldsymbol{k}_u^e \boldsymbol{a}^e - (\boldsymbol{a}^e)^{\mathrm{T}} \boldsymbol{Q}_u \end{aligned} \tag{8.62}$$

where the element stiffness matrix is

$$\begin{aligned} \boldsymbol{k}_u^e &= \boldsymbol{k}_{s2}^e + \boldsymbol{k}_{s1}^e + \boldsymbol{k}_c^e = k_{s2} \boldsymbol{N}_{34} \boldsymbol{N}_{34}^{\mathrm{T}} + k_{s1} \boldsymbol{N}_{45} \boldsymbol{N}_{45}^{\mathrm{T}} + k_c \boldsymbol{N}_{5c} \boldsymbol{N}_{5c}^{\mathrm{T}} \\ &= \begin{bmatrix} 0 & 0 & 0 & 0 & 0 & 0 & 0 \\ & 0 & 0 & 0 & 0 & 0 & 0 \\ & & 0 & 0 & 0 & 0 & 0 \\ & & & 0 & 0 & 0 & 0 \\ & & & & k_{s2} & -k_{s2} & 0 \\ & \text{symmetry} & & & & k_{s2}+k_{s1} & -k_{s1} \\ & & & & & & k_{s1} \end{bmatrix} + k_c \begin{bmatrix} N_1^2 & N_1N_2 & N_1N_3 & N_1N_4 & 0 & 0 & -N_1 \\ & N_2^2 & N_2N_3 & N_2N_4 & 0 & 0 & -N_2 \\ & & N_3^2 & N_3N_4 & 0 & 0 & -N_3 \\ & & & N_4^2 & 0 & 0 & -N_4 \\ & & & & 0 & 0 & 0 \\ & \text{symmetry} & & & & 0 & 0 \\ & & & & & & 1 \end{bmatrix} \end{aligned} \tag{8.63}$$

Element nodal load vector is

$$\boldsymbol{Q}_u = \{\, 0 \quad 0 \quad 0 \quad 0 \quad -m_c g \quad -m_t g \quad -m_w g \,\}^{\mathrm{T}} \tag{8.64}$$

Dissipated energy of the element is

$$R = \frac{1}{2}c_{s2}(\dot{v}_3 - \dot{v}_4)^2 + \frac{1}{2}c_{s1}(\dot{v}_4 - \dot{v}_5)^2 = \frac{1}{2}(\dot{\boldsymbol{a}}^e)^{\mathrm{T}}\boldsymbol{c}_{\mathrm{u}}^e\dot{\boldsymbol{a}}^e \tag{8.65}$$

where the element damping matrix is

$$\boldsymbol{c}_{\mathrm{v}}^e = c_{s2}\boldsymbol{N}_{34}\boldsymbol{N}_{34}^{\mathrm{T}} + c_{s1}\boldsymbol{N}_{45}\boldsymbol{N}_{45}^{\mathrm{T}} = \begin{bmatrix} 0 & 0 & 0 & 0 & 0 & 0 & 0 \\ & 0 & 0 & 0 & 0 & 0 & 0 \\ & & 0 & 0 & 0 & 0 & 0 \\ & & & 0 & 0 & 0 & 0 \\ & & & & c_{s2} & -c_{s2} & 0 \\ & \text{symmetry} & & & & c_{s2}+c_{s1} & -c_{s1} \\ & & & & & & c_{s1} \end{bmatrix} \tag{8.66}$$

Substituting (8.60), (8.62), and (8.65) into Lagrange equations (8.11) and (8.12), it obtains the dynamic equation for moving element of a single wheel with primary and secondary suspension systems as

$$\boldsymbol{m}_{\mathrm{u}}^e\ddot{\boldsymbol{a}} + \boldsymbol{c}_{\mathrm{u}}^e\dot{\boldsymbol{a}} + \boldsymbol{k}_{\mathrm{u}}^e\boldsymbol{a} = \boldsymbol{Q}_{\mathrm{u}}^e \tag{8.67}$$

8.4 Model and Algorithm for Dynamic Analysis of a Single Wheel Moving on the Bridge

In order to illustrate the application of moving element in the dynamic analysis of the train-track coupling system, the vibration response of a single wheel with primary suspension system passing through the bridge is investigated. Finite element mesh is shown by Fig. 8.4.

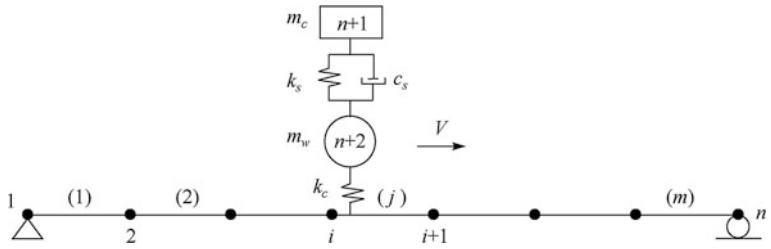

Fig. 8.4 Dynamic analysis model of a single wheel with primary suspension system passing through the bridge

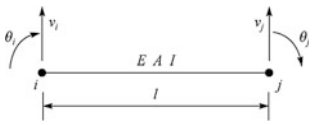

Fig. 8.5 Two-dimensional beam element with 2 nodes and 4 DOFs

The bridge is simulated as a two-dimensional beam element with only vertical displacement and rotation considered, as shown in Fig. 8.5. In the model, E is elasticity modulus of the bridge; I is moment of inertia of the section along the horizontal axis; A is cross-sectional area; and l is length of the beam element. The model for dynamic analysis of a single wheel passing through the bridge is divided into $(m+1)$ elements with $(n+2)$ nodes, in which there are m beam elements and 1 moving element, n nodes for the bridge and 2 nodes for the moving element. The element numbering and the node numbering are shown in Fig. 8.4.

For the two-dimensional beam element with 2 nodes and 4 DOFs, the element mass matrix, stiffness matrix, and damping matrix are as follows [6]

$$\boldsymbol{m}_{\mathrm{b}}^{e} = \frac{\rho A l}{420}\begin{bmatrix} 156 & -22l & 54 & 13l \\ & 4l^2 & -13l & -3l^2 \\ & & 156 & 22l \\ \text{symmetry} & & & 4l^2 \end{bmatrix} \tag{8.68}$$

$$\boldsymbol{k}_{\mathrm{b}}^{e} = \begin{bmatrix} \dfrac{12EI}{l^3} & -\dfrac{6EI}{l^2} & -\dfrac{12EI}{l^3} & -\dfrac{6EI}{l^2} \\ & \dfrac{4EI}{l} & \dfrac{6EI}{l^2} & \dfrac{2EI}{l} \\ & & \dfrac{12EI}{l^3} & \dfrac{6EI}{l^2} \\ \text{symmetry} & & & \dfrac{4EI}{l} \end{bmatrix} \tag{8.69}$$

Applying proportional damping, it has

$$\boldsymbol{c}_{\mathrm{b}}^{e} = \alpha \boldsymbol{m}_{\mathrm{b}}^{e} + \beta \boldsymbol{k}_{\mathrm{b}}^{e} \tag{8.70}$$

where $\boldsymbol{m}_{\mathrm{b}}^{e}$, $\boldsymbol{k}_{\mathrm{b}}^{e}$, and $\boldsymbol{c}_{\mathrm{b}}^{e}$ are the respective mass matrix, stiffness matrix, and damping matrix of the two-dimensional beam element.

For moving element with primary suspension system, the element mass matrix, stiffness matrix, damping matrix, and the element nodal load vector have been given in Sect. 8.2 by Eqs. (8.33), (8.35), (8.38), and (8.36).

Here the major computational steps for the algorithm of dynamic analysis of a single wheel passing through the bridge are given as follows:

I. Calculate the mass matrix, stiffness matrix, and damping matrix of each bridge element by Eqs. (8.68)–(8.70).

II. Form global stiffness matrix, global mass matrix, and global damping matrix of the bridge structure by conventional finite element assembling rule.

$$\boldsymbol{M}_{\mathrm{b}} = \sum_{e} \boldsymbol{m}_{\mathrm{b}}^{e},\ \boldsymbol{K}_{\mathrm{b}} = \sum_{e} \boldsymbol{k}_{\mathrm{b}}^{e},\ \boldsymbol{C}_{\mathrm{b}} = \sum_{e} \boldsymbol{c}_{\mathrm{b}}^{e} \tag{8.71}$$

III. Loop the time steps with Newmark numerical integration method, and in each time step, perform as follows:

(1) Judge the position of the moving element on the bridge by train speed and moving time and then determine the element number of the moving wheel contacting with the bridge.

(2) Calculate the mass matrix, stiffness matrix, damping matrix of the moving element and the element nodal load vector by Eqs. (8.33), (8.35), (8.38), and (8.36).

(3) Assemble the mass matrix, stiffness matrix, and damping matrix of the moving element into the global mass matrix, global stiffness matrix, and global damping matrix of the bridge structure by finite element assembling rule, that is

$$\boldsymbol{M} = \sum_{e} \left(\boldsymbol{M}_{\mathrm{b}} + \boldsymbol{m}_{\mathrm{u}}^{e}\right),\ \boldsymbol{K} = \sum_{e} \left(\boldsymbol{K}_{\mathrm{b}} + \boldsymbol{k}_{\mathrm{u}}^{e}\right),\ \boldsymbol{C} = \sum_{e} \left(\boldsymbol{C}_{\mathrm{b}} + \boldsymbol{c}_{\mathrm{u}}^{e}\right) \tag{8.72}$$

where $\boldsymbol{M}_{\mathrm{b}}$,$\boldsymbol{K}_{\mathrm{b}}$, and $\boldsymbol{C}_{\mathrm{b}}$ are the respective global stiffness matrix, global mass matrix, and global damping matrix of the bridge structure.

(4) Assemble the element nodal load vector of the moving element and formulate the global nodal load vector as

$$\boldsymbol{Q} = \sum_{e} \boldsymbol{Q}_{\mathrm{u}}^{e} \tag{8.73}$$

(5) Solve the following finite element equation by Newmark numerical integration method

$$\boldsymbol{M}\ddot{\boldsymbol{a}} + \boldsymbol{C}\dot{\boldsymbol{a}} + \boldsymbol{K}\boldsymbol{a} = \boldsymbol{Q} \tag{8.74}$$

And it gains the nodal displacement, velocity, and acceleration of the bridge structure and the moving element.

(6) Turn back to step (III) and continue the calculation in next time step until all the calculation finishes.

References

1. Koh CG, Ong JSY, Chua DKH, Feng J (2003) Moving element method for train-track dynamics. Int J Numer Meth Eng 56:1549–1567
2. Ono K, Yamada M (1989) Analysis of railway track vibration. J Sound Vib 130:269–297
3. Filho FV (1978) Finite element analysis of structures under moving loads. Shock Vib Dig 10:27–35
4. Zhai W (2007) Vehicle-track coupling dynamics, 3rd edn. Science Press, Beijing
5. Lei X, Sheng X (2008) Advanced studies in modern track theory, 2nd edn. China Railway Publishing House, Beijing
6. Lei XY, Noda NA (2002) Analyses of dynamic response of vehicle and track coupling system with random irregularity of track vertical profile. J Sound Vib 258(1):147–165

Chapter 9
Model and Algorithm for Track Element and Vehicle Element

With the rapid development of high-speed railway, the train at a high speed results in greater dynamic stress on track structure and larger car body vibration, which directly affects train operation safety and comfort. The dynamic analysis of train-track-subgrade coupling system is the basis to solving this problem. Scholars at home and abroad have done a lot of research work in this field and achieved much [1–12]. Nielsen [1], for example, has established the vehicle-track interaction model; Knothe [2] explores the railway track and vehicle interaction at high frequencies; Koh proposes the moving element method for train-track dynamics [3]; Zhai [6] sets up an analysis model of coupling system with vehicle and track as a whole; Lei [7, 8] has designed a vibration analytic model of vehicle-track nonlinear coupling system with random irregularity by adopting finite element analysis and cross iteration method. These models have distinct characteristics but also have their respective limitations such as low computation efficiency, complex programming, or the only application into the analysis of some special cases.

In this chapter, models of track and vehicle elements applicable to this issue are proposed on the basis of the characteristics of train-track-subgrade coupling system. By adopting finite element method and Lagrange equation, the stiffness matrix, mass matrix, and damping matrix of the track and the vehicle elements are deduced [8–12]. The train-track-subgrade coupling system will be discretized into separate vehicle element and track element, in which the track-subgrade system is simulated as a series of track elements and the train as vehicle elements. In the process of computation, this model only needs to generate the global stiffness matrix, global mass matrix, and global damping matrix of the track-subgrade system once. And in the following computation of each time step, it only needs to assemble the stiffness matrix, mass matrix, and damp matrix of the vehicle element into the global stiffness, mass, and damping matrixes of the track-subgrade system. Therefore, computational efficiency is largely improved. Since the governing equation is based on the energy principle, the stiffness, mass, and damping matrixes are symmetric

X. Lei, *High Speed Railway Track Dynamics*,
DOI 10.1007/978-981-10-2039-1_9

and the train-track-subgrade coupling system only includes vehicle and track elements, thus making programming particularly easier. Therefore, the track and vehicle element models have the characteristics of easy programming and high computation efficiency.

9.1 Ballast Track Element Model

9.1.1 Basic Assumptions

To establish the vertical vibration model of the train-ballast track-subgrade coupling system by using finite element analysis, it is assumed:

(1) Only vertical vibration effect of the vehicle-track-subgrade coupling system is considered.
(2) Since the vehicle and the track are symmetrical about the centerline of the track, only half of the coupling system is used for ease of calculation.
(3) The upper structure in the vehicle and track coupling system is a complete locomotive or rolling stock unit with a primary and secondary suspension systems, in which bouncing and pitch motion for both vehicle and bogie are considered.
(4) The hypothesis of a linear relationship between two elastic contact cylinders perpendicular to each other is used in coupling the vehicle and the track.
(5) The lower structure in the coupling system is the ballast track where rails are discretized into 2D beam element; the stiffness coefficient and damping coefficient of the rail pads and fasteners are denoted by k_{y1} and $c_{y1,}$ respectively.
(6) Sleeper mass is defined as lumped mass, and only vertical vibration effect is considered; the stiffness and damping coefficients of the ballast are denoted by k_{y2} and $c_{y2,}$ respectively.
(7) Ballast mass is simplified as lumped mass, and only vertical vibration effect is considered; the stiffness and damping coefficients of the subgrade are denoted by k_{y3} and $c_{y3,}$ respectively.

9.1.2 Three-Layer Ballast Track Element

Three-layer ballast track element model is shown in Fig. 9.1, in which v_1, v_4 are vertical displacement of the rail, θ_1, θ_4 are rotational angle of the rail, v_2, v_5 are vertical displacement of the sleeper, and v_3, v_6 are vertical displacement of the ballast.

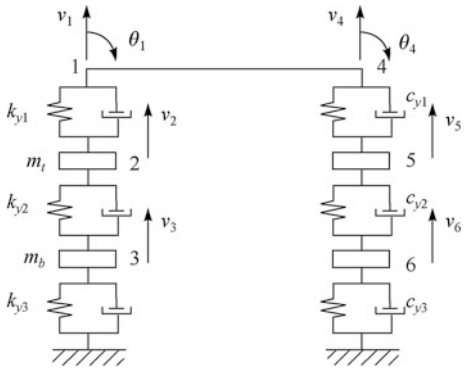

Fig. 9.1 Three-layer ballast track element model

The nodal displacement of the three-layer ballast track element is

$$\boldsymbol{a}_l^e = \{ v_1 \quad \theta_1 \quad v_2 \quad v_3 \quad v_4 \quad \theta_4 \quad v_5 \quad v_6 \}^{\mathrm{T}} \tag{9.1}$$

where $v_i (i = 1, 2, 3, \ldots, 6)$ denotes the vertical displacements of the rail, the sleeper, and the ballast; $\theta_i (i = 1, 4)$ is the rotational angle of the rail at node i.

The mass matrix of the three-layer ballast track element is

$$\boldsymbol{m}_{\mathrm{l}}^e = \boldsymbol{m}_{\mathrm{r}}^e + \boldsymbol{m}_{\mathrm{b}}^e \tag{9.2}$$

where $\boldsymbol{m}_{\mathrm{r}}^e$ is consistent mass matrix of the rail: $\boldsymbol{m}_{\mathrm{b}}^e$ is mass matrix of the sleeper and the ballast.

$$\boldsymbol{m}_{\mathrm{r}}^e = \frac{\rho_{\mathrm{r}} A_{\mathrm{r}} l}{420} \begin{bmatrix} 156 & -22l & 0 & 0 & 54 & 13l & 0 & 0 \\ & 4l^2 & 0 & 0 & -13l & -3l^2 & 0 & 0 \\ & & 0 & 0 & 0 & 0 & 0 & 0 \\ & & & 0 & 0 & 0 & 0 & 0 \\ & & & & 156 & 22l & 0 & 0 \\ & & & & & 4l^2 & 0 & 0 \\ & \text{symmetry} & & & & & 0 & 0 \\ & & & & & & & 0 \end{bmatrix} \tag{9.3}$$

where ρ_{r} is the rail density, A_{r} is the cross-sectional area of the rail, and l is the length of the ballast track element.

Based on the basic assumptions (6) and (7),the sleeper mass m_{t} and the ballast mass m_{b} between two neighboring sleepers are exerted as lumped mass on the three-layer ballast track element, then

$$\boldsymbol{m}_{\mathrm{b}}^e = \mathrm{diag}\left(0 \quad 0 \quad \tfrac{1}{4} m_{\mathrm{t}} \quad \tfrac{1}{4} m_{\mathrm{b}} \quad 0 \quad 0 \quad \tfrac{1}{4} m_{\mathrm{t}} \quad \tfrac{1}{4} m_{\mathrm{b}} \right) \tag{9.4}$$

The stiffness matrix of the three-layer ballast track element is

$$\boldsymbol{k}_{\mathrm{l}}^{e} = \boldsymbol{k}_{\mathrm{r}}^{e} + \boldsymbol{k}_{\mathrm{e}}^{e} \tag{9.5}$$

where $\boldsymbol{k}_{\mathrm{r}}^{e}$ is stiffness matrix caused by rail bending; $\boldsymbol{k}_{\mathrm{e}}^{e}$ is stiffness matrix caused by track elastic support.

$$\boldsymbol{k}_{\mathrm{r}}^{e} = \frac{E_{\mathrm{r}} I_{\mathrm{r}}}{l^3} \begin{bmatrix} 12 & -6l & 0 & 0 & -12 & -6l & 0 & 0 \\ & 4l^2 & 0 & 0 & 6l & 2l^2 & 0 & 0 \\ & & 0 & 0 & 0 & 0 & 0 & 0 \\ & & & 0 & 0 & 0 & 0 & 0 \\ & & & & 12 & 6l & 0 & 0 \\ & & & & & 4l^2 & 0 & 0 \\ & \text{symmetry} & & & & & 0 & 0 \\ & & & & & & & 0 \end{bmatrix} \tag{9.6}$$

$$\boldsymbol{k}_{\mathrm{e}}^{e} = \frac{1}{2} \begin{bmatrix} k_{y1} & 0 & -k_{y1} & 0 & 0 & 0 & 0 & 0 \\ & 0 & 0 & 0 & 0 & 0 & 0 & 0 \\ & & k_{y1}+k_{y2} & -k_{y2} & 0 & 0 & 0 & 0 \\ & & & k_{y2}+k_{y3} & 0 & 0 & 0 & 0 \\ & & & & k_{y1} & 0 & -k_{y1} & 0 \\ & & & & & 0 & 0 & 0 \\ & \text{symmetry} & & & & & k_{y1}+k_{y2} & -k_{y2} \\ & & & & & & & k_{y2}+k_{y3} \end{bmatrix} \tag{9.7}$$

where E_{r} and I_{r} are elasticity modulus and horizontal sectional inertia moment of the rail, respectively. l is the length of the three-layer ballast track element, namely the length between two neighboring sleepers. k_{y1}, k_{y2} and k_{y3} are the stiffness coefficients of the rail pads and fasteners, the ballast, and the subgrade, respectively.

The damping matrix of the three-layer ballast track element is

$$\boldsymbol{c}_{\mathrm{l}}^{e} = \boldsymbol{c}_{\mathrm{r}}^{e} + \boldsymbol{c}_{\mathrm{c}}^{e} \tag{9.8}$$

where $\boldsymbol{c}_{\mathrm{r}}^{e}$ is the damping matrix of the rail influenced by system damping ratio and natural frequency.

$$\boldsymbol{c}_{\mathrm{r}}^{e} = \alpha \boldsymbol{m}_{\mathrm{r}}^{e} + \beta \boldsymbol{k}_{\mathrm{r}}^{e} \tag{9.9}$$

where α, β are proportional damping coefficients.

$\boldsymbol{c}_{\mathrm{c}}^{e}$ is the damping matrix resulted from the rail pads and fasteners, the ballast, and the subgrade.

$$\boldsymbol{c}_{\mathrm{c}}^{e}=\frac{1}{2}\begin{bmatrix} c_{y1} & 0 & -c_{y1} & 0 & 0 & 0 & 0 & 0 \\ & 0 & 0 & 0 & 0 & 0 & 0 & 0 \\ & & c_{y1}+c_{y2} & -c_{y2} & 0 & 0 & 0 & 0 \\ & & & c_{y2}+c_{y3} & 0 & 0 & 0 & 0 \\ & & & & c_{y1} & 0 & -c_{y1} & 0 \\ & & & & & 0 & 0 & 0 \\ & \text{symmetry} & & & & & c_{y1}+c_{y2} & -c_{y2} \\ & & & & & & & c_{y2}+c_{y3} \end{bmatrix} \tag{9.10}$$

where c_{y1}, c_{y2}, and c_{y3} are the damping coefficients of the rail pads and fasteners, the ballast, and the subgrade, respectively.

Based on the finite element assembling rule, the global mass matrix, the global stiffness matrix, and the global damping matrix of the ballast track structure can be obtained by assembling the element mass matrix (9.2), the element stiffness matrix (9.5) and the element damping matrix (9.8).

$$\begin{aligned} \boldsymbol{m}_{\mathrm{l}} &= \sum_{e} \boldsymbol{m}_{\mathrm{l}}^{e} = \sum_{e} \left(\boldsymbol{m}_{\mathrm{r}}^{e} + \boldsymbol{m}_{\mathrm{b}}^{e}\right) \\ \boldsymbol{k}_{\mathrm{l}} &= \sum_{e} \boldsymbol{k}_{\mathrm{l}}^{e} = \sum_{e} \left(\boldsymbol{k}_{\mathrm{r}}^{e} + \boldsymbol{k}_{e}^{e}\right) \\ \boldsymbol{c}_{\mathrm{l}} &= \sum_{e} \boldsymbol{c}_{\mathrm{l}}^{e} = \sum_{e} \left(\boldsymbol{c}_{\mathrm{r}}^{e} + \boldsymbol{c}_{\mathrm{c}}^{e}\right) \end{aligned} \tag{9.11}$$

9.2 Slab Track Element Model

9.2.1 Basic Assumptions

To establish the vertical vibration model of the train-slab track-subgrade coupling system by using finite element analysis, it is assumed:

(1) Only vertical vibration effect of the vehicle-slab track-subgrade coupling system is considered.
(2) The upper structure in the vehicle and track coupling system is a complete locomotive or rolling stock unit with a primary and secondary suspension systems, in which bouncing and pitch motion for both vehicle and bogie are considered.
(3) Since the vehicle and the slab track-subgrade system are symmetrical about the centerline of the track, only half of the coupling system is used for ease of calculation.
(4) The hypothesis of a linear relationship between two elastic contact cylinders perpendicular to each other is used in coupling the vehicle and the track.

(5) The lower structure in the coupling system is the slab track where rails are discretized into 2D beam element supported by discrete viscoelastic supports; the stiffness coefficient and the damping coefficient of the rail pads and fasteners are denoted by k_{y1} and c_{y1}, respectively.
(6) In accordance with the general computation rules of beam and slab on elastic foundations, when the length of the structure is less than three times its width, it is computed as slab, while the length of the structure is more than three times its width, it is computed as beam. Precast track slab is discretized as 2D beam element with continuous viscoelastic support. The stiffness coefficient and the damping coefficient of the cement asphalt mortar layer beneath the precast track slab are denoted by k_{y2} and c_{y2}, respectively.
(7) Concrete support layer is discretized as 2D beam element with continuous viscoelastic support. The stiffness coefficient and the damping coefficient of antifreezing layer beneath it are denoted by k_{y3} and c_{y3}, respectively.
(8) The study is focused on the middle element of the slab track. Relevant matrix of the end elements can be deduced in the same way.

9.2.2 Three-Layer Slab Track Element Model

Three-layer slab track element model is shown in Fig. 9.2, in which v_1, v_4 are vertical displacements of the rail, θ_1, θ_4 are rotational angles of the rail; v_2, v_5 are vertical displacements of the precast track slab, θ_2, θ_5 are rotational angles of the precast track slab, v_3, v_6 are vertical displacements of the concrete support layer, and θ_3, θ_6 are rotational angles of the concrete support layer.

The node displacement vector of the three-layer slab track element is defined as follows:

$$\boldsymbol{a}^e = \{ v_1 \quad \theta_1 \quad v_2 \quad \theta_2 \quad v_3 \quad \theta_3 \quad v_4 \quad \theta_4 \quad v_5 \quad \theta_5 \quad v_6 \quad \theta_6 \}^{\mathrm{T}} \tag{9.12}$$

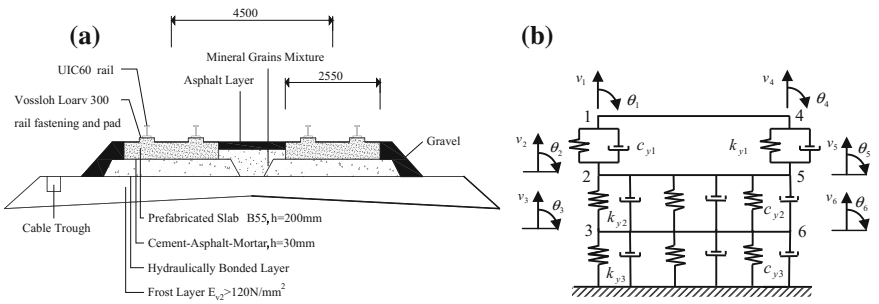

Fig. 9.2 Three-layer slab track element model. **a** Cross section of the slab track and **b** three-layer slab track element

where v_i, θ_i (i = 1, 2, 3, …, 6) denote vertical displacement and rotational angle of the slab track element at note i, respectively.

9.2.3 Mass Matrix of the Slab Track Element

The mass matrix of the slab track element is composed of the mass of the rail, the mass of the precast slab, and the mass of the concrete support layer. The mass matrix is

$$\boldsymbol{m}_{\mathrm{l}}^{e} = \boldsymbol{m}_{\mathrm{r}}^{e} + \boldsymbol{m}_{\mathrm{s}}^{e} + \boldsymbol{m}_{\mathrm{h}}^{e} \tag{9.13}$$

where $\boldsymbol{m}_{\mathrm{r}}^{e}$ is mass matrix of the rail; $\boldsymbol{m}_{\mathrm{s}}^{e}$ is mass matrix of the precast slab; and $\boldsymbol{m}_{\mathrm{h}}^{e}$ is mass matrix of the concrete support layer.

$$\boldsymbol{m}_{\mathrm{r}}^{e} = \frac{\rho_{\mathrm{r}} A_{\mathrm{r}} l}{420} \begin{bmatrix} 156 & -22l & 0 & 0 & 0 & 0 & 54 & 13l & 0 & 0 & 0 & 0 \\ & 4l^2 & 0 & 0 & 0 & 0 & -13l & -3l^2 & 0 & 0 & 0 & 0 \\ & & 0 & 0 & 0 & 0 & 0 & 0 & 0 & 0 & 0 & 0 \\ & & & 0 & 0 & 0 & 0 & 0 & 0 & 0 & 0 & 0 \\ & & & & 0 & 0 & 0 & 0 & 0 & 0 & 0 & 0 \\ & & & & & 0 & 0 & 0 & 0 & 0 & 0 & 0 \\ & & & & & & 156 & 22l & 0 & 0 & 0 & 0 \\ & & & & & & & 4l^2 & 0 & 0 & 0 & 0 \\ & & & & & & & & 0 & 0 & 0 & 0 \\ & & & & \text{symmetry} & & & & & 0 & 0 & 0 \\ & & & & & & & & & & 0 & 0 \\ & & & & & & & & & & & 0 \end{bmatrix} \tag{9.14}$$

$$\boldsymbol{m}_{\mathrm{s}}^{e} = \frac{\rho_{\mathrm{s}} A_{\mathrm{s}} l}{420} \begin{bmatrix} 0 & 0 & 0 & 0 & 0 & 0 & 0 & 0 & 0 & 0 & 0 & 0 \\ & 0 & 0 & 0 & 0 & 0 & 0 & 0 & 0 & 0 & 0 & 0 \\ & & 156 & -22l & 0 & 0 & 0 & 0 & 54 & 13l & 0 & 0 \\ & & & 4l^2 & 0 & 0 & 0 & 0 & -13l & -3l^2 & 0 & 0 \\ & & & & 0 & 0 & 0 & 0 & 0 & 0 & 0 & 0 \\ & & & & & 0 & 0 & 0 & 0 & 0 & 0 & 0 \\ & & & & & & 0 & 0 & 0 & 0 & 0 & 0 \\ & & & & & & & 0 & 0 & 0 & 0 & 0 \\ & & & & & & & & 156 & 22l & 0 & 0 \\ & & \text{symmetry} & & & & & & & 4l^2 & 0 & 0 \\ & & & & & & & & & & 0 & 0 \\ & & & & & & & & & & & 0 \end{bmatrix} \tag{9.15}$$

$$\boldsymbol{m}_{\mathrm{h}}^{e}=\frac{\rho_{\mathrm{h}}A_{\mathrm{h}}l}{420}\begin{bmatrix}0 & 0 & 0 & 0 & 0 & 0 & 0 & 0 & 0 & 0 & 0 & 0\\ & 0 & 0 & 0 & 0 & 0 & 0 & 0 & 0 & 0 & 0 & 0\\ & & 0 & 0 & 0 & 0 & 0 & 0 & 0 & 0 & 0 & 0\\ & & & 0 & 0 & 0 & 0 & 0 & 0 & 0 & 0 & 0\\ & & & & 156 & -22l & 0 & 0 & 0 & 0 & 54 & 13l\\ & & & & & 4l^2 & 0 & 0 & 0 & 0 & -13l & -3l^2\\ & & & & & & 0 & 0 & 0 & 0 & 0 & 0\\ & & & & & & & 0 & 0 & 0 & 0 & 0\\ & & & & & & & & 0 & 0 & 0 & 0\\ & & \text{symmetry} & & & & & & & 0 & 0 & 0\\ & & & & & & & & & & 156 & 22l\\ & & & & & & & & & & & 4l^2\end{bmatrix} \tag{9.16}$$

In the above mass matrixes, ρ_{r}, ρ_{s}, and ρ_{h} refer to the density of the rail, the precast slab, and the concrete support layer, respectively, while A_{r}, A_{s}, and A_{h} denote the area of cross section of the rail, the precast slab, and the concrete support layer, respectively; l means the length of the slab track element.

9.2.4 Stiffness Matrix of the Slab Track Element

The stiffness matrix of the slab track element is made up of the bending stiffness caused by the potential energy of the rail, the precast slab, and the concrete support layer, the stiffness of discrete viscoelastic supports caused by the rail pads and fasteners, and the continuous elastic supporting stiffness of the asphalt cement mortar layer and antifreezing subgrade.

(1) **Bending stiffness of the rail**

$$\boldsymbol{k}_{\mathrm{r}}^{e}=\frac{E_{\mathrm{r}}I_{\mathrm{r}}}{l^3}\begin{bmatrix}12 & -6l & 0 & 0 & 0 & 0 & -12 & -6l & 0 & 0 & 0 & 0\\ & 4l^2 & 0 & 0 & 0 & 0 & 6l & 2l^2 & 0 & 0 & 0 & 0\\ & & 0 & 0 & 0 & 0 & 0 & 0 & 0 & 0 & 0 & 0\\ & & & 0 & 0 & 0 & 0 & 0 & 0 & 0 & 0 & 0\\ & & & & 0 & 0 & 0 & 0 & 0 & 0 & 0 & 0\\ & & & & & 0 & 0 & 0 & 0 & 0 & 0 & 0\\ & & & & & & 12 & 6l & 0 & 0 & 0 & 0\\ & & & & & & & 4l^2 & 0 & 0 & 0 & 0\\ & & & & & & & & 0 & 0 & 0 & 0\\ & & \text{symmetry} & & & & & & & 0 & 0 & 0\\ & & & & & & & & & & 0 & 0\\ & & & & & & & & & & & 0\end{bmatrix} \tag{9.17}$$

where $\boldsymbol{k}_{\mathrm{r}}^{e}$ is the bending stiffness matrix of the rail; E_{r} and I_{r} are the elasticity modulus of the rail and the sectional moment of inertia around the horizontal axis, respectively; and l is the length of the slab track element.

(2) **Bending stiffness of the precast slab**

$$\boldsymbol{k}_{\mathrm{s}}^{e}=\frac{E_{\mathrm{s}}I_{\mathrm{s}}}{l^{3}}\begin{bmatrix}0 & 0 & 0 & 0 & 0 & 0 & 0 & 0 & 0 & 0 & 0 & 0\\ & 0 & 0 & 0 & 0 & 0 & 0 & 0 & 0 & 0 & 0 & 0\\ & & 12 & -6l & 0 & 0 & 0 & 0 & -12 & -6l & 0 & 0\\ & & & 4l^{2} & 0 & 0 & 0 & 0 & 6l & 2l^{2} & 0 & 0\\ & & & & 0 & 0 & 0 & 0 & 0 & 0 & 0 & 0\\ & & & & & 0 & 0 & 0 & 0 & 0 & 0 & 0\\ & & & & & & 0 & 0 & 0 & 0 & 0 & 0\\ & & & & & & & 0 & 0 & 0 & 0 & 0\\ & & & & & & & & 12 & 6l & 0 & 0\\ & & \text{symmetry} & & & & & & & 4l^{2} & 0 & 0\\ & & & & & & & & & & 0 & 0\\ & & & & & & & & & & & 0\end{bmatrix} \tag{9.18}$$

where $\boldsymbol{k}_{\mathrm{s}}^{e}$ is the bending stiffness matrix of the precast slab; E_{s} and I_{s} are the elasticity modulus of the precast slab and the sectional moment of inertia around the horizontal axis, respectively; and l is the length of the slab track element.

(3) **Bending stiffness of the concrete support layer**

$$\boldsymbol{k}_{\mathrm{h}}^{e}=\frac{E_{\mathrm{h}}I_{\mathrm{h}}}{l^{3}}\begin{bmatrix}0 & 0 & 0 & 0 & 0 & 0 & 0 & 0 & 0 & 0 & 0 & 0\\ & 0 & 0 & 0 & 0 & 0 & 0 & 0 & 0 & 0 & 0 & 0\\ & & 0 & 0 & 0 & 0 & 0 & 0 & 0 & 0 & 0 & 0\\ & & & 0 & 0 & 0 & 0 & 0 & 0 & 0 & 0 & 0\\ & & & & 12 & -6l & 0 & 0 & 0 & 0 & -12 & -6l\\ & & & & & 4l^{2} & 0 & 0 & 0 & 0 & 6l & 2l^{2}\\ & & & & & & 0 & 0 & 0 & 0 & 0 & 0\\ & & & & & & & 0 & 0 & 0 & 0 & 0\\ & & & & & & & & 0 & 0 & 0 & 0\\ & & \text{symmetry} & & & & & & & 0 & 0 & 0\\ & & & & & & & & & & 12 & 6l\\ & & & & & & & & & & & 4l^{2}\end{bmatrix} \tag{9.19}$$

where $\boldsymbol{k}_{\mathrm{h}}^{e}$ is the bending stiffness matrix of the concrete support layer; E_{h} and I_{h} are the elasticity modulus of the concrete support layer and the sectional moment of inertia around the horizontal axis, respectively; and l is the length of the slab track element.

(4) **Stiffness caused by discrete elastic support of the rail pads and fasteners**

$$\boldsymbol{k}_{1\mathrm{c}}^{e}=\frac{1}{2}\begin{bmatrix} k_{y1} & 0 & -k_{y1} & 0 & 0 & 0 & 0 & 0 & 0 & 0 & 0 & 0 \\ & 0 & 0 & 0 & 0 & 0 & 0 & 0 & 0 & 0 & 0 & 0 \\ & & k_{y1} & 0 & 0 & 0 & 0 & 0 & 0 & 0 & 0 & 0 \\ & & & 0 & 0 & 0 & 0 & 0 & 0 & 0 & 0 & 0 \\ & & & & 0 & 0 & 0 & 0 & 0 & 0 & 0 & 0 \\ & & & & & 0 & 0 & 0 & 0 & 0 & 0 & 0 \\ & & & & & & k_{y1} & 0 & -k_{y1} & 0 & 0 & 0 \\ & & & & & & & 0 & 0 & 0 & 0 & 0 \\ & & & & & & & & k_{y1} & 0 & 0 & 0 \\ & & \text{symmetry} & & & & & & & 0 & 0 & 0 \\ & & & & & & & & & & 0 & 0 \\ & & & & & & & & & & & 0 \end{bmatrix} \tag{9.20}$$

where $\boldsymbol{k}_{1\mathrm{c}}^{e}$ denotes the stiffness matrix caused by discrete elastic support of the rail pads and fasteners, while k_{y1} refers to its stiffness coefficient.

(5) **Stiffness caused by continuous elastic support of the cement asphalt mortar layer**

The relative displacement of any point in the slab track element between the precast slab and the concrete support layer can be expressed as follows:

$$\begin{aligned} v_{\mathrm{sh}} &= v_{\mathrm{s}}-v_{\mathrm{h}}=N_1v_2+N_2\theta_2+N_3v_5+N_4\theta_5-N_1v_3-N_2\theta_3-N_3v_6-N_4\theta_6 \\ &=\{0\quad 0\quad N_1\quad N_2\quad -N_1\quad -N_2\quad 0\quad 0\quad N_3\quad N_4\quad -N_3\quad -N_4\}\boldsymbol{a}^{e}=\boldsymbol{N}_{\mathrm{sh}}^{\mathrm{T}}\boldsymbol{a}^{e} \end{aligned} \tag{9.21}$$

where N_1–N_4 are interpolation functions of the two-dimensional beam element.

$$\begin{aligned} N_1&=1-\frac{3}{l^2}x^2+\frac{2}{l^3}x^3 \qquad & N_2&=-x+\frac{2}{l}x^2-\frac{1}{l^2}x^3 \\ N_3&=\frac{3}{l^2}x^2-\frac{2}{l^3}x^3 \qquad & N_4&=\frac{1}{l}x^2-\frac{1}{l^2}x^3 \end{aligned} \tag{9.22}$$

The elastic potential energy of the cement asphalt mortar layer can be obtained as follows:

$$\Pi_{2c} = \frac{1}{2}\int_l k_{y2} v_{sh}^2 \mathrm{d}x = \frac{1}{2}\boldsymbol{a}^{e\mathrm{T}} \int_l \left\{k_{y2}\boldsymbol{N}_{sh}\boldsymbol{N}_{sh}^{\mathrm{T}}\right\}\mathrm{d}x\boldsymbol{a}^e = \frac{1}{2}\boldsymbol{a}^{e\mathrm{T}}\boldsymbol{k}_{2c}^e\boldsymbol{a}^e \tag{9.23}$$

where

$$\boldsymbol{k}_{2c}^e = \frac{k_{y2}l}{420}\begin{bmatrix} 0 & 0 & 0 & 0 & 0 & 0 & 0 & 0 & 0 & 0 & 0 & 0 \\ & 0 & 0 & 0 & 0 & 0 & 0 & 0 & 0 & 0 & 0 & 0 \\ & & 156 & -22l & -156 & 22l & 0 & 0 & 54 & 13l & -54 & -13l \\ & & & 4l^2 & 22l & -4l^2 & 0 & 0 & -13l & -3l^2 & 13l & 3l^2 \\ & & & & 156 & -22l & 0 & 0 & -54 & -13l & 54 & 13l \\ & & & & & 4l^2 & 0 & 0 & 13l & 3l^2 & -13l & -3l^2 \\ & & & & & & 0 & 0 & 0 & 0 & 0 & 0 \\ & & & & & & & 0 & 0 & 0 & 0 & 0 \\ & & & & & & & & 156 & 22l & -156 & -22l \\ & & \text{symmetry} & & & & & & & 4l^2 & -22l & -4l^2 \\ & & & & & & & & & & 156 & 22l \\ & & & & & & & & & & & 4l^2 \end{bmatrix} \tag{9.24}$$

$\boldsymbol{k}_{2c}^e$ denotes the stiffness matrix caused by continuous elastic support of the cement asphalt mortar layer, while k_{y2} refers to the stiffness coefficient of the cement asphalt mortar layer.

(6) **Stiffness caused by continuous elastic support of the antifreeze subgrade**

In the same way, the stiffness matrix caused by continuous elastic support of the antifreeze subgrade is available.

$$\boldsymbol{k}_{3c}^e = \frac{k_{y3}l}{420}\begin{bmatrix} 0 & 0 & 0 & 0 & 0 & 0 & 0 & 0 & 0 & 0 & 0 & 0 \\ & 0 & 0 & 0 & 0 & 0 & 0 & 0 & 0 & 0 & 0 & 0 \\ & & 0 & 0 & 0 & 0 & 0 & 0 & 0 & 0 & 0 & 0 \\ & & & 0 & 0 & 0 & 0 & 0 & 0 & 0 & 0 & 0 \\ & & & & 156 & -22l & 0 & 0 & 0 & 0 & 54 & 13l \\ & & & & & 4l^2 & 0 & 0 & 0 & 0 & -13l & -3l^2 \\ & & & & & & 0 & 0 & 0 & 0 & 0 & 0 \\ & & & & & & & 0 & 0 & 0 & 0 & 0 \\ & & & & & & & & 0 & 0 & 0 & 0 \\ & & \text{symmetry} & & & & & & & 0 & 0 & 0 \\ & & & & & & & & & & 156 & 22l \\ & & & & & & & & & & & 4l^2 \end{bmatrix} \tag{9.25}$$

where $\boldsymbol{k}_{3c}^{e}$ denotes the stiffness matrix caused by continuous elastic support of the antifreeze subgrade, while k_{y3} refers to the stiffness coefficient of the antifreeze subgrade.

Finally, the stiffness matrix of the slab track element can be obtained as follows:

$$\boldsymbol{k}_{l}^{e} = \boldsymbol{k}_{r}^{e} + \boldsymbol{k}_{s}^{e} + \boldsymbol{k}_{h}^{e} + \boldsymbol{k}_{1c}^{e} + \boldsymbol{k}_{2c}^{e} + \boldsymbol{k}_{3c}^{e} \tag{9.26}$$

where $\boldsymbol{k}_{l}^{e}$ denotes the stiffness matrix of the slab track element.

9.2.5 Damping Matrix of the Slab Track Element

Damping matrix of the slab track element is composed of the internal friction damping caused by the rail, the precast slab, and the concrete support layer and the support damping caused by the rail pads and fasteners, the cement asphalt mortar layer, and the antifreezing subgrade.

$$\boldsymbol{c}_{l}^{e} = \boldsymbol{c}_{r}^{e} + \boldsymbol{c}_{1c}^{e} + \boldsymbol{c}_{2c}^{e} + \boldsymbol{c}_{3c}^{e} \tag{9.27}$$

where $\boldsymbol{c}_{r}^{e}$ is the damping matrix caused by internal friction of the rail, the precast slab, and the concrete supporting layer, generally adopting proportional damping; $\boldsymbol{c}_{1c}^{e}$, $\boldsymbol{c}_{2c}^{e}$ and $\boldsymbol{c}_{3c}^{e}$ denote the damping matrix caused by the rail pads and fasteners, the cement asphalt mortar layer, and the antifreezing subgrade, respectively.

$$\boldsymbol{c}_{r}^{e} = \alpha_{r}\boldsymbol{m}_{r}^{e} + \beta_{r}\boldsymbol{k}_{r}^{e} + \alpha_{s}\boldsymbol{m}_{s}^{e} + \beta_{s}\boldsymbol{k}_{s}^{e} + \alpha_{h}\boldsymbol{m}_{h}^{e} + \beta_{h}\boldsymbol{m}_{h}^{e} \tag{9.28}$$

where α_r, β_r, α_s, β_s, α_h and β_h denote the proportional damping coefficients of the rail, the precast slab, and the concrete support layer, respectively.

$$\boldsymbol{c}_{1c}^{e} = \frac{1}{2}\begin{bmatrix} c_{y1} & 0 & -c_{y1} & 0 & 0 & 0 & 0 & 0 & 0 & 0 & 0 & 0 \\ & 0 & 0 & 0 & 0 & 0 & 0 & 0 & 0 & 0 & 0 & 0 \\ & & c_{y1} & 0 & 0 & 0 & 0 & 0 & 0 & 0 & 0 & 0 \\ & & & 0 & 0 & 0 & 0 & 0 & 0 & 0 & 0 & 0 \\ & & & & 0 & 0 & 0 & 0 & 0 & 0 & 0 & 0 \\ & & & & & 0 & 0 & 0 & 0 & 0 & 0 & 0 \\ & & & & & & c_{y1} & 0 & -c_{y1} & 0 & 0 & 0 \\ & & & & & & & 0 & 0 & 0 & 0 & 0 \\ & & & & & & & & c_{y1} & 0 & 0 & 0 \\ & & \text{symmety} & & & & & & & 0 & 0 & 0 \\ & & & & & & & & & & 0 & 0 \\ & & & & & & & & & & & 0 \end{bmatrix} \tag{9.29}$$

$$\boldsymbol{c}_{2c}^{e}=\frac{c_{y2}l}{420}\begin{bmatrix}0&0&0&0&0&0&0&0&0&0&0&0\\&0&0&0&0&0&0&0&0&0&0&0\\&&156&-22l&-156&22l&0&0&54&13l&-54&-13l\\&&&4l^2&22l&-4l^2&0&0&-13l&-3l^2&13l&3l^2\\&&&&156&-22l&0&0&-54&-13l&54&13l\\&&&&&4l^2&0&0&13l&3l^2&-13l&-3l^2\\&&&&&&0&0&0&0&0&0\\&&&&&&&0&0&0&0&0\\&&&&&&&&156&22l&-156&-22l\\&&\text{symmetry}&&&&&&&4l^2&-22l&-4l^2\\&&&&&&&&&&156&22l\\&&&&&&&&&&&4l^2\end{bmatrix} \tag{9.30}$$

$$\boldsymbol{c}_{3c}^{e}=\frac{c_{y3}l}{420}\begin{bmatrix}0&0&0&0&0&0&0&0&0&0&0&0\\&0&0&0&0&0&0&0&0&0&0&0\\&&0&0&0&0&0&0&0&0&0&0\\&&&0&0&0&0&0&0&0&0&0\\&&&&156&-22l&0&0&0&0&54&13l\\&&&&&4l^2&0&0&0&0&-13l&-3l^2\\&&&&&&0&0&0&0&0&0\\&&&&&&&0&0&0&0&0\\&&&&&&&&0&0&0&0\\&&\text{symmetry}&&&&&&&0&0&0\\&&&&&&&&&&156&22l\\&&&&&&&&&&&4l^2\end{bmatrix} \tag{9.31}$$

where c_{y1}, c_{y2} and c_{y3} refer to the damping coefficients of the rail pads and fasteners, the cement asphalt mortar, and the antifreeze subgrade, respectively.

Based on the finite element assembling rule, the global mass matrix, the global stiffness matrix, and the global damping matrix of the slab track structure can be obtained by assembling the element mass matrix (9.13), the element stiffness matrix (9.26), and the element damping matrix (9.27).

$$\begin{aligned}\boldsymbol{m}_{l}&=\sum_{e}\boldsymbol{m}_{l}^{e}=\sum_{e}\left(\boldsymbol{m}_{r}^{e}+\boldsymbol{m}_{s}^{e}+\boldsymbol{m}_{h}^{e}\right)\\ \boldsymbol{k}_{l}&=\sum_{e}\boldsymbol{k}_{l}^{e}=\sum_{e}\left(\boldsymbol{k}_{r}^{e}+\boldsymbol{k}_{s}^{e}+\boldsymbol{k}_{h}^{e}+\boldsymbol{k}_{1c}^{e}+\boldsymbol{k}_{2c}^{e}+\boldsymbol{k}_{3c}^{e}\right)\\ \boldsymbol{c}_{l}&=\sum_{e}\boldsymbol{c}_{l}^{e}=\sum_{e}\left(\boldsymbol{c}_{r}^{e}+\boldsymbol{c}_{1c}^{e}+\boldsymbol{c}_{2c}^{e}+\boldsymbol{c}_{3c}^{e}\right)\end{aligned} \tag{9.32}$$

9.3 Slab Track–Bridge Element Model

9.3.1 Basic Assumptions

To establish the vertical vibration model of the train-slab track-bridge coupling system by using finite element analysis, it is assumed:

(1) Only vertical vibration effect of the vehicle-slab track-bridge coupling system is considered.
(2) The upper structure in the vehicle and track coupling system is a complete locomotive or rolling stock unit with a primary and secondary suspension systems, in which bouncing and pitch motion for both vehicle and bogie are considered.
(3) Since the vehicle and the slab track-bridge coupling system are bilaterally symmetrical about the centerline of the track, only half of the coupling system is used for ease of calculation.
(4) The hypothesis of a linear relationship between two elastic contact cylinders perpendicular to each other is used in coupling the vehicle and the track.
(5) The lower structure in the coupling system is the slab track and the bridge where rails are discretized into 2D beam element supported by discrete viscoelastic supports; the stiffness coefficient and the damping coefficient of the rail pads and fasteners are denoted with k_{y1} and $c_{y1,}$ respectively.
(6) Precast track slab is discretized as 2D beam element with continuous viscoelastic support. The stiffness coefficient and the damping coefficient of the cement asphalt mortar layer beneath the precast track slab are denoted by k_{y2} and $c_{y2,}$ respectively.
(7) Concrete bridge is discretized as 2D beam element.
(8) The study is focused on the middle element of the track slab-bridge coupling system. Relevant matrix of the end elements can be deduced in the same way.

9.3.2 Three-Layer Slab Track and Bridge Element Model

As shown in three-layer slab track and bridge element model (Fig. 9.3), v_1, v_4 are vertical displacements of the rail, θ_1, θ_4 are rotational angles of the rail, v_2, v_5 are vertical displacements of the precast slab, θ_2, θ_5 are rotational angles of the precast slab, v_3, v_6 are vertical displacement of the concrete bridge, and θ_3, θ_6 are rotational angles of the concrete bridge.

The node displacement vector of the three-layer slab track and bridge element is defined as follows:

$$\boldsymbol{a}^e = \{ v_1 \quad \theta_1 \quad v_2 \quad \theta_2 \quad v_3 \quad \theta_3 \quad v_4 \quad \theta_4 \quad v_5 \quad \theta_5 \quad v_6 \quad \theta_6 \}^{\mathrm{T}} \tag{9.33}$$

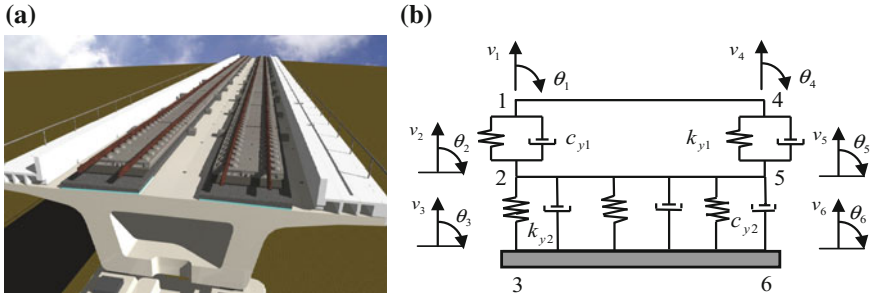

Fig. 9.3 Three-layer slab track-bridge element model. **a** Cross-sectional diagram of elevated slab track and **b** three-layer slab track and bridge element

where v_i and θ_i (i = 1, 2, 3, …, 6) denote vertical displacement and rotational angle of the slab track-bridge element at note i, respectively.

9.3.3 Mass Matrix of the Slab Track-Bridge Element

The mass matrix of the slab track-bridge element is composed of the mass of the rail, the mass of the precast slab, and the mass of the concrete bridge. The mass matrix is as follows:

$$\boldsymbol{m}_{\mathrm{l}}^{e} = \boldsymbol{m}_{\mathrm{r}}^{e} + \boldsymbol{m}_{\mathrm{s}}^{e} + \boldsymbol{m}_{\mathrm{b}}^{e} \tag{9.34}$$

where $\boldsymbol{m}_{\mathrm{r}}^{e}$ is mass matrix of the rail; $\boldsymbol{m}_{\mathrm{s}}^{e}$ is mass matrix of the precast slab; and $\boldsymbol{m}_{\mathrm{b}}^{e}$ is mass matrix of the concrete bridge.

$$\boldsymbol{m}_{\mathrm{r}}^{e} = \frac{\rho_{\mathrm{r}} A_{\mathrm{r}} l}{420} \begin{bmatrix} 156 & -22l & 0 & 0 & 0 & 0 & 54 & 13l & 0 & 0 & 0 & 0 \\ & 4l^2 & 0 & 0 & 0 & 0 & -13l & -3l^2 & 0 & 0 & 0 & 0 \\ & & 0 & 0 & 0 & 0 & 0 & 0 & 0 & 0 & 0 & 0 \\ & & & 0 & 0 & 0 & 0 & 0 & 0 & 0 & 0 & 0 \\ & & & & 0 & 0 & 0 & 0 & 0 & 0 & 0 & 0 \\ & & & & & 0 & 0 & 0 & 0 & 0 & 0 & 0 \\ & & & & & & 156 & 22l & 0 & 0 & 0 & 0 \\ & & & & & & & 4l^2 & 0 & 0 & 0 & 0 \\ & & & & & & & & 0 & 0 & 0 & 0 \\ & & & \text{symmetry} & & & & & & 0 & 0 & 0 \\ & & & & & & & & & & 0 & 0 \\ & & & & & & & & & & & 0 \end{bmatrix} \tag{9.35}$$

$$\boldsymbol{m}_{\mathrm{s}}^{e}=\frac{\rho_{\mathrm{s}}A_{\mathrm{s}}l}{420}\begin{bmatrix}0&0&0&0&0&0&0&0&0&0&0&0\\&0&0&0&0&0&0&0&0&0&0&0\\&&156&-22l&0&0&0&0&54&13l&0&0\\&&&4l^2&0&0&0&0&-13l&-3l^2&0&0\\&&&&0&0&0&0&0&0&0&0\\&&&&&0&0&0&0&0&0&0\\&&&&&&0&0&0&0&0&0\\&&&&&&&0&0&0&0&0\\&&&&&&&&156&22l&0&0\\&&\text{symmetry}&&&&&&&4l^2&0&0\\&&&&&&&&&&0&0\\&&&&&&&&&&&0\end{bmatrix} \tag{9.36}$$

$$\boldsymbol{m}_{\mathrm{b}}^{e}=\frac{\rho_{\mathrm{b}}A_{\mathrm{b}}l}{420}\begin{bmatrix}0&0&0&0&0&0&0&0&0&0&0&0\\&0&0&0&0&0&0&0&0&0&0&0\\&&0&0&0&0&0&0&0&0&0&0\\&&&0&0&0&0&0&0&0&0&0\\&&&&156&-22l&0&0&0&0&54&13l\\&&&&&4l^2&0&0&0&0&-13l&-3l^2\\&&&&&&0&0&0&0&0&0\\&&&&&&&0&0&0&0&0\\&&&&&&&&0&0&0&0\\&&\text{symmetry}&&&&&&&0&0&0\\&&&&&&&&&&156&22l\\&&&&&&&&&&&4l^2\end{bmatrix} \tag{9.37}$$

where ρ_{r}, ρ_{s}, and ρ_{b} refer to the density of the rail, the precast slab, and the concrete bridge, respectively, while A_{r}, A_{s}, and A_{b} denote the cross-sectional area of the rail, the precast slab, and the concrete bridge, respectively; l means the length of the slab track-bridge element.

9.3.4 Stiffness Matrix of the Slab Track-Bridge Element

The stiffness matrix of the slab track-bridge element is made up the stiffness caused by the bending potential energy of the rail, the precast slab, and the concrete bridge, the stiffness of discrete elastic supports caused by the rail pads and fasteners, and the continuous elastic supporting stiffness of the cement asphalt mortar layer.

$$\boldsymbol{k}_{\mathrm{l}}^{e} = \boldsymbol{k}_{\mathrm{r}}^{e} + \boldsymbol{k}_{\mathrm{s}}^{e} + \boldsymbol{k}_{\mathrm{b}}^{e} + \boldsymbol{k}_{1\mathrm{c}}^{e} + \boldsymbol{k}_{2\mathrm{c}}^{e} \tag{9.38}$$

where $\boldsymbol{k}_{\mathrm{l}}^{e}$ denotes the stiffness matrix of the slab track-bridge element

$$\boldsymbol{k}_{\mathrm{r}}^{e} = \frac{E_{\mathrm{r}} I_{\mathrm{r}}}{l^3} \begin{bmatrix} 12 & -6l & 0 & 0 & 0 & 0 & -12 & -6l & 0 & 0 & 0 & 0 \\ & 4l^2 & 0 & 0 & 0 & 0 & 6l & 2l^2 & 0 & 0 & 0 & 0 \\ & & 0 & 0 & 0 & 0 & 0 & 0 & 0 & 0 & 0 & 0 \\ & & & 0 & 0 & 0 & 0 & 0 & 0 & 0 & 0 & 0 \\ & & & & 0 & 0 & 0 & 0 & 0 & 0 & 0 & 0 \\ & & & & & 0 & 0 & 0 & 0 & 0 & 0 & 0 \\ & & & & & & 12 & 6l & 0 & 0 & 0 & 0 \\ & & & & & & & 4l^2 & 0 & 0 & 0 & 0 \\ & & & & & & & & 0 & 0 & 0 & 0 \\ & & & \text{symmetry} & & & & & & 0 & 0 & 0 \\ & & & & & & & & & & 0 & 0 \\ & & & & & & & & & & & 0 \end{bmatrix} \tag{9.39}$$

where $\boldsymbol{k}_{\mathrm{r}}^{e}$ is the bending stiffness matrix of the rail; E_{r} and I_{r} are the elasticity modulus of the rail and the sectional moment of inertia around the horizontal axis, respectively.

$$\boldsymbol{k}_{\mathrm{s}}^{e} = \frac{E_{\mathrm{s}} I_{\mathrm{s}}}{l^3} \begin{bmatrix} 0 & 0 & 0 & 0 & 0 & 0 & 0 & 0 & 0 & 0 & 0 & 0 \\ & 0 & 0 & 0 & 0 & 0 & 0 & 0 & 0 & 0 & 0 & 0 \\ & & 12 & -6l & 0 & 0 & 0 & 0 & -12 & -6l & 0 & 0 \\ & & & 4l^2 & 0 & 0 & 0 & 0 & 6l & 2l^2 & 0 & 0 \\ & & & & 0 & 0 & 0 & 0 & 0 & 0 & 0 & 0 \\ & & & & & 0 & 0 & 0 & 0 & 0 & 0 & 0 \\ & & & & & & 0 & 0 & 0 & 0 & 0 & 0 \\ & & & & & & & 0 & 0 & 0 & 0 & 0 \\ & & & & & & & & 12 & 6l & 0 & 0 \\ & & \text{symmetry} & & & & & & & 4l^2 & 0 & 0 \\ & & & & & & & & & & 0 & 0 \\ & & & & & & & & & & & 0 \end{bmatrix} \tag{9.40}$$

$\boldsymbol{k}_{\mathrm{s}}^{e}$ is the bending stiffness matrix of the precast slab; E_{s} and I_{s} are the elasticity modulus of the precast slab and the sectional moment of inertia around the horizontal axis, respectively.

$$\boldsymbol{k}_{\mathrm{b}}^{e}=\frac{E_{\mathrm{b}}I_{\mathrm{b}}}{l^{3}}\begin{bmatrix}0 & 0 & 0 & 0 & 0 & 0 & 0 & 0 & 0 & 0 & 0 & 0\\ & 0 & 0 & 0 & 0 & 0 & 0 & 0 & 0 & 0 & 0 & 0\\ & & 0 & 0 & 0 & 0 & 0 & 0 & 0 & 0 & 0 & 0\\ & & & 0 & 0 & 0 & 0 & 0 & 0 & 0 & 0 & 0\\ & & & & 12 & -6l & 0 & 0 & 0 & 0 & -12 & -6l\\ & & & & & 4l^{2} & 0 & 0 & 0 & 0 & 6l & 2l^{2}\\ & & & & & & 0 & 0 & 0 & 0 & 0 & 0\\ & & & & & & & 0 & 0 & 0 & 0 & 0\\ & & & & & & & & 0 & 0 & 0 & 0\\ & & \text{symmetry} & & & & & & & 0 & 0 & 0\\ & & & & & & & & & & 12 & 6l\\ & & & & & & & & & & & 4l^{2}\end{bmatrix} \tag{9.41}$$

$\boldsymbol{k}_{\mathrm{b}}^{e}$ is the bending stiffness matrix of the concrete bridge; E_{b} and I_{b} are the elasticity modulus of concrete bridge and the sectional moment of inertia around the horizontal axis, respectively.

$$\boldsymbol{k}_{1\mathrm{c}}^{e}=\frac{1}{2}\begin{bmatrix}k_{y1} & 0 & -k_{y1} & 0 & 0 & 0 & 0 & 0 & 0 & 0 & 0 & 0\\ & 0 & 0 & 0 & 0 & 0 & 0 & 0 & 0 & 0 & 0 & 0\\ & & k_{y1} & 0 & 0 & 0 & 0 & 0 & 0 & 0 & 0 & 0\\ & & & 0 & 0 & 0 & 0 & 0 & 0 & 0 & 0 & 0\\ & & & & 0 & 0 & 0 & 0 & 0 & 0 & 0 & 0\\ & & & & & 0 & 0 & 0 & 0 & 0 & 0 & 0\\ & & & & & & k_{y1} & 0 & -k_{y1} & 0 & 0 & 0\\ & & & & & & & 0 & 0 & 0 & 0 & 0\\ & & & & & & & & k_{y1} & 0 & 0 & 0\\ & & \text{symmetry} & & & & & & & 0 & 0 & 0\\ & & & & & & & & & & 0 & 0\\ & & & & & & & & & & & 0\end{bmatrix} \tag{9.42}$$

$\boldsymbol{k}_{1\mathrm{c}}^{e}$ denotes the stiffness matrix caused by discrete elastic support of the rail pads and fasteners, while k_{y1} refers to the stiffness coefficient of the rail pads and fasteners.

$$\boldsymbol{k}_{2\mathrm{c}}^{e}=\frac{k_{y2}l}{420}\begin{bmatrix}0 & 0 & 0 & 0 & 0 & 0 & 0 & 0 & 0 & 0 & 0 & 0\\ & 0 & 0 & 0 & 0 & 0 & 0 & 0 & 0 & 0 & 0 & 0\\ & & 156 & -22l & -156 & 22l & 0 & 0 & 54 & 13l & -54 & -13l\\ & & & 4l^{2} & 22l & -4l^{2} & 0 & 0 & -13l & -3l^{2} & 13l & 3l^{2}\\ & & & & 156 & -22l & 0 & 0 & -54 & -13l & 54 & 13l\\ & & & & & 4l^{2} & 0 & 0 & 13l & 3l^{2} & -13l & -3l^{2}\\ & & & & & & 0 & 0 & 0 & 0 & 0 & 0\\ & & & & & & & 0 & 0 & 0 & 0 & 0\\ & & & & & & & & 156 & 22l & -156 & -22l\\ & & \text{symmetry} & & & & & & & 4l^{2} & -22l & -4l^{2}\\ & & & & & & & & & & 156 & 22l\\ & & & & & & & & & & & 4l^{2}\end{bmatrix} \tag{9.43}$$

$\boldsymbol{k}_{2c}^{e}$ denotes the stiffness matrix caused by continuous elastic support of the cement asphalt mortar layer, while k_{y2} refers to the stiffness coefficient of the cement asphalt mortar layer.

9.3.5 Damping Matrix of the Slab Track-Bride Element

Damping matrix of the slab track-bride element is composed of the damping caused by the internal friction of the rail, the precast slab, and the concrete bridge, the damping caused by the rail pads and fasteners, and the damping of the cement asphalt mortar layer.

$$\boldsymbol{c}_{l}^{e} = \boldsymbol{c}_{r}^{e} + \boldsymbol{c}_{1c}^{e} + \boldsymbol{c}_{2c}^{e} \tag{9.44}$$

where $\boldsymbol{c}_{r}^{e}$ is the damping matrix caused by internal friction of the rail, the precast slab, and the concrete bridge, generally adopting proportional damping; $\boldsymbol{c}_{1c}^{e}$ and $\boldsymbol{c}_{2c}^{e}$ denote the damping matrix caused by the rail pads and fasteners and the asphalt cement mortar layer, respectively.

$$\boldsymbol{c}_{r}^{e} = \alpha_{r}\boldsymbol{m}_{r}^{e} + \beta_{r}\boldsymbol{k}_{r}^{e} + \alpha_{s}\boldsymbol{m}_{s}^{e} + \beta_{s}\boldsymbol{k}_{s}^{e} + \alpha_{b}\boldsymbol{m}_{b}^{e} + \beta_{b}\boldsymbol{m}_{b}^{e} \tag{9.45}$$

α_r, β_r, α_s, β_s, α_b, and β_b denote the proportional damping coefficients of the rail, the precast slab, and the concrete bridge, respectively.

$$\boldsymbol{c}_{1c}^{e} = \frac{1}{2}\begin{bmatrix} c_{y1} & 0 & -c_{y1} & 0 & 0 & 0 & 0 & 0 & 0 & 0 & 0 & 0 \\ & 0 & 0 & 0 & 0 & 0 & 0 & 0 & 0 & 0 & 0 & 0 \\ & & c_{y1} & 0 & 0 & 0 & 0 & 0 & 0 & 0 & 0 & 0 \\ & & & 0 & 0 & 0 & 0 & 0 & 0 & 0 & 0 & 0 \\ & & & & 0 & 0 & 0 & 0 & 0 & 0 & 0 & 0 \\ & & & & & 0 & 0 & 0 & 0 & 0 & 0 & 0 \\ & & & & & & c_{y1} & 0 & -c_{y1} & 0 & 0 & 0 \\ & & & & & & & 0 & 0 & 0 & 0 & 0 \\ & & & & & & & & c_{y1} & 0 & 0 & 0 \\ & & \text{symmety} & & & & & & & 0 & 0 & 0 \\ & & & & & & & & & & 0 & 0 \\ & & & & & & & & & & & 0 \end{bmatrix} \tag{9.46}$$

$$\boldsymbol{c}_{2c}^{e}=\frac{c_{y2}l}{420}\begin{bmatrix}0 & 0 & 0 & 0 & 0 & 0 & 0 & 0 & 0 & 0 & 0 & 0\\ & 0 & 0 & 0 & 0 & 0 & 0 & 0 & 0 & 0 & 0 & 0\\ & & 156 & -22l & -156 & 22l & 0 & 0 & 54 & 13l & -54 & -13l\\ & & & 4l^2 & 22l & -4l^2 & 0 & 0 & -13l & -3l^2 & 13l & 3l^2\\ & & & & 156 & -22l & 0 & 0 & -54 & -13l & 54 & 13l\\ & & & & & 4l^2 & 0 & 0 & 13l & 3l^2 & -13l & -3l^2\\ & & & & & & 0 & 0 & 0 & 0 & 0 & 0\\ & & & & & & & 0 & 0 & 0 & 0 & 0\\ & & & & & & & & 156 & 22l & -156 & -22l\\ & & \text{symmetry} & & & & & & & 4l^2 & -22l & -4l^2\\ & & & & & & & & & & 156 & 22l\\ & & & & & & & & & & & 4l^2\end{bmatrix} \tag{9.47}$$

c_{y1} and c_{y2} refer to the damping coefficients of the rail pads and fasteners and the cement asphalt mortar, respectively.

Based on the finite element assembling rule, the global mass matrix, the global stiffness matrix, and the global damping matrix of the train-track-bridge coupling system can be obtained by assembling the element mass matrix (9.34), the element stiffness matrix (9.38), and the element damping matrix (9.44).

$$\begin{aligned}\boldsymbol{m}_l&=\sum_e \boldsymbol{m}_l^e=\sum_e\left(\boldsymbol{m}_r^e+\boldsymbol{m}_s^e+\boldsymbol{m}_b^e\right)\\ \boldsymbol{k}_l&=\sum_e \boldsymbol{k}_l^e=\sum_e\left(\boldsymbol{k}_r^e+\boldsymbol{k}_s^e+\boldsymbol{k}_b^e+\boldsymbol{k}_{1c}^e+\boldsymbol{k}_{2c}^e\right)\\ \boldsymbol{c}_l&=\sum_e \boldsymbol{c}_l^e=\sum_e\left(\boldsymbol{c}_r^e+\boldsymbol{c}_{1c}^e+\boldsymbol{c}_{2c}^e\right)\end{aligned} \tag{9.48}$$

By using Lagrange equation, the finite element equation of the ballast track structure, or the slab track structure, or the elevated track structure is available.

$$\boldsymbol{m}_l\ddot{\boldsymbol{a}}_l+\boldsymbol{c}_l\dot{\boldsymbol{a}}_l+\boldsymbol{k}_l\boldsymbol{a}_l=\boldsymbol{Q}_l \tag{9.49}$$

where $\boldsymbol{Q}_l$ denotes the global nodal load vector for the ballast track structure, or the slab track structure, or the elevated track structure.

9.4 Vehicle Element Model

The vehicle element model has 26 degrees of freedom, as shown in Fig. 9.4, where 10 degrees of freedom are used to describe the vertical movement of a car, and 16 degrees of freedom are associated with the rail displacements. In the model, $2M_c$ and $2J_c$ are mass and pitch inertia for the rigid body of the vehicle; $2M_t$ and $2J_t$ are mass and pitch inertia for the bogie; $2k_{s1}$, $2k_{s2}$ and $2c_{s1}$, $2c_{s2}$ stand for stiffness and damping coefficients for the primary and secondary suspension systems of the

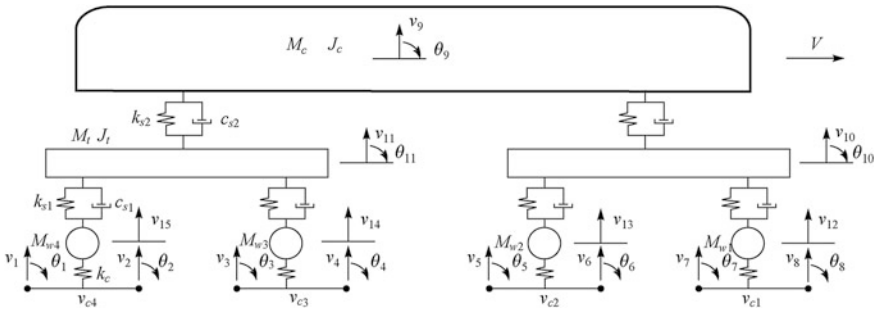

Fig. 9.4 Vehicle element model

vehicle, respectively; $M_{wi}(i = 1, 2, 3, 4)$ is the ith wheel mass; and k_c is the contact stiffness between the wheel and the rail.

The nodal displacement vector for this vehicle element is defined as follows:

$$\boldsymbol{a}^e = \{ v_1 \quad \theta_1 \quad v_2 \quad \theta_2 \quad v_3 \quad \theta_3 \quad v_4 \quad \theta_4 \quad v_5 \quad \theta_5 \quad v_6 \quad \theta_6 \quad v_7 \quad \theta_7 \quad v_8 \quad \theta_8 \quad v_9 \quad \theta_9 \quad v_{10} \quad v_{11} \quad \theta_{10} \quad \theta_{11} \quad v_{12} \quad v_{13} \quad v_{14} \quad v_{15} \}^{\mathrm{T}} \tag{9.50}$$

where v_i and $\theta_i(i = 1, 2, 3, \ldots, 8)$ are the rail vertical displacement and the rail angular displacement for node i; $v_{ci}(i = 1, 2, 3, 4)$ in Fig. 9.4 is the rail vertical displacement at the ith wheel-rail contact point; v_9 and θ_9 are the vertical displacement of bouncing vibration and the angular displacement of pitch vibration of car body, respectively; v_i and $\theta_i(i = 10, 11)$ are the vertical displacement of bouncing vibration and the angular displacement of pitch vibration for these two bogies; and $v_i(i = 12, 13, 14, 15)$ is the vertical displacement for the ith wheel. In terms of track irregularity, the amplitude is denoted by η. The irregularity amplitudes of four wheel-rail contact points are denoted by η_1, η_2, η_3, and η_4, respectively.

In order to formulate finite element equation for the vehicle element, the following Lagrange equation may be used.

$$\frac{d}{dt}\frac{\partial L}{\partial \dot{\boldsymbol{a}}} - \frac{\partial L}{\partial \boldsymbol{a}} + \frac{\partial R}{\partial \dot{\boldsymbol{a}}} = 0 \tag{9.51}$$

where L is Lagrange function, $L = T\text{-}\Pi$; T and Π are kinetic and potential energy, respectively; R is dissipation energy; $\boldsymbol{a}$ and $\dot{\boldsymbol{a}}$ are nodal displacement vector and nodal velocity vector, respectively.

9.4.1 Potential Energy of the Vehicle Element

$$\begin{aligned}\Pi_{\mathrm{u}} = &\frac{1}{2}k_{s2}(v_9 - v_{10} - \theta_9 l_2)^2 + \frac{1}{2}k_{s2}(v_9 - v_{11} + \theta_9 l_2)^2 + \frac{1}{2}k_{s1}(v_{10} - v_{12} - \theta_{10} l_1)^2 \\ &+ \frac{1}{2}k_{s1}(v_{10} - v_{13} + \theta_{10} l_1)^2 + \frac{1}{2}k_{s1}(v_{11} - v_{14} - \theta_{11} l_1)^2 + \frac{1}{2}k_{s1}(v_{11} - v_{15} + \theta_{11} l_1)^2 \\ &+ \frac{1}{2}k_{c}(v_{12} - v_{c1} - \eta_1)^2 + \frac{1}{2}k_{c}(v_{13} - v_{c2} - \eta_2)^2 + \frac{1}{2}k_{c}(v_{14} - v_{c3} - \eta_3)^2 + \frac{1}{2}k_{c}(v_{15} - v_{c4} - \eta_4)^2 \\ &+ v_9 M_{\mathrm{c}} g + v_{10} M_t g + v_{11} M_{\mathrm{t}} g + v_{12} M_{\mathrm{w}} g + v_{13} M_{\mathrm{w}} g + v_{14} M_{\mathrm{w}} g + v_{15} M_{\mathrm{w}} g\end{aligned} \tag{9.52}$$

where

$$\begin{aligned}
v_9 - v_{10} - \theta_9 l_2 &= \{0\ \ 0\ \ 0\ \ 0\ \ 0\ \ 0\ \ 0\ \ 0\ \ 0\ \ 0\ \ 0\ \ 0\ \ 0\ \ 0\ \ 0\ \ 0\ \ 0 \\
&\quad 1\ \ -l_2\ \ -1\ \ 0\ \ 0\ \ 0\ \ 0\ \ 0\ \ 0\ \ 0\}\boldsymbol{a}^e = \boldsymbol{N}_{9-10}^{\mathrm{T}}\boldsymbol{a}^e \\
\dot{v}_9 - \dot{v}_{10} - \dot{\theta}_9 l_2 &= \{0\ \ 0\ \ 0\ \ 0\ \ 0\ \ 0\ \ 0\ \ 0\ \ 0\ \ 0\ \ 0\ \ 0\ \ 0\ \ 0\ \ 0\ \ 0\ \ 0 \\
&\quad 1\ \ -l_2\ \ -1\ \ 0\ \ 0\ \ 0\ \ 0\ \ 0\ \ 0\ \ 0\}\dot{\boldsymbol{a}}^e = \boldsymbol{N}_{9-10}^{\mathrm{T}}\dot{\boldsymbol{a}}^e \\
v_9 - v_{11} + \theta_9 l_2 &= \{0\ \ 0\ \ 0\ \ 0\ \ 0\ \ 0\ \ 0\ \ 0\ \ 0\ \ 0\ \ 0\ \ 0\ \ 0\ \ 0\ \ 0\ \ 0\ \ 0 \\
&\quad 1\ \ l_2\ \ 0\ \ -1\ \ 0\ \ 0\ \ 0\ \ 0\ \ 0\ \ 0\}\boldsymbol{a}^e = \boldsymbol{N}_{9-11}^{\mathrm{T}}\boldsymbol{a}^e \\
\dot{v}_9 - \dot{v}_{11} + \dot{\theta}_9 l_2 &= \{0\ \ 0\ \ 0\ \ 0\ \ 0\ \ 0\ \ 0\ \ 0\ \ 0\ \ 0\ \ 0\ \ 0\ \ 0\ \ 0\ \ 0\ \ 0\ \ 0 \\
&\quad 1\ \ l_2\ \ 0\ \ -1\ \ 0\ \ 0\ \ 0\ \ 0\ \ 0\ \ 0\}\dot{\boldsymbol{a}}^e = \boldsymbol{N}_{9-11}^{\mathrm{T}}\dot{\boldsymbol{a}}^e \\
v_{10} - v_{12} - \theta_{10} l_1 &= \{0\ \ 0\ \ 0\ \ 0\ \ 0\ \ 0\ \ 0\ \ 0\ \ 0\ \ 0\ \ 0\ \ 0\ \ 0\ \ 0\ \ 0\ \ 0\ \ 0 \\
&\quad 0\ \ 0\ \ 1\ \ 0\ \ -l_1\ \ 0\ \ -1\ \ 0\ \ 0\ \ 0\}\boldsymbol{a}^e = \boldsymbol{N}_{10-12}^{\mathrm{T}}\boldsymbol{a}^e \\
\dot{v}_{10} - \dot{v}_{12} - \dot{\theta}_{10} l_1 &= \{0\ \ 0\ \ 0\ \ 0\ \ 0\ \ 0\ \ 0\ \ 0\ \ 0\ \ 0\ \ 0\ \ 0\ \ 0\ \ 0\ \ 0\ \ 0\ \ 0 \\
&\quad 0\ \ 0\ \ 1\ \ 0\ \ -l_1\ \ 0\ \ -1\ \ 0\ \ 0\ \ 0\}\dot{\boldsymbol{a}}^e = \boldsymbol{N}_{10-12}^{\mathrm{T}}\dot{\boldsymbol{a}}^e \\
v_{10} - v_{13} + \theta_{10} l_1 &= \{0\ \ 0\ \ 0\ \ 0\ \ 0\ \ 0\ \ 0\ \ 0\ \ 0\ \ 0\ \ 0\ \ 0\ \ 0\ \ 0\ \ 0\ \ 0\ \ 0 \\
&\quad 0\ \ 0\ \ 1\ \ 0\ \ l_1\ \ 0\ \ 0\ \ -1\ \ 0\ \ 0\}\boldsymbol{a}^e = \boldsymbol{N}_{10-13}^{\mathrm{T}}\boldsymbol{a}^e \\
\dot{v}_{10} - \dot{v}_{13} + \dot{\theta}_{10} l_1 &= \{0\ \ 0\ \ 0\ \ 0\ \ 0\ \ 0\ \ 0\ \ 0\ \ 0\ \ 0\ \ 0\ \ 0\ \ 0\ \ 0\ \ 0\ \ 0\ \ 0 \\
&\quad 0\ \ 0\ \ 1\ \ 0\ \ l_1\ \ 0\ \ 0\ \ -1\ \ 0\ \ 0\}\dot{\boldsymbol{a}}^e = \boldsymbol{N}_{10-13}^{\mathrm{T}}\dot{\boldsymbol{a}}^e \\
v_{11} - v_{14} - \theta_{11} l_1 &= \{0\ \ 0\ \ 0\ \ 0\ \ 0\ \ 0\ \ 0\ \ 0\ \ 0\ \ 0\ \ 0\ \ 0\ \ 0\ \ 0\ \ 0\ \ 0\ \ 0 \\
&\quad 0\ \ 0\ \ 0\ \ 1\ \ 0\ \ -l_1\ \ 0\ \ 0\ \ -1\ \ 0\}\boldsymbol{a}^e = \boldsymbol{N}_{11-14}^{\mathrm{T}}\boldsymbol{a}^e \\
\dot{v}_{11} - \dot{v}_{14} - \dot{\theta}_{11} l_1 &= \{0\ \ 0\ \ 0\ \ 0\ \ 0\ \ 0\ \ 0\ \ 0\ \ 0\ \ 0\ \ 0\ \ 0\ \ 0\ \ 0\ \ 0\ \ 0\ \ 0 \\
&\quad 0\ \ 0\ \ 0\ \ 1\ \ 0\ \ -l_1\ \ 0\ \ 0\ \ -1\ \ 0\}\dot{\boldsymbol{a}}^e = \boldsymbol{N}_{11-14}^{\mathrm{T}}\dot{\boldsymbol{a}}^e \\
v_{11} - v_{15} + \theta_{11} l_1 &= \{0\ \ 0\ \ 0\ \ 0\ \ 0\ \ 0\ \ 0\ \ 0\ \ 0\ \ 0\ \ 0\ \ 0\ \ 0\ \ 0\ \ 0\ \ 0\ \ 0 \\
&\quad 0\ \ 0\ \ 0\ \ 1\ \ 0\ \ l_1\ \ 0\ \ 0\ \ 0\ \ -1\}\boldsymbol{a}^e = \boldsymbol{N}_{11-15}^{\mathrm{T}}\boldsymbol{a}^e \\
\dot{v}_{11} - \dot{v}_{15} + \dot{\theta}_{11} l_1 &= \{0\ \ 0\ \ 0\ \ 0\ \ 0\ \ 0\ \ 0\ \ 0\ \ 0\ \ 0\ \ 0\ \ 0\ \ 0\ \ 0\ \ 0\ \ 0\ \ 0 \\
&\quad 0\ \ 0\ \ 0\ \ 1\ \ 0\ \ l_1\ \ 0\ \ 0\ \ 0\ \ -1\}\dot{\boldsymbol{a}}^e = \boldsymbol{N}_{11-15}^{\mathrm{T}}\dot{\boldsymbol{a}}^e
\end{aligned} \tag{9.53}$$

$$
\begin{aligned}
v_{12}-v_{c1} &= \{0\ \ 0\ \ 0\ \ 0\ \ 0\ \ 0\ \ 0\ \ 0\ \ 0\ \ 0\ \ 0\ \ 0\ \ -N_1\ \ -N_2\ \ -N_3\ \ -N_4 \\
&\quad\ 0\ \ 0\ \ 0\ \ 0\ \ 0\ \ 0\ \ 1\ \ 0\ \ 0\ \ 0\}\boldsymbol{a}^e = \boldsymbol{N}_{c1}^{\mathrm{T}}\boldsymbol{a}^e \\
v_{13}-v_{c2} &= \{0\ \ 0\ \ 0\ \ 0\ \ 0\ \ 0\ \ 0\ \ 0\ \ -N_1\ \ -N_2\ \ -N_3\ \ -N_4\ \ 0\ \ 0\ \ 0\ \ 0 \\
&\quad\ 0\ \ 0\ \ 0\ \ 0\ \ 0\ \ 0\ \ 0\ \ 1\ \ 0\ \ 0\}\boldsymbol{a}^e = \boldsymbol{N}_{c2}^{\mathrm{T}}\boldsymbol{a}^e \\
v_{14}-v_{c3} &= \{0\ \ 0\ \ 0\ \ 0\ \ -N_1\ \ -N_2\ \ -N_3\ \ -N_4\ \ 0\ \ 0\ \ 0\ \ 0\ \ 0\ \ 0\ \ 0\ \ 0 \\
&\quad\ 0\ \ 0\ \ 0\ \ 0\ \ 0\ \ 0\ \ 0\ \ 0\ \ 1\ \ 0\}\boldsymbol{a}^e = \boldsymbol{N}_{c3}^{\mathrm{T}}\boldsymbol{a}^e \\
v_{15}-v_{c4} &= \{-N_1\ \ -N_2\ \ -N_3\ \ -N_4\ \ 0\ \ 0\ \ 0\ \ 0\ \ 0\ \ 0\ \ 0\ \ 0\ \ 0\ \ 0\ \ 0 \\
&\quad\ 0\ \ 0\ \ 0\ \ 0\ \ 0\ \ 0\ \ 0\ \ 0\ \ 0\ \ 1\}\boldsymbol{a}^e = \boldsymbol{N}_{c4}^{\mathrm{T}}\boldsymbol{a}^e
\end{aligned}
\tag{9.54}
$$

$$
\begin{aligned}
v_9 &= \{0\ \ 0\ \ 0\ \ 0\ \ 0\ \ 0\ \ 0\ \ 0\ \ 0\ \ 0\ \ 0\ \ 0\ \ 0\ \ 0\ \ 0\ \ 0 \\
&\quad\ 1\ \ 0\ \ 0\ \ 0\ \ 0\ \ 0\ \ 0\ \ 0\ \ 0\ \ 0\}\boldsymbol{a}^e = \boldsymbol{N}_9^{\mathrm{T}}\boldsymbol{a}^e \\
v_{10} &= \{0\ \ 0\ \ 0\ \ 0\ \ 0\ \ 0\ \ 0\ \ 0\ \ 0\ \ 0\ \ 0\ \ 0\ \ 0\ \ 0\ \ 0\ \ 0 \\
&\quad\ 0\ \ 0\ \ 1\ \ 0\ \ 0\ \ 0\ \ 0\ \ 0\ \ 0\ \ 0\}\boldsymbol{a}^e = \boldsymbol{N}_{10}^{\mathrm{T}}\boldsymbol{a}^e \\
v_{11} &= \{0\ \ 0\ \ 0\ \ 0\ \ 0\ \ 0\ \ 0\ \ 0\ \ 0\ \ 0\ \ 0\ \ 0\ \ 0\ \ 0\ \ 0\ \ 0 \\
&\quad\ 0\ \ 0\ \ 0\ \ 1\ \ 0\ \ 0\ \ 0\ \ 0\ \ 0\ \ 0\}\boldsymbol{a}^e = \boldsymbol{N}_{11}^{\mathrm{T}}\boldsymbol{a}^e \\
v_{12} &= \{0\ \ 0\ \ 0\ \ 0\ \ 0\ \ 0\ \ 0\ \ 0\ \ 0\ \ 0\ \ 0\ \ 0\ \ 0\ \ 0\ \ 0\ \ 0 \\
&\quad\ 0\ \ 0\ \ 0\ \ 0\ \ 0\ \ 0\ \ 1\ \ 0\ \ 0\ \ 0\}\boldsymbol{a}^e = \boldsymbol{N}_{12}^{\mathrm{T}}\boldsymbol{a}^e \\
v_{13} &= \{0\ \ 0\ \ 0\ \ 0\ \ 0\ \ 0\ \ 0\ \ 0\ \ 0\ \ 0\ \ 0\ \ 0\ \ 0\ \ 0\ \ 0\ \ 0 \\
&\quad\ 0\ \ 0\ \ 0\ \ 0\ \ 0\ \ 0\ \ 0\ \ 1\ \ 0\ \ 0\}\boldsymbol{a}^e = \boldsymbol{N}_{13}^{\mathrm{T}}\boldsymbol{a}^e \\
v_{14} &= \{0\ \ 0\ \ 0\ \ 0\ \ 0\ \ 0\ \ 0\ \ 0\ \ 0\ \ 0\ \ 0\ \ 0\ \ 0\ \ 0\ \ 0\ \ 0 \\
&\quad\ 0\ \ 0\ \ 0\ \ 0\ \ 0\ \ 0\ \ 0\ \ 0\ \ 1\ \ 0\}\boldsymbol{a}^e = \boldsymbol{N}_{14}^{\mathrm{T}}\boldsymbol{a}^e \\
v_{15} &= \{0\ \ 0\ \ 0\ \ 0\ \ 0\ \ 0\ \ 0\ \ 0\ \ 0\ \ 0\ \ 0\ \ 0\ \ 0\ \ 0\ \ 0\ \ 0 \\
&\quad\ 0\ \ 0\ \ 0\ \ 0\ \ 0\ \ 0\ \ 0\ \ 0\ \ 0\ \ 1\}\boldsymbol{a}^e = \boldsymbol{N}_{15}^{\mathrm{T}}\boldsymbol{a}^e
\end{aligned}
\tag{9.55}
$$

From Eq. (9.54), v_{c1}, v_{c2}, v_{c3}, and v_{c4} can be expressed by the interpolation of the rail displacements at two ends.

$$
v_{c4} = N_1 v_1 + N_2 \theta_1 + N_3 v_2 + N_4 \theta_2 \tag{9.56}
$$

where N_1–N_4 are interpolation functions as shown in Eq. (9.22). Substituting the local coordinate of the wheel-rail contact point into N_1–N_4 and then into the (9.54), one can obtain $\boldsymbol{N}_{c4.}$ In the same way, substituting the local coordinate x_{c1}, x_{c2}, and x_{c3} into interpolation functions, one can obtain $\boldsymbol{N}_{c1}$, $\boldsymbol{N}_{c2}$, and $\boldsymbol{N}_{c3}$, respectively.

Substituting Eqs. (9.53), (9.54), and (9.55) into (9.52), it has

$$\begin{aligned}\Pi_V &= \frac{1}{2}\boldsymbol{a}^{eT}\{k_{s2}\boldsymbol{N}_{9-10}\boldsymbol{N}_{9-10}^{T} + k_{s2}\boldsymbol{N}_{9-11}\boldsymbol{N}_{9-11}^{T} + k_{s1}\boldsymbol{N}_{10-12}\boldsymbol{N}_{10-12}^{T} + k_{s1}\boldsymbol{N}_{10-13}\boldsymbol{N}_{10-13}^{T} + k_{s1}\boldsymbol{N}_{11-14}\boldsymbol{N}_{11-14}^{T} \\ &\quad + k_{s1}\boldsymbol{N}_{11-15}\boldsymbol{N}_{11-15}^{T} + k_c\boldsymbol{N}_{c1}\boldsymbol{N}_{c1}^{T} + k_c\boldsymbol{N}_{c2}\boldsymbol{N}_{c2}^{T} + k_c\boldsymbol{N}_{c3}\boldsymbol{N}_{c3}^{T} + k_c\boldsymbol{N}_{c4}\boldsymbol{N}_{c4}^{T}\}\boldsymbol{a}^{e} \\ &\quad - \boldsymbol{a}^{eT}(k_c\eta_1\boldsymbol{N}_{c1} + k_c\eta_2\boldsymbol{N}_{c2} + k_c\eta_3\boldsymbol{N}_{c3} + k_c\eta_4\boldsymbol{N}_{c4}) + \frac{1}{2}k_c(\eta_1^2 + \eta_2^2 + \eta_3^2 + \eta_4^2) \\ &\quad + \boldsymbol{a}^{eT}(M_c g\boldsymbol{N}_9 + M_t g\boldsymbol{N}_{10} + M_t g\boldsymbol{N}_{11} + M_w g\boldsymbol{N}_{12} + M_w g\boldsymbol{N}_{13} + M_w g\boldsymbol{N}_{14} + M_w g\boldsymbol{N}_{15}) \\ &= \frac{1}{2}\boldsymbol{a}^{eT}\{\boldsymbol{k}_1 + \boldsymbol{k}_2 + \boldsymbol{k}_3 + \boldsymbol{k}_4 + \boldsymbol{k}_5 + \boldsymbol{k}_6 + \boldsymbol{k}_{c1} + \boldsymbol{k}_{c2} + \boldsymbol{k}_{c3} + \boldsymbol{k}_{c4}\}\boldsymbol{a}^{e} \\ &\quad - \boldsymbol{a}^{eT}(k_c\eta_1\boldsymbol{N}_{c1} + k_c\eta_2\boldsymbol{N}_{c2} + k_c\eta_3\boldsymbol{N}_{c3} + k_c\eta_4\boldsymbol{N}_{c4}) + \frac{1}{2}k_c(\eta_1^2 + \eta_2^2 + \eta_3^2 + \eta_4^2) \\ &\quad + \boldsymbol{a}^{eT}(M_c g\boldsymbol{N}_9 + M_t g\boldsymbol{N}_{10} + M_t g\boldsymbol{N}_{11} + M_w g\boldsymbol{N}_{12} + M_w g\boldsymbol{N}_{13} + M_w g\boldsymbol{N}_{14} + M_w g\boldsymbol{N}_{15}) \\ &= \frac{1}{2}\boldsymbol{a}^{eT}\boldsymbol{k}_u^{e}\boldsymbol{a}^{e} + \boldsymbol{a}^{eT}\boldsymbol{Q}_u^{e} + \frac{1}{2}k_c(\eta_1^2 + \eta_2^2 + \eta_3^2 + \eta_4^2)\end{aligned} \tag{9.57}$$

where $\boldsymbol{k}_u^e$ denotes the stiffness matrix of the vehicle element, while $\boldsymbol{Q}_u^e$ denotes the nodal load vector.

$$\boldsymbol{k}_u^e = \boldsymbol{k}_v + \boldsymbol{k}_c \tag{9.58}$$

$$\boldsymbol{Q}_u^e = \boldsymbol{Q}_v + \boldsymbol{Q}_\eta \tag{9.59}$$

$$\begin{aligned}\boldsymbol{k}_v &= \boldsymbol{k}_1 + \boldsymbol{k}_2 + \boldsymbol{k}_3 + \cdots \boldsymbol{k}_6 = k_{s2}\boldsymbol{N}_{9-10}\boldsymbol{N}_{9-10}^{T} + k_{s2}\boldsymbol{N}_{9-11}\boldsymbol{N}_{9-11}^{T} \\ &\quad + k_{s1}\boldsymbol{N}_{10-12}\boldsymbol{N}_{10-12}^{T} + k_{s1}\boldsymbol{N}_{10-13}\boldsymbol{N}_{10-13}^{T} + k_{s1}\boldsymbol{N}_{11-14}\boldsymbol{N}_{11-14}^{T} + k_{s1}\boldsymbol{N}_{11-15}\boldsymbol{N}_{11-15}^{T} \\ &= \begin{bmatrix}\boldsymbol{0}_{16\times16} & \\ & \boldsymbol{k}_{ve}\end{bmatrix}_{26\times26}\end{aligned} \tag{9.60}$$

$$\boldsymbol{k}_{ve} = \begin{bmatrix}
2k_{s2} & 0 & -k_{s2} & -k_{s2} & 0 & 0 & 0 & 0 & 0 & 0 \\
 & 2k_{s2}l_2^2 & k_{s2}l_2 & -k_{s2}l_2 & 0 & 0 & 0 & 0 & 0 & 0 \\
 & & 2k_{s1} + k_{s2} & 0 & 0 & 0 & -k_{s1} & -k_{s1} & 0 & 0 \\
 & & & 2k_{s1} + k_{s2} & 0 & 0 & 0 & 0 & -k_{s1} & -k_{s1} \\
 & & & & 2k_{s1}l_1^2 & 0 & k_{s1}l_1 & -k_{s1}l_1 & 0 & 0 \\
 & & & & & 2k_{s1}l_1^2 & 0 & 0 & k_{s1}l_1 & -k_{s1}l_1 \\
 & & & & & & k_{s1} & 0 & 0 & 0 \\
 & & & & & & & k_{s1} & 0 & 0 \\
 & & \text{symmetry} & & & & & & k_{s1} & 0 \\
 & & & & & & & & & k_{s1}
\end{bmatrix} \tag{9.61}$$

where $\boldsymbol{0}_{16\times16}$ is the rank 16 zero matrix, $2l_1$ is the wheelbase, and $2l_2$ is the distance between the central lines of two bogies.

$$
\begin{aligned}
\boldsymbol{k}_{\mathrm{c}} &= \boldsymbol{k}_{\mathrm{c1}} + \boldsymbol{k}_{\mathrm{c2}} + \boldsymbol{k}_{\mathrm{c3}} + \boldsymbol{k}_{\mathrm{c4}} \\
&= k_{\mathrm{c}}\boldsymbol{N}_{\mathrm{c1}}\boldsymbol{N}_{\mathrm{c1}}^{\mathrm{T}} + k_{\mathrm{c}}\boldsymbol{N}_{\mathrm{c2}}\boldsymbol{N}_{\mathrm{c2}}^{\mathrm{T}} + k_{\mathrm{c}}\boldsymbol{N}_{\mathrm{c3}}\boldsymbol{N}_{\mathrm{c3}}^{\mathrm{T}} + k_{\mathrm{c}}\boldsymbol{N}_{\mathrm{c4}}\boldsymbol{N}_{\mathrm{c4}}^{\mathrm{T}} \\
&= k_{\mathrm{c}}\begin{bmatrix}
\boldsymbol{NN}_{\mathrm{c4}} & \boldsymbol{0} & \boldsymbol{0} & \boldsymbol{0} & \boldsymbol{0} & \boldsymbol{NI}_{\mathrm{c4}} \\
 & \boldsymbol{NN}_{\mathrm{c3}} & \boldsymbol{0} & \boldsymbol{0} & \boldsymbol{0} & \boldsymbol{NI}_{\mathrm{c3}} \\
 & & \boldsymbol{NN}_{\mathrm{c2}} & \boldsymbol{0} & \boldsymbol{0} & \boldsymbol{NI}_{\mathrm{c2}} \\
 & & & \boldsymbol{NN}_{\mathrm{c1}} & \boldsymbol{0} & \boldsymbol{NI}_{\mathrm{c1}} \\
\text{symmetry} & & & & \boldsymbol{0}_{6\times 6} & \boldsymbol{0} \\
 & & & & & \boldsymbol{I}_{4\times 4}
\end{bmatrix}_{26\times 26}
\end{aligned}
\tag{9.62}
$$

where $\boldsymbol{I}_{4\times 4}$ is the rank 4 identity matrix.

$$
\boldsymbol{NN}_{\mathrm{ci}} = \begin{bmatrix}
N_1^2 & N_1N_2 & N_1N_3 & N_1N_4 \\
 & N_2^2 & N_2N_3 & N_2N_4 \\
 & & N_3^2 & N_3N_4 \\
\text{symmetry} & & & N_4^2
\end{bmatrix}_{x_{\mathrm{ci}}}
\tag{9.63}
$$

$$
\boldsymbol{NI}_{\mathrm{c1}} = \begin{bmatrix}
-N_1 & 0 & 0 & 0 \\
-N_2 & 0 & 0 & 0 \\
-N_3 & 0 & 0 & 0 \\
-N_4 & 0 & 0 & 0
\end{bmatrix}_{x_{\mathrm{c1}}}
\tag{9.64}
$$

$$
\boldsymbol{NI}_{\mathrm{c2}} = \begin{bmatrix}
0 & -N_1 & 0 & 0 \\
0 & -N_2 & 0 & 0 \\
0 & -N_3 & 0 & 0 \\
0 & -N_4 & 0 & 0
\end{bmatrix}_{x_{\mathrm{c2}}}
\tag{9.65}
$$

$$
\boldsymbol{NI}_{\mathrm{c3}} = \begin{bmatrix}
0 & 0 & -N_1 & 0 \\
0 & 0 & -N_2 & 0 \\
0 & 0 & -N_3 & 0 \\
0 & 0 & -N_4 & 0
\end{bmatrix}_{x_{\mathrm{c3}}}
\tag{9.66}
$$

$$
\boldsymbol{NI}_{\mathrm{c4}} = \begin{bmatrix}
0 & 0 & 0 & -N_1 \\
0 & 0 & 0 & -N_2 \\
0 & 0 & 0 & -N_3 \\
0 & 0 & 0 & -N_4
\end{bmatrix}_{x_{\mathrm{c4}}}
\tag{9.67}
$$

$$
\begin{aligned}
\boldsymbol{Q}_{\mathrm{v}} = \{ & 0 \quad 0 \quad 0 \quad 0 \quad 0 \quad 0 \quad 0 \quad 0 \quad 0 \quad 0 \quad 0 \quad 0 \quad 0 \quad 0 \quad 0 \quad -M_{\mathrm{c}}g \quad 0 \quad -M_{\mathrm{t}}g \quad -M_{\mathrm{t}}g \\
& 0 \quad 0 \quad -M_{\mathrm{w}}g \quad -M_{\mathrm{w}}g \quad -M_{\mathrm{w}}g \quad -M_{\mathrm{w}}g \}^{\mathrm{T}}
\end{aligned}
\tag{9.68}
$$

$$
\boldsymbol{Q}_{\eta} = k_{\mathrm{c}}\eta_1\boldsymbol{N}_{\mathrm{c1}} + k_{\mathrm{c}}\eta_2\boldsymbol{N}_{\mathrm{c2}} + k_{\mathrm{c}}\eta_3\boldsymbol{N}_{\mathrm{c3}} + k_{\mathrm{c}}\eta_4\boldsymbol{N}_{\mathrm{c4}}
\tag{9.69}
$$

9.4.2 Kinetic Energy of the Vehicle Element

$$T_{\mathrm{v}} = \frac{1}{2}M_{\mathrm{c}}\dot{v}_9^2 + \frac{1}{2}J_{\mathrm{c}}\dot{\theta}_9^2 + \frac{1}{2}M_{\mathrm{t}}\dot{v}_{10}^2 + \frac{1}{2}M_{\mathrm{t}}\dot{v}_{11}^2 + \frac{1}{2}J_{\mathrm{t}}\dot{\theta}_{10}^2 + \frac{1}{2}J_{\mathrm{t}}\dot{\theta}_{11}^2 + \frac{1}{2}M_{\mathrm{w}}\dot{v}_{12}^2 + \frac{1}{2}M_{\mathrm{w}}\dot{v}_{13}^2 + \frac{1}{2}M_{\mathrm{w}}\dot{v}_{14}^2 + \frac{1}{2}M_{\mathrm{w}}\dot{v}_{15}^2 = \frac{1}{2}\dot{\boldsymbol{a}}^{e\mathrm{T}}\boldsymbol{m}_{\mathrm{u}}^{e}\dot{\boldsymbol{a}}^{e} \tag{9.70}$$

where $\boldsymbol{m}_{\mathrm{u}}^{e}$ denotes the mass matrix of the vehicle element.

$$\boldsymbol{m}_{\mathrm{u}}^{e} = \begin{bmatrix} \mathbf{0}_{16\times 16} & \\ & \boldsymbol{m}_{\mathrm{ve}} \end{bmatrix}_{26\times 26} \tag{9.71}$$

$$\boldsymbol{m}_{\mathrm{ve}} = \mathrm{diag}(\, M_{\mathrm{c}} \quad J_{\mathrm{c}} \quad M_{\mathrm{t}} \quad M_{\mathrm{t}} \quad J_{\mathrm{t}} \quad J_{\mathrm{t}} \quad M_{\mathrm{w}} \quad M_{\mathrm{w}} \quad M_{\mathrm{w}} \quad M_{\mathrm{w}} \,) \tag{9.72}$$

9.4.3 Dissipated Energy of the Vehicle Element

$$R_{\mathrm{V}} = \frac{1}{2}c_{\mathrm{s2}}\left(\dot{v}_9 - \dot{v}_{10} - \dot{\theta}_9 l_2\right)^2 + \frac{1}{2}c_{\mathrm{s2}}\left(\dot{v}_9 - \dot{v}_{11} + \dot{\theta}_9 l_2\right)^2 + \frac{1}{2}c_{\mathrm{s1}}\left(\dot{v}_{10} - \dot{v}_{12} - \dot{\theta}_{10} l_1\right)^2 + \frac{1}{2}c_{\mathrm{s1}}\left(\dot{v}_{10} - \dot{v}_{13} + \dot{\theta}_{10} l_1\right)^2 + \frac{1}{2}c_{\mathrm{s1}}\left(\dot{v}_{11} - \dot{v}_{14} - \dot{\theta}_{11} l_1\right)^2 + \frac{1}{2}c_{\mathrm{s1}}\left(\dot{v}_{11} - \dot{v}_{15} + \dot{\theta}_{11} l_1\right)^2 = \frac{1}{2}\dot{\boldsymbol{a}}^{e\mathrm{T}}\boldsymbol{c}_{\mathrm{u}}^{e}\dot{\boldsymbol{a}}^{e} \tag{9.73}$$

where $\boldsymbol{c}_{\mathrm{u}}^{e}$ denotes the damping matrix of the vehicle element.

$$\boldsymbol{c}_{\mathrm{u}}^{e} = \begin{bmatrix} \mathbf{0}_{16\times 16} & \\ & \boldsymbol{c}_{\mathrm{ve}} \end{bmatrix}_{26\times 26} \tag{9.74}$$

$$\boldsymbol{c}_{\mathrm{ve}} = \begin{bmatrix} 2c_{\mathrm{s2}} & 0 & -c_{\mathrm{s2}} & -c_{\mathrm{s2}} & 0 & 0 & 0 & 0 & 0 & 0 \\ & 2c_{\mathrm{s2}}l_2^2 & c_{\mathrm{s2}}l_2 & -c_{\mathrm{s2}}l_2 & 0 & 0 & 0 & 0 & 0 & 0 \\ & & 2c_{\mathrm{s1}}+c_{\mathrm{s2}} & 0 & 0 & 0 & -c_{\mathrm{s1}} & -c_{\mathrm{s1}} & 0 & 0 \\ & & & 2c_{\mathrm{s1}}+c_{\mathrm{s2}} & 0 & 0 & 0 & 0 & -c_{\mathrm{s1}} & -c_{\mathrm{s1}} \\ & & & & 2c_{\mathrm{s1}}l_1^2 & 0 & c_{\mathrm{s1}}l_1 & -c_{\mathrm{s1}}l_1 & 0 & 0 \\ & & & & & 2c_{\mathrm{s1}}l_1^2 & 0 & 0 & c_{\mathrm{s1}}l_1 & -c_{\mathrm{s1}}l_1 \\ & & & & & & c_{\mathrm{s1}} & 0 & 0 & 0 \\ & & & & & & & c_{\mathrm{s1}} & 0 & 0 \\ & & \text{symmetry} & & & & & & c_{\mathrm{s1}} & 0 \\ & & & & & & & & & c_{\mathrm{s1}} \end{bmatrix} \tag{9.75}$$

9.5 Finite Element Equation of the Vehicle-Track Coupling System

The finite element equation of the vehicle-track coupling system (or the track-bridge coupling system) includes two elements, namely the track element (ballast track, slab track, or slab track-bridge) and the vehicle element. Stiffness matrix, mass matrix, and damping matrix of the track element are denoted by $\boldsymbol{k}_{\mathrm{l}}^{e}$, $\boldsymbol{m}_{\mathrm{l}}^{e}$, and $\boldsymbol{c}_{\mathrm{l}}^{e}$, the calculation of which has been illustrated in Sects. 9.2–9.4, respectively. Stiffness matrix, mass matrix, and damping matrix of the vehicle element are denoted by $\boldsymbol{k}_{\mathrm{u}}^{e}$, $\boldsymbol{m}_{\mathrm{u}}^{e}$, and $\boldsymbol{c}_{\mathrm{u}}^{e}$, the calculation of which has been given in Eqs. (9.58), (9.71) and (9.74). In numerical calculation, it only needs to assemble the global stiffness matrix, the global mass matrix, the global damping matrix, and the global load vector of the track structure once. And in each following calculating time step, by assembling the stiffness matrix, the mass matrix, the damping matrix, and the load vector of the vehicle element into the global stiffness matrix, the global mass matrix, the global damping matrix, and the global load vector of track structure with the standard finite element assembling rule, one can obtain the global stiffness matrix, the global mass matrix, the global damping matrix, and the global load vector of the vehicle-track coupling system(or the track-bridge coupling system).

The resulted dynamic finite element equation of the vehicle-track (or the track-bridge) coupling system is as follows:

$$\boldsymbol{M}\ddot{\boldsymbol{a}} + \boldsymbol{C}\dot{\boldsymbol{a}} + \boldsymbol{K}\boldsymbol{a} = \boldsymbol{Q} \tag{9.76}$$

where $\boldsymbol{M}$, $\boldsymbol{C}$, $\boldsymbol{K}$, and $\boldsymbol{Q}$ denote the global mass matrix, the global damping matrix, the global stiffness matrix, and the global load vector of the vehicle-track (or the track-bridge) coupling system, respectively.

$$\begin{aligned} &\boldsymbol{M} = \sum_{e} \left(\boldsymbol{m}_{\mathrm{l}} + \boldsymbol{m}_{\mathrm{u}}^{e}\right), \quad \boldsymbol{C} = \sum_{e} \left(\boldsymbol{c}_{\mathrm{l}} + \boldsymbol{c}_{\mathrm{u}}^{e}\right), \quad \boldsymbol{K} = \sum_{e} \left(\boldsymbol{k}_{\mathrm{l}} + \boldsymbol{k}_{\mathrm{u}}^{e}\right), \\ &\boldsymbol{Q} = \sum_{e} \left(\boldsymbol{Q}_{\mathrm{l}} + \boldsymbol{Q}_{\mathrm{u}}^{e}\right) \end{aligned} \tag{9.77}$$

The numerical solution to the dynamic finite element equation of the vehicle-track (or the track-bridge) coupling system is available by using direct integration method, such as Newmark integration method. If the solution $\boldsymbol{a}_{\mathrm{t}}, \dot{\boldsymbol{a}}_{\mathrm{t}}, \ddot{\boldsymbol{a}}_{\mathrm{t}}$ of Eq. (9.76) at time step (t) is known, the solution $\boldsymbol{a}_{t+\Delta t}$ at time step $(t + \Delta t)$ can be obtained by Eq. (9.78).

$$(\boldsymbol{K} + c_0\boldsymbol{M} + c_1\boldsymbol{C})\boldsymbol{a}_{\mathrm{t}+\Delta\mathrm{t}} = \boldsymbol{Q}_{\mathrm{t}+\Delta\mathrm{t}} + \boldsymbol{M}(c_0\boldsymbol{a}_{\mathrm{t}} + c_2\dot{\boldsymbol{a}}_{\mathrm{t}} + c_3\ddot{\boldsymbol{a}}_{\mathrm{t}}) + \boldsymbol{C}(c_1\boldsymbol{a}_{\mathrm{t}} + c_4\dot{\boldsymbol{a}}_{\mathrm{t}} + c_5\ddot{\boldsymbol{a}}_{\mathrm{t}}) \tag{9.78}$$

Substituting $\boldsymbol{a}_t, \dot{\boldsymbol{a}}_t, \ddot{\boldsymbol{a}}_t$ and $\boldsymbol{a}_{t+\Delta t}$ into the following equation, the velocity $\dot{\boldsymbol{a}}_{t+\Delta t}$ and the acceleration $\ddot{\boldsymbol{a}}_{t+\Delta t}$ at time step $(t+\Delta t)$ can be calculated as follows:

$$\begin{aligned} \ddot{\boldsymbol{a}}_{t+\Delta t} &= c_0(\boldsymbol{a}_{t+\Delta t} - \boldsymbol{a}_t) - c_2\dot{\boldsymbol{a}}_t - c_3\ddot{\boldsymbol{a}}_t \\ \dot{\boldsymbol{a}}_{t+\Delta t} &= \dot{\boldsymbol{a}}_t + c_6\ddot{\boldsymbol{a}}_t + c_7\ddot{\boldsymbol{a}}_{t+\Delta t} \end{aligned} \tag{9.79}$$

where

$$\begin{aligned} &c_0 = \frac{1}{\alpha\Delta t^2}, \quad c_1 = \frac{\delta}{\alpha\Delta t}, \quad c_2 = \frac{1}{\alpha\Delta t}, \quad c_3 = \frac{1}{2\alpha} - 1 \\ &c_4 = \frac{\delta}{\alpha} - 1, \quad c_5 = \frac{\Delta t}{2}\left(\frac{\delta}{\alpha} - 2\right), \quad c_6 = \Delta t(1-\delta), \quad c_7 = \delta\Delta t \end{aligned} \tag{9.80}$$

Δt denotes the time step; α, δ are Newmark numerical integration parameter. When α, δ equal 0.25 and 0.5, respectively, Newmark numerical integration method is unconditionally stable algorithm.

9.6 Dynamic Analysis of the Train and Track Coupling System

Following are three examples, of which numerical example one is mainly used to verify the algorithm and to analyze the dynamic response of the vehicle and the track structure under a moving vehicle, and numerical Examples 9.2 and 9.3 are used, by consideration of track regularity and track irregularity, respectively.

Example 1 To verify the correctness of the presented model, let us consider the problem defined in Ref. [3]. As shown in Fig. 9.5, the vehicle is simplified into a spring-damping rigid body system with 3 degrees of freedom, and the track is simplified into monolayer continuous elastic beam. Given the train speed is 72 km/h, and the sleeper interval is 0.5 m, let us compare the calculated results of two models.

Track parameters include the following: the elasticity modulus of the rail $E = 2.0 \times 10^5$ MPa, the sectional moment of inertia around the rail horizontal axis $I = 3.06 \times 10^{-5}$ m^4, the track mass per unit length $m = 60$ kg/m, the track stiffness per unit length $k = 1 \times 10^4$ kN/m^2, and the track damping per unit length $c = 4.9$ kNs/m^2.

Vehicle parameters include the following: the wheelset mass $m_1 = 350$ kg, the bogie mass m_2 = 250 kg, the car body mass m_3 = 3500 kg, the wheel-rail contact stiffness $k_1 = 8.0 \times 10^6$ kN/m, the primary spring stiffness $k_2 = 1.26 \times 10^3$ kN/m, the secondary spring stiffness $k_3 = 1.41 \times 10^2$ kN/m, the wheel-rail contact damping $c_1 = 6.7 \times 10^2$ kNs/m, the primary damping coefficient $c_2 = 7.1$ kNs/m, and the secondary damping coefficient $c_3 = 8.87$ kNs/m.

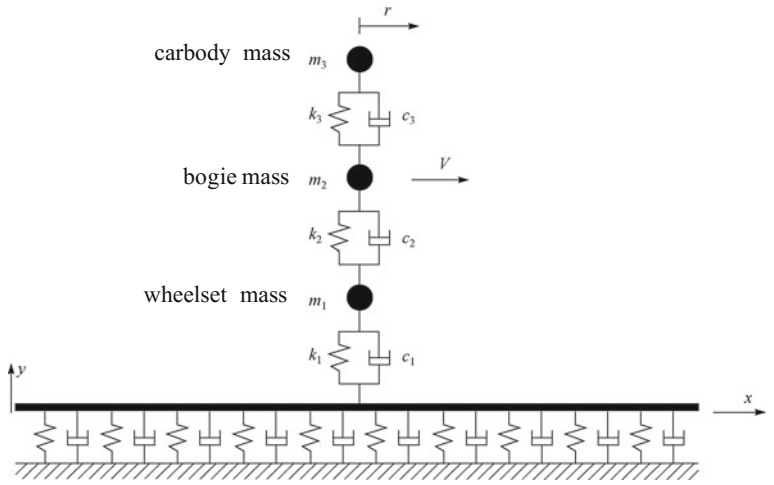

Fig. 9.5 A simplified model for dynamic analysis of the vehicle-track coupling system

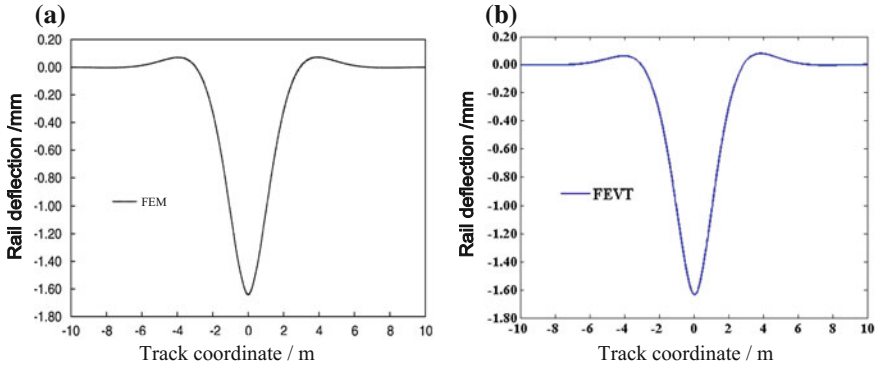

Fig. 9.6 Rail deflection distribution along the track direction. **a** Calculated result of finite element and **b** calculated result of the vehicle and track element

The calculated results are shown in Fig. 9.6, in which Fig. 9.6a shows the results of finite element analysis and Fig. 9.6b shows the results of the vehicle and track element in this chapter. It can be observed that the two results agree well with each other [12].

Example 2 As an application example for the above theory, dynamic response of the vehicle and the track structure is investigated. The vehicle concerned is Chinese high-speed train whose parameters are shown in Table 9.1. The track is the continuously welded rail of 60 kg/m whose flexural modulus is denoted by $EI = 2 \times 6.625\,\text{MN m}^2$, III-type prestressed concrete sleeper with sleeper length of 2.6 m and sleeper interval of 0.60 m, ballast track with ballast thickness 30 cm, and ballast density 2000 kg/m^3. Other parameters are shown in Table 9.2.

Table 9.1 Parameters of Chinese high-speed train HSC

Parameter	Value	Parameter	Value
1/2 car body mass M_c/(kg)	26,000	Vertical stiffness of secondary suspension K_{s2}/(kN/m)	1.72×10^3
1/2 bogie mass M_t/(kg)	1600	Vertical damping of primary suspension C_{s1}/(kN s/m)	500
Wheel mass M_w/(kg)	1400	Vertical damping of secondary suspension C_{s2}/(kN s/m)	196
Car body pitch inertia moment J_c/(kg m^2)	2.31×10^6	Fixed wheelbase $2l_1$/(m)	2.50
Bogie pitch inertia moment J_t/(kg m^2)	3120	Distance between bogie pivot centers $2l_2$/(m)	18.0
Vertical stiffness of primary suspension K_{s1}/(N/m)	1.87×10^6	Wheel radius/m	0.4575

Table 9.2 Parameters of track structure

Track structure	Mass per unit length/(kg)	Stiffness per unit length/(MN/m^2)	Damping per unit length/(kN s/m^2)
Rail	60	133	83.3
Sleeper	284	200	100
Ballast bed	1360	425	150

Assuming that the track is perfect smooth, the train speed is 252 km/h, the time step of Newmark numerical integration method $\Delta t = 0.001$ s, and the wheel-rail contact stiffness coefficient $K_c = 1.325 \times 10^6$ kN/m. In order to reduce the boundary effect of the track, the total track length for computation is 220 m, which includes 20 m extra track lengths on the left and right track ends. The system is discretized to 1 vehicle element and 385 track elements with 1168 nodes.

The calculated results are shown in Fig. 9.7, 9.8, 9.9, 9.10 and 9.11, which denote the deflections of the rail and the sleeper, the vertical accelerations of the rail and the car body, and the wheel-rail contact force, respectively, under a moving vehicle [12]. As is illustrated in them, the four curve peaks of the deflections of the rail and the sleeper are clearly corresponding to the four vehicle wheelsets. In the time history curves of the car body vertical acceleration and the wheel-rail contact force, the calculated results have larger oscillation within the first second because the initial calculation conditions affect the stability of the solution so that the numerical solutions of this period are not accurate. After the first second, calculation tends to stabilize. Because assuming the track is completely smooth, the results of stable dynamic analysis equal the static solution.

Example 3 Dynamic response of the vehicle and the track structure is investigated while the random irregularities of the vertical track profile are considered. To adopt the power spectral density function of track in USA, assuming the irregularity status is level 6, the track irregularity sample is generated by using trigonometric series

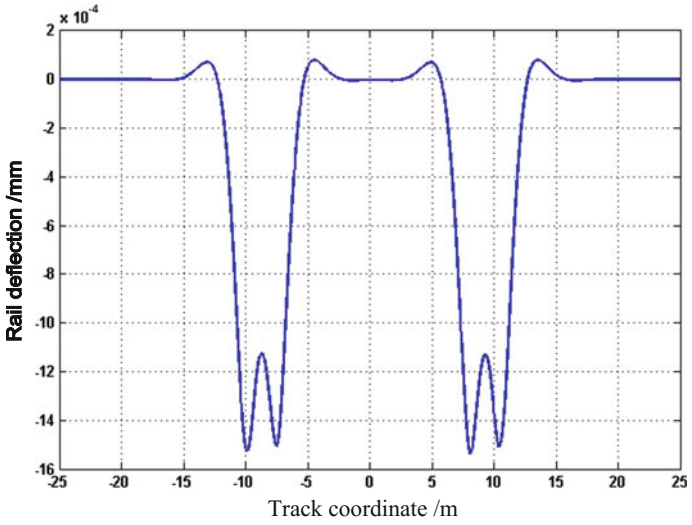

Fig. 9.7 Rail deflection along the track

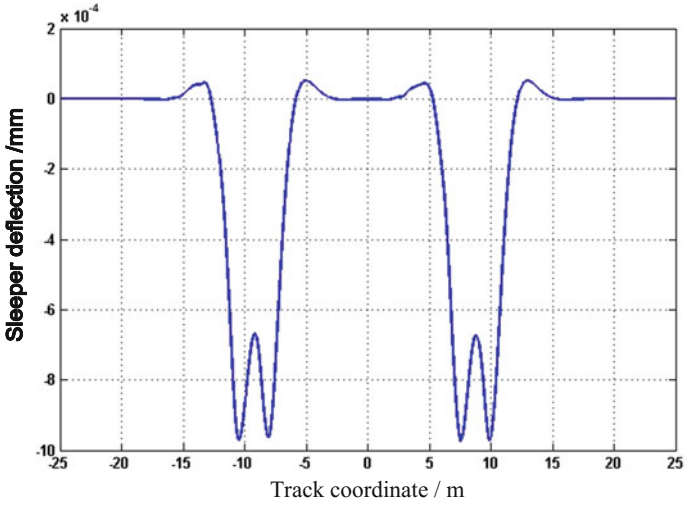

Fig. 9.8 Sleeper deflection along the track

method. By substituting the sample into the Eq. (9.69), the additional dynamic load caused by track irregularity can be obtained. Parameters of the vehicle, the track structure, and the numerical calculation are the same as illustrated in Example 2.

The calculated results are shown in Fig. 9.12, 9.13, 9.14 and 9.15 and 9.16, which denote the deflections of the rail and the sleeper, the vertical accelerations of

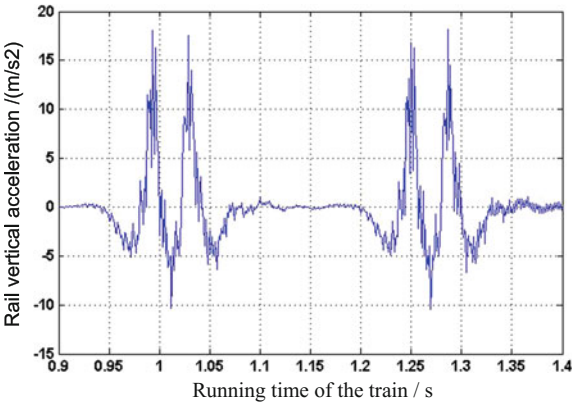

Fig. 9.9 Time history of the vertical acceleration of the rail

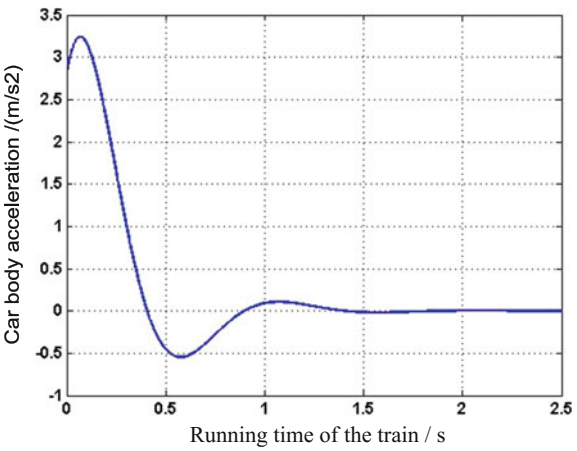

Fig. 9.10 Time history of the vertical acceleration of the car body

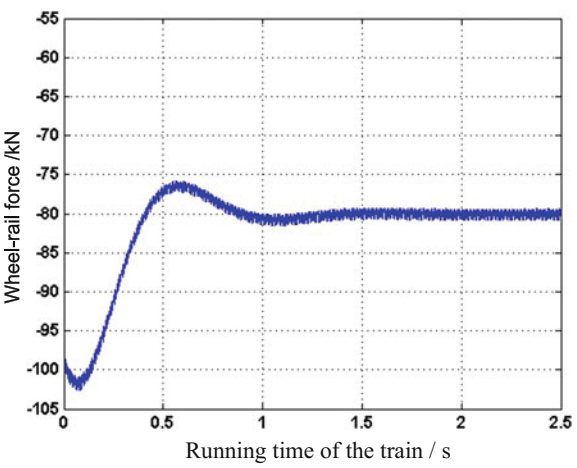

Fig. 9.11 Time history of the wheel-rail contact force

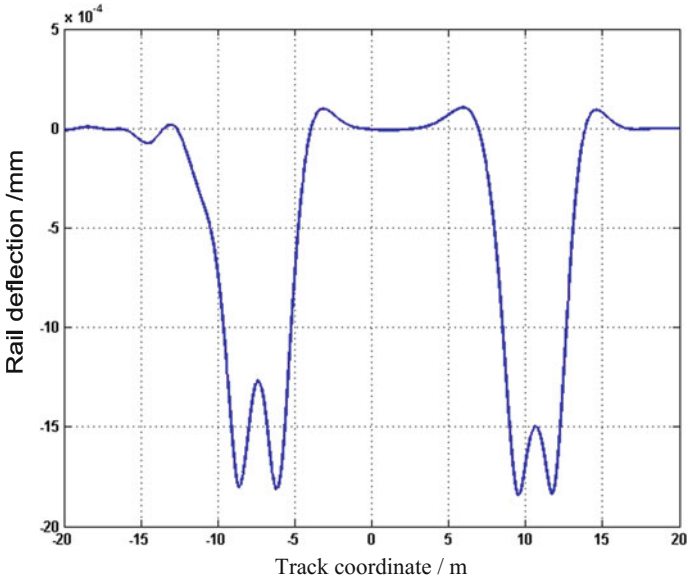

Fig. 9.12 Rail deflection along the track

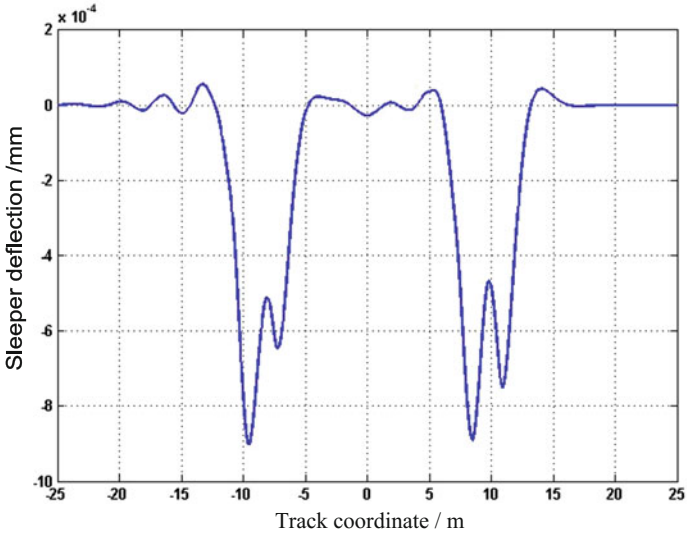

Fig. 9.13 Sleeper deflection along the track

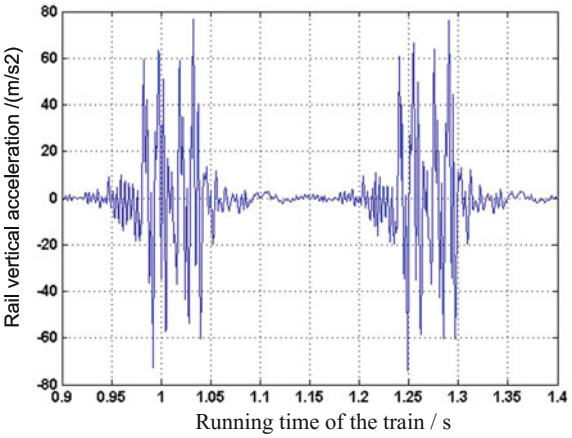

Fig. 9.14 Time history of the rail vertical acceleration

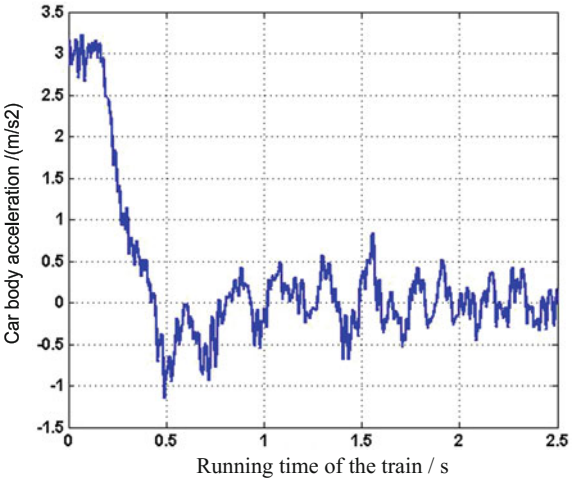

Fig. 9.15 Time history of the vertical acceleration of the car body

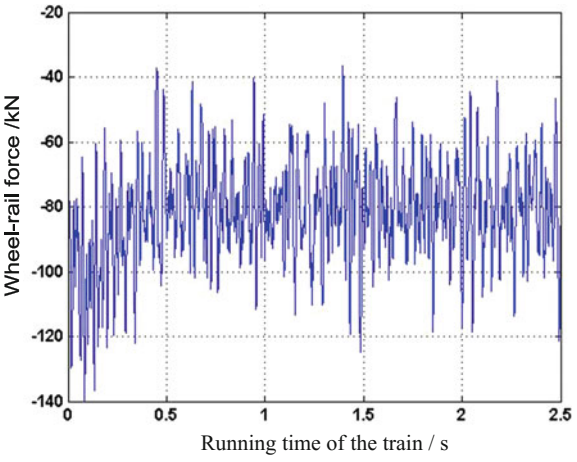

Fig. 9.16 Time history of the wheel-rail contact force

the rail and the car body, and the wheel-rail contact force, respectively, under a moving vehicle [12]. As is illustrated, the track irregularity will trigger additional dynamic load, leading to the increase of dynamic response of the vehicle and the track structure.

References

1. Nielsen JCO (1993) Train/track interaction: coupling of moving and stationary dynamic systems. Ph.D. dissertation, Charles University of technology, Gotebory, Sweden
2. Knothe K, Grassie SL (1993) Modeling of railway track and vehicle/track interaction at high frequencies. Veh Syst Dyn 22(3/4):209–262
3. Koh CG, Ong JSY, Chua DKH, Feng J (2003) Moving element method for train-track dynamics. Int J Numer Meth Eng 56:1549–1567
4. Ono K, Yamada M (1989) Analysis of railway track vibration. J Sound Vib 130:269–297
5. Venancio Filho F (1978) Finite element analysis of structures under moving loads. Shock Vibr Digest 10:27–35
6. Zhai WM (2007) Vehicle-track coupling dynamics (third edition). Science Press, Beijing
7. Lei XY, Sheng XZ (2008) Theoretical research on modern track (second edition). China Railway Publishing House, Beijing
8. Lei XY, Noda NA (2002) Analyses of dynamic response of vehicle and track coupling system with random irregularity of track vertical profile. J Sound Vib 258(1):147–165
9. Lei XY, Zhang B (2010) Influence of track stiffness distribution on vehicle and track interactions in track transition. J Rail Rapid Transit Proc Instit Mech Eng Part F 224(1): 592–604
10. Lei XY, Zhang B (2011) Analysis of dynamic behavior for slab track of high-speed railway based on vehicle and track elements. J Transp Eng 137(4):227–240
11. Lei XY, Zhang B (2011) Analyses of dynamic behavior of track transition with finite elements. J Vib Control 17(11):1733–1747
12. Zhang B (2007) Analyses of dynamic behavior of high speed railway track structure with finite elements. Master's thesis of East China Jiaotong University, Nanchang

Chapter 10
Dynamic Analysis of the Vehicle-Track Coupling System with Finite Elements in a Moving Frame of Reference

With the rapid development of high-speed railways and passenger-dedicated lines, train speed is remarkably improved, and slab track has been the main form for high-speed railways. With giant economic benefit, large increase in railway running speed leads to the adding of wheel-rail interaction, and the vibration noise problem emerges. Slab track structure is a new type of track structure and is very different from the conventional ballast track.

The research of above problems needs the support of dynamics, and therefore it is of great importance to study the effective algorithm of the dynamics in vehicle-track coupling system. Scholars at home and abroad have done huge research in this field. Crassie et al. [1] in Cambridge University have studied the dynamic response of railway track to high frequency vertical excitation; Eisenmann [2] from Munich Engineering & Technology University proposes multi-level theory of ballastless track and applies it into the structure design and load measuring. Chinese Professor Zhai [3, 4] sets up a model of vehicle-track coupling dynamic system and puts it into the study of ballastless track dynamics. Xiang and Zeng [5, 6] propose the principle of "set in the right position" for establishing the dynamic equation of the vehicle-track coupling system and the corresponding matrix assembling method. Lei et al. [7, 8] develop a vibration analysis model and its cross iteration algorithm for the train-track-subgrade nonlinear coupling system with finite element. Xie [9] studies the dynamic response of Winkler beam under a moving load. Koh [10] from Singapore State University proposes moving element method and conducts dynamics analysis of a simplified rail model.

The above mentioned works treat rail beams as continuum and employ some analytical or numerical means to solve the governing differential equations. Furthermore, some boundary conditions have to be introduced artificially to truncate the infinitely long beam at both ends. The moving vehicle will soon come close to the artificial boundary end on the "downstream" side and may even go beyond the artificial boundary end. The numerical solution near the downstream boundary has to be ignored.

X. Lei, *High Speed Railway Track Dynamics*,
DOI 10.1007/978-981-10-2039-1_10

In this chapter, finite elements in a moving frame of reference will be used in the dynamic analysis of the train-slab track coupling system. By establishing the three-layer beam model of the slab track, the element mass, damping, and stiffness matrixes of the slab track in a moving frame of reference are deduced. The research in this chapter adopts the whole vehicle model in Chap. 9, and realizes coupling of the train and the track structure by equilibrium conditions of wheel-rail contact forces and geometrical compatibility conditions, which can effectively avoid the effect from the boundary on the calculated results, thus improving the computation efficiency.

10.1 Basic Assumptions

To establish the three-layer beam element model of CRTS II slab track, it is assumed:

(1) Only vertical vibration effect of the vehicle-track coupling system is considered.
(2) Linear elastic contact between the wheel and the rail is considered
(3) Since the vehicle and the slab track are bilaterally symmetrical about the centerline of the track, only half of the coupling system is used for ease of calculation.
(4) Rails are regarded as 2D beam element with continuous viscoelastic support. The stiffness coefficient and damping coefficient of the rail pads and fasteners are denoted as k_r and c_r, respectively.
(5) Precast track slabs are discretized into 2D beam element with continuous viscoelastic support. The stiffness coefficient and damping coefficient of the cement asphalt mortar layer under the precast track slab are denoted as k_s and c_s, respectively.
(6) The concrete support layer is discretized into 2D beam element with continuous viscoelastic support. The stiffness coefficient and damping coefficient of the subgrade under concrete supporting layer are denoted as k_h and c_h, respectively.
(7) Only the middle part of the track slab is discussed; as for the two sides of the track slab, their related matrices can be deduced with the same method.

10.2 Three-Layer Beam Element Model of the Slab Track in a Moving Frame of Reference

The geometry size of the slab track refers to Fig. 10.1. Figure 10.2 is the simplified three-layer continuous beam model of the slab track.

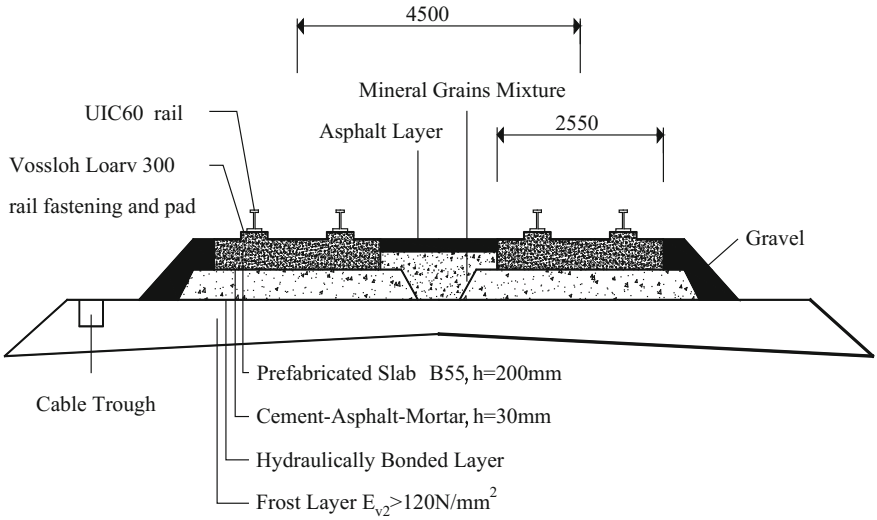

Fig. 10.1 CRTS II slab track

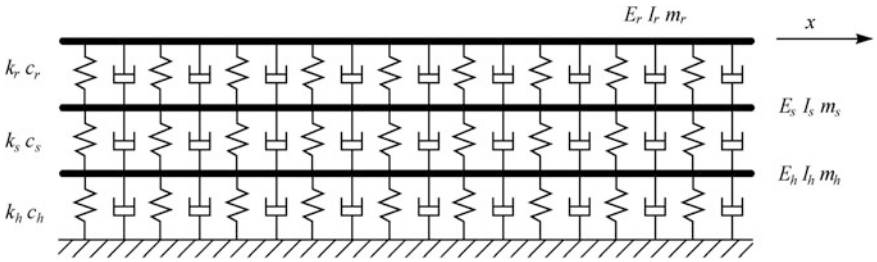

Fig. 10.2 Three-layer continuous beam model of the slab track

In Fig. 10.2, E_r, E_s, and E_h denote the elasticity modulus of the rail, the track slab, and the concrete support layer; I_r, I_s, and I_h denote the moment inertia of the rail, the track slab, and the concrete support layer; m_r, m_s, and m_h denote the mass of unit length of the rail, the track slab, and the concrete support layer.

10.2.1 Governing Equation of the Slab Track

As shown in Fig. 10.3, the dynamic analysis model of the vehicle-track coupling system is divided into upper vehicle subsystem and lower slab track subsystem. The vehicle moves along the track x direction at the speed of V.

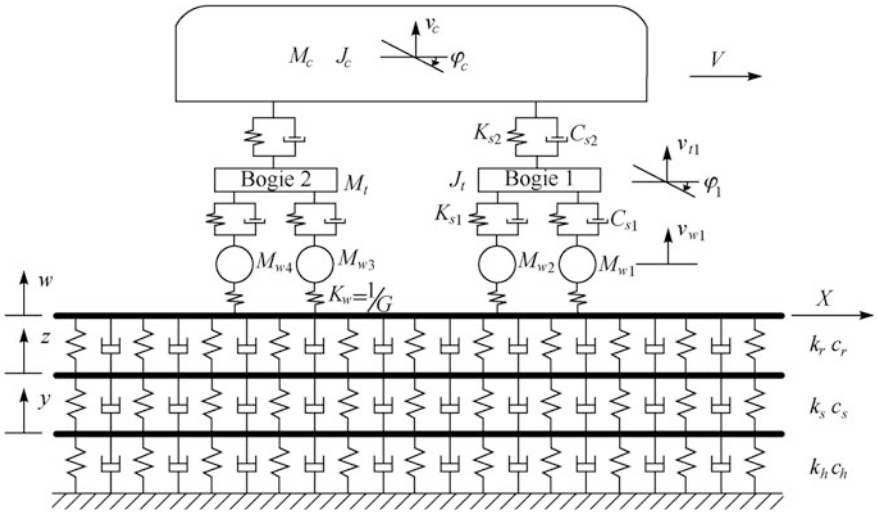

Fig. 10.3 Dynamic analysis model of the vehicle-track coupling system

The vertical vibration displacements of the rail, the precast track slab, and the concrete support layer are defined as w, z and y, and the governing equations of the slab track subsystems are as follows:

$$E_{\mathrm{r}}I_{\mathrm{r}}\frac{\partial^4 w}{\partial x^4}+m_{\mathrm{r}}\frac{\partial^2 w}{\partial t^2}+c_{\mathrm{r}}\left(\frac{\partial w}{\partial t}-\frac{\partial z}{\partial t}\right)+k_{\mathrm{r}}(w-z)=F(t)\delta(x-Vt) \tag{10.1}$$

$$E_{\mathrm{s}}I_{\mathrm{s}}\frac{\partial^4 z}{\partial x^4}+m_{\mathrm{s}}\frac{\partial^2 z}{\partial t^2}+c_{\mathrm{s}}\left(\frac{\partial z}{\partial t}-\frac{\partial y}{\partial t}\right)-c_{\mathrm{r}}\left(\frac{\partial w}{\partial t}-\frac{\partial z}{\partial t}\right)+k_{\mathrm{s}}(z-y)-k_{\mathrm{r}}(w-z)=0 \tag{10.2}$$

$$E_{\mathrm{h}}I_{\mathrm{h}}\frac{\partial^4 y}{\partial x^4}+m_{\mathrm{h}}\frac{\partial^2 y}{\partial t^2}+c_{\mathrm{h}}\frac{\partial y}{\partial t}-c_{\mathrm{s}}\left(\frac{\partial z}{\partial t}-\frac{\partial y}{\partial t}\right)+k_{\mathrm{h}}y-k_{\mathrm{s}}(z-y)=0 \tag{10.3}$$

where $F(t)$ is the dynamic load at the wheel-rail contact point, δ is the Dirac delta function, x is the stationary coordinate in the longitudinal direction of the track, and its origin is arbitrary. For convenience, the origin is usually chosen at the endpoint of the left boundary.

Figure 10.4 shows the truncation of the slab track and the discretization into a finite number of moving elements (not necessarily of equal length) for the numerical modeling. Both the upstream and downstream ends of the truncated track are taken to be sufficiently far from the contact force such that their end forces and moments are zero.

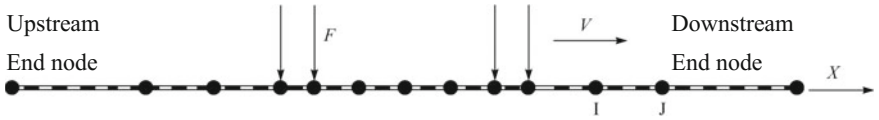

Fig. 10.4 Discretization of the slab track into moving elements

Consider a typical moving element of length l with node I and node J, a moving coordinate can be defined as follows:

$$r = x - x_I - Vt \tag{10.4}$$

where x_I is the stationary coordinate of node I. Accordingly, the origin of the r coordinate moves with the moving force/vehicle. Substituting this simple transformation into Eqs. (10.1)–(10.3), the governing equations for the three-layer beam model of the slab track subsystem in a moving frame of reference are

$$E_{\mathrm{r}}I_{\mathrm{r}}\frac{\partial^4 w}{\partial r^4} + m_{\mathrm{r}}\left[V^2\left(\frac{\partial^2 w}{\partial r^2}\right) - 2V\left(\frac{\partial^2 w}{\partial r \partial t}\right) + \left(\frac{\partial^2 w}{\partial t^2}\right)\right] + c_{\mathrm{r}}\left[\left(\frac{\partial w}{\partial t}\right) - V\left(\frac{\partial w}{\partial r}\right)\right] - c_{\mathrm{r}}\left[\left(\frac{\partial z}{\partial t}\right) - V\left(\frac{\partial z}{\partial r}\right)\right] + k_{\mathrm{r}}(w - z) = F(t)\delta(r + x_I) \tag{10.5}$$

$$E_{\mathrm{s}}I_{\mathrm{s}}\frac{\partial^4 z}{\partial r^4} + m_{\mathrm{s}}\left[V^2\left(\frac{\partial^2 z}{\partial r^2}\right) - 2V\left(\frac{\partial^2 z}{\partial r \partial t}\right) + \left(\frac{\partial^2 z}{\partial t^2}\right)\right] + c_{\mathrm{s}}\left[\left(\frac{\partial z}{\partial t}\right) - V\left(\frac{\partial z}{\partial r}\right)\right] - c_{\mathrm{s}}\left[\left(\frac{\partial y}{\partial t}\right) - V\left(\frac{\partial y}{\partial r}\right)\right] - c_{\mathrm{r}}\left[\left(\frac{\partial w}{\partial t}\right) - V\left(\frac{\partial w}{\partial r}\right)\right] + c_{\mathrm{r}}\left[\left(\frac{\partial z}{\partial t}\right) - V\left(\frac{\partial z}{\partial r}\right)\right] + k_{\mathrm{s}}(z - y) - k_{\mathrm{r}}(w - z) = 0 \tag{10.6}$$

$$E_{\mathrm{h}}I_{\mathrm{h}}\frac{\partial^4 y}{\partial r^4} + m_{\mathrm{h}}\left[V^2\left(\frac{\partial^2 y}{\partial r^2}\right) - 2V\left(\frac{\partial^2 y}{\partial r \partial t}\right) + \left(\frac{\partial^2 y}{\partial t^2}\right)\right] + c_{\mathrm{h}}\left[\left(\frac{\partial y}{\partial t}\right) - V\left(\frac{\partial y}{\partial r}\right)\right] - c_{\mathrm{s}}\left[\left(\frac{\partial z}{\partial t}\right) - V\left(\frac{\partial z}{\partial r}\right)\right] + c_{\mathrm{s}}\left[\left(\frac{\partial y}{\partial t}\right) - V\left(\frac{\partial y}{\partial r}\right)\right] + k_{\mathrm{h}}y - k_{\mathrm{s}}(z - y) = 0 \tag{10.7}$$

Note that most of the elements do not have contact with the vehicle system. For such elements, the force term on the right-hand side of Eq. (10.5) is zero.

10.2.2 Element Mass, Damping, and Stiffness Matrixes of the Slab Track in a Moving Frame of Reference

As shown in Fig. 10.5 for a typical slab track element in a moving frame of reference, v_1, v_4 stand for vertical displacement of the rail, θ_1, θ_4 are the rotational angles of the rail; v_2, v_5 are the vertical displacements of the track slab, θ_2, θ_5 are the rotational angles of the track slab; v_3, v_6 are the vertical displacements of the concrete support layer; θ_3, θ_6 are the rotational angles of the concrete support layer.

Each slab track element in a moving frame of reference has 12 degrees of freedom. Defining the element node displacement vector as follows:

$$\boldsymbol{a}^e = \{ v_1 \quad \theta_1 \quad v_2 \quad \theta_2 \quad v_3 \quad \theta_3 \quad v_4 \quad \theta_4 \quad v_5 \quad \theta_5 \quad v_6 \quad \theta_6 \}^T \tag{10.8}$$

The displacement at any point of the rail can be represented by interpolation function.

$$\begin{aligned} w &= N_1 v_1 + N_2 \theta_1 + N_3 v_4 + N_4 \theta_4 \\ &= [N_1 \quad N_2 \quad 0 \quad 0 \quad 0 \quad 0 \quad N_3 \quad N_4 \quad 0 \quad 0 \quad 0 \quad 0] \boldsymbol{a}^e \\ &= \boldsymbol{N}_\mathrm{r} \boldsymbol{a}^e \end{aligned} \tag{10.9}$$

where $\boldsymbol{N}_\mathrm{r}$ is the interpolation function matrix of the rail displacement, N_1 - N_4 are the displacement interpolation functions of the slab track element.

$$\begin{aligned} N_1 &= 1 - \frac{3}{l^2} r^2 + \frac{2}{l^3} r^3 \qquad & N_2 &= -r + \frac{2}{l} r^2 - \frac{1}{l^2} r^3 \\ N_3 &= \frac{3}{l^2} r^2 - \frac{2}{l^3} r^3 \qquad & N_4 &= \frac{1}{l} r^2 - \frac{1}{l^2} r^3 \end{aligned} \tag{10.10}$$

In the same way, the displacement at any point of the precast slab is as follows:

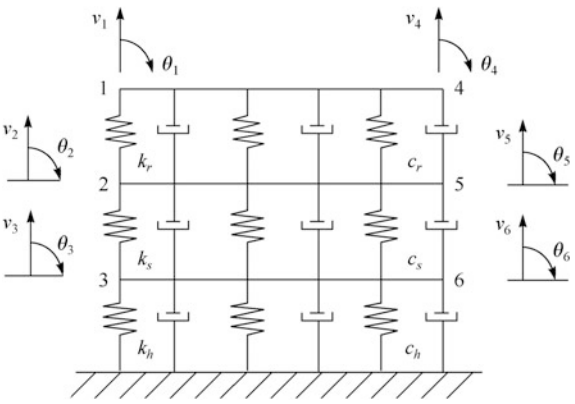

Fig. 10.5 CRTS II slab track element model

$$\begin{aligned} z &= N_1 v_2 + N_2 \theta_2 + N_3 v_5 + N_4 \theta_5 \\ &= [0 \quad 0 \quad N_1 \quad N_2 \quad 0 \quad 0 \quad 0 \quad 0 \quad N_3 \quad N_4 \quad 0 \quad 0] \boldsymbol{a}^e \\ &= \boldsymbol{N}_{\mathrm{s}} \boldsymbol{a}^e \end{aligned} \tag{10.11}$$

where, $\boldsymbol{N}_{\mathrm{s}}$ is the interpolation function matrix of the track slab displacement.

The displacement at any point of the concrete supporting layer is as follows:

$$\begin{aligned} y &= N_1 v_3 + N_2 \theta_3 + N_3 v_6 + N_4 \theta_6 \\ &= [0 \quad 0 \quad 0 \quad 0 \quad N_1 \quad N_2 \quad 0 \quad 0 \quad 0 \quad 0 \quad N_3 \quad N_4] \boldsymbol{a}^e \\ &= \boldsymbol{N}_{\mathrm{h}} \boldsymbol{a}^e \end{aligned} \tag{10.12}$$

where, $\boldsymbol{N}_{\mathrm{h}}$ is the interpolation function matrix of the concrete support layer displacement.

10.2.2.1 The First-Layer Beam's Matrix of the Slab Track Element in a Moving Frame of Reference

The governing equation (10.5) is multiplied by a weighting function (variation) w, and then integrated over the element length, leading to the variational (or weak) form as follows:

$$\begin{aligned} &\int_0^l w(r) \left\{ E_{\mathrm{r}} I_{\mathrm{r}} \frac{\partial^4 w}{\partial r^4} + m_{\mathrm{r}} \left[V^2 \left(\frac{\partial^2 w}{\partial r^2} \right) - 2V \left(\frac{\partial^2 w}{\partial r \partial t} \right) + \left(\frac{\partial^2 w}{\partial t^2} \right) \right] + c_{\mathrm{r}} \left[\left(\frac{\partial w}{\partial t} \right) - V \left(\frac{\partial w}{\partial r} \right) \right] \right. \\ &\left. - c_{\mathrm{r}} \left[\left(\frac{\partial z}{\partial t} \right) - V \left(\frac{\partial z}{\partial r} \right) \right] + k_{\mathrm{r}} (w - z) - F(t) \delta(r) \right\} \mathrm{d}r = 0 \end{aligned} \tag{10.13}$$

Take the integration to each term of above equation by parts over the element length l, namely:

$$\begin{aligned} \int_0^l w(r) E_{\mathrm{r}} I_{\mathrm{r}} \frac{\partial^4 w}{\partial r^4} \mathrm{d}r &= E_{\mathrm{r}} I_{\mathrm{r}} \int_0^l w(r) \mathrm{d} \left(\frac{\partial^3 w}{\partial r^3} \right) = E_{\mathrm{r}} I_{\mathrm{r}} \left[\left(w(r) \cdot \frac{\partial^3 w}{\partial r^3} \right)_o^l - \int_0^l \frac{\partial^3 w}{\partial r^3} \cdot \frac{\partial w}{\partial r} \mathrm{d}r \right] \\ &= -E_{\mathrm{r}} I_{\mathrm{r}} \int_0^l \frac{\partial w}{\partial r} \mathrm{d} \left(\frac{\partial^2 w}{\partial r^2} \right) = -E_{\mathrm{r}} I_{\mathrm{r}} \left[\left(\frac{\partial w}{\partial r} \cdot \frac{\partial^2 w}{\partial r^2} \right)_o^l - \int_0^l \frac{\partial^2 w}{\partial r^2} \cdot \frac{\partial^2 w}{\partial r^2} \mathrm{d}r \right] \\ &= E_{\mathrm{r}} I_{\mathrm{r}} \int_0^l \left(\boldsymbol{N}_{\mathrm{r,rr}} \boldsymbol{a}^e \right)^{\mathrm{T}} \left(\boldsymbol{N}_{\mathrm{r,rr}} \boldsymbol{a}^e \right) \mathrm{d}r = (\boldsymbol{a}^e)^{\mathrm{T}} \cdot E_{\mathrm{r}} I_{\mathrm{r}} \int_0^l \boldsymbol{N}_{\mathrm{r,rr}}^{\mathrm{T}} \boldsymbol{N}_{\mathrm{r,rr}} \mathrm{d}r \cdot (\boldsymbol{a}^e) \end{aligned} \tag{10.14}$$

$$\begin{aligned}\int_0^l w(r)m_{\mathrm{r}}V^2\frac{\partial^2 w}{\partial r^2}\mathrm{d}r &= m_{\mathrm{r}}V^2\int_0^l w(r)\frac{\partial^2 w}{\partial r^2}\mathrm{d}r \\ &= m_{\mathrm{r}}V^2\int_0^l w(r)\mathrm{d}\left(\frac{\partial w}{\partial r}\right) = m_{\mathrm{r}}V^2\left[\left(w(r)\cdot\frac{\partial w}{\partial r}\right)_o^l - \int_0^l \frac{\partial w}{\partial r}\cdot\frac{\partial w}{\partial r}\mathrm{d}r\right] \\ &= -m_{\mathrm{r}}V^2\int_0^l \left(\boldsymbol{N}_{\mathrm{r,r}}\boldsymbol{a}^e\right)^{\mathrm{T}}\left(\boldsymbol{N}_{\mathrm{r,r}}\boldsymbol{a}^e\right)\mathrm{d}r = -(\boldsymbol{a}^e)^{\mathrm{T}}\cdot m_{\mathrm{r}}V^2\int_0^l \boldsymbol{N}_{\mathrm{r,r}}^{\mathrm{T}}\boldsymbol{N}_{\mathrm{r,r}}\mathrm{d}r\cdot(\boldsymbol{a}^e)\end{aligned} \tag{10.15}$$

$$\begin{aligned}-2\int_0^l w(r)m_{\mathrm{r}}V\left(\frac{\partial^2 w}{\partial r\partial t}\right)\mathrm{d}r &= -2m_{\mathrm{r}}V\int_0^l w(r)\left(\frac{\partial^2 w}{\partial r\partial t}\right)\mathrm{d}r \\ &= -2m_r V\int_0^l (\boldsymbol{N}_{\mathrm{r}}\boldsymbol{a}^e)^{\mathrm{T}}\left(\boldsymbol{N}_{\mathrm{r,r}}\dot{\boldsymbol{a}}^e\right)\mathrm{d}r \\ &= -(\boldsymbol{a}^e)^{\mathrm{T}}\cdot 2m_{\mathrm{r}}V\int_0^l \boldsymbol{N}_{\mathrm{r}}^{\mathrm{T}}\boldsymbol{N}_{\mathrm{r,r}}\mathrm{d}r\cdot(\dot{\boldsymbol{a}}^e)\end{aligned} \tag{10.16}$$

$$\begin{aligned}\int_0^l w(r)m_{\mathrm{r}}\left(\frac{\partial^2 w}{\partial t^2}\right)\mathrm{d}r &= m_{\mathrm{r}}\int_0^l w(r)\left(\frac{\partial^2 w}{\partial t^2}\right)\mathrm{d}r \\ &= m_{\mathrm{r}}\int_0^l w(r)\left(\frac{\partial^2 w}{\partial t^2}\right)\mathrm{d}r = m_{\mathrm{r}}\int_0^l (\boldsymbol{N}_{\mathrm{r}}\boldsymbol{a}^e)^{\mathrm{T}}(\boldsymbol{N}_{\mathrm{r}}\ddot{\boldsymbol{a}}^e)\mathrm{d}r \\ &= (\boldsymbol{a}^e)^{\mathrm{T}}\cdot m_{\mathrm{r}}\int_0^l \boldsymbol{N}_{\mathrm{r}}^{\mathrm{T}}\boldsymbol{N}_{\mathrm{r}}\mathrm{d}r\cdot(\ddot{\boldsymbol{a}}^e)\end{aligned} \tag{10.17}$$

$$\begin{aligned}\int_0^l w(r)c_{\mathrm{r}}\left(\frac{\partial w}{\partial t}\right)\mathrm{d}r &= c_{\mathrm{r}}\int_0^l w(r)\left(\frac{\partial w}{\partial t}\right)\mathrm{d}r = c_{\mathrm{r}}\int_0^l (\boldsymbol{N}_{\mathrm{r}}\boldsymbol{a}^e)^{\mathrm{T}}(\boldsymbol{N}_{\mathrm{r}}\dot{\boldsymbol{a}}^e)\mathrm{d}r \\ &= (\boldsymbol{a}^e)^{\mathrm{T}}\cdot c_{\mathrm{r}}\int_0^l \boldsymbol{N}_{\mathrm{r}}^{\mathrm{T}}\boldsymbol{N}_{\mathrm{r}}\mathrm{d}r\cdot(\dot{\boldsymbol{a}}^e)\end{aligned} \tag{10.18}$$

$$
\begin{aligned}
-\int_0^l w(r)c_{\mathrm{r}}V\left(\frac{\partial w}{\partial r}\right)\mathrm{d}r &= -c_{\mathrm{r}}V\int_0^l w(r)\left(\frac{\partial w}{\partial r}\right)\mathrm{d}r \\
&= -c_rV\int_0^l (\boldsymbol{N}_{\mathrm{r}}\boldsymbol{a}^e)^{\mathrm{T}}\left(\boldsymbol{N}_{\mathrm{r,r}}\boldsymbol{a}^e\right)\mathrm{d}r \\
&= -(\boldsymbol{a}^e)^{\mathrm{T}}\cdot c_{\mathrm{r}}V\int_0^l \boldsymbol{N}_{\mathrm{r}}^{\mathrm{T}}\boldsymbol{N}_{\mathrm{r,r}}\mathrm{d}r\cdot(\boldsymbol{a}^e)
\end{aligned}
\tag{10.19}
$$

$$
\begin{aligned}
&-\int_0^l w(r)c_{\mathrm{r}}\left(\frac{\partial z}{\partial t}\right)\mathrm{d}r = -c_{\mathrm{r}}\int_0^l w(r)\left(\frac{\partial z}{\partial t}\right)\mathrm{d}r \\
&= -c_{\mathrm{r}}\int_0^l (\boldsymbol{N}_{\mathrm{r}}\boldsymbol{a}^e)^{\mathrm{T}}(\boldsymbol{N}_{\mathrm{s}}\dot{\boldsymbol{a}}^e)\mathrm{d}r = -(\boldsymbol{a}^e)^{\mathrm{T}}\cdot c_{\mathrm{r}}\int_0^l \boldsymbol{N}_{\mathrm{r}}^{\mathrm{T}}\boldsymbol{N}_{\mathrm{s}}\mathrm{d}r\cdot(\dot{\boldsymbol{a}}^e)
\end{aligned}
\tag{10.20}
$$

$$
\begin{aligned}
\int_0^l w(r)c_{\mathrm{r}}V\left(\frac{\partial z}{\partial r}\right)\mathrm{d}r &= c_{\mathrm{r}}V\int_0^l w(r)\left(\frac{\partial z}{\partial r}\right)\mathrm{d}r \\
&= c_{\mathrm{r}}V\int_0^l (\boldsymbol{N}_{\mathrm{r}}\boldsymbol{a}^e)^{\mathrm{T}}\left(\boldsymbol{N}_{\mathrm{s,r}}\boldsymbol{a}^e\right)\mathrm{d}r = (\boldsymbol{a}^e)^{\mathrm{T}}\cdot c_{\mathrm{r}}V\int_0^l \boldsymbol{N}_{\mathrm{r}}^{\mathrm{T}}\boldsymbol{N}_{\mathrm{s,r}}\mathrm{d}r\cdot(\boldsymbol{a}^e)
\end{aligned}
\tag{10.21}
$$

$$
\begin{aligned}
\int_0^l w(r)k_rw(r)\mathrm{d}r &= k_r\int_0^l w(r)^2\mathrm{d}r = k_r\int_0^l (\boldsymbol{N}_{\mathrm{r}}\boldsymbol{a}^e)^{\mathrm{T}}(\boldsymbol{N}_{\mathrm{r}}\boldsymbol{a}^e)\mathrm{d}r \\
&= (\boldsymbol{a}^e)^{\mathrm{T}}\cdot k_{\mathrm{r}}\int_0^l \boldsymbol{N}_{\mathrm{r}}^{\mathrm{T}}\boldsymbol{N}_{\mathrm{r}}\mathrm{d}r\cdot(\boldsymbol{a}^e)
\end{aligned}
\tag{10.22}
$$

$$
\begin{aligned}
-\int_0^l w(r)k_{\mathrm{r}}z(r)\mathrm{d}r &= -k_{\mathrm{r}}\int_0^l w(r)z(r)\mathrm{d}r = -k_{\mathrm{r}}\int_0^l (\boldsymbol{N}_{\mathrm{r}}\boldsymbol{a}^e)^{\mathrm{T}}(\boldsymbol{N}_{\mathrm{s}}\boldsymbol{a}^e)\mathrm{d}r \\
&= -(\boldsymbol{a}^e)^{\mathrm{T}}\cdot k_{\mathrm{r}}\int_0^l \boldsymbol{N}_{\mathrm{r}}^{\mathrm{T}}\boldsymbol{N}_{\mathrm{s}}\mathrm{d}r\cdot(\boldsymbol{a}^e)
\end{aligned}
\tag{10.23}
$$

By using the principle of the energy, the first-layer beam's mass, damping, and stiffness matrices of the slab track element in a moving frame of reference can be obtained as follows:

$$\boldsymbol{m}_{\mathrm{r}}^{e}=m_{\mathrm{r}}\int_{0}^{l}\boldsymbol{N}_{\mathrm{r}}^{\mathrm{T}}\boldsymbol{N}_{\mathrm{r}}\mathrm{d}r \tag{10.24}$$

$$\boldsymbol{c}_{\mathrm{r}}^{e}=-2m_{\mathrm{r}}V\int_{0}^{l}\boldsymbol{N}_{\mathrm{r}}^{\mathrm{T}}\boldsymbol{N}_{\mathrm{r,r}}\mathrm{d}r+c_{\mathrm{r}}\int_{0}^{l}\boldsymbol{N}_{\mathrm{r}}^{\mathrm{T}}\boldsymbol{N}_{\mathrm{r}}\mathrm{d}r-c_{\mathrm{r}}\int_{0}^{l}\boldsymbol{N}_{\mathrm{r}}^{\mathrm{T}}\boldsymbol{N}_{\mathrm{s}}\mathrm{d}r \tag{10.25}$$

$$\begin{aligned}\boldsymbol{k}_{\mathrm{r}}^{e}=&E_{\mathrm{r}}I_{\mathrm{r}}\int_{0}^{l}\boldsymbol{N}_{\mathrm{r,rr}}^{\mathrm{T}}\boldsymbol{N}_{\mathrm{r,rr}}\mathrm{d}r-m_{\mathrm{r}}V^{2}\int_{0}^{l}\boldsymbol{N}_{\mathrm{r,r}}^{\mathrm{T}}\boldsymbol{N}_{\mathrm{r,r}}\mathrm{d}r-c_{\mathrm{r}}V\int_{0}^{l}\boldsymbol{N}_{\mathrm{r}}^{\mathrm{T}}\boldsymbol{N}_{\mathrm{r,r}}\mathrm{d}r\\&+c_{\mathrm{r}}V\int_{0}^{l}\boldsymbol{N}_{\mathrm{r}}^{\mathrm{T}}\boldsymbol{N}_{\mathrm{s,r}}\mathrm{d}r+k_{\mathrm{r}}\int_{0}^{l}\boldsymbol{N}_{\mathrm{r}}^{\mathrm{T}}\boldsymbol{N}_{\mathrm{r}}\mathrm{d}r-k_{\mathrm{r}}\int_{0}^{l}\boldsymbol{N}_{\mathrm{r}}^{\mathrm{T}}\boldsymbol{N}_{\mathrm{s}}\mathrm{d}r\end{aligned} \tag{10.26}$$

10.2.2.2 The Second-Layer Beam's Matrix of the Slab Track Element in a Moving Frame of Reference

The governing equation (10.6) is multiplied by a weighting function (variation) z, and then integrated over the element length, leading to the variational (or weak) form as follows:

$$\begin{aligned}&\int_{0}^{l}z(r)\left\{E_{\mathrm{s}}I_{\mathrm{s}}\frac{\partial^{4}z}{\partial r^{4}}+m_{\mathrm{s}}\left[V^{2}\left(\frac{\partial^{2}z}{\partial r^{2}}\right)-2V\left(\frac{\partial^{2}z}{\partial r\partial t}\right)+\left(\frac{\partial^{2}z}{\partial t^{2}}\right)\right]+c_{\mathrm{s}}\left[\left(\frac{\partial z}{\partial t}\right)-V\left(\frac{\partial z}{\partial r}\right)\right]\right.\\&\left.-c_{\mathrm{s}}\left[\left(\frac{\partial y}{\partial t}\right)-V\left(\frac{\partial y}{\partial r}\right)\right]-c_{\mathrm{r}}\left[\left(\frac{\partial w}{\partial t}\right)-V\left(\frac{\partial w}{\partial r}\right)\right]+c_{\mathrm{r}}\left[\left(\frac{\partial z}{\partial t}\right)-V\left(\frac{\partial z}{\partial r}\right)\right]+k_{\mathrm{s}}(z-y)-k_{\mathrm{r}}(w-z)\right\}\mathrm{d}r=0\end{aligned} \tag{10.27}$$

Take the integration to each term of above equation by parts over the element length l, namely:

$$\begin{aligned}
&\int_0^l z(r)E_sI_s\frac{\partial^4 z}{\partial r^4}\mathrm{d}r = E_sI_s\int_0^l z(r)\mathrm{d}\left(\frac{\partial^3 z}{\partial r^3}\right)\\
&= E_sI_s\left[\left(z(r)\cdot\frac{\partial^3 z}{\partial r^3}\right)_o^l - \int_0^l \frac{\partial^3 z}{\partial r^3}\cdot\frac{\partial z}{\partial r}\mathrm{d}r\right] = -E_sI_s\int_0^l \frac{\partial z}{\partial r}\mathrm{d}\left(\frac{\partial^2 z}{\partial r^2}\right)\\
&= -E_sI_s\left[\left(\frac{\partial z}{\partial r}\cdot\frac{\partial^2 z}{\partial r^2}\right)_o^l - \int_0^l \frac{\partial^2 z}{\partial r^2}\cdot\frac{\partial^2 z}{\partial r^2}\mathrm{d}r\right]\\
&= E_sI_s\int_0^l \left(\boldsymbol{N}_{s,rr}\boldsymbol{a}^e\right)^{\mathrm{T}}\left(\boldsymbol{N}_{s,rr}\boldsymbol{a}^e\right)\mathrm{d}r = (\boldsymbol{a}^e)^{\mathrm{T}}\cdot E_sI_s\int_0^l \boldsymbol{N}_{s,rr}^{\mathrm{T}}\boldsymbol{N}_{s,rr}\mathrm{d}r\cdot(\boldsymbol{a}^e)
\end{aligned} \tag{10.28}$$

$$\begin{aligned}
&\int_0^l z(r)m_sV^2\left(\frac{\partial^2 z}{\partial r^2}\right)\mathrm{d}r = m_sV^2\int_0^l z(r)\left(\frac{\partial^2 z}{\partial r^2}\right)\mathrm{d}r\\
&= m_sV^2\int_0^l z(r)d\left(\frac{\partial z}{\partial r}\right) = m_sV^2\left[\left(z(r)\cdot\frac{\partial z}{\partial r}\right)_o^l - \int_0^l \frac{\partial z}{\partial r}\cdot\frac{\partial z}{\partial r}\mathrm{d}r\right]\\
&= -m_sV^2\int_0^l \left(\boldsymbol{N}_{s,r}\boldsymbol{a}^e\right)^{\mathrm{T}}\left(\boldsymbol{N}_{s,r}\boldsymbol{a}^e\right)\mathrm{d}r = -(\boldsymbol{a}^e)^{\mathrm{T}}\cdot m_sV^2\int_0^l \boldsymbol{N}_{s,r}^{\mathrm{T}}\boldsymbol{N}_{s,r}\mathrm{d}r\cdot(\boldsymbol{a}^e)
\end{aligned} \tag{10.29}$$

$$\begin{aligned}
&-2\int_0^l m_sVz(r)\left(\frac{\partial^2 z}{\partial r\partial t}\right)\mathrm{d}r = -2m_sV\int_0^l z(r)\left(\frac{\partial^2 z}{\partial r\partial t}\right)\mathrm{d}r\\
&= -2m_sV\int_0^l \left(\boldsymbol{N}_s\boldsymbol{a}^e\right)^{\mathrm{T}}\left(\boldsymbol{N}_{s,r}\dot{\boldsymbol{a}}^e\right)\mathrm{d}r\\
&= -(\boldsymbol{a}^e)^{\mathrm{T}}\cdot 2m_sV\int_0^l \boldsymbol{N}_s^{\mathrm{T}}\boldsymbol{N}_{s,r}\mathrm{d}r\cdot(\dot{\boldsymbol{a}}^e)
\end{aligned} \tag{10.30}$$

$$\begin{aligned}
&\int_0^l z(r)m_s\left(\frac{\partial^2 z}{\partial t^2}\right)\mathrm{d}r = m_s\int_0^l z(r)\left(\frac{\partial^2 z}{\partial t^2}\right)\mathrm{d}r = m_s\int_0^l z(r)\left(\frac{\partial^2 z}{\partial t^2}\right)\mathrm{d}r = m_s\int_0^l \left(\boldsymbol{N}_s\boldsymbol{a}^e\right)^{\mathrm{T}}\left(\boldsymbol{N}_s\ddot{a}^e\right)\mathrm{d}r\\
&= (\boldsymbol{a}^e)^{\mathrm{T}}\cdot m_s\int_0^l \boldsymbol{N}_s^{\mathrm{T}}\boldsymbol{N}_s\mathrm{d}r\cdot(\ddot{\boldsymbol{a}}^e)
\end{aligned} \tag{10.31}$$

$$\int_0^l z(r)c_{\mathrm{s}}\left(\frac{\partial z}{\partial t}\right)\mathrm{d}r = c_{\mathrm{s}}\int_0^l z(r)\left(\frac{\partial z}{\partial t}\right)\mathrm{d}r = c_{\mathrm{s}}\int_0^l (\boldsymbol{N}_{\mathrm{s}}\boldsymbol{a}^e)^{\mathrm{T}}(\boldsymbol{N}_{\mathrm{s}}\dot{\boldsymbol{a}}^e)\mathrm{d}r$$
$$= (\boldsymbol{a}^e)^{\mathrm{T}}\cdot c_{\mathrm{s}}\int_0^l \boldsymbol{N}_{\mathrm{s}}^{\mathrm{T}}\boldsymbol{N}_{\mathrm{s}}\mathrm{d}r\cdot(\dot{\boldsymbol{a}}^e) \tag{10.32}$$

$$-\int_0^l z(r)c_{\mathrm{s}}V\left(\frac{\partial z}{\partial r}\right)\mathrm{d}r = -c_{\mathrm{s}}V\int_0^l z(r)\left(\frac{\partial z}{\partial r}\right)\mathrm{d}r$$
$$= -c_{\mathrm{s}}V\int_0^l (\boldsymbol{N}_{\mathrm{s}}\boldsymbol{a}^e)^{\mathrm{T}}\left(\boldsymbol{N}_{\mathrm{s,r}}\boldsymbol{a}^e\right)\mathrm{d}r = -(\boldsymbol{a}^e)^{\mathrm{T}}\cdot c_{\mathrm{s}}V\int_0^l \boldsymbol{N}_{\mathrm{s}}^{\mathrm{T}}\boldsymbol{N}_{\mathrm{s,r}}\mathrm{d}r\cdot(\boldsymbol{a}^e) \tag{10.33}$$

$$-\int_0^l z(r)c_{\mathrm{s}}\left(\frac{\partial y}{\partial t}\right)\mathrm{d}r = -c_{\mathrm{s}}\int_0^l z(r)\left(\frac{\partial y}{\partial t}\right)\mathrm{d}r$$
$$= -c_{\mathrm{s}}\int_0^l (\boldsymbol{N}_{\mathrm{s}}\boldsymbol{a}^e)^{\mathrm{T}}(\boldsymbol{N}_{\mathrm{h}}\dot{\boldsymbol{a}}^e)\mathrm{d}r = -(\boldsymbol{a}^e)^{\mathrm{T}}\cdot c_{\mathrm{s}}\int_0^l \boldsymbol{N}_{\mathrm{s}}^{\mathrm{T}}\boldsymbol{N}_{\mathrm{h}}\mathrm{d}r\cdot(\dot{\boldsymbol{a}}^e) \tag{10.34}$$

$$\int_0^l z(r)c_{\mathrm{s}}V\left(\frac{\partial y}{\partial r}\right)\mathrm{d}r = c_{\mathrm{s}}V\int_0^l z(r)\left(\frac{\partial y}{\partial r}\right)\mathrm{d}r$$
$$= c_{\mathrm{s}}V\int_0^l (\boldsymbol{N}_{\mathrm{s}}\boldsymbol{a}^e)^{\mathrm{T}}\left(\boldsymbol{N}_{\mathrm{h,r}}\boldsymbol{a}^e\right)\mathrm{d}r = (\boldsymbol{a}^e)^{\mathrm{T}}\cdot c_{\mathrm{s}}V\int_0^l \boldsymbol{N}_{\mathrm{s}}^{\mathrm{T}}\boldsymbol{N}_{\mathrm{h,r}}\mathrm{d}r\cdot(\boldsymbol{a}^e) \tag{10.35}$$

$$-\int_0^l z(r)c_{\mathrm{r}}\left(\frac{\partial w}{\partial t}\right)\mathrm{d}r = -c_{\mathrm{r}}\int_0^l z(r)\left(\frac{\partial w}{\partial t}\right)\mathrm{d}r$$
$$= -c_{\mathrm{r}}\int_0^l (\boldsymbol{N}_{\mathrm{s}}\boldsymbol{a}^e)^{\mathrm{T}}(\boldsymbol{N}_{\mathrm{r}}\dot{\boldsymbol{a}}^e)\mathrm{d}r = -(\boldsymbol{a}^e)^{\mathrm{T}}\cdot c_{\mathrm{r}}\int_0^l \boldsymbol{N}_{\mathrm{s}}^{\mathrm{T}}\boldsymbol{N}_{\mathrm{r}}\mathrm{d}r\cdot(\dot{\boldsymbol{a}}^e) \tag{10.36}$$

$$\int_0^l z(r)c_{\mathrm{r}}V\left(\frac{\partial w}{\partial r}\right)\mathrm{d}r = c_{\mathrm{r}}V\int_0^l z(r)\left(\frac{\partial w}{\partial r}\right)\mathrm{d}r$$
$$= c_{\mathrm{r}}V\int_0^l (\boldsymbol{N}_{\mathrm{s}}\boldsymbol{a}^e)^{\mathrm{T}}\left(\boldsymbol{N}_{\mathrm{r,r}}\boldsymbol{a}^e\right)\mathrm{d}r = (\boldsymbol{a}^e)^{\mathrm{T}}\cdot c_{\mathrm{r}}V\int_0^l \boldsymbol{N}_{\mathrm{s}}^{\mathrm{T}}\boldsymbol{N}_{\mathrm{r,r}}\mathrm{d}r\cdot(\boldsymbol{a}^e) \tag{10.37}$$

$$\int_0^l z(r)c_{\mathrm{r}}\left(\frac{\partial z}{\partial t}\right)\mathrm{d}r = c_{\mathrm{r}}\int_0^l z(r)\left(\frac{\partial z}{\partial t}\right)\mathrm{d}r$$
$$= c_{\mathrm{r}}\int_0^l (\boldsymbol{N}_{\mathrm{s}}\boldsymbol{a}^e)^{\mathrm{T}}(\boldsymbol{N}_{\mathrm{s}}\dot{\boldsymbol{a}}^e)\mathrm{d}r = (\boldsymbol{a}^e)^{\mathrm{T}}\cdot c_{\mathrm{r}}\int_0^l \boldsymbol{N}_{\mathrm{s}}^{\mathrm{T}}\boldsymbol{N}_{\mathrm{s}}\mathrm{d}r\cdot(\dot{\boldsymbol{a}}^e) \tag{10.38}$$

$$-\int_0^l z(r)c_{\mathrm{r}}V\left(\frac{\partial z}{\partial r}\right)\mathrm{d}r = -c_{\mathrm{r}}V\int_0^l z(r)\left(\frac{\partial z}{\partial r}\right)\mathrm{d}r$$
$$= -c_{\mathrm{r}}V\int_0^l (\boldsymbol{N}_{\mathrm{s}}\boldsymbol{a}^e)^{\mathrm{T}}\left(\boldsymbol{N}_{\mathrm{s,r}}\boldsymbol{a}^e\right)\mathrm{d}r = -(\boldsymbol{a}^e)^{\mathrm{T}}\cdot c_{\mathrm{r}}V\int_0^l \boldsymbol{N}_{\mathrm{s}}^{\mathrm{T}}\boldsymbol{N}_{\mathrm{s,r}}\mathrm{d}r\cdot(\boldsymbol{a}^e) \tag{10.39}$$

$$\int_0^l z(r)k_{\mathrm{s}}z(r)\mathrm{d}r = k_{\mathrm{s}}\int_0^l z(r)^2\mathrm{d}r$$
$$= k_{\mathrm{s}}\int_0^l (\boldsymbol{N}_{\mathrm{s}}\boldsymbol{a}^e)^{\mathrm{T}}(\boldsymbol{N}_{\mathrm{s}}\boldsymbol{a}^e)\mathrm{d}r = (\boldsymbol{a}^e)^{\mathrm{T}}\cdot k_{\mathrm{s}}\int_0^l \boldsymbol{N}_{\mathrm{s}}^{\mathrm{T}}\boldsymbol{N}_{\mathrm{s}}\mathrm{d}r\cdot(\boldsymbol{a}^e) \tag{10.40}$$

$$-\int_0^l z(r)k_{\mathrm{s}}y(r)\mathrm{d}r = -k_{\mathrm{s}}\int_0^l z(r)y(r)\mathrm{d}r$$
$$= -k_{\mathrm{s}}\int_0^l (\boldsymbol{N}_{\mathrm{s}}\boldsymbol{a}^e)^{\mathrm{T}}(\boldsymbol{N}_{\mathrm{h}}\boldsymbol{a}^e)\mathrm{d}r = -(\boldsymbol{a}^e)^{\mathrm{T}}\cdot k_{\mathrm{s}}\int_0^l \boldsymbol{N}_{\mathrm{s}}^{\mathrm{T}}\boldsymbol{N}_{\mathrm{h}}\mathrm{d}r\cdot(\boldsymbol{a}^e) \tag{10.41}$$

$$\begin{aligned}-\int_0^l z(r)k_{\mathrm{r}}w(r)\mathrm{d}r &= -k_{\mathrm{r}}\int_0^l z(r)w(r)\mathrm{d}r \\ &= -k_{\mathrm{r}}\int_0^l (\boldsymbol{N}_{\mathrm{s}}\boldsymbol{a}^e)^{\mathrm{T}}(\boldsymbol{N}_{\mathrm{r}}\boldsymbol{a}^e)\mathrm{d}r = -(\boldsymbol{a}^e)^{\mathrm{T}}\cdot k_{\mathrm{r}}\int_0^l \boldsymbol{N}_{\mathrm{s}}^{\mathrm{T}}\boldsymbol{N}_{\mathrm{r}}\mathrm{d}r\cdot(\boldsymbol{a}^e)\end{aligned} \tag{10.42}$$

$$\begin{aligned}\int_0^l z(r)k_{\mathrm{r}}z(r)\mathrm{d}r &= k_{\mathrm{r}}\int_0^l z(r)^2\mathrm{d}r \\ &= k_{\mathrm{r}}\int_0^l (\boldsymbol{N}_{\mathrm{s}}\boldsymbol{a}^e)^{\mathrm{T}}(\boldsymbol{N}_{\mathrm{s}}\boldsymbol{a}^e)\mathrm{d}r = (\boldsymbol{a}^e)^{\mathrm{T}}\cdot k_{\mathrm{r}}\int_0^l \boldsymbol{N}_{\mathrm{s}}^{\mathrm{T}}\boldsymbol{N}_{\mathrm{s}}\mathrm{d}r\cdot(\boldsymbol{a}^e)\end{aligned} \tag{10.43}$$

By using the principle of the energy, the second-layer beam's mass, damping, and stiffness matrices of the slab track element in a moving frame of reference can be obtained as follows:

$$\boldsymbol{m}_{\mathrm{s}}^e = m_{\mathrm{s}}\int_0^l \boldsymbol{N}_{\mathrm{s}}^{\mathrm{T}}\boldsymbol{N}_{\mathrm{s}}\mathrm{d}r \tag{10.44}$$

$$\begin{aligned}\boldsymbol{c}_{\mathrm{s}}^e = &-2m_{\mathrm{s}}V\int_0^l \boldsymbol{N}_{\mathrm{s}}^{\mathrm{T}}\boldsymbol{N}_{\mathrm{s,r}}\mathrm{d}r + c_{\mathrm{s}}\int_0^l \boldsymbol{N}_{\mathrm{s}}^{\mathrm{T}}\boldsymbol{N}_{\mathrm{s}}\mathrm{d}r \\ &- c_{\mathrm{s}}\int_0^l \boldsymbol{N}_{\mathrm{s}}^{\mathrm{T}}\boldsymbol{N}_{\mathrm{h}}\mathrm{d}r - c_{\mathrm{r}}\int_0^l \boldsymbol{N}_{\mathrm{s}}^{\mathrm{T}}\boldsymbol{N}_{\mathrm{r}}\mathrm{d}r + c_{\mathrm{r}}\int_0^l \boldsymbol{N}_{\mathrm{s}}^{\mathrm{T}}\boldsymbol{N}_{\mathrm{s}}\mathrm{d}r\end{aligned} \tag{10.45}$$

$$\begin{aligned}\boldsymbol{k}_{\mathrm{s}}^e = &E_{\mathrm{s}}I_{\mathrm{s}}\int_0^l \boldsymbol{N}_{\mathrm{s,rr}}^{\mathrm{T}}\boldsymbol{N}_{\mathrm{s,rr}}\mathrm{d}r - m_{\mathrm{s}}V^2\int_0^l \boldsymbol{N}_{\mathrm{s,r}}^{\mathrm{T}}\boldsymbol{N}_{\mathrm{s,r}}\mathrm{d}r \\ &- c_{\mathrm{s}}V\int_0^l \boldsymbol{N}_{\mathrm{s}}^{\mathrm{T}}\boldsymbol{N}_{\mathrm{s,r}}dr + c_{\mathrm{s}}V\int_0^l \boldsymbol{N}_{\mathrm{s}}^{\mathrm{T}}\boldsymbol{N}_{\mathrm{h,r}}\mathrm{d}r + c_{\mathrm{r}}V\int_0^l \boldsymbol{N}_{\mathrm{s}}^{\mathrm{T}}\boldsymbol{N}_{\mathrm{r,r}}\mathrm{d}r \\ &- c_{\mathrm{r}}V\int_0^l \boldsymbol{N}_{\mathrm{s}}^{\mathrm{T}}\boldsymbol{N}_{\mathrm{s,r}}\mathrm{d}r + k_{\mathrm{s}}\int_0^l \boldsymbol{N}_{\mathrm{s}}^{\mathrm{T}}\boldsymbol{N}_{\mathrm{s}}\mathrm{d}r - k_{\mathrm{s}}\int_0^l \boldsymbol{N}_{\mathrm{s}}^{\mathrm{T}}\boldsymbol{N}_{\mathrm{h}}\mathrm{d}r \\ &- k_{\mathrm{r}}\int_0^l \boldsymbol{N}_{\mathrm{s}}^{\mathrm{T}}\boldsymbol{N}_{\mathrm{r}}\mathrm{d}r + k_{\mathrm{r}}\int_0^l \boldsymbol{N}_{\mathrm{s}}^{\mathrm{T}}\boldsymbol{N}_{\mathrm{s}}\mathrm{d}r\end{aligned} \tag{10.46}$$

10.2.2.3 The Third Layer Beam's Matrix of the Slab Track Element in a Moving Frame of Reference

The governing equation (10.7) is multiplied by a weighting function (variation) y, and then integrated over the element length, leading to the variational (or weak) form as follows:

$$\int_0^l y(r)\left\{E_\mathrm{h}I_\mathrm{h}\frac{\partial^4 y}{\partial r^4}+m_\mathrm{h}\left[V^2\left(\frac{\partial^2 y}{\partial r^2}\right)-2V\left(\frac{\partial^2 y}{\partial r\partial t}\right)+\left(\frac{\partial^2 y}{\partial t^2}\right)\right]+c_\mathrm{h}\left[\left(\frac{\partial y}{\partial t}\right)-V\left(\frac{\partial y}{\partial r}\right)\right]\right.$$
$$\left.-c_\mathrm{s}\left[\left(\frac{\partial z}{\partial t}\right)-V\left(\frac{\partial z}{\partial r}\right)\right]+c_\mathrm{s}\left[\left(\frac{\partial y}{\partial t}\right)-V\left(\frac{\partial y}{\partial r}\right)\right]+k_\mathrm{h}y-k_\mathrm{s}(z-y)\right\}\mathrm{d}r=0 \tag{10.47}$$

Take the integration to each term of above equation by parts over the element length l, namely:

$$\begin{aligned}\int_0^l y(r)E_\mathrm{h}I_\mathrm{h}\left(\frac{\partial^4 y}{\partial r^4}\right)\mathrm{d}r &= E_\mathrm{h}I_\mathrm{h}\int_0^l y(r)\mathrm{d}\left(\frac{\partial^3 y}{\partial r^3}\right)\\ &= E_\mathrm{h}I_\mathrm{h}\left[\left(y(r)\cdot\frac{\partial^3 y}{\partial r^3}\right)_o^l-\int_0^l\frac{\partial^3 y}{\partial r^3}\cdot\frac{\partial y}{\partial r}\mathrm{d}r\right]=-E_\mathrm{h}I_\mathrm{h}\int_0^l\frac{\partial y}{\partial r}\mathrm{d}\left(\frac{\partial^2 y}{\partial r^2}\right)\\ &= -E_\mathrm{h}I_\mathrm{h}\left[\left(\frac{\partial y}{\partial r}\cdot\frac{\partial^2 y}{\partial r^2}\right)_o^l-\int_0^l\frac{\partial^2 y}{\partial r^2}\cdot\frac{\partial^2 y}{\partial r^2}\mathrm{d}r\right]\\ &= E_\mathrm{h}I_\mathrm{h}\int_0^l\left(\boldsymbol{N}_{\mathrm{h,rr}}\boldsymbol{a}^e\right)^\mathrm{T}\left(\boldsymbol{N}_{\mathrm{h,rr}}\boldsymbol{a}^e\right)\mathrm{d}r=(\boldsymbol{a}^e)^\mathrm{T}\cdot E_\mathrm{h}I_\mathrm{h}\int_0^l\boldsymbol{N}_{\mathrm{h,rr}}^\mathrm{T}\boldsymbol{N}_{\mathrm{h,rr}}\mathrm{d}r\cdot(\boldsymbol{a}^e)\end{aligned} \tag{10.48}$$

$$\begin{aligned}\int_0^l y(r)m_\mathrm{h}V^2\left(\frac{\partial^2 y}{\partial r^2}\right)\mathrm{d}r &= m_\mathrm{h}V^2\int_0^l y(r)\left(\frac{\partial^2 y}{\partial r^2}\right)\mathrm{d}r\\ &= m_\mathrm{h}V^2\int_0^l y(r)\mathrm{d}\left(\frac{\partial y}{\partial r}\right)=m_\mathrm{h}V^2\left[\left(y(r)\cdot\frac{\partial y}{\partial r}\right)_o^l-\int_0^l\frac{\partial y}{\partial r}\cdot\frac{\partial y}{\partial r}\mathrm{d}r\right]\\ &= -m_\mathrm{h}V^2\int_0^l\left(\boldsymbol{N}_{\mathrm{h,r}}\boldsymbol{a}^e\right)^\mathrm{T}\left(\boldsymbol{N}_{\mathrm{h,r}}\boldsymbol{a}^e\right)\mathrm{d}r=-(\boldsymbol{a}^e)^\mathrm{T}\cdot m_\mathrm{h}V^2\int_0^l\boldsymbol{N}_{\mathrm{h,r}}^\mathrm{T}\boldsymbol{N}_{\mathrm{h,r}}\mathrm{d}r\cdot(\boldsymbol{a}^e)\end{aligned} \tag{10.49}$$

$$-2\int_0^l m_\mathrm{h} V y(r)\left(\frac{\partial^2 y}{\partial r\partial t}\right)\mathrm{d}r = -2m_\mathrm{h}V\int_0^l y(r)\left(\frac{\partial^2 y}{\partial r\partial t}\right)\mathrm{d}r = -2m_\mathrm{h}V\int_0^l (\boldsymbol{N}_\mathrm{h}\boldsymbol{a}^e)^\mathrm{T}\left(\boldsymbol{N}_{\mathrm{h,r}}\dot{\boldsymbol{a}}^e\right)\mathrm{d}r$$
$$= -(\boldsymbol{a}^e)^\mathrm{T}\cdot 2m_\mathrm{h}V\int_0^l \boldsymbol{N}_\mathrm{h}^\mathrm{T}\boldsymbol{N}_{\mathrm{h,r}}\mathrm{d}r\cdot(\dot{\boldsymbol{a}}^e) \tag{10.50}$$

$$\int_0^l y(r)m_\mathrm{h}\left(\frac{\partial^2 y}{\partial t^2}\right)\mathrm{d}r = m_\mathrm{h}\int_0^l y(r)\left(\frac{\partial^2 y}{\partial t^2}\right)\mathrm{d}r$$
$$= m_\mathrm{h}\int_0^l y(r)\left(\frac{\partial^2 y}{\partial t^2}\right)\mathrm{d}r = m_\mathrm{h}\int_0^l (\boldsymbol{N}_\mathrm{h}\boldsymbol{a}^e)^\mathrm{T}(\boldsymbol{N}_\mathrm{h}\ddot{\boldsymbol{a}}^e)\mathrm{d}r \tag{10.51}$$
$$= (\boldsymbol{a}^e)^\mathrm{T}\cdot m_\mathrm{h}\int_0^l \boldsymbol{N}_\mathrm{h}^\mathrm{T}\boldsymbol{N}_\mathrm{h}\mathrm{d}r\cdot(\ddot{\boldsymbol{a}}^e)$$

$$\int_0^l y(r)c_\mathrm{h}\left(\frac{\partial y}{\partial t}\right)\mathrm{d}r = c_\mathrm{h}\int_0^l y(r)\left(\frac{\partial y}{\partial t}\right)\mathrm{d}r$$
$$= c_\mathrm{h}\int_0^l (\boldsymbol{N}_\mathrm{h}\boldsymbol{a}^e)^\mathrm{T}(\boldsymbol{N}_\mathrm{h}\dot{\boldsymbol{a}}^e)\mathrm{d}r = (\boldsymbol{a}^e)^\mathrm{T}\cdot c_\mathrm{h}\int_0^l \boldsymbol{N}_\mathrm{h}^\mathrm{T}\boldsymbol{N}_\mathrm{h}\mathrm{d}r\cdot(\dot{\boldsymbol{a}}^e) \tag{10.52}$$

$$-\int_0^l y(r)c_\mathrm{h}V\left(\frac{\partial y}{\partial r}\right)\mathrm{d}r = -c_\mathrm{h}V\int_0^l y(r)\left(\frac{\partial y}{\partial r}\right)\mathrm{d}r$$
$$= -c_\mathrm{h}V\int_0^l (\boldsymbol{N}_\mathrm{h}\boldsymbol{a}^e)^\mathrm{T}\left(\boldsymbol{N}_{\mathrm{h,r}}\boldsymbol{a}^e\right)\mathrm{d}r \tag{10.53}$$
$$= -(\boldsymbol{a}^e)^\mathrm{T}\cdot c_\mathrm{h}V\int_0^l \boldsymbol{N}_\mathrm{h}^\mathrm{T}\boldsymbol{N}_{\mathrm{h,r}}\mathrm{d}r\cdot(\boldsymbol{a}^e)$$

$$-\int_0^l y(r)c_{\mathrm{s}}\left(\frac{\partial z}{\partial t}\right)\mathrm{d}r = -c_{\mathrm{s}}\int_0^l y(r)\left(\frac{\partial z}{\partial t}\right)\mathrm{d}r$$
$$= -c_{\mathrm{s}}\int_0^l (\boldsymbol{N}_{\mathrm{h}}\boldsymbol{a}^e)^{\mathrm{T}}(\boldsymbol{N}_{\mathrm{s}}\dot{\boldsymbol{a}}^e)\mathrm{d}r = -(\boldsymbol{a}^e)^{\mathrm{T}}\cdot c_{\mathrm{s}}\int_0^l \boldsymbol{N}_{\mathrm{h}}^{\mathrm{T}}\boldsymbol{N}_{\mathrm{s}}\mathrm{d}r\cdot(\dot{\boldsymbol{a}}^e) \tag{10.54}$$

$$\int_0^l y(r)c_{\mathrm{s}}V\left(\frac{\partial z}{\partial r}\right)\mathrm{d}r = c_{\mathrm{s}}V\int_0^l y(r)\left(\frac{\partial z}{\partial r}\right)\mathrm{d}r$$
$$= c_{\mathrm{s}}V\int_0^l (\boldsymbol{N}_{\mathrm{h}}\boldsymbol{a}^e)^{\mathrm{T}}\left(\boldsymbol{N}_{\mathrm{s,r}}\boldsymbol{a}^e\right)\mathrm{d}r = (\boldsymbol{a}^e)^{\mathrm{T}}\cdot c_{\mathrm{s}}V\int_0^l \boldsymbol{N}_{\mathrm{h}}^{\mathrm{T}}\boldsymbol{N}_{\mathrm{s,r}}\mathrm{d}r\cdot(\boldsymbol{a}^e) \tag{10.55}$$

$$\int_0^l y(r)c_{\mathrm{s}}\left(\frac{\partial y}{\partial t}\right)\mathrm{d}r = c_{\mathrm{s}}\int_0^l y(r)\left(\frac{\partial y}{\partial t}\right)\mathrm{d}r$$
$$= c_{\mathrm{s}}\int_0^l (\boldsymbol{N}_{\mathrm{h}}\boldsymbol{a}^e)^{\mathrm{T}}(\boldsymbol{N}_{\mathrm{h}}\dot{\boldsymbol{a}}^e)\mathrm{d}r = (\boldsymbol{a}^e)^{\mathrm{T}}\cdot c_{\mathrm{s}}\int_0^l \boldsymbol{N}_{\mathrm{h}}^{\mathrm{T}}\boldsymbol{N}_{\mathrm{h}}\mathrm{d}r\cdot(\dot{\boldsymbol{a}}^e) \tag{10.56}$$

$$-\int_0^l y(r)c_{\mathrm{s}}V\left(\frac{\partial y}{\partial r}\right)\mathrm{d}r = -c_{\mathrm{s}}V\int_0^l y(r)\left(\frac{\partial y}{\partial r}\right)\mathrm{d}r$$
$$= -c_{\mathrm{s}}V\int_0^l (\boldsymbol{N}_{\mathrm{h}}\boldsymbol{a}^e)^{\mathrm{T}}\left(\boldsymbol{N}_{\mathrm{h,r}}\boldsymbol{a}^e\right)\mathrm{d}r = -(\boldsymbol{a}^e)^{\mathrm{T}}\cdot c_{\mathrm{s}}V\int_0^l \boldsymbol{N}_{\mathrm{h}}^{\mathrm{T}}\boldsymbol{N}_{\mathrm{h,r}}\mathrm{d}r\cdot(\boldsymbol{a}^e) \tag{10.57}$$

$$\int_0^l y(r)k_{\mathrm{h}}y(r)\mathrm{d}r = k_{\mathrm{h}}\int_0^l y(r)^2\mathrm{d}r = k_{\mathrm{h}}\int_0^l (\boldsymbol{N}_{\mathrm{h}}\boldsymbol{a}^e)^{\mathrm{T}}(\boldsymbol{N}_{\mathrm{h}}\boldsymbol{a}^e)\mathrm{d}r$$
$$= (\boldsymbol{a}^e)^{\mathrm{T}}\cdot k_{\mathrm{h}}\int_0^l \boldsymbol{N}_{\mathrm{h}}^{\mathrm{T}}\boldsymbol{N}_{\mathrm{h}}\mathrm{d}r\cdot(\boldsymbol{a}^e) \tag{10.58}$$

$$-\int_0^l y(r)k_s z(r)\mathrm{d}r = -k_s\int_0^l y(r)z(r)\mathrm{d}r$$
$$= -k_s\int_0^l (\boldsymbol{N}_h\boldsymbol{a}^e)^T(\boldsymbol{N}_s\boldsymbol{a}^e)\mathrm{d}r = -(\boldsymbol{a}^e)^T\cdot k_s\int_0^l \boldsymbol{N}_h^T\boldsymbol{N}_s\mathrm{d}r\cdot(\boldsymbol{a}^e) \tag{10.59}$$

$$\int_0^l y(r)k_s y(r)\mathrm{d}r = k_s\int_0^l y(r)^2\mathrm{d}r = k_s\int_0^l (\boldsymbol{N}_h\boldsymbol{a}^e)^T(\boldsymbol{N}_h\boldsymbol{a}^e)\mathrm{d}r$$
$$= (\boldsymbol{a}^e)^T\cdot k_s\int_0^l \boldsymbol{N}_h^T\boldsymbol{N}_h\mathrm{d}r\cdot(\boldsymbol{a}^e) \tag{10.60}$$

By using the principle of the energy, the third layer beam's mass, damping, and stiffness matrices of the slab track element in a moving frame of reference can be obtained as follows:

$$\boldsymbol{m}_h^e = m_h\int_0^l \boldsymbol{N}_h^T\boldsymbol{N}_h\mathrm{d}r \tag{10.61}$$

$$\boldsymbol{c}_h^e = -2m_hV\int_0^l \boldsymbol{N}_h^T\boldsymbol{N}_{h,r}\mathrm{d}r + c_h\int_0^l \boldsymbol{N}_h^T\boldsymbol{N}_h\mathrm{d}r - c_s\int_0^l \boldsymbol{N}_h^T\boldsymbol{N}_s\mathrm{d}r + c_s\int_0^l \boldsymbol{N}_h^T\boldsymbol{N}_h\mathrm{d}r \tag{10.62}$$

$$\boldsymbol{k}_h^e = E_hI_h\int_0^l \boldsymbol{N}_{h,rr}^T\boldsymbol{N}_{h,rr}\mathrm{d}r - m_hV^2\int_0^l \boldsymbol{N}_{h,r}^T\boldsymbol{N}_{h,r}\mathrm{d}r$$
$$- c_hV\int_0^l \boldsymbol{N}_h^T\boldsymbol{N}_{h,r}\mathrm{d}r + c_sV\int_0^l \boldsymbol{N}_h^T\boldsymbol{N}_{s,r}\mathrm{d}r$$
$$- c_sV\int_0^l \boldsymbol{N}_h^T\boldsymbol{N}_{h,r}\mathrm{d}r + k_h\int_0^l \boldsymbol{N}_h^T\boldsymbol{N}_h\mathrm{d}r - k_s\int_0^l \boldsymbol{N}_h^T\boldsymbol{N}_s\mathrm{d}r + k_s\int_0^l \boldsymbol{N}_h^T\boldsymbol{N}_h\mathrm{d}r \tag{10.63}$$

Finally, the mass, damping, and stiffness matrices of the slab track element in a moving frame of reference are as follows:

$$\boldsymbol{m}_{\mathrm{l}}^{e} = \boldsymbol{m}_{\mathrm{r}}^{e} + \boldsymbol{m}_{\mathrm{s}}^{e} + \boldsymbol{m}_{\mathrm{h}}^{e} \tag{10.64}$$

$$\boldsymbol{c}_{\mathrm{l}}^{e} = \boldsymbol{c}_{\mathrm{r}}^{e} + \boldsymbol{c}_{\mathrm{s}}^{e} + \boldsymbol{c}_{\mathrm{h}}^{e} \tag{10.65}$$

$$\boldsymbol{k}_{\mathrm{l}}^{e} = \boldsymbol{k}_{\mathrm{r}}^{e} + \boldsymbol{k}_{\mathrm{s}}^{e} + \boldsymbol{k}_{\mathrm{h}}^{e} \tag{10.66}$$

Based on the finite element assembling rule, the global mass matrix, the global damping matrix, and the global stiffness matrix of the slab track element in a moving frame of reference can be obtained by assembling the element mass matrix (10.64), the element damping matrix (10.65), and the element stiffness matrix (10.66).

$$\boldsymbol{m}_{\mathrm{l}} = \sum_{e} \boldsymbol{m}_{\mathrm{l}}^{e}, \quad \boldsymbol{c}_{\mathrm{l}} = \sum_{e} \boldsymbol{c}_{\mathrm{l}}^{e}, \quad \boldsymbol{k}_{\mathrm{l}} = \sum_{e} \boldsymbol{k}_{\mathrm{l}}^{e} \tag{10.67}$$

By using Lagrange equation, the finite element equation of the slab track structure in a moving frame of reference can be obtained as follows:

$$\boldsymbol{m}_{\mathrm{l}}\ddot{\boldsymbol{a}}_{\mathrm{l}} + \boldsymbol{c}_{\mathrm{l}}\dot{\boldsymbol{a}}_{\mathrm{l}} + \boldsymbol{k}_{\mathrm{l}}\boldsymbol{a}_{\mathrm{l}} = \boldsymbol{Q}_{\mathrm{l}} \tag{10.68}$$

where $\boldsymbol{Q}_{\mathrm{l}}$ is the global nodal load vector of the slab track structure.

10.3 Vehicle Element Model

Vehicle element model here is the same as the one in Fig. 9.4 of the Chap. 9. The stiffness matrix ($\boldsymbol{k}_{\mathrm{u}}^{e}$), the mass matrix ($\boldsymbol{m}_{\mathrm{u}}^{e}$), the damping matrix($\boldsymbol{c}_{\mathrm{u}}^{e}$), and the nodal load vector ($\boldsymbol{Q}_{\mathrm{u}}^{e}$) of the vehicle element can refer to (9.58), (9.71), (9.74) and (9.59), respectively.

10.4 Finite Element Equation of the Vehicle-Slab Track Coupling System

Considering that the finite element equation of the vehicle and slab track coupling system consists of two elements, namely the slab track element and the vehicle element, of which the stiffness matrix, the mass matrix, and the damping matrix of the slab track element are $\boldsymbol{k}_{\mathrm{l}}^{e}$, $\boldsymbol{m}_{\mathrm{l}}^{e}$, $\boldsymbol{c}_{\mathrm{l}}^{e}$, respectively, with a calculating formula illustrated in 10.2; while the stiffness matrix, the mass matrix, and the damping matrix of the vehicle element are $\boldsymbol{k}_{\mathrm{u}}^{e}$, $\boldsymbol{m}_{\mathrm{u}}^{e}$, $\boldsymbol{c}_{\mathrm{u}}^{e}$, respectively, shown in (9.58), (9.71) and (9.74) in Chap. 9. In numerical calculation, it only needs to assemble the global

stiffness matrix, the global mass matrix, the global damping matrix, and the global load vector of the track structure once. And in each following calculating time step, by assembling the stiffness matrix, the mass matrix, the damping matrix, and the load vector of the vehicle element into the global stiffness matrix, the global mass matrix, the global damping matrix, and the global load vector of track structure with the standard finite element assembling rule, one can obtain the global stiffness matrix, the global mass matrix, the global damping matrix, and the global load vector of the vehicle-slab track coupling system.

Therefore, the dynamic finite element equation of the vehicle-slab track coupling system is as follows:

$$\boldsymbol{M}\ddot{\boldsymbol{a}} + \boldsymbol{C}\dot{\boldsymbol{a}} + \boldsymbol{K}\boldsymbol{a} = \boldsymbol{Q} \tag{10.69}$$

where $\boldsymbol{M}$, $\boldsymbol{C}$, $\boldsymbol{K}$, and $\boldsymbol{Q}$ are the global mass matrix, the global damping matrix, the global stiffness matrix, and the global load vector of the vehicle-slab track coupling system, respectively.

$$\begin{aligned} \boldsymbol{M} &= \sum_e \left(\boldsymbol{m}_\mathrm{l} + \boldsymbol{m}_\mathrm{u}^e\right), \quad \boldsymbol{C} = \sum_e \left(\boldsymbol{c}_\mathrm{l} + \boldsymbol{c}_\mathrm{u}^e\right), \quad \boldsymbol{K} = \sum_e \left(\boldsymbol{k}_\mathrm{l} + \boldsymbol{k}_\mathrm{u}^e\right), \\ \boldsymbol{Q} &= \sum_e \left(\boldsymbol{Q}_\mathrm{l} + \boldsymbol{Q}_\mathrm{u}^e\right) \end{aligned} \tag{10.70}$$

The numerical solution to the dynamic finite element equation of the vehicle-slab track coupling system can be achieved by the direct integration method, such as Newmark's integration method.

10.5 Algorithm Verification

According to the above algorithm, the computational program FEST (Finite Element program for the Slab Track) is developed by using MATLAB. In order to verify the correctness of the model and the algorithm of this chapter, let us investigate the dynamic response of the vehicle and the track structure for Chinese high-speed train CRH3 running through the CRTS II slab track with the speed of 72 km/h. The calculated results are compared with those by conventional finite element method. Assuming that the railway is completely smooth, the computational time step is 0.001 s. Parameters of the Chinese high-speed train CRH3 and the CRTS II slab track structure are listed in Tables 6.7 and 10.1. The results are shown in Figs. 10.6 and 10.7, in which Fig. 10.6 is the distribution of the rail displacement along the track direction, and Fig. 10.7 is the time history of the wheel-rail contact force.

Table 10.1 Parameters of CRTS II slab track structure

Parameters	Values	Parameters	Values
Rail elasticity modulus/(MPa)	2.1×10^5	Inertia moment of concrete support layer/(m^4)	3.3×10^{-3}
Rail inertia moment/(m^4)	3.217×10^{-5}	Stiffness of rail pads and fasteners/(MN/m)	60
Rail mass/(kg/m)	60	Damping of rail pads and fasteners/(kN s/m)	47.7
Mass of track slab/(kg/m)	1275	CA mortar stiffness/(MN/m)	900
Elasticity modulus of track slab/(MPa)	3.9×10^4	CA mortar damping/(kN s/m)	83
Inertia moment of track slab/(m^4)	8.5×10^{-5}	Subgrade stiffness/(MN/m)	60
Mass of concrete support layer/(kg/m)	2340	Subgrade damping/(kN s/m)	90
Elasticity modulus of concrete support layer/(MPa)	3×10^4	Element length/(m)	0.5

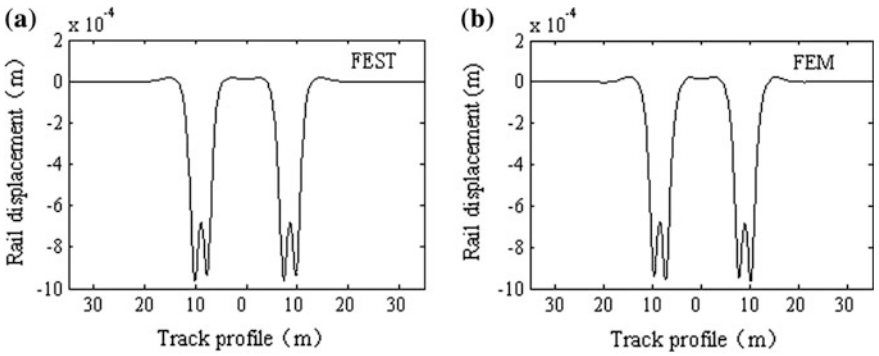

Fig. 10.6 Rail vertical displacement distribution along the track direction. **a** Calculated results with FEST approach and **b** calculated results with FEM approach

As illustrated in Fig. 10.6, the rail vertical displacements obtained by using the model and the algorithm presented in this chapter are in good agreement with those by the conventional finite element method [11]. Figure 10.7 is the time history of the wheel-rail contact force by the two methods. Due to the differences between the two algorithms and the influence of the initial computational conditions, the curves of the calculated results before stability are different, but in the end they all converge to the static load value exerted on the wheels. Since the track is assumed to be completely smooth, it shows that the calculated results are accurate and thus proves the correctness and feasibility of the model and the algorithm.

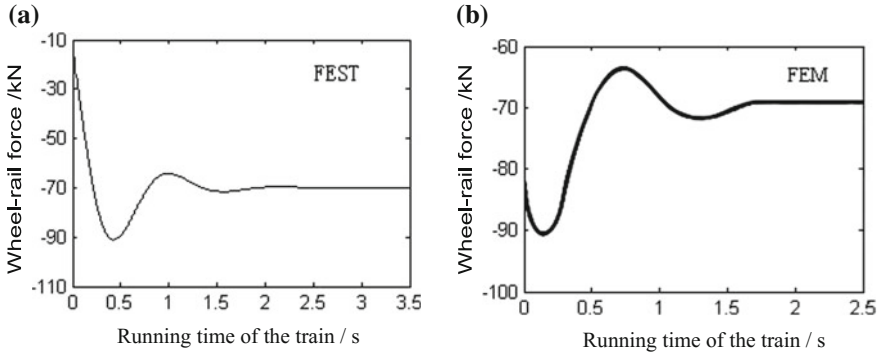

Fig. 10.7 Time history of the wheel-rail contact force. **a** Wheel-rail contact force with FEST approach and **b** wheel-rail contact force with FEM approach

10.6 Dynamic Analysis of High-Speed Train and Slab Track Coupling System

As an application example, dynamic analysis of the high-speed train and the slab track coupling system is carried out by the presented model and algorithm. The vehicle is Chinese high-speed train CRH3; the track structure is CRTS II slab track at the subgrade section, as shown in Figs. 10.8 and 10.9, respectively. The vehicle parameters and the track parameters are as shown in Tables 6.7 and 10.1. The train speed 200 km/h is specified. The German low interference spectrum for high-speed railway is adopted to simulate the track irregularity as shown in Fig. 10.10. Take the time step as 0.001 s in calculation. Because of the influence of the initial conditions, the calculated results of the first few seconds are usually inaccurate. The following is the time history of dynamic response within 5 s after the calculation is stable, including the acceleration of the car body, the displacement of the rail, the

Fig. 10.8 Chinese high-speed train CRH3

Fig. 10.9 Slab track of high-speed railway at the subgrade section

track slab, and the concrete support layer, and their corresponding velocity and acceleration, as well as the wheel-rail contact force [11, 12].

The interaction between the wheel and the rail increases significantly because of the random irregularities of the track. Figures 10.11, 10.12 and 10.13 demonstrate the time history curves of the vertical displacements of the rail, the track slab, and the concrete support layer at the second wheel-rail contact point, respectively. Because of the random irregularities of the track, the displacements of the rail, the track slab, and the concrete support layer are oscillating.

Figures 10.14, 10.15 and 10.16 show the vertical displacement distributions of the rail, the track slab, and the concrete support layer along the track direction, respectively. In Fig. 10.14, there are four obvious peaks in the rail displacement diagram, corresponding to the four wheels' action points. In Fig. 10.15 there are only two pliable peaks in the track slab displacement diagram with the maximum amplitude much smaller than those in Fig. 10.14. The same situation for the

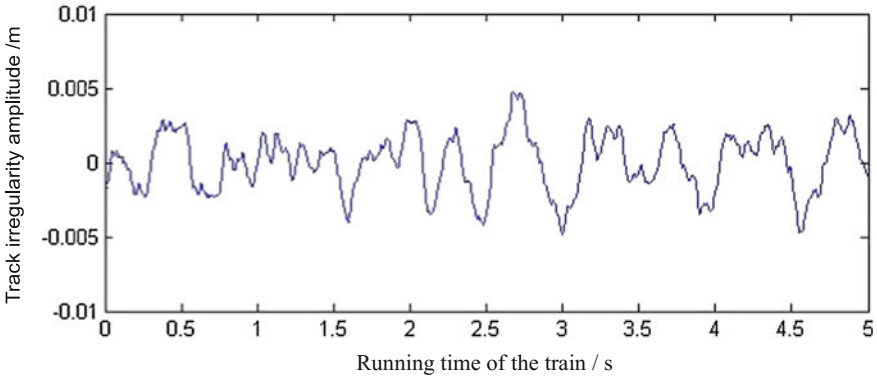

Fig. 10.10 Track irregularity sample with low interference spectrum in Germany

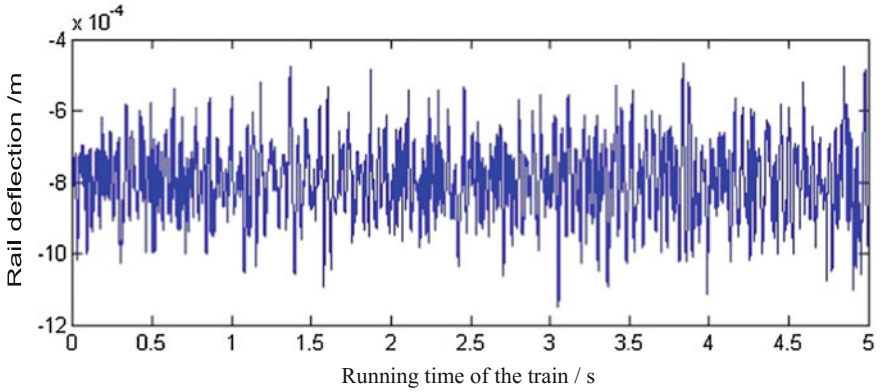

Fig. 10.11 Time history of the rail vertical displacement

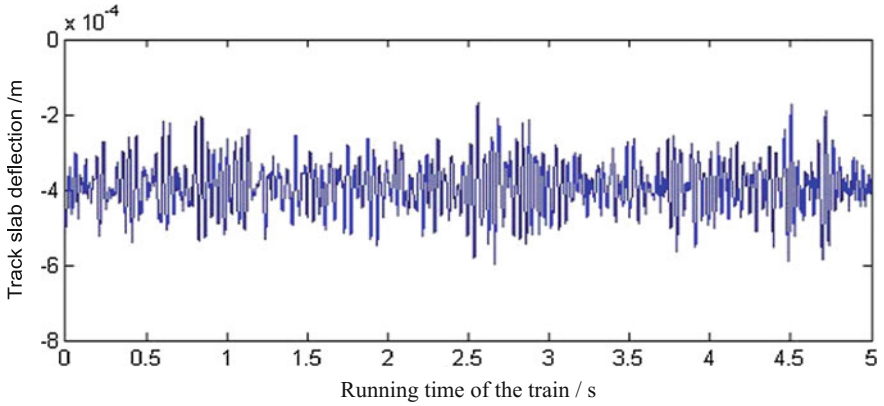

Fig. 10.12 Time history of the slab vertical displacement

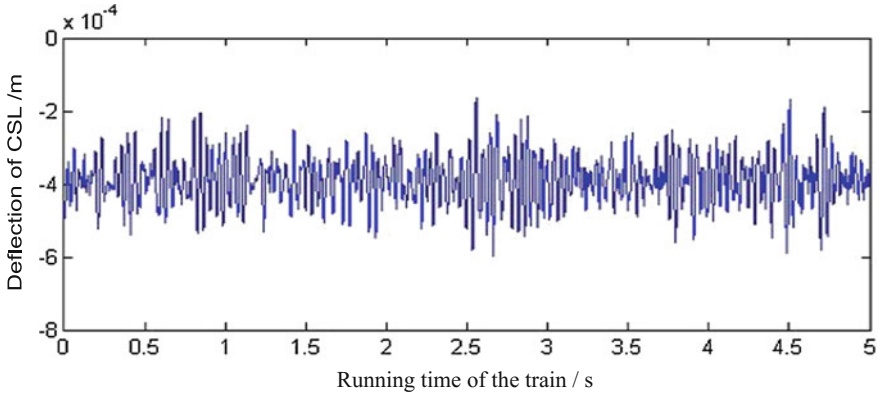

Fig. 10.13 Time history of the vertical displacement of the concrete support layer (CSL)

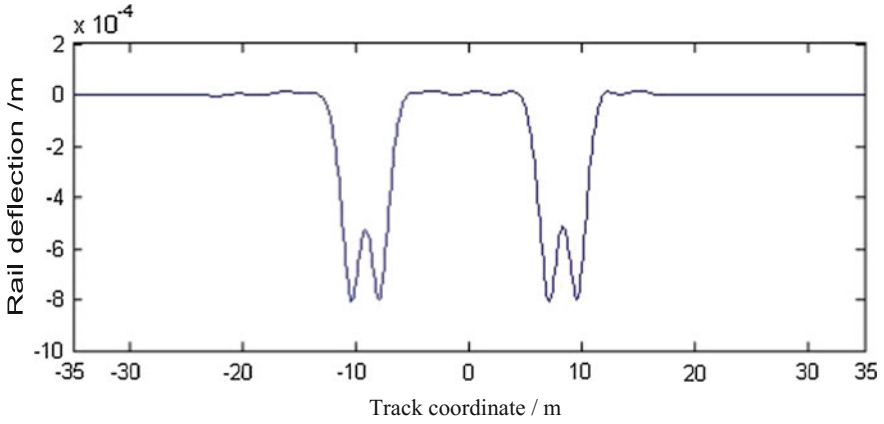

Fig. 10.14 Rail vertical displacement along the track direction

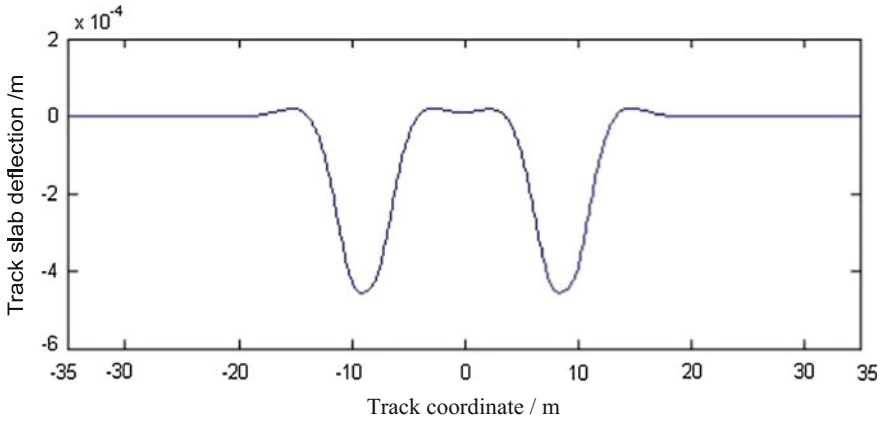

Fig. 10.15 Track slab vertical displacement along the track direction

displacement distribution of the concrete support layer also is observed in Fig. 10.16, which illustrates the additional dynamic load induced by the train operation that is obviously reduced due to the existing of the rail pads and fasteners and the CA mortar.

Figures 10.17, 10.18 and 10.19 represent the time history of the vertical velocity of the rail, the track slab, and the concrete support layer at the second wheel-rail contact point, respectively, which show the vibration velocities of the rail, the track slab, and the concrete support layer attenuating in turn. Figures 10.20, 10.21 and 10.22 are the time history of the vertical acceleration of the rail, the track slab, and the concrete support layer at the second wheel-rail contact point, respectively. Due

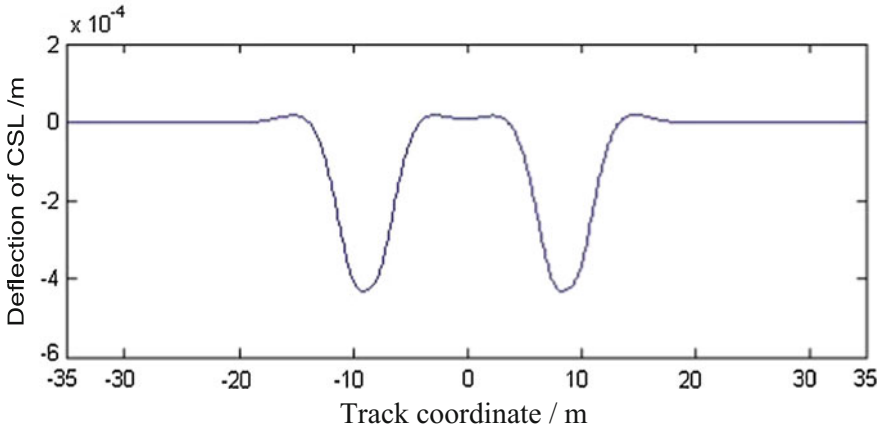

Fig. 10.16 Vertical displacement of the concrete support layer (CSL) along the track direction

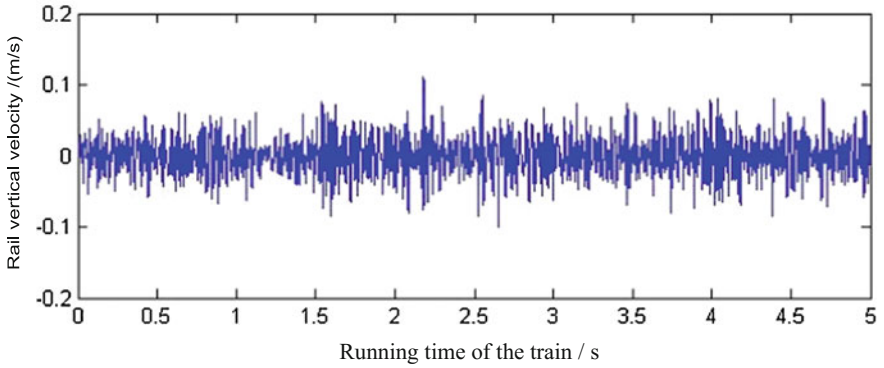

Fig. 10.17 Time history of the rail vertical velocity

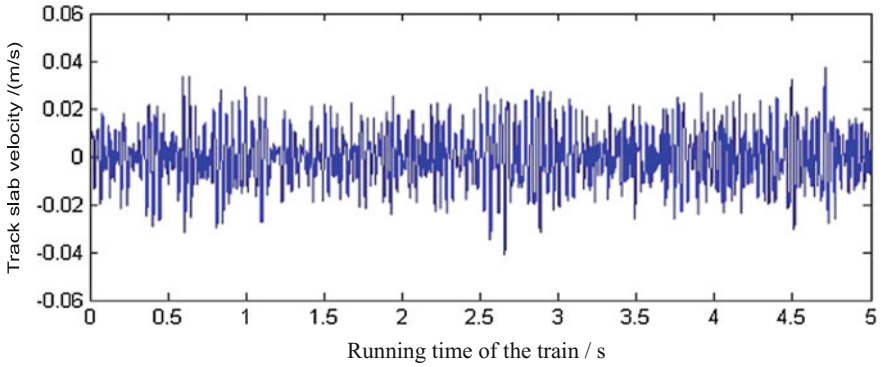

Fig. 10.18 Time history of the track slab vertical velocity

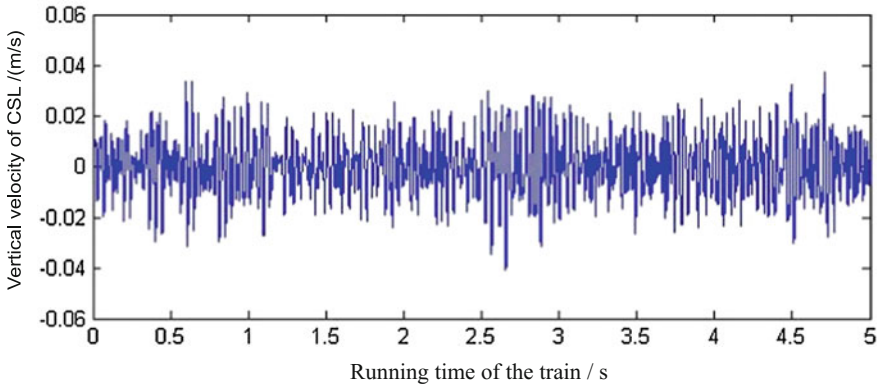

Fig. 10.19 Time history of the vertical velocity of the concrete support layer (CSL)

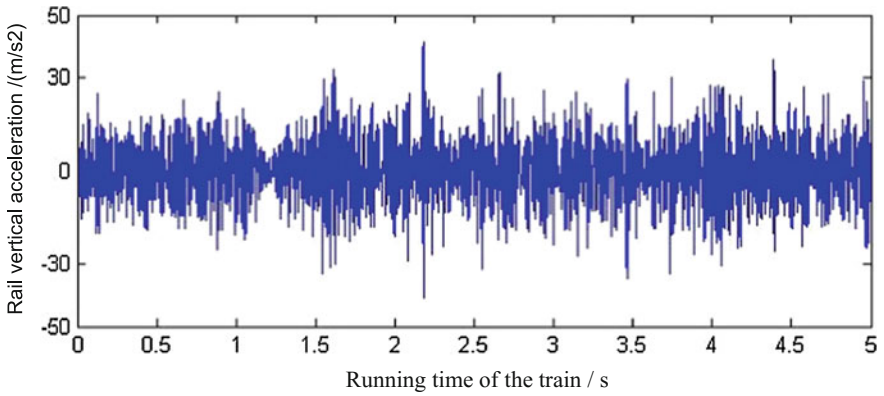

Fig. 10.20 Time history of the rail vertical acceleration

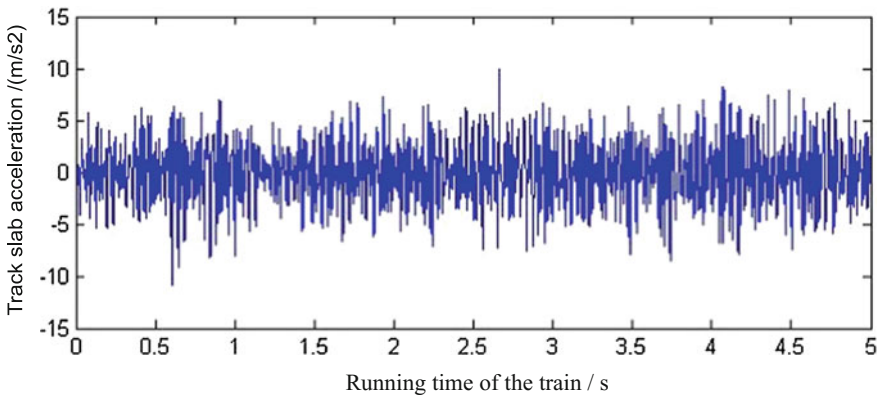

Fig. 10.21 Time history of the track slab vertical acceleration

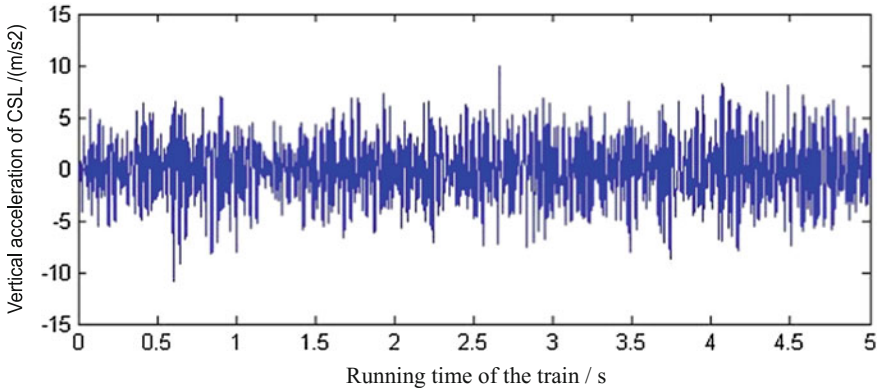

Fig. 10.22 Time history of the vertical acceleration of the concrete support layer (CSL)

to the existing of the rail pads and fasteners and the CA mortar, the acceleration peaks of the track slab and the concrete support layer are also reduced obviously.

Figure 10.23 shows the time history of the car body vibration acceleration. It is an important indicator of measuring passengers' riding comfort. As shown in this Figure, in case of the train speed of 200 m/h and the track irregularity generated by the German low interference spectrum for high-speed railway, the acceleration amplitude of the car body is in a reasonable range, which can guarantee the passengers' comfort.

Figure 10.24 is the time history of the wheel-rail contact force, from which it can be observed that the wheel-rail contact force fluctuates around the static load of 70 kN, with maximum peak not more than 120 kN.

As a conclusion, the slab track element model and the associated algorithm in a moving frame of reference for dynamic analysis of the vehicle-track coupling

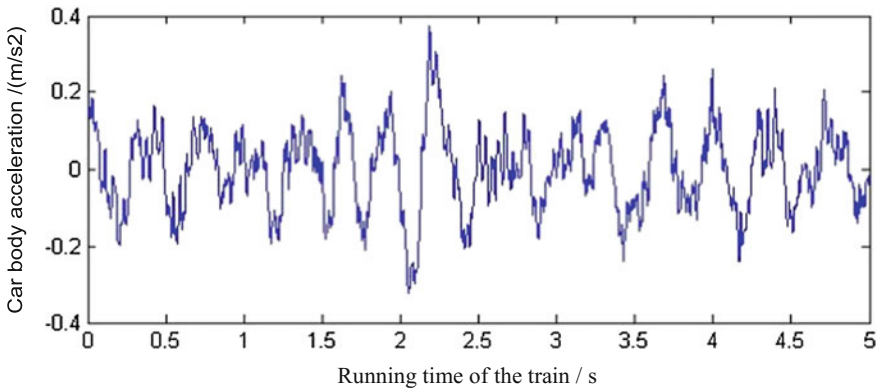

Fig. 10.23 Time history of the car body acceleration

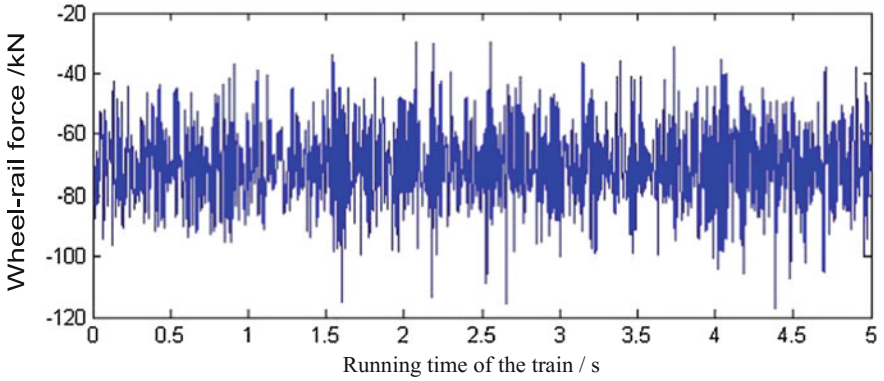

Fig. 10.24 Time history of the wheel-rail contact force

system are presented in this chapter. Three-layer continuous beam model for the slab track is developed, and the mass, damping, and stiffness matrices of the slab track element in a moving frame of reference are deduced. A whole vehicle is taken into account as a vehicle element with 26 degrees of freedom.

The main advantage of the approach is that, unlike in the FEM, the moving vehicle always acts at the same point in the numerical model, thereby eliminating the need for keeping track of the contact point with respect to individual elements. In addition, the moving vehicle will never run out of the truncated model. However, the defect is that the track structure has to be assumed continuous, which is different from the fact that the rail is supported by discrete supports.

References

1. Grassie SL, Gregory RW, Harrison D, Johnson KL (1982) The dynamic response of railway track to high frequency vertical excitation. J Mech Eng Sci 24:77–90
2. Eisenmann J (2002) Redundancy of Rheda-type slab track. Eisenbahningenieur 53(10):13–18
3. Zhai WM (1991) Vehicles-track vertical coupling dynamics. Doctor's dissertation of Southwest Jiaotong University, Chengdu
4. Zhai WM (1992) The vertical model of vehicle-track system and its coupling dynamics. J China Railway Soc 14(3):10–21
5. Xiang J, He D (2007) Analysis model of vertical vibration of high speed train and Bögle slab track system. J Traffic Transp Eng 7(3): l–5
6. He D, Xiang J, Zeng QY (2007) A new method for dynamics modeling of ballastless track. J Central South Univ 12(6):1206–1211
7. Lei XY, Sheng XZ (2008) Theoretical research on modern track, 2nd edn. China Railway Publishing House, Beijing
8. Lei XY, Zhang B, Liu QJ (2009) Model of vehicle and track elements for vertical dynamic analysis of vertical-track system. J Vibr Shock 29(3): 168–173
9. Xie WP, Zhen B (2005) Analysis of stable dynamic response of Winkler beam under moving load. J Wuhan Univ Technol 27(7):61–63

10. Koh CG, Ong JSY, Chua KH, D Feng J (2003) Moving element method for train—track dynamics. Int J Numer Methods Eng 56:1549–1567
11. Wang J (2012) Moving element method for high-speed railway ballastless track dynamic performance analysis. Master thesis. East China Jiaotong University, Nanchang
12. Lei XY, Wang J (2014) Dynamic analysis of the train and slab track coupling system with finite elements in a moving frame of reference. J Vib Control 20(9):1301–1317

Chapter 11
Model for Vertical Dynamic Analysis of the Vehicle-Track-Subgrade-Ground Coupling System

Chapters 6–10 has elaborated several models and their algorithms for vertical dynamic analysis of the vehicle-track coupling system. In the analysis, effects of subgrade and ground have not been considered and the subgrade is simplified into viscoelastic damping elements. In fact, an accurate analysis of the vehicle dynamic action on the track structure has to consider the interactions among vehicle, track, subgrade, and ground [1–6]. In this chapter, a model for vertical dynamic analysis of the integrated vehicle-track-subgrade-ground coupling system is established and its numerical method is explored, based on the previously discussed models.

11.1 Model of the Slab Track-Embankment-Ground System Under Moving Loads

Figure 11.1 is an analytic model of the slab track-embankment-ground coupling system [7]. It is established on the following assumptions: The rail, track slab, and concrete base are infinite Euler beams; stiffnesses and dampings of the rail pads and fasteners, and CA mortar adjustment layer are simulated with uniformly distributed linear springs and dampers; the ground is simplified into three-dimensional layer. In general, due to the big difference between their widths, the subgrade bed and the embankment body are analyzed separately. The subgrade bed is categorized into the track structure model and is regarded as an elastic body with uniformly distributed mass, vertical stiffness, and damping along the track alignment, exclusive of its bending stiffness. The embankment body is taken as a layer of soil covering on the surface of a three-dimensional ground. The slab track-embankment-ground system is divided into two parts: the upper and the lower. The upper part is slab track-subgrade bed system, which is assumed to be a one-dimensional infinite body in the X direction, while the lower part is embankment body-ground system, which is considered to be a three-dimensional semi-infinite body. The two parts keep

X. Lei, *High Speed Railway Track Dynamics*,
DOI 10.1007/978-981-10-2039-1_11

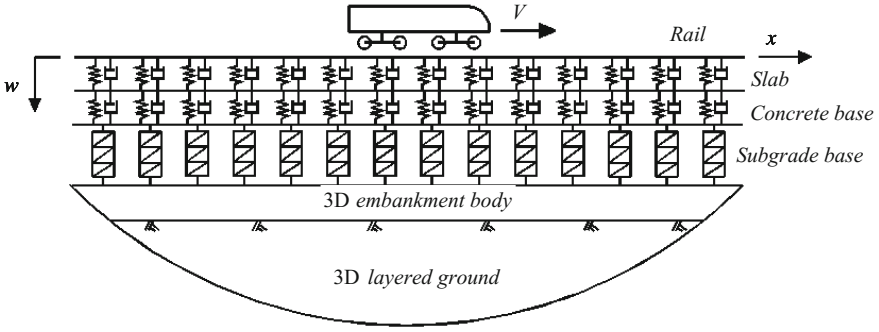

Fig. 11.1 A model of the slab track-embankment-ground coupling system

contact on the central line of the embankment body. Contact width is marked as $2b$ (the width of subgrade bed).

11.1.1 Dynamic Equation and Its Solution for the Slab Track-Subgrade Bed System

Governing equation of the rail vibration is

$$EI_{\mathrm{r}}\frac{\partial^4 w_{\mathrm{r}}}{\partial x^4} + m_{\mathrm{r}}\ddot{w}_{\mathrm{r}} + k_{\mathrm{p}}(w_{\mathrm{r}} - y_{\mathrm{s}}) + c_{\mathrm{p}}(\dot{w}_{\mathrm{r}} - \dot{y}_{\mathrm{s}}) = P(x,t) \tag{11.1}$$

where $P(x,t) = \sum_{l=1}^{M} P_l \mathrm{e}^{i\Omega t}\delta(x - Vt - a_l)$.

Governing equation of the track slab is:

$$EI_{\mathrm{s}}\frac{\partial^4 y_{\mathrm{s}}}{\partial x^4} + m_{\mathrm{s}}\ddot{y}_{\mathrm{s}} - k_{\mathrm{p}}(w_{\mathrm{r}} - y_{\mathrm{s}}) - c_{\mathrm{p}}(\dot{w}_{\mathrm{r}} - \dot{y}_{\mathrm{s}}) + k_{\mathrm{s}}(y_{\mathrm{s}} - y_{\mathrm{d}}) + c_{\mathrm{s}}(\dot{y}_{\mathrm{s}} - \dot{y}_{\mathrm{d}}) = 0 \tag{11.2}$$

Governing equation of the concrete base is:

$$EI_{\mathrm{d}}\frac{\partial^4 y_{\mathrm{d}}}{\partial x^4} + m_{\mathrm{d}}\ddot{y}_{\mathrm{d}} - k_{\mathrm{s}}(y_{\mathrm{s}} - y_{\mathrm{d}}) - c_{\mathrm{s}}(\dot{y}_{\mathrm{s}} - \dot{y}_{\mathrm{d}}) = -F_3 \tag{11.3}$$

Since the subgrade bed is very thick (2.5–3 m in general), the vertical displacement of the bed is assumed to make linear change along the direction of

thickness. Using approximately consistent mass matrix to denote the inertial effect, governing equation of the subgrade bed vibration can be expressed as

$$\frac{m_c}{6}\begin{bmatrix}2 & 1\\ 1 & 2\end{bmatrix}\begin{Bmatrix}\ddot{y}_d\\ \ddot{y}_c\end{Bmatrix}+k_c\begin{bmatrix}1 & -1\\ -1 & 1\end{bmatrix}\begin{Bmatrix}y_d\\ y_c\end{Bmatrix}+c_c\begin{bmatrix}1 & -1\\ -1 & 1\end{bmatrix}\begin{Bmatrix}\dot{y}_d\\ \dot{y}_c\end{Bmatrix}=\begin{Bmatrix}F_3\\ -F_4\end{Bmatrix} \tag{11.4}$$

Indications of the notations in Eqs. (11.1)–(11.4) are as follows : $(\dot{})$ and $(\ddot{})$ are first-order derivative and second-order derivative of t respectively;w_r, y_s, y_d, and y_c are the shortened forms of $w_r(x,t)$, $y_s(x,t)$, $y_d(x,t)$, and $y_c(x,t)$ respectively, standing for the vertical displacement of the rail, track slab, concrete base, and subgrade bed; EI_r, EI_s, and EI_d are the bending stiffness of the rail, track slab, and concrete base, respectively; m_r, m_s, m_d and m_c are the mass for per unit length of the rail, track slab, concrete base, and the subgrade bed, respectively; k_p, k_s, k_c and c_p, c_s, c_c are the stiffnesses and dampings for per unit length of the rail pads and fasteners, CA mortar adjustment layer, and subgrade bed, respectively; F_3 and F_4 are the shortened forms for $F_3(x,t)$ and $F_4(x,t)$, standing for the interaction force between the concrete base and the subgrade bed, and the force between the subgrade bed and the embankment body, respectively; δ is Dirac function; V is the train speed; $P_l e^{i\Omega t}$ is the lth wheel-axle load and indicates moving axle loads or the dynamic wheel-rail force caused by harmonic track irregularities; load frequency is Ω, with a unit of rad/s, load amplitude is P_l, downward direction is positive; a_l means distance between the lth wheel-axle load and the origin when $t = 0$; M is the total number of wheel-axle loads.

Define Fourier transform and inverse Fourier transform in the X direction as

$$\tilde{f}(\beta,t)=\int_{-\infty}^{+\infty} f(x,t)e^{-i\beta x}\,dx,\quad f(x,t)=\frac{1}{2\pi}\int_{-\infty}^{+\infty}\tilde{f}(\beta,t)e^{i\beta x}\,d\beta \tag{11.5}$$

where β is wave number of space coordinate x, with a unit of rad/m.

Applying Fourier transform of X direction to Eqs. (11.1)–(11.4), it yields

$$EI_r\beta^4\tilde{w}_r(\beta,t)+m_r\frac{\partial^2\tilde{w}_r(\beta,t)}{\partial t^2}+k_p[\tilde{w}_r(\beta,t)-\tilde{y}_s(\beta,t)]+c_p\left[\frac{\partial\tilde{w}_r(\beta,t)}{\partial t}-\frac{\partial\tilde{y}_s(\beta,t)}{\partial t}\right]=\tilde{P}(\beta,t) \tag{11.6}$$

$$EI_s\beta^4\tilde{y}_s(\beta,t)+m_s\frac{\partial^2\tilde{y}_s(\beta,t)}{\partial t^2}-k_p[\tilde{w}_r(\beta,t)-\tilde{y}_s(\beta,t)]-c_p\left[\frac{\partial\tilde{w}_r(\beta,t)}{\partial t}-\frac{\partial\tilde{y}_s(\beta,t)}{\partial t}\right]+k_s[\tilde{y}_s(\beta,t)-\tilde{y}_d(\beta,t)]+c_s\left[\frac{\partial\tilde{y}_s(\beta,t)}{\partial t}-\frac{\partial\tilde{y}_d(\beta,t)}{\partial t}\right]=0 \tag{11.7}$$

$$\begin{aligned} EI_{\mathrm{d}}\beta^4\tilde{y}_{\mathrm{d}}(\beta,t)+\left[m_{\mathrm{d}}+\frac{m_{\mathrm{c}}}{3}\right]\frac{\partial^2\tilde{y}_{\mathrm{d}}(\beta,t)}{\partial t^2}+\frac{m_{\mathrm{c}}}{6}\frac{\partial^2\tilde{y}_{\mathrm{c}}(\beta,t)}{\partial t^2}\\ -k_{\mathrm{s}}[\tilde{y}_{\mathrm{s}}(\beta,t)-\tilde{y}_{\mathrm{d}}(\beta,t)]-c_{\mathrm{s}}\left[\frac{\partial\tilde{y}_{\mathrm{s}}(\beta,t)}{\partial t}-\frac{\partial\tilde{y}_{\mathrm{d}}(\beta,t)}{\partial t}\right]\\ +k_{\mathrm{c}}[\tilde{y}_{\mathrm{d}}(\beta,t)-\tilde{y}_{\mathrm{c}}(\beta,t)]+c_{\mathrm{c}}\left[\frac{\partial\tilde{y}_{\mathrm{d}}(\beta,t)}{\partial t}-\frac{\partial\tilde{y}_{\mathrm{c}}(\beta,t)}{\partial t}\right]=0 \end{aligned} \tag{11.8}$$

$$\begin{aligned} &\frac{m_{\mathrm{c}}}{6}\frac{\partial^2\tilde{y}_{\mathrm{d}}(\beta,t)}{\partial t^2}+\frac{m_{\mathrm{c}}}{3}\frac{\partial^2\tilde{y}_{\mathrm{c}}(\beta,t)}{\partial t^2}-k_{\mathrm{c}}[\tilde{y}_{\mathrm{d}}(\beta,t)-\tilde{y}_{\mathrm{c}}(\beta,t)]-c_{\mathrm{c}}\left[\frac{\partial\tilde{y}_{\mathrm{d}}(\beta,t)}{\partial t}-\frac{\partial\tilde{y}_{\mathrm{c}}(\beta,t)}{\partial t}\right]\\ &=-\tilde{F}_4(\beta,t) \end{aligned} \tag{11.9}$$

where $\tilde{w}_{\mathrm{r}}(\beta,t)$, $\tilde{y}_{\mathrm{s}}(\beta,t)$, $\tilde{y}_{\mathrm{d}}(\beta,t)$, $\tilde{y}_{\mathrm{c}}(\beta,t)$, $\tilde{F}_4(\beta,t)$, and $\tilde{P}(\beta,t)$ are the corresponding Fourier transform of $w_{\mathrm{r}}(x,t)$, $y_{\mathrm{s}}(x,t)$, $y_{\mathrm{d}}(x,t)$, $y_{\mathrm{c}}(x,t)$, $F_4(x,t)$, and $P(x,t)$, respectively, $\tilde{P}(\beta,t)=\sum_{l=1}^{M}P_l\mathrm{e}^{-i\beta a_l}\mathrm{e}^{i(\Omega-\beta V)t}$.

Solve the steady displacement of Eqs. (11.6)–(11.9), and suppose

$$\begin{aligned} \tilde{w}_{\mathrm{r}}(\beta,t)&=\bar{w}_{\mathrm{r}}(\beta)\mathrm{e}^{i(\Omega-\beta V)t}\\ \tilde{y}_{\mathrm{s}}(\beta,t)&=\bar{y}_{\mathrm{s}}(\beta)\mathrm{e}^{i(\Omega-\beta V)t}\\ \tilde{y}_{\mathrm{d}}(\beta,t)&=\bar{y}_{\mathrm{d}}(\beta)\mathrm{e}^{i(\Omega-\beta V)t}\\ \tilde{y}_{\mathrm{c}}(\beta,t)&=\bar{y}_{\mathrm{c}}(\beta)\mathrm{e}^{i(\Omega-\beta V)t}\\ \tilde{F}_4(\beta,t)&=\overline{F}_4(\beta)\mathrm{e}^{i(\Omega-\beta V)t}\\ \tilde{P}(\beta,t)&=\overline{P}(\beta)\mathrm{e}^{i(\Omega-\beta V)t} \end{aligned} \tag{11.10}$$

where $\overline{P}(\beta)=\sum_{l=1}^{M}P_l\mathrm{e}^{-i\beta a_l}$.

Letting $\omega=\Omega-\beta V$, and substituting Eq. (11.10) into Eqs. (11.6)–(11.9), it has

$$EI_{\mathrm{r}}\beta^4\bar{w}_{\mathrm{r}}(\beta)-m_{\mathrm{r}}\omega^2\bar{w}_{\mathrm{r}}(\beta)+(k_{\mathrm{p}}+i\omega c_{\mathrm{p}})[\bar{w}_{\mathrm{r}}(\beta)-\bar{y}_{\mathrm{s}}(\beta)]=\overline{P}(\beta) \tag{11.11}$$

$$\begin{aligned} EI_{\mathrm{s}}\beta^4\bar{y}_{\mathrm{s}}(\beta)-m_{\mathrm{s}}\omega^2\bar{y}_{\mathrm{s}}(\beta)-(k_{\mathrm{p}}+i\omega c_{\mathrm{p}})[\bar{w}_{\mathrm{r}}(\beta)-\bar{y}_{\mathrm{s}}(\beta)]\\ +(k_{\mathrm{s}}+i\omega c_{\mathrm{s}})[\bar{y}_{\mathrm{s}}(\beta)-\bar{y}_{\mathrm{d}}(\beta)]=0 \end{aligned} \tag{11.12}$$

$$\begin{aligned} EI_{\mathrm{d}}\beta^4\bar{y}_{\mathrm{d}}(\beta)-\left(m_{\mathrm{d}}+\frac{m_{\mathrm{c}}}{3}\right)\omega^2\bar{y}_{\mathrm{d}}(\beta)-\frac{m_{\mathrm{c}}}{6}\omega^2\bar{y}_{\mathrm{c}}(\beta)-(k_{\mathrm{s}}+i\omega c_{\mathrm{s}})[\bar{y}_{\mathrm{s}}(\beta)-\bar{y}_{\mathrm{d}}(\beta)]\\ +(k_{\mathrm{c}}+i\omega c_{\mathrm{c}})[\bar{y}_{\mathrm{d}}(\beta)-\bar{y}_{\mathrm{c}}(\beta)]=0 \end{aligned} \tag{11.13}$$

$$-\frac{m_{\mathrm{c}}}{6}\omega^2\bar{y}_{\mathrm{d}}(\beta)-\frac{m_{\mathrm{c}}}{3}\omega^2\bar{y}_{\mathrm{c}}(\beta)-(k_{\mathrm{c}}+i\omega c_{\mathrm{c}})[\bar{y}_{\mathrm{d}}(\beta)-\bar{y}_{\mathrm{c}}(\beta)]=-\overline{F}_4(\beta) \tag{11.14}$$

Equations (11.11)–(11.14) have four equations, five unknowns, which need to be solved by considering the coupling relationship between the subgrade bed and the embankment body-layered ground system.

11.1.2 Dynamic Equation and Its Solution for the Embankment Body-Ground System

Taking the embankment body as a layer of soil covering on the ground surface, the embankment body-ground system can be simplified into a three-dimensional-layered model. Supposing the contact force between the subgrade bed and the embankment body is uniformly distributed on the body surface and the contact width is $2b$ (the width of subgrade bed), the harmonic load on the body surface is [7]

$$\begin{aligned} p_x &= 0 \\ p_y &= 0 \\ p_z &= \begin{cases} \frac{F_4(x,t)}{2b} & -b < y < b \\ 0 & \text{else} \end{cases} \end{aligned} \tag{11.15}$$

Performing Fourier transform to Eq. (11.15) and combining (11.10), the harmonic load amplitude in the Fourier transform domain can be expressed as

$$\begin{aligned} \bar{p}_x &= 0 \\ \bar{p}_y &= 0 \\ \bar{p}_z &= \frac{\overline{F}_4(\beta)\sin\gamma b}{\gamma b} \end{aligned} \tag{11.16}$$

where β and γ are wave numbers of space coordinate x and y, respectively, with a unit of rad/m.

Substituting (11.16) into Eq. (2.16) in Chap. 2 of Ref. [7], the surface displacement amplitude of the embankment body in Fourier transform domain can be obtained.

$$\begin{aligned} \bar{u}_{10}(\beta,\gamma,\omega) &= \overline{Q}_{13}(\beta,\gamma,\omega)\frac{\sin\gamma b}{\gamma b}\overline{F}_4(\beta) \\ \bar{v}_{10}(\beta,\gamma,\omega) &= \overline{Q}_{23}(\beta,\gamma,\omega)\frac{\sin\gamma b}{\gamma b}\overline{F}_4(\beta) \\ \bar{w}_{10}(\beta,\gamma,\omega) &= \overline{Q}_{33}(\beta,\gamma,\omega)\frac{\sin\gamma b}{\gamma b}\overline{F}_4(\beta) \end{aligned} \tag{11.17}$$

where $\overline{\boldsymbol{Q}}(\beta,\gamma,\omega)$ is the moving dynamic flexibility matrix in Fourier transform domain, whose derivation process can be found in Sect. 2.2, Chapter two of Ref. [7]. For layered ground in semi-infinite domain, the general expression for $\overline{\boldsymbol{Q}}(\beta,\gamma,\omega)$ is

$$\overline{\boldsymbol{Q}}(\beta,\gamma,\omega)=\begin{bmatrix}\overline{Q}_{11} & \overline{Q}_{12} & \overline{Q}_{13}\\ \overline{Q}_{21} & \overline{Q}_{22} & \overline{Q}_{23}\\ \overline{Q}_{31} & \overline{Q}_{32} & \overline{Q}_{33}\end{bmatrix}=-\left(\boldsymbol{R}\boldsymbol{S}^{-1}\boldsymbol{T}_{21}-\boldsymbol{T}_{11}\right)^{-1}\left(\boldsymbol{T}_{12}-\boldsymbol{R}\boldsymbol{S}^{-1}\boldsymbol{T}_{22}\right) \tag{11.18}$$

where $\boldsymbol{R}$ is the coefficient matrix for top surface soil displacement in elastic half-space in Fourier transform domain, with $\boldsymbol{S}$ as the coefficient matrix for top surface soil stress in elastic half-space in Fourier transform domain, and $\boldsymbol{T}$ as transfer matrix. Specific expressions can be found in Ref. [7].

In special occasions, when the ground is merely an infinite elastic half-space body, it will be

$$\overline{\boldsymbol{Q}}(\beta,\gamma,\omega)=-\boldsymbol{R}\boldsymbol{S}^{-1} \tag{11.19}$$

where when $\omega\neq 0$, it has

$$\boldsymbol{R}=\begin{bmatrix}-\frac{i\beta}{k_{\infty,1}^2} & 1 & 0\\ -\frac{i\gamma}{k_{\infty,1}^2} & 0 & 1\\ \frac{\alpha_{\infty,1}}{k_{\infty,1}^2} & \frac{i\beta}{\alpha_{\infty,2}} & \frac{i\gamma}{\alpha_{\infty,2}}\end{bmatrix} \tag{11.20}$$

$$\boldsymbol{S}=\begin{bmatrix}\frac{2i\mu_\infty\beta\alpha_{\infty,1}}{k_{\infty,1}^2} & -\frac{\mu_\infty(\beta^2+\alpha_{\infty,2}^2)}{\alpha_{\infty,2}} & -\frac{\mu_\infty\beta\gamma}{\alpha_{\infty,2}}\\ \frac{2i\mu_\infty\gamma\alpha_{\infty,1}}{k_{\infty,1}^2} & \frac{-\mu_\infty\gamma\beta}{\alpha_{\infty,2}} & -\frac{\mu_\infty(\gamma^2+\alpha_{\infty,2}^2)}{\alpha_{\infty,2}}\\ \lambda_{n+1}-\frac{2\mu_\infty\alpha_{\infty,1}^2}{k_{\infty,1}^2} & -2i\mu_\infty\beta & -2i\mu_\infty\gamma\end{bmatrix} \tag{11.21}$$

When $\omega=0$, it has

$$\boldsymbol{R}=\begin{bmatrix}0 & 1 & 0\\ 0 & 0 & 1\\ -\frac{\lambda_\infty+3\mu_\infty}{2\alpha_{\infty,1}\mu_\infty} & \frac{i\beta}{\alpha_{\infty,1}} & \frac{i\gamma}{\alpha_{\infty,1}}\end{bmatrix} \tag{11.22}$$

$$\boldsymbol{S}=\begin{bmatrix}-\frac{i\beta\mu_\infty}{\alpha_{\infty,1}} & -\frac{\beta^2\mu_\infty+\alpha_{\infty,1}^2\mu_\infty}{\alpha_{\infty,1}} & -\frac{\beta\gamma\mu_\infty}{\alpha_{\infty,1}}\\ -\frac{i\gamma\mu_\infty}{\alpha_{\infty,1}} & -\frac{\beta\gamma\mu_\infty}{\alpha_{\infty,1}} & -\frac{\gamma^2\mu_\infty+\alpha_{\infty,1}^2\mu_\infty}{\alpha_{\infty,1}}\\ \lambda_\infty+2\mu_\infty & -2i\mu_\infty\beta & -2i\mu_\infty\gamma\end{bmatrix} \tag{11.23}$$

In the above Eqs. (11.20)–(11.23), subscript "∞"indicates physical quantities of the infinite elastic half-space body. In equations

$$\alpha_{\infty,1}^2 = \beta^2 + \gamma^2 - k_{\infty,1}^2, \quad k_{\infty,1}^2 = \frac{\rho_\infty \omega^2}{\lambda_\infty + 2\mu_\infty}$$

$$\alpha_{\infty,2}^2 = \beta^2 + \gamma^2 - k_{\infty,2}^2, \quad k_{\infty,2}^2 = \frac{\rho_\infty \omega^2}{\mu_\infty}$$

$$\lambda_\infty = \frac{v_\infty E_\infty (1 + i\eta_\infty \mathrm{sgn}(\omega))}{(1 + v_\infty)(1 - 2v_\infty)}, \quad \mu_\infty = \frac{E_\infty (1 + i\eta_\infty \mathrm{sgn}(\omega))}{2(1 + v_\infty)}$$

$E_\infty[1 + i\eta_\infty \mathrm{sgn}(\omega)]$ is elasticity modulus of infinite elastic half-space body with damping included, where $\mathrm{sgn}(\omega)$ denotes notation function. When $\omega > 0$, $\mathrm{sgn}(\omega) = 1$, and when $\omega < 0$, $\mathrm{sgn}(\omega) = -1$, with ω for angular frequency of vibration, η_∞ for loss factor and v_∞ for Poisson's ratio.

Substituting Eq. (11.17) into Eq. (2.13) in Chap. 2 of Ref. [7], the steady surface displacement of the embankment body in Fourier transform domain can be expressed as

$$\begin{aligned}
\tilde{u}_{10}(\beta,\gamma,t) &= \bar{u}_{10}(\beta,\gamma)\mathrm{e}^{i(\Omega-\beta V)t} = \overline{Q}_{13}(\beta,\gamma,\omega)\frac{\sin\gamma b}{\gamma b}\overline{F}_4(\beta)\mathrm{e}^{i(\Omega-\beta V)t} \\
\tilde{v}_{10}(\beta,\gamma,t) &= \bar{v}_{10}(\beta,\gamma)\mathrm{e}^{i(\Omega-\beta V)t} = \overline{Q}_{23}(\beta,\gamma,\omega)\frac{\sin\gamma b}{\gamma b}\overline{F}_4(\beta)\mathrm{e}^{i(\Omega-\beta V)t} \\
\tilde{w}_{10}(\beta,\gamma,t) &= \bar{w}_{10}(\beta,\gamma)\mathrm{e}^{i(\Omega-\beta V)t} = \overline{Q}_{33}(\beta,\gamma,\omega)\frac{\sin\gamma b}{\gamma b}\overline{F}_4(\beta)\mathrm{e}^{i(\Omega-\beta V)t}
\end{aligned} \tag{11.24}$$

Applying inverse Fourier transform to (11.24), the surface displacement of the embankment body $u_{10}(x,y,t)$, $v_{10}(x,y,t)$, and $w_{10}(x,y,t)$ in space domain can be obtained.

11.1.3 Coupling Vibration of the Slab Track-Embankment-Ground System

Considering consistent conditions of the vertical displacement at the point of $y = 0$ along the central line of the subgrade bed and the embankment body contact surface [7], it has

$$y_c(x,t) = w_{10}(x,y,t)|_{y=0} = w_{10}(x,0,t) \tag{11.25}$$

where

$$\begin{aligned} w_{10}(x,0,t) &= \frac{1}{4\pi^2}\int_{-\infty}^{\infty}\int_{-\infty}^{\infty}\tilde{w}_{10}(\beta,\gamma,t)\mathrm{e}^{i(\beta x+\gamma y)}\,\mathrm{d}\beta\mathrm{d}\gamma\Big|_{y=0} \\ &= \frac{1}{4\pi^2}\int_{-\infty}^{\infty}\int_{-\infty}^{\infty}\tilde{w}_{10}(\beta,\gamma,t)\mathrm{e}^{i\beta x}\,\mathrm{d}\beta\mathrm{d}\gamma \end{aligned} \tag{11.26}$$

Applying Fourier transform of X direction to Eq. (11.25) and combining Eq. (11.26), it gets

$$\tilde{y}_{\mathrm{c}}(\beta,t) = \frac{1}{2\pi}\int_{-\infty}^{\infty}\tilde{w}_{10}(\beta,\gamma,t)\,\mathrm{d}\gamma \tag{11.27}$$

Substituting Eq. (11.24) into Eq. (11.27) and combining (11.10), it has

$$\bar{y}_{\mathrm{c}}(\beta) = \left(\frac{1}{2\pi}\int_{-\infty}^{\infty}\overline{Q}_{33}(\beta,\gamma,\omega)\frac{\sin\gamma b}{\gamma b}\mathrm{d}\gamma\right)\cdot\overline{F}_4(\beta) = \overline{H}(\beta)\cdot\overline{F}_4(\beta) \tag{11.28}$$

where

$$\overline{H}(\beta) = \frac{1}{2\pi}\int_{-\infty}^{\infty}\overline{Q}_{33}(\beta,\gamma,\omega)\frac{\sin\gamma b}{\gamma b}\mathrm{d}\gamma \tag{11.29}$$

Simultaneously solving for Eqs. (11.11)–(11.14) and (11.28), it has

$$\bar{w}_{\mathrm{r}}(\beta) = \overline{P}(\beta)/\left[EI_{\mathrm{r}}\beta^4 - m_{\mathrm{r}}\omega^2 + i\omega c_{\mathrm{p}} + k_{\mathrm{p}} - \frac{(k_{\mathrm{p}}+i\omega c_{\mathrm{p}})^2}{K_{14}}\right] \tag{11.30}$$

$$\bar{y}_{\mathrm{s}}(\beta) = \frac{k_{\mathrm{p}}+i\omega c_{\mathrm{p}}}{K_{14}}\bar{w}_{\mathrm{r}}(\beta) \tag{11.31}$$

$$\bar{y}_{\mathrm{d}}(\beta) = \frac{k_{\mathrm{s}}+i\omega c_{\mathrm{s}}}{K_{13}}\bar{y}_{\mathrm{s}}(\beta) \tag{11.32}$$

$$\overline{F}_4(\beta) = K_{12}\cdot\bar{y}_{\mathrm{d}}(\beta) \tag{11.33}$$

where

$$
\begin{aligned}
K_{11} &= EI_{\mathrm{d}}\beta^4 - \left(m_{\mathrm{d}} + \frac{m_{\mathrm{c}}}{3}\right)\omega^2 + (k_{\mathrm{s}} + k_{\mathrm{c}}) + i\omega(c_{\mathrm{s}} + c_{\mathrm{c}}),\\
K_{12} &= \frac{m_{\mathrm{c}}\omega^2/6 + k_{\mathrm{c}} + i\omega c_{\mathrm{c}}}{(-m_{\mathrm{c}}\omega^2/3 + k_{\mathrm{c}} + i\omega c_{\mathrm{c}})\overline{H}(\beta) + 1},\\
K_{13} &= K_{11} + (-m_{\mathrm{c}}\omega^2/6 - k_{\mathrm{c}} - i\omega c_{\mathrm{c}})\overline{H}(\beta)K_{12},\\
K_{14} &= EI_{\mathrm{s}}\beta^4 - m_{\mathrm{s}}\omega^2 + (k_{\mathrm{p}} + k_{\mathrm{s}}) + i\omega(c_{\mathrm{p}} + c_{\mathrm{s}}) - \frac{(k_{\mathrm{s}} + i\omega c_{\mathrm{s}})^2}{K_{13}}.
\end{aligned}
$$

Substituting Eqs. (11.30)–(11.33) and (11.28) to Eq. (11.10) and performing inverse Fourier transform, it obtains the solution in space-time domain.

Let the inverse Fourier transform of $\bar{w}_{\mathrm{r}}(\beta)$, $\bar{y}_{\mathrm{s}}(\beta)$, $\bar{y}_{\mathrm{d}}(\beta)$, $\overline{F}_4(\beta)$, $\bar{y}_{\mathrm{c}}(\beta)$, $\bar{u}_{10}(\beta,\gamma)$, $\bar{v}_{10}(\beta,\gamma)$, and $\bar{w}_{10}(\beta,\gamma)$ be $\hat{w}_{\mathrm{r}}(x)$, $\hat{y}_{\mathrm{s}}(x)$, $\hat{y}_{\mathrm{d}}(x)$, $\hat{F}_4(x)$, $\hat{y}_{\mathrm{c}}(x)$, $\hat{u}_{10}(x,y)$, $\hat{v}_{10}(x,y)$, and $\hat{w}_{10}(x,y)$, the solution of the slab track-embankment-ground system in space-time domain can be expressed as

$$
\begin{aligned}
w_{\mathrm{r}}(x,t) &= \hat{w}_{\mathrm{r}}(x - Vt)\mathrm{e}^{i\Omega t}\\
y_{\mathrm{s}}(x,t) &= \hat{y}_{\mathrm{s}}(x - Vt)\mathrm{e}^{i\Omega t}\\
y_{\mathrm{d}}(x,t) &= \hat{y}_{\mathrm{d}}(x - Vt)\mathrm{e}^{i\Omega t}\\
y_{\mathrm{c}}(x,t) &= \hat{y}_{\mathrm{c}}(x - Vt)\mathrm{e}^{i\Omega t}\\
F_4(x,t) &= \hat{F}_4(x - Vt)\mathrm{e}^{i\Omega t}\\
u_{10}(x,y,t) &= \hat{u}_{10}(x - Vt, y)\mathrm{e}^{i\Omega t}\\
v_{10}(x,y,t) &= \hat{v}_{10}(x - Vt, y)\mathrm{e}^{i\Omega t}\\
w_{10}(x,y,t) &= \hat{w}_{10}(x - Vt, y)\mathrm{e}^{i\Omega t}
\end{aligned}
\tag{11.34}
$$

When the wheel load is moving axle load, and its frequency $\Omega = 0$, solution to the vibration displacement of the slab track-embankment-ground system induced by the moving axle load can be directly calculated through the above equation.

11.2 Model of the Ballast Track-Embankment-Ground System Under Moving Loads

Figure 11.2 is the analysis model of the ballast track-embankment-ground system [7]. The rail is still assumed to be infinite Euler beam acting on discretely supported sleepers. When the wheelset masses move along the rail, parameter excitation will be produced. For conventional ballast track, when the frequency is lower than 200 Hz, sleepers' impact of discrete support can be ignored. Low frequency means longer wavelength of irregularities. Irregularity amplitude of large wavelength is

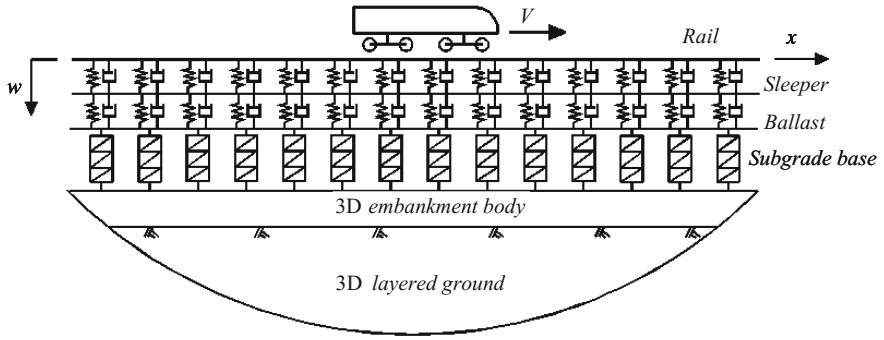

Fig. 11.2 A model of the ballast track-embankment-ground coupling system

usually big and its impact usually exceeds parameter excitation. Therefore, the sleepers are simplified as uniformly distributed masses. Stiffness and damping of the rail pads and fasteners are simulated with uniformly distributed linear springs and dampers. Due to the weak constraints among the components of the track structure, the ballast is regarded as an elastic body with uniformly distributed mass, vertical stiffness, and damping along the track alignment. The model of the subgrade bed, embankment body, and ground is the same as that in Sect. 11.1. And similarly, the ballast track-embankment-ground system is also divided into the upper part and the lower part. The upper part is the ballast track-subgrade bed system, which is assumed to be a one-dimensional infinite body along the X direction, while the lower part is the embankment body-ground system, which is considered to be a three-dimensional semi-infinite body. The two parts contact with each other on the central line of the embankment body. The contact width is marked as $2b$ (the width of subgrade bed).

11.2.1 Dynamic Equation and Its Solution for the Ballast Track-Subgrade Bed System

Governing equation of the rail vibration is the same as Eq. (11.1), that is

$$EI_{\mathrm{r}}\frac{\partial^4 w_{\mathrm{r}}}{\partial x^4} + m_{\mathrm{r}}\ddot{w}_{\mathrm{r}} + k_{\mathrm{p}}(w_{\mathrm{r}} - y_{\mathrm{s}}) + c_{\mathrm{p}}(\dot{w}_{\mathrm{r}} - \dot{y}_{\mathrm{s}}) = P(x,t) \tag{11.35}$$

where $P(x,t) = \sum_{l=1}^{M} P_l \mathrm{e}^{i\Omega t}\delta(x - Vt - a_l)$.

Governing equation of the sleeper vibration is:

$$m_s\ddot{y}_s - k_p(w_r - y_s) - c_p(\dot{w}_r - \dot{y}_s) + k_s(y_s - y_d) + c_s(\dot{y}_s - \dot{y}_d) = 0 \tag{11.36}$$

Governing equation of the ballast vibration is:

$$m_d\ddot{y}_d - k_s(y_s - y_d) - c_s(\dot{y}_s - \dot{y}_d) = -F_3 \tag{11.37}$$

Governing equation of the subgrade bed vibration is the same as Eq. (11.4), that is

$$\frac{m_c}{6}\begin{bmatrix}2 & 1\\ 1 & 2\end{bmatrix}\begin{Bmatrix}\ddot{y}_d\\ \ddot{y}_c\end{Bmatrix} + k_c\begin{bmatrix}1 & -1\\ -1 & 1\end{bmatrix}\begin{Bmatrix}y_d\\ y_c\end{Bmatrix} + c_c\begin{bmatrix}1 & -1\\ -1 & 1\end{bmatrix}\begin{Bmatrix}\dot{y}_d\\ \dot{y}_c\end{Bmatrix} = \begin{Bmatrix}F_3\\ -F_4\end{Bmatrix} \tag{11.38}$$

Indications of the notations from Eqs. (11.35) to (11.38) are as follows: $(\cdot)$ and $(\ddot{\cdot})$ are first-order derivative and second-order derivative of t, respectively; y_s and y_d are the shortened forms of $y_s(x,t)$ and $y_d(x,t)$, respectively, symbolizing vertical displacements of the sleeper and ballast; m_s and m_d are masses of the sleeper and ballast per unit length, respectively; k_s and c_s are stiffness and damping of the ballast per unit length; F_3 is the shortened form of $F_3(x,t)$, standing for the interaction between the ballast and the subgrade bed; the meanings of the other notations are the same as those in Sect. 11.1.1.

Applying Fourier transform of X direction to Eqs. (11.35)–(11.38) and supposing the solution of steady displacement in the transform domain as harmonic function, it yields

$$EI_r\beta^4\bar{w}_r(\beta) - m_r\omega^2\bar{w}_r(\beta) + (k_p + i\omega c_p)[\bar{w}_r(\beta) - \bar{y}_s(\beta)] = \overline{P}(\beta) \tag{11.39}$$

$$-m_s\omega^2\bar{y}_s(\beta) - (k_p + i\omega c_p)[\bar{w}_r(\beta) - \bar{y}_s(\beta)] + (k_s + i\omega c_s)[\bar{y}_s(\beta) - \bar{y}_d(\beta)] = 0 \tag{11.40}$$

$$\begin{aligned} &-\left(m_d + \frac{m_c}{3}\right)\omega^2\bar{y}_d(\beta) - \frac{m_c}{6}\omega^2\bar{y}_c(\beta) - (k_s + i\omega c_s)[\bar{y}_s(\beta) - \bar{y}_d(\beta)]\\ &\quad + (k_c + i\omega c_c)[\bar{y}_d(\beta) - \bar{y}_c(\beta)] = 0 \end{aligned} \tag{11.41}$$

$$-\frac{m_c}{6}\omega^2\bar{y}_d(\beta) - \frac{m_c}{3}\omega^2\bar{y}_c(\beta) - (k_c + i\omega c_c)[\bar{y}_d(\beta) - \bar{y}_c(\beta)] = -\overline{F}_4(\beta) \tag{11.42}$$

There are five unknowns in (11.39)–(11.42) four equations, which needs to be solved by considering the coupling relationship between the subgrade bed and the embankment body-layered ground system.

11.2.2 Coupling Vibration of the Ballast Track-Embankment-Ground System

The model of the embankment body-ground system is the same as the three-dimensional-layered ground model in Sect. 11.1. In light of the balanced contact force and the equal contact displacement at the interface of the subgrade bed and the embankment body, the relationship of amplitudes between $y_c(x,t)$ and $F_4(x,t)$ in the Fourier transform domain can finally be established by the similar deduction as in Sect. 11.1, as shown in Eq. (11.28).

Simultaneously solving for Eqs. (11.39)–(11.42) and (11.28), it has

$$\bar{w}_r(\beta) = \overline{P}(\beta) / \left[EI_r\beta^4 - m_r\omega^2 + i\omega c_p + k_p - \frac{(k_p + i\omega c_p)^2}{K_{14}} \right] \tag{11.43}$$

$$\bar{y}_s(\beta) = \frac{k_p + i\omega c_p}{K_{14}} \bar{w}_r(\beta) \tag{11.44}$$

$$\bar{y}_d(\beta) = \frac{k_s + i\omega c_s}{K_{13}} \bar{y}_s(\beta) \tag{11.45}$$

$$\overline{F}_4(\beta) = K_{12} \cdot \bar{y}_d(\beta) \tag{11.46}$$

$$\bar{y}_c(\beta) = \overline{H}(\beta) \cdot \overline{F}_4(\beta) \tag{11.47}$$

where

$$\begin{aligned}
K_{11} &= -\left(m_d + \frac{m_c}{3}\right)\omega^2 + (k_s + k_c) + i\omega(c_s + c_c), \\
K_{12} &= \frac{m_c\omega^2/6 + k_c + i\omega c_c}{(-m_c\omega^2/3 + k_c + i\omega c_c)\overline{H}(\beta) + 1} \\
K_{13} &= K_{11} + \overline{H}(\beta)(-m_c\omega^2/6 - k_c - i\omega c_c)K_{12}, \\
K_{14} &= -m_s\omega^2 + (k_p + k_s) + i\omega(c_p + c_s) - \frac{(k_s + i\omega c_s)^2}{K_{13}}
\end{aligned}$$

Applying inverse Fourier transform to $\bar{w}_r(\beta)e^{i\omega t}$, $\bar{y}_s(\beta)e^{i\omega t}$, $\bar{y}_d(\beta)e^{i\omega t}$, $\overline{F}_4(\beta)e^{i\omega t}$, $\bar{y}_c(\beta)e^{i\omega t}$, the solution in space-time domain can be obtained.

11.3 Analytic Vibration Model of the Moving Vehicle-Track-Subgrade-Ground Coupling System

In this section, a vibration model of the moving vehicle-track-subgrade-ground coupling system is built by wave number-frequency domain method. Firstly, flexibility matrixes of the moving vehicles at wheelset points and the track-subgrade-ground system at wheel-rail contact points are deduced, and then an analytic vibration model of the moving vehicle-track-subgrade-ground coupling system is established by taking account of the track irregularities and the displacement constraint condition at the wheel-rail contact points [7].

11.3.1 Flexibility Matrix of Moving Vehicles at Wheelset Points

A moving vehicle with primary and secondary suspension systems is considered, as is shown in Fig. 11.3[7, 8]. The vehicle is simulated into a multi-body system moving on the track structure at the speed of V. The car body and bogies, and the bogies and wheelsets are connected by linear springs and viscous dampers. Bouncing and pitch vibration of the car body and the bogies, and the bouncing vibration of the wheelsets are taken into account. In order to make the analysis in frequency domain, the nonlinear characteristics of the actual vehicle's suspension system is treated as linear springs and viscous dampers. The vertical displacement downward and the rotational angle clockwise are defined as positive. The wheel-rail contact force is positive for pressure. The vehicle model has 10 degrees of freedom.

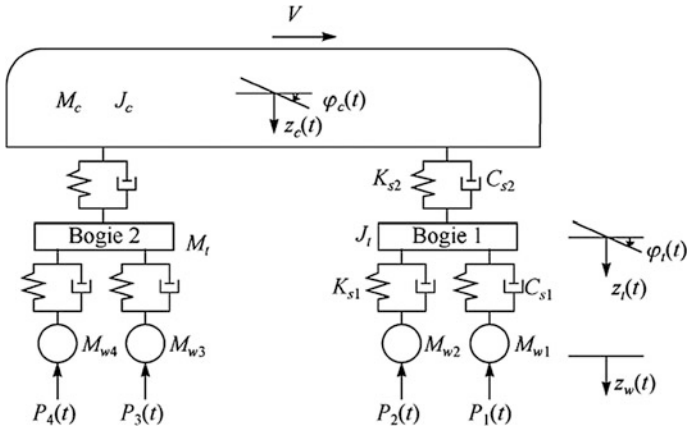

Fig. 11.3 A vehicle model with primary and secondary suspension systems

Governing equation of the moving vehicle vibration is:

$$\boldsymbol{M}_{\mathrm{u}}\ddot{\boldsymbol{Z}}_{\mathrm{u}}(t)+\boldsymbol{C}_{\mathrm{u}}\dot{\boldsymbol{Z}}_{\mathrm{u}}(t)+\boldsymbol{K}_{\mathrm{u}}\boldsymbol{Z}_{\mathrm{u}}(t)=\boldsymbol{Q}_{\mathrm{u}}(t) \tag{11.48}$$

In the equation, $\boldsymbol{M}_{\mathrm{u}}$, $\boldsymbol{C}_{\mathrm{u}}$, and $\boldsymbol{K}_{\mathrm{u}}$ stand for mass matrix, damping matrix, and stiffness matrix of the vehicle, respectively; $\boldsymbol{Z}_{\mathrm{u}}(t)$, $\dot{\boldsymbol{Z}}_{\mathrm{u}}(t)$, and $\ddot{\boldsymbol{Z}}_{\mathrm{u}}(t)$ are displacement, velocity, and acceleration vectors of the vehicle, respectively; $\boldsymbol{Q}_{\mathrm{u}}(t)$ stands for vehicle dynamic load vector due to track irregularity, ignoring other impacts on the vehicle dynamic loads. Gravity load of the vehicle directly acts on the track structure in the form of dynamic axle load, without considering its participation in the vehicle-track coupling vibration. Explicit expressions for the variables in the above equations are as follows

$$\boldsymbol{M}_{\mathrm{u}}=\mathrm{diag}\{\,M_{\mathrm{C}}\quad J_{\mathrm{C}}\quad M_{\mathrm{t}}\quad M_{\mathrm{t}}\quad J_{\mathrm{t}}\quad J_{\mathrm{t}}\quad M_{\mathrm{w1}}\quad M_{\mathrm{w2}}\quad M_{\mathrm{w3}}\quad M_{\mathrm{w4}}\,\} \tag{11.49}$$

$$\boldsymbol{Z}_{\mathrm{u}}(t)=\{\,z_{\mathrm{c}}(t)\quad \varphi_{\mathrm{c}}(t)\quad z_{\mathrm{t1}}(t)\quad z_{\mathrm{t2}}(t)\quad \varphi_{\mathrm{t1}}(t)\ \varphi_{\mathrm{t2}}(t)\quad z_{\mathrm{w1}}(t)\quad z_{\mathrm{w2}}(t)\quad z_{\mathrm{w3}}(t)\quad z_{\mathrm{w4}}(t)\,\}^{\mathrm{T}} \tag{11.50}$$

$$\dot{\boldsymbol{Z}}_{\mathrm{u}}(t)=\{\,\dot{z}_{\mathrm{c}}(t)\quad \dot{\varphi}_{\mathrm{c}}(t)\quad \dot{z}_{\mathrm{t1}}(t)\quad \dot{z}_{\mathrm{t2}}(t)\quad \dot{\varphi}_{\mathrm{t1}}(t)\ \dot{\varphi}_{\mathrm{t2}}(t)\quad \dot{z}_{\mathrm{w1}}(t)\quad \dot{z}_{\mathrm{w2}}(t)\quad \dot{z}_{\mathrm{w3}}(t)\quad \dot{z}_{\mathrm{w4}}(t)\,\}^{\mathrm{T}} \tag{11.51}$$

$$\ddot{\boldsymbol{Z}}_{\mathrm{u}}(t)=\{\,\ddot{z}_{\mathrm{c}}(t)\quad \ddot{\varphi}_{\mathrm{c}}(t)\quad \ddot{z}_{\mathrm{t1}}(t)\quad \ddot{z}_{\mathrm{t2}}(t)\quad \ddot{\varphi}_{\mathrm{t1}}(t)\ \ddot{\varphi}_{\mathrm{t2}}(t)\quad \ddot{z}_{\mathrm{w1}}(t)\quad \ddot{z}_{\mathrm{w2}}(t)\quad \ddot{z}_{\mathrm{w3}}(t)\quad \ddot{z}_{\mathrm{w4}}(t)\,\}^{\mathrm{T}} \tag{11.52}$$

$$\boldsymbol{Q}_{\mathrm{u}}(t)=\{\,0\quad 0\quad 0\quad 0\quad 0\quad 0\quad -P_1(t)\quad -P_2(t)\quad -P_3(t)\quad -P_4(t)\,\}^{\mathrm{T}} \tag{11.53}$$

$$\boldsymbol{K}_{\mathrm{u}}=\begin{bmatrix}
2K_{\mathrm{s2}} & 0 & -K_{\mathrm{s2}} & -K_{\mathrm{s2}} & 0 & 0 & 0 & 0 & 0 & 0\\
 & 2L_2^2K_{\mathrm{s2}} & -L_2K_{\mathrm{s2}} & L_2K_{\mathrm{s2}} & 0 & 0 & 0 & 0 & 0 & 0\\
 & & 2K_{\mathrm{s1}}+K_{\mathrm{s2}} & 0 & 0 & 0 & -K_{\mathrm{s1}} & -K_{\mathrm{s1}} & 0 & 0\\
 & & & 2K_{\mathrm{s1}}+K_{\mathrm{s2}} & 0 & 0 & 0 & 0 & -K_{\mathrm{s1}} & -K_{\mathrm{s1}}\\
 & & & & 2L_1^2K_{\mathrm{s1}} & 0 & -K_{\mathrm{s1}}L_1 & K_{\mathrm{s1}}L_1 & 0 & 0\\
 & & & & & 2L_1^2K_{\mathrm{s1}} & 0 & 0 & -K_{\mathrm{s1}}L_1 & K_{\mathrm{s1}}L_1\\
 & & \text{Symmetry} & & & & K_{\mathrm{s1}} & 0 & 0 & 0\\
 & & & & & & & K_{\mathrm{s1}} & 0 & 0\\
 & & & & & & & & K_{\mathrm{s1}} & 0\\
 & & & & & & & & & K_{\mathrm{s1}}
\end{bmatrix} \tag{11.54}$$

$$\boldsymbol{C}_{\mathrm{u}}=\begin{bmatrix}
2C_{\mathrm{s2}} & 0 & -C_{\mathrm{s2}} & -C_{\mathrm{s2}} & 0 & 0 & 0 & 0 & 0 & 0\\
 & 2L_2^2C_{\mathrm{s2}} & -L_2C_{s2} & L_2C_{\mathrm{s2}} & 0 & 0 & 0 & 0 & 0 & 0\\
 & & 2C_{s1}+C_{s2} & 0 & 0 & 0 & -C_{\mathrm{s1}} & -C_{\mathrm{s1}} & 0 & 0\\
 & & & 2C_{\mathrm{s1}}+C_{\mathrm{s2}} & 0 & 0 & 0 & 0 & -C_{\mathrm{s1}} & -C_{\mathrm{s1}}\\
 & & & & 2L_1^2C_{\mathrm{s1}} & 0 & -C_{\mathrm{s1}}L_1 & C_{\mathrm{s1}}L_1 & 0 & 0\\
 & & & & & 2L_1^2C_{\mathrm{s1}} & 0 & 0 & -C_{\mathrm{s1}}L_1 & C_{\mathrm{s1}}L_1\\
 & & \text{Symmetry} & & & & C_{\mathrm{s1}} & 0 & 0 & 0\\
 & & & & & & & C_{\mathrm{s1}} & 0 & 0\\
 & & & & & & & & C_{\mathrm{s1}} & 0\\
 & & & & & & & & & C_{\mathrm{s1}}
\end{bmatrix} \tag{11.55}$$

In the above equations, M_c, J_c are mass and inertia moment for the car body; M_t, J_t are mass and inertia moment for the bogie; $M_{wi}(i = 1, 2, 3, 4)$ represents mass of the ith wheelset; K_{s1}, C_{s1} and K_{s2}, C_{s2} stand for stiffness and damping coefficients for the primary and secondary suspension systems of the vehicle, respectively; z_c is vertical displacement of the car body with downward as the positive; φ_c is rotational angle of the car body around the horizontal axis, with clockwise as the positive; z_t is vertical displacement of the bogie; φ_t is rotational angle of the bogie around the horizontal axis; z_w is vertical displacement of the wheelsets; $2L_2$ is the distance between the bogie pivot centers of the car body; $2L_1$ is fixed wheel base.

Assuming dynamic loads of the vehicle caused by track irregularities are harmonic loads, vibration of the vehicle is also harmonic.

$$\boldsymbol{Q}_u(t) = \boldsymbol{Q}_u(\Omega)e^{i\Omega t} \tag{11.56}$$

$$\boldsymbol{Z}_u(t) = \boldsymbol{Z}_u(\Omega)e^{i\Omega t} \tag{11.57}$$

where Ω is the frequency of exciting source.

Substituting Eqs. (11.56) and (11.57) into Eq. (11.48), it yields

$$\boldsymbol{Z}_u(\Omega) = (\boldsymbol{K}_u + i\Omega\boldsymbol{C}_u - \Omega^2\boldsymbol{M}_u)^{-1}\boldsymbol{Q}_u(\Omega) = \boldsymbol{A}_u\boldsymbol{Q}_u(\Omega) \tag{11.58}$$

where $\boldsymbol{A}_u = (\boldsymbol{K}_u + i\Omega\boldsymbol{C}_u - \Omega^2\boldsymbol{M}_u)^{-1}$ is flexibility matrix of the vehicle.

Let $\boldsymbol{P}(\Omega)$, the amplitude of the dynamic wheel-rail force caused by track irregularities, and $\boldsymbol{Z}_w(\Omega)$, the amplitude of wheel displacement, be as follows:

$$\boldsymbol{P}(\Omega) = \{\, P_1(\Omega) \quad P_2(\Omega) \quad P_3(\Omega) \quad P_4(\Omega) \,\}^T \tag{11.59}$$

$$\boldsymbol{Z}_w(\Omega) = \{\, z_{w1}(\Omega) \quad z_{w2}(\Omega) \quad z_{w3}(\Omega) \quad z_{w4}(\Omega) \,\}^T \tag{11.60}$$

And it has

$$\boldsymbol{Q}_u(\Omega) = -\boldsymbol{H}^T\boldsymbol{P}(\Omega) \tag{11.61}$$

$$\boldsymbol{H}\boldsymbol{Z}_u(\Omega) = \boldsymbol{Z}_w(\Omega) \tag{11.62}$$

where $\boldsymbol{H} = [\,\boldsymbol{0}_{4\times6} \quad \boldsymbol{I}_{4\times4}\,]$.

Multiplying $\boldsymbol{H}$ to the left side of Eq. (11.54), and substituting Eqs. (11.61) and (11.62) into it, it has

$$\boldsymbol{Z}_w(\Omega) = -\boldsymbol{H}\boldsymbol{A}_u\boldsymbol{H}^T\boldsymbol{P}(\Omega) = -\boldsymbol{A}_w\boldsymbol{P}(\Omega) \tag{11.63}$$

where $\boldsymbol{A}_{\mathrm{w}} = \boldsymbol{H}\boldsymbol{A}_{\mathrm{u}}\boldsymbol{H}^{\mathrm{T}}$ is flexibility matrix of the vehicle at wheelset points. When the train has N vehicles, the flexibility matrix of the train at wheelset points will be

$$\boldsymbol{A}_{\mathrm{TW}} = \mathrm{diag}[\boldsymbol{A}_{\mathrm{w}1}, \ldots \boldsymbol{A}_{\mathrm{w}i}, \ldots, \boldsymbol{A}_{\mathrm{w}N}] \tag{11.64}$$

where $\boldsymbol{A}_{\mathrm{w}i}$ stands for flexibility matrix of the ith vehicle at wheelset points.

11.3.2 Flexibility Matrix of the Track-Subgrade-Ground System at Wheel-Rail Contact Points

We have discussed and obtained the displacements of the separate parts in the track-subgrade-ground system under moving harmonic loads in Sects. 11.1and 11.2. Supposing a unit harmonic load acts on the track structure, and when $t = 0$, the load is located in the origin, it is easy to get the rail displacement as

$$w_{\mathrm{r}}^{e}(x,t) = \bar{w}_{\mathrm{r}}^{e}(x - ct)\mathrm{e}^{i\Omega t} \tag{11.65}$$

where superscript e stands for unit harmonic load. When a number of wheel-axle loads are acting on the structure, the rail displacement at the jth wheel-rail contact point induced by unit force at the kth wheel-rail contact point will be

$$w_{\mathrm{r},jk}^{e} = \bar{w}_{\mathrm{r}}^{e}(l_{jk})\mathrm{e}^{i\Omega t} \tag{11.66}$$

where $l_{jk} = a_j - a_k$ is the distance between two wheelsets.

Define displacement amplitude as

$$\delta_{jk} = \bar{w}_{\mathrm{r}}^{e}(l_{jk}) \tag{11.67}$$

In a single vehicle model, it bears the action of four wheels, so the rail displacement $\boldsymbol{Z}_{\mathrm{R}}(\Omega)$ at wheel-rail contact point generated by dynamic wheel-rail force should be

$$\boldsymbol{Z}_{\mathrm{R}}(\Omega) = \{\, z_{\mathrm{R}1}(\Omega) \quad z_{\mathrm{R}2}(\Omega) \quad z_{\mathrm{R}3}(\Omega) \quad z_{\mathrm{R}4}(\Omega) \,\}^{\mathrm{T}} = \boldsymbol{A}_{\mathrm{R}}\boldsymbol{P}(\Omega) \tag{11.68}$$

where $\boldsymbol{A}_{\mathrm{R}} = \begin{bmatrix} \delta_{11} & \delta_{12} & \delta_{13} & \delta_{14} \\ \delta_{21} & \delta_{22} & \delta_{23} & \delta_{24} \\ \delta_{31} & \delta_{32} & \delta_{33} & \delta_{34} \\ \delta_{41} & \delta_{42} & \delta_{43} & \delta_{44} \end{bmatrix}$ is flexibility matrix of the track-subgrade-ground system at wheel-rail contact point. And similarly, a train with N vehicles has $4N$ wheel-rail contact points, so it is easy to solve the flexibility matrix of the track-subgrade-ground system at wheel-rail contact points of the moving train.

11.3.3 Coupling of Moving Vehicle-Subgrade-Ground System by Consideration of Track Irregularities

Supposing the wheel-rail contact is linear elastic contact, the contact stiffness is

$$K_{\mathrm{W}} = \frac{3}{2G} p^{1/3} \tag{11.69}$$

where G is the contact deflection coefficient, $G = 4.57R^{-0.149} \times 10^{-8}\,(\mathrm{m/N^{2/3}})$ for the wheel with conical tread, and $G = 3.86R^{-0.115} \times 10^{-8}\,(\mathrm{m/N^{2/3}})$ for the wheel with worn profile tread. p approximately equals to the static axle load.

In a single vehicle model, relative displacement amplitude $\boldsymbol{\eta}(\Omega)$ at wheel-rail contact point is

$$\boldsymbol{\eta}(\Omega) = \{\, \eta_1(\Omega) \quad \eta_2(\Omega) \quad \eta_3(\Omega) \quad \eta_4(\Omega) \,\}^{\mathrm{T}} = \boldsymbol{A}_{\Delta}\boldsymbol{P}(\Omega) \tag{11.70}$$

where $\boldsymbol{A}_{\Delta} = \mathrm{diag}(\, 1/K_{\mathrm{W}} \quad 1/K_{\mathrm{W}} \quad 1/K_{\mathrm{W}} \quad 1/K_{\mathrm{W}} \,)$.

Assuming track surface irregularity $\Delta z(x)$ is harmonic function, that is

$$\Delta z(x) = -A\mathrm{e}^{i(2\pi/\lambda)x} \tag{11.71}$$

where A is the amplitude of track surface irregularity, and λ is wavelength of the irregularity. Track irregularity at the lth wheel-rail contact point can be expressed as

$$\Delta z_l(x) = -A\mathrm{e}^{i(2\pi/\lambda)(a_l + Vt)} = -A\mathrm{e}^{i(2\pi/\lambda)a_l}\mathrm{e}^{i2\pi(V/\lambda)t} = -\Delta z_l(\Omega)\mathrm{e}^{i\Omega t} \tag{11.72}$$

where $\Delta z_l(\Omega) = A\mathrm{e}^{i(2\pi/\lambda)a_l}$, $\Omega = 2\pi V/\lambda$.

In the single vehicle model, the amplitude of track surface irregularity at wheel-rail contact point is

$$\Delta \boldsymbol{Z}(\Omega) = -\left\{ A\mathrm{e}^{i(2\pi/\lambda)a_1} \quad A\mathrm{e}^{i(2\pi/\lambda)a_2} \quad A\mathrm{e}^{i(2\pi/\lambda)a_3} \quad A\mathrm{e}^{i(2\pi/\lambda)a_4} \right\}^{\mathrm{T}} \tag{11.73}$$

Supposing the wheel always keeps contacting with the rail, the displacement constraint condition at the wheel-rail contact point is

$$\boldsymbol{Z}_{\mathrm{w}}(\Omega) = \boldsymbol{Z}_{\mathrm{R}}(\Omega) + \boldsymbol{\eta}(\Omega) + \Delta \boldsymbol{Z}(\Omega) \tag{11.74}$$

Substituting Eqs. (11.63), (11.68), (11.70), and (11.73) into Eq. (11.74), it has

$$(\boldsymbol{A}_{\mathrm{w}} + \boldsymbol{A}_{\mathrm{R}} + \boldsymbol{A}_{\Delta})\boldsymbol{P}(\Omega) = \Delta \boldsymbol{Z}(\Omega) \tag{11.75}$$

From Eq. (11.75), amplitude of dynamic wheel-rail force generated by track irregularity can be derived, and dynamic wheel-rail force can be calculated by

$\boldsymbol{P}(t) = \boldsymbol{P}(\Omega)e^{i\Omega t}$. Hence, based on the derivation in Sects. 11.1 and 11.2, dynamic response can be obtained for all parts of the track-subgrade-ground system under dynamic wheel-rail force generated by track irregularity.

11.4 Dynamic Analysis of the High-Speed Train-Track-Subgrade-Ground Coupling System

Based on the presented theory, a computational program is designed for dynamic analysis of the high-speed train-track-subgrade-ground coupling system. For the sake of easier calculation, single TGV high-speed motor car is considered.

11.4.1 Influence of Train Speed and Track Irregularity on Embankment Body Vibration

Parameters for the TGV high-speed motor car are given in Chap. 6. Conditions of the track structure are as follows: ballast track structure with 60 kg/m continuous welded rails, bending stiffness of the rails: $EI = 2 \times 6.625\,\text{MN m}^2$; type-III sleepers, sleeper interval: 0.6 m, sleeper length: 2.6 m; ballast thickness: 35 cm, ballast width: 50 cm, ballast shoulder ratio: 1:1.75, ballast density: 1900 kg/m$^{3;}$ subgrade thickness: 3.0 m, subgrade width: 8.2 m, subgrade shoulder ratio: 1:1.5, and subgrade density: 1900 kg/m^3. Other parameters of the track and the subgrade bed are shown in Table 11.1. Embankment body is 2 m thick with hard soil, as is shown in Table 11.2; the ground is elastic half-space body and its detailed parameters are shown in Table 11.2. Profile irregularity values in the French track irregularity evaluation and management standard are adopted here, in which half-peak value A = 3 mm and wavelength l = 12.2 m.

The calculated results are shown in Figs. 11.4 and 11.5 [9, 10]. Figure 11.4 shows the vertical displacement of the embankment body with different train speeds, and Fig. 11.5 illustrates that, with other parameters unchanged and only consideration of different half-peak values of profile irregularity, the vertical displacement of the embankment body attenuates with the distance from the track center.

Table 11.1 Parameters for the track

Parameters	Stiffness per unit length/ (MN/m^2)	Damping per unit length/ (kN s/m^2)
Rail pads and fasteners	80/0.6	50/0.6
Ballast	120/0.6	60/0.6
Subgrade bed	1102	275

Table 11.2 Parameters for the embankment body and ground

Layer of soil	Type of soil	Elasticity modulus/(10^3 kN/m^2)	Poisson's ratio	Density/(kg/m^3)	Loss factor
Embankment body	Hard soil	269	0.257	1550	0.1
	Medium-hard soil	60	0.44	1550	0.1
	Soft soil	30	0.47	1500	0.1
Ground	Half-space body	2040	0.179	2450	0.1

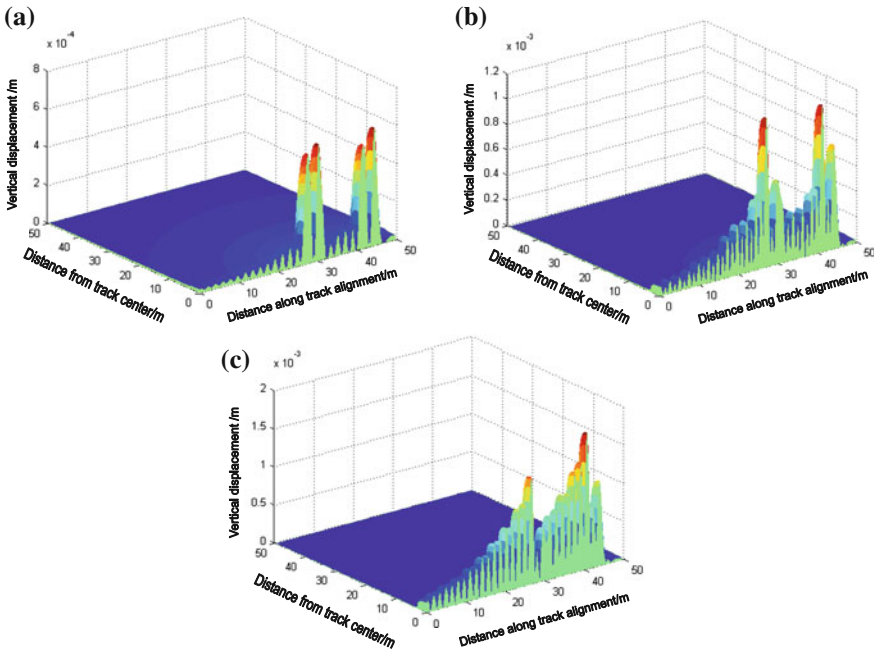

Fig. 11.4 Influence of train speed on the vertical displacement of the embankment body. **a** Train speed V = 200 km/h; **b** Train speed V = 250 km/h; **c** Train speed V = 300 km/h

It can be observed from Fig. 11.4 that with the increase of train speed, volatility of the vertical displacement of the embankment body is more and more obvious. When the train speed reaches 200 km/h, the vertical displacement of the embankment body is large only at the wheel load point but very small at other points; when the train speed reaches 300 km/h, huge vertical displacement occurs at all other points beside the wheel load point. It is shown in Fig. 11.5 that with the increase of half-peak value of track profile irregularity, the vertical displacement of the embankment body also increases, but the increase is not significant and only

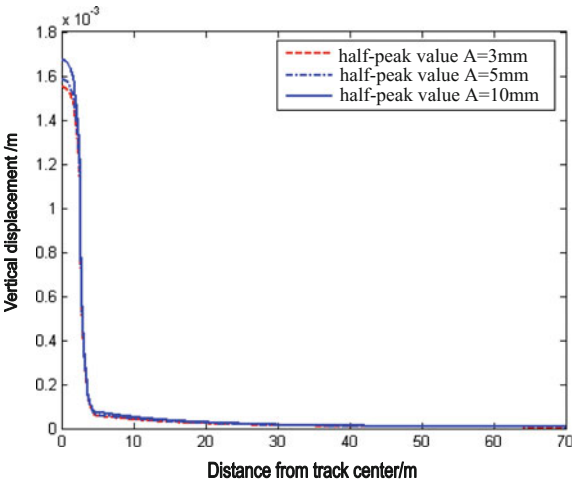

Fig. 11.5 Influence of track irregularity on the vertical displacement of the embankment body

influences the vibration displacement of the embankment body near the track. Therefore, it can be inferred that the vertical displacement of the embankment body is mainly resulted from the moving axle loads.

11.4.2 Influence of Subgrade Bed Stiffness on Embankment Body Vibration

Supposing the train speed is 200 km/h, and the other parameters are the same as those in Sect. 11.4.1, let us compare distribution of the vertical displacement of the embankment body with different subgrade bed stiffness. The calculated results are shown in Fig. 11.6 [10].

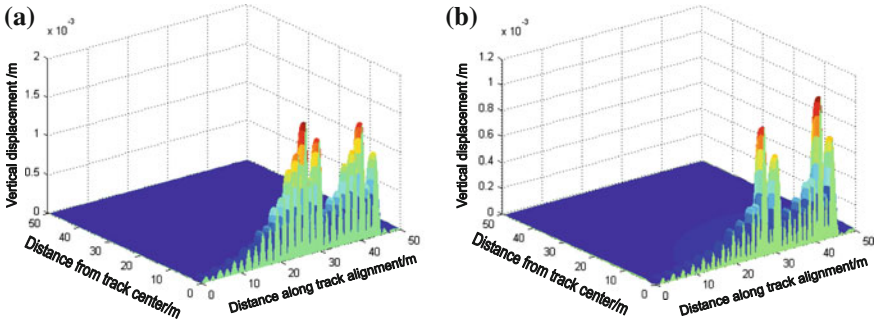

Fig. 11.6 Influence of subgrade bed stiffness on the vertical displacement of the embankment body. **a** Subgrade bed stiffness $k_c = 0.5 \times 1102$ MN/m^2; **b** Subgrade bed stiffness $k_c = 0.25 \times 1102$ MN/m^2

The comparison between Figs. 11.4a and 11.6 shows subgrade bed stiffness has a significant influence on the vertical displacement of the embankment body. With the decrease of stiffness, the vertical displacement of the embankment body increases dramatically and volatility also increases markedly.

11.4.3 Influence of Embankment Soil Stiffness on Embankment Body Vibration

Supposing the train speed is 200 km/h, and the other parameters are the same as those in Sect. 11.4.1, let us investigate distribution of the vertical displacement of the embankment body with different soil types. The calculated results are shown in Fig. 11.7 [10]. Parameters of the embankment soil type are shown in Table 11.2. It is shown in Fig. 11.7 that parameters of soil type have significant influence on the vertical displacement of the embankment body. Compared with hard soil, the vertical displacement of soft soil embankment increases greatly. Therefore, in engineering applications, special attention should be paid to the influence of soft soil embankment and particular measures such as increasing embankment soil stiffness to decrease the vibration displacement should be taken.

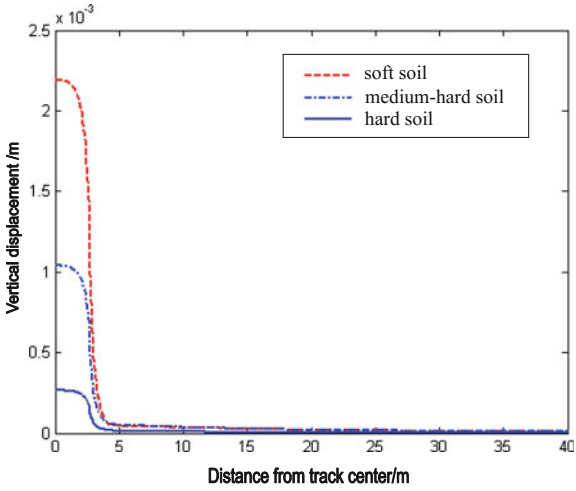

Fig. 11.7 Influence of embankment soil type on the vertical displacement of the embankment body

References

1. Xie W, Hu J, Xu J (2002) Dynamic responses of track-ground system under high-speed moving loads. Chin J Rock Mech Eng 21(7):1075–1078
2. Xuecheng Bian, Yunmin Chen (2005) Dynamic analyses of track and ground coupled system with high-speed train loads. Chin J Theor Appl Mech 37(4):477–484
3. Li Z, Gao G, Feng S, Shi G (2007) Analysis of ground vibration induced by high-speed train. J Tongji Univ (Sci) 35(7):909–914
4. Sheng X, Jones CJC, Thompson DJ (2004) A theoretical model for ground vibration from trains generated by vertical track irregularities. J Sound Vib 272:937–965
5. Lombaert G, Degrande G, Kogut J (2006) The experimental validation of a numerical model for the prediction of railway induced vibrations. J Sound Vib 297:512–535
6. Sheng X, Jones CJC, Petyt M (1999) Ground vibration generated by a harmonic load acting on a railway track. J Sound Vib 225(1):3–28
7. Feng Q (2013) Research on ground vibration induced by high-speed trains. Doctor's dissertation, Tongji University, Shanghai
8. Lei X, Sheng X (2008) Advanced studies in modern track theory, 2nd edn. China Railway Publishing House, Beijing
9. Feng Q, Lei X, Lian S (2008) Vibration analysis of high-speed railway tracks with geometric irregularities. J Vib Eng 21(6):559–564
10. Feng Q, Lei X, Lian S (2010) Vibration analysis of high-speed railway subgrade-ground system. J Railway Sci Eng 7(1):1–6

Chapter 12
Analysis of Dynamic Behavior of the Train, Ballast Track, and Subgrade Coupling System

With the large-scale construction of high speed railways and the completion of speed-rising projects, rail transportation in China has entered a high-speed era. As a result, the increase in train speed naturally induces greater dynamic force on the track, which will gradually lead to functional deterioration and failure of the track structure. Meanwhile, with the adoption and promotion of new track structure, such as broad sleepers, integrated ballast beds, and heavy rails, the wheel-rail shock and track vibration will be much more violent, which results in problems such as track surface shelling and spelling, adulatory wear, ballast flaking, and ballast hardening. Hence, a thorough research on the induction of track vibration and its transfer mechanism among all the track components, the destructive influence of vibration on the track, and effective vibration reduction and vibration isolation measures to improve vibration resistance ability is one of the most important ways to enhance track load capacity and to ensure running safety of the vehicle. To achieve the above aims, an analysis on the track dynamics is the premise. In this chapter, analysis of dynamic behavior of the train-ballast track-subgrade coupling system is carried out. Especially, to the problem of the frequent occurrence of track faults caused by vehicle bumping at roadbed-bridge joints of high-speed railways, computational software is developed based on the model and the algorithm of the vehicle element and track element in Chap. 9 [1–5]. And simulation analyses are performed to investigate the influence factors such as varying train speeds, varying patterns of track stiffness distribution, and transition irregularity on the dynamic responses of the vehicle and the track structure on track transitions.

12.1 Parameters for Vehicle and Track Structure

In analyzing the dynamic responses of the vehicle and the track structure on roadbed-bridge transitions, the vehicle concerned is Chinese high-speed train CRH3, as shown in Fig. 12.1. Parameters of the high-speed train CRH3 are given in

X. Lei, *High Speed Railway Track Dynamics*,
DOI 10.1007/978-981-10-2039-1_12

Fig. 12.1 Chinese high-speed train CRH3

Table 12.1 Parameters for ballast track

Parameter		Value	Parameter		Value
Rail	Mass/(kg/m)	60	Sleeper	Sleeper interval/(m)	0.57
	Density/(kg/m^3)	7800		Mass/(kg)	340
	Sectional area/(cm^2)	77.45	Ballast	Stiffness/(MN/m)	120
	Inertia moment around the horizontal axis/(cm^4)	3217		Damping/(kN·s/m)	60
	Elasticity modulus/(Mpa)	2.06×10^5		Mass/(kg)	2718
Rail pad and fastener	Stiffness/(MN/m)	80	Subgrade	Stiffness/(MN/m)	60
	Damping/(kN·s/m)	50		Damping/(kN·s/m)	90

Table 6.7 of chap. 6. The track is the ballast track with 60 Kg/m continuous welded rails and type-III sleepers. Parameters of the track structure are given in Table 12.1. The time step of numerical integration for the Newmark scheme adopts $\Delta t = 0.001$ s.

12.2 Influence Analysis of the Train Speed

In railway lines, there exist a large number of roadbed-bridge transitions, roadbed-culvert transitions, and crossings, which are fault-prone sections. Scholars both at home and abroad have achieved a wealth of findings about track transition [6–11], but the studies are mainly confined to experiments and engineering measures, which lacks in-depth theoretical analysis. From this section, the laws and influence factors of the dynamic responses of vehicle and track structure on track transitions will be investigated by starting with the influence analysis of the train speed.

A computational model for analysis of dynamic responses of the vehicle and the track structure in roadbed-bridge transition is shown in Fig. 12.2. In the simulation, total track length for computation is 300 m, which includes 100 m and 20 m extra track lengths on left and right track ends to eliminate the boundary effect. The start point is 100 m from the left track boundary. The change of track stiffness occurs in position 170 m. Suppose the stiffness of rigid subgrade at bridge section K_f is five times as that of the conventional ballast track $K_{f0,}$ that is $K_f = 5K_{f0,}$ where $K_{f0} = 60$ MN/m. The track structure model is discretized into 526 track elements with 1591 nodes.

Taking the boundary effect into account, seven observation points along the track, denoted with O1, O2,…, O7, are chosen at distances of 25, 45, 65, 70, 80, 100 and 120 m from the start point to analyze the dynamic responses of the vehicle and the track structure. Among the seven output points, three are located on the conventional subgrade ballast track, three on rigid bridge track, and one is exactly at the point of the stiffness change of the roadbed-bridge joints. Four kinds of the train speeds (V = 160, 200, 250, and 300 km/h) are specified to investigate the distribution of the dynamic responses of the vehicle and the track structure, as shown in Fig. 12.2.

To comprehensively analyze and assess the influence of train speeds, parts of the results including the time history curves obtained for the rail vertical acceleration, the vertical acceleration of car body, and the wheel-rail force are shown in Figs. 12.3, 12.4 and 12.5 [11].

It can be observed from Figs. 12.3, 12.4 and 12.5 that the changing subgrade stiffness has significant influence on the rail vertical acceleration and the wheel-rail contact force. With the increase in the train speed, the dynamic response increases remarkably. The influence of train speed is quite effective. At the change point of subgrade stiffness, the rail vertical acceleration and the wheel-rail contact force

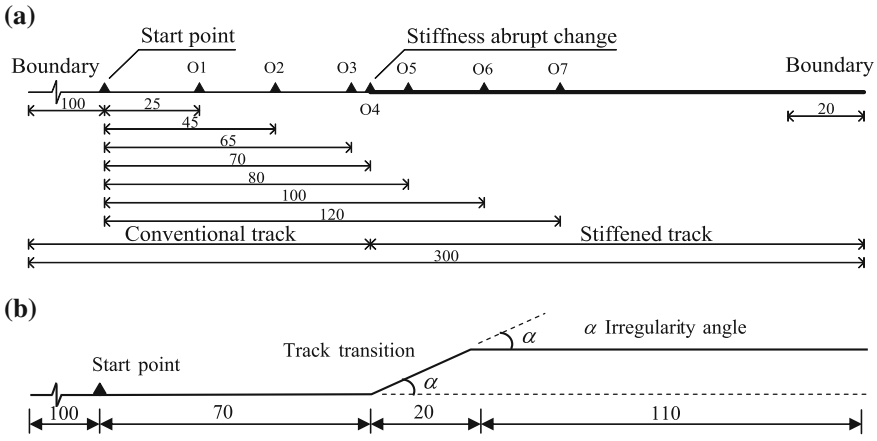

Fig. 12.2 A computational model for analysis of the dynamic responses of the vehicle and the track structure in roadbed-bridge transition/m

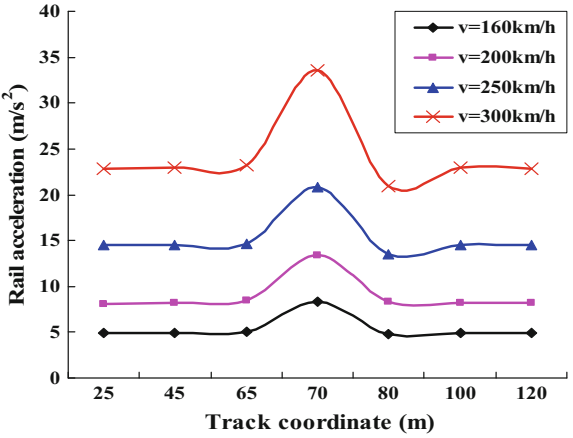

Fig. 12.3 Influence of train speeds on rail vertical acceleration

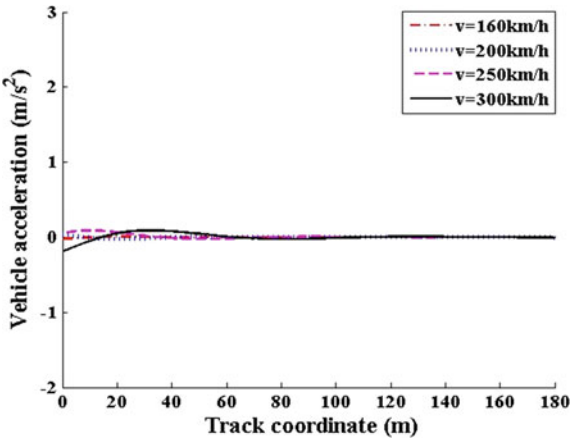

Fig. 12.4 Influence of train speeds on vertical acceleration of car body

display marked peak values. And the peak values multiply with the increase in train speed, which imposes great impact on the track structure. But the train speed has essentially no influence on the vertical acceleration of car body because of the excellent vibration isolation resulting from the primary and secondary suspension systems of the vehicle.

12.3 Influence Analysis of the Track Stiffness Distribution

A computational model for influence analysis of the different transition pattern for track stiffness distribution on the dynamic responses of track transition is shown in Fig. 12.6. The total track length for computation is 300 m, which includes 100 and 20 m extra track lengths on left and right track ends to eliminate the boundary

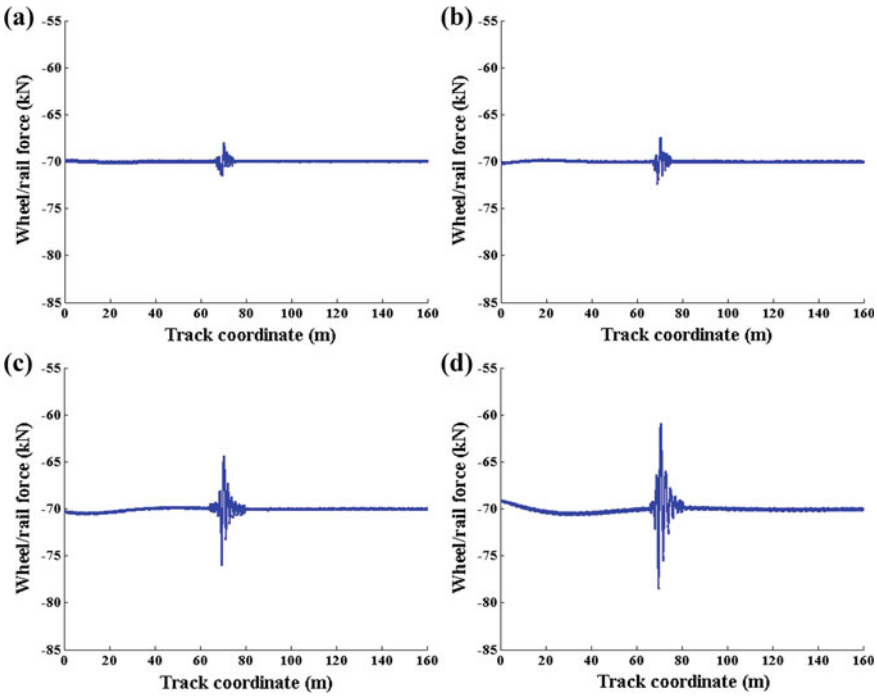

Fig. 12.5 Influence of train speeds on wheel-rail contact force ($K_f = 5K_{f0}$). **a** V = 160 km/h. **b** V = 200 km/h. **c** V = 250 km/h. **d** V = 300 km/h

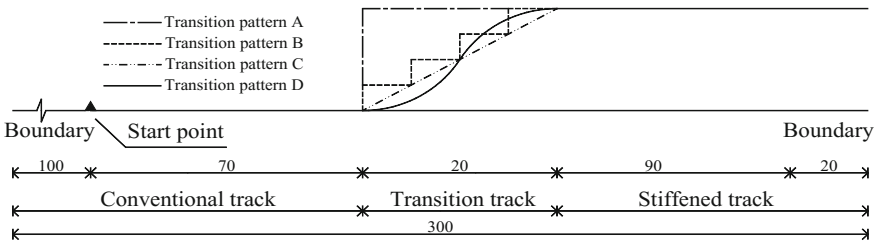

Fig. 12.6 Four kinds of transition pattern for track stiffness distribution

effect. The transition section is 20 m long and the subgrade stiffness changes in position 170 m, that is, 70 m after the start point. Suppose the train speed is V = 250 km/h, and the track structure model is discretized into 526 track elements with 1591 nodes.

To comprehensively understand the influence of the track stiffness distribution, four transition patterns are studied which are as follows:

Pattern A Abrupt change. The stiffness of ballast changes 5 times abruptly, and the stiffness of subgrade changes 40 times accordingly

Pattern B Step-by-step change. The stiffness of ballast changes 1–2–3–4–5 times in a ladder, and the stiffness of subgrade changes 1–5–10–20–40 times accordingly

Pattern C Linear change. The stiffness of ballast makes a linear change from 1 to 5 times; the stiffness of subgrade also changes linearly from 1 to 40 times

Pattern D Cosine change. The stiffness of ballast changes in a cosine curve, adopting a 1–5 cosine interpolation; accordingly the stiffness of subgrade also makes a cosine change, adopting a 1–40 cosine interpolation computing method

The output results include the time history curves of the vertical acceleration of car body, the rail vertical acceleration, and the wheel-rail contact force, as shown in Figs. 12.7, 12.8 and 12.9, respectively [11].

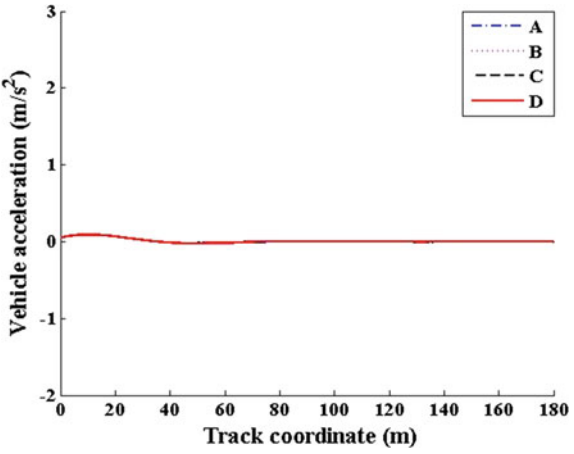

Fig. 12.7 Influence of track stiffness distribution on vertical acceleration of car body

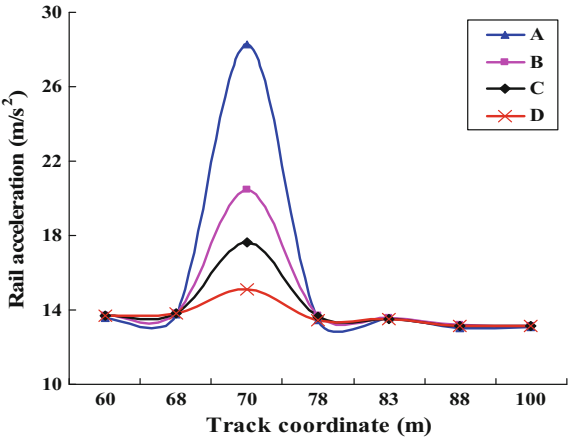

Fig. 12.8 Influence of track stiffness distribution on rail vertical acceleration

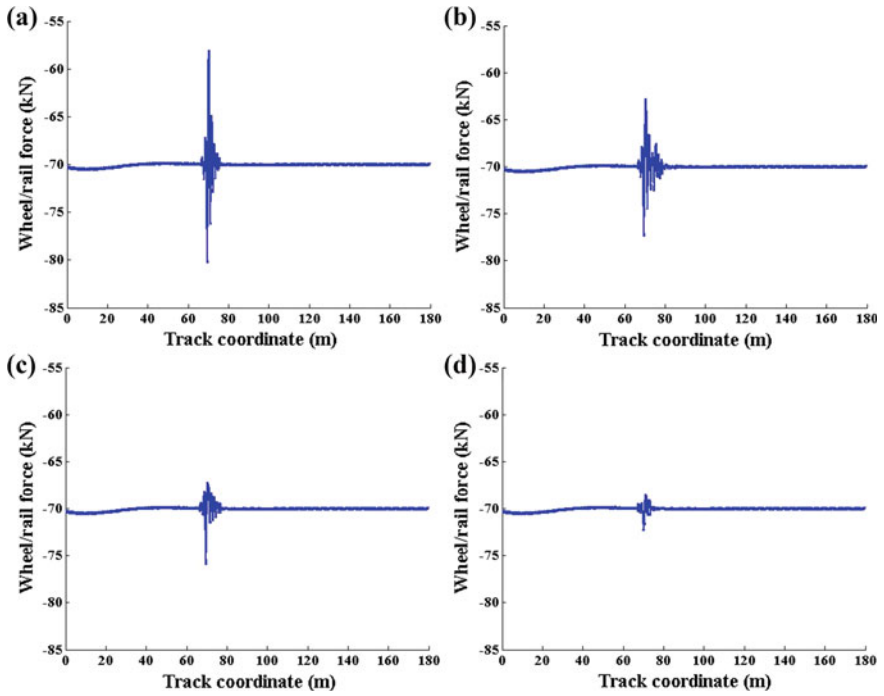

Fig. 12.9 Influence of track stiffness distribution on wheel-rail contact force. **a** Pattern A. **b** Pattern B. **c** Pattern C. **d** Pattern D

As shown in Fig. 12.7, the vertical accelerations of the car body corresponding to the four kinds of the track stiffness transition patterns are completely overlapped, which means changing track stiffness has little influence on the car body acceleration. Influence of the track stiffness distribution on the car body acceleration is not effective, due to the excellent vibration isolation resulting from the primary and secondary suspension systems of the vehicle. Figure 12.8 shows that the rail vertical acceleration does not change either on conventional track foundation or rigid track foundation, which indicates that the track stiffness has little influence on the rail vertical acceleration. But at the variation point of track stiffness in the transition section, the rail vertical acceleration changes dramatically. With the change of the track stiffness transition patterns, the rail vertical acceleration differs greatly, among which the cosine pattern has the least influence. In addition, the wheel-rail contact force differs with the change of the four kinds of the track stiffness transition patterns. Figure 12.9 and Table 12.2 reveal that when the track stiffness of roadbed-bridge transition changes in cosine pattern, the wheel-rail contact force changes the least, and the additional dynamic action is also the least, which can significantly reduce the impact on the vehicle and the track structure and thus to improve passenger comfortableness and to ensure high-speed running.

Table 12.2 Influence of track stiffness distribution on wheel-rail contact force and rail acceleration

Wheel-rail contact force	Abrupt change	Step-by-step change	Linear change	Cosine change
Maximum/(kN)	−58.050	−62.755	−67.18	−68.406
Minimum/(kN)	−80.253	−77.382	−75.937	−72.301
Amplitude/(kN)	22.203	14.627	8.757	3.895
Reduction ratio compared with transition pattern A/%	0	34.12	60.56	82.46
Maximum rail acceleration (m/s^2)	28.248	20.442	17.638	15.138
Reduction ratio compared with transition pattern A/%	0	27.63	37.56	46.41

12.4 Influence Analysis of the Transition Irregularity

When the train is moving on roadbed-bridge transitions, vehicle bumping at bridge head occurs frequently. The bumping is caused by a number of factors, such as post-construction settlement of the roadbed-bridge joints on newly built railways, roadbed settlement resulting from the more compact and condensed abutment fillings under cyclic vehicle loading, and the uneven stiffness between the roadbed and bridge. Previous studies show that changing track stiffness of the roadbed-bridge transition has little influence on the running safety of vehicles and the comfortableness of passengers, while the transition irregularity caused by roadbed-bridge settlement differences has a profound influence on the safe running of vehicles [6–9]. In the following analysis, only the dynamic response induced by the transition irregularity is studied, exclusive of the influence of the track stiffness of roadbed-bridge transition. And in order to truly simulate the real conditions of the railway, the random track profile irregularity is considered with the method proposed in Chap. 5. In the following analyses, three kinds of irregularity pattern are examined.

Pattern A Regular transition. The vehicle moves into the transition at the speed of 250 km/h

Pattern B Irregular transition. The roadbed-bridge settlement difference is 5 cm. Two types of transition irregularities, linear and cosine, are considered, and the vehicle moves into the transition at the speed of 250 km/h

Pattern C Irregular transition. The vehicle moves out of the transition at the speed of 250 km/h, and the other conditions are the same as Pattern B

In the model, the total track length for computation is 300 m, which includes 100 and 20 m boundary regions on the track start and track end. The transition section is 20 m long.

The sample of track irregularity is generated by use of trigonometric series based on railway track profile irregularity spectrum for line level 6, which is specified in standards of American ARR (Association of American Railroads). Here listed are

only some of the typical dynamics evaluation index curves. The calculated results for the diversified transition irregularity patterns are shown in Figs. 12.10, 12.11, 12.12, 12.13, 12.14, 12.15, 12.16, 12.17, 12.18, 12.19, 12.20 and 12.21, respectively [11].

Based on the above computation, the conclusions can be summarized as follows:

(1) Figures 12.11, 12.12, 12.13, 12.14, 12.15, 12.16, 12.17, 12.18, 12.19, 12.20 and 12.21 show that the calculated results for the car body acceleration and the wheel-rail contact force are distributed in a reasonable range. When the vehicle moves into the transition section, it goes through a step-up process, which exerts an additional impact on start point O1 of the transition section. Therefore, there appears a downward minimum wheel-rail contact force. When the step-up process comes to an end, there exists a possibility of transient wheel-rail separation. Hence, at the point of O2, the peak value of the wheel-rail contact force appears again, but it is an upward maximum value. When the vehicle moves out of the transition, it goes through a step-down process. At the point of O3, the vehicle may be in a suspension state and is in danger of derailment. When the step-down process finishes, the vehicle imposes an additional impact on point O4. Simulation of the vehicle moving into and out of the transition is consistent with what happens in reality, which proves that the computation model is effective and the results are reliable.

(2) As it can be seen from Table 12.3, when the transition irregularity is in a linear change, impact of the vehicle on the transition track at the point of O1 is weaker than that at the point of O4, that is, the destruction on the track structure caused by the vehicle moving out of the transition is more severe than moving into the transition. The maximum wheel-rail contact force at the point of O3 is bigger than that at the point of O2, which means the danger of derailment is greater when the vehicle moves out of the transition than when it moves into the transition. When the transition irregularity is in cosine change, impact by the vehicle moving out of the transition is also greater than that by the vehicle moving into the transition. Different from linear change, danger of derailment is greater when the vehicle is moving into the transition. It illustrates that irregularity is the principal factor for the dynamic changes of transition section.

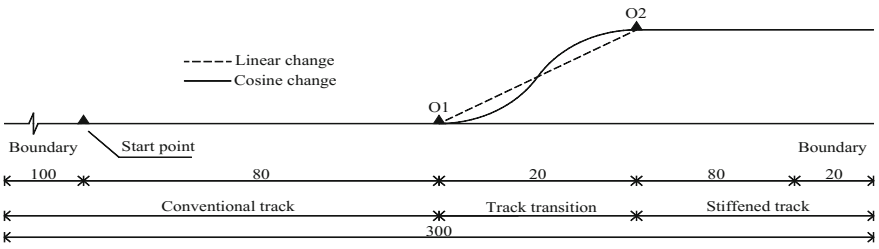

Fig. 12.10 Analysis model for the vehicle moving into the bridge deck/m

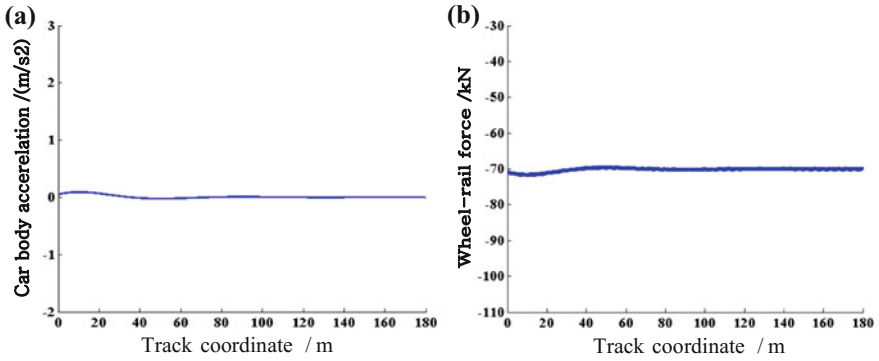

Fig. 12.11 Car body acceleration and wheel-rail contact force under the train moving into the transition (Pattern A). **a** Car body acceleration. **b** Wheel-rail contact force

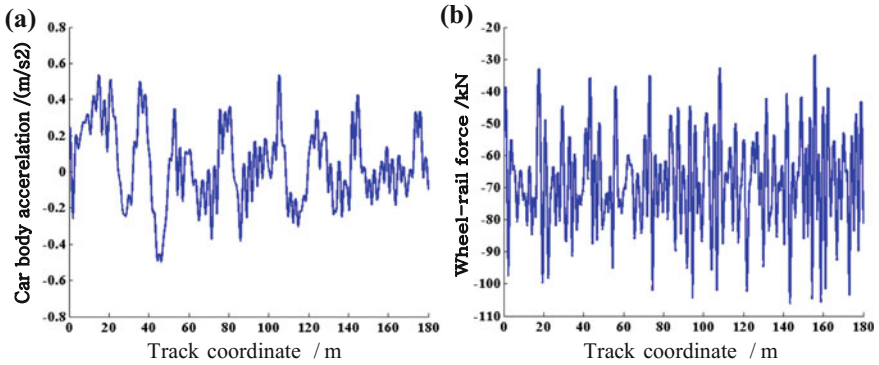

Fig. 12.12 Car body acceleration and wheel-rail contact force under the train moving into the transition (Pattern A + random irregularity). **a** Car body acceleration. **b** Wheel-rail contact force

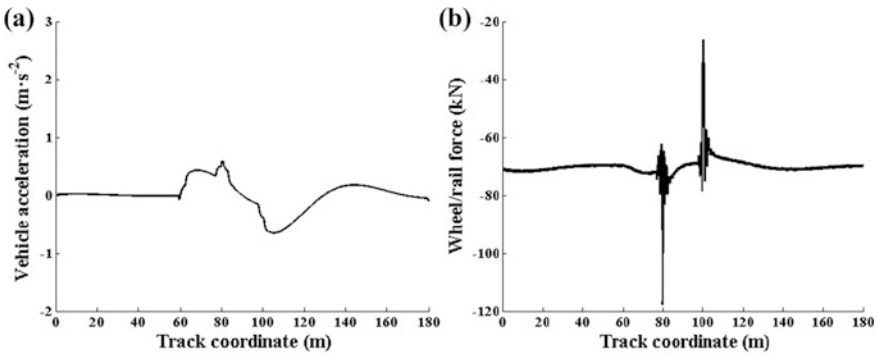

Fig. 12.13 Car body acceleration and wheel-rail contact force under the train moving into the linear transition (Pattern B). **a** Car body acceleration. **b** Wheel-rail contact force

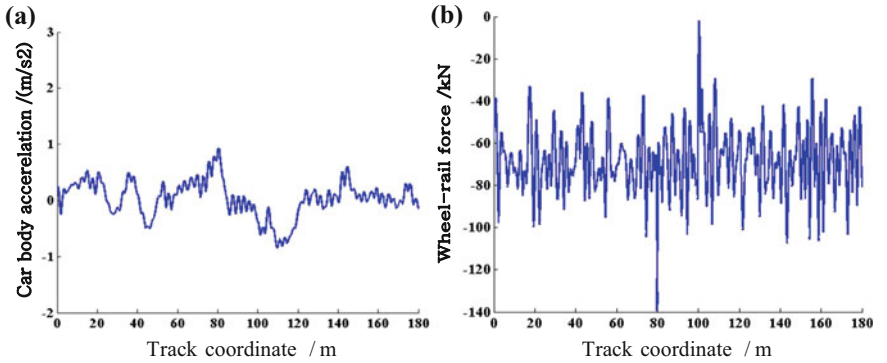

Fig. 12.14 Car body acceleration and wheel-rail contact force under the train moving into the linear transition (Pattern B + random irregularity). **a** Car body acceleration. **b** Wheel-rail contact force

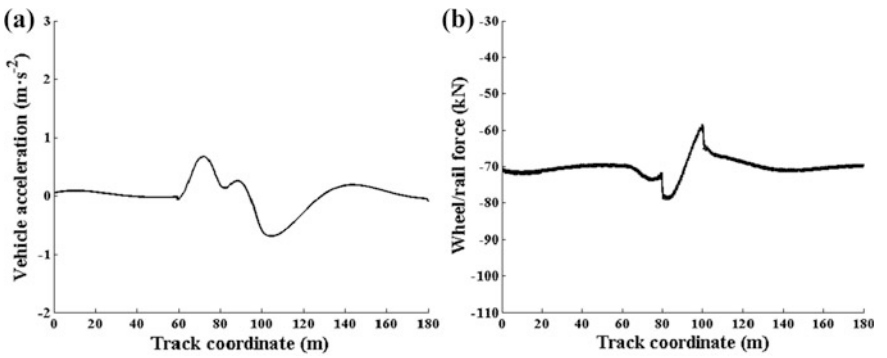

Fig. 12.15 Car body acceleration and wheel-rail contact force under the train moving into the cosine transition (Pattern B). **a** Car body acceleration. **b** Wheel-rail contact force

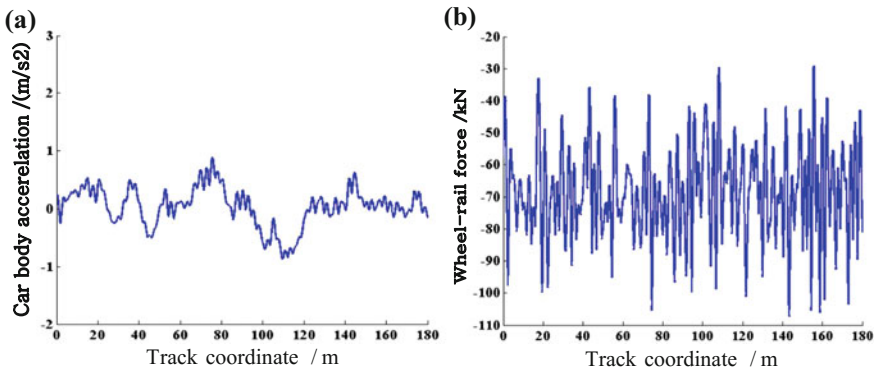

Fig. 12.16 Car body acceleration and wheel-rail contact force under the train moving into the cosine transition (Pattern B + random irregularity). **a** Car body acceleration. **b** Wheel-rail contact force

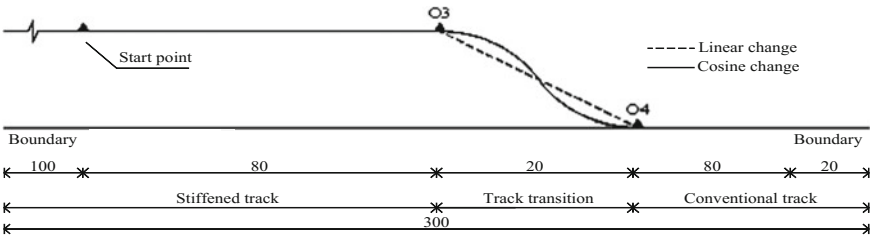

Fig. 12.17 Analysis model for the vehicle moving out of the bridge deck/m. **a** Car body acceleration. **b** Wheel-rail contact force

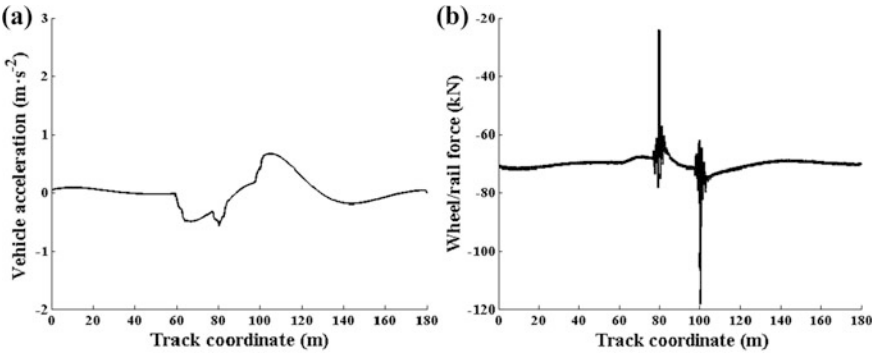

Fig. 12.18 Car body acceleration and wheel-rail contact force under the train moving out of the linear transition (Pattern C). **a** Car body acceleration. **b** Wheel-rail contact force

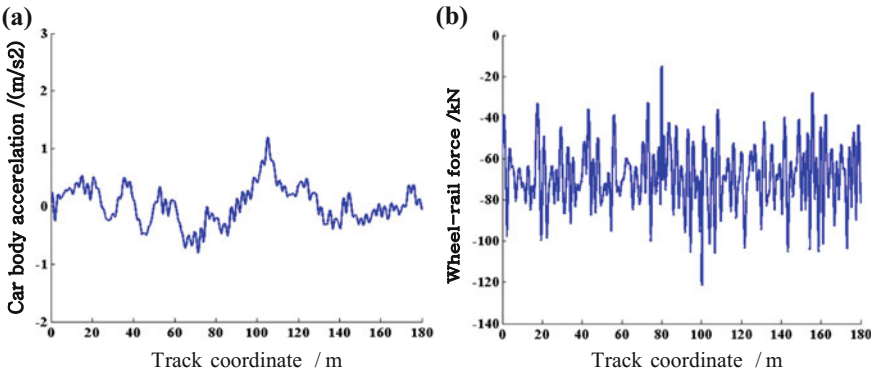

Fig. 12.19 Car body acceleration and wheel-rail contact force under the train moving out of the linear transition (Pattern C + random irregularity). **a** Car body acceleration. **b** Wheel-rail contact force

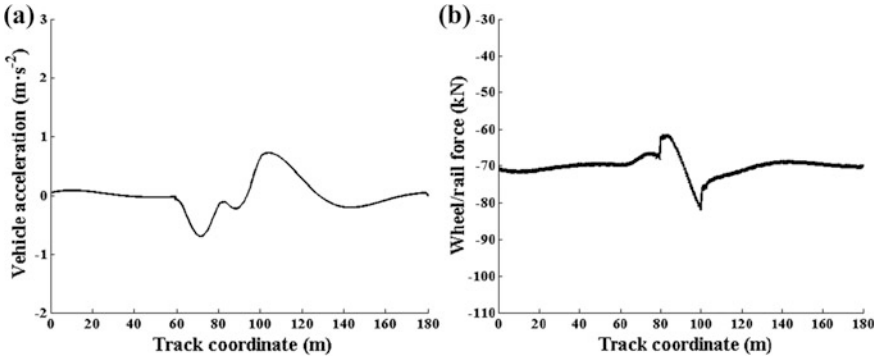

Fig. 12.20 Car body acceleration and wheel-rail contact force under the train moving out of the cosine transition (Pattern C). **a** Car body acceleration. **b** Wheel-rail contact force

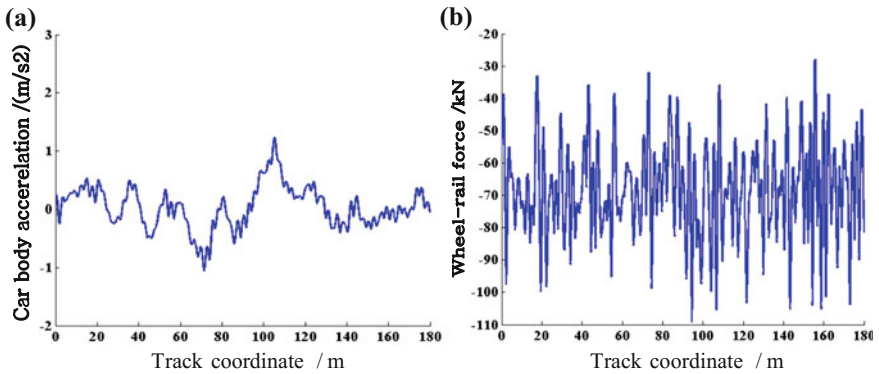

Fig. 12.21 Car body acceleration and wheel-rail contact force under the train moving out of the cosine transition (Pattern C + random irregularity). **a** Car body acceleration. **b** Wheel-rail contact force

Table 12.3 Wheel-rail contact force for different transition irregularity patterns

Wheel-rail contact force	Regular transition	Irregular transition			
		Linear, into	Cosine, into	Linear, out of	Cosine, out of
Maximum/(kN)	−70	−26.192	−58.30	−23.873	−61.25
Minimum/(kN)	−70	−117.81	−79.17	−118.34	−81.82
Amplitude/(kN)	0	91.618	20.87	94.467	20.57

(3) Transition patterns of track irregularity have a dramatic influence on the dynamic indexes of the vehicle and the track structure. When the transition is in a linear change, the dynamic response is quite great, while when the transition is in a moderate cosine change, the response is evidently weakened.

(4) Random irregularity of the track is the major exciting source of the vehicle and the track vibration, which directly affects the train's smooth and safety operation. Car body acceleration is an important index to evaluate passenger comfortableness and is sensitive to random irregularity of the track, but the primary and secondary suspension systems of the vehicle can effectively isolate and reduce the system vibration.

12.5 Influence Analysis of the Combined Track Stiffness and Transition Irregularity

Influence analysis of the combined track stiffness and transition irregularity is based on practical conditions of the roadbed-bridge transition. On track transition, there exist both the random irregularity and stiffness change of the roadbed-bridge track foundation. Therefore, the following analysis mainly focuses on the combined influence of the track surface irregularity and track stiffness change on the dynamic response of the vehicle and the track structure under high-speed moving vehicles.

A computational model for influence analysis of the combined track stiffness and transition irregularity is shown in Fig. 12.22. The total track length for computation is 300 m, which includes 100 and 20 m extra track lengths on left and right track ends to eliminate the boundary effect. The start point is 100 m from the left boundary, and the transition begins in position 170 m. Total length of the transition is 20 m. Suppose the train speed V = 250 km/h, and the track structure model is discretized into 526 track elements with 1591 nodes.

In view of different irregularity angles of the track transition, as shown in Fig. 12.22, six cases are considered as α = 0, 0.0010, 0.0015, 0.0020, 0.0025, and 0.0030 rad. The following analysis are based on assumptions: (1) Suppose the stiffness of rigid subgrade at bridge section K_f is five times as that of the conventional ballast track $K_{f0,}$ that is $K_f = 5K_{f0,}$ where K_{f0} = 60 MN/m. (2) The train speed V = 250 km/h. (3) Seven observation points along the track (denoted with

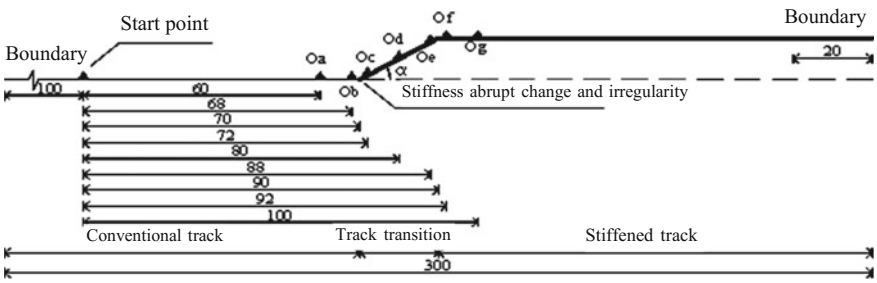

Fig. 12.22 A computational model for influence analysis of the combined track stiffness and irregularity on the dynamic response of the vehicle and the track/m

Oa, Ob, …, Og) are chosen to analyze the dynamic responses of the vehicle and the track structure. The track coordinates are 60, 68, 72, 80, 88, 92 and 100 m accordingly. The calculated results are shown in Figs. 12.23, 12.24 and 12.25 [11].

Influence analysis of the combined track stiffness and transition irregularity in different cases proves that when the train moves at a constant speed and there exist abrupt change of track stiffness, the irregularity angle of the track transition has substantial influence on the rail vertical acceleration and the wheel-rail contact force. And the larger the irregularity angle is, the greater the influence becomes. The combined influence is much more evident than the separate influence of track stiffness or transition irregularity. As shown in Fig. 12.23, two peaks of the rail vertical acceleration are observed at track coordinates 68 and 91 m. The magnitude of the first peak is 2.1 times as that of the second. This is because the first peak of

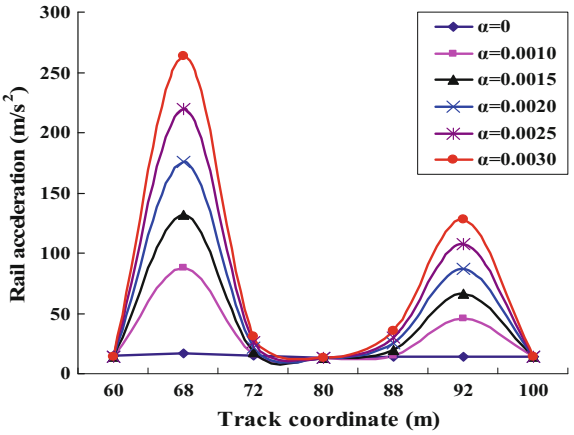

Fig. 12.23 Influence of combined track stiffness and irregularity angles on rail vertical acceleration

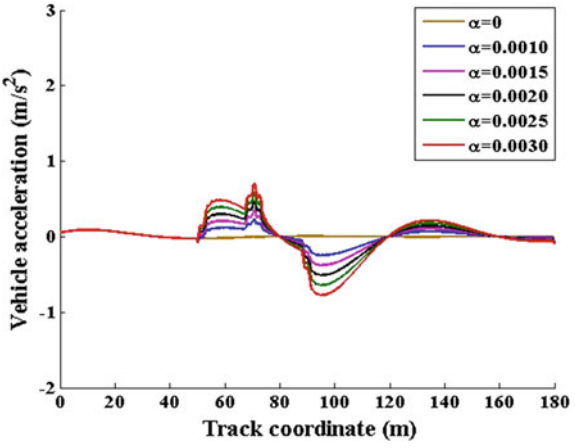

Fig. 12.24 Influence of combined track stiffness and irregularity angles on vehicle acceleration

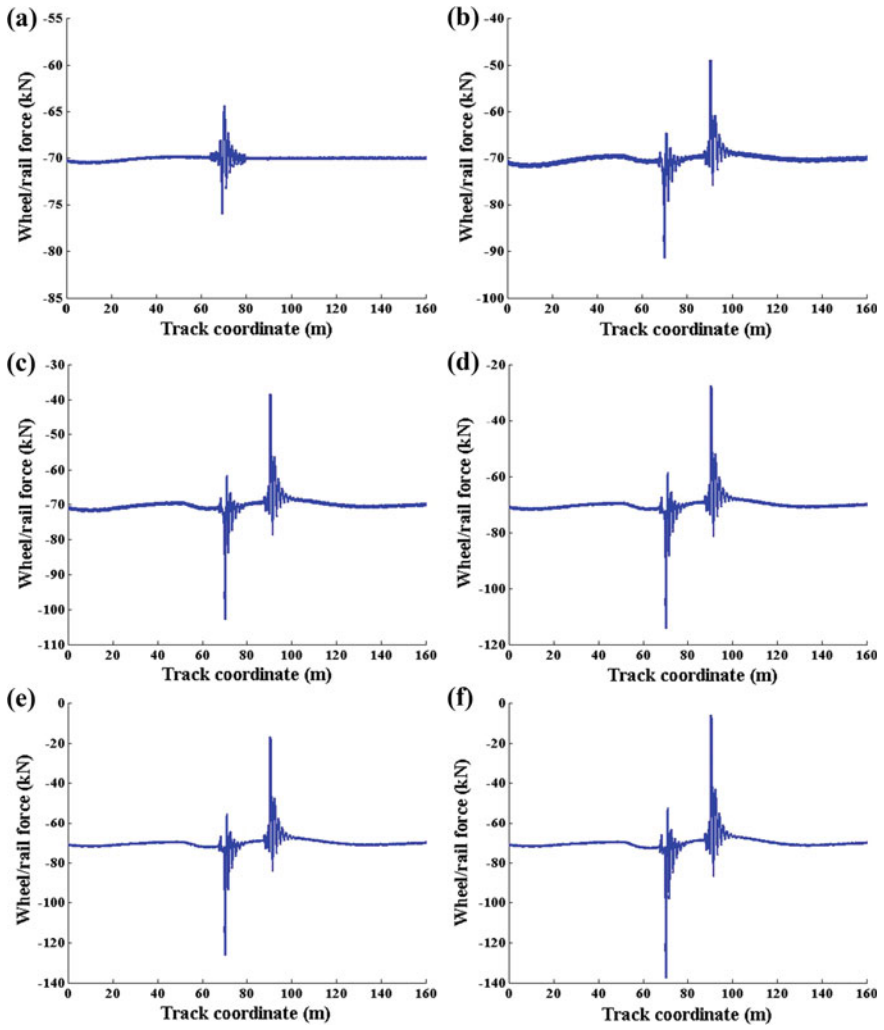

Fig. 12.25 Influence of combined track stiffness and irregularity angles on wheel-rail contact force (V = 250 km/h). **a** $\alpha = 0$. **b** $\alpha = 0.0010$ rad. **c** $\alpha = 0.0015$ rad. **d** $\alpha = 0.0020$ rad. **e** $\alpha = 0.0025$ rad. **f** $\alpha = 0.0030$

the rail vertical acceleration is induced simultaneously by the irregularity angle of the track transition and the abrupt change of the subgrade stiffness, whereas the second peak is only generated by the irregularity angle of the track transition. In Fig. 12.24, curves of the vertical acceleration of the car body for different kinds of irregularity angles have slight differences in magnitudes due to the well vibration reduction of the primary and the secondary suspension system of the vehicle.

This chapter makes an in-depth investigation to the dynamic behavior of the ballast track system, especially the mechanism of track faults caused by train

bumping at bridge head. Up to now, due to the great difficulty in technology and the lagging-behind theoretical research to engineering applications, ultimate solution to the fault has not been realized yet. The problem not only limits the train's speed and increases the operation cost, but also endangers the running safety of vehicles in extreme cases. Consequently, it lowers the railway service level to a large extent and affects the railway's social benefits and economic returns. Even in countries where the railway is highly developed, vehicle bumping at bridge head is still one of the tough problems, waiting to be successfully tackled. To ensure a good track condition, maintenance and repairs in the track transition should be performed frequently by relative department. In this sense, a theoretical research on the causes of vehicle bumping at bridge head can provide some guidance to the specific problems in engineering applications.

In this chapter, a computational software is developed and coded with MATLAB. Typical track transitions are chosen. Influence factors such as varying train speeds, different patterns of track stiffness distribution, and transition irregularity on the dynamic responses of the vehicle and the track structure are simulated, analyzed, and evaluated comprehensively.

Through the analysis, the conclusions can be obtained as follows:

(1) Influence analysis of the train speed on the roadbed-bridge transition shows as follows: Once there is a change in track stiffness, the train speed will have evident influence on all the dynamic indexes of the vehicle and the track structure. And if the speed is very fast and the stiffness change is very great, the combined influence will be more evident.
(2) Stiffness change of the roadbed-bridge track foundation has influence on the dynamic indexes of the vehicle-track coupling system to different degrees but has slight influence on the train's operation safety. Influence analysis for track stiffness distribution shows cosine change of the track stiffness is preferable and should be adopted as the theoretical guidance for engineering maintenance, because it can effectively reduce the impact and destruction on the track.
(3) Transition irregularity resulted from roadbed-bridge settlement differences has notable influence on all the dynamic indexes. The vehicle and the track structure are very sensitive to the track irregularity and require a higher level of the track regularity. The influence of the track stiffness distribution on train's operation safety is not as great as that of the track irregularity.
(4) Analysis of the combined influence indicates that when there are both track stiffness change and track irregularity, the combined influence is much more obvious than the separate influence of the track stiffness or the track irregularity. Adopting reasonable track transition pattern can reduce the vehicle impact on track structure in transition sections, and thus meet the requirement of passenger comfortableness and high-speed operation.
(5) The influence of track irregularity on passenger comfortableness and operation safety has become one of the major constraints to the development of the high-speed railways. Efforts and attentions of the railway maintenance

technicians have to be directed at eliminating track irregularity. Abating and smoothing irregularity to the greatest extent so as to prevent and avoid vehicle bumping at bridge head is of great significance to reduce the transition faults and ensure the operation safety.

References

1. Lei X, Zhang B (2010) Influence of track stiffness distribution on vehicle and track interactions in track transition. J Rail Rapid Transit Proc Inst Mech Eng Part F 224(1):592–604
2. Lei Xiaoyan, Zhang Bin (2011) Analysis of dynamic behavior for slab track of high-speed railway based on vehicle and track elements. J Transp Eng 137(4):227–240
3. Lei Xiaoyan, Zhang Bin (2011) Analyses of dynamic behavior of track transition with finite elements. J Vib Control 17(11):1733–1747
4. Xiaoyan Lei, Bin Zhang, Qingjie Liu (2010) Model of vehicle and track elements for vertical dynamic analysis of vehicle-track system. J Vib Shock 29(3):168–173
5. Bin Zhang, Xiaoyan Lei (2011) Analysis on dynamic behavior of ballastless track based on vehicle and track elements with finite element method. J China Railw Soc 33(7):78–85
6. Kerr AD, Moroney BE (1993) Track transition problems and remedies. Bull 742 Am Railw Eng Assoc 267–298
7. Moroney BE (1991) A study of railroad track transition points and problems. Master's thesis of University of Delaware, Newark
8. Linya Liu, Xiaoyan Lei (2004) Designing and dynamic performance evaluation of roadbed-bridge transition on existing railways. Railw Stan Des 1:9–10
9. Chengbiao Cai, Wanming Zhai, Tiejun Zhao (2001) Research on dynamic interaction of train and track on roadbed-bridge transition section. J Traffic Transp Eng 1(1):17–19
10. Xiaoyan Lei, Bin Zhang, Qingjie Liu (2009) Finite element analysis on the dynamic characteristics of the track transition. China Railw Sci 30(5):15–21
11. Zhang Bin (2007) Finite element analysis on the dynamic characteristics of track structure for high-speed railway. Master's thesis of East China Jiaotong University, Nanchang

Chapter 13
Analysis of Dynamic Behavior of the Train, Slab Track, and Subgrade Coupling System

With several competitive advantages over conventional ballast tracks, slab tracks are widely applied in countries where high-speed railways are well developed. Today, China is actively developing passenger-dedicated lines, with slab tracks laid section by section as the major type of track structure. But in terms of this advanced slab track structure type, experience in the systematic designing, construction, supervision, operation, and maintenance of the structure is still lacking. As for the vibration and deformation characteristics, operation reliability and safety of the slab track under moving train loads, theoretical, and experimental research are also in great need. In this sense, it is of great practical value to make a dynamic behavior analysis on the slab track. The dynamic interaction between the high-speed train and the slab track is the key issue for the vibration analysis of the train-track coupling system. The forced vibration of the slab track structure under moving train loads directly influences the working state and service life of the structure. Meanwhile, the riding quality and safety are the important indexes to evaluate whether the parameters of the slab track structure are reasonably designed or not.

Compared with the ballast track, the slab track has a higher stiffness, which induces stronger vibration of the high-speed wheel-rail system. Track foundation stiffness is not only one of the key factors which influence the riding performance of the train, but also an important parameter in influencing the dynamic characteristics of the wheel-rail system. With the rapid development of high-speed railways, slab track foundation stiffness has become one of the hot issues for researchers both at home and abroad.

Based on the model and the algorithm of the vehicle element and track element proposed in Chap. 9 [1–6], dynamic behavior of slab track structure under moving train loads is investigated in this chapter. Especially, parameter analysis of the structure will be carried out. Through the parameter analysis, it attempts to optimize parameters of the slab track structure so as to abate track deformation, prolong track service life, and improve track stability.

X. Lei, *High Speed Railway Track Dynamics*,
DOI 10.1007/978-981-10-2039-1_13

13.1 Example Validation

In order to verify the model and the algorithm of the train-slab track-subgrade coupling system presented in this chapter, a vertical vibration characteristic analysis of the train–Bögle slab track coupling system is performed by the consideration of two kinds of track conditions, i.e., the smooth track and the irregularity track. The vehicle concerned is China-star high-speed train which is marshaled by a motor car and a trailer. Parameters for China-star high-speed train and for the Bögle slab track adopt those in Reference [7]. The calculated results with the proposed model are compared with those obtained from the dynamic analysis model of the lateral finite strip and slab segment element in Reference [7] and the static model of slab track (double-layer beams) in Reference [8], respectively.

Case 1 Assume the track is absolutely smooth and the China-star high-speed train moves on the Bögle slab track at the speed of 50 km/h. The maximum vertical vibration displacements of the rail and the Bögle slab are calculated and compared with those in Reference [7] and Reference [8], as is shown in Table 13.1. Time history curves of the rail deflection and the Bögle slab deflection are shown in Figs. 13.1 and 13.2 [6].

Case 2 Considering the China-star high-speed train marshaled by a motor car and a trailer moves on the Bögle slab track at the speed of 200 km/h [7].

Table 13.1 Maximum vertical displacements of the rail and the Bögle slab

Maximum vertical displacements	Calculated result of this chapter	Calculated result of Reference [7]	Calculated result of Reference [8]
Rail/(mm)	0.815	0.817	0.802
Bögle slab/(μm)	2.038	1.700	0.800

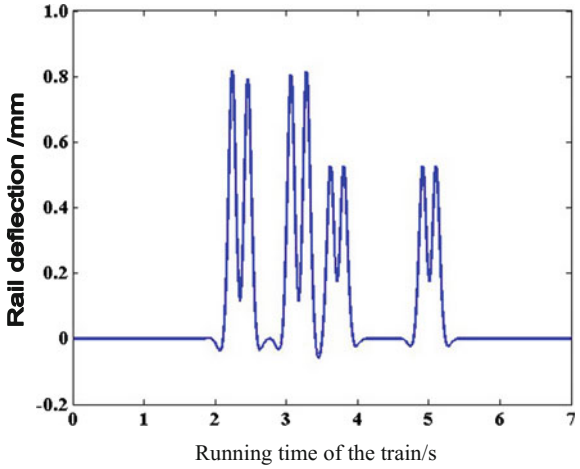

Fig. 13.1 Time history of the rail deflection

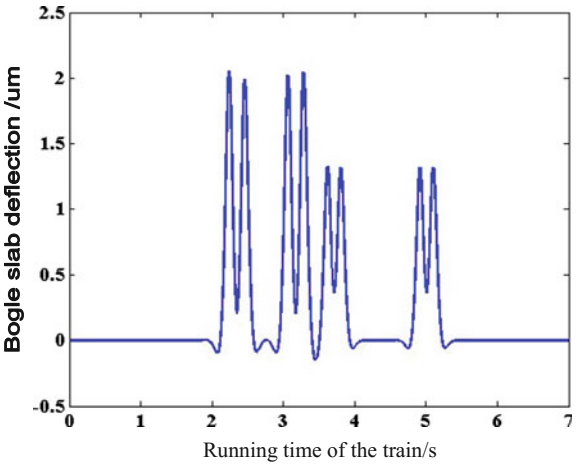

Fig. 13.2 Time history of the Bögle slab deflection

Simulation is performed to analyze the vertical vibration displacements of the track structure. Excitation source adopts a periodic sine function of track profile irregularity with 20 m wavelength and 6 mm amplitude. Time history curves of the rail vertical displacement and the Bögle slab vertical displacement are compared with those calculated by finite element method, as is shown in Figs. 13.3 and 13.4 [6].

The calculated results for the two cases are highly consistent, which valid the model and the algorithm proposed in this chapter. And in addition, the trace of the wheels is clearly observed.

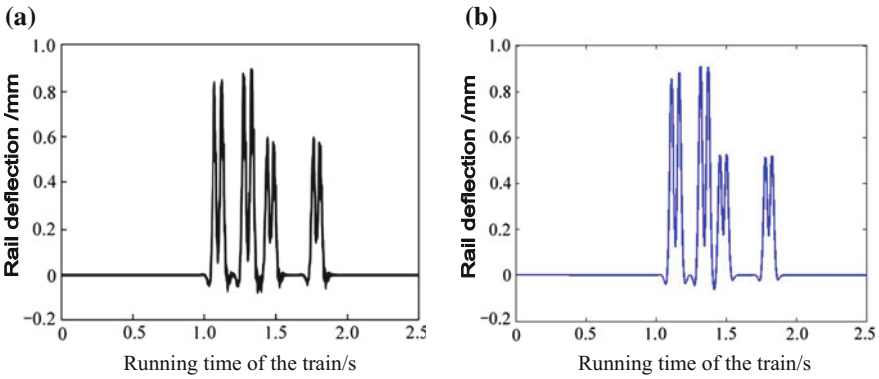

Fig. 13.3 Time history of the rail vertical displacements. **a** Results with FEM. **b** Results with the proposed method

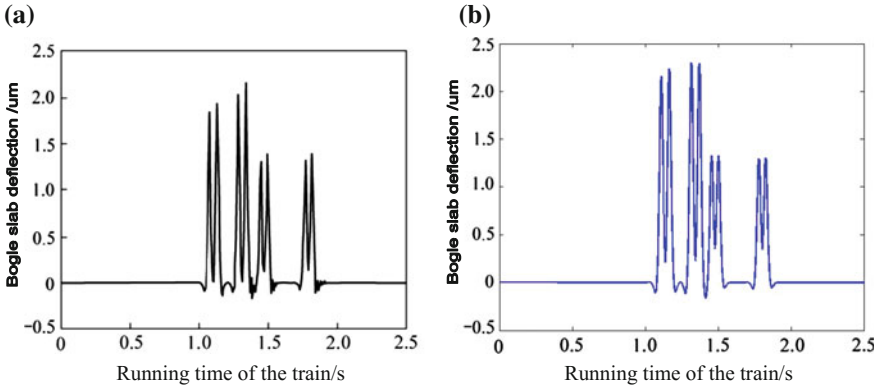

Fig. 13.4 Time history of the Bögle slab vertical displacements. **a** Results with FEM. **b** Results with the proposed method

13.2 Parameter Analysis of Dynamic Behavior of the Train, Slab Track, and Subgrade Coupling System

In the following simulation, the vehicle concerned is China high-speed train CRH3. The slab track involved is German track laid on Beijing-Tianjin intercity railway. Parameters of the high-sped train CRH3 and the Bögle slab track structure are given in Tables 6.7 and 6.10 of Chap. 6, respectively.

The feature of the Bögle slab track is the CA mortar laid between the track slab and the concrete support layer. As the support layer of precast reinforced concrete track slab, CA mortar can fill the gap between the track slab and the concrete support layer, jointly adjust the track profile difference with the rail pads and make the track structure precisely located. Meanwhile, it can also provide sufficient track strength and certain track elasticity. Therefore, reasonably chosen parameters of the CA mortar is very significant to improve the comprehensive dynamic performance of the slab track structure. In the slab track system, stiffness and damping of the rail pad and fastener and the subgrade also has an influence on the dynamic performance of the vehicle and the track structure.

The following parameter analysis is based on the assumptions: the model and the algorithm is the vehicle element and track element presented in Chap. 9; the track is perfect smooth; the train speed is V = 250 km/h; the time step of numerical integration for the Newmark Scheme is $\Delta t = 0.001$ s. Simulation is performed to analyze the influence of the stiffness and the damping of the rail pad and fastener,

the CA mortar and the subgrade on the dynamic performance of the slab track structure. Evaluation indexes include the vertical acceleration of the car body, the wheel-rail contact force, the deflections, and the vertical accelerations of the rail, the track slab and the concrete support layer. Through the analysis, it aims to provide a theoretical basis for the reasonable choice of parameters for the Bögle slab track structure.

13.3 Influence of the Rail Pad and Fastener Stiffness

With other parameters unchanged, six cases of the rail pad and fastener stiffness coefficient are considered to investigate its influence on the dynamic performance of the vehicle and the track structure: 2×10^7 N/m, 4×10^7 N/m, 6×10^7 N/m, 8×10^7 N/m, 1.0×10^8 N/m, and 1.2×10^8 N/m. The calculated results are illustrated by Figs. 13.5, 13.6, 13.7, 13.8 and 13.9 [6].

Figures 13.5, 13.6, 13.7, 13.8 and 13.9 reveal that changing the rail pad and fastener stiffness has significant influence on rail vibration. With the increase in the rail pad and fastener stiffness, more vibration energy is transferred to track foundation, which dramatically decreases the rail deflection and the rail vertical acceleration. The strong vibration of the rail, especially the rail vertical acceleration, is prone to damage the rail. Therefore, reasonably increasing the rail pad and fastener stiffness can help to decrease the rail dynamic response. But with the increase in the rail pad and fastener stiffness, the force directly exerted on the track slab will be more centralized, which leads to the increase in the track slab acceleration. Consequently, the track slab vibration acceleration will affect the stress of the CA mortar. As illustrated by Fig. 13.9d, the track slab vertical acceleration increases

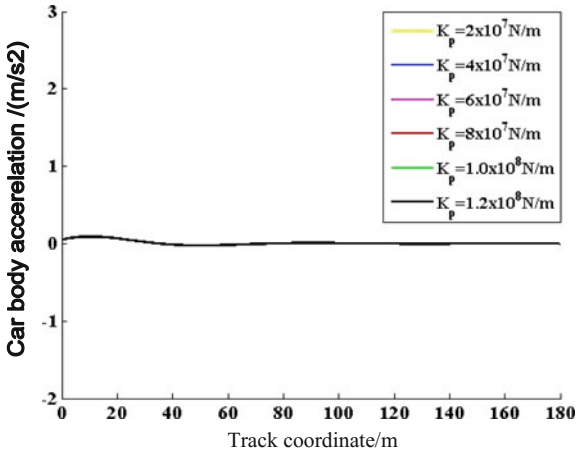

Fig. 13.5 Influence of different rail pad and fastener stiffness on the car body acceleration

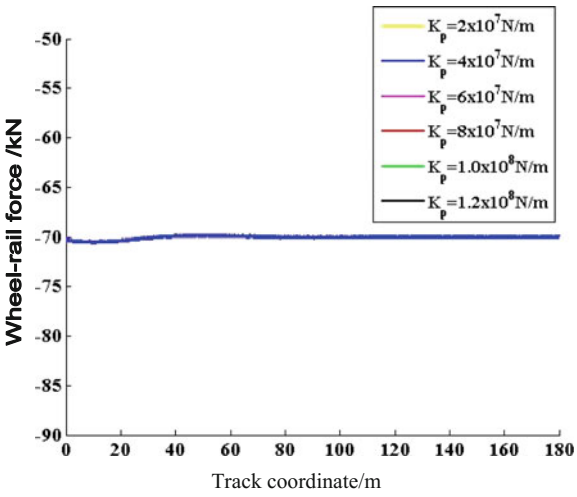

Fig. 13.6 Influence of different rail pad and fastener stiffness on the wheel-rail contact force

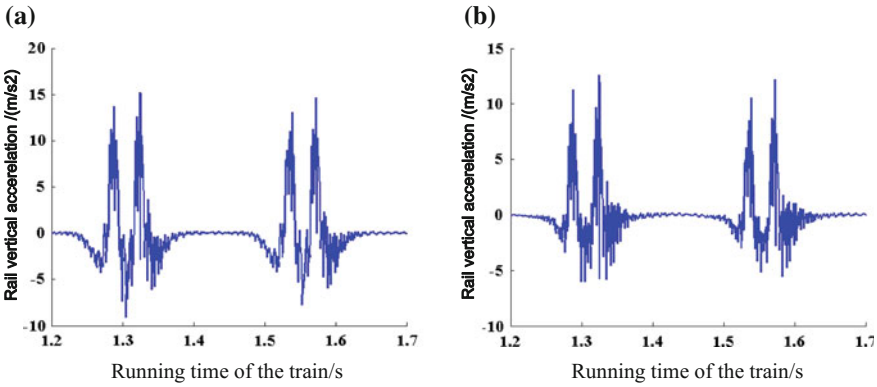

Fig. 13.7 Influence of different rail pad and fastener stiffness on the rail vertical acceleration. **a** $K_p = 2 \times 10^7$ N/m. **b** $K_p = 1.2 \times 10^8$ N/m

with the increase in the rail pad and fastener stiffness. Hence, from the mere perspective of depressing the CA mortar stress, the raid pad and fastener stiffness should be appropriately reduced.

The above analysis proves that changing the rail pad and fastener stiffness has a reverse effect on the rail and the track slab. In track structure designing, the response of the rail and the track slab should be controlled in a reasonable value range and thus to keep the comprehensive dynamic performance of the track

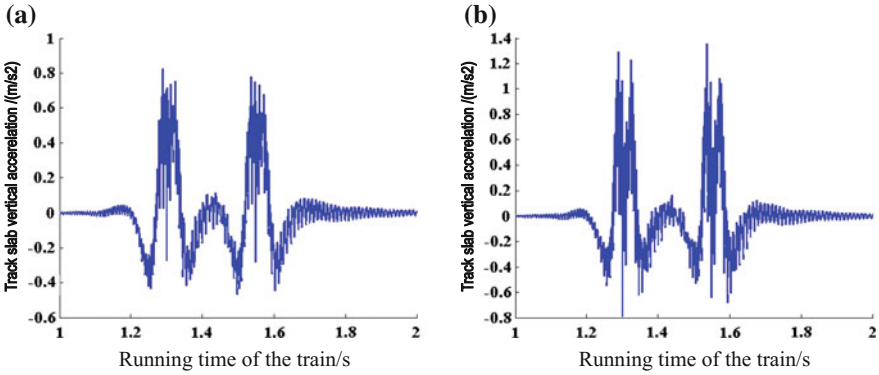

Fig. 13.8 Influence of different rail pad and fastener stiffness on the track slab vertical acceleration. **a** $K_p = 2 \times 10^7$ N/m. **b** $K_p = 1.2 \times 10^8$ N/m

structure in its best condition. Analysis shows the reasonable range of the rail pad and fastener stiffness is 60–80 kN/mm. In addition, Figs. 13.5, 13.6, 13.7, 13.8 and 13.9 also reveal that nearly no changes occur to the deflections of the track slab and the concrete support layer. And the influence on the wheel-rail contact force and the vertical acceleration of the car body are insignificant.

13.4 Influence of the Rail Pad and Fastener Damping

A reasonable choice of the rail pad and fastener damping is very important for the improvement of track dynamic performance. Six cases of the rail pad and fastener damping coefficients are considered to investigate its influence on the dynamic performance of the vehicle and the track structure: 3.63×10^4 N s/m, 4.77×10^4 N s/m, 1.0×10^5 N s/m, 3.0×10^5 N s/m, 6.0×10^5 N s/m, and 10×10^5 N s/m. The calculated results are illustrated by Figs. 13.10, 13.11, 13.12, 13.13 and 13.14 [6].

As shown in Figs. 13.10, 13.11, 13.12, 13.13 and 13.14, the rail deflection and the rail vertical acceleration decrease with the increase in the rail pad and fastener damping, while the vertical accelerations of the track slab and the concrete support layer increase dramatically with the increase in the rail pad and fastener damping; the rail pad and fastener damping have some influence on the wheel-rail contact force, but little influence on the car body acceleration; its influence on the deflections of the track slab and the concrete support layer can be ignored. When the rail pad and fastener damping is larger than 1×10^5 N s/m, the vibration response for each component of the track structure will change dramatically. In general, the

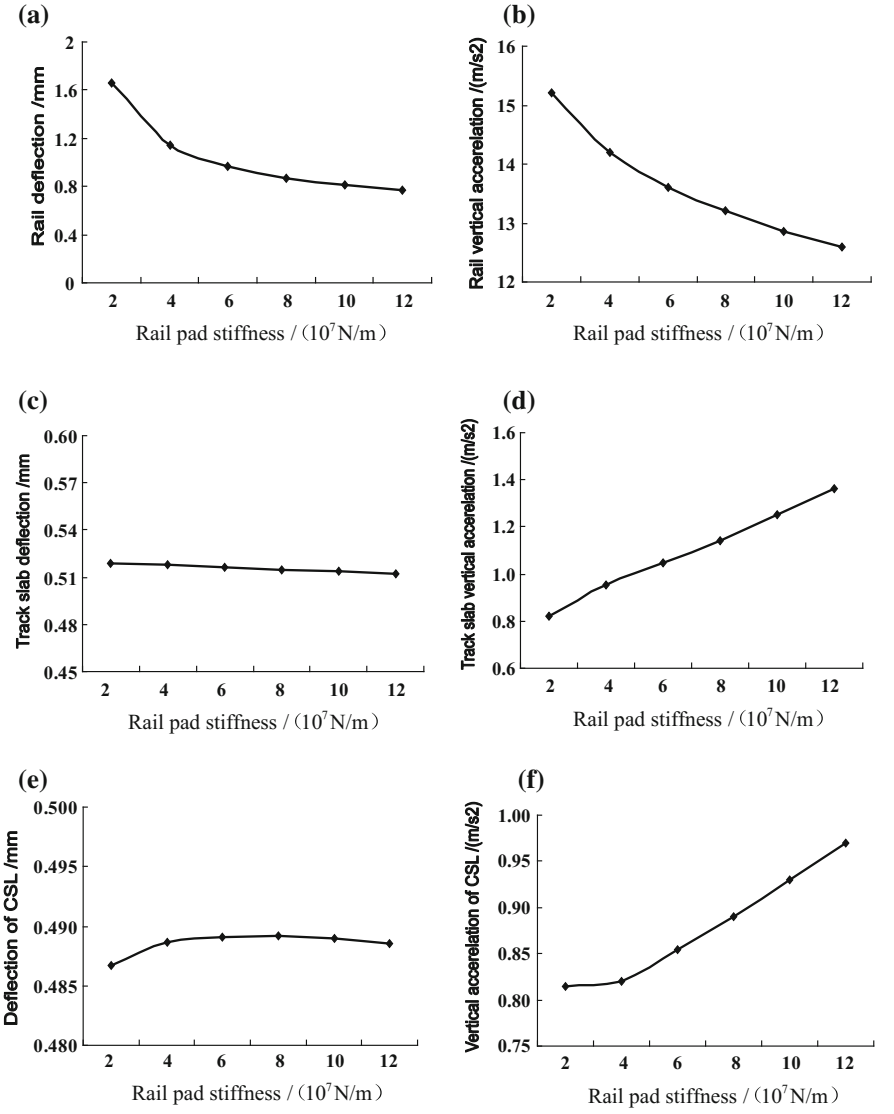

Fig. 13.9 Influence of the rail pad and fastener stiffness on different dynamic evaluation indexes. **a** Rail deflection. **b** Rail vertical acceleration. **c** Track slab deflection. **d** Track slab vertical acceleration. **e** Deflection of the concrete support layer (CSL). **f** Acceleration of the concrete support layer (CSL)

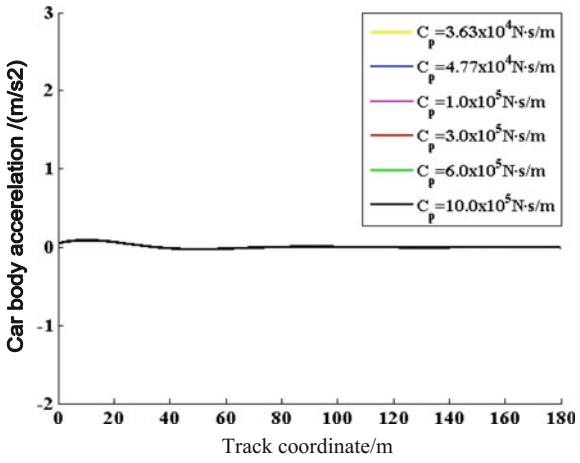

Fig. 13.10 Influence of the rail pad and fastener damping on the car body acceleration

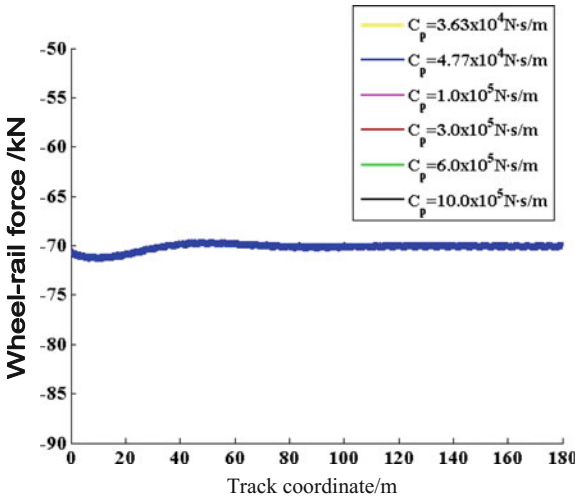

Fig. 13.11 Influence of the rail pad and fastener damping on the wheel-rail contact force

reasonable value for the rail pad and fastener damping should be controlled around 1×10^5 N s/m. To summarize, increasing the rail pad and fastener damping can reduce rail vibration, but will increase dynamic response of the track slab and the concrete support layer at the same time. Therefore, the rail pad and fastener damping coefficient should be reasonably chosen on the basis that the vibration responses from each component of the track structure are comprehensively considered, so as to extend the service life of the slab tracks.

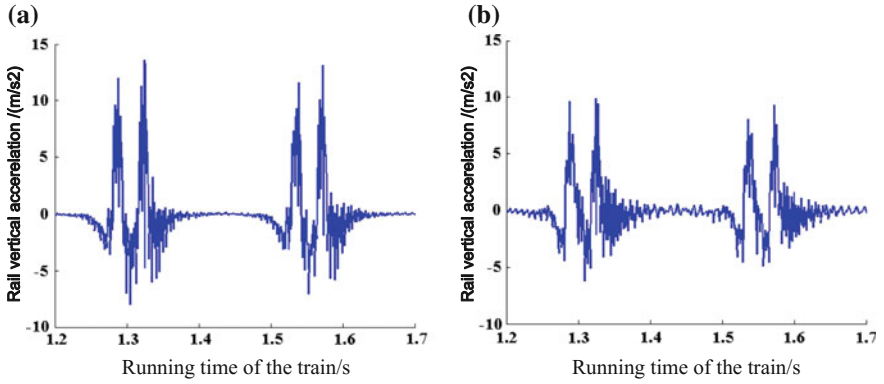

Fig. 13.12 Influence of different rail pad and fastener damping on the rail vertical acceleration. **a** $C_p = 3.63 \times 10^4$ N s/m. **b** $C_p = 10 \times 10^5$ N s/m

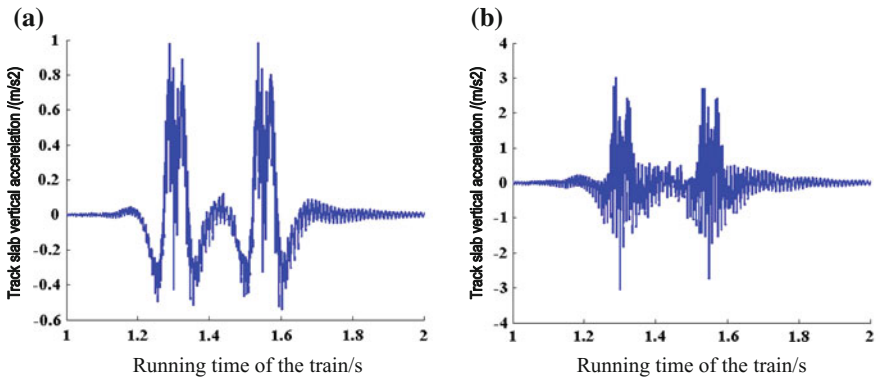

Fig. 13.13 Influence of different rail pad and fastener damping on the track slab vertical acceleration. **a** $C_p = 3.63 \times 10^4$ N s/m. **b** $C_p = 10 \times 10^5$ N s/m

13.5 Influence of the CA Mortar Stiffness

With other parameters unchanged, six cases of the CA mortar stiffness are considered to investigate its influence on the dynamic performance of the vehicle and the track structure: 3×10^8 N/m, 6×10^8 N/m, 9×10^8 N/m, 1.2×10^9 N/m, 1.5×10^9 N/m and 3.0×10^9 N/m. The calculated results are shown in Figs. 13.5, 13.6, 13.7, 13.8 and 13.9 [6].

As shown in Figs. 13.15, 13.16, 13.17, 13.18 and 13.19, changing the CA mortar stiffness has obvious influence on the rail deflection and the track slab deflection, but little influence on the deflection of the concrete support layer. The curves of the rail deflection and the track slab deflection reveal that the maximum rail deflection and the maximum track slab deflection decrease with the increase in

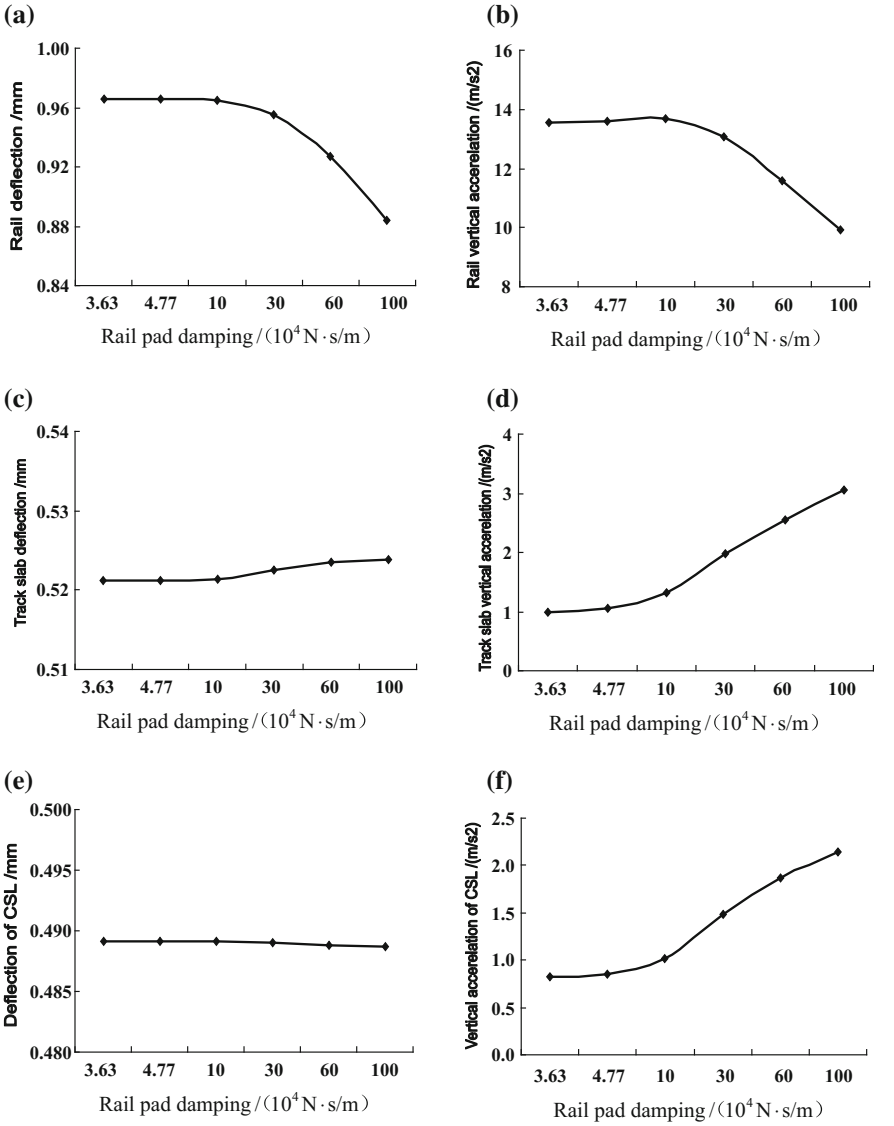

Fig. 13.14 Influence of the rail pad and fastener damping on different dynamic evaluation indexes. **a** Rail deflection. **b** Rail vertical acceleration. **c** Track slab deflection. **d** Track slab vertical acceleration. **e** Deflection of the concrete support layer (CSL). **f** Acceleration of the concrete support layer (CSL)

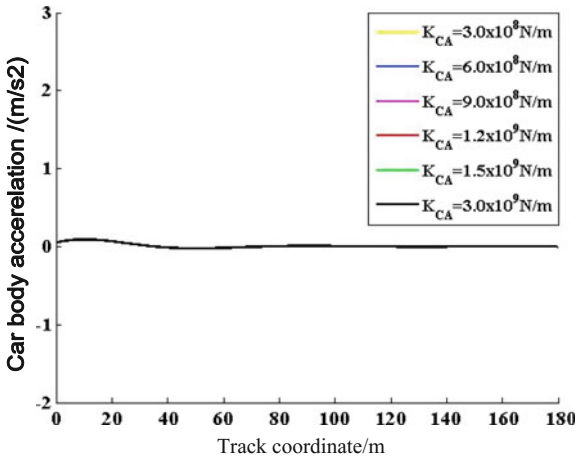

Fig. 13.15 Influence of the CA mortar stiffness on the car body acceleration

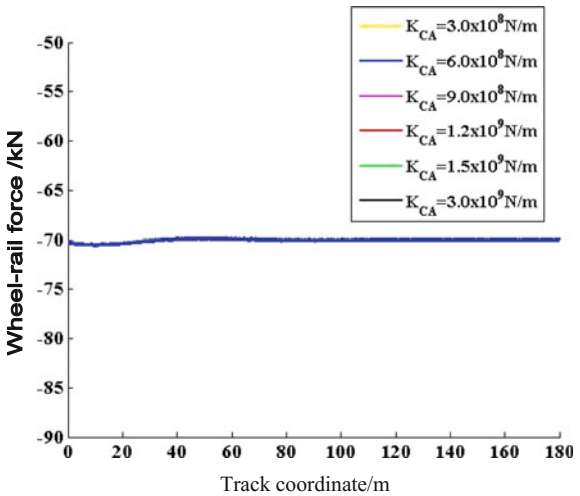

Fig. 13.16 Influence of the CA mortar stiffness on the wheel-rail contact force

the CA mortar stiffness. The CA mortar stiffness has little influence on the rail vertical acceleration, and practically no influence on the car body acceleration and the wheel-rail contact force. While the vertical accelerations of the track slab and the concrete support layer decrease with the increase in the CA mortar stiffness. Therefore, it can be safely concluded that increasing the CA mortar stiffness can reduce track deformation to a certain extent, but excessive CA mortar stiffness can weaken the slab track elasticity, which is not favorable to vibration reduction of the track structure. In short, the influence of the CA mortar stiffness on the train and the track structure is not as strong as that of the rail pad and fastener stiffness.

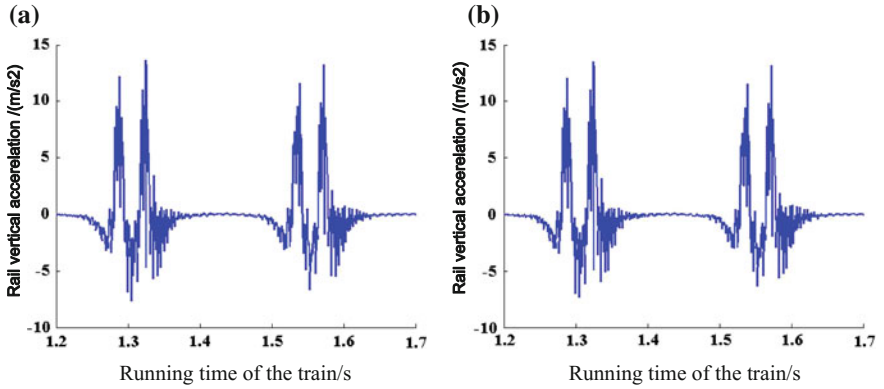

Fig. 13.17 Influence of different CA mortar stiffness on the rail vertical acceleration. **a** $K_{CA} = 3.0 \times 10^8$ N/m. **b** $K_{CA} = 3.0 \times 10^9$ N/m

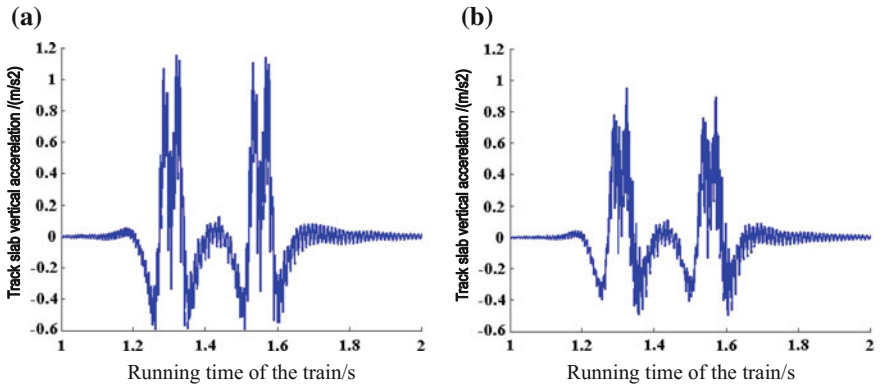

Fig. 13.18 Influence of different CA mortar stiffness on the track slab vertical acceleration. **a** $K_{CA} = 3.0 \times 10^8$ N/m. **b** $K_{CA} = 3.0 \times 10^9$ N/m

13.6 Influence of the CA Mortar Damping

With other parameters unchanged, five cases of the CA mortar damping coefficients are considered to investigate its influence on the dynamic performance of the vehicle and the track structure: 2×10^4 N s/m, 4×10^4 N s/m, 8.3×10^4 N s/m, 1.6×10^5 N s/m and 3.2×10^5 N s/m. The calculated results are illustrated by Figs. 13.20, 13.21, 13.22, 13.23 and 13.24 [6].

As shown in Figs. 13.20, 13.21, 13.22, 13.23 and 13.24, with the increase in the CA mortar damping, nearly no changes occur to the rail deflection, the rail vertical acceleration, the track slab deflection and the deflection of the concrete support

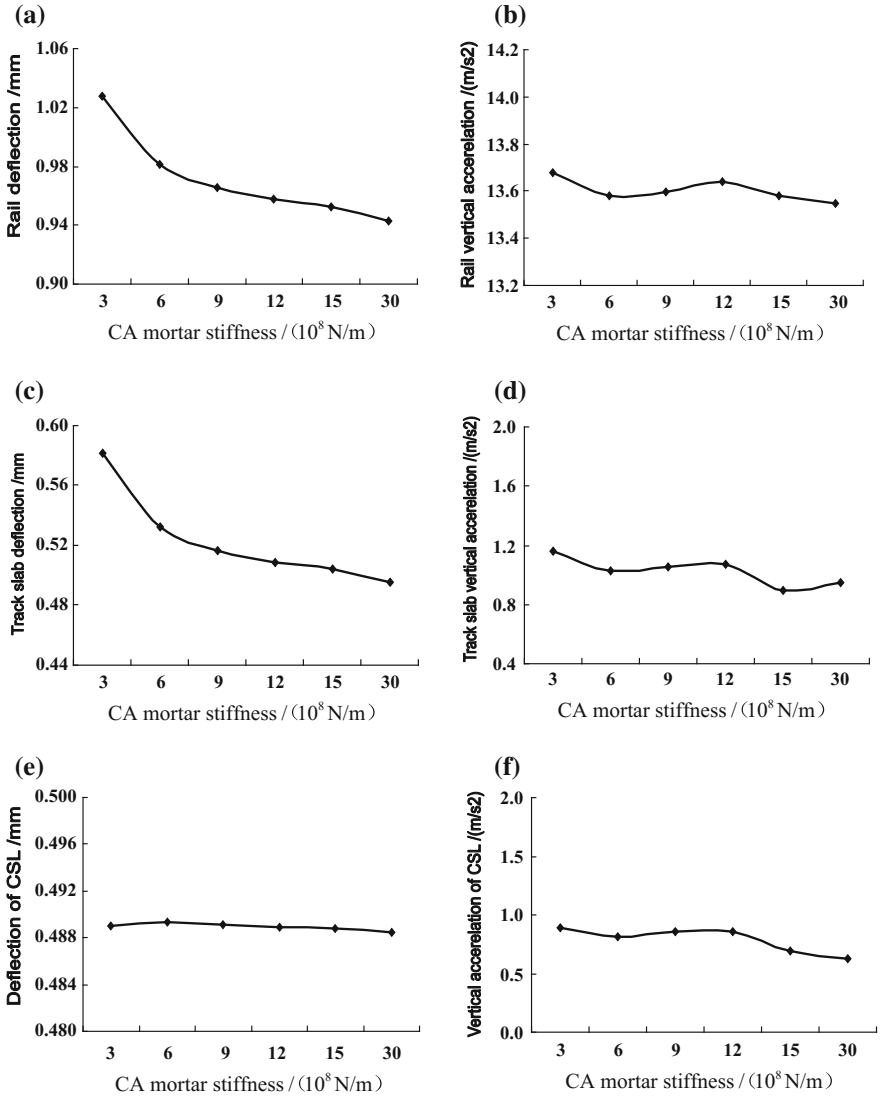

Fig. 13.19 Influence of the CA mortar stiffness on different dynamic evaluation indexes. **a** Rail deflection. **b** Rail vertical acceleration. **c** Track slab deflection. **d** Track slab vertical acceleration. **e** Deflection of the concrete support layer (CSL). **f** Acceleration of the concrete support layer (CSL)

layer, whereas the vertical accelerations of the track slab and the concrete support layer decrease greatly. The influence of the CA mortar damping on the wheel-rail contact force and the vertical acceleration of the car body is not obvious, almost with no changes. From the above analysis, it can be concluded that the CA mortar

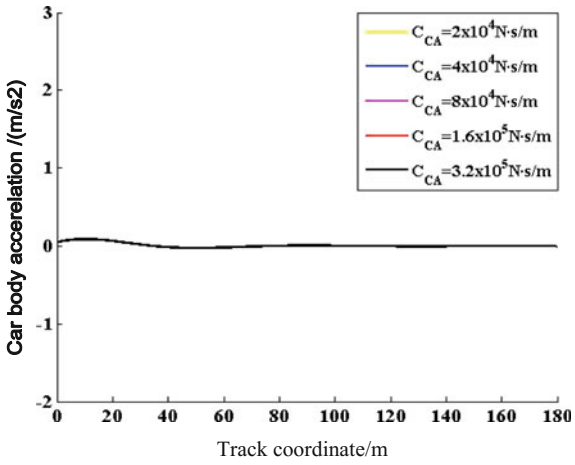

Fig. 13.20 Influence of the CA mortar damping on the car body acceleration

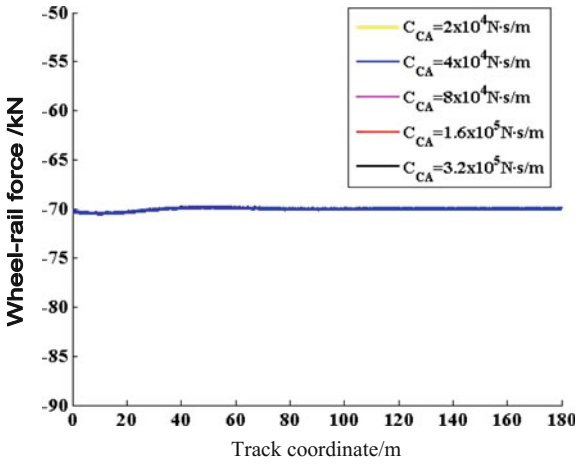

Fig. 13.21 Influence of the CA mortar damping on the wheel-rail contact force

with greater damping should be applied, so as to effectively reduce the vibration of the track structure, extend the service life of the slab track, and lighten the workload of the track structure maintenance.

13.7 Influence of the Subgrade Stiffness

With other parameters unchanged, six cases of the subgrade stiffness are considered to investigate its influence on the dynamic performance of the vehicle and the track structure: 2×10^7 N/m, 4×10^7 N/m, 6×10^7 N/m, 8×10^7 N/m, 1.0×10^8 N/m,

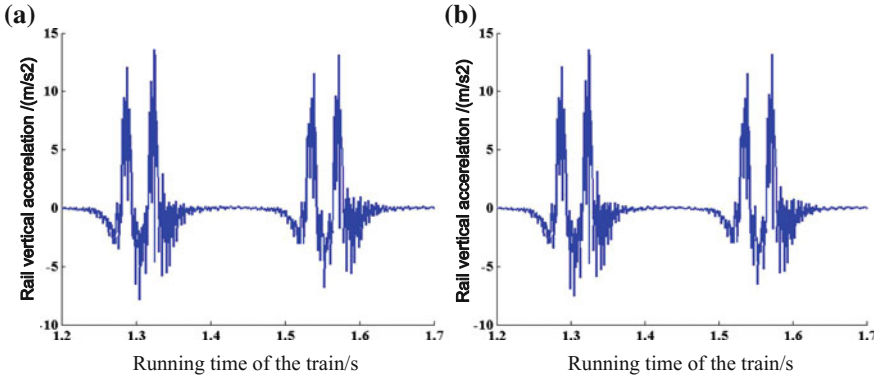

Fig. 13.22 Influence of different CA mortar damping on the rail vertical acceleration. **a** $C_{CA} = 2 \times 10^4$ N s/m. **b** $C_{CA} = 3.2 \times 10^5$ N s/m

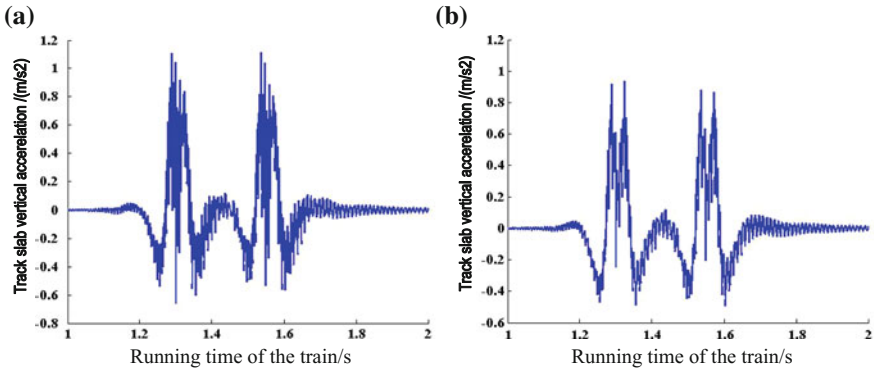

Fig. 13.23 Influence of different CA mortar damping on the track slab vertical acceleration. **a** $C_{CA} = 2 \times 10^4$ N s/m. **b** $C_{CA} = 3.2 \times 10^5$ N s/m

and 1.2×10^8 N/m. The calculated results are shown in Figs. 13.25, 13.26, 13.27, 13.28 and 13.29 [6].

As shown in Figs. 13.25, 13.26, 13.27, 13.28 and 13.29, changing the subgrade stiffness has significant influence on the vibration of the whole track structure. When the subgrade stiffness increases, the dynamic indexes of each component of the track structure are on the decrease. By comparison, the decreased margins of the deflection for the rail, the track slab, and the concrete support layer are larger than their corresponding accelerations. It indicates that the influence of the subgrade stiffness on the track structure deflection is much more effective than that on the

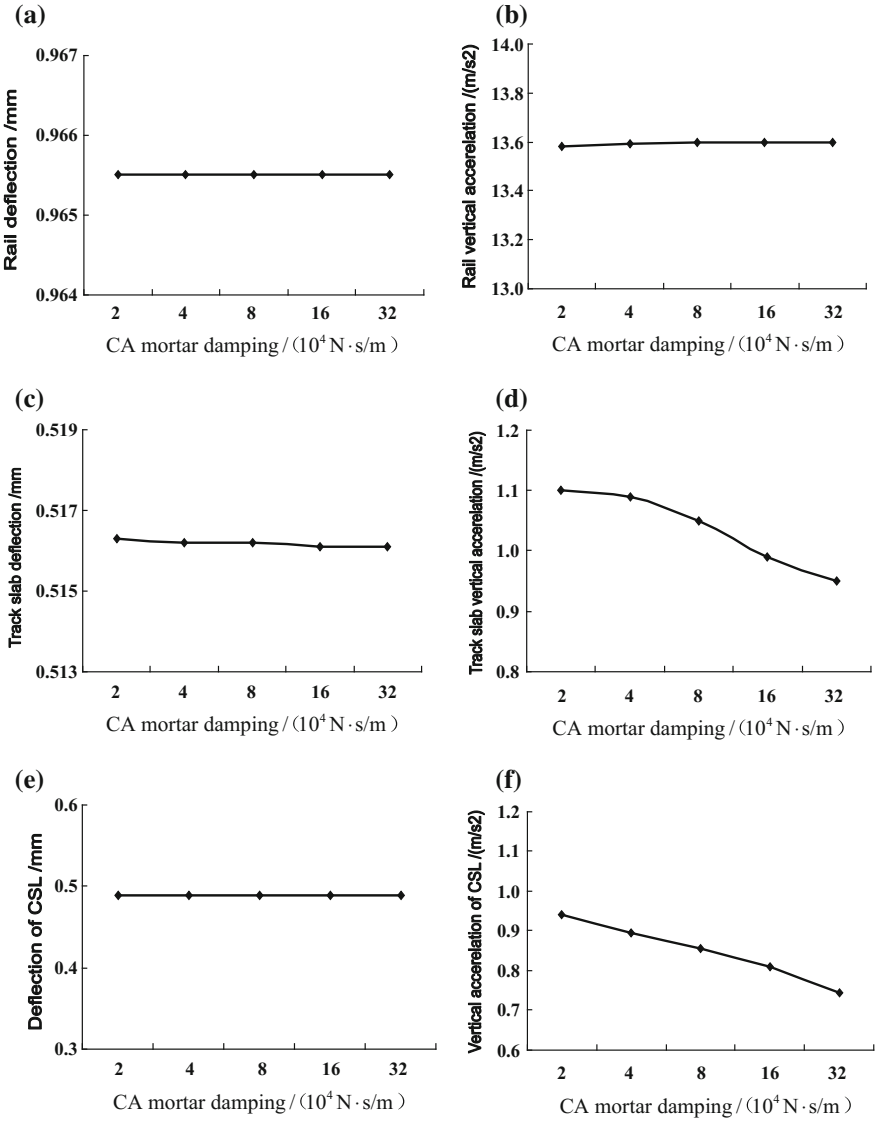

Fig. 13.24 Influence of the CA mortar damping on different dynamic evaluation indexes. **a** Rail deflection. **b** Rail vertical acceleration. **c** Track slab deflection. **d** Track slab vertical acceleration. **e** Deflection of the concrete support layer (CSL). **f** Acceleration of the concrete support layer (CSL)

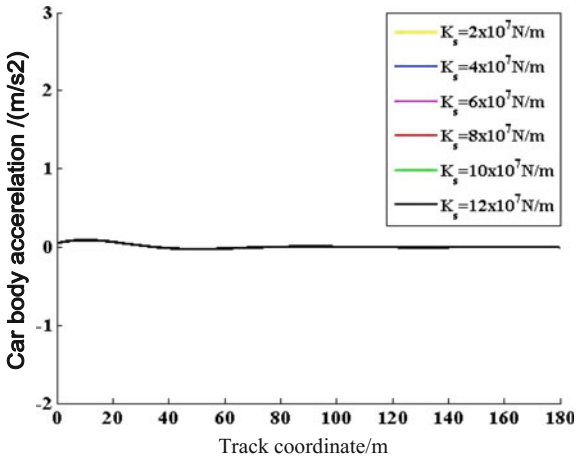

Fig. 13.25 Influence of the subgrade stiffness on the car body acceleration

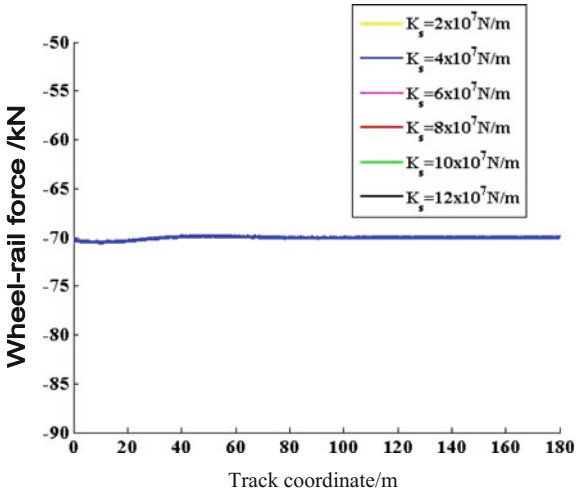

Fig. 13.26 Influence of the subgrade stiffness on the wheel-rail contact force

vertical acceleration. Besides, a small subgrade stiffness coefficient may induce huge dynamic response of the track structure. When the train speed keeps rising to reach or exceed the critical velocity of the track, it will induce strong vibration of the track structure. The subgrade stiffness coefficient is the major factor which can influence the critical velocity of the track, and the critical velocity increases with the increase in the subgrade stiffness. Therefore, increasing the subgrade stiffness can contribute to track safety and track stability.

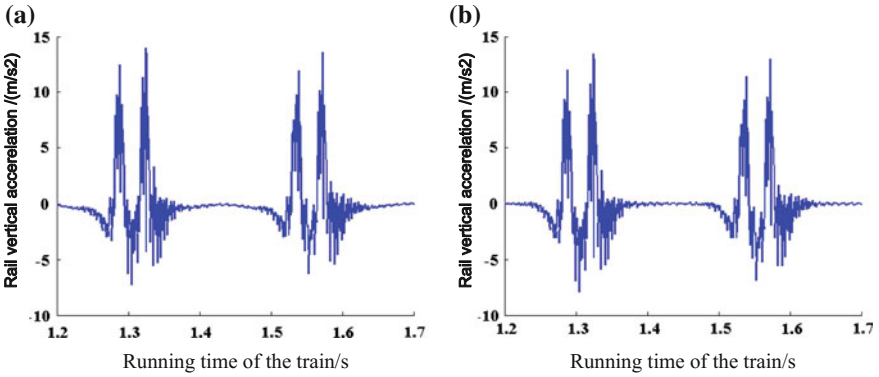

Fig. 13.27 Influence of different subgrade stiffnesses on the rail vertical acceleration. **a** $K_s = 2 \times 10^7$ N/m. **b** $K_s = 1.2 \times 10^8$ N/m

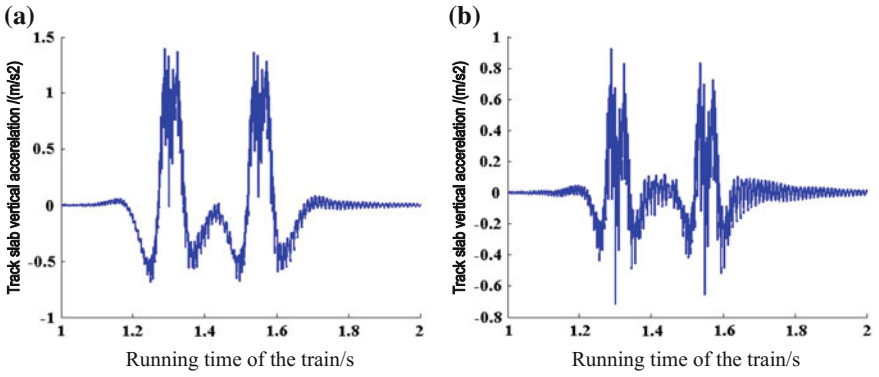

Fig. 13.28 Influence of different subgrade stiffness on the track slab vertical acceleration. **a** $K_s = 2 \times 10^7$ N/m. **b** $K_s = 1.2 \times 10^8$ N/m

13.8 Influence of the Subgrade Damping

With other parameters unchanged, six cases of the subgrade damping are considered to investigate its influence on the dynamic performance of the vehicle and the track structure: 3×10^4 N s/m, 6×10^4 N s/m, 9×10^4 N s/m, 1.2×10^5 N s/m,

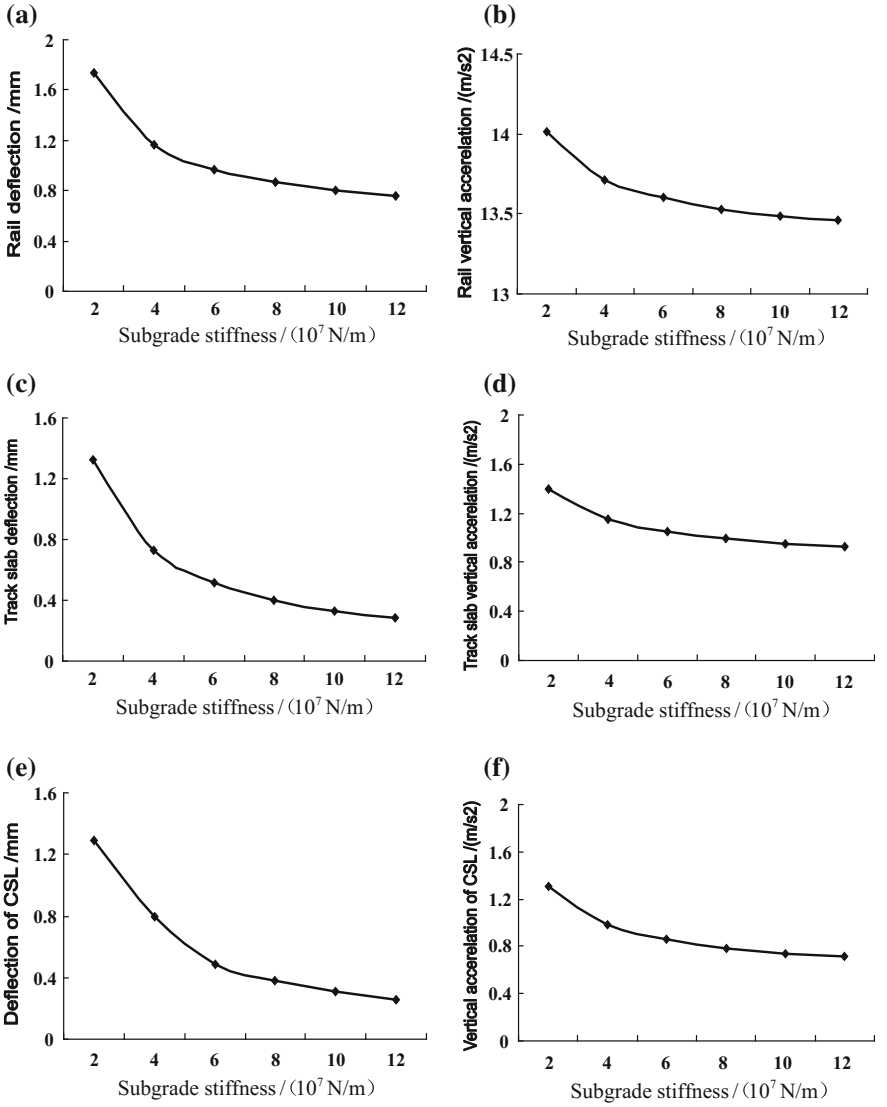

Fig. 13.29 Influence of the subgrade stiffness on different dynamic evaluation indexes. **a** Rail deflection. **b** Rail vertical acceleration. **c** Track slab deflection. **d** Track slab vertical acceleration. **e** Deflection of the concrete support layer (CSL). **f** Acceleration of the concrete support layer (CSL)

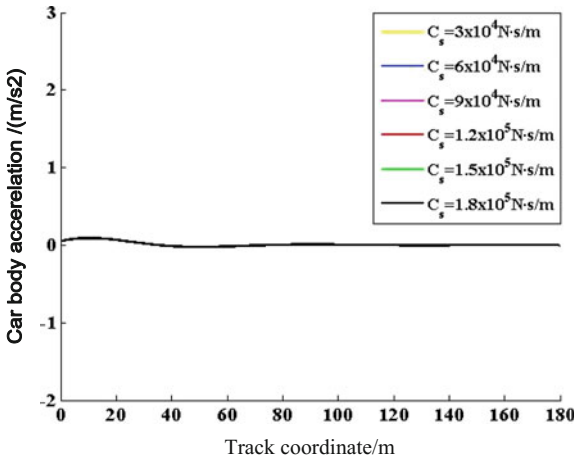

Fig. 13.30 Influence of the subgrade damping on the car body acceleration

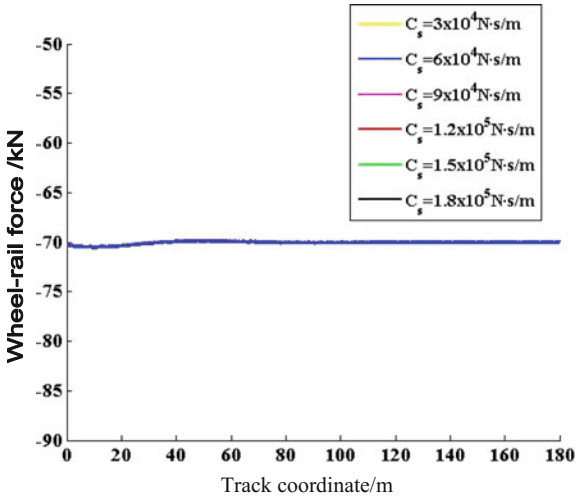

Fig. 13.31 Influence of the subgrade damping on the wheel-rail contact force

1.5×10^5 N s/m, and 1.8×10^5 N s/m. The calculated results are illustrated by Figs. 13.30, 13.31, 13.32, 13.33, and 13.34 [6].

As shown in Figs. 13.30, 13.31, 13.32, 13.33, and 13.34 that, with the increase in the subgrade damping coefficient, little changes occur to the rail deflection, the rail vertical acceleration, the track slab deflection, and the deflection of the concrete

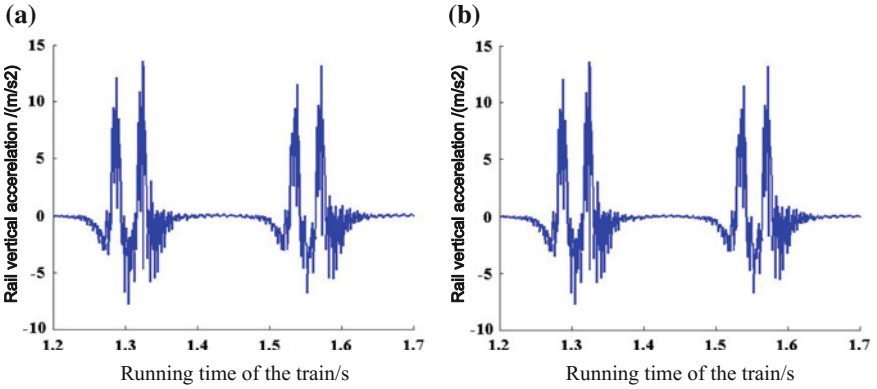

Fig. 13.32 Influence of different subgrade damping on the rail vertical acceleration. **a** $C_s = 3 \times 10^4$ N s/m. **b** $C_s = 1.8 \times 10^5$N s/m

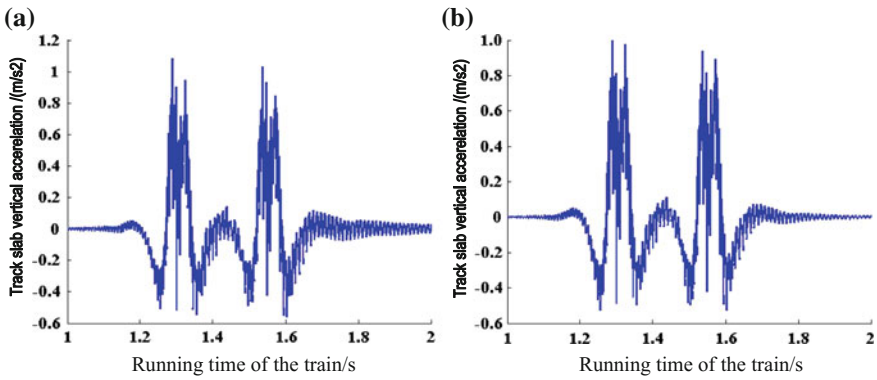

Fig. 13.33 Influence of different subgrade damping on the track slab vertical acceleration. **a** $C_s = 3 \times 10^4$ N s/m. **b** $C_s = 1.8 \times 10^5$ N s/m

support layer, but the vertical accelerations of the track slab and the concrete support layer are on the decrease. No changes occur to the wheel-rail contact force and the vertical acceleration of the car body. In short, the subgrade damping has little influence on the vibration of the track structure.

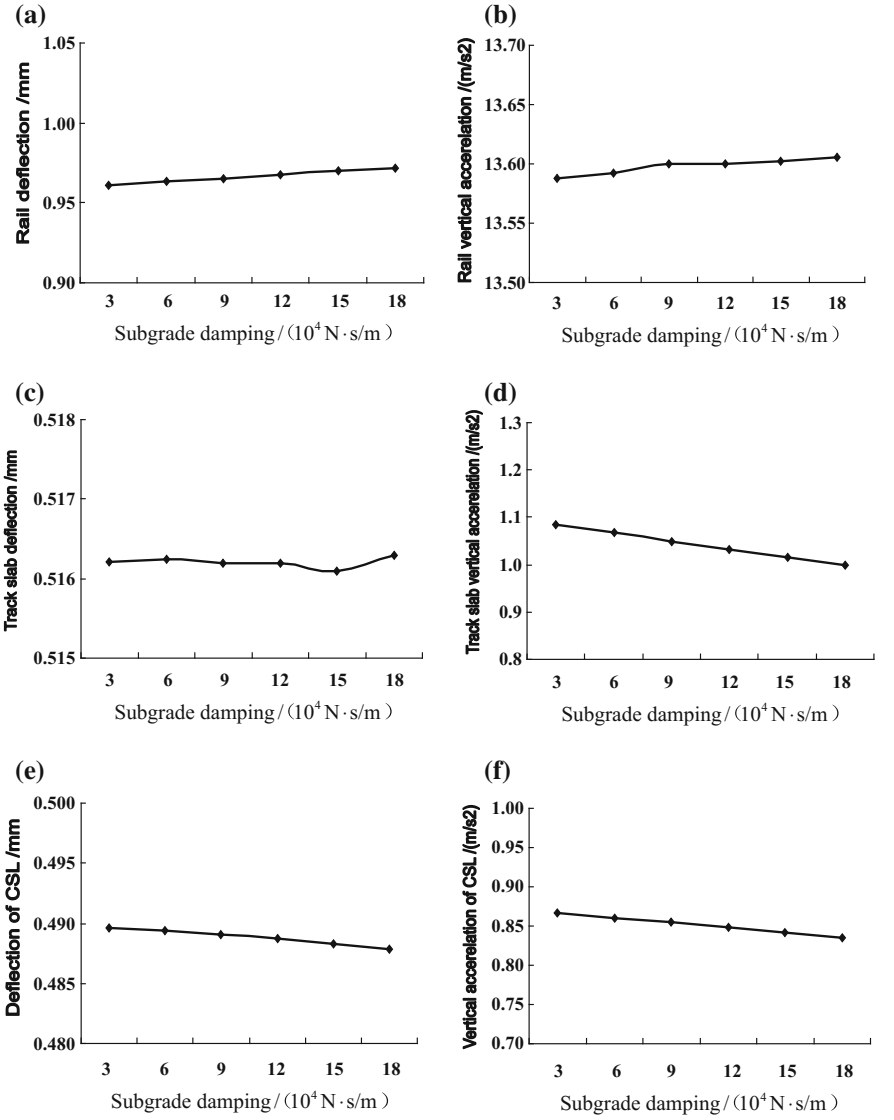

Fig. 13.34 Influence of the subgrade damping on different dynamic evaluation indexes. **a** Rail deflection. **b** Rail vertical acceleration. **c** Track slab deflection. **d** Track slab vertical acceleration. **e** Deflection of the concrete support layer (CSL). **f** Acceleration of the concrete support layer (CSL)

References

1. Lei XY, Zhang B (2011) Analyses of dynamic behavior of track transition with finite elements. J Vib Control 17(11):1733–1747
2. Lei XY, Zhang B (2011) Analysis of dynamic behavior for slab track of high-speed railway based on vehicle and track elements. J Transp Eng 137(4):227–240
3. Lei XY, Zhang B (2010) Influence of track stiffness distribution on vehicle and track interactions in track transition. J Rail Rapid Transit Proc Inst Mech Eng Part F 224(1):592–604
4. Lei X, Zhang B, Qingjie Liu (2010) Model of vehicle and track elements for vertical dynamic analysis of vehicle-track system. J Vib Shock 29(3):168–173
5. Zhang B, Lei X (2011) Analysis on dynamic behavior of ballastless track based on vehicle and track elements with finite element method. J China Railway Soc 33(7):78–85
6. Zhang B (2007) Finite element analysis on the dynamic characteristics of track structure for high-speed railway. Master's Thesis of East China Jiaotong University, Nanchang
7. He D, Xiang J, Zeng Q (2007) A new method for dynamics modeling of ballastless track. J Central South Univ (Sci Technol) 38(6):1206–1211
8. Chen X (2005) Track engineering. China Architecture and Building Press, Beijing

Chapter 14
Analysis of Dynamic Behavior of the Transition Section Between Ballast Track and Ballastless Track

There are a large number of bridges, grade crossings and rigid culverts involved in railway transportation, which result in plenty of track transitions. Track transition regions are the locations where a railway track exhibits abrupt changes in vertical stiffness. These usually occur at the ballast track compare to the ballastless track, at the abutments of open deck bridges, where a concrete sleeper track changes to a wooden sleeper track, and at the ends of tunnels, highway grade crossings and locations where rigid culverts are placed close to the bottom of the sleepers in a ballast track. The abrupt change in the vertical stiffness of the track causes the wheels to experience an equally abrupt change in elevation because of the uneven track deflection.

Tests reveal that when the train moves over the region of vertical stiffness with abrupt change, additional dynamic interaction will be increased obviously, and the subgrade deformation will be induced in track transition, which in turn will result in track irregularity. This problem will be more serious with the increase in the train speed. Surveys conducted abroad for track transition between the ballast track and the ballastless track indicate that under the long-term action of the vehicle loads, a series of problems come out and more or less lead to the damage of the track structure in track transition. These problems include the following:

(1) When the train moves at the speed of 200 km/h or higher, the influence of the track irregularity on the moving train will be amplified. Therefore, maintenance cost will be enormous to meet the requirement of track regularity and stability.
(2) The conventional design approach for transition region between the ballast track and the ballastless track is to set up reinforced concrete slabs with length of 10 m or 20 m. However, under the repeated actions of the vehicle loads, there will be some partial suspension of slabs which will result in the change of the ballastless track stress and seriously affect the track structure intensity and stability, as well as the dynamic interaction between the vehicle and the ballastless track.

X. Lei, *High Speed Railway Track Dynamics*,
DOI 10.1007/978-981-10-2039-1_14

(3) Irregularity of the ballast track can be removed by tamping or eliminating railway ballast, while irregularity of the ballastless track can only be reduced or eliminated by adjusting the rail pads. As there is a strict limit for adjusting the value of the rail pads, it is limited for the ballastless track. However, under the repeated action of the vehicle loads, the ballastless track deformation will exceed the adjustment allowance of the rail pads with the accumulation of the deformation in track transition.
(4) There is warping in the track slabs in the track transition. The pull force caused by the impact force, acting on the track slab, exceeds the tensile strength of concrete, which in turn leads to cracking of the track slab surface and corrosion of the internal reinforcement in slab, and finally results in the reduction of the slab strength.
(5) The residual track deformation in the track transition is obviously larger than that in other sections of the track. It is difficult to repair and recover the track when big deformation occurs in the ballastless track. And a new line should be laid in a serious situation.

The reason for the above problems is that the overall stiffness of the ballastless track is far larger than that of the ballast track. To reduce the additional dynamic force due to the stiffness difference in the track transition, smooth transition of the track stiffness between the ballast track and the ballastless track is required.

Many researches on dynamic characteristics of the vehicle and the track structure conducted at home and abroad mainly focus on experiment [1–10], with few theoretical and numerical analysis [5–10]. This chapter, based on major structure patterns and design parameters of the transition track between the ballast track and the ballastless track, together with the vehicle model and the track model and their algorithm suggested in Chap. 9 while taking into account of the influence of the train speed and the track stiffness, offers parameter analyses, by using the software developed from dynamic characteristic of the transition section between the ballast track and the ballastless track [11, 12]. Hopefully, such an analysis provides a theoretical guidance for designing and choosing of the track stiffness in the track transition.

14.1 Influence Analysis of the Train Speed for the Transition Section Between the Ballast Track and the Ballastless Track

In the following parameter analyses, the vehicle concerned is Chinese high-speed train CRH3, as shown in Fig. 12.1, and the parameters of the high-speed train CRH3 are given in Table 6.7 of Chap. 6. The ballast track is 60 kg/m continuous

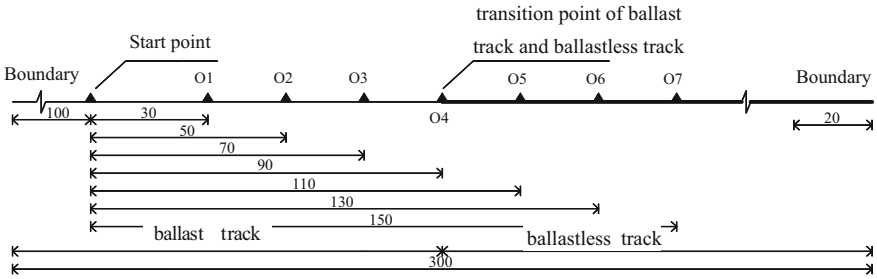

Fig. 14.1 Computational model for the influence of the train speed/m

welded rail with type III sleepers, and the parameters of the ballast track structure are shown in Table 12.1. The ballastless track involved is German Bögle slab track with the parameters given in Table 6.10 of Chap. 6.

The time step of numerical integration for the Newmark scheme adopts $\Delta t = 0.001$ s.

The computational model for the dynamic responses of the vehicle and the track structure in the transition section between the ballast track and the ballastless track is shown in Fig. 14.1. In the simulation, the total track length for computation is 300 m, which includes 100 and 20 m extra track lengths on left and right track ends to eliminate the boundary effect. To begin with, consider the effect of the train speed without transition section, that is, the ballast track and the ballastless track connects directly at position 190 m of the line. The track structure model is discretized into 502 track elements with 1516 nodes.

To eliminate the effect of model boundary, seven observation points along the track, denoted with O1, O2, …, O7, are chosen at the distances of 30, 50, 70, 90, 110, 130 and 150 m from the starting point to analyze the dynamic responses of the vehicle and the track structure. Among the seven output points, three are located on the conventional ballast track, three on the ballastless track and one is exactly at the joint of the ballast track and the ballastless track. Four kinds of the train speeds (V = 160, 200, 250 and 300 km/h) are specified to investigate the distribution of the dynamic responses of the vehicle and the track structure, as shown in Fig. 14.1.

To comprehensively analyze and assess the influence of the train speed, parts of the results including the time history curves obtained for the rail vertical acceleration, the vertical acceleration of car body and the wheel-rail contact force are shown in Figs. 14.2, 14.3 and 14.4 [13].

As can be observed from Fig. 14.2, 14.3 and 14.4, the overall structural stiffness of the ballastless track is several times as that of the ballast track and there is significant difference in terms of vertical stiffness along the longitudinal track direction. Such a stiffness difference results in the larger wheel-rail contact force, which increases with the increase in the train speed. In some cases, the tensile stress

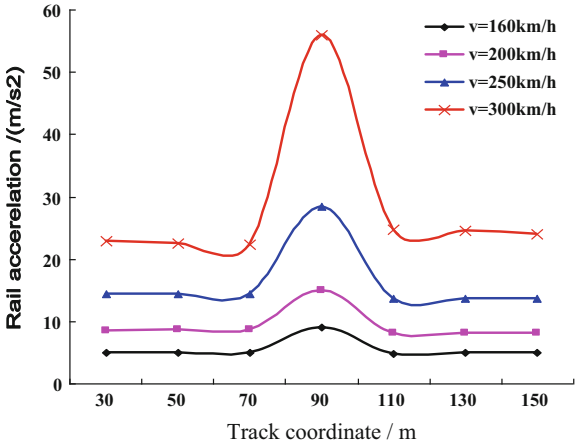

Fig. 14.2 Influence of train speeds on rail vertical acceleration

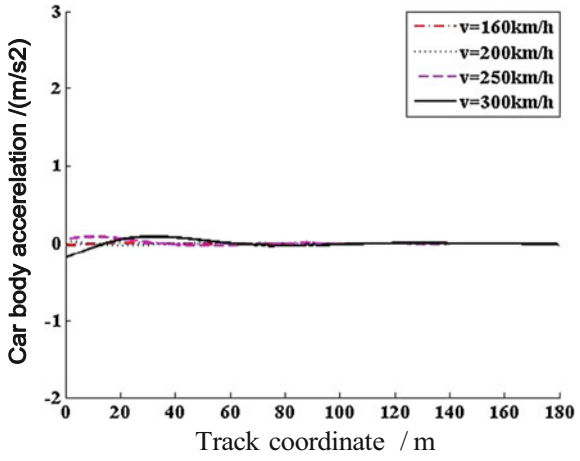

Fig. 14.3 Influence of train speeds on vertical acceleration of car body

induced by the larger wheel-rail contact force may exceed the tensile strength of reinforced concrete in track slab, which ultimately results in the crack and warp of the slab. At the track transition joint, the rail vertical acceleration and the wheel-rail contact force reach the maximum, especially when the train speed reaches 200 km/h or higher, and the two peaks doubled to have a great impact on track structure. But the train speed has essentially no influence on the vertical acceleration of car body because of the excellent vibration isolation resulting from the primary and secondary suspension systems of the vehicle.

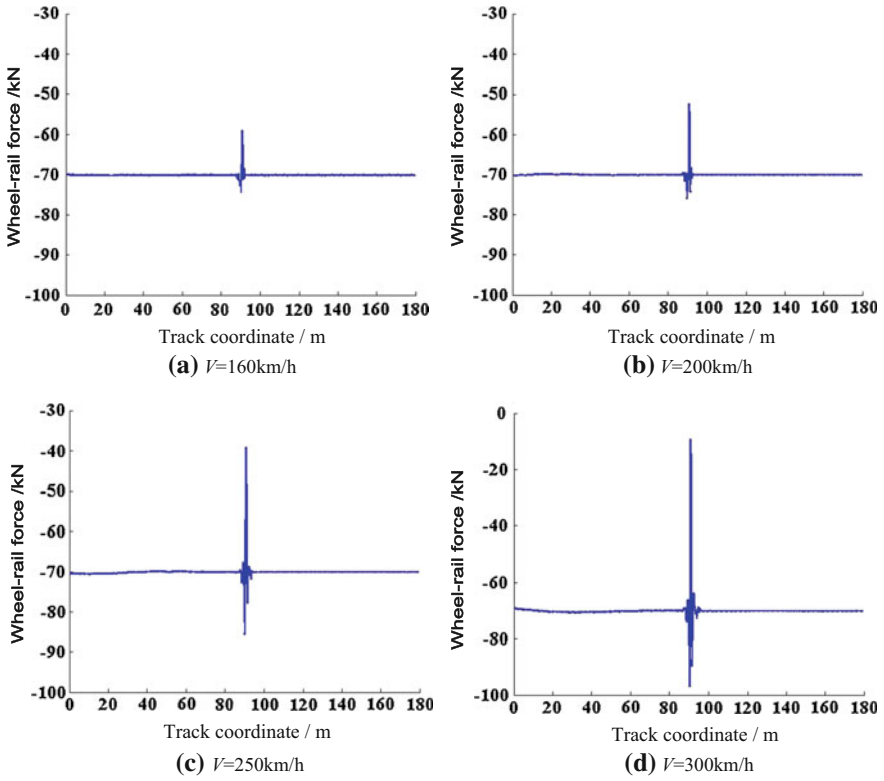

Fig. 14.4 Influence of train speeds on wheel-rail contact force

14.2 Influence Analysis of the Track Foundation Stiffness for the Transition Section between the Ballast Track and the Ballastless Track

Usually, the transition section is constructed inside the ballast track in passenger lines, and a 20-m-long transition track is laid between the ballast track and the ballastless track. The total track length for the computation is 300 m, which includes 100 and 20 m extra track lengths on left and right track ends to eliminate the boundary effect. The length of the transition section is 20 m, and the ballast track and the ballastless track connect at the distance of 190 m of the line as shown in Fig. 14.5. Suppose the train speed is V = 250 km/h the track structure model is discretized into 526 track elements with 1591 nodes.

In engineering practice, track transition is usually installed by constructing subgrade transition section in the ballast track side. In the following, four kinds of transition patterns are considered in the influence analysis of the track foundation stiffness:

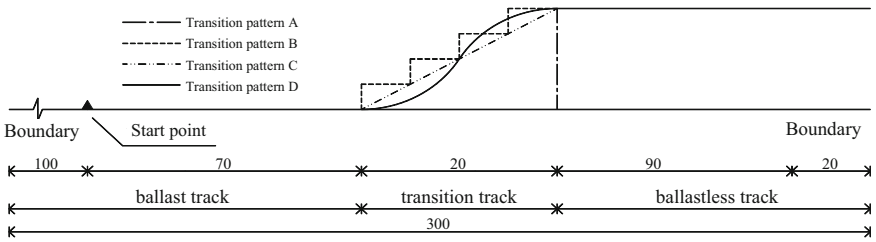

Fig. 14.5 Computational model for the influence of the track foundation stiffness/m

Pattern A The transition pattern is abrupt change, namely there is no transition section between the ballast track and the ballastless track

Pattern B Step-by-step change. The stiffness of the ballast changes 1–2—3—4—5 times in a ladder; the stiffness of the subgrade changes 1—5—10—20—40 times accordingly

Pattern C Linear change. The stiffness of the ballast changes linearly from 1 to 5 times; the stiffness of the subgrade also changes linearly from 1 to 40 times

Pattern D Cosine change. The stiffness of the ballast changes in a cosine curve adopting 1–5 cosine interpolation; accordingly the stiffness of the subgrade also changes from 1–5 times in a cosine interpolation

The output results including the time history of the vertical acceleration of car body, the rail vertical acceleration and the wheel-rail contact force, as shown in Figs. 14.6, 14.7 and 14.8, respectively [11].

As can be observed from Fig. 14.6, the vertical acceleration of car body corresponding to the four kinds of the track stiffness transition patterns is completely overlapped, which means changing track stiffness has little influence on the car body acceleration. Influence of the track stiffness distribution on the car body

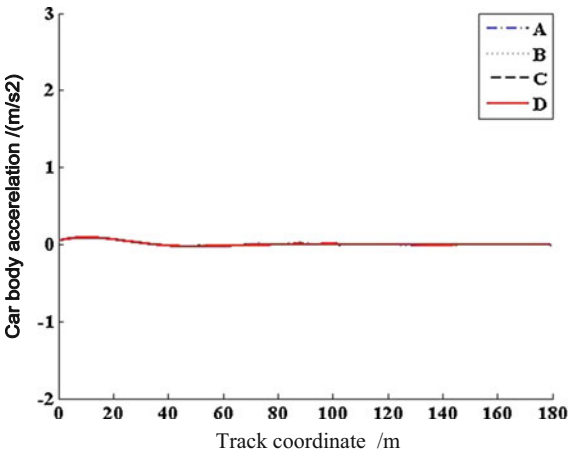

Fig. 14.6 Influence of transition patterns on vertical acceleration of car body

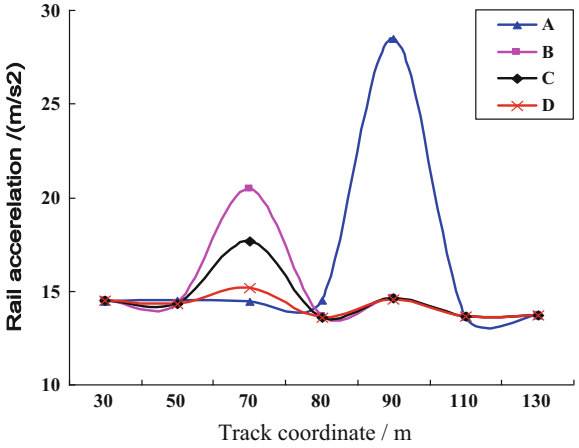

Fig. 14.7 Influence of transition patterns on rail vertical acceleration

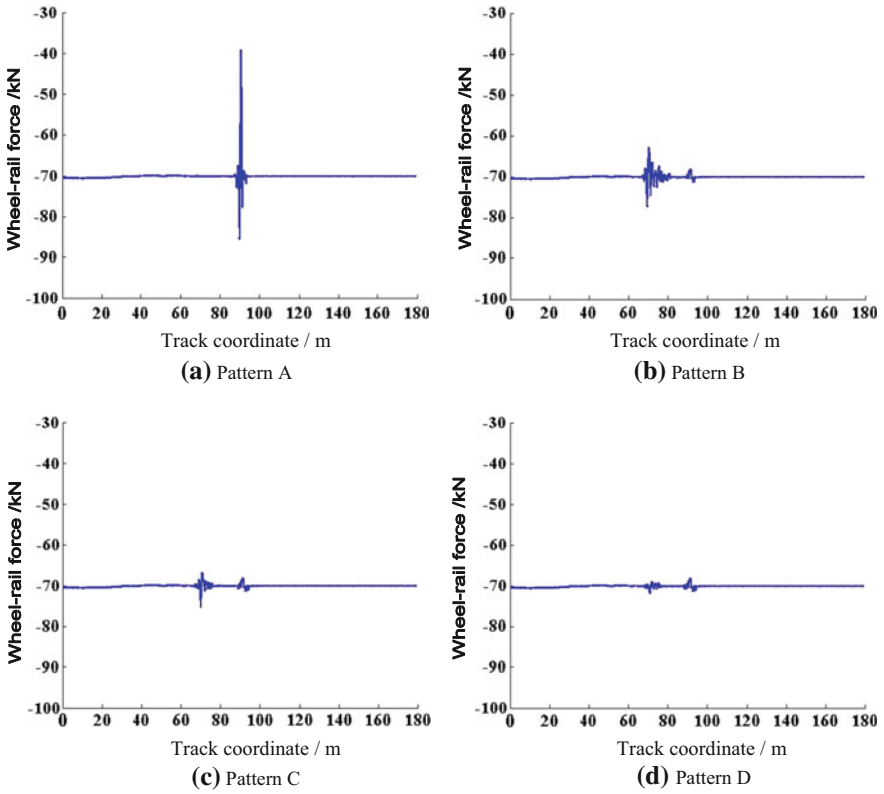

Fig. 14.8 Influence of transition patterns on wheel-rail contact force

acceleration is not effective, due to the excellent vibration isolation resulting from the primary and secondary suspension systems of the vehicle.

Secondly, as shown in Fig. 14.7, in the ballast track side, when track stiffness changes, namely at the position of 70 m away from the starting point, the rail vertical acceleration changes dramatically. As the track stiffness transition patterns change, the rail vertical acceleration increases significantly, among which influence of the cosine pattern is the least. In the transition section between the ballast track and the ballastless track, namely at the position of 90 m away from the starting point, the rail vertical acceleration has a peak again. For transition patterns B, C and D, all with transition section, the rail vertical accelerations are far smaller than that for transition pattern A without transition section. This indicates that constructing the transition section between the ballast track and the ballastless track can greatly reduce the track structure vibration.

As shown in Fig. 14.8, for transition patterns B, C and D with transition section, the wheel-rail contact force peaks twice. The first peaks at the position of 70 m are induced by the ballast track stiffness change, and the minimum wheel-rail contact force is corresponding to the cosine transition pattern, while the peaks at the position of 90 m are induced by track stiffness difference between the ballast track and the ballastless track. For transition pattern A without transition section, the maximum wheel-rail contact force is dozens of times of that for transition patterns B, C and D, all of which with transition sections. The powerful wheel-rail contact force results in great damage on track structure, which again indicates the importance of constructing the transition section between the ballast track and the ballastless track.

As shown by the wheel-rail contact force peaks in 70 and 90 m, setting up the ballast and subgrade stiffness transition can effectively solve the problem of track stiffness uneven between the ballast track and the ballastless track. But when the train enters into the transition section of the ballast track, its impact exceeds the impact of the connection section between the ballast track and the ballastless track, and hence the second peak comes along. In this case, extending the length of the transition section can reduce the wheel-rail contact force on the ballast track and avoid the secondary impact on the train and the track structure, thus to ensure passengers comfortableness and high-speed operation.

14.3 Remediation Measures of the Transition Section between the Ballast Track and the Ballastless Track

Many experimental researches concerning track transition have been conducted in China. Based on relevant testing data and drew on the experience of other countries, regulations such as *Interim Provisions on Ballastless Track Design for Passenger-dedicated Railway*, *Interim Provisions on Design for Beijing–shanghai High-speed*

Railway, *Provisional Design Regulations for the new 200–250 km/h Passenger-dedicated Railway* and *Provisional Design Regulations for the new 300–350 km/h Passenger-dedicated Railway* set guidelines for constructing the transition section [14, 15].

Track transition is generally constructed in the ballast track side. Major construction measures include setting up transition section with stiffness change to increase the vertical stiffness of the track, for instance, filling the subgrade with quality stuffing, adopting higher subgrade compaction standard, using graded broken stone with cement, setting up trapezium reinforced concrete slabs on the surface layer of subgrade, solidifying ballast layer, achieving gradual change in the thickness of ballast bed, adjusting stiffness of the rubber pads under the rail and setting up auxiliary rail to increase vertical bending stiffness of the rail. In addition, the overall stiffness of ballastless track should be reduced by using rail pads with low-stiffness or setting up elastic cushion layer under the slab, and pasting microcellular rubber cushion layer to the bottom of track slab. Some of the technical measures applied in the engineering construction are given as follows:

Measure 1 As specified in China's industry standard for railway construction [2007]47 *Provisional Design Regulations for the new 300–350 km/h Passenger-dedicated Railway,* the transition section should be constructed in connection section between the bridge abutment and the ballast track with subgrade. Usually, the transition section with longitudinal inverted trapezoidal graded broken stone, as shown in Fig. 14.9, can be adopted along the line. The following equation should be satisfied:

$$L = a + (H - h)\, n \tag{14.1}$$

where L denotes the length of transition section, generally not less than 20 m;H for height of graded broken stone with cement; h for the thickness of surface layer of subgrade; a for constant coefficient,taking 3–5 m; and n for constant coefficient, taking 2–5 m.

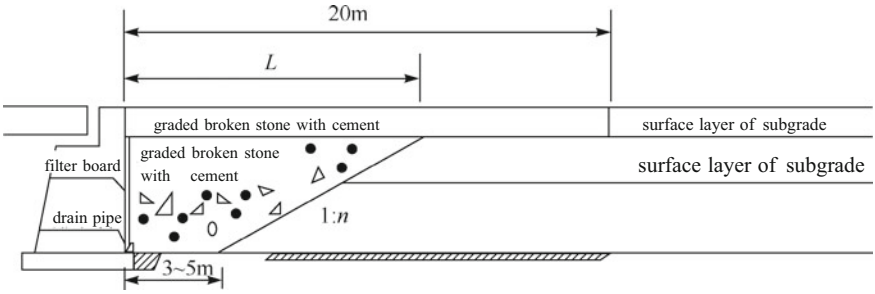

Fig. 14.9 Transition section with longitudinal inverted trapezoidal graded broken stone along the line

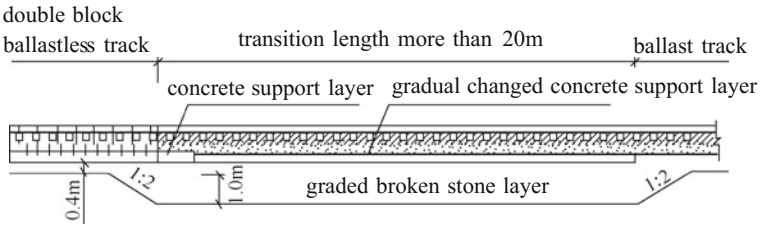

Fig. 14.10 Transition section between the ballast track and the ballastless track

Measure 2 In the construction of passenger lines, the conventional measure is to improve the ballast track stiffness. The typical practice is to lay concrete support layer with varied thickness and graded broken stones with different proportion of cement at different positions. A minimum of 20-m-long transition section should be constructed between the ballast track and the ballastless track. Graded broken stone (with 3–5 % cement) is laid at the bottom of subgrade. Figure 14.10 is longitudinal profile for the transition section between the ballast track and the ballastless track.

Measure 3 Ballastless track slabs are laid in Fengshupai tunnel of the Ganzhou-Longyan railway. In the transition section between the ballast track and the ballastless track, five vibration reduction slabs are used at the connection region in the ballast track side to reduce the stiffness difference between the ballast track and the ballastless track and to improve the stability of the train's operation.

Measure 4 In ballastless track testing section of Suining-Chongqing Railway, measures for reducing the ballastless track stiffness while increasing the ballast track stiffness are adopted simultaneously. The length of the transition section between the ballast track and the ballastless track is 25 m, whereas it is 20 m for ballast track. In the ballast track transition, ballast thickness is gradually changed from 250 to 350 mm. Measures for reducing the ballastless track stiffness include pasting microcellular rubber cushion layer to the bottom of the five track slabs, laying five railway sleepers of 2.8 m long close to slab track section, adopting lower rail pad and fastener stiffness as 35–55 kN/mm and using 50 kg/m guard rail as auxiliary rail of transition section.

Measure 5 Figure 14.11 shows the longitudinal profile of the transition section between the ballast track and German Bögle slab track on subgrade. It shows in Figure that hydraulically bearing layer of the slab track is extended into the ballast track with the length of 10 m, and within the range of the first 15 m of the ballast track, the ballast bed is completely bonded with epobond epoxy, while within the range of the second 15 m the ballast bed is partly bonded, as for the third 15 m the ballast shoulder is partly bonded.

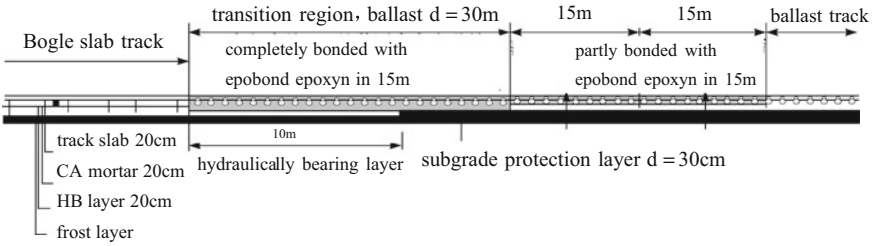

Fig. 14.11 Transition section between the ballast track and German Bögle slab track on subgrade

Measure 6 To ensure smooth operation of high-speed trains from the ballast track on subgrade to the slab track on bridge, it is necessary to reduce the stiffness difference and the differential settlements between the ballast track and the slab track so as to ensure track regularity. To construct the transition section between the ballast track on subgrade and the slab track on bridge, some technical measures can be taken:

(1) Refill the foundation ditches of abutment with concrete and construct subgrade close to abutment with quality graded broken stones with higher strength and lower deformation. The compact density and the void ratio of embankment subgrade surface layer have to meet the requirements, $K_{30} \geq 190$ MPa, $\eta < 15$ %, while for the compact density and the void ratio beneath the subgrade bed, $K_{30} \geq 150$ MPa, $\eta < 20$ %.
(2) Elastic rubber buffer cushion is attached to the bottom of the track slab on the bridge near to the ballast track on subgrade.
(3) Two auxiliary rails are employed in the ballast track of transition section.

Measure 7 To avoid stiffness abrupt change between the ballast track and the ballastless track, hydraulically bearing layer of the slab track is extended into the ballast track with the length of 10 m. At the end of the ballastless track, the concrete supporting board and the hydraulically bearing layer have to be anchored together to ensure satisfactory connection stiffness between the two. In engineering practice, to smooth different track stiffness, the ballast bed in the track transition is completely bonded with epobond epoxy. The bonding strength of the ballast bed decreases gradually from the ballastless track to the ballast track. Transition section is constructed in the ballast track side with a total length of 45 m, which is divided into three parts with equal length, namely the complete bonded part among the ballast bed, boundary beam and sleepers; the partial bonded part between the ballast bed and boundary beam; and the partial bonded part in the ballast bed.

References

1. Kerr AD, Moroney BE (1995) Track transition problems and remedies. Bull 742 Am Railw Eng Assoc (742):267–297
2. Kerr AD (1987) A method for determining the track modulus using a locomotive or car on multi-axle trucks. Proc Am Railw Eng Assoc 84(2):270–286
3. Kerr AD (1989) On the vertical modulus in the standard railway track analyses. Railw Int 235 (2):37–45
4. Moroney BE (1991) A study of railroad track transition points and problems. Master's thesis of University of Delaware, Newark
5. Xiaoyan Lei, Lijun Mao (2004) Dynamic response analyses of vehicle and track coupled system on track transition of conventional high speed railway. J Sound Vib 271(3):1133–1146
6. Xiaoyan Lei (2006) Effects of abrupt changes in track foundation stiffness on track vibration under moving loads. J Vib Eng 19(2):195–199
7. Qichang Wang (1999) High-speed railway engineering. Southwest Jiaotong University Press, Chengdu
8. Xiaoyan Lei (2006) Influences of track transition on track vibration due to the abrupt change of track rigidity. China Railw Sci 27(5):42–45
9. Linya Liu, Xiaoyan Lei (2004) Designing and dynamic performance evaluation of roadbed-bridge transition on existing railways. Railw Stand Des 1:9–10
10. Xiaoyan Lei, Bin Zhang, Qingjie Liu (2009) Finite element analysis on the dynamic characteristics of the track transition. China Railw Sci 30(5):15–21
11. Lei Xiaoyan, Zhang Bin (2011) Analyses of dynamic behavior of track transition with finite elements. J Vib Control 17(11):1733–1747
12. Lei Xiaoyan, Zhang Bin (2011) Analysis of dynamic behavior for slab track of high-speed railway based on vehicle and track elements. J Transp Eng 137(4):227–240
13. Zhang B (2007) Finite element analysis on the dynamic characteristics of track structure for high-speed railway. Master's thesis of East China Jiaotong University, Nanchang
14. Provisional Design Regulations for the new 200–250 km/h Passenger-dedicated Railway (2005) Railway Consruction [2005]140. China Railway Publishing House, Beijing
15. Provisional Design Regulations for the new 300–350 km/h Passenger-dedicated Railway (2005) Railway Consruction [2007]47. China Railway Publishing House, Beijing

Chapter 15
Environmental Vibration Analysis Induced by Overlapping Subways

China is in the golden period of constructing urban mass transit. In urban subway network planning and layout, the overlapping of two or even more subway lines are inevitable. Environmental vibration induced by the overlapping of two or more subway lines does not equal the sum of each one and differs greatly from that induced by a single line. Since the transport organization and the train's operation in overlapping subways differ greatly and are quite complicated, their influence on the environmental vibration can be amplified or exceeds the environmental vibration standard. Currently there are a small number of researches addressing this problem in China, such as researches done by Jia [1], Ma [2], and Xu [3]. But compared with the rapid development of urban mass transit and its construction speed, relevant research is far from enough, especially those concerning environmental vibration induced by trains moving simultaneously in the 4 holes or more holes of subways are fewer.

Nanchang subway 1 and subway 2 converge at Bayi Square, forming an overlapping subway. Nearby the square locates the key provincial cultural relic protection units, namely the Exhibition Hall of Mao Zedong, also known as the Exhibition Center of Jiangxi Province. Taking the complicated 4-hole overlapping subways as engineering background, a 3D finite element model of the track-tunnel-ground-building coupling system is established, and simulation analyses of vibration response of the ground and the building and their propagation characteristics induced by trains moving in overlapping subways are carried out in this chapter. Moreover, vibration influences on the ground and the building, induced by separate operation of subway 1 and subway 2, and simultaneous operation of the two subways, are compared.

X. Lei, *High Speed Railway Track Dynamics*,
DOI 10.1007/978-981-10-2039-1_15

15.1 Vibration Analysis of the Ground Induced by Overlapping Subways

15.1.1 Project Profile

Nanchang subway 1 and subway 2 converge under the Bayi Avenue, the west of Bayi Square which locates in the old city center. Bayi Square station is situated at the intersection of the two subways. Up to now, tunnel excavation construction of subway 1 and design of subway 2 are under way. Both subways are of double tunnel sections with paralleled uplink and downlink. They are 15 m away from each other, forming a right-angle intersection with subway 1 beneath subway 2. Tunnel buried depth of subway 1 is 17 m, while that of subway 2 is 9 m. Subways are constructed by shield tunneling method with round tunnel structure section. Tunnel lining thickness measures 0.3 m, internal and external diameters are 5.4 and 6 m, respectively. The overlapping subways divide the ground around Bayi Square into 4 blocks as shown in the plan sketch of Fig. 15.1.

Due to the centrosymmetry of the four blocks, it is feasible to select any one of the four to make environmental vibration analysis. The following is environmental vibration analysis based on the third block (quadrant), i.e., the section from the Bayi museum station to Bayi Square station of subway 1 and Bayi Square station to Yongshu Road station of subway 2.

15.1.2 Material Parameters

As environmental vibration induced by subways falls into the category of microvibration, it is advisable to take related materials as linear elastic media in

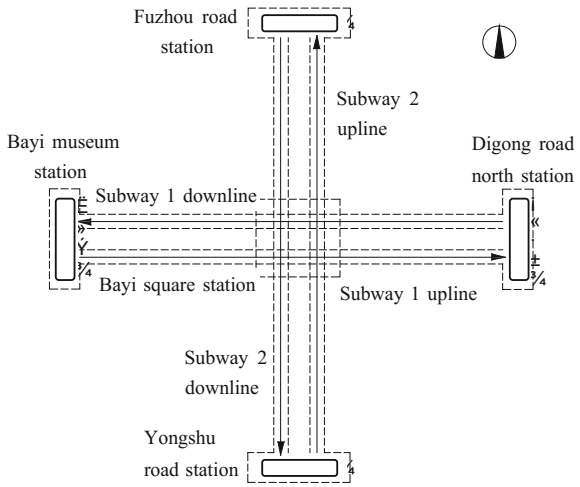

Fig. 15.1 Plan sketch of overlapping subways

Table 15.1 Bayi Square underground soil parameters

Soil property	Thickness/(m)	Density/(kg/m^3)	Shear wave velocity/(m/s)	Modulus of elasticity/(MPa)	Poisson's ratio	Soil type
Miscellaneous fill	1.5	1850	150.7	115.96	0.38	Soft soil
Silty clay	3.0	1950	189.9	194.09	0.38	Soft soil
Fine sand	6.0	1950	174.2	159.77	0.35	Soft soil
Gravel sand and gravel	10.0	1990	285.5	428.22	0.32	Hard soil
Medium-weathered pelitic siltstone	15.5	2300	813.2	3802.44	0.25	Rock
Microweathered pelitic siltstone	–	2500	1098.8	7364.90	0.22	Rock

Table 15.2 Parameters of track structure and tunnel

Structure	Material	Density/(kg/m^3)	Modulus of elasticity/(MPa)	Poisson's ratio
Tunnel foundation	C35 concrete	2500	31500	0.2
Tunnel lining	C35 concrete	2500	31500	0.2
Rail	U75V Ordinary hot rolled rail	7800	210000	0.3
Floating slab	C50 concrete	3000	32500	0.2

dynamic analysis. Referring to engineering geological exploration report [4–6], the corresponding soil layers are weighted evenly by using the weighted average method. The underground soil layers of Bayi Square are simplified to six layers, and the corresponding material parameters in each soil layer are shown in Table 15.1. Parameters of the track structure and the tunnel in finite element computation are given in Table 15.2.

In addition, while the stiffness and damping coefficients of the ordinary rail pad and fastener are 50 kN/mm and 75kN s/m, respectively, the sleeper interval is 0.625 m; while the stiffness and damping coefficients of the steel spring floating slab are 6.9 kN/mm and 100 kN s/m, respectively, the interval between the steel spring bearings is 1.25 m and the thickness and the breadth of floating slab are 0.35 and 3.2 m.

15.1.3 Finite Element Model

A 3D dynamic analysis model of track-tunnel-ground coupling system is established by using large-scale finite element software ANSYS. Generally, vibration influence induced by subway is within the range of 60 m on both sides of the vibration source. In order to make sure the finite element model is of moderate size to achieve computational accuracy, it is suitable to take the distance between model boundary and vibration source as 70 m. Considering a certain amount of surplus, the size of the model is 115 m longitudinally and transversely, and 60 m vertically. The distance between the downlink of subway 1 and the model boundary and that between the uplink of subway 2 and the model boundary are 25 m, while the distance between the uplink of subway 1 and the model boundary and that between the downlink of subway 2 and the model boundary are 75 m. The interval between the downlink and the uplink for both subways is 15 m. 3D equivalent viscoelastic boundary is adopted in the model boundary, which can be implemented by extending a layer of equivalent elements along the normal direction of the boundary elements [7]. The outer boundary constraints of the layer of equivalent elements are fixed. The influence of boundary reflection waves can be eliminated by defining the material properties of the equivalent elements. The finite element model is shown in Fig. 15.2 [8].

As specified by designing data, the track with the integrated ballast bed is used in general region of Nanchang subways, and the track with the shock absorber is adopted in normal vibration reduction area, while the track with the steel spring floating slab is employed in special vibration reduction region. In the following analysis, the track model with the integrated ballast bed and that with the steel spring floating slab are established, respectively, as shown in Fig. 15.3, which are used to compare the influence of different track structures in subway 1 and 2 on environmental vibration [8].

Elements in 3D finite element model include the spatial beam element BEAM 188 used to simulate the rail, the spring, and damping element COMBIN 14 to the rail pad and fasteners and the steel spring bearing of the floating slab, the shell

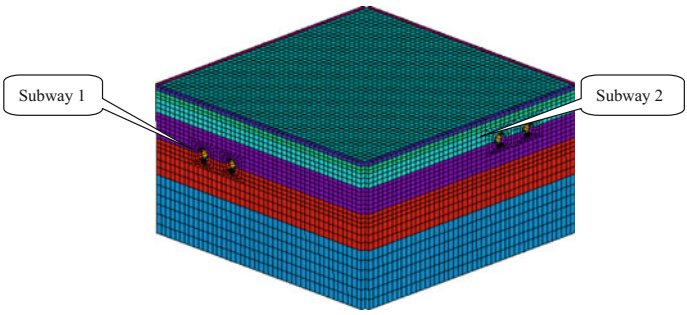

Fig. 15.2 3D finite element model for the track-tunnel-ground system

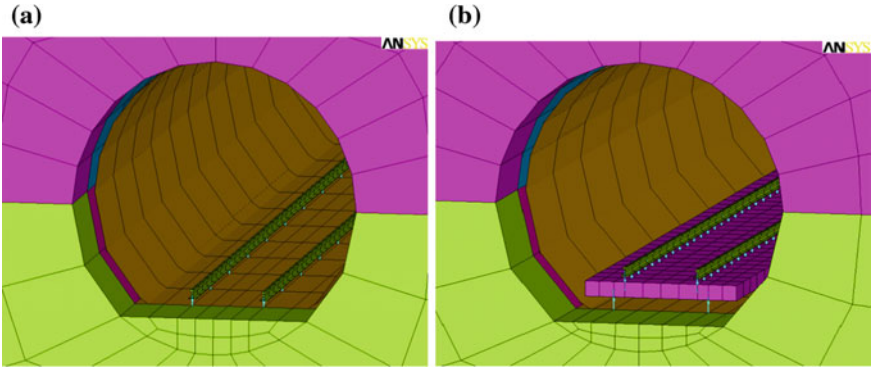

Fig. 15.3 Partial enlarged view of the finite element model. **a** Track with integrated ballast bed. **b** Track with steel spring floating slab

element SHELL 63 to the floating slab and the tunnel lining, and the solid element SOLID 45 to the tunnel foundation and the soil. The element size is 0.25–3 m, and the fine elements are used to the region close to the vibration source, which is smaller than 1/12 of material's shear wave. While the sparse elements are adopted to the domain far from the vibration source, which are smaller than 1/6 of material's shear wave. All element sizes meet the accuracy requirements.

15.1.4 Damping Coefficient and Integration Step

Rayleigh damping is generally adopted in structural dynamic analysis, that is,

$$\boldsymbol{C} = \alpha \boldsymbol{M} + \beta \boldsymbol{K} \tag{15.1}$$

Damping coefficient α and β relate to the system's natural frequency and the damping ratio. Based on the experiment data, the damping ratio of the soil structure is taken as 0.05 in modal analysis of finite element model, while the first two orders of natural frequencies are taken as 16.96 and 18.21 rad/s, Rayleigh damping coefficient α and β can be calculated as follows:

$$\alpha = \frac{2\omega_1\omega_2}{\omega_1 + \omega_2}\xi_0 = \frac{2 \times 16.96 \times 18.21}{16.96 + 18.21} \times 0.05 = 0.878 \tag{15.2}$$

$$\beta = \frac{2}{\omega_1 + \omega_2}\xi_0 = \frac{2}{16.96 + 18.21} \times 0.05 = 0.0028 \tag{15.3}$$

Considering vibration response in the range of f = 0–100 Hz, the numerical integration step should be

$$\Delta t = 1/2f = 0.005 \text{ s}. \tag{15.4}$$

15.1.5 Vehicle Dynamic Load

In actual operation, the vehicle dynamic loads on railway track are random due to the track irregularity. The vehicle dynamic loads are composed of the vehicle axle loads and additional dynamic loads, and the latter is known as inertia force generated by the wheel loads of the vehicle.

The dynamic load of the moving vehicle on the track can be expressed as [9]

$$F(t) = -\sum_{l=1}^{n}\left(F_l + m_w \frac{\partial^2 \eta}{\partial t^2}\right)\delta(x - Vt - a_l) \tag{15.5}$$

where $F(t)$ stands for the dynamic load of the moving vehicle on the track; F_l for 1/2 axle load of the lth wheelset; m_w for wheel mass; $\eta(x = Vt)$ for track random irregularity; δ for Dirac function; V for the vehicle moving speed; a_l is the distance between the lth wheelset and the coordinate origin when $t = 0$, and n is the total number of the wheelsets.

Up to now, there is no universal domestic track irregularity spectrum density function specified for urban mass transit; hence, in numerical analysis, the American track irregularity spectra for line level 6 are adopted and its mathematical expression is as follows:

$$S_{\mathrm{v}}(\omega) = \frac{kA_{\mathrm{v}}\omega_{\mathrm{c}}^2}{(\omega^2 + \omega_{\mathrm{c}}^2)\omega^2} \tag{15.6}$$

where $S_{\mathrm{v}}(\omega)$ is track irregularity power spectral density function ($\mathrm{cm}^2/\mathrm{rad/m}$), ω is spatial frequency (rad/m), ω_c and ω_s are cutoff frequency (rad/m), A_{v} is roughness coefficient (cm^2 rad/m), related to line level, and their values are shown in Table 5.1 of Chap. 5, and k is coefficient, generally taking 0.25.

Figure 15.4 shows the track vertical profile irregularity sample for line level 6 generated by trigonometric series method.

By establishing a three-layer continuous elastic beam model of track structure and substituting the dynamic load of the moving vehicle expressed by Eq. (15.5) into the vibration governing equation of three-layer beam model of track structure, the track structure vibration response and the wheel-rail contact forces can be evaluated by Fourier transform method.

Type-B vehicle is adopted in subway 1 and subway 2. Parameters of the type-B vehicle include the length between bogie pivot centers 12.6 m, the fixed wheel base

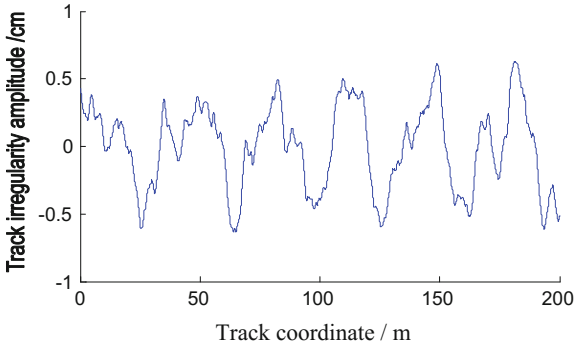

Fig. 15.4 The track vertical profile irregularity sample for line level 6

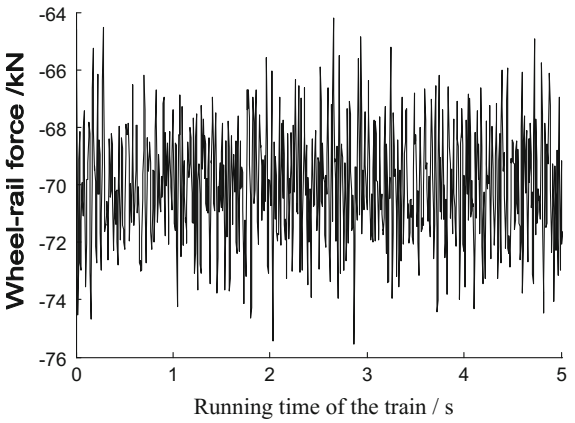

Fig. 15.5 Time history of a typical wheel dynamic load

2.2 m, the axle load 140 kN, and the wheelset mass 1539 kg. The subway train is composed of six type-B vehicles. Figure 15.5 shows the time history of a typical wheel dynamic load when the train moves at the speed of 80 km/h.

Applying the subway train's dynamic load shown in Fig. 15.5 on the rails of ANSYS 3D finite element model, analysis of environmental vibration induced by overlapping subways can be performed with the complete matrix method of Newmark implicit integration method.

15.1.6 Environmental Vibration Evaluation Index

Based on *Standard of vibration in urban area environment* GB10070-88 [10], the environmental vibration evaluation index is vibration level *Z*, namely vertical vibration acceleration obtained after correction by different frequency weighting factor. The recommended value of ISO2631-1: 1985 is adopted in weighted curve of vibration level *Z* [11]. The calculated formula for vibration level *Z* is as follows:

$$\mathrm{VL}_Z = 20\ \lg\left(\frac{a'_{\mathrm{rms}}}{a_0}\right) \tag{15.7}$$

where a_0 is reference acceleration, generally $a_0 = 10^{-6}\ \mathrm{m/s^2}$; a'_{rms} is effective value of acceleration RMS ($\mathrm{m/s^2}$) obtained after correction by different frequency weighting factor. a'_{rms} can be derived by the following formula:

$$a'_{\mathrm{rms}} = \sqrt{\sum a^2_{f\mathrm{rms}}\ 10^{0.1c_f}} \tag{15.8}$$

where a'_{rms} stands for effective value of vibration acceleration corresponding to frequency f; c_f for sensory modification value of vertical vibration acceleration. The specific values are shown in Table 1.21 of Chap. 1.

Plenty of tests and researches indicate that vertical vibration is larger than horizontal and longitudinal vibration [12–14], and it is the main source of vibration accounting for environmental vibration induced by subway trains. Therefore, in evaluating environmental vibration induced by urban mass transit, the vertical vibration acceleration and vibration level Z are generally adopted as evaluation index.

15.1.7 *Influence of Operation Direction of Uplink and Downlink on Vibration*

As four trains move simultaneously on overlapping subways, their intersections are much complicated. To simplify the analyses, environmental vibrations induced by subway 1 under three operation cases are investigated and compared. The three operation cases include the following:

Case A Train in subway 1 with single uplink operation,

Case B Trains in subway 1 with intersection operation of both uplink and downlink,

Case C Trains in subway 1 with same direction operation of both uplink and downlink.

Track foundation of subway 1 is integrated ballast bed. Eight vibration response points at interval of 10 m are specified along the ground line perpendicular to the centerline of subway 1. Among these, the response point 1 is right above the center of the subway, and the response point 8 is horizontally located 70 m away from the center of the subway. Due to the limited space, Fig. 15.6 only shows the time history of the vibration acceleration and the acceleration amplitude-frequency curve at the response point 1 for the above three operation cases. Figure 15.7 shows the acceleration peak and the vibration level Z attenuate with distance [15–17].

As shown in Fig. 15.6, the time history of the acceleration and the amplitude differs slightly for both Case B and Case C. However, the acceleration amplitude

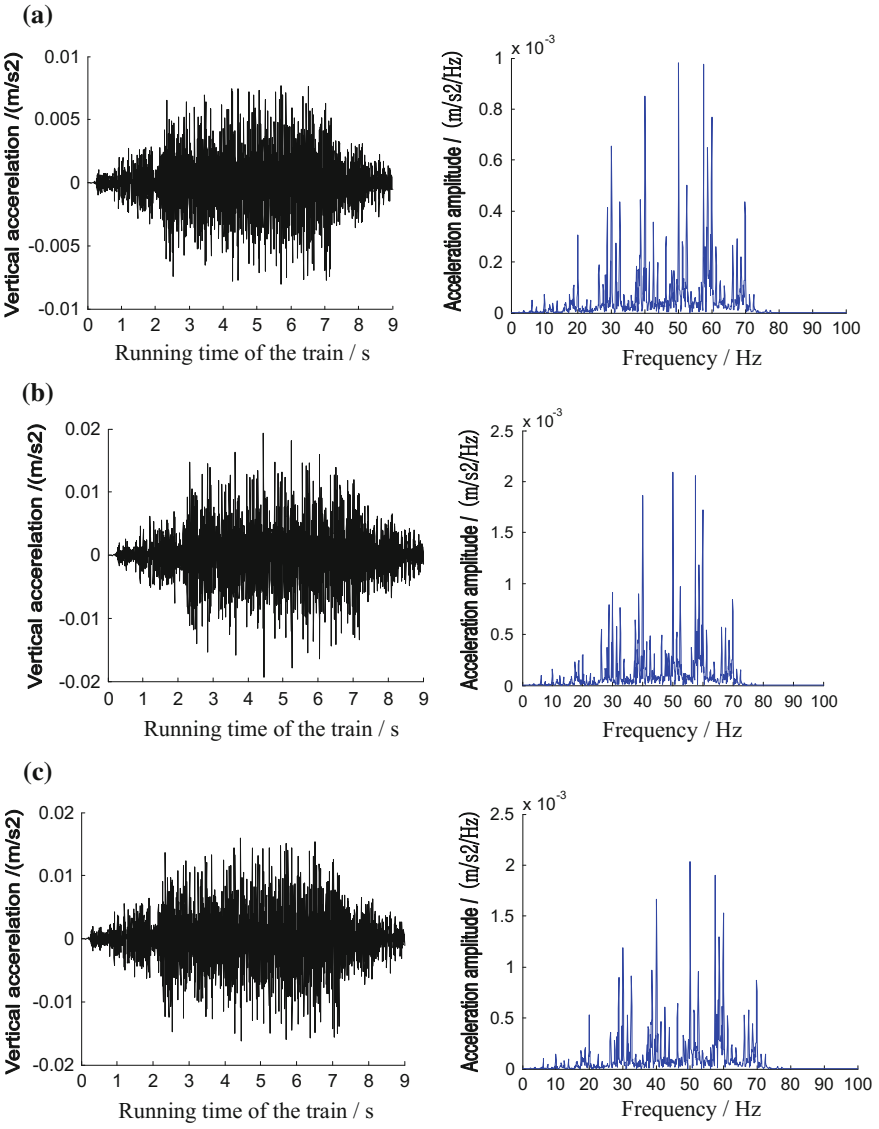

Fig. 15.6 Time history of the vibration acceleration and the acceleration amplitude-frequency curve at the response point 1. **a** Train in subway 1 with single uplink operation. **b** Trains in subway 1 with intersection operation of both uplink and downlink. **c** Trains in subway 1 with same direction operation of both uplink and downlink

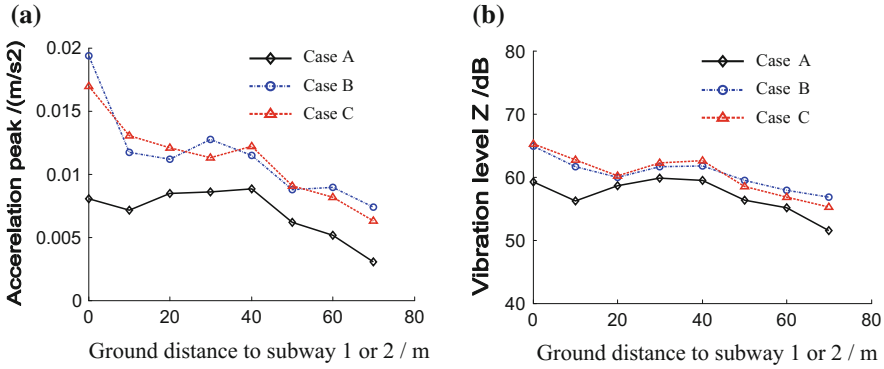

Fig. 15.7 Acceleration peak and vibration level Z attenuate with distance. **a** Acceleration peak. **b** Vibration level Z

for Case A is small and only half of that for Case B and Case C. The acceleration amplitude-frequency curves in three operation cases are similar, with basic frequency in the range of 30–60 Hz. As shown in Fig. 15.7, variation trends of the acceleration peak and the vibration level Z are similar with approximate equal value for both Case B and Case C. While the acceleration peak and the vibration level Z for Case A differ greatly from those for Case B and Case C, to be more specific, the peak value is half of that of the other two operation cases, and the vibration level Z is less than that of the other two operation cases by 5 dB.

Therefore, it is possible to analyze the environmental vibration induced by trains in subway 1 with the same direction operation of both uplink and downlink rather than the intersection operation condition. The advantage of such an approach is greatly simplified the complicated conditions of trains moving in 4-hole tunnels, without distinction of intersection points to save the trouble of taking into account of various load combinations, nor to differentiate the most unfavorable load combination to ground vibration. As when the trains in subway 1 move from Bayi museum station to Bayi Square station and the trains in subway 2 move from Yongshu Road station to Bayi Square station with the same direction operation of both uplink and downlink, it is the most unfavorable load combination to ground vibration. In the following, investigations on environmental vibration induced by both the trains in subway 1 and subway 2 with the same direction operation will be carried out.

15.1.8 Vibration Reduction Scheme Analysis for Overlapping Subways

To study the influence of different vibration reduction combination scheme on environmental vibration, six cases are examined as shown in Table 15.3. The train's moving directions and the vibration response points on the ground are shown

Table 15.3 Computational cases

Case	Track type		Subway combination
	Subway 1	Subway 2	
1	Integrated ballast bed	–	Subway 1
2	–	Integrated ballast bed	Subway 2
3	Integrated ballast bed	Integrated ballast bed	Subway 1 + subway 2
4	Floating slab track	Integrated ballast bed	Subway 1 + subway 2
5	Integrated ballast bed	Floating slab track	Subway 1 + subway 2
6	Floating slab track	Floating slab track	Subway 1 + subway 2

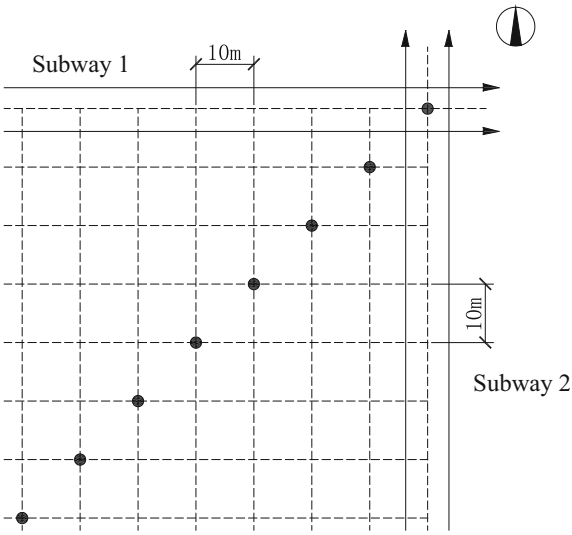

Fig. 15.8 Train's moving directions and vibration response points on the ground

in Fig. 15.8. Eight response points are specified along the diagonal line, with distance of $10\sqrt{2}$ m between two neighbor points. Distance between each response point and the centerline of any subway is the multiple of 10 m.

Figure 15.9 shows the comparisons of the ground vibration Level Z corresponding to computational Case 1, Case 2, and Case 3 when the track structure is integrated ballast bed, where the horizontal coordinate means the distance of the response point on diagonal line in Fig. 15.8 from the centerline of subway 1 or subway 2. As shown in Fig. 15.9, the ground vibration induced in Case 1 is much smaller than that induced in Case 2, and the vibration level Z is about 10 dB less. The ground vibration induced in Case 3 is greater than that in Case 2 except at the point of 70 m, and the vibration level Z is about 2–3 dB greater. In addition, attenuation behavior of vibration Level Z in 3 cases with distance from the centerline of the track is similar. It is noteworthy that at the distance of 40 m, there is a peak corresponding to Case 3, and the vibration level Z exceeds that at the distance of 0 m. This shows

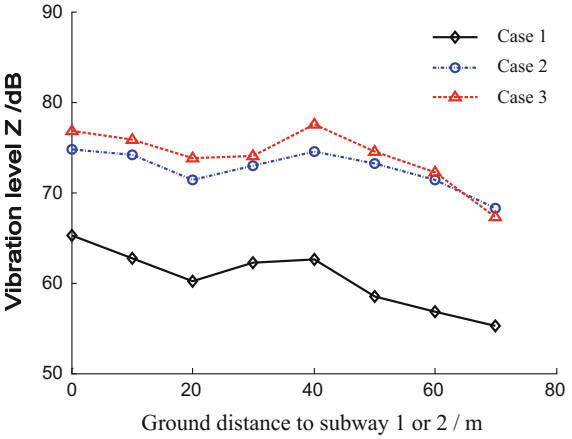

Fig. 15.9 Comparisons of vibration level Z in Case 1, 2, and 3

that in case of the same direction operation of subway 1 and 2, vibration level at the distance of 40 m is more obvious than that in case of a single subway operation.

According to *Environmental Vibration Standards in Urban Area*, the daytime vibration level Z in mixed area and CBDs should be smaller than 75 dB, while that for the nighttime should be smaller than 72 dB. As shown in Fig. 15.9, the maximum ground vibration level Z is 77.6 dB when subway 1 and 2 operate simultaneously, and altogether there are 3 response points where the ground vibration level Z is bigger than 75 dB, exceeding the specified vibration limit. Although rarely do 4-hole tunnel subways operating simultaneously at the speed of 80 km/h, appropriate measures of vibration reduction should be adopted to ensure a certain amount of surplus between the environmental vibration and the limited value and take into account of the influence of long term operation of the subways.

Figure 15.10 shows the influences of different computational cases on environmental vibration by adopting steel spring floating slabs as vibration reduction measure, where the horizontal coordinate means the distance of the response point on diagonal line in Fig. 15.8 from the centerline of subway 1 or subway 2. As shown in Fig. 15.10, the ground vibration reduction is not obvious when the floating slab track is used only in subway 1, and the vibration reduction value is less 1 dB, while the ground vibration reduction is significant when the floating slab track is used only in subway 2, and the vibration reduction value is up to 9–12 dB. The ground vibration reduction effect by employing the floating slab track both in subway 1 and subway 2 is similar to that by employing the floating slab track only in subway 2, and the vibration reduction value is 9–14 dB. This shows in the condition of simultaneous operation of subway 1 and subway 2, the most economic vibration reduction measure is to implement vibration reduction in shallowly embedded subway 2, while no measures in deeply embedded subway 1.

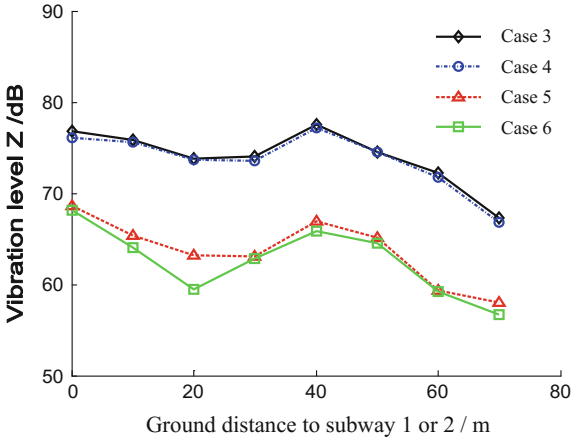

Fig. 15.10 Comparisons of vibration level Z in Case 3, 4, 5, and 6

15.1.9 Vibration Frequency Analysis

Taking Case 3 and Case 6 for instances, vibration response points of 0 m, 20 m, 40 m, and 60 m on diagonal line in Fig. 15.8 are selected to analyze ground vibration frequency when subway 1 and subway 2 operate simultaneously, as shown in Fig. 15.11. It demonstrates in Fig. 15.11a that the principal vibration frequency at the point of 0 and 20 m is between 40 and 70 Hz and at the point of 40 and 60 m is between 20 and 40 Hz when both subway 1 and subway 2 are integrated ballast tracks. This indicates that with the increase of the distance, the frequency of above 40 Hz attenuates while the frequency below 40 Hz attenuates slowly. In addition, by comparisons with Fig. 15.6b and c it shows the principal vibration frequency of ground vibration induced by simultaneous operation of

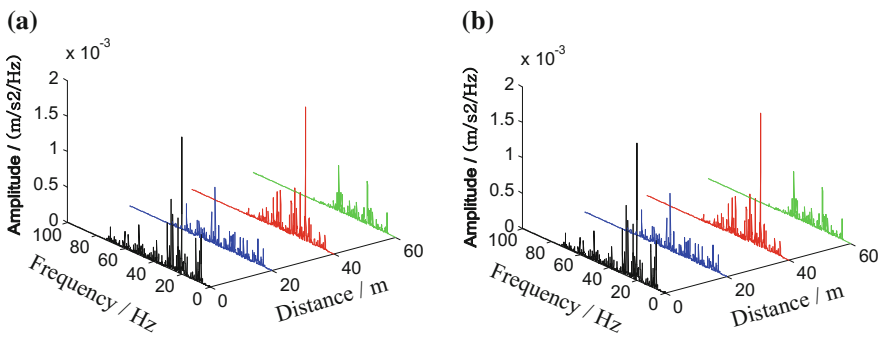

Fig. 15.11 Vibration acceleration amplitude-frequency curves. **a** Case 3. **b** Case 6

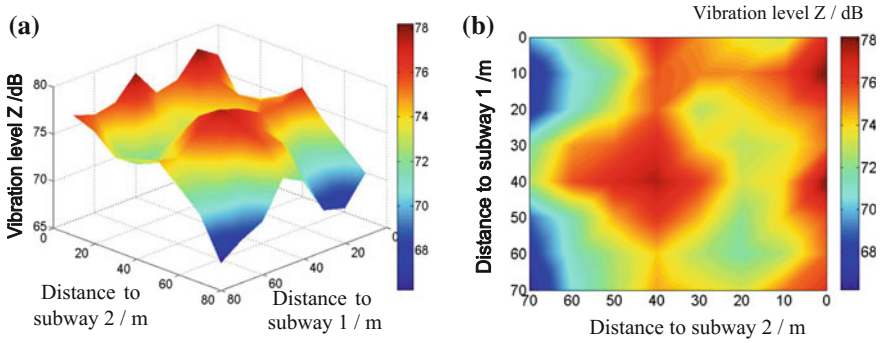

Fig. 15.12 Color chart of the ground vibration level *Z*. **a** 3-D diagram. **b** Vertical view

subway 1 and subway 2 is similar to that by independent operation of subway 1. As shown in Fig. 15.11b, when the floating slab tracks are adopted both in subway 1 and subway 2, the principal vibration frequency of ground vibration is near 7, 20, and 40 Hz. Besides, with the increase of the distance, the frequency varied slightly and the frequencies of 7 and 20 Hz are dominant in frequency domain [8].

15.1.10 Ground Vibration Distribution Characteristics

Taking Case 3 for instance, a total of 64 vibration response points with 10-m intervals between two neighbor points are selected. Color chart of the ground vibration level *Z* can be obtained by linear interpolation, as shown in Fig. 15.12. As observed in the figure, there are four vibration-amplified areas on the ground when subway 1 and subway 2 operate simultaneously: ① the intersection of subway 1 and subway 2 with maximum value 78.2 dB; ② the center of subway 1 with 40 m away from subway 2 with maximum value of 76.5 dB; ③ the center of subway 2 with 40 m away from subway 1 with maximum value of 78.2 dB; and ④ the area with 40 m away both from subway 1 and subway 2 with maximum value of 77.6 dB. Due to the symmetry, vibration distribution characteristics in other three quadrants of Fig. 15.1 are similar. This shows that there are vibration-amplified areas with 40 m away from subways, which are induced by subway 1 or subway 2. Such an amplified effect is more obvious when subway 1 and subway 2 operate simultaneously. Therefore, higher grade of vibration reduction measures should be adopted to the vibration-sensitive buildings located in the vibration-amplified area.

15.2 Vibration Analysis of the Historic Building Induced by Overlapping Subways

Bayi Square locates at the downtown of Nanchang with shopping malls nearby and some major buildings such as the Memorial Tower of Bayi Revolution, Jiangxi Exhibition Center, Post and Telecommunication Buildings. Among these buildings, Jiangxi Exhibition Center, one of the provincial key cultural relics protection units, is the closest to subway 1 and subway 2 and is more sensitive to environmental vibration as shown in Fig. 15.13. Taking the Exhibition Center as engineering background, a 3D finite element model of the track-tunnel-ground-building coupling system is established, and prediction and evaluation of the building vibration induced by recent subway 1 and the later simultaneous operation of both subway 1 and 2 are carried out.

15.2.1 Project Profile

The Jiangxi Exhibition Center locates at the right side of Bayi Square, which is collectively designed by famous architectural design experts at that time and its construction began in Oct 1968. It is the iconic building with the characteristics of the times in the 1960s and 1970s, originally named as Long Live Mao Zedong Thought Pavilion and renamed several times afterward. Since 1992 it was renamed as Jiangxi Exhibition Center and became one of the provincial key cultural relics protection units.

The building is of reinforced concrete frame structure with the cast-in-place reinforced concrete beam slab foundation. The building plane shapes as an "E" with the longitudinal length of 155.5 m, and the lateral length 57.5 m. The total height of the building is 32.6 m with 6 floors of the main structure. The nearest distance

Fig. 15.13 Jiangxi Exhibition Center

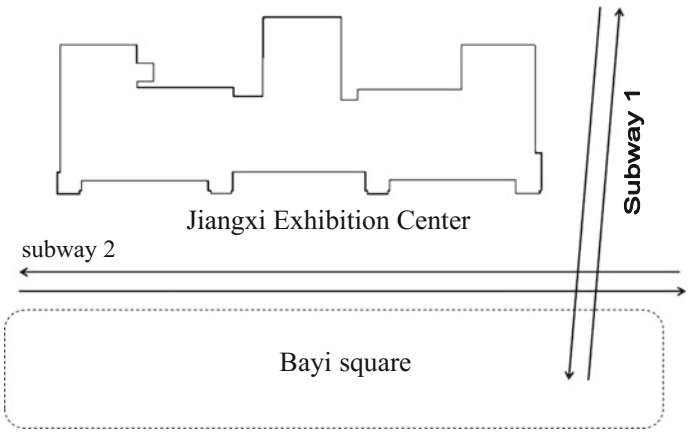

Fig. 15.14 Plan sketch of Jiangxi Exhibition Center and the subways

between the building and subway 1 is 17.5 m, while the distance between the building and subway 2 is 32.5 m. The plan sketch of the location relationship between the subway and the building is shown in Fig. 15.14.

15.2.2 Finite Element Model

As the building plane shapes as an "E" with three parts, namely the left, right, and the center, each is independent from the other two with deformation joints. Therefore, to reduce the element number and to improve computation efficiency, a 3D finite element model involving only the building and the ground on the right side near the subway intersection is established, as shown in Fig. 15.15 [8]. Subway 1 and 2 is roughly considered as a right-angle intersection, and the size of the ground in the model is 135 m × 135 m × 60 m. The closest distance between the center of subway 1 or subway 2 and the model boundary is 32.5, while the farthest distance between the center of subway 1 or subway 2 and the model boundary is 102.5 m. Three-dimensional equivalent artificial viscoelastic boundary is adopted in the boundaries around the model, and the bottom is fixed support. The building is reinforced concrete frame structure being composed of beam, column and floor. The building geometry size is determined by the design drawings.

Material for beams, columns, and floors of the building is concrete C30 with elasticity modulus 300 GPa, density 2500 kg/m^3, and Poisson's ratio 0.25. Parameters for other material are given in Sect. 15.1.2. The beam and column are simulated with element BEAM 4, the floor with element SHELL 63, and the foundation with element SOLID 45. Elements for other structure are the same as in Sect. 15.1.3.

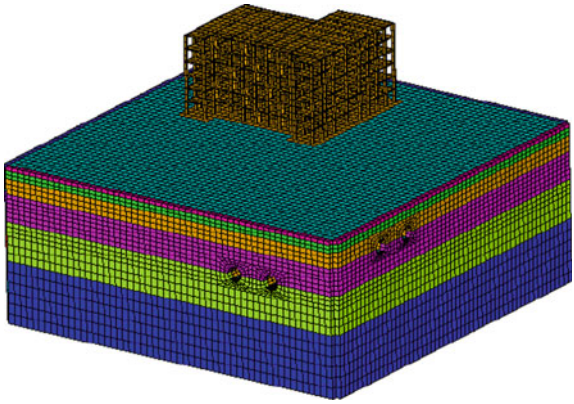

Fig. 15.15 3D finite element model of track-overlapping tunnels-ground-building

Models for the integrated ballast bed and the steel spring floating slab track bed are established, respectively, and the six computational cases shown as in Table 15.3 are taken into account. In the dynamic analysis, the complete matrix method of Newmark implicit integration algorithm is adopted with the train speed of 80 km/h and the time step of 0.005 s.

15.2.3 Modal Analysis of Building

Block Lanczos method is adopted in modal analysis of the building model. The first calculated 20 natural frequencies are given in Table 15.4, and the first 10 vibration modes are shown in Fig. 15.16. As can be seen from Table 15.4, the first 20 natural vibration frequencies range from 0.96 to 7.26 Hz, which fall into low frequency.

Table 15.4 The first calculated 20 natural vibration frequencies

Order	Natural vibration frequency/(Hz)	Order	Natural vibration frequency/(Hz)
1	0.96137	11	7.1317
2	0.98083	12	7.1400
3	1.1321	13	7.1414
4	3.4159	14	7.1815
5	3.4872	15	7.1991
6	3.9310	16	7.2169
7	6.9235	17	7.2402
8	7.0622	18	7.2420
9	7.0946	19	7.2447
10	7.1191	20	7.2583

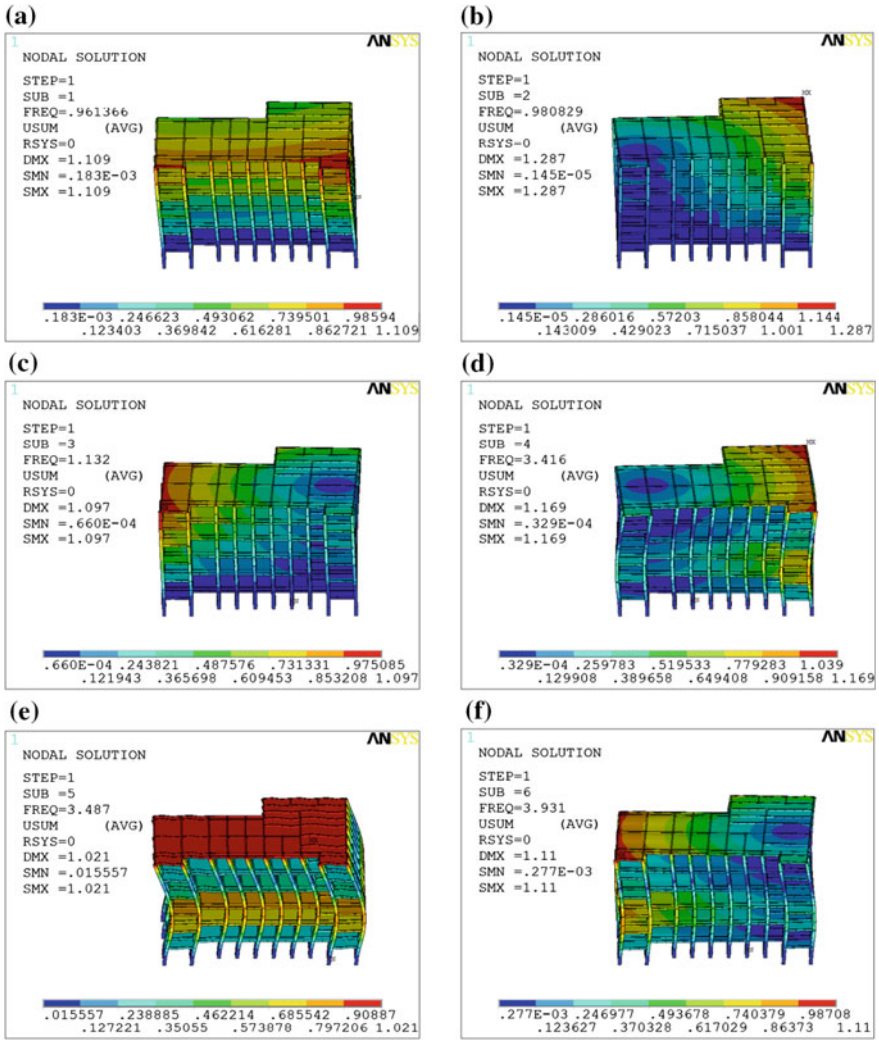

Fig. 15.16 The first 10 vibration mode of the building. **a** The first order. **b** The second order. **c** The third order. **d** The 4th order. **e** The 5th order. **f** The 6th order. **g** The 7th order. **h** The 8th order. **i** The 9th order. **j** The 10th order

The first 6 vibration modes of the building are corresponding to rigid translation and rigid rotation with the maximum displacements at the top floor. Starting from the 7th floor, vibration mode turns to partial vertical vibration of the floor of open-space room. Therefore, the whole building mainly features horizontal vibration with partial larger vertical vibration. In the dynamic analysis, vibration response points are selected at the center of each floor of the open-space room near the subway.

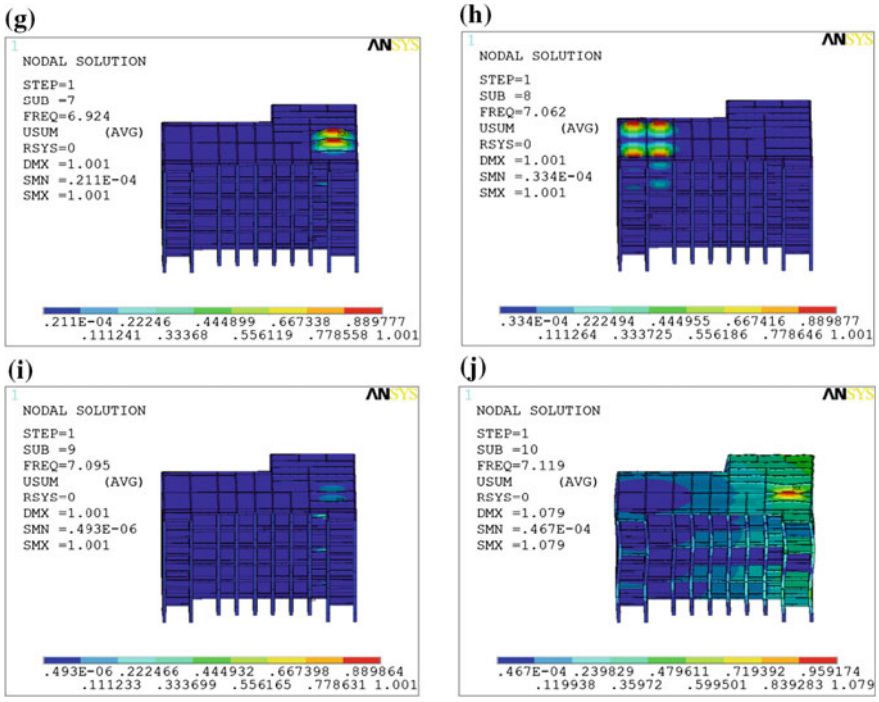

Fig. 15.16 (continued)

15.2.4 Horizontal Vibration Analysis of the Building

Based on *Technical specifications for protection of historic buildings against man-made vibration* GB/T 50452-2008, the evaluation index of structural vibration of historic buildings is vibration velocity. Hence, environmental vibration analysis and evaluation are performed based on vibration velocity collected at each vibration response points.

(1) Analysis in time domain and frequency domain

Figure 15.17 shows the time history and the amplitude-frequency curves of vibration velocity for vibration response points along the *X* (transversal direction, perpendicular to subway 1), *Y* (longitudinal direction, parallel to subway 1) and *Z* (vertical) directions [8]. These vibration response points are selected at the center of the top floor of open-space rooms when train moves on subway 1 with integrated ballast trackbed.

Figure 15.17 shows that for the top floor of open-space room, its vibration velocity amplitude of *X* direction and that of *Y* direction are similar, with peak amplitude of about 0.1 mm/s, and the dominant frequency is around 5 Hz. However, vibration velocity of *X* direction above 20 Hz is greater than that of

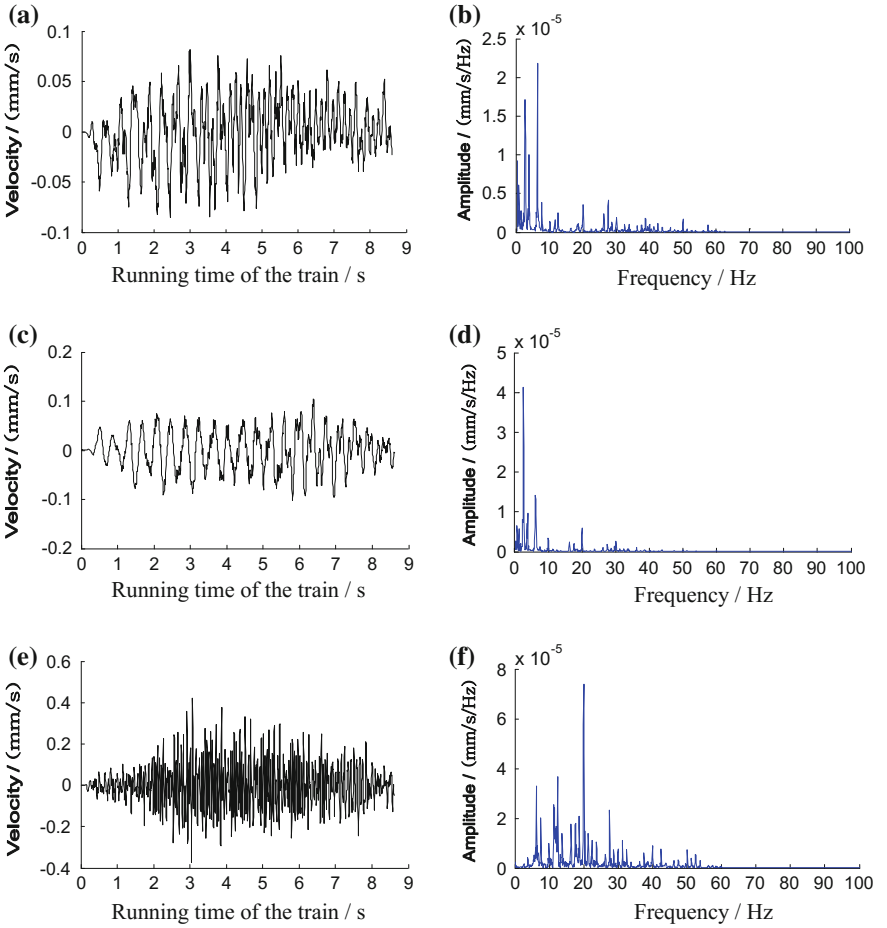

Fig. 15.17 Time history and amplitude-frequency curve of vibration velocity for top floor when train moves on subway 1. **a** Time-history of vibration velocity along *X*-direction. **b** Amplitude frequency curve of vibration velocity along *X*-direction. **c** Time-history of vibration velocity along *Y*-direction. **d** Amplitude frequency curve of vibration velocity along *Y*-direction. **e** Time-history of vibration velocity along *Z*-direction. **f** Amplitude frequency curve of vibration velocity along *Z*-direction

Y direction. As for vibration velocity of *Z* direction, its amplitude is greater than that of both *X* direction and *Y* direction, being 5 times of the latter. It is the same case with its dominant frequency 20 Hz, being greater than that of both *X* direction and *Y* direction. Such a law can be applied to other floors in terms of vibration characteristics of *X*, *Y*, and *Z* directions. These show that building floor vibration is of low frequency, with vertical vibration greater than horizontal vibration, and the horizontal vibration mode is low while the vertical vibration mode is high.

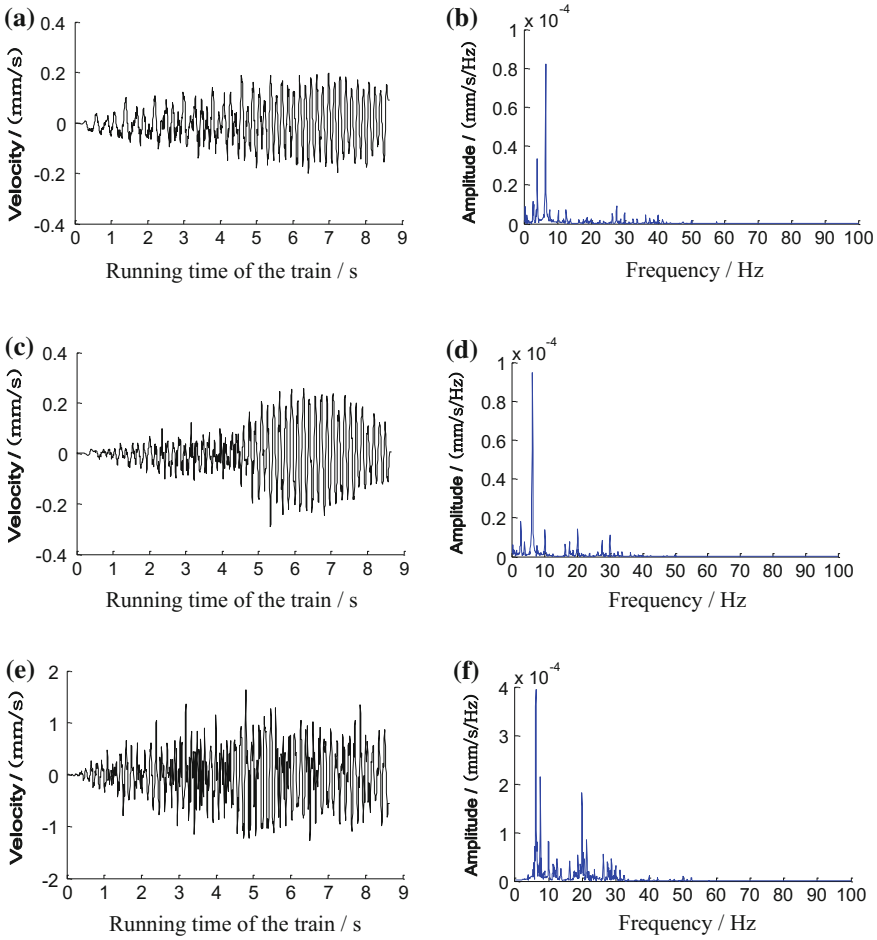

Fig. 15.18 Time history and amplitude-frequency curve of vibration velocity for top floor when trains move on both subway 1 and subway 2 simultaneously. **a** Time-history of vibration velocity along *X*-direction. **b** Amplitude frequency curve of vibration velocity along *X*-direction. **c** Time-history of vibraion velocity along *Y*-direction. **d** Amplitude frequency curve of vibraion velocity along *Y*-direction. **e** Time-history of vibraion velocity along *Z*-direction. **f** Amplitude frequency curve of vibraion velocity along *Z*-direction

Figure 15.18 shows the time history and the amplitude-frequency curves of vibration velocity when trains move in both subway 1 and subway 2 simultaneously, where the integrated ballast trackbed is adopted. Figure 15.18 demonstrates that when both subways operate simultaneously, vibration velocity amplitude of the top floor is doubly greater than that when only a single subway 1 operates, and the vibration lasts longer. Moreover, frequency distribution and other vibration characteristics are similar in the two operating conditions.

(2) Vibration evaluation

Selecting the center of each floor of open-space room by the side of the subway, and inputting the vibration velocity collected at each points, the maximum value of vibration velocity of each floor can be obtained, which are checked against the limit value specified by the technical specifications for protection of historic buildings against man-made vibration GB/T 50452-200t. The results are listed in Table 15.5, which show, without any vibration reduction measures, the horizontal vibration maximum velocity of each floor induced by a single subway operation and that by simultaneous operation of two subways. As specified by the standard, horizontal vibration is adopted as the sole evaluation index concerning building of brick and stone structure, the table only lists the maximum velocity of *X* direction, *Y* direction, and synthetic direction of *X* and *Y*. Figure 15.19 shows, based on Table 15.5, the distribution of vibration velocity of synthetic direction varies with the floor.

As shown in Table 15.5 and Fig. 15.19, when either subway 1 or subway 2 operates independently, vibration velocities of *X* direction, *Y* direction, and synthetic direction do not exceed the limit values. When both subways operate simultaneously, vibration velocity of *Y* direction, and vibration velocity of the top floor and 2nd floor as well as 5th floor along the synthetic direction exceed the limit values, with the maximum exceeded value of 0.082 mm/s. The building vibration of any direction induced by simultaneous operation of subway 1 and subway 2 is greater than that by independent operation of subway 1 or subway 2, and the vibration induced by subway 2 is obviously greater than that by subway 1. This accounts for the fact that the influence of shallowly embedded subway on building vibration is greater than that of deeply embedded subway. Apart from this, when subway 1 or subway 2 operates independently, vibration velocity of *X* direction is similar to that of *Y* direction of each floor. With increase of the floor, vibration velocity of *X* direction and *Y* direction decreases gradually, but increases abruptly at the top floor with the value greater than that of the first floor. While subway 1 and subway 2 operate simultaneously, vibration velocity of *X* direction is smaller than that of *Y* direction in each floor except the first floor. The maximum vibration velocities for both *X* and *Y* directions are detected at the top floor, while there is no regularity for other floors.

Therefore, by considering simultaneous operation of both subways in future, vibration reduction measures should be adopted in subways to leave an appropriate margins for allowable vibration values so as to ensure building safety. Table 15.6 shows horizontal maximum vibration velocity of each floor when both subways operate simultaneously with vibration reduction measures. Figure 15.20 shows, based on Table 15.6, the distribution of vibration velocity of synthetic direction varies with the floor.

As shown in Table 15.6 and Fig. 15.20, when vibration reduction measure is adopted, vibration velocities of *X* direction and *Y* direction induced by simultaneous operation of both subways are similar, with maximum value at the top floor. While there is no regularity for other floors and value variation is insignificant. As for vibration velocity of synthetic direction, only that of the top floor exceeds the limit

Table 15.5 The maximum vibration velocity of each floor without vibration reduction measures (mm/s)

Floor	Operation of subway 1			Operation of subway 2			Simultaneous operationof subway 1 and 2			Limit value
	X direction	*Y* direction	Synthetic direction	*X* direction	*Y* direction	Synthetic direction	*X* direction	*Y* direction	Synthetic direction	Horizontal
1	0.090	0.089	0.126	0.127	0.123	0.177	0.155	0.139	0.208	0.27
2	0.082	0.087	0.120	0.124	0.103	0.161	0.180	0.239	0.299	0.27
3	0.070	0.083	0.108	0.111	0.090	0.143	0.126	0.207	0.242	0.27
4	0.056	0.075	0.093	0.085	0.094	0.126	0.125	0.151	0.197	0.27
5	0.060	0.062	0.086	0.092	0.092	0.130	0.168	0.249	0.300	0.27
6	0.053	0.060	0.080	0.066	0.066	0.093	0.108	0.134	0.172	0.27
Top floor	0.085	0.105	0.135	0.149	0.146	0.208	0.201	0.289	0.352	0.27

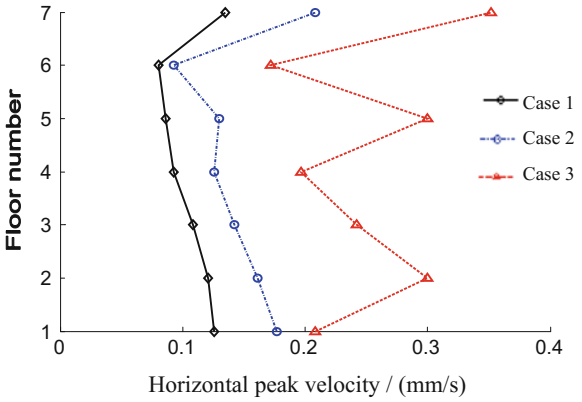

Fig. 15.19 Vibration velocity of each floor along the synthetic direction without vibration reduction measures (Case 1: a single operation of subway 1 with integrated ballast bed; Case 2: a single operation of subway 2 with integrated ballast bed; and Case 3: simultaneous operation of both subways with integrated ballast bed)

value when floating slab track is adopted in subway 1. Vibration velocity of each floor is below the limit value when floating slab track is adopted in subway 2 or in both subways. Moreover, as shown in Fig. 15.20, vibration reduction results are not significant when floating slab track is solely used in shallowly embedded subway 1. While vibration reduction results are similar when floating slab track is used in shallowly embedded subway 2 and in both subways. Therefore, the most economic vibration reduction measure is that it should be adopted in shallowly embedded subway, which is consistent with the conclusion obtained in vertical vibration analysis of the former section.

15.2.5 Vertical Vibration Analysis of the Building

As specified by GB10070-88 *Standard of Environmental Vibration in Urban Area* and JGJ/T170-2009 *Standard for Limit and Measuring Method of Building Vibration and Secondary Noise Caused by Urban Rail Transit,* the environmental vibration evaluation index is vertical vibration acceleration. In the following, vertical vibration analysis and environmental vibration evaluation of the Jiangxi exhibition center are carried out.

(1) Analysis in time domain and frequency domain

Figure 15.21 shows the time history and the amplitude-frequency curves of vibration acceleration of top floor when integrated ballast track is used in both subway 1 and 2 [8].

As shown in Fig. 15.21, the vertical vibration acceleration amplitudes induced by subway 2 and jointly induced by subway 1 and 2 are similar, being 3 times as much as that induced by subway 1. This is consistent with the case of horizontal vibration velocity. In terms of frequency domain, frequency distributions are similar in cases of each independent subway operation with principal frequency locating

Table 15.6 The maximum vibration velocity of each floor when both subways operate with vibration reduction measures (mm/s)

Floor	Subway 1 with floating slabs			Subway 2 with floating slabs			Both subways with floating slabs			Limit value
	X direction	*Y* direction	Synthetic direction	*X* direction	*Y* direction	Synthetic direction	*X* direction	*Y* direction	Synthetic direction	Horizontal
1	0.140	0.158	0.212	0.107	0.097	0.144	0.045	0.053	0.070	0.27
2	0.178	0.208	0.274	0.131	0.102	0.166	0.119	0.080	0.143	0.27
3	0.120	0.164	0.203	0.095	0.127	0.158	0.082	0.061	0.102	0.27
4	0.095	0.145	0.174	0.082	0.082	0.117	0.067	0.057	0.088	0.27
5	0.165	0.217	0.273	0.112	0.093	0.146	0.121	0.086	0.149	0.27
6	0.100	0.114	0.152	0.078	0.066	0.102	0.056	0.050	0.075	0.27
Top floor	0.194	0.239	0.307	0.147	0.158	0.216	0.154	0.101	0.184	0.27

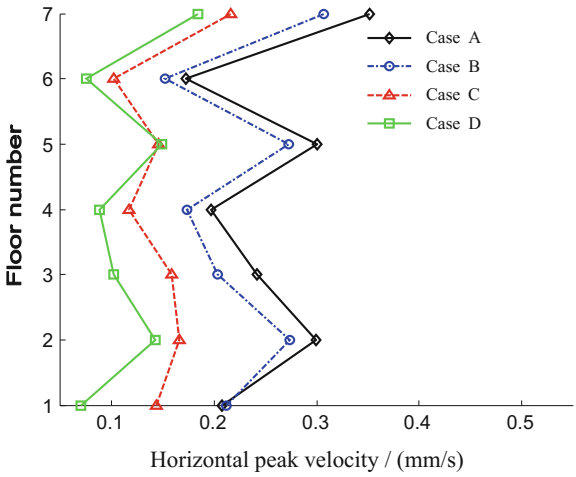

Fig. 15.20 Vibration velocity of synthetic direction of each floor when both subways operate (Case A: both subways with integrated ballast track; Case B: subway 1 with floating slab track; Case C: subway 2 with floating slab track; and Case D: Both subways with floating slab track)

near 20 Hz. And the lower frequency components below 10 Hz when subway 1 and 2 operate simultaneously are more than those of a single subway operation.

(2) Analysis of vibration level *Z*

Figure 15.22 shows the distribution of vibration level *Z* of each floor induced by a single subway or both subways where the integrated ballast track is used while Fig. 15.23 shows the similar distribution of vibration level *Z* of each floor when vibration reduction measure is adopted [8].

As shown in Fig. 15.22, the building's vertical vibration induced by the operation of subway 2 is significantly greater than that induced by subway 1, with the former 8–11 dB greater than the latter. Moreover, the building's vertical vibration induced by the operation of both subways is greater than that induced by subway 2, yet the difference decreases gradually with the increase of floors. Both the building's maximum vertical vibration induced by subway 2 and that by both subways exceed the vibration limit of daytime, which is 75 dB, for mixed zone and central business district specified by *Standard of Environmental Vibration in Urban Area.* Therefore, vibration reduction measures should be taken in subways.

As shown in Fig. 15.23, by comparing different vibration reduction conditions when both subways operate simultaneously, the vibration reduction effect on vertical vibration of the building is consistent with that on vertical vibration of the ground and horizontal vibration of the building. That is, adopting vibration reduction measure merely in deeply embedded subway 1 cannot achieve satisfactory effect; the most economic alternative is adopting of vibration reduction measure in shallowly embedded subway 2.

In addition, as shown in Figs. 15.22 and 15.23, vertical vibration of the building gradually increases with the increase of floors, while that between each floor varies slightly.

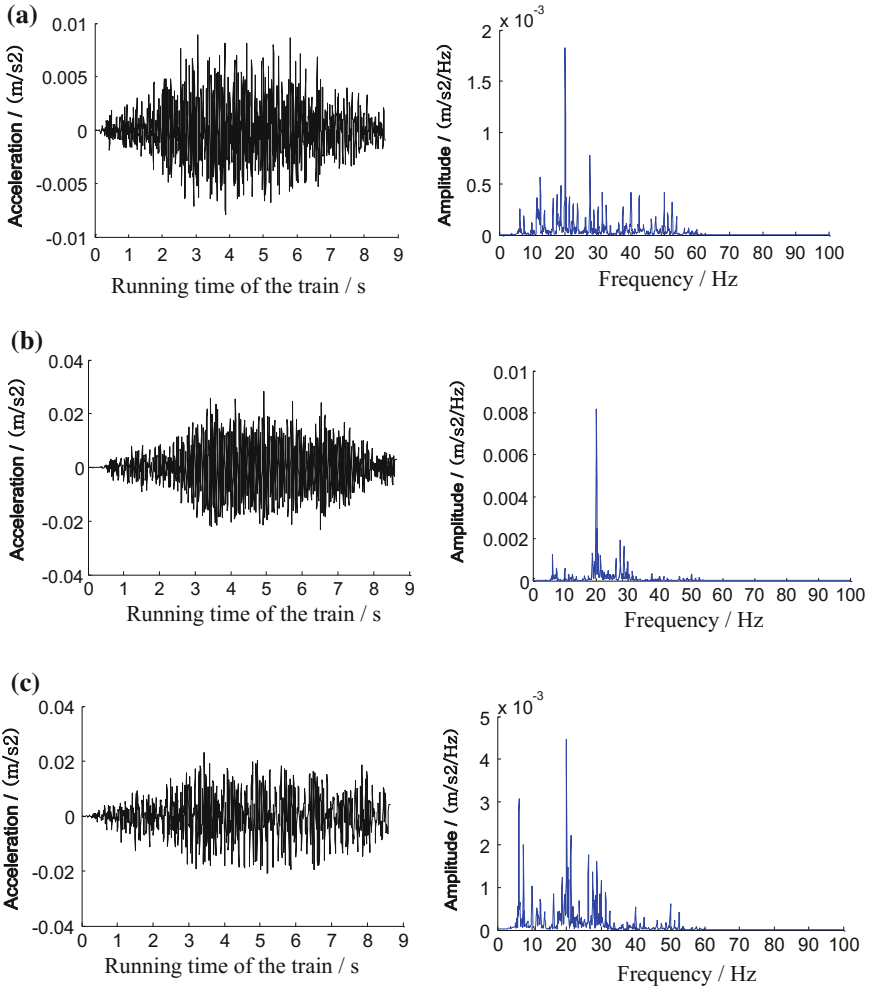

Fig. 15.21 Time history and amplitude-frequency curves of vibration acceleration of top floor. **a** Subway 1 in operation. **b** Subway 2 in operation. **c** Both subway 1 and 2 in operation

(3) 1/3 Octave band analysis

The following is the vibration analysis of the building roof in 1/3 octave band induced by computational cases 1, 2, 3, and 5 shown in Table 15.3. The vibration acceleration levels in 1/3 octave band corresponding to each computational case are shown in Fig. 15.24, among which the vibration levels are corrected by weighted factor of the frequency specified by Standard for Limit and Measuring Method of Building Vibration and Secondary Noise Caused by Urban Rail Transit.

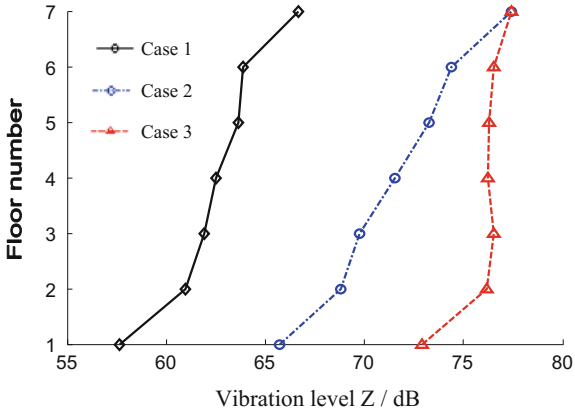

Fig. 15.22 Vibration level Z of each floor with integrated ballast track (Case 1: subway 1 in operation; Case 2: subway 2 in operation; and Case 3: both subway 1 and 2 in operation)

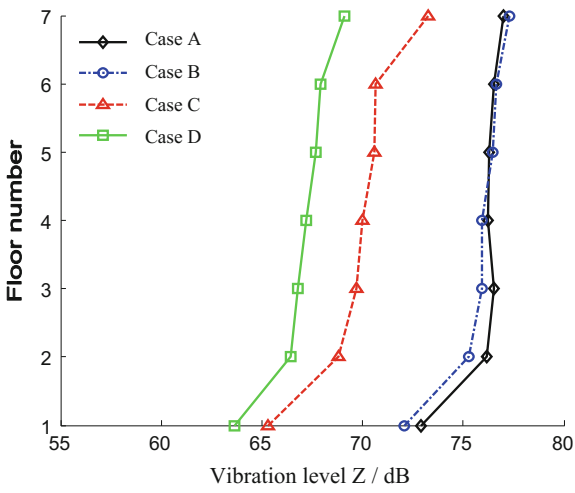

Fig. 15.23 Vibration level Z of each floor when both subways operate (Case A: both subways with integrated ballast track; Case B: subway 1 with floating slab track; Case C: subway 2 with floating slab track; and Case D: both subways with floating slab track)

As shown in Fig. 15.24, the maximum vibration acceleration levels corresponding to each computational case are detected at the dominant frequency 20 Hz, and these values are given in Table 15.7.

As shown in Table 15.7, the vibration acceleration levels induced by subway 2 and those by both subways exceed the vibration limit of nighttime 70 dB for mixed areas and CBDs specified by *Standard for Limit and Measuring Method of Building Vibration and Secondary Noise Caused by Urban Rail Transit*, while those induced by subway 1 and by subway 2 with floating slab track are lower than the vibration limit, which is consistent with the evaluation results based on *Standard of Vibration in Urban Area Environment.*

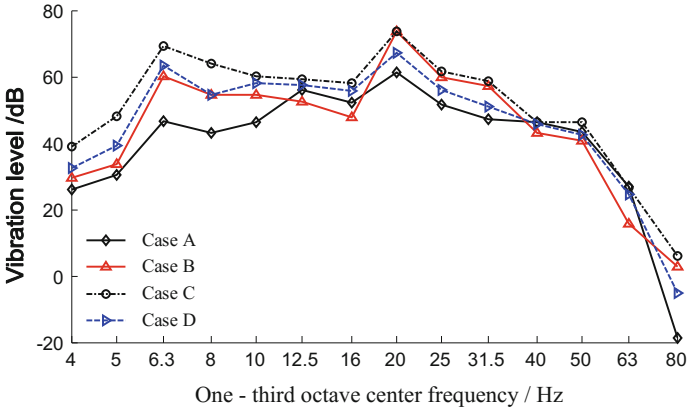

Fig. 15.24 Vibration acceleration level of the building roof in 1/3 octave frequency (Case A: subway 1 in operation; Case B: subway 2 in operation; Case C: both subway 1 and 2 in operation; and Case D: subway 2 in operation with floating slab track)

Table 15.7 Maximum vibration acceleration level of the building roof in 1/3 octave frequency

Operation of subway 1		Operation of subway 2		Simultaneous operation of both subways		Floating slabs of subway 2	
Frequency/ (Hz)	Vibration level/(dB)	Frequency/ (Hz)	Vibration level/(dB)	Frequency/ (Hz)	Vibration level/(dB)	Frequency/ (Hz)	Vibration level/(dB)
20	61.3	20	73.8	20 Hz	73.8	20	67.3

15.3 Conclusions

Based on the analyses of the ground and historic building vibration induced by overlapping subways, the following major conclusions can be summarized as follows:

(1) The amplitude and frequency distribution of the most unfavorable environmental vibration caused by uplink and downlink operation in the same direction and that by intersection operation of uplink and downlink are similar. Therefore, in analyzing environmental vibration induced by overlapping subways, it is advisable to substitute uplink and downlink operation in the same direction for intersection operation of uplink and downlink for simplifying the analysis.

(2) Several vibration-amplifying domains are detected in ground vibration induced by overlapping subways, which are around the intersection of subways and 40 m away from the center of any subway. There are a total of nine vibration-amplifying domains in the vibration influence range induced by overlapping subways. If vibration-sensitive buildings are located in these

vibration-amplifying domains, higher grade vibration reduction measures should be taken in the subways.

(3) Modal analysis of the building reveals that the first ten natural vibration frequencies are lower than 8 Hz and belong to low-frequency vibration. The first six modes are featured by horizontal vibration with the maximum deformation at the top floor. From the 7th mode, greater vertical vibrations are detected in building floor of open-space room.

(4) The principal frequency of horizontal vibration of the building floor is near 6 Hz and falls into the first six vibration modes, while that of vertical vibration of the building floor is near 20 Hz, belonging to a higher order vibration mode.

(5) No regularity is observed for horizontal vibration of the building floor with increase of the building floor under simultaneous operation of two subways. Vertical vibration of the building floor increases with increase of the building floor, while the increased value between the adjacent floors is a few.

(6) Results of vibration evaluation of the Jiangxi Exhibition Center induced by subways are similarly based on the technical specifications for protection of historic buildings against man-made vibration, and the Standard of Vibration in Urban Area and Standard for Limit and Measuring Method of Building Vibration and Secondary Noise Caused by Urban Rail Transit.

(7) The shallowly embedded subway 2 has a great influence on environmental vibration. When both subways operate simultaneously, ground vibration and building floor vibration in some domains will exceed the vibration limit with a small margin. Adopting vibration reduction measure in deeply embedded subway 1 cannot achieve satisfactory effect, and the most economic alternative is adopting of vibration reduction measure in shallowly embedded subway 2.

References

1. Jia Y, Liu W, Sun X et al (2009) Vibration effect on surroundings induced by passing trains in spatial overlapping tunnels. J China Railway Soc 231(2):104–109
2. Ma M, Liu W, Ding D (2010) Influence of metro train-induced vibration on xi'an bell tower. J Beijing Jiaotong Univ 34(4):88–92
3. Xu H, Fu Z, Liang L (2011) Analysis of environmental vibration adjacent to the vertical porous tunnel under the train load in the subway. Chin J Rock Eng 32(6):1869–1873
4. Wu F, Wang Z (2010) Environmental impact statement of Phase 1 Project of Nanchang rail transit line 2. China Railway Siyuan Survey and Design Group Co., LTD, Wuhan 4
5. Survey and Design Institute of Jiangxi Province (2009) Geological engineering survey report of Phase 1 of Nanchang rail transit line 1. Survey and Design Institute of Jiangxi Province, Nanchang
6. He L, Liang K (2011) Preliminary geological engineering survey report of Phase 1 of Nanchang rail transit line 2. Henan Geological Mining Construction Engineering (group) co., LTD, Zhengzhou, 10
7. Gu Y, Liu J, Du Y (2007) 3-D uniform viscoelasticity artificial boundary and viscoelasticity boundary element. Eng Mech 24(12):31–37

8. Tu Q (2014) Exploration into environment vibration induced by subway and vibration reduction technology. Master's Thesis of East China Jiaotong University, Nanchang
9. Lei X, Sheng X (2008) Advanced studies in modern track theory, 2nd edn. China Railway Publishing House, Beijing
10. Ministry of Environmental Protection (1988) Standard of vibration in urban area environment (GB 10070-88). China Standard Publishing House, Beijing
11. International Standard (1985) ISO2631-1 Mechanical vibration and shock evaluation of human exposure to whole-body vibration
12. Jia B, Lou M, Zong G et al (2013) Field measurements for ground vibration induced by vehicle load. J Vib Shock 32(4):10–14
13. Wei H, Lei X, Lv S (2008) Field testing and numerical analysis of ground vibration induced by trains. Environ Pollut Control 30(9):17–22
14. Li R (2008) Research on ground vibration induced by subway trains and vibration isolation measures. Doctor's Dissertation of Beijing Jiaotong University, Beijing
15. Tu Q, Lei X (2013) Finite element model analysis of ground vibration induced by subway. J East China Jiaotong Univ 30(1):26–31
16. Tu Q, Lei X, Mao S (2014) Prediction analysis of environmental vibration induced by Nanchang subways. Urban Mass Transit 17(10):30–36
17. Tu Q, Lei X, Mao S (2014) Analyses of subway induced environment vibration and vibration reduction of rail track structure. Noise Vibr Control 34(4):178–183

Index

X. Lei, *High Speed Railway Track Dynamics*,
DOI 10.1007/978-981-10-2039-1